frontiers | Research Topics

Experimental and numerical studies on liquid metal cooled fast reactors

Edited by
Songbai Cheng, Wenzhong Zhou, Long Gu, Hongli Chen, Di Yun, Koji Morita, Hidemasa Yamano and Shripad T. Revankar

Published in
Frontiers in Energy Research

ISSN 1664-8714
ISBN 978-2-83251-676-8
DOI 10.3389/978-2-83251-676-8

About Frontiers

Frontiers is more than just an open access publisher of scholarly articles: it is a pioneering approach to the world of academia, radically improving the way scholarly research is managed. The grand vision of Frontiers is a world where all people have an equal opportunity to seek, share and generate knowledge. Frontiers provides immediate and permanent online open access to all its publications, but this alone is not enough to realize our grand goals.

Frontiers journal series

The Frontiers journal series is a multi-tier and interdisciplinary set of open-access, online journals, promising a paradigm shift from the current review, selection and dissemination processes in academic publishing. All Frontiers journals are driven by researchers for researchers; therefore, they constitute a service to the scholarly community. At the same time, the *Frontiers journal series* operates on a revolutionary invention, the tiered publishing system, initially addressing specific communities of scholars, and gradually climbing up to broader public understanding, thus serving the interests of the lay society, too.

Dedication to quality

Each Frontiers article is a landmark of the highest quality, thanks to genuinely collaborative interactions between authors and review editors, who include some of the world's best academicians. Research must be certified by peers before entering a stream of knowledge that may eventually reach the public - and shape society; therefore, Frontiers only applies the most rigorous and unbiased reviews. Frontiers revolutionizes research publishing by freely delivering the most outstanding research, evaluated with no bias from both the academic and social point of view. By applying the most advanced information technologies, Frontiers is catapulting scholarly publishing into a new generation.

What are Frontiers Research Topics?

Frontiers Research Topics are very popular trademarks of the *Frontiers journals series*: they are collections of at least ten articles, all centered on a particular subject. With their unique mix of varied contributions from Original Research to Review Articles, Frontiers Research Topics unify the most influential researchers, the latest key findings and historical advances in a hot research area.

Find out more on how to host your own Frontiers Research Topic or contribute to one as an author by contacting the Frontiers editorial office: frontiersin.org/about/contact

Experimental and numerical studies on liquid metal cooled fast reactors

Topic editors

Songbai Cheng — Sun Yat-sen University, China
Wenzhong Zhou — Sun Yat-sen University, China
Long Gu — Institute of Modern Physics, Chinese Academy of Sciences (CAS), China
Hongli Chen — University of Science and Technology of China, China
Di Yun — Xi'an Jiaotong University, China
Koji Morita — Kyushu University, Japan
Hidemasa Yamano — Japan Atomic Energy Agency, Japan
Shripad T. Revankar — Purdue University, United States

Citation

Cheng, S., Zhou, W., Gu, L., Chen, H., Yun, D., Morita, K., Yamano, H., Revankar, S. T., eds. (2023). *Experimental and numerical studies on liquid metal cooled fast reactors*. Lausanne: Frontiers Media SA. doi: 10.3389/978-2-83251-676-8

Table of contents

frontiers | Frontiers in Energy Research

TYPE Editorial
PUBLISHED 31 January 2023
DOI 10.3389/fenrg.2023.1140962

OPEN ACCESS

EDITED AND REVIEWED BY
Uwe Schröder,
University of Greifswald, Germany

*CORRESPONDENCE
Wenzhong Zhou,
zhouwzh3@mail.sysu.edu.cn

SPECIALTY SECTION
This article was submitted to Nuclear Energy, a section of the journal Frontiers in Energy Research

RECEIVED 09 January 2023
ACCEPTED 17 January 2023
PUBLISHED 31 January 2023

CITATION
Cheng S, Zhou W, Gu L, Chen H, Yun D, Morita K, Yamano H and Revankar ST (2023), Editorial: Experimental and numerical studies on liquid metal cooled fast reactors.
Front. Energy Res. 11:1140962.
doi: 10.3389/fenrg.2023.1140962

Editorial: Experimental and numerical studies on liquid metal cooled fast reactors

Songbai Cheng[1], Wenzhong Zhou[1]*, Long Gu[2], Hongli Chen[3], Di Yun[4], Koji Morita[5], Hidemasa Yamano[6] and Shripad T. Revankar[7]

[1]Sino-French Institute of Nuclear Engineering and Technology, Sun Yat-Sen University, Guangzhou, China, [2]Institute of Modern Physics, Chinese Academy of Sciences, Lanzhou, China, [3]University of Science and Technology of China, Hefei, China, [4]School of Nuclear Science and Technology, Xi'an Jiaotong University, Xi'an, China, [5]Department of Applied Quantum Physics and Nuclear Engineering, Kyushu University, Fukuoka, Japan, [6]Japan Atomic Energy Agency, Oarai, Japan, [7]School of Nuclear Engineering, Purdue University, West Lafayette, IN, United States

KEYWORDS

liquid metal cooled fast reactors, experimental/numerical thermal hydraulics, experimental/computational fuels and materials, neutronics, severe accident analysis, multi-phase flow and heat/mass transfer

Editorial on the Research Topic
Experimental and numerical studies on liquid metal cooled fast reactors

Liquid metal cooled fast reactors (LMFRs) use liquid metal as a coolant instead of water commonly used in commercial nuclear power plants. This allows the coolant to operate at a higher temperature and a lower pressure than current reactors, thus improving the efficiency and safety of the reactor system. They also use the fast neutron spectrum, which means that neutrons can cause fission without having to be slowed down first, as in current reactors. This allows liquid metal cooled fast reactors to use fissile materials and spent fuels from the current reactor to generate electricity. Due to their much higher power density, higher thermodynamic efficiency, and higher temperature, liquid metal cooled fast reactors have become more and more attractive among different countries for improving reactor designs, power outputs, and nuclear waste management (Alemberti et al., 2014; Ohshima and Kubo, 2016). Understanding physical phenomena in liquid metal cooled fast reactors is thus vital in increasing innovation for reactor design and operation optimization. To address the challenges related to liquid metal cooled fast reactors, the team of editors organizes the Research Topic "Experimental and Numerical Studies on Liquid Metal Cooled Fast Reactors" in the journal *Frontiers in Energy Research*. Finally, 16 articles are collected, covering different yet essential aspects of liquid metal cooled fast reactors, including neutronics, thermal hydraulics and severe accident analysis, and nuclear fuels/materials performance. Both experimental and computational approaches have been collected to significantly contribute to advances in liquid metal cooled fast reactors.

There are eleven original research articles about nuclear thermal hydraulics and severe accident analysis for liquid metal cooled fast reactors. Low-Prandtl number liquid metal is a promising candidate coolant for various designs of advanced nuclear systems such as liquid metal–cooled fast reactors and accelerator-driven sub-critical systems (ADS) due to their high thermal conductivity. Huang et al. proposed a turbulent Prandtl number model for the Reynolds-averaged Navier–Stokes approach on the modeling of turbulent heat transfer of low-Prandtl number liquid metal, which is validated with the LES/DNS results available. To increase the accuracy of low Prandtl flow prediction in a bare 19-rod bundle, Li et al. used a four-equation model, consisting of a two-equation turbulence model and a two-equation heat transfer model, in OpenFOAM. Its effectiveness and feasibility are validated through the comparison with the empirical correlations. Yi et al. develop a methodology to

predict CEFR core thermal hydraulic parameters based on the adaptive radial basis function neural network. The proposed RBF neural network model can provide real-time forecasting in a short time under unstable flow conditions. Bubble columns represent an extreme case of gas-liquid two-phase flow. Wang et al. develop drift-flux correlation for vertical forward bubble column-type gas-liquid lead-bismuth two-phase flow. The statistical analysis results show that the new correlation gives the best prediction for gas-LBE two-phase flow in the void fraction range of 0. 018–0.313. In order to research and compare the effect of wire-wrapped on the sub-channels and inner flow field of the fast reactor annular fuel assembly, Guo et al. investigate the thermal-hydraulic characteristics in inner and outer wire-wrapped for a fast reactor annular fuel assembly, providing a reference for the optimization design of the fuel assembly. Duan and Huang. perform an unsteady RANS study of thermal striping in a T-junction with sodium streams mixing at different temperatures. To better understand the mechanisms of stainless-steel corrosion behavior in the LBE flow, Chen and Wan. numerically investigate the iron mass transfer phenomenon on roughened walls under various LBE pipe flow conditions. Liu et al. numerically study the heat transfer characteristics of a liquid lead–bismuth eutectic in a D-type channel, and the simulation results lay a good foundation for the development of printed circuit heat exchanger (PCHE) with an LBE as the working fluid.

When a sodium leakage accident occurs in the sodium-cooled fast reactor, the leaked sodium reacts violently with the air in the form of droplets, resulting in a sodium spray fire. Zou et al. proposed a semi-empirical model of sodium spray droplet size distribution based on the theory of the maximum entropy principle, which shows good agreement with the experimental data. Under postulated severe accidents, the fuel rod of LFR may be damaged, which would cause the release of fission gas, and the migration of fission gas bubbles in the reactor molten pool will affect the release and absorption of radioactive substances in the reactor. Mai et al. perform a three-dimensional numerical study on the release and migration behavior of fission gas in a molten LBE pool based on the VOF method. Fuel-coolant interaction (FCI) has a pivotal role in the development of core disruptive accidents in a sodium-cooled fast reactor. Wang et al. present an improved multiphase smoothed particle hydrodynamics (SPH) algorithm corrected with kernel gradient correction (KGC) technique is presented for multiphase flow with large density ratio and complex interfacial behaviors.

One paper discusses the power optimization methodology of the natural circulation lead-bismuth cooled fast reactor SPALLER-100 design, considering different constraint parameters such as neutronics, materials, and thermal-hydraulics. Xiao et al. develop a platform to calculate the maximum neutronic power produced by the reactor at different core heights using Latin hypercube sampling and the Kriging proxy model. The cooling power of the reactor at different core heights is calculated by considering its natural circulation capacity. Finally, a design scheme that meets the requirements of neutronic and thermal-hydraulic assessments while producing maximum power is obtained.

Three articles focus on reactor fuels/materials performance, trying to overcome the challenges from the materials aspect of liquid metal cooled fast reactors. Mun et al. successfully modify the fuel performance code FRAPCON-4.0 for normal operation of light water reactors (LWRs) to evaluate the thermal and mechanical performance of the highest linear power rod of MicroURANUS, an innovative ultra-long-life lead-bismuth eutectic (LBE)-cooled fast reactor. Cai et al. successfully model and simulate an annular uranium-plutonium mixed oxide (MOX) fuel operating in a liquid lead/lead-bismuth cooled fast reactor to predict its behavior under transient and steady-state operation based on COMSOL Multiphysics. Oxide Dispersion Strengthened (ODS) steels with nano-scale oxides have become one of the potential candidate materials used in advanced nuclear reactor systems. Yun et al. irradiate a novel MX-ODS steel with uniformly distributed Y_2O_3 nano-precipitates and extremely low carbon content under 3 MeV Fe ions at 550°C and peak damage up to 70 dpa. The MX-ODS steel exhibits good irradiation tolerance.

Finally, this Research Topic also includes one review article to overview state-of-the-art research approaches on liquid metal cooled fast reactors. A specific type of sloshing motion may occur in the molten pool during core disruptive accidents (CDAs) of sodium-cooled fast reactors due to local neutronic power excursion or pressure developments, thereby significantly influencing recriticality. Recognizing the importance of improving the evaluation of CDAs of SFRs, Xu and Cheng contribute a comprehensive review of experimental and numerical investigations into molten-pool sloshing motion for severe accident analysis of sodium-cooled fast reactors, which is valuable not only for improving and verifying SFR safety analysis codes but also for providing reference data for studies of sloshing motion in other fields of engineering.

After almost 1 year's revisions and updates, this Research Topic finally selected those 16 articles and published them in the journal *Frontiers in Energy Research*. The collection shows the ongoing research on liquid metal cooled fast reactors from different perspectives and also allows us to exhibit the high-quality work to the public. More high-quality topics and articles are welcomed at this open platform in the future. All the editors are open to further information and communications.

Author contributions

All authors listed have made a substantial, direct, and intellectual contribution to the work and approved it for publication.

Conflict of interest

The authors declare that the research was conducted in the absence of any commercial or financial relationships that could be construed as a potential conflict of interest.

Publisher's note

References

Alemberti, A., Smirnov, V., Smith, C. F., and Takahashi, M. (2014). Overview of lead-cooled fast reactor activities. *Prog. Nucl. Energy* 77, 300–307. doi:10.1016/j.pnucene.2013.11.011

Ohshima, H., and Kubo, S. (2016). "Sodium-cooled fast reactor," in *Handbook of generation IV nuclear reactors* (Duxford: Woodhead Publishing Series in Energy, JAEA). doi:10.1016/B978-0-08-100149-3.00005-7

frontiers | Frontiers in Energy Research

ORIGINAL RESEARCH
published: 10 May 2022
doi: 10.3389/fenrg.2022.888738

Semi-Empirical Model of Droplet Size Distribution From the Maximum Entropy Principle in Sodium Spray

Wenbin Zou[1], *Zhenyu Zou*[1], *Lili Tong*[1]* *and Cheng Peng*[2]

[1]School of Mechanical Engineering, Shanghai Jiao Tong University, Shanghai, China, [2]College of Energy and Mechanical Engineering, Shanghai University of Electric Power, Shanghai, China

When a sodium leakage accident occurs in the sodium-cooled fast reactor, the leaked sodium reacts violently with the air in the form of droplets, resulting in the phenomenon of sodium spray fire. The droplet size distribution formed by liquid sodium injection is the key factor affecting the accident analysis of sodium spray fire. Based on the theory of the maximum entropy principle, a semi-empirical model of sodium spray droplet size distribution is constructed, which is constrained by the mass equation or the momentum equation with viscous resistance, respectively. Based on the existing liquid fuel droplet size distribution experiment results and the sodium spray fire experiment results, the semi-empirical model is verified, which shows that the prediction result with the semi-empirical model constrained by the momentum equation is in good agreement with the experimental result with the error of about 20%. Furthermore, the proposed sodium spray droplet model is compared with other models of the empirical model, the semi-empirical model, and the model based on the maximum entropy principle constrained by the simplified mass equation. The simulation result with the proposed model matches the experimental data better with minor error.

Keywords: sodium-cooled fast reactor, sodium spray fire, maximum entropy principle, drop size distribution, semi-empirical model

OPEN ACCESS

Edited by:
Songbai Cheng,
Sun Yat-sen University, China

Reviewed by:
Xiaoxue Huang,
The University of Sheffield, United Kingdom
Huai-En Hsieh,
Xiamen University, China

***Correspondence:**
Lili Tong
lltong@sjtu.edu.cn

Specialty section:
This article was submitted to Nuclear Energy, a section of the journal Frontiers in Energy Research

Received: *03 March 2022*
Accepted: *04 April 2022*
Published: *10 May 2022*

Citation:
Zou W, Zou Z, Tong L and Peng C (2022) Semi-Empirical Model of Droplet Size Distribution From the Maximum Entropy Principle in Sodium Spray. Front. Energy Res. 10:888738. doi: 10.3389/fenrg.2022.888738

1 INTRODUCTION

As a recommended reactor type in the Generation IV advanced nuclear energy system, sodium-cooled fast reactors (SFRs) have attracted worldwide attention due to their mature technology and inherent safety (GIF, 2002). However, sodium shows a high chemical reactivity with oxygen, which entails a fire hazard risk in the case of leaks into the containment, named sodium pool fire and sodium spray fire accident, resulting in equipment damages (Sathiah and Roelofs, 2014). The consequences of spray sodium fire are the most serious, in which the liquid sodium is dispersed into a large number of small droplets in the spray, making a violent sodium burning. According to the research of Sandia National Laboratory (SNL) on sodium spray fire accident phenomenon identification and ranking table, it is found that the prediction of droplet size distribution is very important in sodium spray dynamics (Olivier et al., 2010). However, there is still a lack of relevant physical phenomena, and the empirical model is also lack of experiment verification (Ohno et al., 2012).

The process of sodium spray can be regarded as the breakup process of molten sodium. The distribution of spray diameter determines the heat-transfer interface of sodium droplets, which is related to the subsequent combustion behavior and the aerosol generation and removal behavior

(Srinivas et al., 2019). Many experiments and theoretical studies have been carried out. The large-scale sodium spray experiment is conducted on the FAUNA device (Cherdron, 1980; Garcia et al., 2016). It is found that when the initial spray mass is 7, 20, and 40 kg, the average diameter of the sodium droplet is 1.3, 2.15, and 4.8 μm, respectively. The results show that the average diameter of sodium spray droplets is positively correlated with the amount of sodium. However, when the injection mass reaches the maximum value of 60 kg, the pressure also reaches the maximum value of 1.8 bar. The medium-scale sodium spray experiment with an initial spray mass of 0.4–5.25 kg and a pressure of 2.6 bar is conducted (Malet et al., 1982). It is believed that smaller spray size is conducive to pressure propagation. The small-scale sodium spray experiment is carried out on the LISOF device (Torsello et al., 2012; Manzini and Torsello, 2013) using an LDV/PDA system to collect and characterize the sodium spray dynamic parameters. It is found that the droplet number density relative to droplet size is similar to Gaussian distribution. A sodium spray test under a pressure difference of 0.2 MPa is also conducted by Japan Nuclear Cycle Development Institute (JNC) (Nagai et al., 1999) using a laser droplet size analyzer to measure the sodium spray droplet size distribution. The number density distribution with the size of sodium droplets conforms to the Nukiyama–Tanasawa model.

The spray phenomenon widely exists in various fields such as nuclear industries, engine research, and medical treatment. Babinsky and Sojka (2002) of Purdue University in the United States have summarized three basic methods to deal with droplet distribution in the spray process, namely, the empirical correlation method, discrete probability function (DPF) method, and maximum entropy principle. The expression form of the model based on the empirical method is simple and easy to apply. Rosin and Rammler (1933) has developed the Rosin–Rammler empirical relation based on the droplet size distribution in the breakup process of pulverized coal and cement slurry, which can be regarded as a special form of expression of the Nukiyama–Tanasawa model. In addition, the Nukiyama–Tanasawa model, obtained by measuring the droplet size distribution, is adopted in the sodium spray and fire analysis programs of NACOM (Tsai, 1980), CONTAIN-LMR (Murata et al., 1993), and SPHINCS (Yamaguchi and Tajima, 2002). However, the model relies heavily on the determination of the average droplet size. The extension of the pure empirical model under different droplet conditions may be controversial. The DPF method was first applied to modeling drop size distributions in Newtonian sprays by Sovani et al. (1999). A drop size distribution is produced because of the fluctuation of initial conditions. The DPF method requires a set of initial conditions and a model of the breakup mechanism. The DPF has not been validated because of the difficulties involved in obtaining the fluctuating initial conditions (Babinsky and Sojka, 2002). The maximum entropy principle was first proposed by Jaynes (1957), which characterizes the droplet number distribution obtained under a series of physical constraints, and its corresponding system entropy function reaches the maximum value. Cheng et al. (2002) have proposed the droplet size distribution function based on the principle of maximum entropy and established an exponential model that does not change with different test conditions with the constraints of the simplified mass equation. Therefore, Lee et al. (2004); Wu et al. (2020) have used this method to conduct preliminary explorations on fuel combustion in the energy field. Peng et al. (2021) have coupled the continuity and momentum equations to build a droplet size distribution model based on the principle of maximum entropy and have used the present experiment results and current models to validate. However, the model took the basic mass equation and momentum equation as constraints without considering the influence of viscous resistance. Besides, the distribution of the experimental data used for verification is similar, most of which are normally distributed and are not adequate. However, based on the study of the droplet fragmentation mechanism by Zhao et al. (2011) and Cao and Ma (1997), viscous resistance plays an important role. Therefore, it is necessary to develop a maximum entropy droplet size distribution model considering the influence of viscous resistance and to use multiple experimental data types in the form of distribution to validate the model.

Based on the maximum entropy principle, two semi-empirical models of the droplet size distribution, with the main constraint condition of the mass equation and the momentum equation including the viscous resistance term as the main constraint condition, are developed and verified.

2 ESTABLISHMENT OF THE DROPLET SIZE DISTRIBUTION MODEL

2.1 Maximum Entropy Principle With the Mass Equation as the Constraint Condition

The derivation of the sodium droplet size distribution model based on the maximum entropy principle requires the establishment of appropriate physical constraints. Jaynes (1957) applied the maximum entropy principle to physics to obtain the droplet distribution law, shown as **Eq. 1**.

$$S = -T \sum_k P_k \ln P_k \tag{1}$$

where S is the entropy, T is a constant, and P_k is the probability of the number of droplets under a certain volume of the leaked sodium droplet.

When the entropy takes a maximum value, the most probable event occurs, that is, the sodium droplet size distribution function with the largest probability of occurrence is obtained (Cao et al., 2008), shown as **Eq 2**

$$\sum_k P_k \cdot \ln P_k = Max. \tag{2}$$

From the mass conservation of sodium droplets in the system (Cheng et al., 2002), **Eq. 3** can be obtained

$$\sum_k P_k m_k N_0 (1 + \varepsilon) = \dot{m} \tag{3}$$

where m_k is the ejection mass under the action of the pressure difference when the loop system is broken, N_0 is the total number of sodium droplets produced in unit time, ε is the loss of sodium droplets due to chemical reaction or physical actions like pressure difference, and $\dot{m}$ is the mass flow rate of sodium droplets ejected from the break.

Considering that the sodium droplet is an incompressible fluid, **Eq. 3** can be transformed into **Eq. 4**

$$\sum_k P_k v_k N_0 (1+\varepsilon) = \dot{V} \tag{4}$$

where v_k is the volume of a single sodium droplet and $\dot{V}$ is the total volume flow of sodium droplets ejected from the break.

In various cases, the sum of the number probabilities is 1, shown as **Eq. 5**

$$\sum_k P_k = 1 \tag{5}$$

For the above three basic constraints of **Eqs 2**, **4**, and **5**, the Lagrange method is used to obtain the function of G_{ma} as **Eqs 6**, **7** (Mojaver et al., 2020)

$$G_{ma} = \sum_k P_k \cdot \ln P_k + (\phi - 1)\Big(\sum_k P_k - 1\Big) + \omega\Big(\sum_k P_k v_k N_0 (1+\varepsilon) - \dot{V}\Big) \tag{6}$$

$$\frac{dG_{\mathrm{ma}}}{dP_k} = 0 \tag{7}$$

Then, **Eq. 8** can be obtained

$$P_k = \exp\big[-\phi - \omega v_k N_0 (1+\varepsilon)\big] \tag{8}$$

where ϕ and ω are the undetermined Lagrange multipliers.

Eqs 9, **10** can be obtained through inserting **Eq. 8** into **Eqs 4**, **5**

$$\sum_k \exp\big[-\phi - \omega v_k N_0 (1+\varepsilon)\big] \cdot v_k N_0 (1+\varepsilon) = \dot{V} \tag{9}$$

$$\phi = \ln \sum_k \exp\big[-\omega v_k N_0 (1+\varepsilon)\big] \tag{10}$$

Thus, **Eq. 11** is obtained

$$\dot{V} = \frac{\sum_k v_k N_0 (1+\varepsilon) \cdot \exp\big[-\omega v_k N_0 (1+\varepsilon)\big]}{\sum_k \exp\big[-\omega v_k N_0 (1+\varepsilon)\big]} \tag{11}$$

Assuming that the droplet diameter of the particles of atomization sodium droplets ejected from the break of the loop system, denoted as D, conforms to the continuous distribution, **Eqs 12**, **13** can be obtained

$$\phi = \ln \int_{D_{\min}}^{D_{\max}} \exp\Big[-\omega \frac{\pi}{6} D^3 \cdot N_0 (1+\varepsilon)\Big] \frac{\pi}{2} D^2 dD \tag{12}$$

$$\dot{V} = \frac{\pi^2}{12} N_0 (1+\varepsilon) \int_{D_{\min}}^{D_{\max}} D^5 \exp\Big[-\phi - \frac{\pi}{6}\omega N_0 (1+\varepsilon) D^3\Big] dD \tag{13}$$

Eq. 14 can be obtained by solving **Eq. 12**. Insert **Eq. 14** into **Eq. 13** and integrate it, and **Eq. 15** is obtained

$$\phi = \ln\left\{\frac{1}{\omega N_0 (1+\varepsilon)}\left\{\exp\Big[-\omega N_0 (1+\varepsilon)\frac{\pi}{6} D_{\min}^3\Big] - \exp\Big[-\omega N_0 (1+\varepsilon)\frac{\pi}{6} D_{\max}^3\Big]\right\}\right\} \tag{14}$$

$$\dot{V} = \frac{1}{\omega}\frac{\exp\Big[-\frac{\pi}{6}\omega N_0 (1+\varepsilon) D_{\max}^3\Big]\Big[-\frac{\pi\omega N_0 (1+\varepsilon) D_{\max}^3}{6} - 1\Big]}{\Big\{\exp\Big[-\frac{\pi}{6}\omega N_0 (1+\varepsilon) D_{\min}^3\Big] - \exp\Big[-\frac{\pi}{6}\omega N_0 (1+\varepsilon) D_{\max}^3\Big]\Big\}} - \frac{1}{\omega}\frac{-\exp\Big[-\frac{\pi}{6}\omega N_0 (1+\varepsilon) D_{\min}^3\Big]\Big[-\frac{\pi\omega N_0 (1+\varepsilon) D_{\min}^3}{6} - 1\Big]}{\Big\{\exp\Big[-\frac{\pi}{6}\omega N_0 (1+\varepsilon) D_{\min}^3\Big] - \exp\Big[-\frac{\pi}{6}\omega N_0 (1+\varepsilon) D_{\max}^3\Big]\Big\}} \tag{15}$$

Finally, Lagrange multipliers ϕ and ω can be uniquely solved by **Eqs 14**, **15**.

Define P_{ni} as the probability of droplet size distribution, which can be expressed with the integration of P_k in the range of volume intervals $[v_i - \frac{\Delta v_i}{2}, v_i + \frac{\Delta v_i}{2}]$. **Eq. 16** can be obtained as follows

$$P_{ni} = \int_{v_i - \frac{\Delta v_i}{2}}^{v_i + \frac{\Delta v_i}{2}} P_k dv = \int_{v_i - \frac{\Delta v_i}{2}}^{v_i + \frac{\Delta v_i}{2}} \exp\big[-\phi - w v_k N_0 (1+\varepsilon)\big] dv = \int_{D_i - \frac{\Delta D_i}{2}}^{D_i + \frac{\Delta D_i}{2}} \exp\Big[-\phi - w\frac{\pi D^3}{6} N_0 (1+\varepsilon)\Big] \frac{\pi D^2}{2} dD \tag{16}$$

When the droplet diameter size is in the range of $[D_i - \frac{\Delta D_i}{2}, D_i + \frac{\Delta D_i}{2}]$, the probability density function of a sodium droplet of diameter D is defined as dN/dD, and N means the number percentage of sodium droplet diameter. Assuming that the droplet size of the particles of atomization sodium droplets ejected from the break of the loop system conforms to the continuous distribution, the probability of droplet diameter distribution of P_{ni} can be expressed as **Eq. 17**

$$P_{ni} = \int_{D_i - \frac{\Delta D_i}{2}}^{D_i + \frac{\Delta D_i}{2}} \frac{dN}{dD} dD \tag{17}$$

The probability density function of a sodium droplet of diameter D can be obtained as **Eq. 18**

$$\frac{dN}{dD} = \frac{\pi}{2} D^2 \exp\Big[-\phi - \omega\frac{\pi}{6} D^3 N_0 (1+\varepsilon)\Big] \tag{18}$$

Consider that there is a pressure differential drive between the sodium circuit system and the external environment where the pipe breaks. Assume that the minimum diameter $D_{\min}$ of the sodium droplet after ejection is 0 and the maximum diameter is $D_{\max}$, which can also be denoted as D_{cr} and determined by We_{cr} (Hinze, 1955)

$$D_{cr} = \frac{\sigma We_{cr}}{\rho_A \bar{u}^2} \tag{19}$$

where ρ_A is the density of the ambient medium; σ is the surface tension of the sodium droplet; We_{cr} is the critical value of We; and

$\bar{u}^2$ is the average value across the whole flow field of the squares of velocity differences over a distance equal to D_{cr}, which is related to the kinetic energy per unit mass. Therefore, **Eq. 20** can be obtained by simplifying **Eq. 14**

$$\phi = \ln \frac{\left\{1 - \exp\left[- \omega N_0 (1+\varepsilon) \frac{\pi}{6} D_{cr}^3 \right]\right\}}{\omega N_0 (1+\varepsilon)} \tag{20}$$

Insert **Eq. 20** into **Eq. 18**

$$\frac{dN}{dD} = \frac{\pi}{2} D^2 \left\{ \frac{\omega N_0 (1+\varepsilon)}{1 - \exp\left[- \omega N_0 (1+\varepsilon) \frac{\pi}{6} D_{cr}^3 \right]} \right\} \cdot \exp\left[- \omega N_0 (1+\varepsilon) \frac{\pi}{6} D^3 \right] \tag{21}$$

where ω can be given by the implicit expression of (1–15). However, for the calculation of the safety analysis of the sodium spray fire accident, it is inconvenient to use the mathematical model of the implicit expression. The semi-empirical relationship based on the constraint of the mass equation will be determined by the method of fitting the experimental data. **Eq. 21** can be simplified as **Eq. 22**

$$\frac{dN}{dD} = aD^2 \cdot \exp\left(bD^3\right) \tag{22}$$

The mathematical expression form with the maximum entropy principle with the mass equation as the constraint condition can be obtained as **Eq. 23**

$$\ln\left(\frac{dN}{dD}\right) = a + 2\ln D + bD^3 \tag{23}$$

where a and b are the coefficients determined by fitting the experimental data.

2.2 Maximum Entropy Principle With the Momentum Equation as the Constraint Condition

The momentum equation considering the viscous resistance term of the sodium droplet is as follows

$$\sum_i P_i \nu_i N_0 \left[u_0^2 + \frac{4\mu_l}{\pi^2 D_i^3 \rho_A} \left(\frac{\sigma}{D_i \rho_l} \right)^{1/2} \right] = AU_0^3 \tag{24}$$

where P_i represents the probability of the number of droplets with atomization volume ν_i , u_0 is the volume-weighted average velocity, μ_l is the integral of the kinetic viscosity of the sodium droplet for the droplet surface, D_i is the diameter of the sodium droplet, ρ_l is the density of the sodium droplet, A is the cross-sectional area of the break, and U_0 is the average flow velocity of sodium droplets at the break.

Using the Lagrange method, **Eq. 25** is obtained between G_{mo} and the probability of the number of sodium droplets

$$G_{mo} = \sum_i P_i \ln(P_i) + \lambda \left\{ \sum_i P_i \nu_i N_0 \left[u_0^2 + \frac{4\mu_l}{\pi^2 D_i^3 \rho_A} \left(\frac{\sigma}{D_i \rho_l} \right)^{1/2} \right] \right\} - \lambda A U_0^3 + (\beta - 1) \left(\sum_i P_i - 1 \right) \tag{25}$$

The derivation of G_{mo} with respect to the number probability is 0. Thus, **Eqs 26**, **27** can be obtained as follows

$$\ln P_i + 1 + \lambda \nu_i N_0 \left[u_0^2 + \frac{4\mu_l}{\pi^2 D_i^3 \rho_A} \left(\frac{\sigma}{D_i \rho_l} \right)^{1/2} \right] + \beta - 1 = 0 \tag{26}$$

$$P_i = \exp\left\{ - \beta - \lambda \nu_i N_0 \left[u_0^2 + \frac{4\mu_l}{\pi^2 D_i^3 \rho_A} \left(\frac{\sigma}{D_i \rho_l} \right)^{1/2} \right] \right\} \tag{27}$$

where λ and β are the Lagrange multipliers.

The probability of droplet size distribution P_{ni} can be expressed with the integration of P_i in the range of volume intervals $[\nu_i - \frac{\Delta\nu_i}{2}, \nu_i + \frac{\Delta\nu_i}{2}]$, and **Eq. 28** can be obtained

$$\begin{aligned} P_{ni} &= \int_{\nu_i - \frac{\Delta\nu_i}{2}}^{\nu_i + \frac{\Delta\nu_i}{2}} P_i d\nu = \int_{\nu_i - \frac{\Delta\nu_i}{2}}^{\nu_i + \frac{\Delta\nu_i}{2}} \exp\left\{ - \beta - \lambda \nu_i N_0 \left[u_0^2 + \frac{4\mu_l}{\pi^2 D_i^3 \rho_A} \left(\frac{\sigma}{D_i \rho_l} \right)^{1/2} \right] \right\} d\nu \\ &= \int_{D_i - \frac{\Delta D_i}{2}}^{D_i + \frac{\Delta D_i}{2}} \exp\left\{ - \beta - \lambda \frac{\pi D^3}{6} N_0 \left[u_0^2 + \frac{4\mu_l}{\pi^2 D^3 \rho_A} \left(\frac{\sigma}{D \rho_l} \right)^{1/2} \right] \right\} \frac{\pi D^2}{2} dD \\ &= \int_{D_i - \frac{\Delta D_i}{2}}^{D_i + \frac{\Delta D_i}{2}} \exp\left\{ - \beta - \lambda \frac{\pi D^3}{6} N_0 u_0^2 - \frac{2}{3} \lambda N_0 \frac{\mu_l}{\pi \rho_A} \left(\frac{\sigma}{D \rho_l} \right)^{1/2} \right\} \frac{\pi D^2}{2} dD \end{aligned} \tag{28}$$

Set **Eqs 29**, **30** as follows. Also, assuming that the droplet size of the sodium droplets ejected from the main system break follows a continuous distribution, **Eq. 31** can be obtained from **Eq. 28**

$$\alpha = \frac{\pi}{6} \lambda N_0 \tag{29}$$

$$K = \frac{2}{3} N_0 \frac{\mu_l}{\pi \rho_A} \left(\frac{\sigma}{\rho_l} \right)^{1/2} \tag{30}$$

$$\frac{dN}{dD} = \exp\left\{ - \beta - \alpha u_0^2 D^3 - \lambda K D^{-1/2} \right\} \frac{\pi D^2}{2} \tag{31}$$

According to **Eq. 12**, **Eq. 32** can be obtained

$$\phi = \ln \int_{D_{\min}}^{D_{\max}} \exp\left\{ - \alpha u_0^2 D^3 - \lambda K D^{-1/2} \right\} \frac{\pi D^2}{2} dD \tag{32}$$

Insert **Eq. 32** into **Eq. 31**

$$\frac{dN}{dD} = \frac{D^2 \exp\left(- \alpha D^3 u_0^2 - \lambda K D^{-1/2} \right)}{\int_{D_{\min}}^{D_{\max}} D^2 \exp\left(- \alpha D^3 u_0^2 - \lambda K D^{-1/2} \right) dD} \tag{33}$$

Define the coefficient W_1 as follows

$$W_1 = \int_{D_{\min}}^{D_{\max}} D^2 \exp\left(- \alpha D^3 u_0^2 - \lambda K D^{-1/2} \right) dD \tag{34}$$

The mathematical expression form with the maximum entropy principle with the momentum equation as the constraint condition can be obtained as **Eq. 35**

$$\ln \frac{dN}{dD} = -\ln(W_1) + W_2 \ln D - W_3 D^3 - W_4 D^{-1/2} \tag{35}$$

where W_1, W_2, W_3, and W_4 are the coefficients determined by fitting the experimental data.

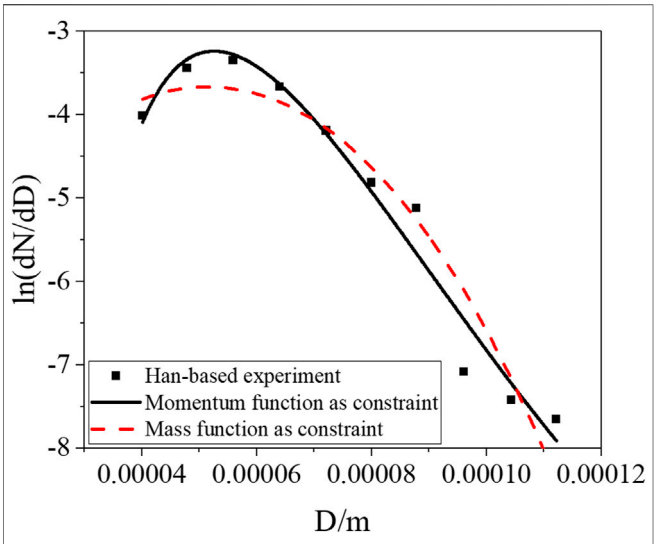

FIGURE 1 | Results of droplet size distribution of HAN-based liquid droplets under the pressure difference of 1.8 MPa.

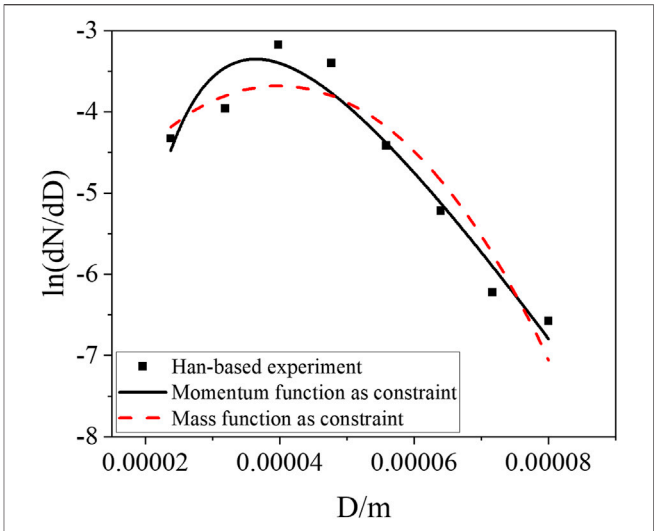

FIGURE 2 | Results of droplet size distribution of HAN-based liquid droplets under the pressure difference of 2.2 MPa.

3 VERIFICATION BY COMPARISON WITH EXPERIMENTS

3.1 Verification by Liquid Fuel Spray Experiment Results

The HAN-based liquid spray experiment (Wang, 2017) is selected, in which the density and viscosity are 1300 kg/m^3 and 1.2 × 10^{-3} Pas, respectively, for the simulated working fluid of the HAN-based liquid. The droplet size distribution experiments of spray droplets under the pressure differences of 1.8, 2.2, and 2.6 MPa were carried out, where the droplet size distribution of spray droplets was measured with phase Doppler analysis (PDA). The semi-empirical model with the mass conservation equation as the constraint condition and the momentum conservation equation as the constraint condition was used to simulate the experimental data, and the result is shown in **Figures 1–3**. Under different pressure differences, the two models can both reflect the spray size distribution of HAN-based liquids. In addition, both models can reflect the trend that the median diameter gradually decreases with the increase of the nozzle pressure difference, which is consistent with the experimental conclusion. The result of the semi-empirical model with the momentum equation as the constraint is in good agreement with the experimental data, with little error, especially for the smaller spray diameter.

The model is also verified by the spray droplet distribution experiment of injecting diesel into the air combustion chamber (Hiroyasu, 1985) with the pressure differences of 8.8 and 9.8 MPa, respectively. In addition, the sampling time of the experimental data is 4.5 ms after injection. At this time, the atomization state and droplet size are basically stable. The experimental data under the pressure difference of 8.8 MPa show a normal distribution, that is, the distribution of data points near the peak of probability density is nearly symmetrical, shown as **Figure 4**. However, under the

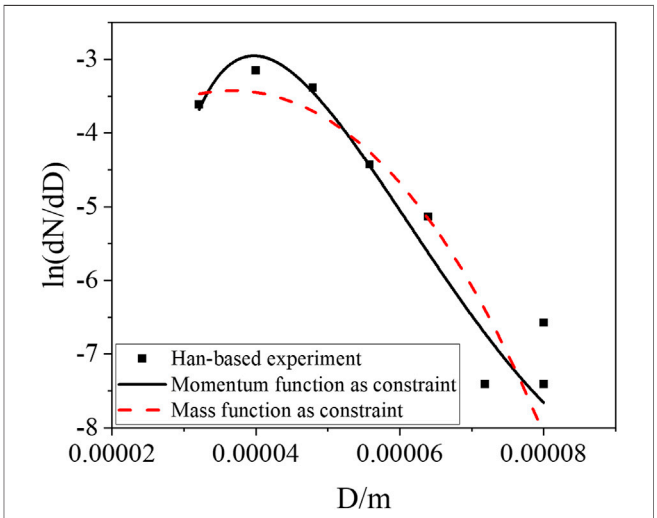

FIGURE 3 | Results of droplet size distribution of HAN-based liquid droplets under the pressure difference of 2.6 MPa.

experimental condition of the pressure difference of 9.8 MPa, the overall distribution of the experimental data is asymmetric and is barbed, shown as **Figure 5**. The results calculated with the both models can reflect the normal distribution very well. However, when the pressure difference reaches 9.8 MPa, the model with the mass equation as the constraint cannot correctly reflect the spray size distribution. The spray size distribution simulated by the semi-empirical model with the momentum equation as the constraint is in good agreement with the experimental data under a higher pressure difference. It is shown that when the peak of the probability density appears at a small diameter under a high pressure difference, the model

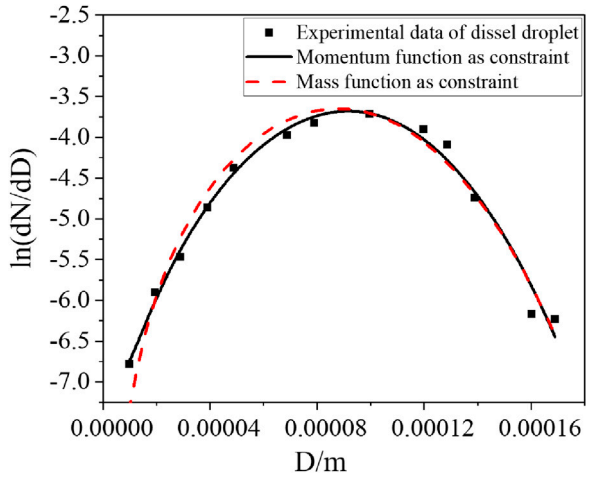

FIGURE 4 | Results of diesel droplet size distribution under the pressure difference of 8.8 MPa.

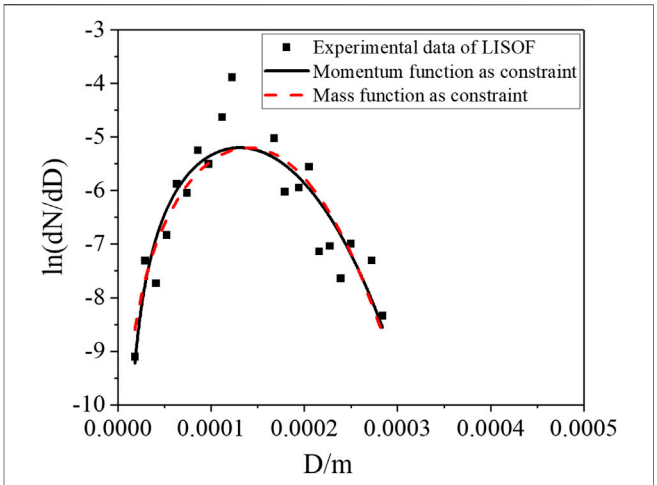

FIGURE 6 | Results of LISOF sodium droplet size distribution under the pressure difference of 0.6 MPa.

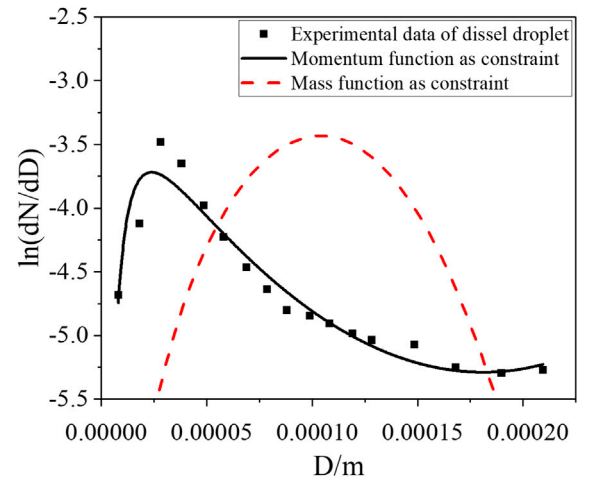

FIGURE 5 | Results of diesel droplet size distribution under the pressure difference of 9.8 MPa.

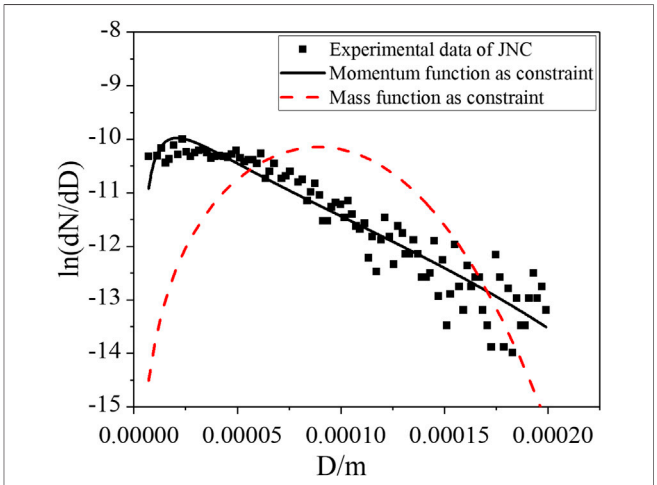

FIGURE 7 | Results of JNC sodium droplet size distribution under the pressure difference of 0.2 MPa.

constrained by the momentum equation also has better applicability due to the influence of viscous force.

3.2 Verification by Sodium Spray Fire Experiments Results

The model is verified by the Italian LISOF sodium spray fire experiment (Torsello et al., 2012) and the sodium spray fire test of JNC (Nagai et al., 1999). The LISOF experiment is carried out for the droplet leakage phenomenon under the small break of the sodium-cooled fast reactor, and it uses sodium with a temperature of 550°C and a 0.2 mm nozzle to simulate the phenomenon of sodium spray under microdefects in a cooling circuit, which is similar to those in SFR. The pressure difference is 0.6 MPa, and the initial mass flow rate is 0.9 g/s. The JNC sodium droplet size distribution experiment is carried out for large-scale sodium spray fire under the pressure nozzle with a pressure difference of 0.2 MPa, an initial mass flow rate of 49.6 g/s, and a sodium temperature of 140°C.

The comparison between the calculation results of the two models and the experimental data of two sodium sprays is shown in **Figures 6**, **7**, which shows similar conclusions with the experimental verification of the liquid fuel spray. In other words, the semi-empirical model with the momentum equation as the constraint can reflect the particle size distribution of sodium spray, whether it is normal distribution or asymmetric distribution, such as barb distribution.

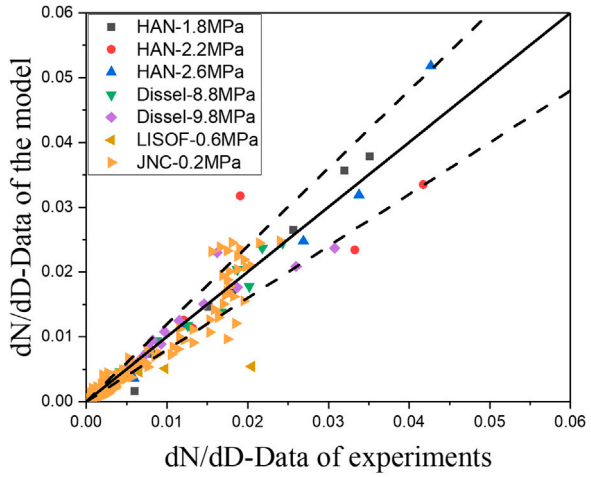

FIGURE 8 | Relative error of droplet size number obtained by the model constrained with momentum equation.

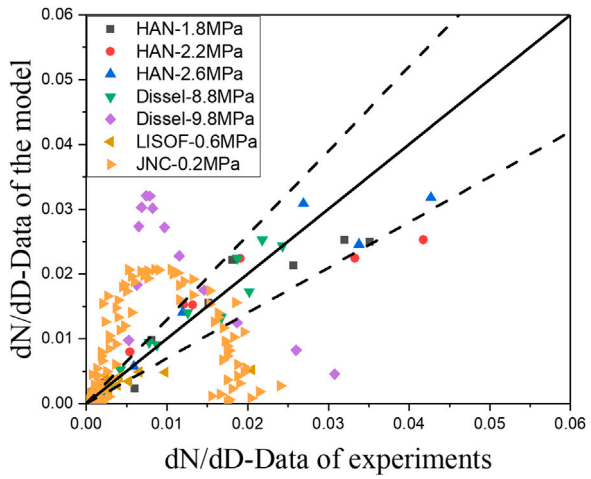

FIGURE 9 | Relative error of droplet size number obtained by the model constrained with mass equation.

3.3 Comparison of Two Models

The data from the liquid fuel spray experiment and the sodium spray fire experiment are summarized and compared with the both semi-empirical prediction models. The results are shown as **Figures 8**, **9**. The horizontal axis represents the probability density value measured by the four experiments, and the vertical axis represents the predicted value of the model corresponding to the experiments. The error of the semi-empirical model with momentum as a constraint is in the range of 20%. In addition, the error of the semi-empirical model with the mass equation as a constraint is in the range of 30%, except for some data with large deviation.

The semi-empirical model with the mass equation as a constraint does not seem to be able to correctly reflect the slow reduction of the number of large particles with the increase of particle size. This is because after the droplet is ejected, the momentum will decrease due to viscous force and surface tension; as a result, the reduction is not conducive to breaking the droplets into small particles, leading to an increase in the proportion of large droplets. There exists the same problem in the HAN-based liquid experiment, only due to the small amount of data; the fitting results under the two constraints have little difference.

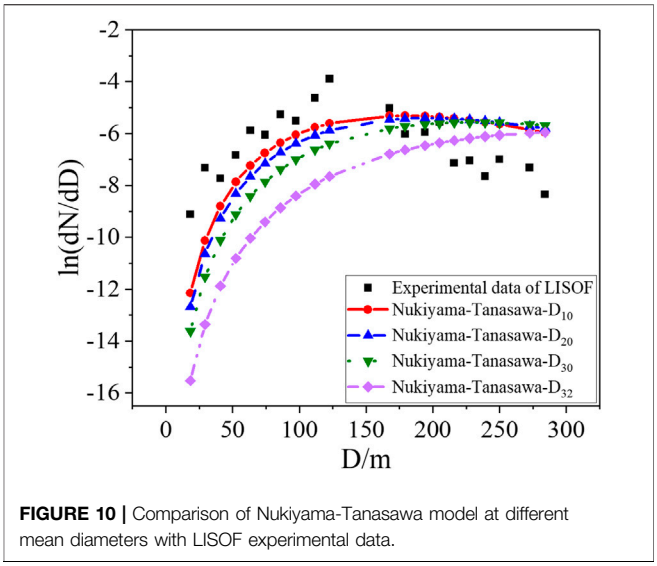

FIGURE 10 | Comparison of Nukiyama-Tanasawa model at different mean diameters with LISOF experimental data.

4 COMPARISON WITH CURRENT DISTRIBUTION MODELS

The existing typical spray droplet size distribution models include the Nukiyama–Tanasawa model (Tsai, 1980), Rosin-Rammler model (Rosin and Rammler, 1933), and Cheng model (Cheng et al., 2002) based on the maximum entropy principle and considering the simplified mass conservation equation, expressed as **Eqs 36**, **37**, **38**, where b and q are undetermined coefficients and $\bar{D}$ is the average diameter of droplets. Combined with the proposed sodium spray model constrained with the momentum equation in the paper, the droplet size distribution is compared and verified with the LISOF sodium spray fire experiment and JNC experiment

$$\frac{dN}{dD} = \left(\frac{3.915}{\bar{D}}\right)^6 \frac{D^5}{120} \exp\left(-\frac{3.915D}{\bar{D}}\right) \tag{36}$$

$$\frac{dN}{dD} = bq \cdot D^{q-4} \exp\left(-bD^q\right) \tag{37}$$

$$\frac{dN}{dD} = \frac{\pi}{2} D^2 \frac{\rho_l N_0}{\dot{m}} \exp\left(-\frac{\pi}{6} \frac{\rho_l N_0}{\dot{m}} D^3\right) \tag{38}$$

The Nukiyama–Tanasawa model with an arithmetic mean diameter of 138.6 μm, a surface area mean diameter of 152.9 μm, a volume mean diameter of 180.7 μm, and a Sauter mean diameter of 252.7 μm is used to compare with

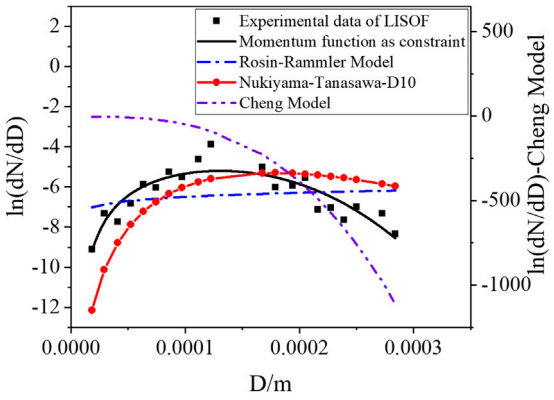

FIGURE 11 | Comparison of Nukiyama-Tanasawa model with D10, Cheng model, Rosin-Rammler model and the proposed sodium spray model with LISOF experimental data.

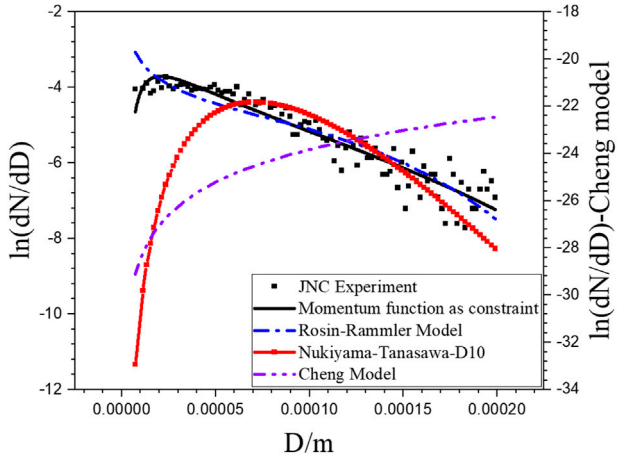

FIGURE 12 | Comparison of Nukiyama-Tanasawa model with D10, Cheng model, Rosin-Rammler model and the proposed sodium spray model with JNC experimental data.

LISOF experimental data, shown as **Figure 10**. The error between the Nukiyama–Tanasawa model with the arithmetic mean diameter (named D_{10}) and experiment data is relatively small.

The proposed sodium spray model constrained with the momentum equation, the Nukiyama–Tanasawa model with arithmetic mean diameter D_{10}, the Rosin–Rammler model, and the Cheng model are used to predict LISOF experiment and JNC experiment data, shown as **Figures 11**, **12**. It can be found that the Rosin–Rammler model, the Nukiyama–Tanasawa model with the arithmetic mean diameter, and the Cheng model have serious distortions in the prediction. The proposed sodium spray model constrained with the momentum equation is in good agreement with the experimental data for different distribution forms, which means that it has a wider range of applications.

5 CONCLUSION

The semi-empirical model of drop size distribution from the maximum entropy principle is developed and verified with different experimental data. The main conclusions are achieved as follows.

Theoretical analysis is carried out on the size distribution of sodium droplets in sodium spray based on the maximum entropy principle, a semi-empirical model with the mass equation as the main constraint or the semi-empirical model with the momentum equation including the viscous resistance term as the main constraint is developed. Through the comparing with the experimental data of liquid fuel and sodium droplet size distributions, the rationality of the proposed sodium spray model is proved. Regardless of normal distribution or barb distribution, the proposed model is in good agreement with experimental data, with an error of 20%. The proposed model semi-empirical model with the momentum equation constraint considering the influence of viscous force can reflect an increase in the proportion of large droplets due to the decrease in momentum. Compared with other existing models, the proposed sodium spray model constrained with the momentum equation is in better agreement with the experimental data for different distribution forms with minor error.

This study provides a new prediction model for the prediction of the size distribution for the safety analysis of sodium spray fire accidents.

DATA AVAILABILITY STATEMENT

The original contributions presented in the study are included in the article/Supplementary Material, further inquiries can be directed to the corresponding author.

AUTHOR CONTRIBUTIONS

WZ: model and draft. ZZ: analysis and writing—original. LT: methodology, investigation, and writing—review and editing. CP: analysis.

FUNDING

This work was financially supported by the National Natural Science Foundation of China (U1967202).

REFERENCES

Babinsky, E., and Sojka, P. E. (2002). Modeling Drop Size Distributions. *Prog. Energ. Combustion Sci.* 28 (4), 303–329. doi:10.1016/s0360-1285(02)00004-7

Cao, J. M., He, J., and Li, X. G. (2008). Droplet Size and Velocity Distribution Function in Sprays Based on Maximum Entropy Principle. *J. Traffic Transportation Eng.* 8 (5), 1–8.

Cheng, X. B., Huang, R. H., and Zhu, M. L. (2002). Application of Information Entropy to Calculating Drop Size Distribution of spray. *J. Huazhong Univ. Sci. Technology* 30, 30–32.

Cherdron, W. (1980). *Determination of Sodium Fire Aerosol Process Coefficients from FAUNA-experimentsNUREG/CR-1724*.

Garcia, M., Herranz, L. E., and Kissane, M. P. (2016). Theoretical Assessment of Particle Generation from Sodium Pool Fires. *Nucl. Eng. Des.* 310, 470–483. doi:10.1016/j.nucengdes.2016.10.024

GIF (2002). *A Technology Roadmap for Generation IV Nuclear Energy Systems*. U.S. DOE Nuclear Energy Research Advisory Committee and the Generation IV International Forum. GIF 002-00.

Hinze, J. O. (1955). Fundamentals of the Hydrodynamic Mechanism of Splitting in Dispersion Processes. *Aiche J.* 1 (3), 289–295. doi:10.1002/aic.690010303

Hiroyasu, H. (1985). Diesel Engine Combustion and its Modeling. *Comodia* 85, 53–75.

Jaynes, E. T. (1957). Information Theory and Statistical Mechanics. *Phys. Rev.* 106, 620–630. doi:10.1103/PhysRev.106.620

Lee, K. H., Lee, C. H., and Lee, C. S. (2004). An Experimental Study on the spray Behavior and Fuel Distribution of GDI Injectors Using the Entropy Analysis and PIV Method. *Fuel* 83 (7-8), 971–980. doi:10.1016/j.fuel.2003.10.021

Malet, J. C., Casselman, C., Duverger de Guy, G., Rzekiecki, R., and Charpenel, J. (1982). Potential Results of spray and Pool Fires. *Nucl. Eng. Des.* 68 (2), 195–206. doi:10.1016/0029-5493(82)90031-0

Manzini, G., and Torsello, G. (2013). "Sodium Safety- spray and Pool Fires ECART Modeling," in 15th International Topical Meeting on Nuclear Reactor Thermal-hydraulics, Pisa, Italy, May 12-17.

Mojaver, P., Khalilarya, S., and Chitsaz, A. (2020). Multi-objective Optimization and Decision Analysis of a System Based on Biomass Fueled SOFC Using Couple Method of Entropy/VIKOR. *Energ. Convers. Management* 203, 112260. doi:10.1016/j.enconman.2019.112260

Murata, K. K., Carroll, D. E., Bergeron, K. D., and Valdez, G. D. (1993). *CONTAIN LMR/1B-Mod.1, A Computer Code for Containment Analysis of Accidents in Liquid-Metal-Cooled Nuclear Reactors*. USA: Sandia National Laboratories. SAND 91-1490.

Nagai, K., Hirabayashi, M., Onojima, T., Oki, Y., Gunji, M., and Ara, K. (1999). *Sodium Leakage and Combustion Tests-Measurement and Distribution of Droplet Size Using Various spray Nozzles*. JAPAN: JNC TN. 9400 99-030.

Ohno, S., Ohshima, H., Tajima, Y., and Ohki, H. (2012). Development of PIRT and Assessment Matrix for Verification and Validation of Sodium Fire Analysis Codes. *Jpes* 6 (2), 241–254. doi:10.1299/jpes.6.241

Olivier, T. J., Blanchat, T. K., Figueroa, V. G., Hewson, J. C., and Nowlen, S. P. (2010). *Metal Fires and Their Implications for advance Reactors Part 3: Experimental and Modeling Results*. USA: Sandia National Laboratories. SAND 2010-7113, 2010.

Peng, C., Qiao, D. L., Li, D., and Wu, J. (2021). Liquid spray Modeling under Sodium Fire Accidents. *Nucl. Eng. Des.* 379, 111260. doi:10.1016/j.nucengdes.2021.111260

Rosin, P., and Rammler, E. (1933). The Laws Governing the Fineness of Powdered Coal. *J. Inst. Fuel* 7, 29–36.

Sathiah, P., and Roelofs, F. (2014). Numerical Modeling of Sodium Fire-Part I: Spray Combustion. *Nucl. Eng. Des.* 278, 723–738. doi:10.1016/j.nucengdes.2013.11.081

Sovani, S. D., Sojka, P. E., and Sivathanu, Y. R. (1999). Prediction of Drop Size Distributions from First Principles: the Influence of Fluctuations in Relative Velocity and Liquid Physical Properties. *Atomization and Sprays* 9 (2). doi:10.1615/atomizspr.v9.i2.20

Srinivas, C. V., Subramanian, V., Kumar, A., Usha, P., Sujatha, N., Bagavath Singh, A., et al. (2019). Modeling of Atmospheric Dispersion of Sodium Fire Aerosols for Environmental Impact Analysis during Accidental Leaks. *J. Aerosol Sci.* 137, 105432. doi:10.1016/j.jaerosci.2019.105432

Torsello, G., Parozzi, F., Nericcio, L., Araneo, L., Cozzi, F., Carcassi, M., et al. (2012). "Characterization of the Liquid Sodium spray Generated by a Pipework Hole," in Proceedings of ICAPP '12, Chicago, USA, June 24-28, 2012. Paper 12152.

Tsai, S. S. (1980). *NACOM Code for Analysis of Postulated Sodium spray Fires in LMFBRS*. Upton, NY (USA): Brookhaven National Lab.

Wang, J. (2017). *Experimental and Simulation Studies on the spray Characteristics of Impinging Nozzle*. NANJING University of Science and Technology. M.S. Dissertation https://kns.cnki.net/KCMS/detail/detail.aspx?dbname=CMFD201702&filename=1017053166.nh

Wu, S., Lao, C. T., Akroyd, J., Mosbach, S., Yang, W., and Kraft, M. (2020). A Joint Moment Projection Method and Maximum Entropy Approach for Simulation of Soot Formation and Oxidation in Diesel Engines. *Appl. Energ.* 258, 114083. doi:10.1016/j.apenergy.2019.114083

Yamaguchi, A., and Tajima, Y. (2002). Validation Study of Computer Code SPHINCS for Sodium Fire Safety Evaluation of Fast Reactor. *Nucl. Eng. Des.* 219, 19–34.

Conflict of Interest: The authors declare that the research was conducted in the absence of any commercial or financial relationships that could be construed as a potential conflict of interest.

frontiers | Frontiers in Energy Research

ORIGINAL RESEARCH
published: 20 June 2022
doi: 10.3389/fenrg.2022.922169

Numerical Study of Low Pr Flow in a Bare 19-Rod Bundle Based on an Advanced Turbulent Heat Transfer Model

Xianwen Li[1,2], *Xingkang Su*[1,2]*, *Long Gu*[1,2,3]*, *Lu Zhang*[1] *and Xin Sheng*[1]

[1]Institute of Modern Physics, Chinese Academy of Sciences, Lanzhou, China, [2]School of Nuclear Science and Technology, University of Chinese Academy of Sciences, Beijing, China, [3]School of Nuclear Science and Technology, Lanzhou University, Lanzhou, China

OPEN ACCESS

Edited by:
Yixiang Liao,
Helmholtz Association of German Research Centres (HZ), Germany

Reviewed by:
Jinbiao Xiong,
Shanghai Jiao Tong University, China
Hui Cheng,
Sun Yat-sen University, China

***Correspondence:**
Long Gu
gulong@impcas.ac.cn
Xingkang Su
suxingkang@impcas.ac.cn

Specialty section:
This article was submitted to Nuclear Energy, a section of the journal Frontiers in Energy Research

Received: *17 April 2022*
Accepted: *06 May 2022*
Published: *20 June 2022*

Citation:
Li X, Su X, Gu L, Zhang L and Sheng X (2022) Numerical Study of Low Pr Flow in a Bare 19-Rod Bundle Based on an Advanced Turbulent Heat Transfer Model. Front. Energy Res. 10:922169. doi: 10.3389/fenrg.2022.922169

Compared to assuming a constant turbulent Prandtl number model, an advanced four-equation model has the potential to improve the numerical heat transfer calculation accuracy of low–Prandtl number (*Pr*) fluids. Generally, a four-equation model consists of a two-equation $k-\varepsilon$ turbulence model and a two-equation $k_\theta-\varepsilon_\theta$ heat transfer model. It is essential to analyze the influence of dissimilar turbulence models on the overall calculation accuracy of the four-equation model. The present study aims to study the effect of using different turbulence models on the same $k_\theta-\varepsilon_\theta$ heat transfer model. First, based on the open-source computational fluid dynamics software OpenFOAM, an advanced two-equation $k_\theta-\varepsilon_\theta$ heat transfer model was introduced into the solver buoyant2eqnFoam, which was developed based on the self-solver buoyantSimpleFoam of OpenFOAM. In the solver buoyant2eqnFoam, various turbulence models built into OpenFOAM can be conveniently called to close the Reynolds stress and an advanced two-equation heat transfer model can be utilized to calculate the Reynolds heat flux of low-*Pr* fluids. Subsequently, the solver buoyant2eqnFoam was employed to study the fully developed flow heat transfer of low-*Pr* fluids in a bare 19-rod bundle. The numerical results were compared and analyzed with the experimental correlations and other simulation results to validate the effectiveness and feasibility of the solver buoyant2eqnFoam. Furthermore, the influence of combining different turbulence models with the same two-equation $k_\theta-\varepsilon_\theta$ heat transfer model was also presented in this study. The results show that the turbulence model has a considerable influence on the prediction of turbulent heat transfer in the high Peclet number range, suggesting that it should be prudent when picking a turbulence model in the simulations of low-*Pr* fluids.

Keywords: low Pr fluid, liquid metal, turbulence model, turbulent heat transfer model, OpenFOAM

1 INTRODUCTION

Nuclear energy is playing an increasingly irreplaceable role in the future energy structure as the demand for energy increases rapidly (Gu and Su, 2021). Lead-cooled fast reactor (LFR) is one of the six types of innovative nuclear power systems proposed by the Generation IV International Forum (Abram and Ion, 2008; Pacio et al., 2015). Benefiting from the excellent performance in chemical inertness, neutron economy, and thermohydraulic properties, lead–bismuth eutectic (LBE) is considered as one of most promising coolants for LFR. It is indispensable to research the thermohydraulic behaviors of the LBE inner fuel assembly, which influences the security and economic performance of LFRs but is poorly understood (Martelli et al., 2017; Pacio et al., 2017).

Since it is expensive, parlous, and complicated to conduct an experiment with LBE under a high-temperature state, computational fluid dynamics (CFD) methods are widely employed to study the thermohydraulic characteristics of LBE. The CFD methods can be subdivided into three categories: direct numerical simulation (DNS), large eddy simulation (LES), and Reynolds-averaged Navier–Stokes simulation (RANS). Despite the high calculation accuracy of DNS and LES, they have a high demand for computational resources, and as a result, they are only suitable for some specific and straightforward geometric models (Kawamura et al., 1999). Since the computational cost of the RANS approach is much lower than that of the DNS and LES, the RANS approach is the most widely adopted CFD method in engineering calculation. In the RANS method, the linear eddy-viscosity $k-\varepsilon$ or $k-\omega$ turbulence model is ordinarily sufficient to accurately predict the momentum transport of various fluids (Nagano, 2002). On the other hand, for reproducing the heat transfer, the Reynolds-analogy hypothesis assuming a constant turbulent Prandtl number $Pr_t = 0.85 \sim 0.9$ is adopted in almost all commercial codes (Manservisi and Menghini, 2014a). For the simulation of ordinary fluids like water and air, having a relatively high Prandtl number, the rational results can be obtained with a constant Pr_t (He et al., 2021). However, LBE is characterized by high thermal diffusivity and low viscosity values, resulting in low Prandtl numbers ($Pr \approx 0.01 \sim 0.03$). Consequently, the Reynolds-analogy hypothesis is no longer appropriate to be employed to study the thermohydraulic characteristics of LBE by the CFD methods (Cheng and Tak, 2006). For this reason, some advanced turbulent heat transfer models which can reproduce the heat transfer behaviors of LBE with high precision are highly desirable.

In the past four decades, to improve the calculation accuracy of heat transfer for low-Pr fluids, various heat flux models to close the energy conservation equation in the framework of RANS have been developed.

1.1 Differential Heat Flux Model

DHFM is a full second-moment differential model for the transport of Reynolds heat fluxes. Compared with the constant Pr_t model, DHFM fully considers the convection, diffusion, generation, and dissipation terms of Reynolds heat flux in the differential equations. Carteciano (1995), Carteciano et al. (1997), Carteciano et al. (2001), and Carteciano and Grötzbach (2003) developed a kind of DHFM named turbulence model for buoyant flows (TMBF). The simulations of two-dimensional forced convection and mixed convection with different fluids were carried out to evaluate the accuracy of TMBF. The numerical results obtained by TMBF demonstrate that stratified flows and buoyant effects were well reproduced compared with the constant Pr_t model, especially in mixed convection conditions. Based on a summary of the various DHFM models developed in recent years, Shin et al. (2008) proposed a new set of DHFM models with an

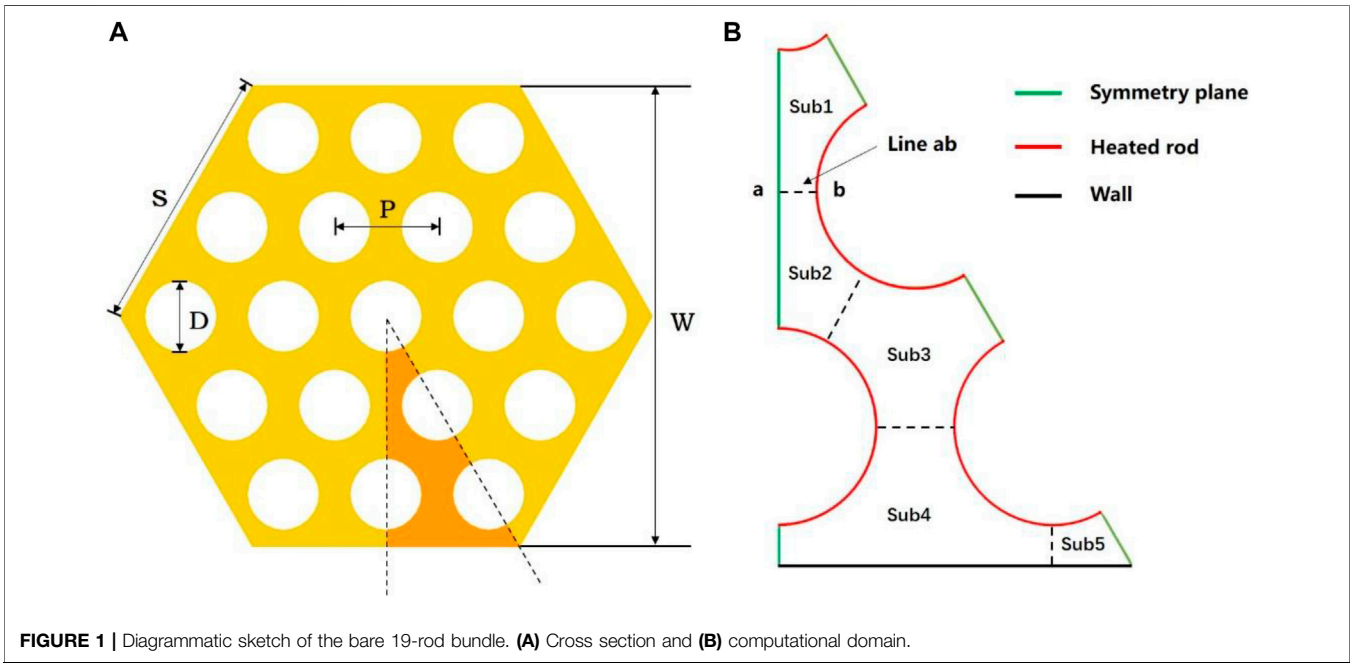

FIGURE 1 | Diagrammatic sketch of the bare 19-rod bundle. **(A)** Cross section and **(B)** computational domain.

TABLE 1 | Geometric parameters of the bare 19-rod bundle.

Parameter	Symbol	Value	Unit
Rod diameter	D	8.2	mm
Pitch	P	11.48	mm
P/D ratios	X	1.4	
The side length of a regular hexagon	S	29.68	mm
Opposite edge distance of a regular hexagon	W	51.4	mm
The hydraulic diameter of the bare 19-rod bundle	$D_{h,bun}$	7.70	mm
The hydraulic diameter of $Sub1$	$D_{h,sub1}$	9.52	mm
The height of bundle	L	$15D_{h,bun}$	mm

TABLE 2 | Flow parameters of LBE.

Parameter	Symbol	Value	Unit
Prandtl numbers	Pr	0.01	
Density	ρ	10340	kg/m^3
Dynamic viscosity	μ	0.00181	$Pa \cdot s$
Thermal conductivity	λ	26.3808	$W/(m \cdot K)$
Specific heat capacity	C_p	145.75	$J/(kg \cdot K)$
Heat flux	q_w	360000	W/m^2
Peclet numbers	Pe_{bun}	250–3000	

TABLE 3 | The model constants of the Abe $k-\varepsilon$ turbulence model.

C_μ	σ_k	σ_ε	$C_{1\varepsilon}$	$C_{2\varepsilon}$
0.09	1.4	1.4	1.5	1.9

TABLE 4 | The constant empirical coefficients of the Manservisi $k_\theta - \varepsilon_\theta$ turbulent heat transfer model.

C_θ	C_γ	σ_{k_θ}	$\sigma_{\varepsilon_\theta}$	C_{p1}	C_{d1}	C_{d2}
0.1	0.3	1.4	1.4	0.925	1.0	0.9

elliptic blending model. The new model was utilized to study the fully developed square duct flow, rotating, and nonrotating channel flow. The numerical results show good agreement with the LES and DNS results.

1.2 Algebraic Heat Flux Model

AHFM is a simplified second-moment form of DHFM, which transports Reynolds heat flux by establishing algebraic equations. Hanjalić et al. (1996), Kenjereš et al. (2005), Otić et al. (2005), and Otić and Grotzbach. (2007) developed and analyzed an implicit algebraic transport equation for the Reynolds heat flux term to close the energy equation. Evaluations and calibrations of AHFM for low-Pr fluids were implemented by Shams et al. (2014), Shams (2018), Shams et al. (2018), and De Santis et al. (2018) and De Santis and Shams (2018). AHFM has been validated in their works by comparison with the DNS data for turbulent flows in forced, mixed, and natural convection of different fluids. The numerical results obtained by AHFM illustrate that temperature, heat flux field, buoyant effects in-plane, backward-facing step, corium pool, rod bundle, etc. are well predicted.

1.3 A two-equation $k_\theta - \varepsilon_\theta$ model for Reynolds heat flux

The $k_\theta - \varepsilon_\theta$ model is a first-order 2-equation model for the calculation of Reynolds heat flux, which can be developed in a way similar to that of a first-order 2-equation $k-\varepsilon$ model for the turbulent transport of momentum formulated. Compared with DHFM and AHFM, the two-equation model has been widely applied in recent years because of its lower calculation cost. To precisely reproduce the heat transfer of low-Pr fluids, extensive contributions of model coefficient and function, wall boundary conditions, and near-wall thermal turbulence effect of a two-equation $k_\theta - \varepsilon_\theta$ model had been made by Nagano and Kim (1988); Nagano and Shimada (1996); Nagano et al. (1997); Nagano (2002), Sommer et al. (1992), and Youssef et al. (1992); and Youssef (2006), Abe et al. (1994), Hattori et al. (1993), Hwang and Lin (1999), Deng et al. (2001), and Karcz and Badur (2005). In recent years, based on previous study, Manservisi and Menghini (2014a); Manservisi and Menghini (2014b); Manservisi and Menghini (2015), Cerroni et al. (2015), Cervone et al. (2020), Chierici et al. (2019), and Da Via et al. (2016); Da Vià and Manservisi (2019); and Da Vià et al. (2020) proposed a two-equation $k_\theta - \varepsilon_\theta$ model suitable for the LBE turbulent heat transfer simulation, and improved new numerical near-wall boundary conditions for turbulence variables. The numerical results obtained by the literature (Manservisi and Menghini, 2014a; Manservisi and Menghini, 2014b; Manservisi and Menghini, 2015; Su et al., 2022) indicate that turbulent heat transfer statistics such as in-plane, tube, backward-facing step, triangular rod bundle, square lattice bare rod bundle, and hexagonal rod bundle of forced convection of LBE are well reproduced based on their $k_\theta - \varepsilon_\theta$ turbulent heat transfer model.

In recent years, the interest in reliable CFD methods used to investigate the turbulent heat transfer of low-Pr fluids in complicated industrial configurations has increased dramatically. Nevertheless, commercial codes are still lacking, except for an AHFM model available on software STAR-CCM+ (Simcenter, 2016). A two-equation $k-\varepsilon$ model utilized to calculate Reynolds stress with a two-equation $k_\theta - \varepsilon_\theta$ model used to calculate Reynolds heat flux is usually called a four-equation $k-\varepsilon-k_\theta-\varepsilon_\theta$ model, which is expected to improve the numerical CFD accuracy of turbulent heat transfer for LBE. However, different turbulence models will have a certain impact on the time-scale transport of a two-equation $k_\theta - \varepsilon_\theta$ model. It is necessary to evaluate the sensitivity of various turbulence models to a two-equation $k_\theta - \varepsilon_\theta$ model.

Thus, in the present study, an improved CFD solver buoyant2eqnFoam, which introduces a two-equation $k_\theta - \varepsilon_\theta$ model to calculate the Reynolds heat flux and can directly call different turbulence models to calculate the Reynolds stress, was first developed based on the solver buoyantSimpleFoam of open-source CFD program OpenFOAM. The fully developed turbulent heat transfer results of LBE inner flow and a bare 19-rod bundle geometry with different Peclet numbers were investigated and

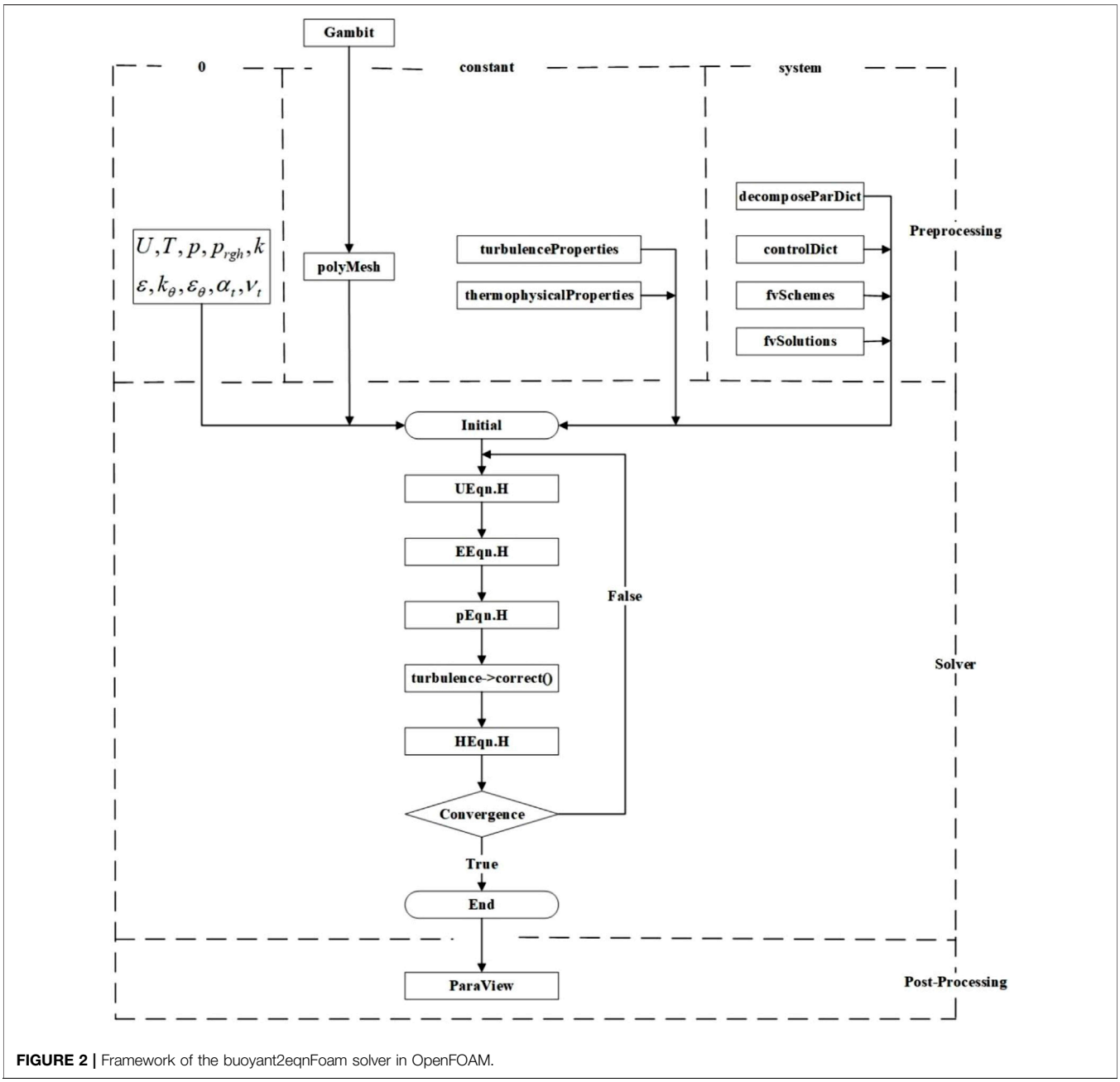

FIGURE 2 | Framework of the buoyant2eqnFoam solver in OpenFOAM.

compared with experimental relations to verify the effectiveness of the solver buoyant2eqnFoam and the numerical algorithm. Finally, the heat transfer sensitivity of different turbulence models to the two-equation $k_\theta - \varepsilon_\theta$ model was presented.

2 MATHEMATICAL MODEL

2.1 Physical Model

Thermal-hydraulic phenomena in a 19-rod bundle geometry are an essential research topic. In the past decades, numerous experimental and simulation researches have been conducted to precisely obtain flow characteristics and heat transfer correlations of coolant (Pacio et al., 2014; Martelli et al., 2017). In the present study, a bare 19-rod bundle with a fully developed turbulent LBE flow is considered. **Figure 1A** displays the cross section of the bare 19-rod bundle. Since the cross-flow in the bare 19-rod bundle is negligible and its construction is symmetrical, one-twelfth of the whole bundle is selected to carry out simulation for the sake of economizing computational cost. The computational domain is sketched in **Figure 1B**, together with the definitions of sub-channels and boundary regions. *Sub*1, *Sub*2, and *Sub*3 are defined as inner sub-channels, while *Sub*4 and *Sub*5 are the edge sub-channel and corner sub-channel, respectively. The more detailed geometric parameters are summarized in **Table 1**, which are consistent with Pacio's experiment (Pacio et al., 2015), except that there are no grid

TABLE 5 | Boundary conditions imposed on each boundary.

Boundary	k	ε	ε_θ	k_θ	U	T
Inlet	cyclic	cyclic	cyclic	cyclic	cyclic	cyclic
Outlet	cyclic	cyclic	cyclic	cyclic	cyclic	cyclic
Symmetry plane	symmetry	symmetry	symmetry	symmetry	symmetry	symmetry
Heated rod	kLowReWallFunction	epsilonWallFunction	zeroGradient	zeroGradient	noSlip	fixedGradient (q_w/λ)
Wall	kLowReWallFunction	epsilonWallFunction	zeroGradient	zeroGradient	noSlip	zeroGradient

spacers in the current study. $D_{h,bun}$ and $D_{h,sub1}$ are the hydraulic diameter of the bundle and hydraulic diameter of *Sub*1, respectively. The length of the whole computational domain is set to 15 $D_{h,bun}$ to eliminate the effect of employing periodic inlet boundary conditions. The flow parameters of LBE are reported in **Table 2**, where $Pe_{bun} = PrU_{bun}D_{h,bun}\rho/\mu$ is the Peclet number of the bundle.

2.2 Conservation Equations

For forced convection, the incompressible RANS equations with constant physical properties and no gravity are considered

$$\frac{\partial u_i}{\partial x_i} = 0 \tag{1}$$

$$\frac{\partial u_i}{\partial t} + u_j\frac{\partial u_i}{\partial x_j} = -\frac{1}{\rho}\frac{\partial P}{\partial x_i} + \frac{\partial}{\partial x_j}\left(\nu\frac{\partial u_i}{\partial x_j}\right) - \frac{\partial}{\partial x_j}\overline{u_i^{'}u_j^{'}} \tag{2}$$

where ν, u_i, and P are the molecular viscosity, Reynolds-averaged velocity, and the so-called average pressure, respectively. To obtain the unknown Reynolds stress $\overline{u'_i u'_j}$, the linear eddy-viscosity model can be adopted as follows:

$$\overline{u'_i u'_j} = -\nu_t\left(\frac{\partial u_i}{\partial x_j} + \frac{\partial u_j}{\partial x_i}\right) + \frac{2k}{3}\delta_{ij} \tag{3}$$

where k and ν_t, both derived from the turbulence model, represent the turbulent kinetic energy and the turbulent viscosity, respectively.

It should be noted that, in OpenFOAM, the energy conservation equation can be expressed in terms of enthalpy (Darwish and Moukalled, 2021):

$$\frac{\partial h}{\partial t} + u_j\frac{\partial h}{\partial x_j} + \frac{\partial K}{\partial t} + u_j\frac{\partial K}{\partial x_j} = \frac{1}{\rho}\frac{\partial P}{\partial t} + \frac{\partial}{\partial x_j}\left((\alpha + \alpha_t)\frac{\partial h}{\partial x_j}\right) \tag{4}$$

where h, $K = |U|^2/2$, α, and α_t are the enthalpy per unit of mass, the kinetic energy per unit of mass, molecular thermal diffusivity, and the turbulent thermal diffusivity, respectively. The unknown α_t needs to be derived from a two-equation $k_\theta - \varepsilon_\theta$ turbulent heat transfer model. After solving **Eq. 4**, the distribution of h can be obtained. Subsequently, the Reynolds-averaged temperature T can be calculated by using the function Thermo.T () coming with OpenFOAM. The derivation of periodic momentum and energy equations in OpenFOAM can be found in the reference (Ge et al., 2017).

2.3 Turbulence Model for Momentum Field

Benefiting from replacing the friction velocity u_τ with Kolmogorov velocity u_ε, the turbulence model proposed by Abe et al. (1994), which can well reproduce the low Reynolds number and near-wall effects of both separated and attached flows, was widely adopted in the calculation of LBE (Manservisi and Menghini, 2014a; Manservisi and Menghini, 2014b; Cerroni et al., 2015; Manservisi and Menghini, 2015; Da Via et al., 2016; Chierici et al., 2019; Da Và and Manservisi, 2019; Cervone et al., 2020; Da Và et al., 2020). However, the Abe $k-\varepsilon$ turbulence model does not exist in the current turbulence model library of OpenFOAM. Therefore, in the current study, the Abe $k-\varepsilon$ turbulence model is compiled into the turbulence model library that comes with OpenFOAM so as to utilize the wall functions of OpenFOAM in this self-compiled turbulence model. In the Abe $k-\varepsilon$ turbulence model, the turbulent viscosity ν_t is computed as follows:

$$\nu_t = C_\mu f_\mu\frac{k^2}{\varepsilon} \tag{5}$$

where C_μ is a constant. f_μ is the model function, defined as follows:

$$f_\mu = \left(1 - \exp\left(-\frac{y^*}{14}\right)\right)^2\left(1 + \frac{5}{R_t^{3/4}}\exp\left(-\left(\frac{R_t}{200}\right)^2\right)\right) \tag{6}$$

$$y^* = \frac{u_\varepsilon\delta}{\nu} \tag{7}$$

where $R_t = k^2/\nu\varepsilon$ and $u_\varepsilon = (\nu\varepsilon)^{1/4}$. Moreover, δ is the distance from the wall. The equations for k and its dissipation ε can be written as follows:

$$\frac{\partial k}{\partial t} + u_j\frac{\partial k}{\partial x_j} = \frac{\partial}{\partial x_j}\left(\left(\nu + \frac{\nu_t}{\sigma_k}\right)\frac{\partial k}{\partial x_j}\right) + P_k - \varepsilon \tag{8}$$

$$P_k = -\overline{u_i^{'}u_j^{'}}\frac{\partial u_i}{\partial x_j} = \nu_t\left(\frac{\partial u_i}{\partial x_j} + \frac{\partial u_j}{\partial x_i}\right)\frac{\partial u_i}{\partial x_j} - \frac{2k\delta_{ij}}{3}\frac{\partial u_i}{\partial x_j} \tag{9}$$

$$\frac{\partial \varepsilon}{\partial t} + u_j\frac{\partial \varepsilon}{\partial x_j} = \frac{\partial}{\partial x_j}\left(\left(\nu + \frac{\nu_t}{\sigma_\varepsilon}\right)\frac{\partial \varepsilon}{\partial x_j}\right) + C_{1\varepsilon}\frac{\varepsilon}{k}P_k - C_{2\varepsilon}f_\varepsilon\frac{\varepsilon^2}{k} \tag{10}$$

$$f_\varepsilon = \left(1 - \exp\left(-\frac{y^*}{3.1}\right)\right)^2\left(1 - 0.3\exp\left(-\frac{R_t^2}{6.5}\right)\right) \tag{11}$$

The model constants utilized in the Abe $k-\varepsilon$ turbulence model are reported in **Table 3**.

2.4 Two-Equation Model for Thermal Field

In the current work, the $k_\theta - \varepsilon_\theta$ turbulent heat transfer model developed and improved by Manservisi and Menghini (2014a), Manservisi and Menghini (2014b), and Manservisi and Menghini (2015), which introduces the average square temperature

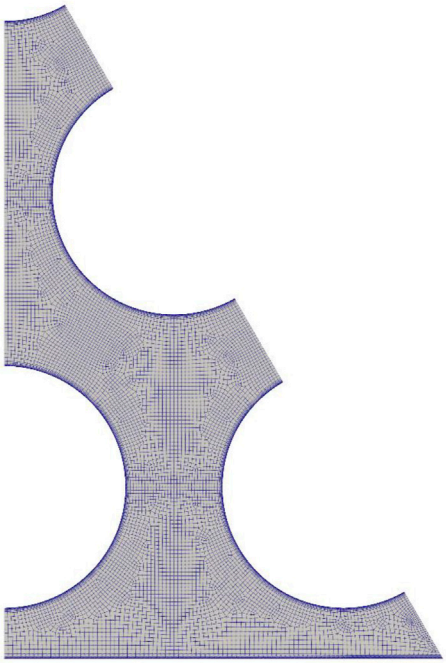

FIGURE 3 | The mesh of computational domain.

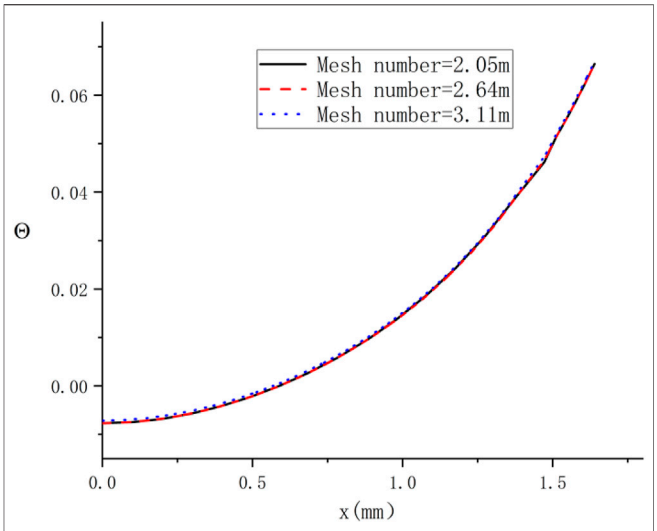

FIGURE 4 | The dimensionless temperature profiles along line ab of the three sets of mesh.

fluctuation k_θ and its dissipation ε_θ in order to well reproduce the near-wall turbulent heat transfer behaviors of LBE having Pr in the range of 0.01–0.03, is adopted to calculate the turbulent thermal diffusivity α_t. In the Manservisi $k_\theta - \varepsilon_\theta$ model, α_t is computed as follows:

$$\alpha_t = C_\theta k \tau_{l\theta} \tag{12}$$

where C_θ is the constant empirical coefficient and $\tau_{l\theta}$ is the local thermal characteristic time, modeled as follows:

$$\tau_{l\theta} = f_{1\theta} B_{1\theta} + f_{2\theta} B_{2\theta} \tag{13}$$

with the appropriate functions set as follows:

$$f_{1\theta} = \left(1 - \exp\left(-\frac{R_\delta}{19\sqrt{Pr}}\right)\right)\left(1 - \exp\left(-\frac{R_\delta}{14}\right)\right) \tag{14}$$

$$B_{1\theta} = 0.9\tau_u = 0.9\frac{k}{\varepsilon} \tag{15}$$

$$f_{2\theta} B_{2\theta} = \tau_u \left(f_{2a\theta}\frac{2R}{R + C_\gamma} + f_{2b\theta}\sqrt{\frac{2R}{Pr}}\ \frac{1.3}{\sqrt{Pr}R_t^{3/4}}\right) \tag{16}$$

$$f_{2a\theta} = f_{1\theta}\exp\left(-\left(\frac{R_t}{500}\right)^2\right) \tag{17}$$

$$f_{2b\theta} = f_{1\theta}\exp\left(-\left(\frac{R_\delta}{200}\right)^2\right) \tag{18}$$

where $R_\delta = \delta\varepsilon^{1/4}/\nu^{3/4}$, $\tau_u = k/\varepsilon$, and $R = \tau_\theta/\tau_u$ with the thermal turbulent characteristic time $\tau_\theta = k_\theta/\varepsilon_\theta$. In addition, $\tau_u = k/\varepsilon$ represents the dynamical turbulent characteristic time. The equations for k_θ and its dissipation ε_θ can be written as follows:

$$\frac{\partial k_\theta}{\partial t} + u_j\frac{\partial k_\theta}{\partial x_j} = \frac{\partial}{\partial x_j}\left(\left(\alpha + \frac{\alpha_t}{\sigma_{k_\theta}}\right)\frac{\partial k_\theta}{\partial x_j}\right) + P_\theta - \varepsilon_\theta \tag{19}$$

$$P_\theta = \alpha_t\left(\frac{\partial T}{\partial x_j}\right)\left(\frac{\partial T}{\partial x_j}\right) \tag{20}$$

$$\frac{\partial \varepsilon_\theta}{\partial t} + u_j\frac{\partial \varepsilon_\theta}{\partial x_j} = \frac{\partial}{\partial x_j}\left(\left(\alpha + \frac{\alpha_t}{\sigma_{\varepsilon_\theta}}\right)\frac{\partial \varepsilon_\theta}{\partial x_j}\right) + \frac{\varepsilon_\theta}{k_\theta}\left(C_{P1}P_\theta - C_{d1}\varepsilon_\theta\right) + \frac{\varepsilon_\theta}{k}\left(C_{P2}P_k - C_{d2}\varepsilon\right) \tag{21}$$

$$C_{d2} = \left(1.9\left(1 - 0.3\exp\left(-\left(\frac{R_t}{6.5}\right)^2\right)\right) - 1\right)\left(1 - \exp\left(-\frac{R_\delta}{5.7}\right)\right)^2 \tag{22}$$

The constant empirical coefficients used in the Manservisi $k_\theta - \varepsilon_\theta$ turbulent heat transfer are reported in **Table 4**.

3 SOLVER AND BOUNDARY CONDITIONS

To calculate the thermal-hydraulic characteristics of LBE, a CFD solver named buoyant2eqnFoam was developed on the OpenFOAM platform having user-friendly programming language features based on the turbulence model and the aforementioned turbulent heat transfer model. The SIMPLE algorithm is adopted to handle pressure–velocity coupling equations and the coupled multigrid iterations technique is utilized for matrix solutions. All calculations were performed using double precision on OpenFOAM and the convergence conditions of residual error are set as follows:

$$\mathrm{Max}\left|\frac{Q^{n+1}}{Q^n} - 1\right| < 10^{-6} \tag{23}$$

TABLE 6 | Correlations of the Nusselt number for triangular lattices.

Investigator	Correlation	*X*	*Pe*
Subbotin	$Nu = 0.58(\frac{2\sqrt{3}}{\pi}X^2 - 1)^{0.55}Pe^{0.45}$	1.1–1.5	80–4000
Mikityuk	$Nu = 0.047(1 - e^{-3.8(X-1)})(Pe^{0.77} + 250)$	1.1–1.95	30–5000
Graber	$Nu = 0.25 + 6.2X + (0.032X - 0.007)Pe^{0.8-0.024X}$	1.2–2.0	150–4000
Mareska	$Nu = 6.66 + 3.126X + 1.184X^2 + 0.0155(\psi Pe)^{0.86}$	1.3–3.0	70–10000

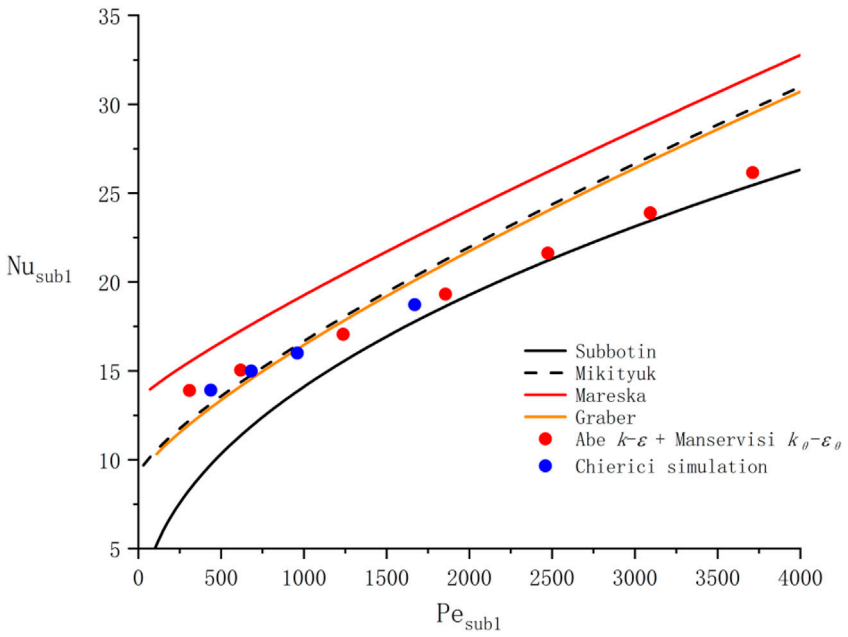

FIGURE 5 | Comparison of the Nusselt number with Chierici simulation and experimental correlations.

where Q stands for u_i, T, P, k_θ, ε_θ, k, and ε. The index i represents the number of iterations. The framework of the buoyant2eqnFoam solver is presented in **Figure 2**. The buoyant2eqnFoam solver mainly includes main-program buoyant2eqnFoam.C, velocity equation **UEqn.H**, energy equation **EEqn.H**, pressure–Poisson equation **pEqn.H**, call function of turbulence model **turbulence- > correct()**, and a two-equation $k_\theta - \varepsilon_\theta$ heat transfer model **HEqn.H**. The boundary condition data, mesh data, physical property data, calculation control, discrete format of each differential operator, algebraic equation solver, and relaxation factor required by buoyant2eqnFoam to perform calculation are included in the 0 folder, constant/polyMesh, constant/thermophysicalProperties, system/controlDict, system/fvSchemes, and system/fvSolutions.

In the computational domain, periodic boundary conditions are set on the region of inlet and outlet, considering the fully developed turbulent inner flow in the bundle. It is worth noting that the energy source term needs to be added to the energy **Eq. 4** in order to apply periodic boundary conditions to temperature variables. The calculation method of energy source term refers to this literature (Ge et al., 2017). For k_θ and ε_θ, the boundary condition zeroGradient is employed on the wall under the uniform heat flux condition, according to the research of Deng et al. (2001). The boundary conditions imposed on each boundary are summarized in **Table 5**. Since the wall functions kLowReWallFunction for k and epsilonWallFunction for ε are both suitable for the low–Reynolds number turbulence model and can well reproduce the near-wall turbulence behaviors when y^+ is very low (Darwish and Moukalled, 2021), they are employed in this study. Given that there are no wall functions accessible for k_θ and ε_θ in OpenFOAM, y^+ must be less than or equal to 1 in order to accurately reproduce the thermal turbulent behaviors near the wall (Manservisi and Menghini, 2014a).

4 RESULTS AND DISCUSSIONS

4.1 Mesh Independence Analysis

In this section, the buoyant2eqnFoam, which utilizes the Abe $k - \varepsilon$ turbulence model for turbulence fields and uses the Manservisi $k_\theta - \varepsilon_\theta$ model for thermal fields, is employed to investigate the thermohydraulic characteristics of LBE inner flow in the bare 19-rod bundle in a wide range of Pe_{bun}. As shown in **Figure 3**, the

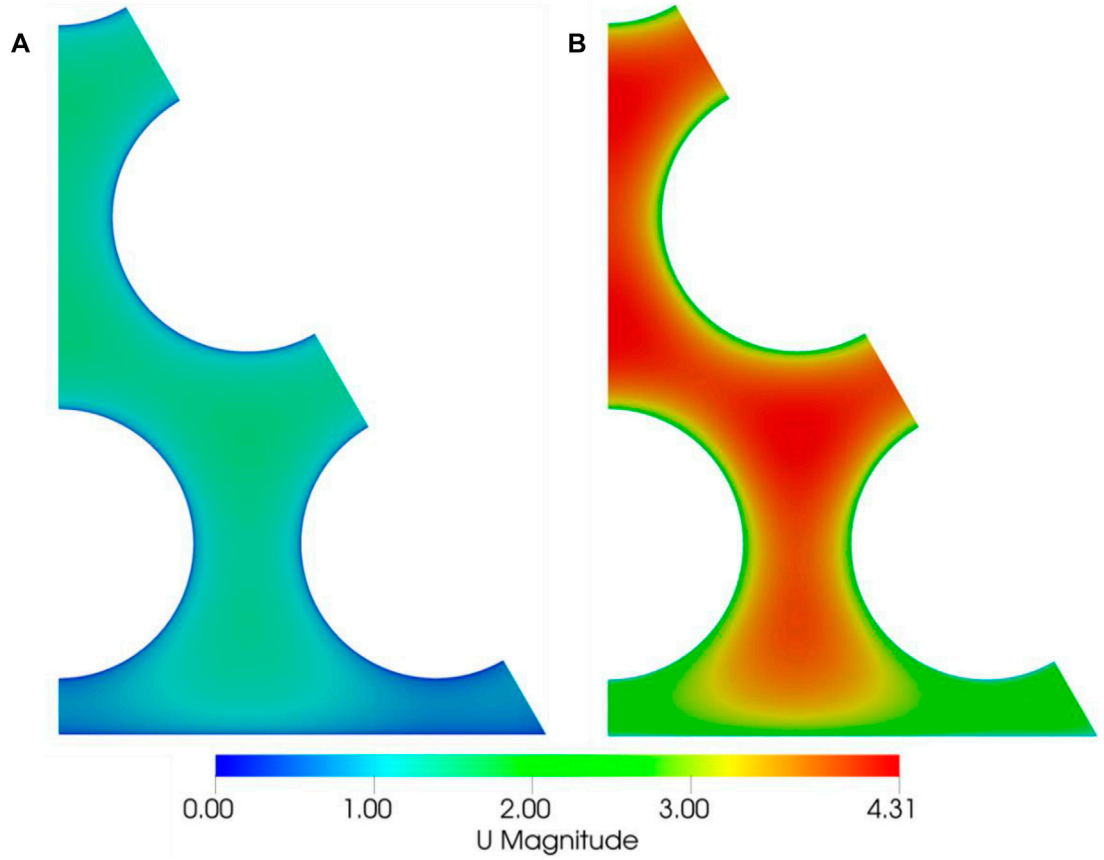

FIGURE 6 | Profiles of velocity magnitude on a computational domain. **(A)** Pe_{bun} = 500 and **(B)** Pe_{bun} = 1500.

TABLE 7 | Mean velocity of each sub-channel.

Pe_{bun}	U_b (m/s)				
	Sub1	**Sub2**	**Sub3**	**Sub4**	**Sub5**
500	1.255	1.254	1.250	1.025	0.665
1500	3.754	3.753	3.737	3.085	2.044
3000	7.498	7.495	7.462	6.179	4.146

computational domain was discretized by GAMBIT unstructured meshes (tetrahedral and hexahedral mesh blending). The first layer grid was set with a height of 0.001 mm in order to satisfy the criterion of the low–Reynolds number turbulence model for $y^+ \leq 1$. A total of 15 layers of boundary grids with a height ratio of 1.3 were designed.

Three sets of mesh with different mesh numbers of 2.05 million, 2.64 million, and 3.11 million were adopted to analyze the mesh sensitivity. The dimensionless coolant temperature Θ is defined as follows:

$$\Theta = \frac{(T - T_{b,bun})\lambda}{D_{h,bun} \cdot q_w} \tag{24}$$

where $T_{b,bun}$ is the bulk temperature of the computational domain. The dimensionless temperature profiles along line ab (shown in **Figure 1B**) of three sets of mesh are displayed in **Figure 4** under Pe_{bun} = 1500. It is evident that the difference in the dimensionless temperature profile between three sets of mesh is negligible. Consequently, the mesh with a mesh number of 2.05 million is selected, taking the calculation cost into consideration.

4.2 Solver Verification

The fully developed turbulent heat transfer characteristics of LBE inner flow in the bare 19-rod bundle were studied by Chierici et al. (2019), using a four-equation model in logarithmic specific dissipation form $k - \Omega - k_\theta - \Omega_\theta$, which was developed based on the Abe $k - \varepsilon$ turbulence model and the Manservisi $k_\theta - \varepsilon_\theta$ model. The numerical results of Chierici et al. (2019) can provide some reference for developing a CFD solver of LBE turbulent heat transfer. Therefore, the simulation results of Chierici et al. (2019) and some experimental data are picked for comparison to verify the validity of the solver buoyant2eqnFoam. The Nusselt number is selected for comparison since it is a critical parameter in engineering. **Table 6** presents some Nusselt number experimental correlations of the triangular

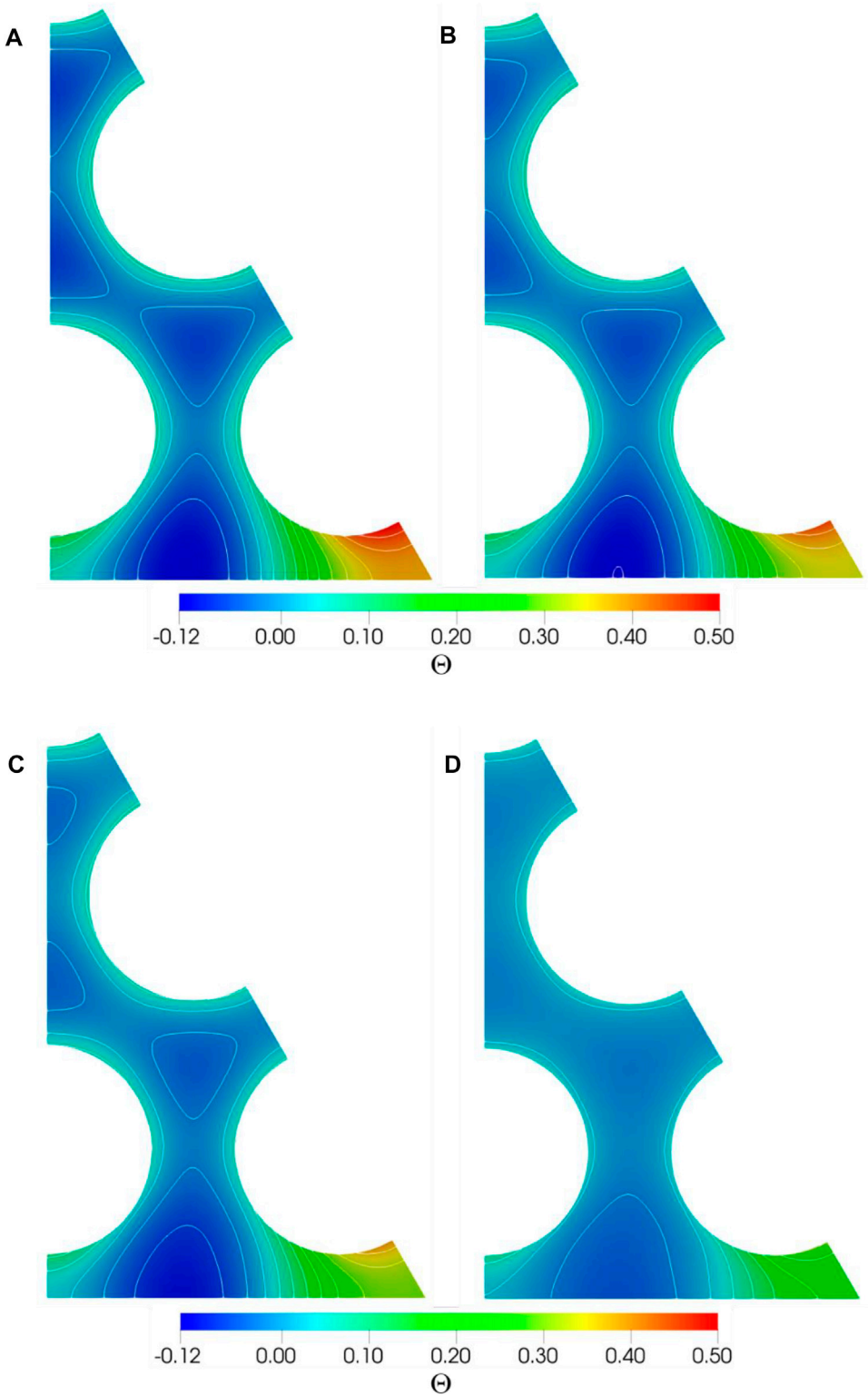

FIGURE 7 | Profiles of dimensionless temperature on computational domain. **(A)** Pe_{bun} = 250; **(B)** Pe_{bun} = 500; **(C)** Pe_{bun} = 1000; and **(D)** Pe_{bun} = 3000.

rod bundle channel cooled by liquid metal, obtained by Subbotin et al. (1965), Mikityuk (2009), Gräber and Rieger (1972), and Mareska and Dwyer (1964), respectively.

Because these reported correlations were developed for triangular lattices, the Nusselt number of inner sub-channel *Sub*1 is picked for comparison. The Nu_{sub1} is calculated as follows:

TABLE 8 | Results of hot spot factor for sub-channels.

Pe_{bun}	Sub1		Sub2		Sub3		Sub4		Sub5	
	Pe_{sub}	ϕ	Pe_{sub}	ϕ	Pe_{sub}	ϕ	Pe_{sub}	ϕ	Pe_{sub}	ϕ
250	309	1.058	309	1.063	309	1.091	215	5.201	127	8.154
500	619	1.064	619	1.086	619	1.080	431	5.280	253	7.923
1000	1237	1.070	1237	1.101	1237	1.101	861	5.391	506	7.762
1500	1856	1.074	1856	1.111	1856	1.112	1292	5.488	760	7.583
2000	2474	1.075	2474	1.105	2474	1.110	1722	5.567	1013	7.280
2500	3093	1.074	3093	1.107	3093	1.110	2153	5.670	1266	7.000
3000	3712	1.074	3712	1.103	3712	1.107	2583	5.700	1519	6.667

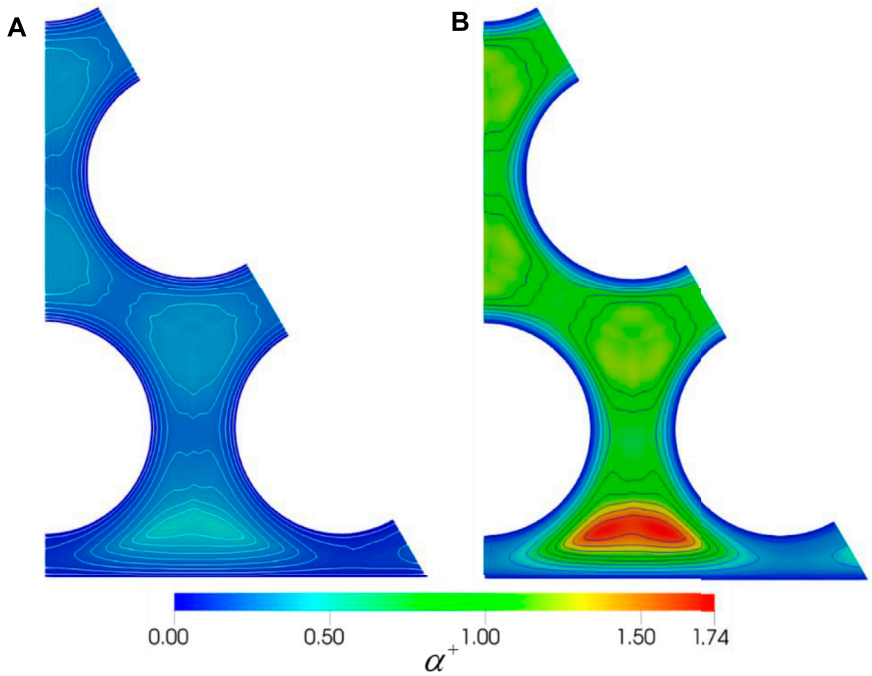

FIGURE 8 | Dimensionless thermal diffusivity distribution on a computational domain. **(A)** Pe_{bun} = 500 and **(B)** Pe_{bun} = 1500.

$$Nu_{sub1} = \frac{q_w D_{h,sub1}}{\lambda\left(T_{w,sub1} - T_{b,sub1}\right)} \tag{25}$$

where $T_{w,sub1}$ and $T_{b,sub1}$ are the mean wall temperature and mean coolant temperature of *Sub*1, respectively. Correspondingly, $Pe_{sub1} = PrU_{sub1}D_{h,sub1}\rho/\mu$ is the Peclet number of the inner sub-channel *Sub*1. **Figure 5** displays the comparison of the Nusselt number with Chierici simulation and experimental correlations. From this figure, it can be clearly observed that the tendency of Nu_{sub1} is consistent with the simulation results of Chierici and shows good agreements with experimental data in a specific Peclet number range, illustrating that the rational prediction of LBE turbulent heat transfer can be obtained by the self-compiled solver buoyant2eqnFoam which can use the Abe $k-\varepsilon$ turbulence model with wall functions for turbulence fields and the Manservisi $k_\theta - \varepsilon_\theta$ model with zero-gradient boundary for thermal fields.

4.3 Flow and Heat Transfer Analysis

4.3.1 Velocity Field

The profiles of velocity magnitude on the computational domain of the bare 19-rod bundle are reported in **Figure 6**, with Pe_{bun} = 500 and Pe_{bun} = 1500, respectively. It is obvious that the mean velocity in the inner sub-channels is higher than that in the edge sub-channel *Sub*4 and corner sub-channel *Sub*5 because the hydraulic diameter of inner sub-channels is relatively higher, resulting in much lower flow resistance. For the same reason, the average velocity of *Sub*5 is much lower compared with that of other sub-channels, as summarized in **Table 7**.

4.3.2 Dimensionless Temperature and Hot Spot Factor Distributions

Figure 7 shows the distribution of dimensionless temperature from where it can be seen that the maximum temperature is located in the corner sub-channel *Sub*5, which is mainly due to the lower mean coolant velocity of the corner sub-channel

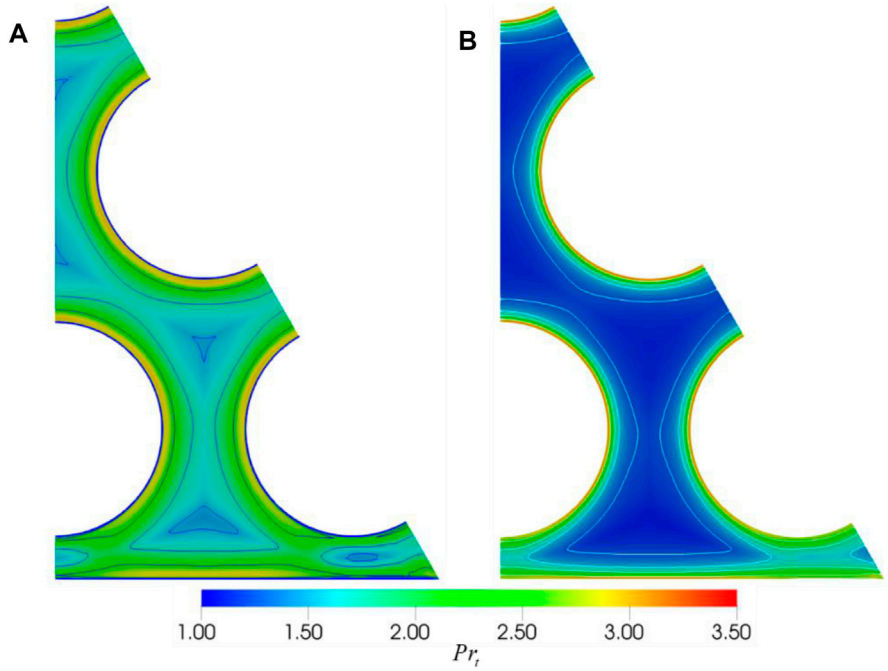

FIGURE 9 | Turbulent Prandtl number distribution on a computational domain. **(A)** Pe_{bun} = 1000 and **(B)** Pe_{bun} = 3000.

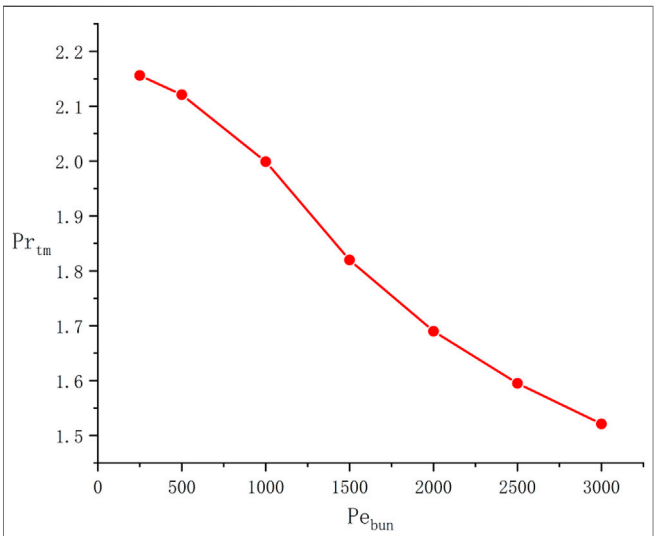

FIGURE 10 | Mean turbulent Prandtl number of the bare 19-rod bundle.

*Sub*5. Owing to the larger hydraulic diameter of the edge sub-channel *Sub*4 and the adiabatic boundary condition applied on the outer casing wall, the coolant with the lowest temperature can be found in the area of the edge sub-channel *Sub*4 near the outer casing wall. Comparing the four cases reported in **Figure 7**, it can be found that the convective heat transfer of the coolant in each sub-channel is enhanced as the Reynolds number increases, leading to the decrease of maximum temperature and the increase of bulk coolant temperature.

The dimensionless hot spot factor characterizing the inhomogeneity of wall temperature is defined as follows:

$$\phi = \frac{\theta_{wmax,sub} - \theta_{b,sub}}{\theta_{wb,sub} - \theta_{b,sub}} \tag{26}$$

where $\theta_{wmax,sub}$, $\theta_{b,sub}$, and $\theta_{wb,sub}$ are the maximum wall temperature of the sub-channel, the bulk temperature of the sub-channel, and the mean wall temperature of the sub-channel, respectively. As ϕ = 1, it means that the maximum wall temperature of the sub-channel is equal to the average wall temperature. The calculated results of the hot spot factor of each sub-channel are summarized in **Table 8**, from where it can be deduced that the wall temperature distribution of the inner sub-channel *Sub*1 is the most homogeneous. On the other hand, due to the coexistence of the heated rod wall and adiabatic wall in the edge sub-channel *Sub*4 and the corner sub-channel *Sub*5, the phenomenon of nonhomogeneous wall temperature distribution in these channels is more dramatic.

4.3.3 Dimensionless Thermal Diffusivity Distribution

To analyze the dependence of heat transfer on Pe_{bun}, defining the dimensionless thermal diffusivity α^+ as follows:

$$\alpha^+ = \frac{\alpha_t}{\alpha} \tag{27}$$

α^+ is the ratio between turbulent thermal diffusivity and molecular thermal diffusivity. **Figure 8** reports the calculated dimensionless thermal diffusivity distribution on the computational domain for Pe_{bun} = 500 and Pe_{bun} = 1500. From this figure, it can be clearly seen that the α^+ in the center of each sub-channel is higher than that near the wall,

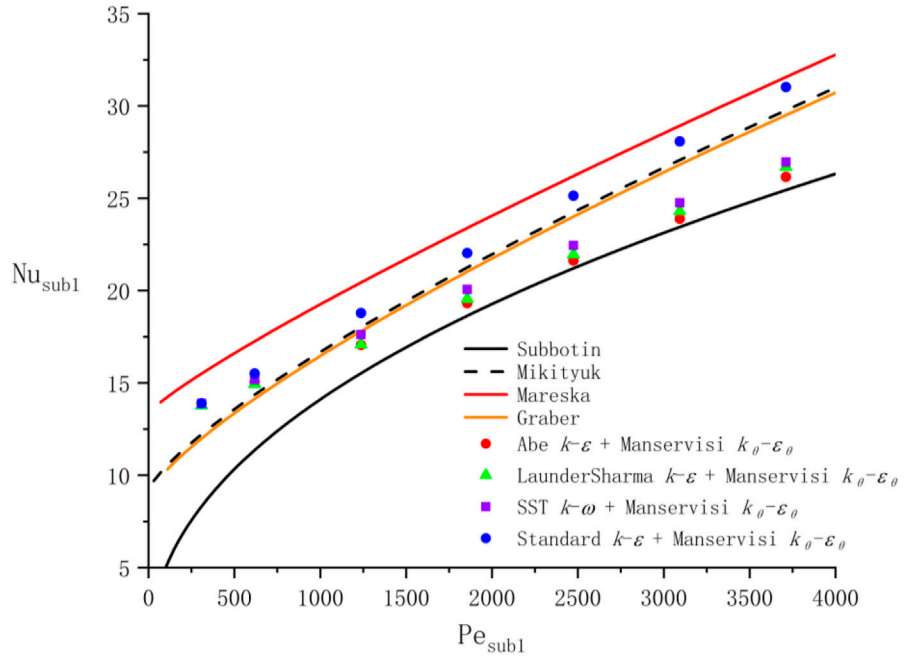

FIGURE 11 | Comparison of Nu_{sub1} calculated by different turbulence models.

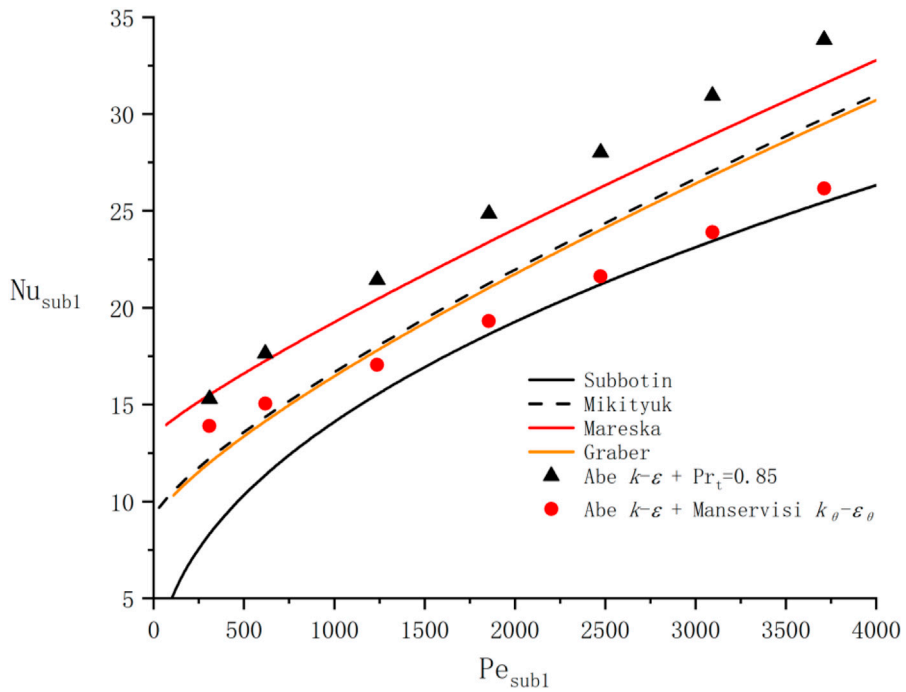

FIGURE 12 | Comparison of Nu_{sub1} calculated by different turbulent heat transfer models.

where the heat is mainly derived by the molecular heat conduction. Moreover, in the center of the edge sub-channel *Sub*4, the maximum dimensionless thermal diffusivity can be found, indicating that the thermal diffusion caused by turbulent flow reaches its peak in this region. It should be mentioned that when Pe_{bun} = 500, the α^+ in the whole computational domain is less than 1, suggesting that the molecular heat conduction affects the entire computational domain dominantly. In addition, with

the increase of Pe_{bun}, a region where turbulent thermal diffusion is stronger than molecular heat conduction begins to appear.

4.3.4 Turbulent Prandtl Number Distribution

The distribution of Pr_t in the computational domain is plotted against different Pe_{bun} numbers and displayed in **Figure 9**. As revealed in this figure, the Pr_t is higher in the district close to the wall of the heated rod. Moreover, the overall turbulent Prandtl number in the computational domain decreases with the increase of Pe_{bun}. In particular, the turbulent Prandtl number in the turbulent core region decreases significantly with the increase of Pe_{bun}.

The mean turbulent Prandtl number Pr_{tm} of the computational domain is defined as follows:

$$Pr_{tm} = \frac{\int_A Pr_t dA}{\int_A dA} \tag{28}$$

In order to investigate the influence of Pe_{bun} on the Pr_{tm}, **Figure 10** plots the Pr_{tm} against different Pe_{bun}. From this figure, it can be concluded that the Pr_{tm} tends to decrease as the Pe_{bun} increases. However, the rate of decline also decreases with the increase of Pe_{bun}. Furthermore, the Pr_{tm} of the computational domain is higher than 1, suggesting that the analogy about Pr_t = 0.85 is not appropriate in such low-Pr fluids.

4.4 Assessment of Different Turbulence Models and Turbulent Heat Transfer Models

To analyze the effect of the turbulence model on the simulation of heat transfer, in this sub-section, various turbulence models of OpenFOAM are also employed in buoyant2eqnFoam, including standard $k-\varepsilon$ (Launder and Spalding, 1972; 1983), SST $k-\omega$ (Menter and Esch, 2001; Menter et al., 2003; Hellsten, 2012), and LaunderSharma $k-\varepsilon$ (Launder and Sharma, 1974). The specific definitions of these turbulence models can be found in the literature (Launder and Spalding, 1972; Launder and Sharma, 1974; Launder and Spalding, 1983; Menter and Esch, 2001; Menter et al., 2003; Hellsten, 2012). A comparison of Nu_{sub1} calculated by different turbulence models with heat transfer experimental correlations is displayed in **Figure 11**. As demonstrated in this figure, the Nu_{sub1} calculated by four turbulence models is pretty close when $Pe_{sub1} < 1000$, mainly because the molecular heat conduction is dominant in this Peclet number range. It should be noted, however, that the deviations of Nu_{sub1} obtained by each turbulence model gradually increase as the Peclet number grows. As indicated in **Figure 11**, all Nu_{sub1} predicted by the standard $k-\varepsilon$ turbulence model is located between Mareska and Mikityuk correlations. However, for Abe $k-\varepsilon$, LaunderSharma $k-\varepsilon$, and SST $k-\omega$, the calculated Nu_{sub1} lies between the Graber and Subbotin correlations when $Pe_{sub1} > 1000$. Although the Nu_{sub1} results obtained by Abe $k-\varepsilon$, LaunderSharma $k-\varepsilon$, and SST $k-\omega$ are very similar, in general, Abe $k-\varepsilon$ is the most conservative. In addition, the maximum deviation of the Nusselt number obtained by the Abe $k-\varepsilon$ and the standard $k-\varepsilon$ is close to 19%. It is worth mentioning that due to the significant deviation between the various Nusselt number experimental correlations, the quality of these turbulence models cannot be evaluated. Therefore, great care and caution should be exercised when selecting a turbulence model in simulation. More precise experimental and analytical studies are required in the future to identify the thermohydraulic characteristics of heavy liquid metals like LBE.

Moreover, the Nu_{sub1} calculated by the Manservisi $k_\theta-\varepsilon_\theta$ model and the Pr_t = 0.85 model is reported in **Figure 12**. It is evident that compared with the experimental correlations plotted in **Figure 12**, the Nu_{sub1} obtained by the Pr_t = 0.85 heat transfer model is higher under almost all Peclet numbers. Oppositely, the Manservisi $k_\theta-\varepsilon_\theta$ heat transfer model provides the more conservative results of Nu_{sub1}.

5 CONCLUSION

In the current study, the Abe $k-\varepsilon$ turbulence model was compiled into the turbulence model library coming with OpenFOAM. A CFD solver buoyant2eqnFoam, which introduces the Manservisi $k_\theta-\varepsilon_\theta$ turbulent heat transfer model, was developed. Subsequently, the Abe $k-\varepsilon$ turbulence model with wall functions and Manservisi $k_\theta-\varepsilon_\theta$ turbulent heat transfer model with zero-gradient boundary were employed to analyze the thermohydraulic characteristics of LBE inner flow in the bare 19-rod bundle. In addition, the influence of the turbulence model on the prediction of turbulent heat transfer was investigated by employing various turbulence models in the self-compiled solver buoyant2eqnFoam, including Abe $k-\varepsilon$, standard $k-\varepsilon$, SST $k-\omega$, and LaunderSharma $k-\varepsilon$. Based on the aforementioned discussions, conclusions obtained from the present work can be summarized as follows:

1) The Nusselt numbers obtained by the self-compiled solver buoyant2eqnFoam are in good agreement with experimental correlations and Chierici simulation research, indicating the validity and reliability of the self-compiled solver.
2) In the bare 19-rod bundle with P/D = 1.4, the flow resistance of the corner sub-channel is higher than that of other sub-channels due to the smaller hydraulic diameter, leading to the appearance of higher temperature distribution and larger hot spot factor in this region.
3) Although the turbulent Prandtl number of LBE inner flow in the bare 19-rod bundle will decrease as the Peclet number increases, the overall turbulent Prandtl number is higher than 0.85, revealing that the Reynolds-analogy hypothesis about Pr_t = 0.85 is not appropriate for low-Pr number fluids like LBE.
4) The turbulence model has a considerable influence on the calculation of turbulent heat transfer of low–Pr number fluids in the high Peclet number range, suggesting that it should be prudent and rigorous when picking a turbulence model in the simulations. Moreover, compared with the $k_\theta-\varepsilon_\theta$ turbulent heat transfer model, the Reynolds-analogy hypothesis about Pr_t = 0.85 may give the much higher Nusselt numbers in the simulation of low–Pr number fluids.

The applicability of the solver developed in the present study for the more complicated geometry like fuel assembly with grid spacer or wire-wrapped configurations requires further verification.

DATA AVAILABILITY STATEMENT

The original contributions presented in the study are included in the article/supplementary material, further inquiries can be directed to the corresponding authors.

AUTHOR CONTRIBUTIONS

XL: concept, research, writing, editing, code, and data processing; XS: modification, concept, research, and code; LG: fund, project management, concept, and research; LZ: editing and research; and XS: editing and research.

FUNDING

This study was supported by the Research on key technology and safety verification of primary circuit, Grant No. 2020YFB1902104; the Experimental study on thermal hydraulics of fuel rod bundle, Grant No. Y828020XZ0; and the National Natural Science Foundation of China, Grant No.12122512.

REFERENCES

Abe, K., Kondoh, T., and Nagano, Y. (1994). A New Turbulence Model for Predicting Fluid Flow and Heat Transfer in Separating and Reattaching Flows-I. Flow Field Calculations. *Int. J. Heat Mass Transf.* 37 (1), 139–151. doi:10.1016/0017-9310(94)90168-6

Abram, T., and Ion, S. (2008). Generation-IV Nuclear Power: A Review of the State of the Science. *Energy Policy* 36 (12), 4323–4330. doi:10.1016/j.enpol.2008.09.059

Carteciano, L., Dorr, B., Grötzbach, G., Olbrich, W., and Jin, X. J. F. (2001). Two- and Three-Dimensional Thermal and Fluid-Dynamical Analysis of the Complete MEGAPIE-Module with the Computer Code. *FLUTAN* 6653, 443–458.

Carteciano, L. J. H. (1995). Analysis of a Turbulence Model for Buoyant Flows Implemented in the 3d Thermal-Hydraulic Computer Code FLUTAN and Comparison with the Standard Kε-Σt Model. *Turbulence* 1.

Carteciano, L. N., and Grötzbach, G. (2003). *Validation of Turbulence Models in the Computer Code FLUTAN for a Free Hot Sodium Jet in Different Buoyancy Flow Regimes*. ETDEWEB.

Carteciano, L., Weinberg, D., and Müller, U. (1997). "Development and Analysis of a Turbulence Model for Buoyant Flows," in Proc. of the 4th World Conf. on Experimental Heat Transfer, Fluid Mechanics and Thermodynamics, Bruxelles, Belgium, 2–6. June: Citeseer).

Cerroni, D., Da Via, R., Manservisi, S., Menghini, F., Pozzetti, G., and Scardovelli, R. (2015). Numerical Validation of a κ-ω-κθ-ωθ Heat Transfer Turbulence Model for Heavy Liquid Metals. *J. Phys. Conf. Ser.* 655 (1), 012046. IOP Publishing). doi:10.1088/1742-6596/655/1/012046

Cervone, A., Chierici, A., Chirco, L., Da Vià, R., Giovacchini, V., and Manservisi, S. (2020). CFD Simulation of Turbulent Flows over Wire-Wrapped Nuclear Reactor Bundles Using Immersed Boundary Method. *J. Phys. Conf. Ser.* 1599 (1), 012022. IOP Publishing). doi:10.1088/1742-6596/1599/1/012022

Cheng, X., and Tak, N.-I. (2006). Investigation on Turbulent Heat Transfer to Lead-Bismuth Eutectic Flows in Circular Tubes for Nuclear Applications. *Nucl. Eng. Des.* 236 (4), 385–393. doi:10.1016/j.nucengdes.2005.09.006

Chierici, A., Chirco, L., Da Vià, R., and Manservisi, S. (2019). Numerical Simulation of a Turbulent Lead Bismuth Eutectic Flow inside a 19 Pin Nuclear Reactor Bundle with a Four Logarithmic Parameter Turbulence Model. *J. Phys. Conf. Ser.* 1224 (1), 012030. IOP Publishing). doi:10.1088/1742-6596/1224/1/012030

Da Vià, R., Giovacchini, V., and Manservisi, S. (2020). A Logarithmic Turbulent Heat Transfer Model in Applications with Liquid Metals for Pr= 0.01–0.025. *Appl. Sci.* 10 (12), 4337. doi:10.3390/app10124337

Da Vià, R., Manservisi, S., and Menghini, F. (2016). A K-Ω-Kθ-Ωθ Four Parameter Logarithmic Turbulence Model for Liquid Metals. *Int. J. Heat Mass Transf.* 101, 1030–1041. doi:10.1016/j.ijheatmasstransfer.2016.05.084

Da Vià, R., and Manservisi, S. (2019). Numerical Simulation of Forced and Mixed Convection Turbulent Liquid Sodium Flow over a Vertical Backward Facing Step with a Four Parameter Turbulence Model. *Int. J. Heat Mass Transf.* 135, 591–603. doi:10.1016/j.ijheatmasstransfer.2019.01.129

Darwish, M., and Moukalled, F. (2021). *The Finite Volume Method in Computational Fluid Dynamics: An Advanced Introduction with OpenFOAM® and Matlab®*. Springer.

De Santis, A., and Shams, A. (2018). Application of an Algebraic Turbulent Heat Flux Model to a Backward Facing Step Flow at Low Prandtl Number. *Ann. Nucl. Energy* 117, 32–44. doi:10.1016/j.anucene.2018.03.016

De Santis, D., De Santis, A., Shams, A., and Kwiatkowski, T. (2018). The Influence of Low Prandtl Numbers on the Turbulent Mixed Convection in an Horizontal Channel Flow: DNS and Assessment of RANS Turbulence Models. *Int. J. Heat Mass Transf.* 127, 345–358. doi:10.1016/j.ijheatmasstransfer.2018.07.150

Deng, B., Wu, W., and Xi, S. (2001). A Near-Wall Two-Equation Heat Transfer Model for Wall Turbulent Flows. *Int. J. Heat Mass Transf.* 44 (4), 691–698. doi:10.1016/s0017-9310(00)00131-9

Ge, Z., Liu, J., Zhao, P., Nie, X., and Ye, M. (2017). Investigation on the Applicability of Turbulent-Prandtl-Number Models in Bare Rod Bundles for Heavy Liquid Metals. *Nucl. Eng. Des.* 314, 198–206. doi:10.1016/j.nucengdes.2017.01.032

Gräber, H., and Rieger, M. J. A. (1972). Experimentelle Untersuchung des Wärmeübergangs an Flüssigmetalle (NaK) in parallel durchströmten Rohrbündeln bei konstanter und exponentieller Wärmeflussdichteverteilung. *Atomkernenergie (ATKE) Bd.* 19 23-40.

Gu, L., and Su, X. (2021). Latest Research Progress for LBE Coolant Reactor of China Initiative Accelerator Driven System Project. *Front. Energy* 15 (4), 810–831. doi:10.1007/s11708-021-0760-1

Hanjalić, K., Kenjereš, S., and Durst, F. (1996). Natural Convection in Partitioned Two-Dimensional Enclosures at Higher Rayleigh Numbers. *Int. J. Heat Mass Transf.* 39 (7), 1407–1427.

Hattori, H., Nagano, Y., and Tagawa, M. (1993). Analysis of Turbulent Heat Transfer under Various Thermal Conditions with Two-Equation Models. *In Engineering Turbulence Modelling and Experiments*, 43–52. Elsevier

He, S., Wang, M., Zhang, J., Tian, W., Qiu, S., Su, G. H., et al. (2021). Numerical Simulation of Three-Dimensional Flow and Heat Transfer Characteristics of Liquid Lead-Bismuth. *Nucl. Eng. Technol.* 53 (6), 1834–1845. doi:10.1016/j.net.2020.12.025

Hellsten, A. (2012). "Some Improvements in Menter's K-Omega SST Turbulence Model," in 29th AIAA, Fluid Dynamics Conference, 2554.

Hwang, C. B., and Lin, C. A. (1999). A Low Reynolds Number Two-Equation Model to Predict Thermal Fields. *Int. J. Heat Mass Transf.* 42 (17), 3217–3230. doi:10.1016/s0017-9310(98)00382-2

Karcz, M., and Badur, J. (2005). An Alternative Two-Equation Turbulent Heat Diffusivity Closure. *Int. J. Heat Mass Transf.* 48 (10), 2013–2022. doi:10.1016/j.ijheatmasstransfer.2004.12.006

Kawamura, H., Abe, H., Matsuo, Y., and Flow, F. (1999). DNS of Turbulent Heat Transfer in Channel Flow with Respect to Reynolds and Prandtl Number Effects. *Int. J. Heat Fluid Flow* 20 (3), 196–207. doi:10.1016/s0142-727x(99)00014-4

Kenjereš, S., Gunarjo, S., and Hanjalić, K. (2005). Contribution to Elliptic Relaxation Modelling of Turbulent Natural and Mixed Convection. *Int. J. Heat Fluid Flow* 26 (4), 569–586.

Launder, B. E., and Sharma, B. I. (1974). Application of the Energy-Dissipation Model of Turbulence to the Calculation of Flow Near a Spinning Disc. *Lett. Heat Mass Transf.* 1 (2), 131–137. doi:10.1016/0094-4548(74)90150-7

Launder, B. E., and Spalding, D. B. (1972). *Lectures in Mathematical Models of Turbulence*. Academic Press.

Launder, B. E., and Spalding, D. B. (1983). "The Numerical Computation of Turbulent Flows," in *Numerical Prediction of Flow, Heat Transfer, Turbulence and Combustion* (Elsevier), 96–116. doi:10.1016/b978-0-08-030937-8.50016-7

Manservisi, S., and Menghini, F. (2014a). A CFD Four Parameter Heat Transfer Turbulence Model for Engineering Applications in Heavy Liquid Metals. *Int. J. Heat Mass Transf.* 69, 312–326. doi:10.1016/j.ijheatmasstransfer.2013.10.017

Manservisi, S., and Menghini, F. (2015). CFD Simulations in Heavy Liquid Metal Flows for Square Lattice Bare Rod Bundle Geometries with a Four Parameter Heat Transfer Turbulence Model. *Nucl. Eng. Des.* 295, 251–260. doi:10.1016/j.nucengdes.2015.10.006

Manservisi, S., and Menghini, F. (2014b). Triangular Rod Bundle Simulations of a CFD κ-ϵ-κ-ϵ Heat Transfer Turbulence Model for Heavy Liquid Metals. *Nucl. Eng. Des.* 273, 251–270. doi:10.1016/j.nucengdes.2014.03.022

Mareska, M. W., and Dwyer, O. E. (1964). Heat Transfer in a Mercury Flow along Bundles of Cylindrical Rods. *J. Heat. Transf.* 86 (2), 180–186.)

Martelli, D., Marinari, R., Barone, G., Di Piazza, I., and Tarantino, M. (2017). CFD Thermo-Hydraulic Analysis of the CIRCE Fuel Bundle. *Ann. Nucl. Energy* 103, 294–305. doi:10.1016/j.anucene.2017.01.031

Menter, F., and Esch, T. (2001). "Elements of Industrial Heat Transfer Predictions," in 16th Brazilian Congress of Mechanical Engineering (COBEM), 650.

Menter, F. R., Kuntz, M., and Langtry, R. J. T. (2003). Ten Years of Industrial Experience with the SST Turbulence Model. *Heat Mass Transf.* 4 (1), 625–632.

Mikityuk, K. (2009). Heat Transfer to Liquid Metal: Review of Data and Correlations for Tube Bundles. *Nucl. Eng. Des.* 239 (4), 680–687. doi:10.1016/j.nucengdes.2008.12.014

Nagano, Y., Hattori, H., and Abe, K. (1997). Modeling the Turbulent Heat and Momentum Transfer in Flows under Different Thermal Conditions. *Fluid Dyn. Res.* 20 (1-6), 127–142. doi:10.1016/s0169-5983(96)00049-4

Nagano, Y., and Kim, C. (1988). A Two-Equation Model for Heat Transport in Wall Turbulent Shear Flows. *J. Heat. Transf.* 110 (3), 583–589. doi:10.1115/1.3250532

Nagano, Y. (2002). *Modelling Heat Transfer in Near-Wall Flows*, 188–247.

Nagano, Y., and Shimada, M. (1996). Development of a Two-equation Heat Transfer Model Based on Direct Simulations of Turbulent Flows with Different Prandtl Numbers. *Phys. Fluids* 8 (12), 3379–3402. doi:10.1063/1.869124

Otić, I., and Grötzbach, G. (2007). Turbulent Heat Flux and Temperature Variance Dissipation Rate in Natural Convection in Lead-Bismuth. *Nucl. Sci. Eng.* 155 (3), 489–496.

Otić, I., Grötzbach, G., and Wörner, M. (2005). Analysis and Modelling of the Temperature Variance Equation in Turbulent Natural Convection for Low-Prandtl-Number Fluids. *J. Fluid Mech.* 525, 237–261.

Pacio, J., Daubner, M., Fellmoser, F., Litfin, K., Marocco, L., Stieglitz, R., et al. (2014). Heavy-liquid Metal Heat Transfer Experiment in a 19-rod Bundle with Grid Spacers. *Nucl. Eng. Des.* 273, 33–46. doi:10.1016/j.nucengdes.2014.02.020

Pacio, J., Litfin, K., Batta, A., Viellieber, M., Class, A., Doolaard, H., et al. (2015). Heat Transfer to Liquid Metals in a Hexagonal Rod Bundle with Grid Spacers: Experimental and Simulation Results. *Nucl. Eng. Des.* 290, 27–39. doi:10.1016/j.nucengdes.2014.11.001

Pacio, J., Wetzel, T., Doolaard, H., Roelofs, F., and Van Tichelen, K. (2017). Thermal-hydraulic Study of the LBE-Cooled Fuel Assembly in the MYRRHA Reactor: Experiments and Simulations. *Nucl. Eng. Des.* 312, 327–337. doi:10.1016/j.nucengdes.2016.08.023

Shams, A., Mikuž, B., and Roelofs, F. (2018). Numerical Prediction of Flow and Heat Transfer in a Loosely Spaced Bare Rod Bundle. *Int. J. Heat Fluid Flow* 73, 42–62. doi:10.1016/j.ijheatfluidflow.2018.07.006

Shams, A., Roelofs, F., Baglietto, E., Lardeau, S., and Kenjeres, S. (2014). Assessment and Calibration of an Algebraic Turbulent Heat Flux Model for Low-Prandtl Fluids. *Int. J. Heat Mass Transf.* 79, 589–601. doi:10.1016/j.ijheatmasstransfer.2014.08.018

Shams, A. (2018). Towards the Accurate Numerical Prediction of Thermal Hydraulic Phenomena in Corium Pools. *Ann. Nucl. Energy* 117, 234–246. doi:10.1016/j.anucene.2018.03.031

Shin, J. K., An, J. S., Choi, Y. D., Kim, Y. C., and Kim, M. S. (2008). Elliptic Relaxation Second Moment Closure for the Turbulent Heat Fluxes. *J. Turbul.* 9 (9), N3. doi:10.1080/14685240701823101

Simcenter (2016). *STAR-CCM+ Documentation*.

Sommer, T. P., So, R. M. C., and Lai, Y. G. (1992). A Near-Wall Two-Equation Model for Turbulent Heat Fluxes. *Int. J. Heat Mass Transf.* 35 (12), 3375–3387. doi:10.1016/0017-9310(92)90224-g

Su, X., Li, X., Wang, X., Liu, Y., Chen, Q., Shi, Q., et al. (2022). Development and Assessment of an Isotropic Four-Equation Model for Heat Transfer of Low Prandtl Number Fluids. *Front. Energy Res.* 57. doi:10.3389/fenrg.2022.816560

Subbotin, V., Ushakov, P., Kirillov, P., Ibragimov, M., Ivanovski, M., Nomofilov, E., et al. (1965). "Heat Transfer in Elements of Reactors with a Liquid Metal Coolant," in Proceedings of the 3rd International Conference on Peaceful Use of Nuclear Energy, 192–200.

Youssef, M. S. (2006). A Two-Equation Heat Transfer Model for Wall Turbulent Shear Flows. *JES. J. Eng. Sci.* 34 (6), 1877–1903. doi:10.21608/jesaun.2006.111184

Youssef, M. S., Nagano, Y., and Tagawa, M. (1992). A Two-Equation Heat Transfer Model for Predicting Turbulent Thermal Fields under Arbitrary Wall Thermal Conditions. *Int. J. Heat Mass Transf.* 35 (11), 3095–3104. doi:10.1016/0017-9310(92)90329-q

Conflict of Interest: The authors declare that the research was conducted in the absence of any commercial or financial relationships that could be construed as a potential conflict of interest.

Publisher's Note: All claims expressed in this article are solely those of the authors and do not necessarily represent those of their affiliated organizations, or those of the publisher, the editors, and the reviewers. Any product that may be evaluated in this article, or claim that may be made by its manufacturer, is not guaranteed or endorsed by the publisher.

frontiers | Frontiers in Energy Research

TYPE Original Research
PUBLISHED 18 July 2022
DOI 10.3389/fenrg.2022.928693

OPEN ACCESS

EDITED BY
Wenzhong Zhou,
Sun Yat-sen University, China

REVIEWED BY
Yaou Shen,
Laboratory of Reactor System Design Technology (LRSDT), China
Hui Cheng,
Sun Yat-sen University, China

*CORRESPONDENCE
Bo Pang,
bo.pang@szu.edu.cn

SPECIALTY SECTION
This article was submitted to Nuclear Energy,
a section of the journal
Frontiers in Energy Research

RECEIVED 26 April 2022
ACCEPTED 27 June 2022
PUBLISHED 18 July 2022

CITATION
Huang X, Pang B, Chai X and Yin Y (2022), Proposal of a turbulent Prandtl number model for Reynolds-averaged Navier–Stokes approach on the modeling of turbulent heat transfer of low-Prandtl number liquid metal. *Front. Energy Res.* 10:928693. doi: 10.3389/fenrg.2022.928693

Proposal of a turbulent Prandtl number model for Reynolds-averaged Navier–Stokes approach on the modeling of turbulent heat transfer of low-Prandtl number liquid metal

Xi Huang[1], Bo Pang[1,2]*, Xiang Chai[3] and Yuan Yin[1,2]

[1]Department of Nuclear Science and Technology, College of Physics and Optoelectronic Engineering (CPOE), Shenzhen University (SZU), Shenzhen, China, [2]Institute of Nuclear Power Operation Safety Technology, Affiliated to the National Energy R & D Center on Nuclear Power Operation and Life Management, Shenzhen, China, [3]School of Nuclear Science and Engineering, Shanghai Jiao Tong University (SJTU), Shanghai, China

Because of their high molecular heat conductivity, low-Prandtl number liquid metal is a promising candidate coolant for various designs of advanced nuclear systems such as liquid metal–cooled fast reactors and accelerator-driven sub-critical system (ADS). With the fast-growing computational capacity, more and more attention has been paid to applying computational fluid dynamics (CFD) methods in thermal design and safety assessment of such systems for a detailed analysis of three-dimensional thermal–hydraulic behaviors. However, numerical modeling of turbulent heat transfer for low-Prandtl number liquid metal remains a challenging task. Numerical approaches such as wall-resolved large eddy simulation (LES) or direct numerical simulation (DNS), which can provide detailed insight into the physics of the liquid metal flow and the associated heat transfer, were widely applied to investigate the turbulent heat transfer phenomenon. However, these approaches suffer from the enormous computational consumption and are hence limited only to simple geometrical configurations with low to moderate Reynolds numbers. The Reynolds-averaged Navier–Stokes (RANS) approach associated with a turbulent Prandtl number Pr_t accounting for the turbulent heat flux based on Reynolds analogy is still, at least in the current state in most of the circumstances, the only feasible approach for practical engineering applications. However, the conventional choice of Pr_t in the order of 0.9~unity in many commercial computational fluid dynamics codes is not valid for the low-Prandtl number liquid metal. In this study, LES/DNS simulation results of a simple forced turbulent channel flow up to a friction Reynolds number Re_τ of 2000 at Pr of 0.01 and 0.025 were used as references, to which the Reynolds-averaged Navier–Stokes approach with varying Pr_t was compared. It was found that the appropriate Pr_t for the RANS approach decreases with bulk Peclet number Pe_b and approaches a constant value of

1.5 when Pe_b becomes larger than 2000. Based on this calibrated relation with Pe_b, a new model for Pr_t used in the RANS approach was proposed. Validation of the proposed model was carried out with available LES/DNS results on the local temperature profile in the concentric annulus and bare rod bundle, as well as with experimental correlations on the Nusselt number in a circular tube and bare rod bundle.

KEYWORDS

low-Prandtl number liquid metal, turbulent heat transfer, turbulent Prandtl number, RANS, CFD

Highlights

1) Proposal of a new model for the turbulent Prandtl number in the RANS approach for engineering applications.
2) Validation of the proposed model with available LES/DNS results of the local temperature profile in the concentric annulus and bare rod bundle.
3) Validation of the proposed model with experimental correlations on the Nusselt number in a circular tube and bare rod bundle.

1 Introduction

Low-Prandtl number liquid metals are considered as promising candidate coolants in various innovative nuclear systems, such as the sodium-cooled fast reactor (SFR), the liquid lead–cooled fast reactor (LFR), and the accelerator-driven sub-critical system (ADS), due to their high molecular heat conductivity in favor of the reactors' reliability and safety (Roelofs, 2019). With the fast development of computational power, more and more attention has been paid to applying the computational fluid dynamics (CFD) methods for detailed analysis of three-dimensional thermal–hydraulic behavior, especially in nuclear fuel assembly design (Cheng and Tak, 2006b; Marinari et al., 2019; Chai et al., 2019). However, modeling of turbulent heat flux in low-Prandtl number liquid metal flow remains a challenging task when using CFD methods to solve the turbulent flow heat transfer behavior (Shams, 2019). Advanced high-fidelity numerical approaches represented by the wall-resolved large eddy simulation (LES) method and the direct numerical simulation (DNS) method can provide detailed insight into the physics of the flow and the associated heat transfer (Tiselj et al., 2019). However, these approaches are limited to simple flow configurations and low to moderate Reynolds numbers due to their rather high requirement of computational capacities. Hence, Reynolds-averaged Navier–Stokes (RANS) method is still at least in the current state, in most cases, the only practically feasible approach to deal with high Reynolds industrial flows, especially those in complex geometries such as those encountered in typical nuclear fuel assemblies (Shams et al., 2019). It is thus important to assess and improve the accuracy of the RANS approach and the associated models for turbulent heat transfer. With this objective in mind, simulation results of the velocity and temperature field obtained by LES or DNS are, hence, very valuable references to which RANS models can be compared and calibrated.

Compared to conventional fluids with the Prandtl number in the order of unity, such as water or air, heat transfer in the low-Prandtl number liquid metal is characterized by the high contribution of molecular heat conduction even in high turbulent flow. Consequently, temperature change in the boundary layer is much smoother, even in the very thin laminar sub-layer. In the classical RANS approach with conventional turbulence models, turbulent heat transfer is often predicted solely from the knowledge of turbulent momentum transfer based on the concept of the so-called Reynolds analogy (Cheng and Tak, 2006a), in which the turbulent heat conductivity a_t (or eddy conductivity) is given by the ratio between turbulent momentum conductivity ν_t (or eddy diffusivity) and a turbulent Prandtl number (Pr_t) according to:

$$a_t = \frac{\nu_t}{\mathrm{Pr}_t}. \tag{1}$$

It is well acknowledged that an accurate prediction of Pr_t is of crucial importance in modeling turbulent heat transfer in the low-Prandtl number liquid metal flows. For instance, as pointed out by Cheng and Tak (2006b), a decrease in the Nusselt number of about 30% can be obtained by increasing Pr_t from 0.9 to 1.5. However, the conventional choice of Pr_t as a constant value of 0.85–0.9, with which satisfying results of the turbulent heat flux can be obtained for most of the engineering purposes with fluid of Prandtl number in the order of unity, is not valid for a low-Prandtl number liquid metal.

In the past, extensive studies were carried out to derive appropriate expressions for Pr_t for the low-Prandtl number liquid metal. In general, two types of models can be found in the open literature, the first type specifies Pr_t as a global value depending on the bulk flow parameters such as the bulk

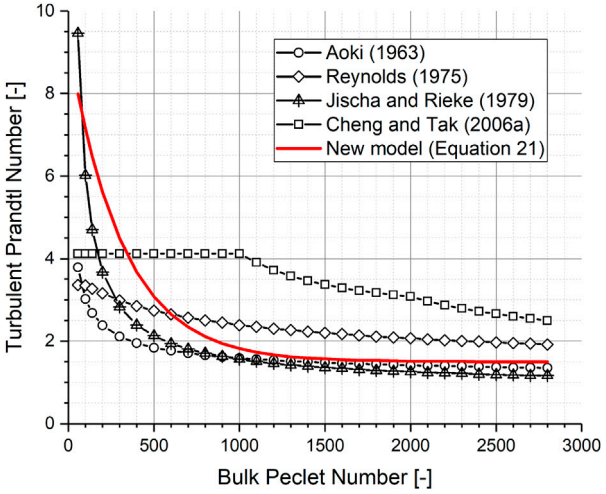

FIGURE 1
Comparison of turbulent Prandtl numbers obtained with different models (molecular Prandtl **Pr** = 0.01).

Reynolds number Re_b or/and the bulk Peclet number Pe_b represented by the early model of Aoki (1963).

$$Pr_t^{-1} = 0.014\, Re_b^{0.45}\, Pr^{0.2}\left[1 - exp\left(\frac{-1}{0.014\, Re_b^{0.45}\, Pr^{0.2}}\right)\right]. \quad (2)$$

The models of Reynolds (1975).

$$Pr_t = \left(1 + 100 Pe_b^{-0.5}\right)\cdot\left(\frac{1}{1 + 120 Re_b^{-0.5}} - 0.15\right). \quad (3)$$

Also, the model of Jischa and Rieke (1979).

$$Pr_t = 0.9 + \frac{182.4}{Pr Re_b^{0.888}}. \quad (4)$$

The model by Cheng and Tak (2006b).

$$Pr_t = \begin{cases} 4.12, & if\ Pe_b \le 1000 \\ \dfrac{0.01 Pe_b}{\left[0.018 Pe_b^{0.8} - (7.0 - A)\right]^{1.25}}, & if\ 1000 < Pe_b \le 6000 \end{cases}, \quad (5)$$

in which the constant A is given as:

$$\begin{aligned} A &= 5.4 - 9 \times 10^{-4} Pe_b, \quad if\ 1000 < Pe_b \le 2000, \\ A &= 3.6, \quad if\ 2000 < Pe_b \le 6000. \end{aligned} \quad (6)$$

The second type gives Pr_t as a local varying value depending on the local flow parameters such as the local eddy diffusivity, represented by the model of Kays (1994).

$$Pr_t = 0.85 + \frac{0.7}{Pe_t}, \quad (7)$$

where the turbulent Peclet number $\mathbf{Pe_t}$ is defined as:

$$Pe_t = \frac{\nu_t}{\nu} Pr. \quad (8)$$

Figure 1 compares the Pr_t calculated with the model of Aoki (1963), Reynolds (1975), Jischa and Rieke (1979), and Cheng and Tak (2006b) for bulk Peclet number Pe_b up to 2,800 at Pr of 0.01 (corresponding to a Re_b up to 280,000). Also included in the figure is the proposed model for Pr_t in the current study given by Eq. 21. It is observed that first, Pr_t generally decreases with increasing Pe_b. Second, Pr_t tends to approach a constant value between 1 and 2 as Pe_b becomes larger than 2000 except for the model of Cheng and Tak (2006b). Pr_t predicted by the model of Cheng and Tak (2006b) is generally larger than all the other models. Finally, a rather scattering distribution exists in the predicted values of Pr_t obtained by different models proposed in the literature, especially in the range of Pe_b lower than 1,000. A possible reason for the scattering is due to the lack of reliable and consistent experimental data on turbulent heat transfer in liquid metal flows.

With the fast-growing computational capacities, advanced high-fidelity numerical approaches such as wall-resolved LES method and DNS method become more and more attractive to provide detailed insight into the physics of the flow and the associated heat transfer. Due to their high demands of computational capacities, LES and DNS simulations are often, at least in the current state, limited to rather simple geometrical configurations. Nevertheless, simulation results of LES and DNS are very valuable references to which RANS models can be compared and calibrated. In the current study, LES and DNS results of a simple fully developed forced turbulent channel flow of low-Prandtl number fluid (Pr = 0.01 and 0.025) up to Re_τ of 2000 were used as references to assess RANS modeling of the turbulent heat transfer by means of the turbulent Prandtl number concept. RANS simulations of the forced turbulent channel flow with boundary conditions following those in LES/DNS settings were performed by systematically varying Pr_t from 0.9 up to 8.0. Based on the comparison of the dimensionless temperature field and/or bulk Nusselt number Nu_b calculated by the RANS approach with those obtained by LES/DNS simulations, an appropriate choice of the Pr_t associated with the RANS approach can be obtained and a new model for Pr_t was then proposed and validated.

2 Large eddy simulation and direct numerical simulation results on fully developed forced turbulent channel flow of low-Prandtl number fluid

As depicted in Figure 2, a fully developed forced turbulent channel flow of low-Prandtl number fluid heated by a uniform heat flux q_w on both walls is a simple scenario which has been extensively investigated in the open literature by means of LES and DNS. Table 1 summarizes the representative LES and DNS simulations in the ascending order of the bulk Peclet number Pe_b.

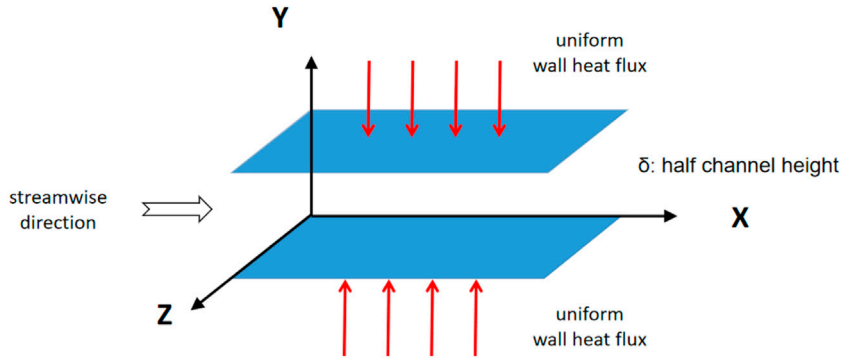

FIGURE 2
Sketch of the fully developed forced turbulent channel flow heated by a uniform heat flux q_w on both sides of the walls.

TABLE 1 Summary of LES/DNS simulation on fully developed turbulent channel flow for low-Prandtl number fluid.

Source	Pr [-]	Re_τ [-]	Re_b [-]	Pe_b [-]	Nu_b [-]	CFD method
Bricteux et al., (2012)	0.01	180	5,600	56	Not available	DNS
Kawamura et al., (1999)	0.025	180	5,600	140	Not available	DNS
Bricteux et al., (2012)	0.01	590	22,000	220	6.02	LES
Kawamura et al., (1999)	0.025	395	13,500	337.5	Not available	DNS
Duponcheel et al., (2014)	0.01	2000	87,000	870	8.44	LES
Abe et al., (2004)	0.025	1,020	41,000	1,025	Not available	DNS
Duponcheel et al., (2014)	0.025	2000	87,000	2,175	14.39	LES

The channel flow is characterized by the friction Reynolds number Re_τ which is defined with the friction velocity u_τ and the channel half height δ according to:

$$Re_\tau = \frac{u_\tau \cdot \delta \cdot \rho}{\mu}, \tag{9}$$

in which the friction velocity u_τ is defined with relation to the wall shear stress τ_w as:

$$u_\tau = \sqrt{\frac{\tau_w}{\rho}}, \tag{10}$$

where ρ and μ stand for the fluid density and dynamic viscosity, respectively. The bulk velocity u_b is an average channel flow velocity defined as:

$$u_b = \frac{1}{\delta}\int_0^\delta u dy, \tag{11}$$

which is then used to define the bulk Reynolds number Re_b as:

$$Re_b = \frac{u_b \cdot 2\delta \cdot \rho}{\mu}. \tag{12}$$

The bulk Peclet number Pe_b is defined as:

$$Pe_b = Re_b \cdot Pr. \tag{13}$$

Also included in Table 1 is the global heat transfer performance characterized by the bulk Nusselt number Nu_b defined as:

$$Nu_b = \frac{q_w \cdot 2\delta}{\lambda \cdot (T_w - T_b)}, \tag{14}$$

where the bulk temperature T_b is the average channel flow temperature which is defined as:

$$T_b = \frac{1}{u_b \cdot \delta}\int_0^\delta (u \cdot T) dy. \tag{15}$$

For the purpose of assessing RANS approach, DNS results of Kawamura et al. (1999) with $Pr = 0.025$ and $Re_\tau = 180, 395$, DNS results of Abe et al. (2004) with $Pr = 0.025$ and $Re_\tau = 1020$, as well as DNS results of Bricteux et al. (2012) with $Pr = 0.01$ and $Re_\tau = 180, 590$, LES results of Duponcheel et al. (2014) with $Pr = 0.01, 0.025$ and $Re_\tau = 2000$ were chosen as references. The corresponding bulk Reynolds number Re_b covers a wide range

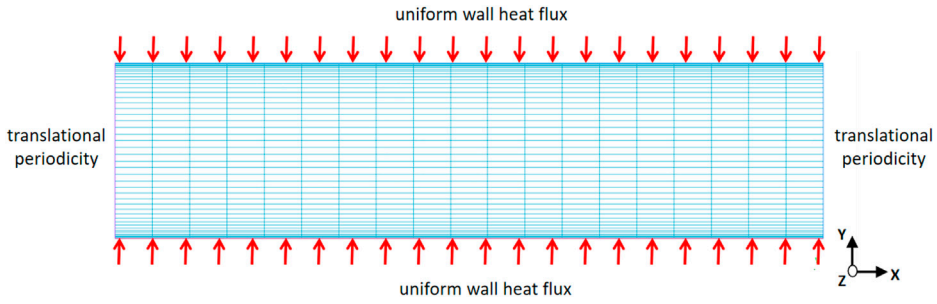

FIGURE 3
Sketch of the mesh structure and boundary conditions used in RANS simulation of the fully developed forced turbulent channel flow.

TABLE 2 Summary of boundary parameters for RANS simulations of fully developed forced turbulent channel flow for low-Prandtl number fluid.

Turbulent Prandtl number	**0.9, 1.5, 2.0, 4.0, 6.0, 8.0**
Turbulence model	$k-\omega$, $k-\epsilon$, SST
Mesh size: y_1^+	0.1, 0.2, 0.6
Boundary type: streamwise (X)	Translational periodic
Boundary type: channel height (Y)	No-slip wall with uniform heat flux
Boundary type: spanwise (Z)	Symmetric

from 5,600 up to 87,000, while the bulk Peclet number Pe_b is varied in the range from 56 up to 2,175.

3 Reynolds-averaged Navier–Stokes approach associated with turbulent Prandtl number concept

3.1 Geometrical setups and boundary conditions

As depicted in Figure 3, a quasi-2D RANS simulation of the fully developed channel flow was performed in the current study with the commercial CFD software package Ansys CFX. An arbitrary channel half height δ of 0.01 m (y-direction) was chosen, while the channel streamwise (x-direction) length was set as 80 times of δ. For a quasi-2D simulation, only 1 cell element was extruded in the spanwise direction (z-direction) and symmetrical conditions were specified on the two boundaries of the spanwise direction. A translational periodic boundary condition was specified on the two boundaries of the streamwise direction, in order to obtain the fully developed flow conditions. A constant uniform heat flux was given for the top and bottom boundaries following the LES/DNS settings.

Table 2 summarizes the most important boundary parameters of the RANS simulations performed in the current study. The flow is assumed to be incompressible with constant thermal–physical properties as in consistency with the LES/DNS settings. The governing equations are the RANS equations for incompressible flow with constant thermal–physical properties and the energy conservation equation for temperature. Due to the periodic boundary condition in the streamwise direction and the constant wall heat flux on the top and bottom walls, the temperature will continuously increase in the streamwise direction and a fully developed flow condition will never be achieved. Therefore, a negative volumetric heat source was specified in the RANS simulation, which takes exactly the same amount of energy away as given to the domain by the heat flux on the top and bottom walls. High-resolution advection scheme and turbulence numerics were chosen to ensure a second order accuracy. The buoyancy effect due to the temperature difference in the channel height direction (y-direction) is negligibly small, hence not considered in the RANS simulations. This is justified by the fact that the bulk Richardson number Ri_b for the RANS setups according to the following equation is quite small (<<1):

$$Ri_b = \frac{g \cdot \beta \cdot (T_w - T_b) \cdot \delta}{u_b^2}, \tag{16}$$

where g and β are the gravitational acceleration and the thermal expansivity, respectively.

3.2 Presentation of the Reynolds-averaged Navier–Stokes results: normalization in friction units

The mean streamwise velocity profile and mean temperature profile in the channel height direction (y-direction) are normalized with the friction velocity u_τ and friction temperature T_τ, respectively. The friction velocity is already

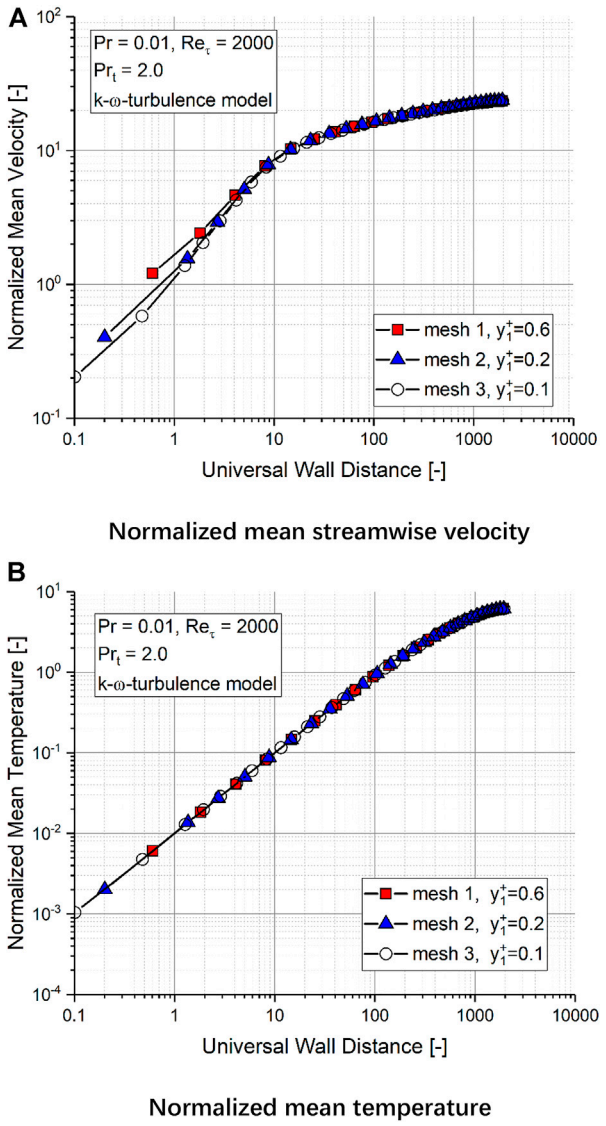

FIGURE 4
Mesh sensitivity study: comparison of the **(A)** mean velocity profile and **(B)** mean temperature profile normalized in a friction unit obtained with different meshes.

defined in Eq. 10 with relation to the wall shear stress τ_w. The friction temperature T_τ is defined with relation to the wall heat flux q_w as follows:

$$T_\tau = \frac{q_w}{\rho \cdot c_p \cdot u_\tau}, \tag{17}$$

where c_p stands for the specific heat capacity at constant pressure.

The mean streamwise velocity profile is hence characterized by the normalized dimensionless mean velocity u^+ given as:

$$u^+ = \frac{u}{u_\tau}. \tag{18}$$

The mean temperature profile is characterized by the normalized dimensionless mean temperature θ^+ according to:

$$\theta^+ = \frac{T_w - T}{T_\tau}, \tag{19}$$

where T_w is the wall temperature of the heated top or bottom wall. Both the dimensionless velocity and dimensionless temperature profile are specified in terms of a dimensionless universal wall distance y^+ defined as:

$$y^+ = \frac{u_\tau \cdot y \cdot \rho}{\mu}, \tag{20}$$

where y is the actual distance to the wall.

3.3 Effect of mesh refinement and turbulence model

As also included in Figure 3, a block-structured mesh consisting of only hexahedra was used in RANS simulations. The mesh nodes are uniformly distributed among the streamwise direction (x-direction), while local refinement was specified in the y-direction when approaching the top and bottom wall, in order to ensure at least a dimensionless universal wall distance of the first interior node $y_1^+ < 1$ as required for the wall-resolved low-Reynolds number turbulence model in RANS simulations, that is, the $k-\omega$ model and the shear stress transport (SST) model. The mesh sensitivity study was performed for the LES case of $Pr = 0.01$ and $Re_\tau = 2000$ (Duponcheel et al., 2014) (corresponding Re_b and Pe_b are 87,000 and 870, respectively). The wall-resolved $k-\omega$ turbulence model and a constant turbulent Prandtl number Pr_t of 2.0 were used for all the tested meshes. For the mesh sensitivity study, three different levels of mesh refinement were studied with the same block structure as displayed in Figure 3. The total cell numbers of the three meshes were 3,713, 5,841, and 15,721, respectively, meaning that the highest density mesh is 4.23 times finer than the smallest-density mesh. The corresponding values of y_1^+ were 0.6, 0.2, and 0.1, respectively.

Figure 4 compares the normalized mean streamwise velocity profile (u^+) and the normalized mean temperature profile (θ^+) obtained with the three tested meshes. It is observed that the mean streamwise velocity calculated with mesh 1 is slightly higher than that obtained with mesh 2 and mesh 3 in the near wall region with y^+ lower than 5, while the difference among the velocity profile obtained with mesh 2 and mesh 3 is negligibly small. Furthermore, the mean temperature profile obtained with the three tested meshes agrees well with each other, despite a large difference in the total cell number and mesh refinement. The bulk Nusselt number Nu_b obtained by RANS simulations with the three different meshes are 8.81, 8.81, and 8.84, respectively. In conclusion, mesh 2 with y_1^+

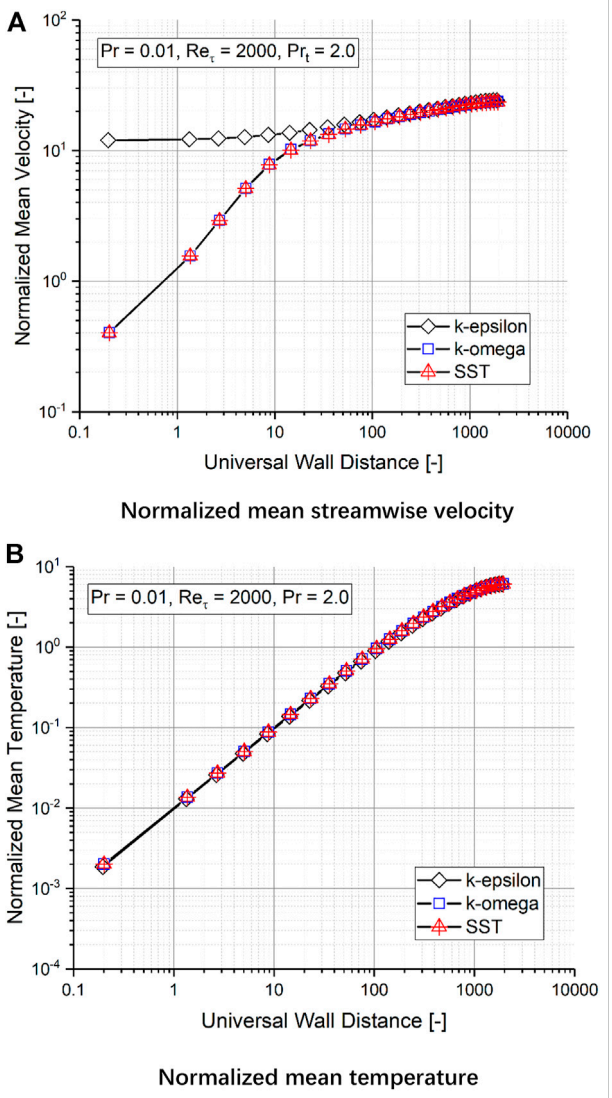

FIGURE 5
Effect of different turbulence models on **(A)** mean velocity and, **(B)** mean temperature profile in friction unit.

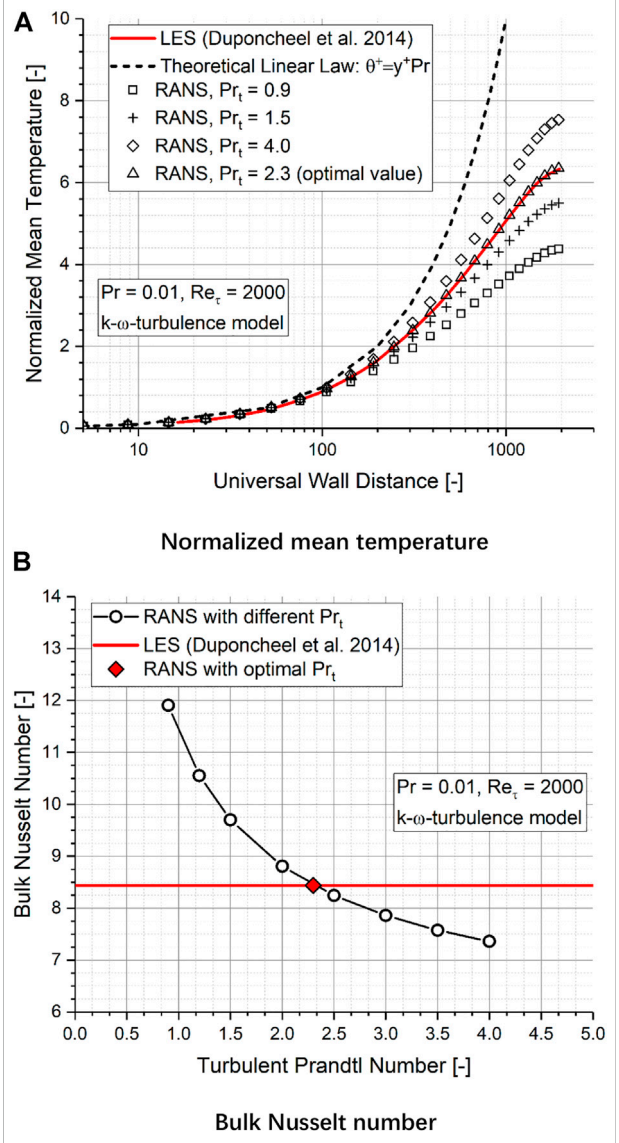

FIGURE 6
RANS approach with varying turbulent Prandtl numbers: **(A)** effect on normalized mean temperature; **(B)** effect on bulk Nusselt number.

of 0.2 was hence chosen for the RANS simulations henceforth in the current study.

Two types of turbulence models are available in CFX, that is, the wall-resolved low-Reynolds number turbulence model with which the boundary layer is fully resolved, and the wall-unresolved high-Reynolds number turbulence model with which the boundary layer is approximated relying on a logarithmic wall function. For the present analysis, the wall-resolved $k-\omega$ and *SST* turbulence model as well as the wall-unresolved $k-\epsilon$ turbulence model were tested. Figure 5 shows the mean streamwise velocity profile and the mean temperature profile normalized in fiction unit for the case of $Pr = 0.01$ and $Re_\tau = 2000$. A constant turbulent Prandtl number Pr_t of 2.0 was specified for all the RANS simulations. It is observed that the temperature profile is hardly influenced by the turbulence model. In the logarithmic region where y^+ becomes larger than 60, the velocity profile calculated by the different turbulence model agrees well with each other. The difference in the velocity profile in the near wall region ($y^+ < 30$) is to be expected, since the $k-\epsilon$ model applies the logarithmic wall function for the complete boundary layer. The bulk Nusselt numbers Nu_b obtained with $k-\epsilon$, $k-\omega$, and SST model are 8.72, 8.81, and 8.84, respectively. The $k-\omega$ turbulence model was chosen for the RANS simulations henceforth in the current study.

3.4 Effect of turbulent Prandtl number Pr_t

To study the effect of the turbulent Prandtl number Pr_t, the same case of Pr = 0.01 at Re_τ = 2000 as in the mesh sensitivity study was further investigated. In the RANS simulations, Pr_t was systematically varied from 0.9, 1.2, 1.5, 2.0, 2.5, 3.0, 3.5 up to 4.0. The same mesh with y_1^+ of 0.2 (mesh 2) and the same $k-\omega$ turbulence model were employed. Since the velocity field is hardly affected by Pr_t for incompressible flow with constant thermal–physical properties, Figure 6A shows only the normalized mean temperature profile obtained by the RANS simulations. For a better demonstration of the results, only RANS results of Pr_t = 0.9, 2.0, and 4.0 are shown in the figure (the RANS simulation results with the optimum value of Pr_t = 2.3 are also included in Figure 6A and will be discussed later.). The corresponding LES results obtained by Duponcheel et al. (2014) are shown as a straight line in the subfigure for comparison with RANS results. Also included in the figure is the theoretical linear law of the temperature profile $\theta^+ = Pr \cdot y^+$ (dashed line) (Kader, 1981). It is shown as follows:

1) Compared to conventional fluid with the Prandtl number in the order of unity, for which the linear law is valid only in the very thin laminar sub-layer of y^+ generally much smaller than 30, the theoretical linear law is still valid at a wall distance of y^+ up to 60~70 for low-Prandtl number fluid. This indicates that the heat transfer in this region is dominated by the molecular effect of heat conduction. Consequently, no difference can be observed in the temperature profiles obtained with RANS of different Pr_t and they all agree well with the temperature profile obtained by LES.
2) As y^+ becomes larger than 100, the theoretical linear law is no longer valid. The temperature profile given by the linear law is much steeper than that calculated by LES, which indicates that the turbulent diffusivity also becomes important in the heat transfer in addition to the molecular effect of heat conduction. It is clearly seen that the temperature profile now depends strongly on Pr_t. The temperature profile obtained with the conventional choice of Pr_t= 0.9 is much smoother than that calculated by LES, which indicates that the global heat transfer, that is, the heat transfer contribution due to turbulent diffusivity is obviously overestimated. With Pr_t increasing from 0.9 to 1.5 and 4.0, the temperature profile becomes steeper and an optimum value of Pr_t for the RANS approach exists apparently in the range of 1.5–4.0.

In order to obtain the optimum value of Pr_t for the investigated case of Pr = 0.01 at Reτ = 2000, the global heat transfer behavior was also studied. Figure 6B shows the bulk Nusselt number Nu_b obtained in the RANS simulations with different Pr_t (shown as line with circular symbols), compared with that obtained by LES (red straight line) of Duponcheel et al. (2014). It is observed that with Pr_t = 0.9, the bulk Reynolds number was overestimated by about 40%. The conventional choice of Pr_t = 0.9 is clearly not valid for low-Prandtl number fluid. The bulk Nusselt number Nu_b decreases with increasing turbulent Prandtl number Pr_t and an optimum value of Pr_t is apparently located in the interval between 2.0 and 2.5. Therefore, further RANS simulations with Pr_t = 2.1, 2.2, 2.3, and 2.4 were carried out and the optimum value was finally found at Pr_t = 2.3 (shown as the diamond symbol in Figure 6B), for this value; the Nu_b obtained by RANS simulation is equal to that obtained by LES. The temperature profile obtained with Pr_t = 2.3 was also included in Figure 6A with triangular symbols and it agrees well with that obtained by LES (straight line).

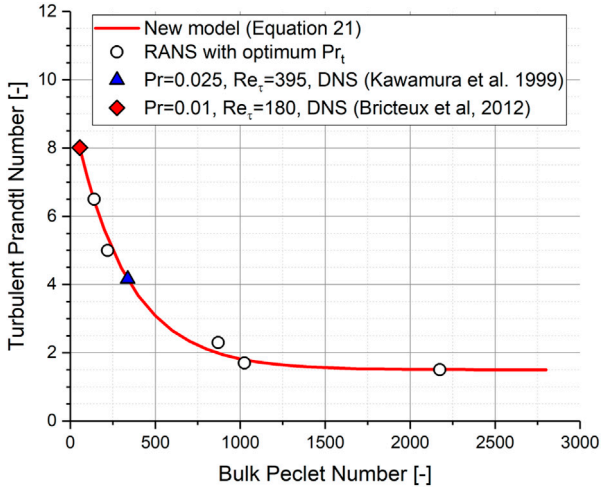

FIGURE 7
Development of a new model of the turbulent Prandtl number for RANS with LES/DNS results in turbulent channel flow as a reference.

4 Development of a new turbulent Prandtl number model for Reynolds-averaged Navier–Stokes approach

4.1 Proposal of a new turbulent Prandtl number model for Reynolds-averaged Navier–Stokes approach

The aforementioned approach to determine the optimum value of Pr_t for the RANS approach was also conducted for further selected LES/DNS cases listed in Table 1, for which the bulk Nusselt numbers Nu_b were reported in the respective sources, that is, for the case with Pr = 0.01 at Re_τ = 590 (Bricteux et al., 2012) and for the case with Pr = 0.025 at Re_τ = 2000 (Duponcheel et al., 2014). For the purpose of developing a suitable model for Pr_t, RANS simulations were also performed for the case with Pr = 0.01 at Re_τ = 180 (Bricteux et al., 2012)

and for the case with $Pr = 0.025$ at $Re_\tau = 1020$ (Abe et al., 2004). Although no values of Nu_b were provided in the DNS simulations of the aforementioned two cases, the optimum value of Pr_t for the RANS simulation was found solely by comparing the temperature profile. Overall, RANS simulations were performed for five cases of different Pr and Re_τ (corresponding Re_b and Pe_b covering the range from 5,600 to 87,000 and from 140 to 2,175, respectively). By comparing the temperature profile or/and bulk Nusselt number obtained in RANS simulations with those obtained in their respective LES/DNS simulations, the optimum values of Pr_t for the RANS approach were determined for the five cases, as shown with the five circular symbols in Figure 7.

It is observed that

1) Apparently, the turbulent Prandtl number Pr_t can be correlated solely with the bulk Peclet number Pe_b independent of Prandtl number Pr.
2) Furthermore, Pr_t decreases with increasing Pe_b and tends to approach a constant value of 1.5 when Pe_b becomes larger than 2000. This behavior is in general agreement with other models proposed in the literature as shown in Figure 1.
3) More importantly, the fact that Pr_t approaches a constant value for large bulk Peclet number Pe_b (corresponding also to a large bulk Reynolds number Re_b) means that no further LES/DNS simulations are required for those large Reynolds numbers when developing a suitable model for Pr_t.
4) Therefore, the following simple model for Pr_t was proposed for the usage in the RANS approach, in which Pr_t was assumed as a function of the bulk Peclet number Pe_b (shown with the red straight line in Figure 7).

$$Pr_t = 1.5 + 7.745 \cdot e^{-0.00318 \cdot Pe_b}. \quad (21)$$

5) Since the proposed new model in Eq. 21 was derived based on LES/DNS results, the validity range of the new model should be limited to the range as specified in LES/DNS simulations as summarized in Table 1. Therefore, the validity range of Pe_b should be from 56 to 2,175 with a validity range of Pr from 0.025 to 0.01.

For assessment of the proposed model for the turbulent Prandtl number, RANS simulation was performed with Pr_t calculated from the new model for the case of $Pr = 0.01$ at $Re_\tau = 180$ (corresponding bulk Reynolds number Re_b is 5,600 and bulk Peclet number Pe_b is 56) for which DNS results of the temperature profile are given in Bricteux et al. (2012), and for the case of $Pr = 0.025$ at $Re_\tau = 395$ (corresponding Re_b is 13,500 and Pe_b is 337.5), for which DNS results of the temperature profile are given in Kawamura et al. (1999). In the RANS simulations, Pr_t was then calculated with the proposed model given by Eq. 21. For the case of $Pr = 0.025$ at $Re_\tau = 395$, the Pr_t calculated with the proposed model is 4.15, while for the case of $Pr = 0.01$ at $Re_\tau = 180$ the calculated Pr_t is 7.98. Figure 8 compares the two cases of the normalized temperature profiles calculated by RANS simulations with those obtained by their respective DNS simulations. It is observed that, despite the fact that only five points were used to develop the new model for Pr_t, the agreement between the RANS and DNS results is acceptable, which justifies the adequacy of the proposed model.

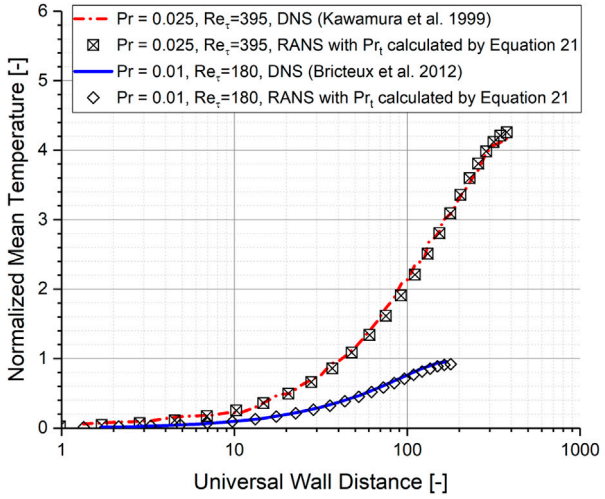

FIGURE 8
Assessment of the proposed model for the turbulent Prandtl number with DNS results for Pr = 0.025 at Reτ = 395, and for Pr = 0.01 at Reτ = 180: comparison of the mean temperature profile normalized in a friction unit.

4.2 Validation of the proposed turbulent Prandtl number model for Reynolds-averaged Navier–Stokes approach

The general strategy for validation of the proposed new model for the turbulent Prandtl number for the RANS approach is divided into the following two phases:

1) Phase I: taking LES/DNS results on the local temperature profile in the concentric annulus and bare rod bundle heated by constant uniform heat flux as a reference, with which RANS simulations results with the new model for Pr_t will be compared. In the current study, we chose the LES/DNS simulation performed in a concentric annular channel by Lyu et al. (2015) and Marocco (2018) with a bulk Reynolds number of 8,900 at $Pr = 0.026$ and the LES simulation performed in a bare rod bundle by Shams et al. (2018) with a bulk Reynolds number of 54650 at $Pr = 0.016$ as a reference.
2) Phase II: LES/DNS simulations in the concentric annulus and bare rod bundle can provide detailed information about the

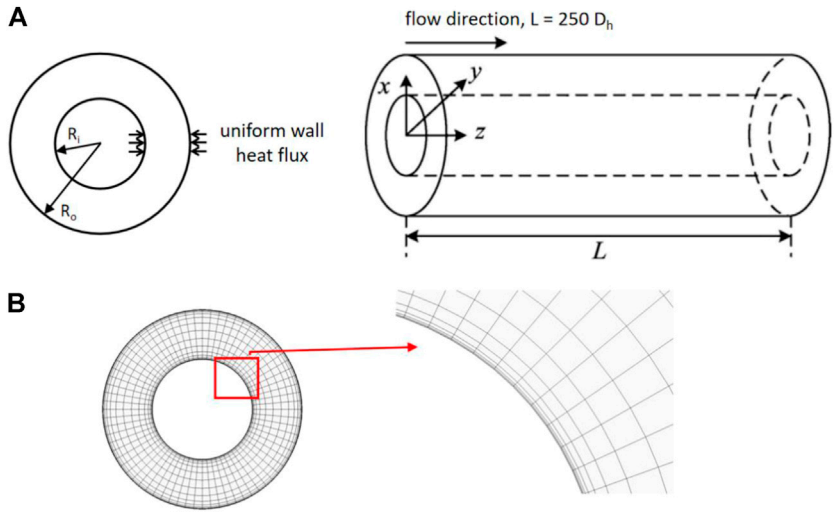

FIGURE 9
(A) Sketch of a concentric annular channel heated uniformly on both walls and **(B)** mesh used in the RANS simulations.

local temperature profile, but are only available to a rather low-Reynolds number and Peclet number due to the enormous computational requirement. From the engineering point of view, the most important parameter to be considered is the heat transfer behavior in terms of the bulk Nusselt number Nu_b. Therefore, in the second phase of the validation process, experimental correlations on the bulk Nusselt number Nu_b developed for a circular tube and bare triangular rod bundle were taken as a reference, with which RANS simulations results with the new model for Pr_t will be compared. The reason for selecting a circular tube and bare triangular rod bundle lies mainly in the fact, that most of the experimental investigations on turbulent heat transfer with the low-Prandtl number liquid metal were actually conducted with these two kinds of geometries and various experimental correlations were available in the open literature as summarized in OECD (2015).

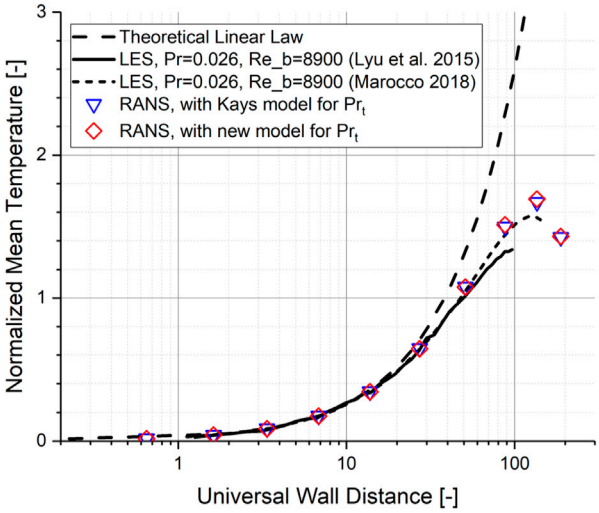

FIGURE 10
Validation of the proposed model on turbulent Prandtl number: a heated concentric annular channel.

4.2.1 Phase I: validation based on large eddy simulation/direct numerical simulation results for a local temperature profile in the concentric annulus and bare rod bundle

As the first step of the validation process phase I, a concentric annular channel heated on both walls as depicted in Figure 9A was considered due to its closeness to the sub-channel in a bare rod bundle (Ma et al., 2012). LES/DNS simulations on the fully developed state of turbulent heat transfer in the annular channel were performed at Pr = 0.026 with a bulk Reynolds number Re_b = 8900 by Lyu et al. (2015) and Marocco (2018). The ratio of the outer diameter R_o to the inner diameter R_i is 2. In the LES simulation, the annular channel was heated with a constant uniform heat flux on both walls. Since the flow and heat transfer situation on the inner wall is closer to that in a rod bundle, only the LES results normalized based on the parameters of the inner wall were taken as a reference.

Following the LES setting, RANS simulation was performed with the Pr_t given by the new model proposed in the current study. With Pr = 0.026 at Re_b = 8900, the corresponding bulk Peclet number Pe_b is 231 and the turbulent Prandtl number Pr_t

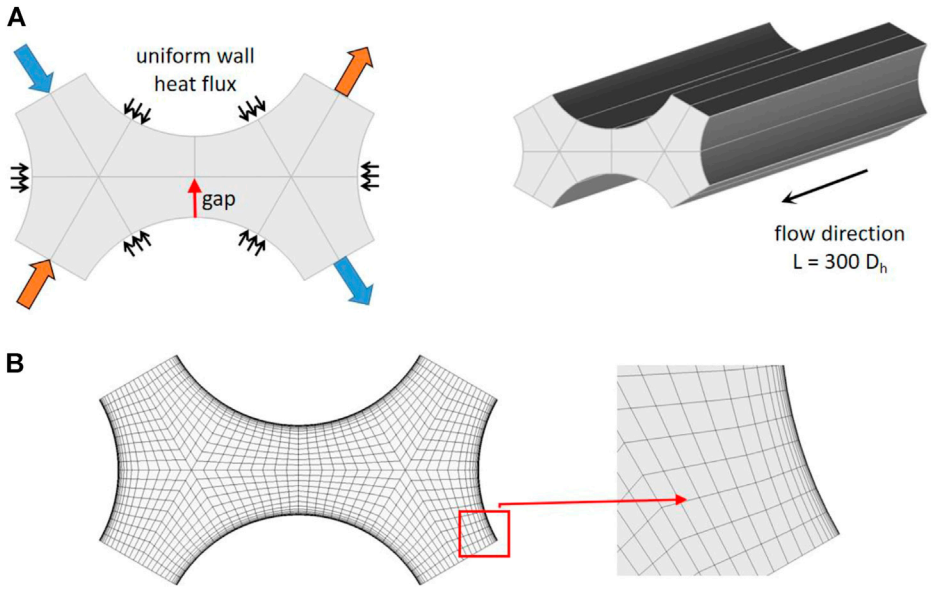

FIGURE 11
(A) Sketch of a hexagonal rod bundle heated uniformly on walls and **(B)** mesh used in the RANS simulations.

calculated with the new model is hence 5.2. Lead–bismuth eutectic (LBE) with constant thermal–physical properties taken from the OECD Handbook on a heavy liquid metal (OECD, 2015) was chosen as a working fluid. An arbitrary inner diameter R_i of 10 mm was chosen for the RANS simulation, while the outer diameter R_o is 20 mm following the setting in the LES simulation. The hydraulic diameter of the annular channel is then 10 mm. The channel length in the flow direction L was set as 250 times of the channel hydraulic meter in the RANS simulations, in order to assure the establishment of a fully developed state in the channel. Constant and uniform velocity and temperature were given to the inlet boundary, while a constant pressure was specified at the outlet boundary. Both inner and outer walls of the annular channel were modeled as no-slip walls for the velocity field and a constant uniform heat flux was imposed for the temperature field. Also included in Figure 9B is the detail of the mesh structure in RANS simulation. As recommended in the mesh sensitivity study in Section 3.3, the block-structured hexahedral mesh was used with local refinement close to both heated walls.

Figure 10 shows the fully developed normalized mean temperature profile in the radial direction of the annular channel. The wall distance was determined relative to the inner wall and the mean temperature was also normalized with friction temperature and wall temperature on the inner wall. It is observed that the temperature profile obtained by the RANS simulation with the new model for Pr_t agrees well with that given by LES simulation in the literature (Lyu et al., 2015; Marocco, 2018). RANS simulation with the Kays model, which gives local varying Pr_t depending on local flow parameters (Eq. 7), was also performed. As depicted in Figure 10, temperature profiles predicted by the Kays model and by the new model proposed in this study agree well with each other.

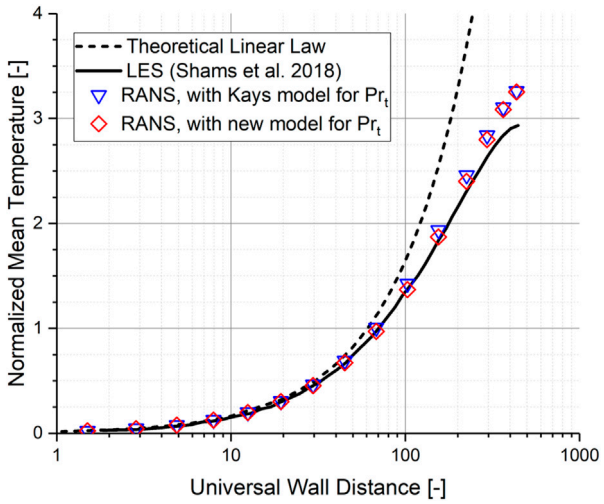

FIGURE 12
Validation of the proposed model on the turbulent Prandtl number: a hexagonal rod bundle.

A further validation of the proposed new model for the turbulent Prandtl number was performed in a loosely spaced bare

rod bundle, for which wall-resolved large eddy simulation (LES) on the fully developed state of turbulent heat transfer with liquid lead at an operating temperature of 440°C (corresponding to a $Pr = 0.016$) was performed at a bulk Reynolds number of 54,650 (Shams et al., 2018). As depicted in Figure 11A, the diameter (D) of the rod is 10.5 mm and the pitch (P) between the rods is 13.86 mm, corresponding to a pitch-to-diameter ratio P/D of 1.32. The computational domain consists of two adjacent sub-channels with a hydraulic diameter of 9.67 mm. Liquid lead with constant thermal–physical properties at 440°C is considered as a working fluid. In the RANS simulation, the channel flow length was set at 300 times of the hydraulic diameter for the establishment of a fully developed state. All the rods were modeled as no-slip walls imposed with a constant uniform wall heat flux. Following the LES settings, the arrows of the same color (Figure 11A) indicate that the side planes have been connected with the periodic boundary conditions. Also included in Figure 11B is the block-structured mesh used in the RANS simulation, following the recommendation derived from the mesh sensitivity study in Section 3.3.

Figure 12 compares, then, the fully developed temperature profile in the gap region of the two sub-channels (as indicated with a red arrow in Figure 11A). It is observed that the temperature profile obtained by RANS simulation with the new model for Pr_t agrees well with that provided by LES (Shams et al., 2018). Similar to the case in the annular channel, temperature profiles predicted by the Kays model and by the new model proposed in this study agree well with each other.

4.2.2 Phase II: validation based on experimental correlations for the Nusselt number in a circular tube and bare rod bundle

The first step of validation phase II was performed in a circular tube, for this geometry has been studied intensively from an experimental point of view. Many correlations on the turbulent heat transfer behavior (in terms of the bulk Nusselt number Nu_b) are available in the open literature. However, a common agreement is not yet available, as often contradictory conclusions were reported by different authors (OECD, 2015). We take, as recommended in the OECD Handbook on the heavy liquid metal (OECD, 2015) based on a critical review of the available literature for the experimental data and proposed correlations, the following three correlations as references for comparison with RANS results. All the correlations predict the heat transfer behavior of liquid metal in a similar way as represented by the bulk Nusselt number Nu_b and bulk Peclet number Pe_b.

1) Correlation of Lyon (1949), Lyon (1951) as an upper limit for the bulk Nusselt number.

$$Nu_b = 7.0 + 0.025 \cdot Pe_b^{0.8}. \tag{22}$$

2) Correlation of Kutateladze et al. (1959) as a lower limit for the bulk Nusselt number.

$$Nu_b = 5.0 + 0.0021 \cdot Pe_b^{1.0}. \tag{23}$$

3) Correlation of Notter and Sleicher (1972) as the best general applicable correlation for all the investigated liquid metals including sodium (Na) and sodium–potassium alloys (NaK), pure lead (Pb), and lead–bismuth eutectic (LBE) as well as pure mercury (Hg).

$$Nu_b = 6.3 + 0.0167 \cdot Pe_b^{0.85} Pr^{0.08}. \tag{24}$$

It should be noted that all the aforementioned correlations were proposed for the thermal boundary condition of the uniform wall heat flux and have been developed for fully developed turbulent flow conditions with bulk Reynolds numbers Re_b in the range between 10^4 and 10^6. As depicted in Figure 13, RANS simulations were, hence, performed in a circular tube heated with a uniform wall heat flux. Constant uniform velocity and inlet temperature were given at the inlet boundary, while a constant pressure boundary condition was set at the outlet boundary. In order to achieve the fully developed state, the streamwise length of the tube was set as 250 times of the tube diameter. RANS simulations were performed for a lead–bismuth eutectic (LBE) with constant thermal–physical properties at $Pr = 0.025$. The bulk Reynolds number Re_b determined with the bulk flow velocity of the tube, covers a wide range between 10^4 and 4×10^5, while the corresponding bulk Peclet number Pe_b varies between 250 and 1,000. The block-structured mesh with local refinement toward the heated tube wall was used in all the RANS simulations, in accordance with the recommendation given by the mesh sensitivity study in Section 3.3.

Figure 14 compares then the bulk Nusselt number Nu_b obtained in RANS simulations with that calculated with the experimental correlations of Eqs. 22–24. With the conventional choice of $Pr_t = 0.9$, the bulk Nusselt number is largely overpredicted. RANS simulations with the Kays model for Pr_t still overpredict the bulk Nusselt number, since a good agreement with the upper limit defined by the correlation of Lyon (1949), Lyon (1951) is observed. With the proposed new model for Pr_t, on the other hand, a much better agreement with the experimental correlations is achieved. The bulk Nusselt number Nu_b obtained with the proposed new model for Pr_t lies within the range of the upper and lower limit defined by the correlation of Lyon (1949), Lyon (1951), and Kutateladze et al. (1959), respectively, and it agrees well with that given by the correlation of Notter and Sleicher (1972), which is recommended as the best general applicable correlation for all the investigated liquid metals including sodium (Na) and sodium–potassium alloys (NaK), pure lead (Pb) and lead–bismuth eutectic (LBE) as well as pure mercury (Hg).

In the second step of validation phase II, a bare rod bundle in the hexagonal arrangement was investigated, for which most of

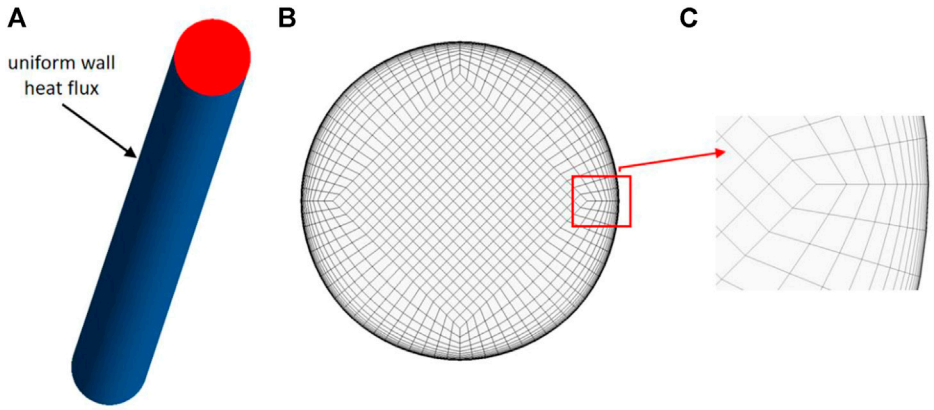

FIGURE 13
(A) Sketch of a tube heated uniformly on the wall; **(B)** and **(C)** mesh used in the RANS simulations.

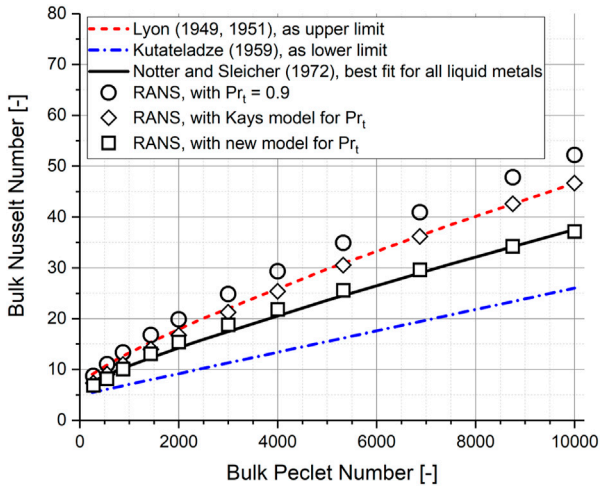

FIGURE 14
Validation of the proposed model on the turbulent Prandtl number: heated tube.

the experiments were performed in hexagonal arrays or bundles (OECD, 2015). Based on a review of available experimental data, the following three correlations were chosen as references. All the correlations express the bulk Nusselt number Nu_b in a similar way in terms of the bulk Peclet number Pe_b and the pitch-to-diameter ratio (P/D).

1) Correlation of Gräber and Rieger (1972).

$$Nu_b = 0.25 + 6.2\left(\frac{P}{D}\right) + \left[0.032\left(\frac{P}{D}\right) - 0.007\right] \cdot Pe_b^{0.8-0.024\left(\frac{P}{D}\right)}. \quad (25)$$

TABLE 3 Summary of experimental correlations on the bulk Nusselt number in a bare rod bundle of the hexagonal arrangement for the low-Prandtl number liquid metal.

Source	P/D [-]	Peb [-]
(Gräber and Rieger, 1972)	1.2–2.0	150–4,000
Ushakov et al., (1977)	1.3–2.0	1–4,000
Mikityuk, (2009)	1.1–1.95	30–5,000

2) Correlation of Ushakov et al. (1977).

$$Nu_b = 7.55 - 20\left(\frac{P}{D}\right)^{-13} + \frac{3.67}{90}\left(\frac{P}{D}\right)^{-2} \cdot Pe_b^{0.19\left(\frac{P}{D}\right)+0.56}. \quad (26)$$

3) Correlation of Mikityuk (2009).

$$Nu_b = 0.047 \cdot \left[1 - e^{-3.8\left(\frac{P}{D}-1\right)}\right] \cdot \left(Pe_b^{0.77} + 250\right). \quad (27)$$

It should be noted, that the aforementioned Eqs. 25–27 were developed based on the experimental data of alkali metals such as liquid sodium (Na) or sodium–potassium alloy (NaK). However, as reviewed by Mikityuk (2009), the three correlations were recommended in the OECD Handbook on the heavy liquid metal (OECD, 2015) as the most relevant engineering heat transfer correlations for heavy liquid metal flows, that is, LBE or liquid lead. Similar to the correlations proposed for a circular tube, the aforementioned three correlations for the bare rod bundle are defined for the fully developed state. Table 3 summarizes the validity range of the respective correlations in terms of the pitch-to-diameter ratio and bulk Peclet number. However, it should be noted that in the review conducted by Mikityuk (2009), all the three correlations were recommended for use in the range of P/D = 1.1 ~ 1.95 and bulk Peclet number Pe_b of 30 ~ 5000.

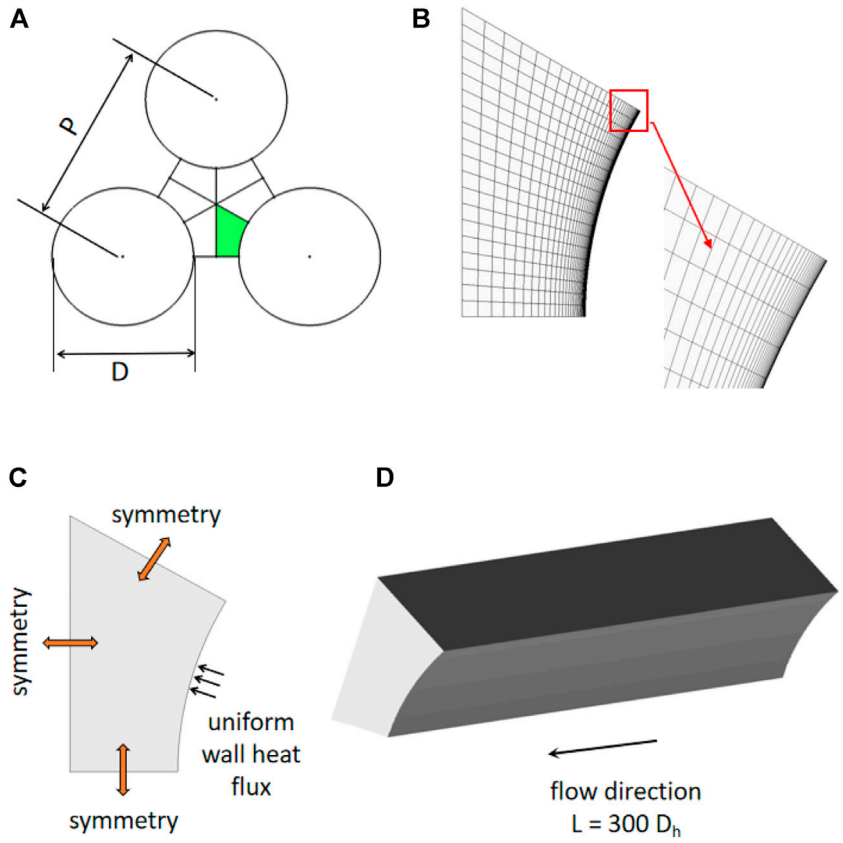

FIGURE 15
(A) Sketch of a bare rod bundle uniformly on the wall; **(B)** mesh used in the RANS simulations. **(C)** boundary conditions is the RNAS simulations; **(D)** sketch of the streamwise domain length.

Figure 15A defines the geometry investigated in the current study, where a triangular bundle configuration is shown. One-sixth of a sub-channel (a colored region in the figure) was defined as a computational domain, in which a block-structured hexahedral mesh was defined (Figure 15B). The definition of the boundary conditions was specified in Figure 15C. The rod was defined as a no-slip wall with a constant uniform heat flux, while the symmetry boundary condition was imposed on the other three side planes. In order to achieve a fully developed state, a domain length of 300 times of the hydraulic diameter was given in the flow direction. Constant uniform velocity and temperature were specified in the inlet boundary and a constant pressure condition was defined at the outlet boundary. LBE with constant thermal–physical properties (corresponding Prandtl number is 0.025) was chosen as a working fluid. In the current study, four pitch-to-diameter ratios P/D = 1.1, 1.2, 1.3, and 1.5 were investigated. For each pitch-to-diameter ratio, RANS simulations were performed for bulk Reynolds numbers Re_b = 10000, 20000, 40000, 60000, 100000, and 120000, respectively. The corresponding bulk Peclet numbers Pe_b are 250, 500, 1000, 1500, 2500 , and 3000, respectively. The turbulent Prandtl numbers Pr_t for RANS simulations calculated with the new model are then 5.00, 3.08, 1.80, 1.57, 1.50, and 1.50, respectively.

Figures 16A–D compare, then, the bulk Nusselt number obtained by RANS simulations with that given by the experimental correlations Eqs. 25–27 for P/D = 1.1, 1.2, 1.3, and 1.5, respectively. It is shown as follows:

1) The same trend of the bulk Nusselt numberNu_b increasing with the bulk Peclet number Pe_b but decreasing with the P/D ratio is predicted by all the three experimental correlations, as well as by the RANS simulations.
2) For the tight-spaced bundle of P/D = 1.1, a large scattering exists among the experimental correlations. Although the values of Nu_b calculated with the correlation of Gräber and Rieger (1972) and Ushakov et al. (1977) are still comparable, they are both much higher than those predicted by the correlation of Mikityuk (2009). Nu_b obtained by the RANS approach with Pr_t = 0.9 is higher than that obtained by the RANS approach with the new

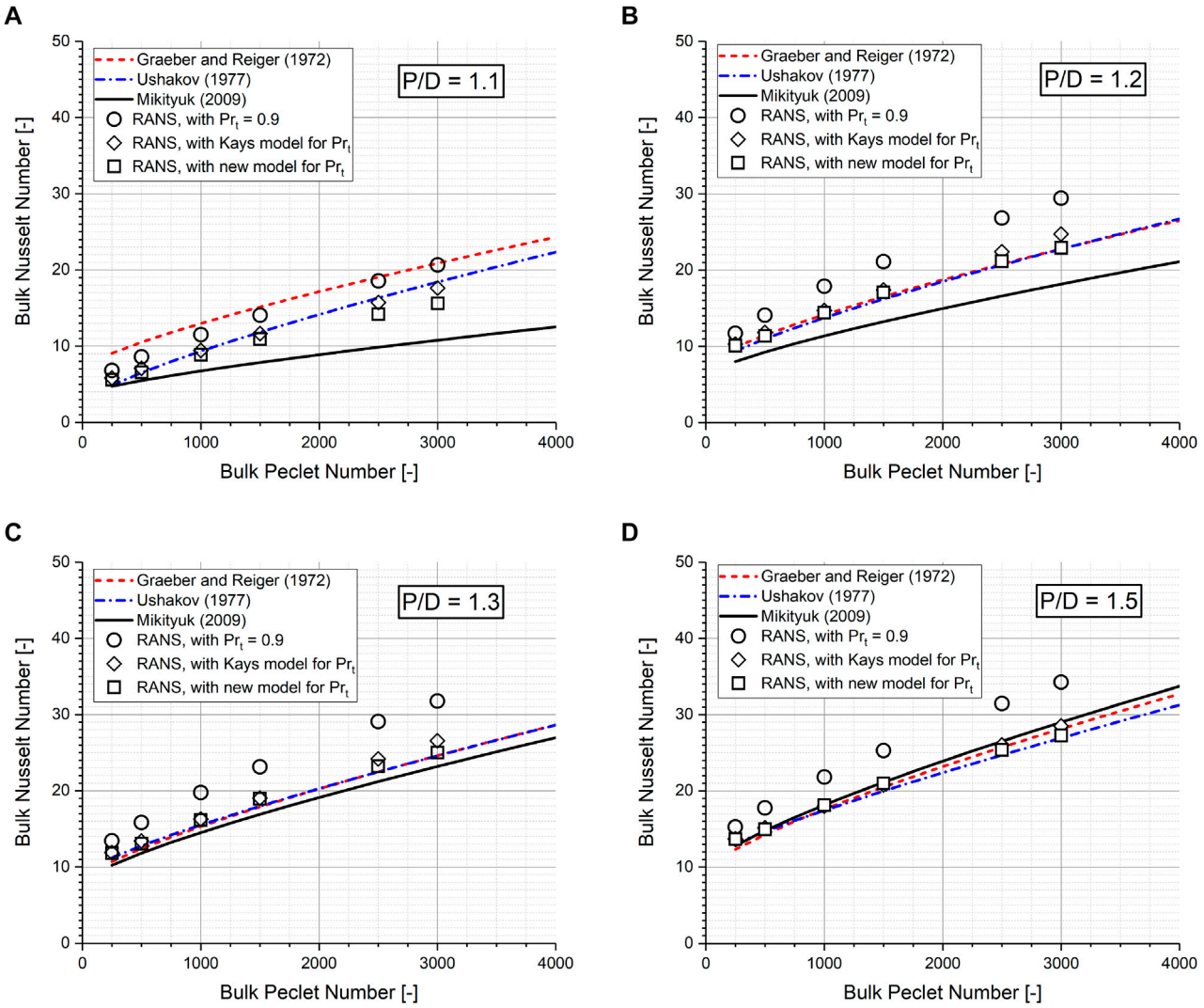

FIGURE 16
Validation of the proposed model on turbulent Prandtl number: bare rod bundle of P/D ratio equals **(A)** 1.1; **(B)** 1.2; **(C)** 1.3 and **(D)** 1.5.

model for Pr_t. But they all lie within the range defined by the three experimental correlations.

3) However, the situation is much different for the loosely spaced rod bundle of P/D ratio larger than 1.2. Nu_b predicted by the three correlations agrees well with each other. In general, for the loosely spaced rod bundle, the bulk Nusselt number obtained by the RANS approach with the conventional choice of $Pr_t = 0.9$ is much higher than that predicted by the experimental correlations. With the new proposed model for Pr_t, however, a much better agreement with the experimental correlations was able to be achieved. Compared to the RANS simulations with the Kays model, RANS simulations with the new model proposed in this study show a comparable yet slightly better agreement with the three experimental correlations.

5 Conclusion and outlook

In this study, LES/DNS simulation results of a fully developed forced turbulent channel flow up to $Re_\tau = 2000$ at $Pr = 0.01$ and 0.025 were used as a reference, to which the RANS approach with the simple turbulent Prandtl number concept was compared and calibrated. Based on the calibrated relation with bulk Peclet number Pe_b , a new model for turbulent Prandtl number Pr_t used in the RANS approach was proposed and validated. The main conclusions derived are summarized as follows:

1) Heat transfer characteristics of the low-Prandtl number liquid metal depend strongly on the turbulent Prandtl number Pr_t. An accurate estimation of Pr_t is of essential importance when

applying the RANS approach to simulate the turbulent heat transfer of liquid metal. The conventional choice of Pr_t = 0.9 is proven to be not suitable for the liquid metal, with which the bulk Nusselt number Nu_b could be overestimated by up to 40%.

2) Taking the LES/DNS simulation results of the fully developed forced turbulent channel flow as a reference, the RANS approach with the turbulent Prandtl number concept was assessed. It was found that the optimum value of Pr_t used in the RANS approach for the low-Prandtl number liquid metal decreases with bulk Peclet Number Pe_b and tends to approach a constant value of 1.5 as Pe_b becomes larger than 2000.
3) Based on the aforementioned relation between Pr_t and Pe_b, a new model expressing Pr_t solely in dependence on Pe_b was proposed in this study. Validation of the proposed model was carried out with available LES/DNS results of a local temperature profile in a concentric annulus and a loosely spaced bare rod bundle, as well as with experimental correlations on bulk Nusselt number Nu_b in a circular tube and bare rod bundle in a triangular arrangement. An overall good agreement of the RANS simulation results with the LES/DNS results, as well as with the experimental correlations was achieved, which demonstrates the adequacy of the proposed new model for Pr_t in this study.
4) To summarize, it could be concluded that the RANS approach with the simple concept of a constant global turbulent Prandtl number Pr_t is a suitable tool for simulating the forced convective turbulent heat transfer with the low-Prandtl number liquid metal, provided an appropriate Pr_t is specified. The RANS approach with the turbulent Prandtl number concept is, and will still be the only feasible approach when dealing with industrial application of turbulent heat transfer with the low-Prandtl number liquid metal. Therefore, it is believed that the model developed in the current study will have a promising perspective for engineering applications.

Data availability statement

The raw data supporting the conclusions of this article will be made available by the authors, without undue reservation.

Author contributions

XH—writing–original draft preparation; methodology; investigation; data curation; visualization. BP—conceptualization; methodology; investigation; writing–original draft preparation; writing–review and editing; project administration; funding acquisition. XC—software; investigation; writing–review and editing YY—methodology; project administration; writing–review and editing.

Funding

This work was financially supported by the Natural Science Foundation of Guangdong Province (2021A1515010391).

Conflict of interest

The authors declare that the research was conducted in the absence of any commercial or financial relationships that could be construed as a potential conflict of interest.

Publisher's note

All claims expressed in this article are solely those of the authors and do not necessarily represent those of their affiliated organizations, or those of the publisher, the editors, and the reviewers. Any product that may be evaluated in this article, or claim that may be made by its manufacturer, is not guaranteed or endorsed by the publisher.

References

Abe, H., Kawamura, H., and Matsuo, Y. (2004). Surface Heat-Flux Fluctuations in a Turbulent Channel Flow up to Reτ=1020 with Pr=0.025 and 0.71. *Int. J. Heat Fluid Flow* 25 (3), 404–419. doi:10.1016/j.ijheatfluidflow.2004.02.010

Aoki, S. (1963). *A Consideration on the Heat Transfer in Liquid Metal*. Tokyo, Japan: Bulletin of the Tokyo Institute of Technology, 63–73.

Bricteux, L., Duponcheel, M., Winckelmans, G., Tiselj, I., and Bartosiewicz, Y. (2012). Direct and Large Eddy Simulation of Turbulent Heat Transfer at Very Low Prandtl Number: Application to Lead-Bismuth Flows. *Nucl. Eng. Des.* 246, 91–97. doi:10.1016/j.nucengdes.2011.07.010

Chai, X., Liu, X., Xiong, J., and Cheng, X. (2019). Numerical Investigation of Thermal-Hydraulic Behaviors in a LBE-Cooled 19-pin Wire-Wrapped Rod Bundle. *Prog. Nucl. Energy* 119, 103044. In press, corrected proof, Available online 1 May 2019, Article 103044. doi:10.1016/j.pnucene.2019.103044

Cheng, X., and Tak, N.-I. (2006). Investigation on Turbulent Heat Transfer to Lead-Bismuth Eutectic Flows in Circular Tubes for Nuclear Applications. *Nucl. Eng. Des.* 236, 385–393. doi:10.1016/j.nucengdes.2005.09.006

Duponcheel, M., Bricteux, L., Manconi, M., Winckelmans, G., and Bartosiewicz, Y. (2014). Assessment of RANS and Improved Near-Wall Modeling for Forced Convection at Low Prandtl Numbers Based on LES up to Reτ=2000. *Int. J. Heat Mass Transf.* 75, 470–482. doi:10.1016/j.ijheatmasstransfer.2014.03.080

Graber, H., and Rieger, M. (1972). Experimentelle Untersuchung des Wärmebergangs an Flüssigmetalle (NaK) in parallel durchströmten Rohrbündeln bei konstanter und exponentieller Wärmeflussdichteverteilung. *Atomkernenergie* 19 (1), 23–40.

Jischa, M., and Rieke, H. B. (1979). About the Prediction of Turbulent Prandtl and Schmidt Numbers from Modeled Transport Equations. *Int. J. Heat Mass Transf.* 22, 1547–1555. doi:10.1016/0017-9310(79)90134-0

Kader, B. A. (1981). Temperature and Concentration Profiles in Fully Turbulent Boundary Layers. *Int. J. Heat Mass Transf.* 24, 1541–1544. doi:10.1016/0017-9310(81)90220-9

Kawamura, H., Abe, H., and Matsuo, Y. (1999). DNS of Turbulent Heat Transfer in Channel Flow with Respect to Reynolds and Prandtl Number Effects. *Int. J. Heat Fluid Flow* 20, 196–207. doi:10.1016/s0142-727x(99)00014-4

Kays, W. M. (1994). Turbulent Prandtl Number-Where Are We? *J. Heat Transf.* 116, 284–295. doi:10.1115/1.2911398

Kirillov, P., and Ushakov, P. A. (2001). Heat Transfer to Liquid Metals: Specific Features, Methods of Investigation, and Main Relationships. *Therm. Eng.* 48 (1), 50–59.

Kutateladze, S., Borishanskii, V., and Novikov, I. (1959). Heat Transfer in Liquid Metals. *J. Nucl. Energy, Part B, React. Technol.* 9 (1-4), 214–229. doi:10.1016/0368-3265(59)90177-x

Lyon, R. (1949). *Forced Convection Heat Transfer Theory and Experiments with Liquid Metals*. Oak Ridge, Tennessee: Oak Ridge National Laboratory.

Lyon, R. (1951). Liquid Metal Heat-Transfer Coefficients. *Chem. Eng. Prog.* 47 (2), 75–79. doi:10.1080/00223131.2014.980349

Lyu, Y., Ge, Z., and Zhao, P. (2015). Large Eddy Simulation for the Turbulent Heat Transfer of Liquid Metal in an Annulus. *J. Univ. Sci. Technol. China* 45 (11), 917–922. doi:10.3969/j.issn.0253-2778.2015.11.006

Ma, Z., Wu, Y., Qiu, Z., Tian, W., Su, G., and Qiu, S. (2012). An Innovative Method for Prediction of Liquid Metal Heat Transfer Rate for Rod Bundles Based on Annuli. *Ann. Nucl. Energy* 47, 91–97. doi:10.1016/j.anucene.2012.04.023

Marinari, R., Di Piazza, I., Tarantino, M., Angelucci, M., and Martelli, D. (2019). Experimental Tests and Post-test Analysis of Non-uniformly Heated 19-pins Fuel Bundle Cooled by Heavy Liquid Metal. *Nucl. Eng. Des.* 343, 166–177. doi:10.1016/j.nucengdes.2018.12.024

Marocco, L. (2018). Hybrid LES/DNS of Turbulent Forced and Aided Mixed Convection to a Liquid Metal Flowing in a Vertical Concentric Annulus. *Int. J. Heat Mass Transf.* 121, 488–502. doi:10.1016/j.ijheatmasstransfer.2018.01.006

Mikityuk, K. (2009). Heat Transfer to Liquid Metal: Review of Data and Correlations for Tube Bundles. *Nucl. Eng. Des.* 239 (4), 680–687. doi:10.1016/j.nucengdes.2008.12.014

Notter, R. H., and Sleicher, C. A. (1972). A Solution to the Turbulent Graetz Problem-III Fully Developed and Entry Region Heat Transfer Rates. *Chem. Eng. Sci.* 27 (11), 2073–2093. doi:10.1016/0009-2509(72)87065-9

OECD (2015). *Handbook on Lead-Bismuth Eutectic Alloy and Lead Properties, Materials Compatibility, Thermal-hydraulics and Technologies*. Paris, France No: OECD/NEA, 7268.

Reynolds, A. J. (1975). The Prediction of Turbulent Prandtl and Schmidt Numbers. *Int. J. Heat Mass Transf.* 18, 1055–1069. doi:10.1016/0017-9310(75)90223-9

Roelofs, F. (2019). "Chapter 1: Introduction to Liquid Metal Cooled Reactors," in *Thermal Hydraulics Aspects of Liquid Metal Cooled Nuclear Reactors*. Editor F. Roelofs (Cambridge: Woodhead Publishing, Elsevier Ltd).

Shams, A. (2019). "Chapter 6.2.1 Turbulent Heat Transport," in *Thermal Hydraulics Aspects of Liquid Metal Cooled Nuclear Reactors*. Editor F. Roelofs (Cambridge: Woodhead Publishing, Elsevier Ltd).

Shams, A., De Santis, A., Koloszar, L. K., Villa Oritz, A., and Narayanan, C. (2019). Status and Perspectives of Turbulent Heat Transfer Modelling in Low-Prandtl Number Fluids. *Nucl. Eng. Des.* 353, 110220. doi:10.1016/j.nucengdes.2019.110220

Shams, A., Mikuž, B., and Roelofs, F. (2018). Numerical Prediction of Flow and Heat Transfer in a Loosely Spaced Bare Rod Bundle. *Int. J. Heat Fluid Flow* 73, 42–62. doi:10.1016/j.ijheatfluidflow.2018.07.006

Tiselj, I., Flageul, C., and Oder, J. (2019). Direct Numerical Simulation and Wall-Resolved Large Eddy Simulation in Nuclear Thermal Hydraulics. *Nucl. Technol.* 206, 164–178. doi:10.1080/00295450.2019.1614381

Ushakov, P., Zhukov, A., and Matyukhin, N. (1977). Heat Transfer to Liquid Metals in Regular Arrays of Fuel Elements. *High. Temp. (USSR)* 15 (10), 1027–1033.

frontiers | Frontiers in Energy Research

TYPE Original Research
PUBLISHED 08 August 2022
DOI 10.3389/fenrg.2022.964841

OPEN ACCESS

EDITED BY
Liangming Pan,
Chongqing University, China

REVIEWED BY
Longxiang Zhu,
Chongqing University, China
Liangxing Li,
Xi'an Jiaotong University, China

*CORRESPONDENCE
Hui Cheng,
chengh78@mail.sysu.edu.cn
Songbai Cheng,
chengsb3@mail.sysu.edu.cn

SPECIALTY SECTION
This article was submitted to Nuclear Energy,
a section of the journal
Frontiers in Energy Research

RECEIVED 09 June 2022
ACCEPTED 12 July 2022
PUBLISHED 08 August 2022

CITATION
Mai Z, Zhao Z, Cheng H, Cheng S and Zhao J (2022), Numerical study on the release and migration behavior of fission gas in a molten LBE pool.
Front. Energy Res. 10:964841.
doi: 10.3389/fenrg.2022.964841

Numerical study on the release and migration behavior of fission gas in a molten LBE pool

Zijun Mai[1], Zichen Zhao[2], Hui Cheng[1]*, Songbai Cheng[1]* and Jiyun Zhao[3]

[1]Sino-French Institute of Nuclear Engineering and Technology, Sun Yat-Sen University, Zhuhai, Guangdong, China, [2]Reactor Engineering Center/Serious Accident Department, China Nuclear Power Technology Research Institute Co., Ltd., Shenzhen, Guangdong, China, [3]Department of Mechanical Engineering, City University of Hong Kong, Hong Kong, China

The lead-cooled fast reactor (LFR) is one of the most promising fast neutron reactors using molten lead or the lead–bismuth eutectic (LBE) alloy as a coolant. Under postulated severe accidents, the fuel rod of LFR may be damaged, which would cause the release of fission gas, and the migration of fission gas bubbles in the reactor molten pool will affect the release and absorption of radioactive substances in the reactor. In this paper, a three-dimensional numerical study on the release and migration behavior of fission gas in the molten LBE pool of LFR is carried out based on the volume of fluid method. The bubbles are continuously released by gas injection, and the research mainly focuses on the detachment time, the rising velocity, and the size of the bubble when it detaches at the orifice. The coalescence of bubbles is observed, and the acceleration effect of the bubble wake is confirmed. The distribution of the bubble terminal rising velocity with diameter has no simple or linear relationship. The effects of the gas injection velocity, the release depth, and the gas injection angle are studied. A lower gas injection velocity will delay the detachment and reduce the size of the bubble. The increase of release depth tends to release smaller bubbles. The bubbles released from a vertical surface will attach to the wall. The simulations and theoretical analysis are comparable and have similar tendencies. The distribution of the bubble terminal rising velocity with equivalent diameter may predict the migration behavior of bubbles in molten LBE.

KEYWORDS

lead-cooled fast reactor, lead–bismuth eutectic alloy, bubble migration, VOF method, nuclear safety

Introduction

Fast neutron reactors can greatly improve the utilization rate of uranium resources and reduce nuclear contamination through transmutation as well as improve the safety during operation (Kelly, 2014; Pioro, 2016). As one of the members of fast neutron reactors using a liquid metal as a coolant (Pioro, 2016), the lead-cooled fast reactor (LFR) utilizes lead or lead-based alloys such as the lead–bismuth Eutectic alloy (LBE) as the primary coolant, which has favorable characteristics in terms of thermal properties,

chemical inertness, and a harder neutron spectrum (Tuček et al., 2006; Fazio et al., 2015). However, LFRs have not reached the level of commercial operation and exist only for a few experimental use and military applications (Cinotti et al., 2009).

In a pool-type LFR, the fuel assemblies are deployed in the molten LBE pool, and the fuel pellet undergoes the fission reaction, producing neutrons, solid fission products, and gas fission products. In a postulated severe accident, the core fuel rods suffer damages, the fission gas contained will be released from the crack, and gas bubbles will be formed in the LBE pool, which will affect the natural circulation of the primary loop and then influence the safety of the operation. Fission gas is a component of the radioactive source item of the coolant of the primary circuit. When the fission gas bubbles are formed, their volumes and migration behavior will directly affect the distribution of radioactive substances in the molten pool, causing changes in the absorption and release among the core, the coolant of the primary circuit, and the gas environment, which will affect the safety analysis of LFR, such as the analysis of the radioactive source term. Hence, fully understanding of the release and migration behavior of fission gas in the molten LBE pool is crucial for the safety design of LFR.

As a common phenomenon in various scenarios, the migration behavior of bubbles in the liquid has been studied by numerous researchers with theoretical analyses, experiments, and simulations. Dating back to 1917, the Rayleigh equation (Rayleigh, 1917) can describe the instantaneous pressure of the external liquid and the radius with time of a large bubble. Based on this, viscosity and surface tension have been considered in the Rayleigh–Plesset equation (Plesset and Chapman, 1971). The viscous drag is an important factor affecting the migration of bubbles; many researches have carried out studies on the drag coefficient (Prosperetti, 1977; Bhaga and Weber, 1981; Kang and Leal, 1988a; Kang and Leal, 1988b; Tomiyama et al., 1998). A large number of experiments and theoretical analyses have shown that the rising velocity of bubbles in the liquid is related to the size of the bubbles, and many scholars have proposed methods to calculate the rising velocity of bubbles based on different assumptions. Davies and Taylor (Davies and Taylor, 1950) studied the rising velocity of large bubbles and proposed the formula for the calculation. Based on this, Joseph's formula has considered viscosity and surface tension (Joseph, 2003). The analogy of the wave theory has been applied for the prediction of the terminal rising velocity of bubbles in surface tension- and inertia-dominated regions (Mendelson, 1967). In Wallis's drift model, the formulas of the terminal rising velocity of bubbles in still liquids under flow conditions distinguished by the Re number and Ga number are given (Wallis, 1974). Grace's graphical empirical correlation (Clift et al., 1987) interprets the shape of bubbles by three dimensionless numbers, namely, the Reynolds number (Re), the Morton number (Mo), and the Eötvös number (Eo), and it can be used to predict the terminal rising velocities of bubbles. Tomiyama et al. (2002) analyzed the relationship between the terminal rising velocity of the bubble and the aspect ratio that characterizes the deformation of the bubble through experiments and theoretical analysis and proposed a model of the relationship between the terminal rising velocity and the aspect ratio of the bubble.

Although theoretical and experimental studies have achieved certain results, most of them are based on spherical bubbles. For other complex flow conditions such as a high Reynolds number, large bubble deformation, and interaction between multiple bubbles, numerical simulation study shows its advantages. Zhang et al. (2012) used the volume of fluid (VOF) method to study the dynamic characteristics of the formation, growth, release, and rise of a single bubble in three dimensions, and the effects of fluid properties, fluid velocities, orifice number, and nozzle size on bubble behavior are investigated. Based on the finite element lattice Boltzmann method of mass conservation (FE-LBE), a two-dimensional (2D) numerical simulation study of bubbles rising in a viscous liquid at a high Reynolds number was carried out (Baroudi and Lee, 2021). The pressure fluctuation and velocity fluctuation are numerically studied during the bubble detachment (Cai et al., 2018). In an unsteady turbulence of the venturi bubble generator, the numerical simulation on the bubble dynamics is carried out (Song et al., 2021).

Most of the research studies on multiphase flow are based on water or other transparent viscous liquids, whereas it is hard to conduct experiments and visualize the bubbles in liquid metals such as molten LBE. The rising motion of single bubbles in the LBE pool is studied by neutron radiography (Hibiki et al., 2000), indicating that the migration behavior is similar to the typical characteristics of bubble migration in two-phase flow, and the results agree well with 1D and 2D simulations using the SIMMWE-III code. The bubble coalescence in the GaInSn eutectic alloy is investigated by X-ray photography (Keplinger et al., 2018). The rising velocity and the shape of small helium bubbles are indirectly measured by a layer of glycerol above the molten LBE pool (Konovalenko et al., 2017). The drag coefficient of single bubbles in molten LBE is obtained by analogy with several transparent liquids; then the prediction of the terminal rising velocity of single bubbles in molten LBE is carried out (Zhang et al., 2018). The diffusive interface method is applied for the 2D simulation of nitrogen single bubbles, and the results agree with Grace's graphical correlation (Wang and Cai, 2018). Nevertheless, the experimental research on the bubble migration behavior in molten LBE is restricted due to the opacity, and 2D simulation studies cannot completely describe the movements and forces of bubbles in three dimensions. Thus, the research on the bubble migration behavior in molten lead and bismuth is still insufficient.

In order to study the release and migration behavior of fission gas bubbles in the molten LBE pool of LFR, 3D numerical simulation based on the VOF method was carried out. The effects of gas injection velocity, release depth, and gas injection angle on the bubble release and migration behavior in molten LBE were

investigated. The bubble rising velocity, bubble equivalent diameter, and bubble detachment time, which are of great importance in bubble dynamics, were measured. The results were compared with theoretical analysis. This paper contributes to deepening the understanding of the mechanism of the release and migration behavior of fission gas bubbles in the molten LBE pool of LFR, and it provides a reference for system design optimization as well as safety analysis of LFR.

Numerical method

Governing equations

For incompressible fluids, the continuity equation and the momentum equation with surface tension are as follows:

$$\nabla.\vec{u} = 0 \tag{1}$$

$$\rho\left(\frac{\partial\vec{u}}{\partial t} + \left(\vec{u}.\nabla\right)\vec{u}\right) = -\nabla p + \nabla.\left(\mu\left(\nabla\vec{u} + \left(\nabla\vec{u}\right)^{T}\right)\right) + \rho\vec{g} + \vec{F_s} \tag{2}$$

where $\vec{u}$ denotes the fluid velocity, ρ denotes the density, p denotes the pressure, μ denotes the dynamic viscosity coefficient, $\vec{g}$ denotes the acceleration of gravity, and $\vec{F_s}$ denotes the equivalent body force of the surface tension. The system of Navier–Stokes equations consists of the continuity equation and the momentum equation.

The VOF method (Hirt and Nichols, 1981) is a free interface tracking method based on a fixed Euler grid, which has the advantages of a high efficiency and good precision. In this method, two or more immiscible fluids share a set of momentum equations, and the interface in the computational domain is tracked by the volume fraction C as follows:

$$\begin{cases} C = 0, & gas \\ 0 < C < 1, & interface \\ C = 1, & liquid \end{cases} \tag{3}$$

For the i^{th} phase, the volume fraction satisfies the volume fraction equation as follows:

$$\frac{\partial C_i}{\partial t} + \vec{u_i} \cdot \nabla C_i = 0 \tag{4}$$

In the current case, gas and liquid phases satisfy

$$\sum_{i=1}^{2} C_i = 0 \tag{5}$$

In the continuum surface force (CSF) model (Brackbill et al., 1992), with the divergence theorem, the surface tension at the interface can be expressed as an equivalent body force as follows:

$$F_S = \frac{\rho\sigma\kappa\nabla C_l}{0.5\left(\rho_g + \rho_l\right)} \tag{6}$$

where ρ is the density; g and l denote, respectively, the gas phase and liquid phase; σ denotes the surface tension coefficient; and κ denotes the interface curvature; the density and the viscosity are respectively obtained by the following scalar equations:

$$\rho\left(\vec{x},t\right) = \rho_l C\left(\vec{x},t\right) + \rho_g\left(1 - C\left(\vec{x},t\right)\right) \tag{7}$$

$$\mu\left(\vec{x},t\right) = \mu_l C\left(\vec{x},t\right) + \mu_g\left(1 - C\left(\vec{x},t\right)\right) \tag{8}$$

Boundary conditions and solution strategy

In this paper, the gas injection is divided into two modes: gas injection at the bottom orifice and gas injection at the wall orifice. As shown in Figure 1A, the simulation computational domain for the migration of bubbles continuously generated through ∇gas injection at the bottom orifice is a cuboid of 30 mm × 30 mm × 75 mm, and the orifice is located at the center of the bottom surface. In Figure 1B, when simulating the bubbles released by gas injection through the wall orifice, in order to further reduce the unnecessary computation, one of the dimensions of the bottom surface of the computational domain is shortened to 20 mm, and the height of the orifice is 10 mm. The orifices are 1 mm in diameter. The meshing of the entire computational domain is based on a structured mesh with a size of 0.5 mm. Since the shape of the orifice is circular, an O-grid is applied for the meshing. The processes of geometry and meshing were performed using ANSYS ICEM. The velocity inlet is set at the orifice. The top surface of the computational domain is set as the pressure outlet, and other surfaces are non-slip walls. The operation condition of the simulation is under an atmospheric pressure, that is, $1.013 \times 10^5\ Pa$. Initially, the liquid in the domain was in a static state.

In view of the huge difference in magnitude of physical properties such as density and viscosity between the gas and liquid, the volume of the bubble, which is affected by temperature, pressure, and physical properties, would be mainly concerned. Therefore, air is used as the general representative of the gas phase. At the same time, it is assumed that the effect of heat transfer between the bubble and the external fluid could be neglected. The physical properties of the studied fluids are given in Table 1.

The simulations are performed with ANSYS Fluent. The pressure-based and transient solver is selected. The gravity is $-9.81\ m/s^2$ in the z-direction. In the VOF model, the volume fraction discretization method is explicit, and the interface modeling is sharp. The CSF model is selected in the phase interaction section. The pressure–velocity coupling scheme is the Pressure-Implicit with Splitting of Operators (PISO) method, the pressure discretization method is PREssure STaggering Option (PRESTO), the momentum discretization method is the QUICK mode, and the volume

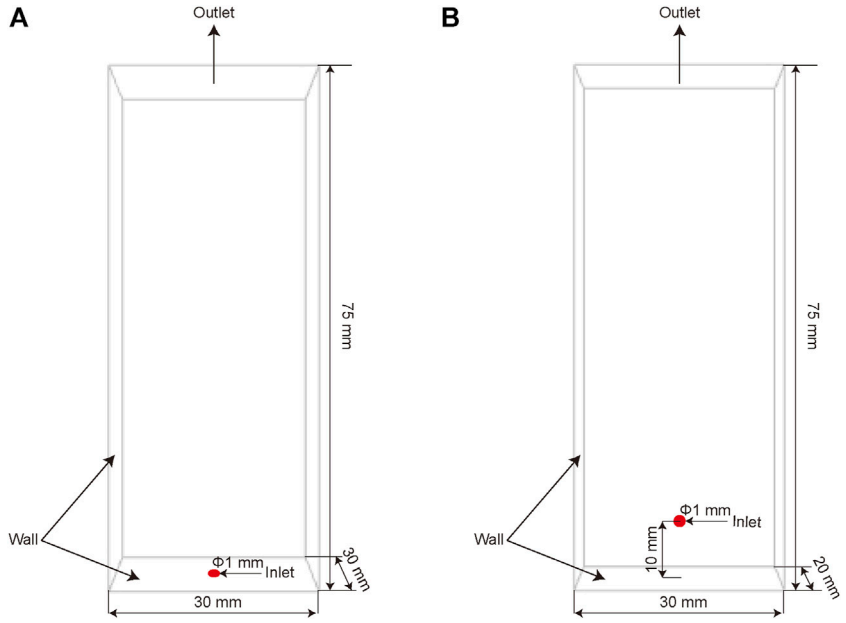

FIGURE 1
Schematic of the computational domain. **(A)** Bottom injection. **(B)** Wall injection.

TABLE 1 Material properties.

Material	Air	Water	LBE
Temperature (°C)	25	25	400
Density (kg/m^3)	1.225	998.2	10194.62
Viscosity (kg/m/s)	1.7894e-5	0.001003	0.001514
Surface tension (N/m)	—	0.0728	0.3947

TABLE 2 Detachment time and diameter of the first bubble in water when $v_g = 1\,m/s$.

Grid size (mm)	0.25	0.4	0.5	1.0
Total numbers of nodes	660,049–992,052	1,122,094	604,505	77,824
Detachment time (s)	0.110	0.100	0.100	0.135
Equivalent diameter (mm)	5.34	5.05	4.98	5.44

fraction discretization method is Geo-Reconstruct. Considering the calculation speed and convergence, the Courant number is controlled between 0.1 and 0.8; then the time step is adapted from 10^{-5} to 10^{-3} s, and the time interval of output data is 0.005 s.

The post-processing is conducted with CFD-Post. The bubble edge is defined by the iso-surface where the air bubble volume fraction is 0.4, and the acquisition of the data is based this iso-surface. The bubble's length, width, and height are measured; then the rising velocity and aspect ratio are calculated. The instantaneous rising velocity is defined as the average velocity calculated from the distance that the bubble rises in 0.005 s, while the terminal rising velocity is the average of the instantaneous rising velocity after the bubble has finished accelerating. The volume of the bubble is obtained by volume integration of the grids, and the equivalent diameter of the bubble is calculated from the bubble volume.

Grid independent test

In order to study the effect of mesh size on the simulation results, the grid-independent test is conducted through the simulation of bubbles released by gas injection in water. Air passes through the orifice with a diameter of 1 mm at the gas velocity of 1 m/s, and bubbles emerge, grow and detach from the orifice, and rise in the computational domain of a cuboid of 30 mm × 30 mm × 75 mm with grid sizes of 0.25, 0.4, 0.5, and 1.0 mm, respectively. In the computational domain, the overall mesh is based on structured meshes. The total numbers of nodes are given in Table 2, and it should be noted that the 0.25 mm grid is only applied near the gas–liquid interface.

Figure 2 shows the meshes before the first bubble detaches under grids of different sizes. It can be observed that the bubbles all show the shape of a rounded upper part and a shrinking neck shape before they are released. The finer the mesh is, the

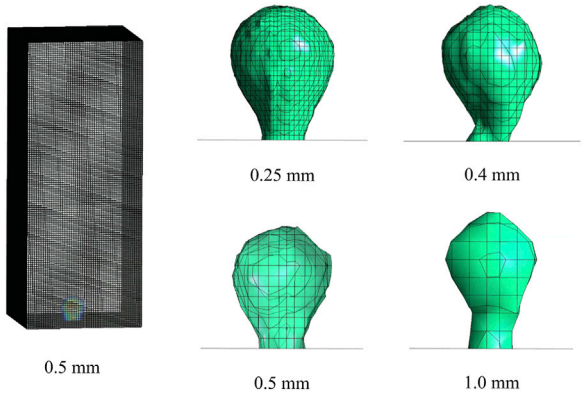

FIGURE 2
Mesh of the bubble before detachment with different grid sizes.

smoother and rounder the bubble interface is described, and when the mesh is thicker, the surface of the bubble gradually appears angular, and the position of the bubble center is higher. The grid-independent analysis mainly focuses on the detachment time and size of the first bubble released from the orifice under different mesh sizes as well as the instantaneous rising velocity and aspect ratio of the bubble after the detachment.

The detachment time of the first bubble emerging from the orifice and the corresponding equivalent diameter are shown in Table 2. The detachment time and equivalent diameter of the first bubble in grids under 0.5 mm are close, and the detachment is obviously delayed in the grid of 1.0 mm. The rising velocity in different grids is shown in Figure 3A; similar behaviors are found where the rising velocity increases rapidly after the bubble detaches and then fluctuates within a certain range. Figure 3B shows that the aspect ratio drops rapidly and then fluctuates around a stable value. The results of grids under 0.5 mm are close, while the result with the 1.0 mm grid is sometimes unstable and the values of aspect ratio are generally higher.

The above simulations verify the independence of the grid and show that a grid size of 0.5 mm is sufficient to reasonably and accurately simulate and analyze the migration characteristics of bubbles in liquids. For a typical bubble with an equivalent diameter of 5 mm, the number of grids is about 500. Therefore, considering the rationality and accuracy of the calculation and taking into account the convergence and speed of the calculation, a grid with a size of 0.5 mm is used for the following 3D numerical simulations.

Model verification

Model verification is an indispensable part of numerical study. In order to verify the rationality and applicability of the

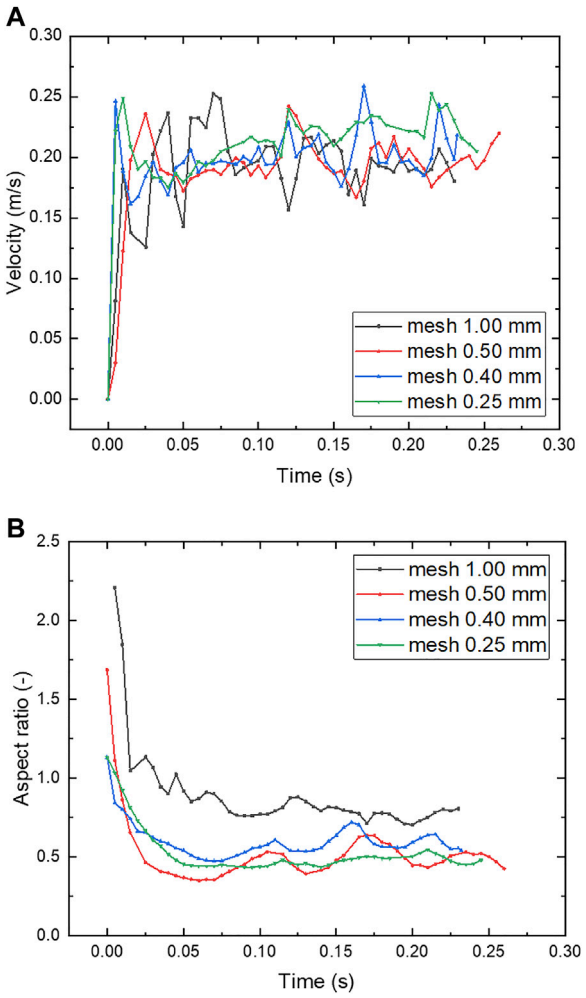

FIGURE 3
(A) Rising velocity and **(B)** aspect ratio of the bubble in water with different grid sizes, $v_g = 1\,m/s$.

model, the 3D simulation of a bubble released in water is conducted. A bubble with an equivalent diameter of 4 mm, which is found typical for the study of bubble migration in liquids, is released and rises under the action of buoyancy. The simulation of the bubble rising in water is compared to the experiment conducted in the laboratory of Sun Yat-Sen University, and the process of bubble rising in water was captured using a high-speed camera.

Simulation snapshots and experimental results of a 4 mm bubble rising in quiescent water are compared in Figure 4. It is found that the simulation results of the height, the deformation, and the motion of the bubble agree well with the experiment. After the bubble is released, the bottom of the bubble rapidly becomes flat, and the shape of the bubble becomes ellipsoidal. The rising trajectory of the bubble is zigzag on the 2D view, while it is flat and upward spiral in 3D

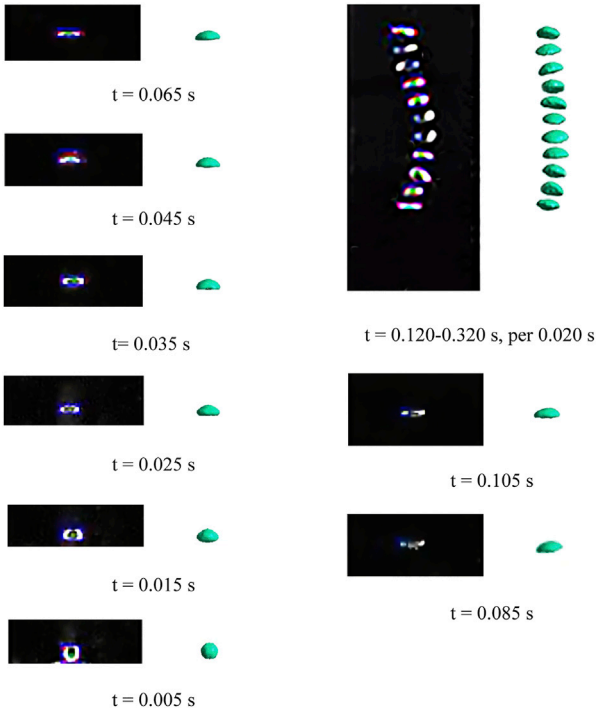

FIGURE 4
Comparison of experiments and 3D simulation of the bubble rising in water, $d = 4\,mm$.

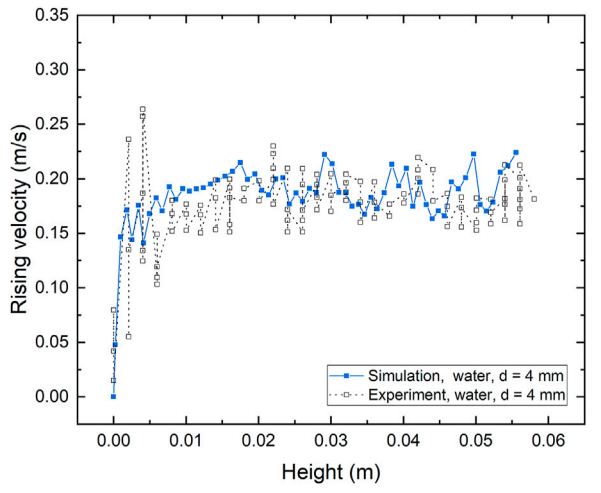

FIGURE 5
Comparison of 3D simulation and experiments of bubble rising velocity with height in water.

FIGURE 6
Snapshots of 3D simulation of bubbles released by gas injection in molten LBE, $v_g = 1\,m/s$.

view. The wobble of the bubble has a similar direction in simulation and experiments, but the deviation is less important in simulation. Due to the purity of the fluid and the actual situation of the field, the difference between simulation and experiments is inevitable. It is hard to make sure that the liquid is absolutely quiescent in experiments, and the gas velocity and pressure will affect the result, which lead to the motion of the bubble in experiments being more violent. Generally, the result of simulation agrees well with experiments.

Figure 5 shows the rising velocities of a 4 mm bubble in water with height in simulation as well as in experiments. The rising velocities increase rapidly once the bubbles are released and then fluctuate within certain ranges. The results in simulation and in experiments are similar and comparable. Considering the complexity of the bubble migration behavior, the agreement between simulation and experimental results of the bubble in water is acceptable, which indicates that the methodology is reasonable and feasible to study the bubble migration behavior in the liquid, and the modifications in material properties from water to molten LBE would be possible. Hence, this model can be applied to the study on the bubble migration behavior in molten LBE.

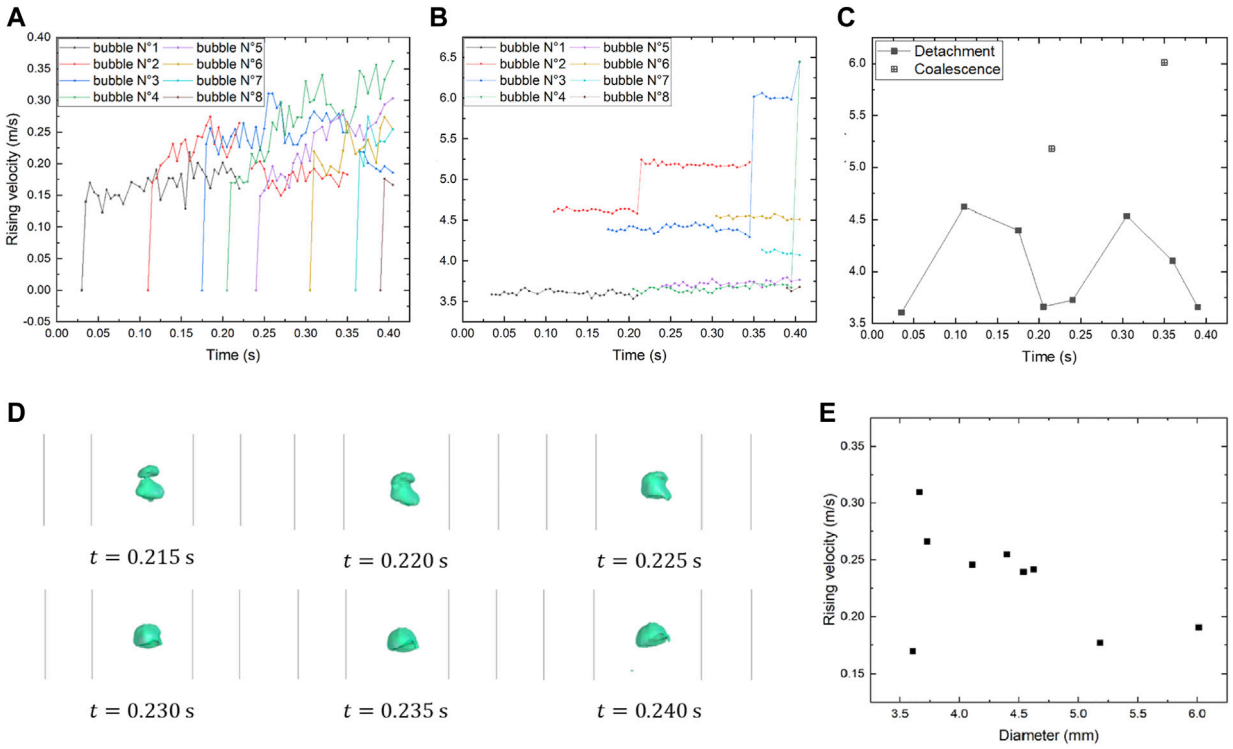

FIGURE 7
Simulation results of bubbles released by gas injection in molten LBE, $v_g = 1\,m/s$. **(A)** Rising velocity. **(B)** Equivalent diameters. **(C)** Detachment and coalescence. **(D)** Coalescence of bubbles No. 1 and 2. **(E)** Terminal rising velocity.

Results and discussion

Bubbles released by gas injection in the molten lead–bismuth eutectic

In a postulated severe accident in LFR, the damage of the fuel rods could cause the ejection of the high-pressure fission gas contained within and thereby generate bubbles. In order to better understand the release and migration behavior of fission gas bubbles in molten LBE pools under severe accidents, a 3D numerical study of bubble migration behavior under the condition that gas bubbles are continuously generated by gas injection is carried out in this part. At the same time, in order to study the potential influencing factors of bubble migration behavior in the postulated severe accident of LFR, the effects of different parameters including gas injection velocity, release depth, and gas injection angle were studied. The results of the bubble rising velocity, bubble detachment time, and bubble equivalent diameter were measured.

Figure 6 shows the snapshots of 3D simulation of bubbles continuously generated at a gas injection velocity $v_g = 1\,m/s$ through the orifice with a diameter of 1 mm at the bottom of the computational domain. The bubbles undergo the generation, growth, and detachment. Then, the bubbles float upward in the computational domain under the action of inertia and buoyancy. After the bubbles detach from the orifice, the lower surface quickly becomes flat or even concave and then becomes hemispherical or ellipsoidal, and the bubbles rise with wobbling. Within 0.4 s of the simulation, eight bubbles have detached at the orifice, which are named bubble No. 1 to bubble No. 8 according to the detachment order. Figure 7A shows the instantaneous rising velocities of these bubbles. It is observed that the bubbles continuously generated by gas injection in molten LBE have typical bubble rising characteristics; that is, the rising velocities of the bubbles first increase rapidly after detaching at the orifice and then fluctuate around stable values.

Under the current conditions, the coalescence of bubbles can be clearly observed. The coalescence of bubble No. 1 and No. 2, the coalescence of bubble of No. 2 and No. 3, and the coalescence of bubble of No. 3 and No. 4 occurred at 0.215, 0.350, and 0.405 s, respectively, forming a bigger bubble at each time. It is found in Figure 7B that the equivalent diameter of the bubbles remains basically stable during the rising process except during the coalescence process. Among them, the bubbles with a too short simulation duration were not analyzed. It can be seen in Figure 7C that at the gas injection velocity $v_g = 1\,m/s$, the equivalent diameter of the bubbles has a certain periodicity. The equivalent diameter of the bubbles detaching from the

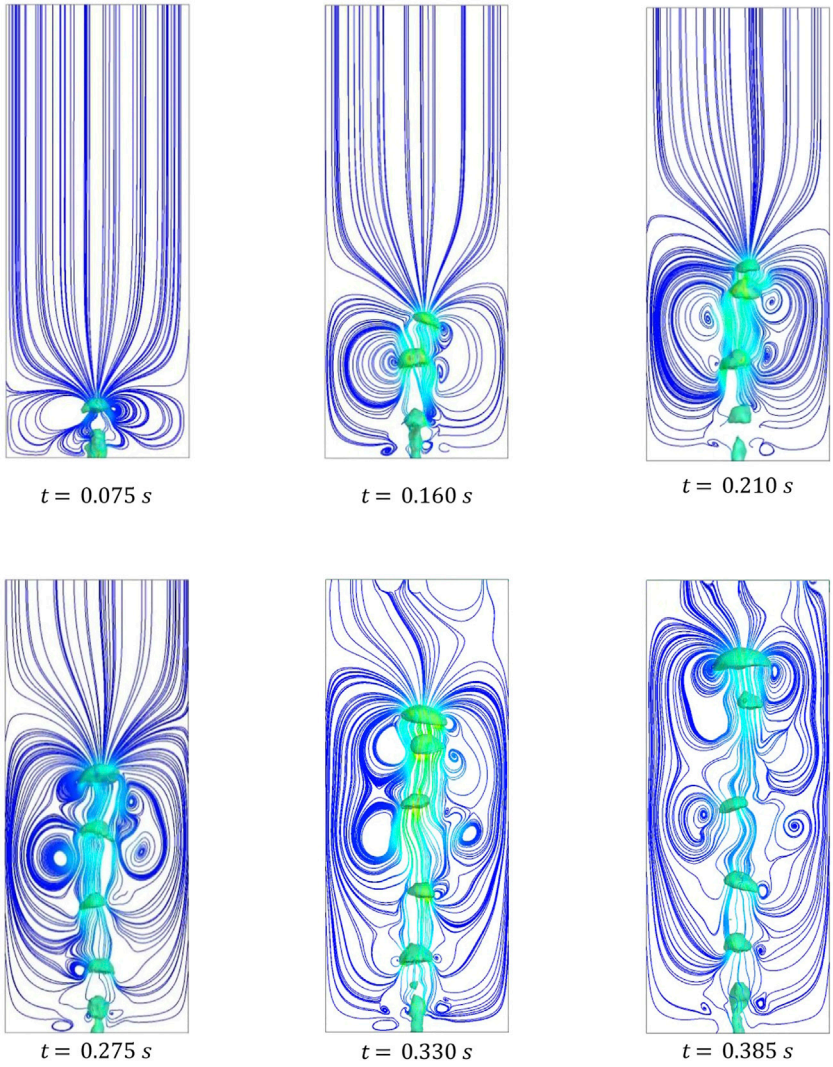

FIGURE 8
Streamlines of the velocity field of bubbles released by gas injection in molten LBE, $v_g = 1\,m/s$.

orifice is between 3.5 and 4.6 mm, and the fluctuation period of its value is about 0.2 s. The frequency of releasing bubbles is 0.049, and the equivalent diameters of the bubbles after coalescence are all greater than 5 mm.

Figure 7D shows the process of coalescence of bubble No. 1 and bubbles No. 2. The leading bubble usually has a lower rising velocity, and due to the effect of the wake of the leading bubble, the trailing bubble is accelerated and its top surface extends to reach the leading bubble's lower surface and then eventually merges with the leading bubble. The coalescence of bubbles leads to the formation of a bigger bubble. This phenomenon is also found in the study of Hasan (Hasan and Zakaria, 2011). It can be seen in Figure 7A that the rising velocity of the bubble after coalescence is slightly higher than the leading bubble.

Figure 8 shows the streamlines of the velocity field during the release and rising of bubbles. It is observed that the streamlines around the first bubble have good symmetry and the field above is tranquil. While it is found that the bubble wake has a long distance and straight impact on the bubbles down below, most of the bubbles detaching afterward get in the wake of the upper bubbles. The bubbles in the wake not only are accelerated but also could be deviated horizontally. With the continuous release and rising of bubbles, the streamlines become more complex but maintain a relatively good symmetry, which keeps the bubbles being influenced by the bubble wake.

Therefore, it can be seen in Figure 7E that no simple or linear relationship exists for the terminal rising velocity of bubbles released by gas injection in molten LBE and it is divided into two cases. One of the cases is the bubbles not being influenced by the

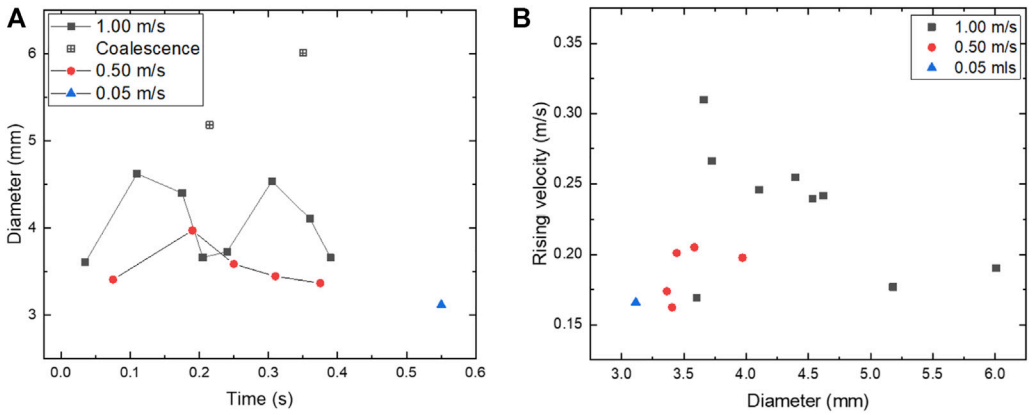

FIGURE 9
Effect of gas injection velocity on the release and migration behavior of bubbles in molten LBE. **(A)** Equivalent diameter. **(B)** Terminal rising velocity.

bubble wake, and the other is the bubbles influenced by the bubble wake. The first bubble detaching at the orifice and the bubbles after merging with it are not influenced by the wake, and their terminal rising velocities are lower than 0.20 m/s, as shown in Figure 7E, and only after the coalescence, the rising velocity increases slightly. While the bubbles get influenced by the wake of the upper bubble, the wake causes the decrease of the pressure, the increase of fluid velocity, and the formation of vortexes. These differences in the flow field accelerate the bubbles that are in the wake, making their terminal rising velocities greater than 0.20 m/s.

Effect of gas injection velocity

In order to study the effect of gas injection velocity on the bubble migration behavior, the simulations were conducted under the condition of gas injection though the orifice at the bottom surface of the computational domain, with the typical gas injection velocity $v_g = 1m/s$, $0.5m/s$, $0.05\,m/s$. It is found that the gas injection velocity has a great impact on the number of bubbles and the detachment time. Moreover, the coalescence of bubbles is found when $v_g = 1m/s$, while it is not observed when $v_g = 0.5m/s$ and $v_g = 0.05m/s$.

The detachment time and equivalent diameter of bubbles in molten LBE at each gas injection velocity are shown in Figure 9A, where the coalescence of bubbles occurs at $v_g = 1m/s$. Reducing the gas injection velocity can significantly delay the detachment time. At a smaller gas injection velocity, the equivalent diameter of the bubble is smaller when the bubble detaches at the orifice. For example, when $v_g = 1m/s$, the range of equivalent diameters of the bubble is 3.6–4.6 mm, and it increases with the coalescence of bubbles, while when $v_g = 0.5m/s$, the range of equivalent diameters of the bubble reduces to 3.4–4.0 mm; when $v_g = 0.05m/s$, only one bubble with an equivalent diameter of 3.1 mm is released. It is observed that the equivalent diameter of the first bubble increases slightly with the increase of gas injection velocity. However, there is no obvious difference in the terminal rising velocity.

Figure 9B shows the distribution of bubble terminal rising velocity with equivalent diameter at the gas injection velocities of $v_g = 1m/s$, $0.5m/s$, $0.05\,m/s$. There is no simple and linear relationship existing, and there are two zones when $d \leq 4.5\,mm$: one of the zones when $3.5\,mm \leq d \leq 4.5\,mm$, where the terminal rising velocity drops from 0.31 m/s to 0.24 m/s, and the other when $3.0\,mm \leq d \leq 4.0\,mm$, where the terminal rising velocity increases from 0.16 m/s to 0.20 m/s. When $d > 4.5\,mm$, the terminal rising velocity is around 0.18 m/s. For the first bubble detaching at the orifice and the bubbles after merging with the first bubble, they are less likely to be affected by the bubble wake, and the flow field above these bubbles is tranquil and quiescent. Therefore, these bubbles are not obviously accelerated and their terminal rising velocities are relatively low. However, the bubbles that are greatly affected by the wake of the upper bubble will accelerate. At a higher gas injection velocity, the time between bubbles leaving the orifice is shorter, and there is a greater chance of entering the wake of the upper bubble, so it is easier to be accelerated. For example, when $v_g = 1m/s$, the terminal rising velocity can be accelerated up to 0.30 m/s. At a lower gas injection velocity, the time between bubble detachments prolongs, weakening the influence of the wake between bubbles, so the bubbles are less accelerated. When $v_g = 0.5m/s$, the terminal rising velocity can be accelerated up to 0.20 m/s. When $v_g = 0.05m/s$, the second bubble does not detach when the first bubble leaves the computational domain and the effect of the wake could be neglected.

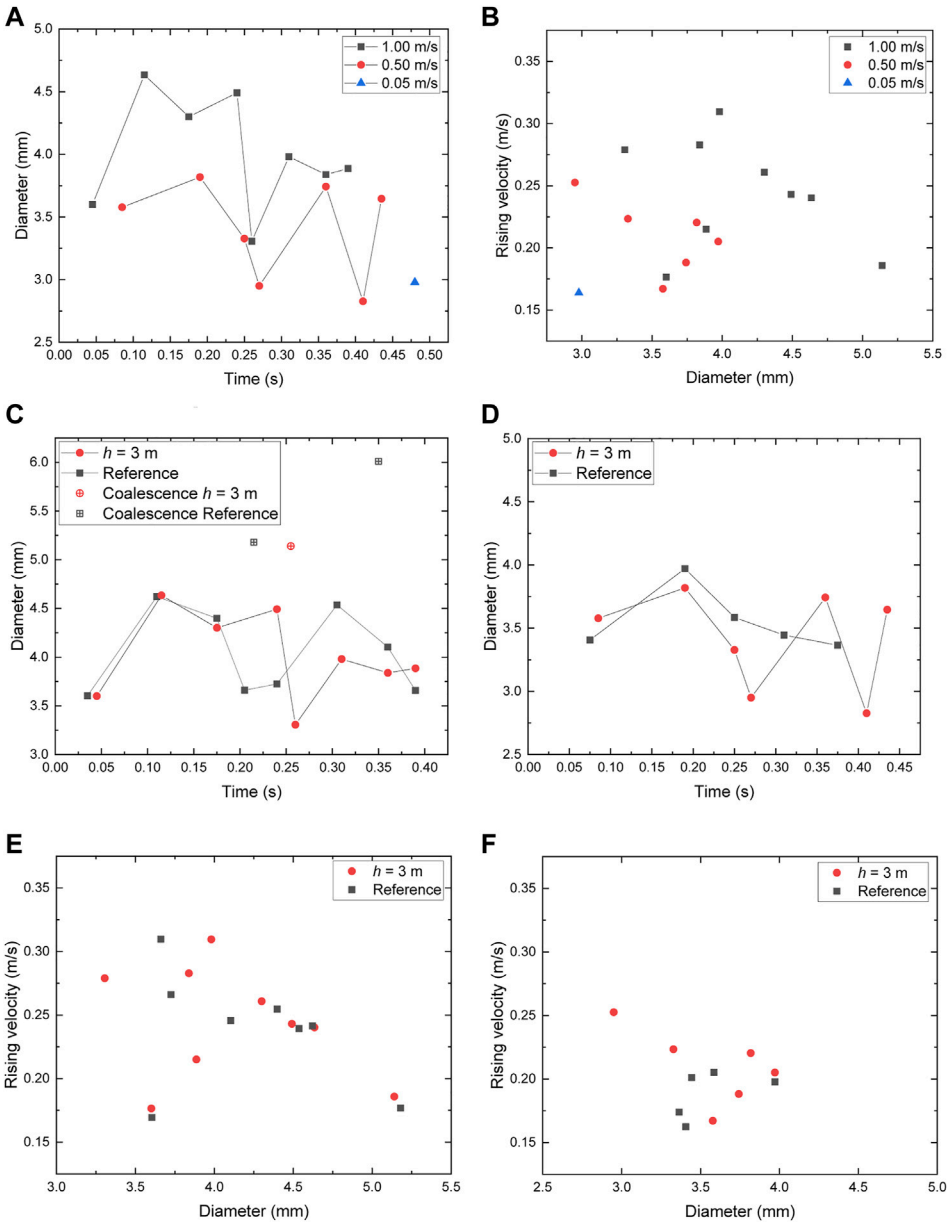

FIGURE 10
Influence of release depth on the release and migration behavior of bubbles in molten LBE. **(A)** Equivalent diameter. **(B)** Terminal rising velocity. **(C)** Equivalent diameter, v_o = 1 m/s. **(D)** Equivalent diameter, v_o = 0.5 m/s. **(E)** Terminal rising velocity, v_o = 1 m/s. **(F)** Terminal rising velocity, v_o = 0.5 m/s.

Effect of release depth

In order to study the effect of release depth on the bubble migration behavior in molten LBE, a layer of molten LBE of 3 m is added above the computational domain. Due to the limitation of computing resources, it is not possible to directly lengthen the computational domain by 3 m. Instead, the change in the length of the computational domain is equivalent by increasing the back pressure at the pressure outlet. The back pressure of $p_b = 0.3\ MPa$ is applied to the pressure outlet, which is equivalent to adding molten LBE with a thickness of 3 m above the computational domain, and the position of the orifice is equivalent to the lower middle position of the molten LBE pool. Studying the effect of release depth helps to better simulate the conditions of bubbles in the melt pool of LFR.

Simulations were carried out with the increase of release depth $h = 3\,m$ at the gas injection velocities of $v_g = 1m/s$, $0.5m/s$, $0.05\,m/s$. It is found in Figure 10A that the decrease of the gas injection velocity also causes the delay of detachment time and the decrease of the equivalent diameter, which is the same as the effect of the gas injection velocity without the increase of the depth.

Figures 10C,D show the influence of release depth on the detachment time and equivalent diameter of bubbles at $v_g = 1m/s$ and $v_g = 0.5m/s$. Only slight delay in the detachment is found after increasing the release depth, while the equivalent diameter of the bubble varies more violently at each detachment, and the coalescence of bubbles is also delayed when $v_g = 1m/s$. Moreover, when $h = 3\,m$ and $v_g = 1m/s$, the range of equivalent diameters shrinks from 3.6–4.6 mm to 3.3–4.6 mm, and for $v_g = 0.5m/s$, this range turns from 3.4–4.0 mm to 2.9–4.0 mm. This result indicates that the increase of release depth tends to reduce the lower limit of the range of equivalent diameters of the bubble released. Similarly, when $v_g = 0.05m/s$, the increase of depth turns out the decrease of the size of bubbles by about 1%. However, the gas volume of the bubble reduces and the detachment is in advance.

Figure 10B shows the distribution of bubble terminal rising velocity with equivalent diameter when $h = 3\,m$ at different gas injection velocities, and two zones of the terminal rising velocity are also observed. It infers that the bubbles with lower terminal rising velocities are less influenced by the bubble wake, while the bubbles with higher terminal rising velocities are accelerated by the wake of the upper bubbles. When the gas injection velocity decreases, the equivalent diameter of the bubble decreases, and the distance between bubbles extends at the same time, weakening the acceleration effect of the bubble wake. With the decrease of gas injection velocity, the distribution map of terminal rising velocity moves to the bottom left as a whole and finally gets gathered at the bottom left at a very low gas injection velocity. After the increase of release depth, the distribution is more dispersed than that in Figure 9B.

Figures 10E,F show the effect of release depth on the distribution of bubble terminal rising velocity with equivalent diameter at $v_g = 1m/s$ and $v_g = 0.5m/s$. At the gas injection velocity of 1 m/s, the difference of the distribution is not obvious by the change of release depth: when the equivalent diameter is greater than 4 mm, the terminal rising velocity decreases; when the equivalent diameter is below 4 mm, the terminal rising velocity is divided into a higher branch and a lower branch. At the gas injection velocity of 0.5 m/s, the bubbles are smaller than 4 mm, and the bubbles with an equivalent diameter of 3.4–4.0 mm have close terminal rising velocities before and after the increase of release depth. The increase of release depth can cause the generation of smaller bubbles within a shorter duration, making these bubbles more easily accelerated by the wake of the upper bubble.

Effect of gas injection angle

In the reactor, the fuel rods are in a vertical position. Under a postulated severe accident, the damage could happen on a vertical surface, in which the shear force applied on the bubble would be different. Hence, the gas injection angle is to be studied. The orifice with a diameter of 1 mm is located on the midline of a vertical wall, and the distance to the bottom surface is 10 mm. The gas injection velocities of 1 m/s, 0.5 m/s, and 0.05 m/s are applied.

Figure 11 shows the snapshots of simulation of the bubbles generated by gas injection at the wall orifice in molten LBE. It can be observed that the bubbles released at the wall orifice will rise and attach to the wall. The bubbles with a large gas volume tend to form half-cut bubbles, while the bubbles with a smaller gas volume tend to form gas films and the tiny bubbles on the wall surface. Compared to the previous cases where the orifice is on the bottom surface, more bubbles are generated at the orifice on the wall, and the bubbles that attach to the wall are more favorable to the coalescence of bubbles.

Figure 12A shows the instantaneous rising velocities of bubbles numbered by the order of detachment when $v_g = 1\,m/s$. There are nine bubbles released within 0.335 s, indicating that the bubbling frequency is higher than previous cases. The instantaneous rising velocity of the bubble is similar to those of the bubbles released at the orifice on the bottom surface; that is, the rising velocity of the bubble accelerates at the beginning and then fluctuates within a certain range. The bubbles attaching to the wall generally have higher rising velocities because of the guidance of the wall. Before the coalescence of bubbles, the wake of the upper bubble has an acceleration effect on the bubble below so that the bubble can reach a higher instantaneous rising velocity. The breakpoint of the curve in Figure 12A indicates the coalescence of bubbles. It is observed that the instantaneous rising velocity of the bubble after coalescence is lower than that of the trailing bubble and slightly higher than that of the original leading bubble. At the same time, it is found that sometimes, the phenomenon of bubble coalescence occurs the very moment after a bubble is just released from the orifice. For example, after bubble No. 5 is separated from the orifice, it accelerates to a high rising velocity so that it merges quickly with bubble No. 4.

The detachment time and equivalent diameter of bubbles generated by gas injection at the wall orifice in molten LBE at the gas injection velocities of 1 m/s and 0.5 m/s are shown in Figures 12C,D. The first bubble released at the orifice takes a longer waiting time than the rest of the bubbles, and therefore, more gas is accumulated to form a bigger bubble. Meanwhile, the flow field for the first bubble is tranquil, so its rising velocity is relatively low. The rest of the bubbles are smaller, and the time intervals between the bubble detachments are shorter; then these bubbles have short distances with each other. Therefore, theses bubbles are more easily accelerated under the effect of the wake of upper

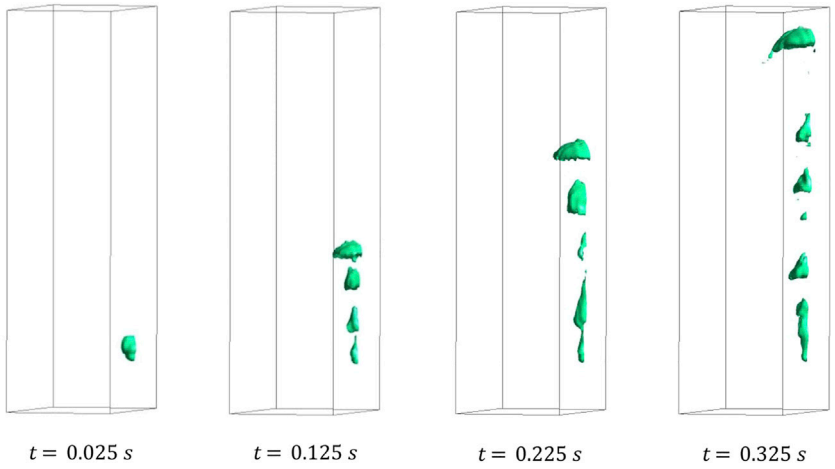

FIGURE 11
Snapshots of simulation of the bubbles generated by gas injection at the wall orifice in molten LBE, $v_g = 1\,m/s$.

bubbles and the coalescence of bubbles is facilitated. It should be noted that some of the bubbles merge right after their detachment with tiny bubbles, which detach almost at the same time, or with the gas column underneath, such as bubble No. 5 when $v_g = 1m/s$, and it is not shown in Figure 12C.

Figure 12B shows the detachment time and equivalent diameter at different gas injection velocities at the wall orifice. Compared with the results of the bubbles released at the orifice on the bottom surface in Figure 9A, it is found that bubbles are more easily released at the wall orifice and the bubbles are smaller. When $v_g = 1\,m/s$, the range of equivalent diameters decreases from 3.6–4.6 mm to 2.9–4.5 mm; when $v_g = 0.5\,m/s$, the range of equivalent diameters decreases from 3.4–4.0 mm to 2.0–3.4 mm; when $v_g = 0.05\,m/s$, the equivalent diameter drops from 3.1 mm to about 1.9 mm. The decrease of gas injection velocity delays the detachment time and the number of bubbles. In addition, the equivalent diameter decreases, and the fluctuation of the bubble equivalent diameter is less violent.

Figure 12E shows the distribution of terminal rising velocity with equivalent diameter of the bubbles generated by gas injection at the wall orifice in molten LBE. The existence of two zones which depend on the influence of the bubble wake is observed referring to the previous cases. Most of the small bubbles tend to chase after bigger bubbles; then these small bubbles are accelerated and reach higher rising velocities. The bubbles with larger diameters usually formed after merging with other bubbles, and their terminal rising velocities maintain around 0.20 m/s. With the decrease in the gas injection velocity, the equivalent diameter of the bubble decreases, and the terminal rising velocity decreases, which is equivalent to moving the overall distribution to the bottom left. Finally, when the gas injection velocity is very low, the data point converges at the bottom left of the diagram. Compared with Figure 9B, the terminal rising velocity of the bubble released by the wall orifice is generally higher than that of the bubble released by the orifice on the bottom surface.

Theoretical analysis

Numerical simulation provides a more economical and feasible path for more difficult and complex experimental research, especially for the molten LBE of opaque and complicated operations to carry out general experimental research. However, in order to discuss the rationality and accuracy of numerical simulation results, it is still useful to compare the results of numerical simulation with theoretical analysis.

Grace's graphical empirical correlation (Clift et al., 1987) describes the shape and rising characteristics of the bubble by the dimensionless numbers, namely, the Reynolds number (Re), Morton number (Mo), and Eötvös number (Eo), as follows:

$$Re = \frac{\rho_l U d}{\mu_l} \tag{9}$$

$$Mo = \frac{g\mu_l^4}{\rho_l \sigma^3} \tag{10}$$

$$Eo = \frac{\rho_l g d^2}{\sigma} \tag{11}$$

where the subscript l denotes the liquid phase, σ denotes the surface tension coefficient, d denotes the equivalent diameter of the bubble, μ denotes the dynamic viscosity coefficient, U denotes the rising velocity of the bubble, and g denotes the acceleration of gravity.

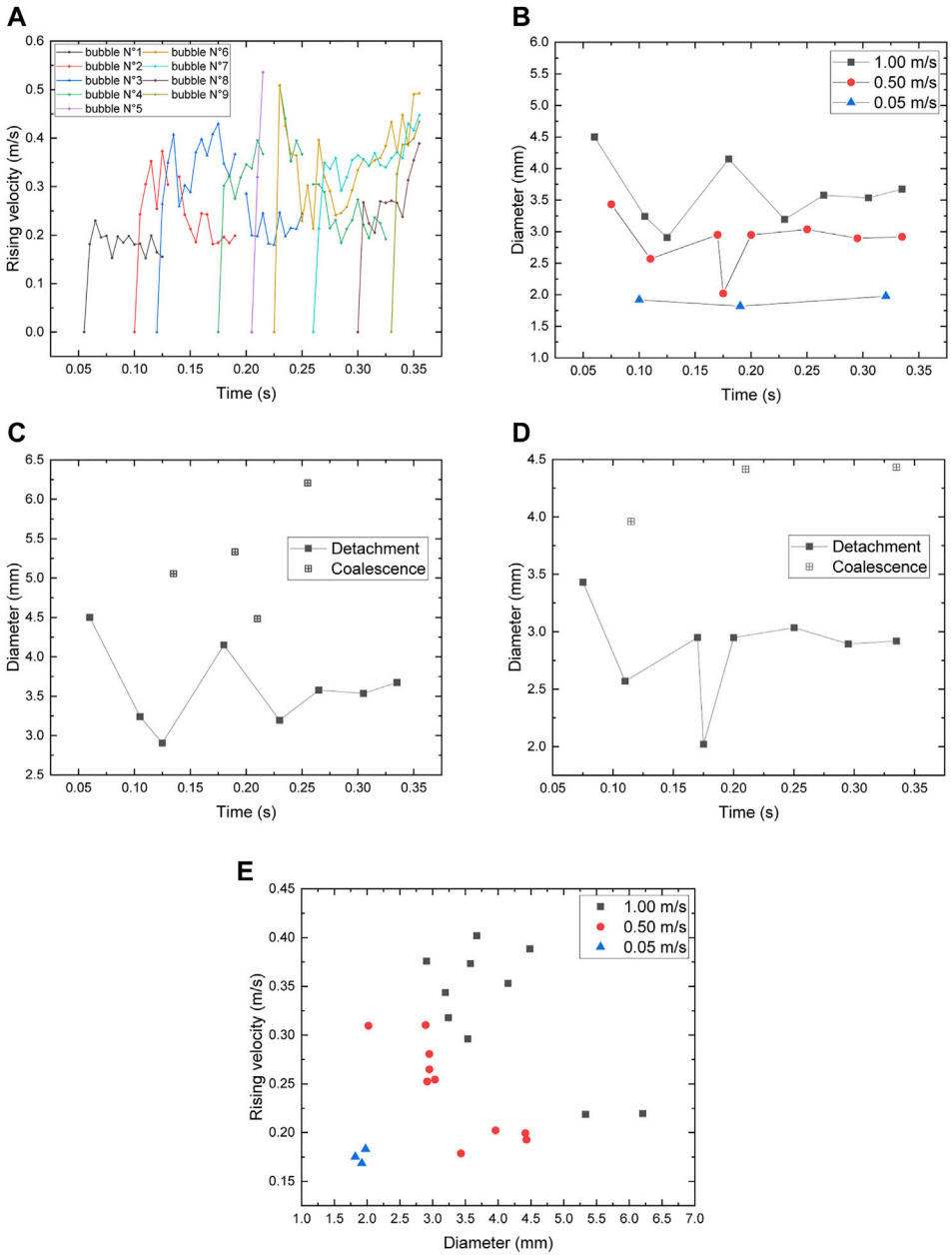

FIGURE 12
Release and migration behavior the bubbles generated by gas injection at the wall orifice in molten LBE. **(A)** Instantaneous rising velocity. **(B)** Equivalent diameter. **(C)** Equivalent diameter, v_o = 1 m/s. **(D)** Equivalent diameter, v_o = 0.5 m/s. **(E)** Terminal rising velocity.

Grace did not provide the curves at an extreme density ratio. The ranges of the dimensionless numbers including *Mo*, *Re*, and *Eo* are respectively 8.2×10^{-14}, $2.1 \times 10^{3} - 1.1 \times 10^{4}$, and 0.8 – 10. The high density and low viscosity of molten LBE result in the extreme situation of a high Reynolds number and a low Morton number. Therefore, the simulation results are located at the blank area of Figure 13, but the points tend to distribute with a similar tendency to the closest curve, where the Reynolds number increases with the Eötvös number. In addition, the shape of the bubbles is generally ellipsoidal with wobble, which agrees with the description of the bubbles located in the nearby region. The results of the cases of gas injection velocity and release depth almost have the same distributions. However, the distribution of the case of the wall orifice is wider and higher due a larger range of bubble sizes and a higher bubble terminal rising velocity. Hence, Grace's graphical empirical correlation

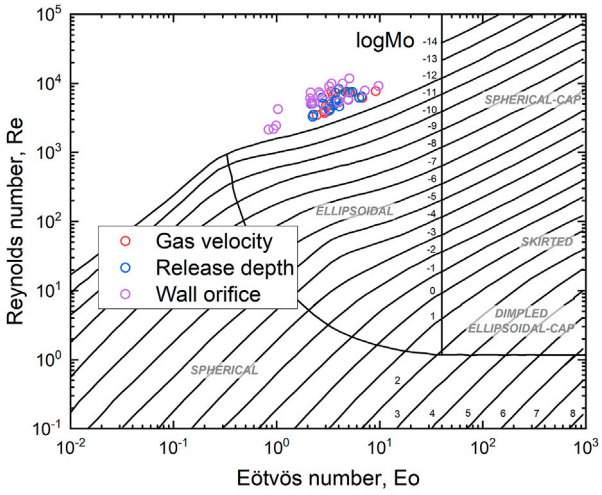

FIGURE 13
Simulation results on Grace's graphical empirical correlation.

and the results of simulation are still comparable, and it may be possible to predict the migration behavior of the bubbles in molten LBE, such as bubble shape and terminal rising velocity, by completing Grace's graphical empirical correlation at a higher Reynolds number.

Conclusion

In this paper, a 3D numerical study on the release and migration behavior of the fission gas bubbles in the molten LBE pool of LFR is carried out based on the VOF method. The acceleration effect of the wake of the upper bubble is confirmed, and coalescence of bubbles could be facilitated. The distribution of the terminal rising velocity with equivalent diameter of the bubble has no simple and linear relationship, and it depends on the influence of bubble wake. Decreasing the gas injection velocity delays the detachment time, decreases the bubbling frequency, and releases smaller bubbles. The increase of release depth tends to decrease the lower limit of the range of the bubble equivalent diameters, and the variation of bubble size may be more intense. The bubbles released at the orifice on the wall would reach higher rising velocities under the guidance of the wall and the acceleration effect of the bubble wake. The results of simulation are still comparable to Grace's graphical empirical correlation at the area of a higher Reynolds number, and the distribution of the terminal rising velocity with equivalent diameter may predict the migration characteristics of the bubbles in molten LBE. This paper contributes to deepening the understanding of the mechanism of the release and migration behavior of fission gas bubbles in the molten LBE pool of LFR and provides references for the system design optimization and safety analysis of LFR.

Data availability statement

The raw data supporting the conclusion of this article will be made available by the authors, without undue reservation.

Author contributions

ZM performed the investigation, analysis, and the writing of the first draft of the manuscript. HC wrote and edited sections of the manuscript. All authors contributed to manuscript revision, read, and approved the submitted version.

Funding

The research is funded by the Science and Technology Program of Guangdong Province (No. 2021A0505030026), the China Postdoctoral Science Foundation (No. 2019M663128), and the Basic and Applied Basic Research Foundation of Guangdong province (No. 2021A1515010343, No. 2022A1515011582).

Conflict of interest

ZZ was employed by China Nuclear Power Technology Research Institute Co., Ltd.

The remaining authors declare that the research was conducted in the absence of any commercial or financial relationships that could be construed as a potential conflict of interest.

Publisher's note

References

Baroudi, L., and Lee, T. (2021). Simulation of a bubble rising at high Reynolds number with mass-conserving finite element lattice Boltzmann method. *Comput. Fluids* 220, 104883. doi:10.1016/j.compfluid.2021.104883

Bhaga, D., and Weber, M. E. (1981). Bubbles in viscous liquids: Shapes, wakes and velocities. *J. Fluid Mech.* 105, 61–85. doi:10.1017/s002211208100311x

Brackbill, J. U., Kothe, D. B., and Zemach, C. (1992). A continuum method for modeling surface tension. *J. Comput. Phys.* 100, 335–354. doi:10.1016/0021-9991(92)90240-y

Cai, K., Song, Y., Li, J., Wang, D., Yin, J., Liu, W., et al. (2018). Pressure and velocity fluctuation in the numerical simulation of bubble detachment in a venturi-type bubble generator. *Nucl. Technol.* 205, 94–103. doi:10.1080/00295450.2018.1479575

Cinotti, L., Smith, C. F., and Sekimoto, H. (2009). *Lead-cooled fast reactor (LFR) overview and perspectives*. Livermore, CA, United States: Lawrence Livermore National Lab. LLNL.

Clift, R., Grace, J. R., and Weber, M. E. (1987). *Bubbles, drops, and particles*. New York: Academic Press.

Davies, R. M., and Taylor, G. I. (1950). The mechanics of large bubbles rising through liquids in tubes. *Proc. R. Soc. Lond. A* 200, 375–390.

Fazio, C., Sobolev, V. P., Aerts, A., Gavrilov, S., Lambrinou, K., Schuurmans, P., et al. (2015). *Handbook on lead-bismuth eutectic alloy and lead properties, materials compatibility, thermal-hydraulics and technologies-2015 edition*. Issy-les-Moulineaux, France: Organisation for Economic Co-Operation and Development.

Hasan, N., and Zakaria, Z. B. (2011). Computational approach for a pair of bubble coalescence process. *Int. J. Heat Fluid Flow* 32, 755–761. doi:10.1016/j.ijheatfluidflow.2011.02.004

Hibiki, T., Saito, Y., Mishima, K., Tobita, Y., Konishi, K., Matsubayashi, M., et al. (2000). Study on flow characteristics in gas-molten metal mixture pool. *Nucl. Eng. Des.* 196, 233–245. doi:10.1016/s0029-5493(99)00293-9

Hirt, C. W., and Nichols, B. D. (1981). Volume of fluid (VOF) method for the dynamics of free boundaries. *J. Comput. Phys.* 39, 201–225. doi:10.1016/0021-9991(81)90145-5

Joseph, D. D. (2003). Rise velocity of a spherical cap bubble. *J. Fluid Mech.* 488, 213–223. doi:10.1017/s0022112003004968

Kang, I. S., and Leal, L. G. (1988b). Small-amplitude perturbations of shape for a nearly spherical bubble in an inviscid straining flow (steady shapes and oscillatory motion). *J. Fluid Mech.* 187, 231–266. doi:10.1017/s0022112088000412

Kang, I. S., and Leal, L. G. (1988a). The drag coefficient for a spherical bubble in a uniform streaming flow. *Phys. Fluids (1994).* 31, 233–237. doi:10.1063/1.866852

Kelly, J. E. (2014). Generation IV international forum: A decade of progress through international cooperation. *Prog. Nucl. Energy* 77, 240–246. doi:10.1016/j.pnucene.2014.02.010

Keplinger, O., Shevchenko, N., and Eckert, S. (2018). Visualization of bubble coalescence in bubble chains rising in a liquid metal. *Int. J. Multiph. Flow* 105, 159–169. doi:10.1016/j.ijmultiphaseflow.2018.04.001

Konovalenko, A., Sköld, P., Kudinov, P., Bechta, S., and Grishchenko, D. (2017). Controllable generation of a submillimeter single bubble in molten metal using a low-pressure macrosized cavity. *Metall. Materi. Trans. B* 48, 1064–1072. doi:10.1007/s11663-017-0914-z

Mendelson, H. D. (1967). The prediction of bubble terminal velocities from wave theory. *AIChE J.* 13, 250–253. doi:10.1002/aic.690130213

Pioro, I. (2016). *Handbook of generation IV nuclear reactors*. Duxford, United Kingdom: Woodhead Publishing.

Plesset, M. S., and Chapman, R. B. (1971). Collapse of an initially spherical vapour cavity in the neighbourhood of a solid boundary. *J. Fluid Mech.* 47, 283–290. doi:10.1017/s0022112071001058

Prosperetti, A. (1977). Viscous effects on perturbed spherical flows. *Q. Appl. Math.* 34, 339–352. doi:10.1090/qam/99652

Rayleigh, L. (1917). VIII. On the pressure developed in a liquid during the collapse of a spherical cavity. *Lond. Edinb. Dublin Philos. Mag. J. Sci.* 34, 94–98. doi:10.1080/14786440808635681

Song, Y., Xu, R., Cai, K., Yin, J., and Wang, D. (2021). Numerical studies on bubble dynamics in an unsteady turbulence of the venturi bubble generator applied to TMSR. *Ann. Nucl. Energy* 160, 108322. doi:10.1016/j.anucene.2021.108322

Tomiyama, A., Celata, G., Hosokawa, S., and Yoshida, S. (2002). Terminal velocity of single bubbles in surface tension force dominant regime. *Int. J. Multiph. flow* 28, 1497–1519. doi:10.1016/s0301-9322(02)00032-0

Tomiyama, A., Kataoka, I., Zun, I., and Sakaguchi, T. (1998). Drag coefficients of single bubbles under normal and micro gravity conditions. *JSME Int. J. Ser. B Fluids. Therm. Eng.* 41, 472–479. doi:10.1299/jsmeb.41.472

Tuček, K., Carlsson, J., and Wider, H. (2006). Comparison of sodium and lead-cooled fast reactors regarding reactor physics aspects, severe safety and economical issues. *Nucl. Eng. Des.* 236, 1589–1598. doi:10.1016/j.nucengdes.2006.04.019

Wallis, G. B. (1974). The terminal speed of single drops or bubbles in an infinite medium. *Int. J. Multiph. Flow* 1, 491–511. doi:10.1016/0301-9322(74)90003-2

Wang, C., and Cai, J. (2018). Numerical simulation of bubble rising behavior in liquid LBE using diffuse interface method. *Nucl. Eng. Des.* 340, 219–228. doi:10.1016/j.nucengdes.2018.09.041

Zhang, C., Zhou, D., Sa, R., and Wu, Q. (2018). Investigation of single bubble rising velocity in LBE by transparent liquids similarity experiments. *Prog. Nucl. Energy* 108, 204–213. doi:10.1016/j.pnucene.2018.05.011

Zhang, Y., Liu, P., Xu, Y., and Tang, C. (2012). Three-dimensional volume of fluid simulations on bubble formation and dynamics in bubble columns. *Chem. Eng. Sci.* 73, 55–78. doi:10.1016/j.ces.2012.01.012

frontiers | Frontiers in Energy Research

TYPE Original Research
PUBLISHED 16 August 2022
DOI 10.3389/fenrg.2022.961547

OPEN ACCESS

EDITED BY
Hongli Chen,
University of Science and Technology of China, China

REVIEWED BY
Xiang Chai,
Shanghai Jiao Tong University, China
Donny Hartanto,
Oak Ridge National Laboratory (DOE), United States

*CORRESPONDENCE
Pengcheng Zhao,
zpc1030@mail.ustc.edu.cn
Tao Yu,
taoyu0626@163.com

SPECIALTY SECTION
This article was submitted to Nuclear Energy, a section of the journal Frontiers in Energy Research

RECEIVED 04 June 2022
ACCEPTED 22 July 2022
PUBLISHED 16 August 2022

CITATION
Xiao Y, Yang J, Zhao P, Yu T and Liu Z (2022), Research on core power maximization method of natural circulation lead-bismuth cooled fast reactor.
Front. Energy Res. 10:961547.
doi: 10.3389/fenrg.2022.961547

Research on core power maximization method of natural circulation lead-bismuth cooled fast reactor

Yingjie Xiao[1], Junkang Yang[1], Pengcheng Zhao[1,2]*, Tao Yu[1]* and Zijing Liu[1]

[1]School of Nuclear Science and Technology, University of South China, Hengyang, Hunan, China, [2]Science and Technology on Reactor System Design Technology Laboratory, Nuclear Power Institute of China, Chengdu, Sichuan, China

To improve the inherent safety and cost-effectiveness of lead-bismuth cooled fast reactors, the SPALLER-100 reactor designed by the University of South China has been selected as the research object to determine the maximum power it can produce. This is a multi-objective, complex, multi-dimensional, nonlinear, and constrained optimization problem. To maintain the transportability, material durability, and long-term operation stability of the reactor core and ensure safety under accident conditions, three steady-state limitations and three accident limitations are proposed. The platform used to calculate the maximum neutronic power produced by the reactor at different core heights has been built using Latin hypercube sampling and the Kriging proxy model. Meanwhile, the cooling power of the reactor at different core heights is calculated by considering its natural circulation capacity. Finally, a design scheme is obtained that meets the requirements of neutronic and thermal-hydraulic assessments, while producing maximum power. Consequently, during the entire life-cycle of SPALLER-100, a safety analysis of three typical accident scenarios (unprotected loss of heat sink, unprotected transient over power, and unprotected coolant inlet temperature undercooling) is performed using a Quasi-Static Reactivity Balance (QSRB) approach. The results show that the platform used to calculate the maximum neutronic power exhibits high accuracy, and that the design scheme with maximum power is safe and economical. Overall, this study can provide reference ideas for designing natural circulation reactors that can maximize power output.

KEYWORDS

lead-bismuth reactor, maximum neutronic power, natural circulation, quasi-static reactivity balance approach, SPALLER-100

1 Introduction

Although new energy sources are being continuously developed globally, nuclear energy is still one of the important energy sources for humans. Currently, the development and commercialization of small- and medium-sized reactors is increasing since they exhibit a short construction cycle, low investment risk, and flexible layout (Cao et al., 2014). Small natural circulation lead-bismuth reactors are novel nuclear reactors that are safe, compact, cost-effective, and exhibit a long service life; thus, they have good development prospects.

A long-life nuclear reactor requires a sustainable core and fast neutron spectrum for reducing its refueling cost, which allows it to utilize uranium more efficiently than thermal neutron reactors. Moreover, the structural materials of the reactor should be able to withstand irradiation for a long time. The cladding materials of current reactors, such as HT-9 or T-91 steel, can withstand material irradiation of 200 dpa (Cheon et al., 2009). Lead-bismuth eutectic (LBE) exhibits the advantages of stable chemical properties, high thermal conductivity, and favorable natural circulation. However, for a lead-bismuth reactor, LBE has two main disadvantages as a coolant (Zhao, 2017): first, LBE seriously corrodes the structural materials in the reactor; second, LBE leads to the production of radionuclide ^{210}Po with a half-life of 138 days. Zrodniko et al. (2006) have developed a method for treating ^{210}Po during the refueling and maintenance of the reactor. Meanwhile, Muller (Müller et al., 2002) and Rivai (Rivai and Takahashi, 2008) have developed coating materials for aluminum and silicon that can overcome the corroding effect of LBE. A decreased fuel loading in the core and small core size are essential for meeting the national road transportation regulations. Thus, miniaturization technology enables the transportation of reactors and allows a flexible reactor layout. Furthermore, to ensure natural circulation, a significant difference between the heat levels of the heat exchanger and core is necessary. Owing to the balance between buoyancy and resistance, steady-state natural convection leads to a uniform core temperature distribution, which effectively avoids overheating and even burning accidents of fuel components and core structures, and reduces material damage caused by thermal stress.

To achieve the above-mentioned objectives and improve the safety and cost-effectiveness of reactors, this study uses the Small Passive Long-life LBE-cooled fast Reactor (Liu et al., 2020) (SPALLER) designed by the University of South China (USC) as the research object to achieve maximal output power. First, this study analyzes various design limitations of the LBE reactor under natural circulation. Second, we build a platform that determines the maximum power produced by the reactor, while considering the physical and thermal performance of the reactor. Finally, an accident analysis is performed through the Quasi-static Reactivity Balance (QSRB) approach (Wade and Chang, 1988) proposed by Argonne National Laboratory (ANL). The results show that the proposed reactor scheme exhibits a good thermal safety performance, which can be used to engineer other reactors.

2 Core model and related theory

2.1 SPALLER-100 reactor

The SPALLER-100 reactor has been independently designed by the USC. The thermal power of the reactor core is 100 MW, and the refueling cycle is 20 years. The operating temperature is 320–480°C, and its coolant is LBE. The height of the reactor core active zone is 1.5 m, and the equivalent diameter is 1.7 m. The reactor fuel is PuN-ThN. Furthermore, the reactor exhibits a loading capacity of 5475.88 kg, with fuel assemblies in the inner and outer zones. There are 61 fuel rods in each fuel assembly, with a 4 mm assembly box in the outer layer. The pellet cladding material is made of HT-9 steel. Meanwhile, BeO is used as the moderator, which is filled between the assembly box and the outermost fuel rod.

The SPALLER-100 reactor is shown in Figure 1. The core is composed of 48 fuel assemblies (including inner and outer zones), 66 reflector assemblies, and 126 shielding assemblies. Moreover, the core is also equipped with 3 shutdown assemblies and 10 control assemblies. Among them, the inner zone contains 12 fuel assemblies (Pu mass fraction is 20.5%), and the outer zone contains 36 fuel assemblies (Pu mass fraction is 30.8%).

In a reactor, the effective multiplication factor k_{eff} (defined *via* the neutron equilibrium relationship) is the ratio of the neutron production rate to the total neutron disappearance rate. To quantitatively analyze the effect of changes in the SPALLER core reactivity on reactor operation, the following definitions of reactivity ρ and reactivity swing $\Delta\rho$ are used:

$$\rho = \frac{k_{eff} - 1}{k_{eff}} \tag{1}$$

$$\Delta\rho = \frac{k_{eff}(Max) - k_{eff}(Min)}{k_{eff}(Max)k_{eff}(Min)} \tag{2}$$

2.2 Latin hypercube sampling

Sampling points are the basis of proxy model construction. In this study, the Latin Hypercube Sampling (LHS) method (Li and Zhang, 2011) is used for data collection. The Monte Carlo (MC) method is often used for reactor physics calculations,

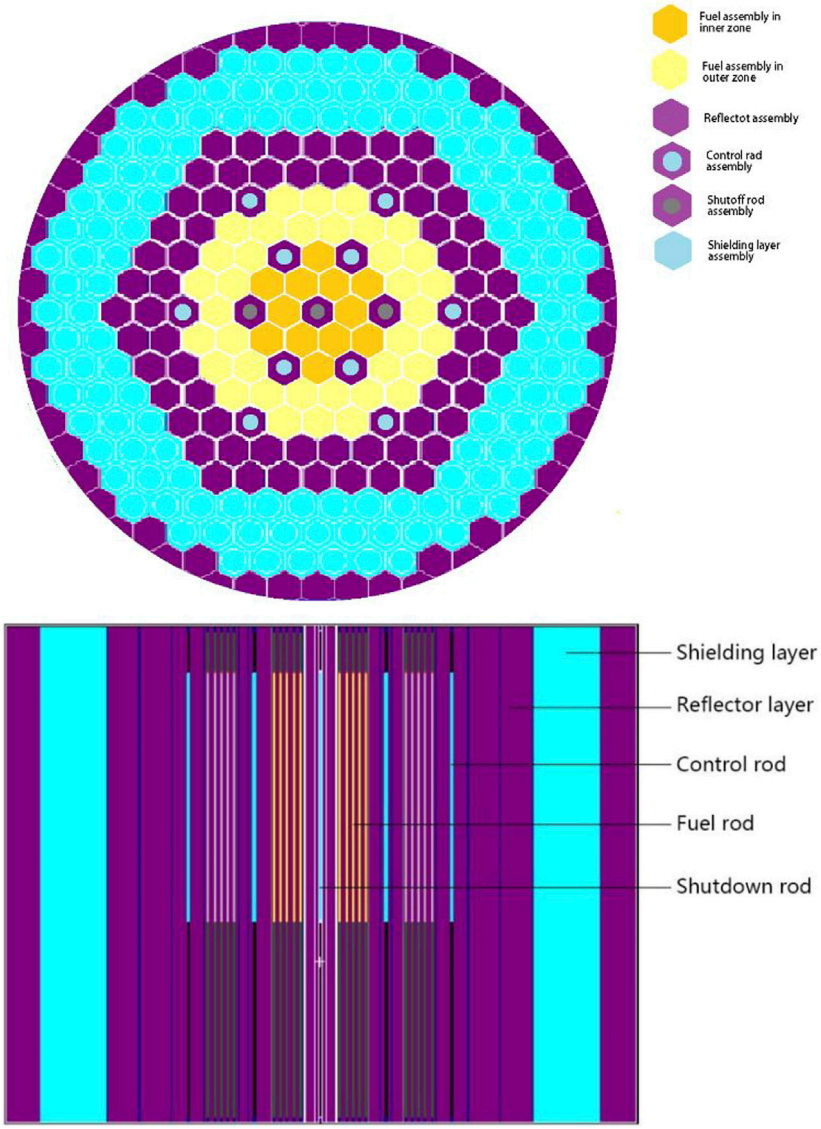

FIGURE 1
Cross-sections of the SPALLER-100 core.

which is a traditional sampling method that utilizes the probability distribution of random numbers or pseudorandom numbers. However, low probability results lead to the aggregation of MC sampling data. In contrast to the MC method, LHS can achieve nonoverlapping and space-filling sampling to effectively avoid the problem of sample point aggregation.

The main aim of employing the LHS method is to stratify the input probability distribution (that is, to extract the samples with sample size n from multiple variables) for maximizing the stratification of samples for each single variable. Its general calculation formula is:

$$x_{ij} = \frac{\left[x_j(i) - U_{ij}\right]}{n}, 1 \le i \le n, 1 \le j \le d \tag{3}$$

where $x_j(1) \ldots x_j(n)$ is a random arrangement of integers 1 to n, $U_{ij} \sim U[0,1]$ is a uniform random distribution obeying $U[0,1]$, n is the number of samples, and d is the sample dimension.

2.3 Kriging proxy model

Kriging (Kempf et al., 2012) interpolation is implemented using the following steps: for any point in the specified area, x_0

TABLE 1 Steady-state limitations.

Design criterion	Principle	Design parameters	Design limitations
Transportation limitations (China)	Road transportation width limit	Active zone core diameter	<2.5 m
	Miniaturization design limit	Active zone core height	<2.5 m
Material limitations	Coolant melting point	Coolant temperature	>124.5°C
	Corrosion of oxide film without cladding	Coolant flow rate	<2 m/s
	Melting without cladding (normal condition)	Maximum cladding temperature	<550°C
	Melting without cladding (accident condition)		<650°C
	Pellet melting point	Maximum fuel temperature	<2300°C
Neutronic limitations	Passive safety	Reactivity swing	<8$
	Shutdown depth	Excess reactivity	<8$
	Embrittlement without cladding	Displacement per atom	<200 dpa

is set as the point to be predicted, $x_1, x_2 \ldots x_n$ are selected as the observation points near x_0 the corresponding observation values are $y(x_1), y(x_2) \ldots y(x_n)$, and the prediction value of the point to be predicted is recorded as $\hat{y}(x_0)$. Then, the predicted value is obtained by determining the weighted sum of the observed values:

$$\hat{y}(x_0) = \sum_{i=1}^{N} \lambda_i y(x_i) \tag{4}$$

where λ_i is the undetermined weighting coefficient. The key to kriging prediction is that the weighting coefficient λ_i must satisfy the following two conditions:

(1) Assuming that the actual value of the measured point is $y(x_0)$, the unbiased estimation conditions are as follows:

$$E[\hat{y}(x_0) - y(x_0)] = 0, \ \sum_{i=1}^{N} \lambda_i = 1 \tag{5}$$

(2) The variance between the estimated value and true value $y(x_0)$ is minimal.

The kriging model is mainly composed of a regression model and residual error. Its mathematical expression is as follows:

$$y(x) = F(\beta, x) + Z(x) = f^T(x)\beta + Z(x) \tag{6}$$

where β is the regression coefficient; $f^T(x)$ is a regression model used to simulate global approximation; and $Z(x)$ is the residual error, which is used to simulate local error approximation.

3 Design limitations of analysis

To explore the method that maximizes the power produced by the natural circulation LBE reactor, it is necessary to ensure the safety of the reactor during long-term operation. Therefore, this study elucidates the original design limitations (Liu et al., 2020) of SPALLER-100 and puts forward many safety-related guidelines related to accident status and normal operation. Overall, this section mainly includes steady-state limitations and accident limitations.

3.1 Steady state limitations

Steady-state limitations can be divided into three categories based on road transportation, structural materials, and reactor physics: transportation limitations, material limitations, and neutronic limitations (Table 1).

3.1.1 Transportation limitations

According to China's road transportation restrictions (Geng, 2004), the width of transportation vehicles should not exceed 2.5 m and their height should not be more than 4 m. The initial design goal of SPALLER-100 is to achieve a height of less than 2 m for the active zone of the core, with an equivalent diameter of less than 2 m. To explore the maximum power that can be output from the core, design limitations (an active zone height of less than 2.5 m and an equivalent diameter of less than 2.5 m) have been established by considering the above factors and widely referring to the design scheme of international long-life small natural circulation reactors.

3.1.2 Material limitations

Material limitations are greatly affected by fuels, structural materials, coolants, etc. SPALLER-100 utilizes PuN-ThN as the fuel and its melting point (corresponding to an enrichment of 30% and a burnup of 50 MWd/kgHM) is selected as the maximum temperature limit (2300°C). The cladding material of SPALLER-100 is composed of HT-9. To ensure that cladding materials are damaged and melted under normal and accident conditions, 550°C and 650°C are selected as the maximum cladding temperature limits under normal and accident

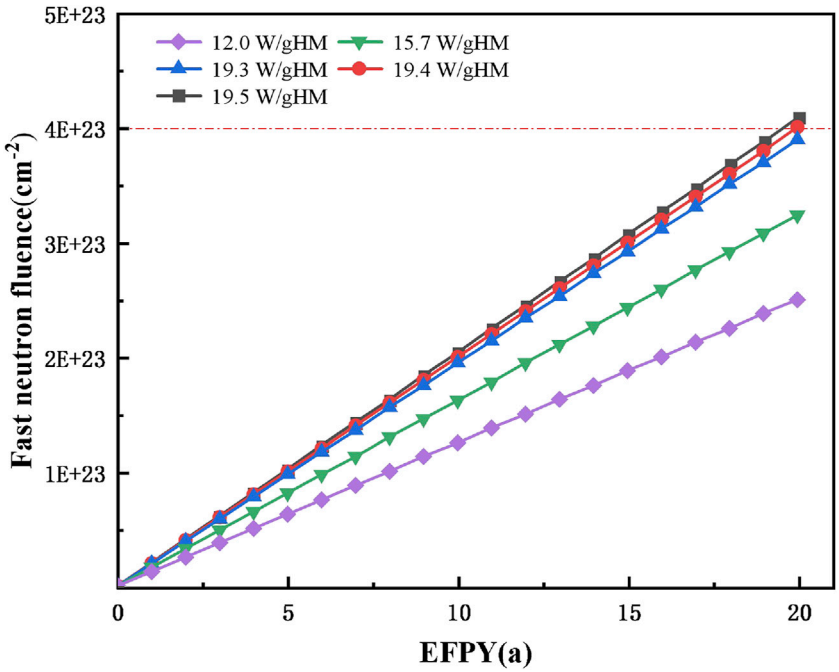

FIGURE 2
Fast neutron fluence for different EFPY.

conditions, respectively, based on an extensive investigation of the temperature limits of lead cooled fast reactors with HT-9 cladding. Each channel design must ensure that the coolant does not boil. Meanwhile, to prevent material corrosion, the speed of the LBE is limited to approximately 2.0 m/s (Hong et al., 2015).

3.1.3 Neutronic limitations

To provide a greater shutdown depth and meet safety requirements, the reactivity swing and maximum excess reactivity should be limited to less than 8 $. The delayed neutron share (β) of the core is 0.3% (approximately 300 pcm). Since fast neutrons cause significant radiation damage to cladding and structural materials, the radiation resistance of cladding materials determines the neutron fluence limit during reactor operation. With the operation of the reactor, HT-9 neutron fluence will continue to accumulate. Specific power is proportional to neutron fluence, as shown in Figure 2. Meanwhile, the irradiation limit of HT-9 is 200 dpa and the corresponding neutron fluence is $4 \times 10^{23} cm^{-2}$. When the core is operated for 20 effective full power years (EFPY), the neutron fluence rate in the reactor is limited to $6.34 \times 10^{14} cm^{-2} \cdot s^{-1}$ and the specific power does not exceed 19.4 W/gHM.

3.2 Accident limitations

In case of an expected transient accident in a nuclear power plant, an automatic shutdown of the reactor emergency system is needed; however, a subsequent failure of the reactor protection system results in shutdown failure. Such an accident scenario is termed as the Anticipated Transient Without Scram (ATWS). In these scenarios, the reactor does not implement any shutdown protection measures. The ATWS scenarios can be analyzed *via* the QSRB approach and include five unprotected scenarios: unprotected loss of heat sink (ULOHS) accident, unprotected transient over power (UTOP) accident, unprotected loss of flow (ULOF) accident, unprotected coolant inlet temperature (UCIT) undercooling accident, and unprotected pump over-speed (UPOS) accident. The following equation shows the QSRB equation applicable to natural circulation (Cho et al., 2015):

$$\sum \Delta\rho = (P-1)A + \left(\frac{P}{F} - 1\right)B + \delta T_{in}C = 0 \tag{7}$$

where P is the normalized power, F is the normalized flow, A is the reactive power coefficient (cents), B is the reactive power/flow coefficient (cents), and C is the reactive inlet temperature coefficient (cents/°C). δT_{in} is the change in the coolant inlet temperature.

$$A = (\alpha_D + \alpha_A)\Delta T_{FC} \tag{8}$$

$$B = (\alpha_D + \alpha_A + \alpha_C + 2\alpha_R)\Delta T_C/2 \tag{9}$$

$$C = \alpha_D + \alpha_A + \alpha_R + \alpha_C \tag{10}$$

$$A' = \alpha_D \Delta T_{FC} \tag{11}$$

α_D is the fuel Doppler coefficient, α_A is the core axial expansion reactivity coefficient, α_R is the core radial expansion reactivity

coefficient, α_c is the reactivity coefficient of coolant density, ΔT_{FC} is the difference between the average fuel temperature and the average coolant temperature under normal scenarios, and ΔT_c is the temperature rise of core coolant under normal scenarios.

The QSRB approach has an applicable assumption; that is, the reactor can reach its equilibrium state with a total reactivity of 0 through self-regulation after any accident or transient operation for a significant time. The temperature rise at the coolant outlet δT_{out} can be expressed using the following formula:

$$\delta T_{out} = \delta T_{in} + \left(\frac{P}{F} - 1\right)\Delta T_C \tag{12}$$

SPALLER-100 is driven *via* natural circulation without a coolant pump. It is assumed that the relationship between flow (F) and power (P) under natural circulation is represented as follows: $F \sim P^{1/3}$ (Duffey and Sursock, 1987). Therefore, ULOFS and UPOS accidents will not occur; however, ULOHS, UTOP, and UCIT accidents may still occur. For UTOP and UCIT, it should be noted that coefficient A is applicable to Eq. 11.

3.2.1 Unprotected loss of heat sink

In ULOHS, the heat removal function of the primary coolant system is lost, core heat cannot be exported in time, and average circulation coolant temperature keeps increasing; this leads to a negative reactivity in the core. The decay heat power after the accident depends on the fuel burn-up. It is conservatively assumed that the core power after a long transition is reduced to 7% of the normal full operating power (Todreas Neil and Kazimi Mujid, 1990), which ensures that reactivity stays at 0. If the effect of reactor residual heat is considered, the temperature rise of the coolant at the core exit according to Eqs 7, 12 is:

$$\delta T_{\text{out}} = \frac{0.93A + 0.83B}{C} - 0.83\Delta T_C \tag{13}$$

3.2.2 Unprotected transient over power

In UTOP, assuming that certain control fuel rods operating at maximum power become out of control and cannot be withdrawn, the reactor core introduces additional positive reactivity, resulting in a rapid increase in core power; the negative reactivity arising from the power rise will eventually smooth out the total core reactivity to 0. In this accident, it is assumed that the core power increases by 10% of the normal operating power due to reactivity insertion. The reactor generates more heat due to the increase in power, and the primary heat trap is unable to effectively absorb the excess heat, causing the average primary coolant temperature to rise; the resulting decrease in reactivity will be compensated for by a reduction in core power, thereby ultimately causing the reactor to shut down. If residual heat is considered, the outlet temperature fluctuation at this point can be expressed as:

$$\delta T_{out} = \frac{-\Delta\rho_{TOP} - 0.1A - 0.07B}{C} + 0.07\Delta T_c \tag{14}$$

3.2.3 Unprotected coolant inlet temperature undercooling

In UCIT, the inlet temperature of the primary coolant decreases; the resulting positive reactivity is compensated by boosting the core power, assuming that the relationship between F and P is $F \sim P^{1/3}$. At this point, no external reactivity is introduced and the rise in coolant temperature at the coolant outlet is:

$$\delta T_{out} = \delta T_{in} - \frac{\delta T_{in} C \Delta T_C}{A + B} \tag{15}$$

To ensure the inherent safety of SPALLER-100 and allow the reactor to stop safely under accident conditions, three passive safety design limitations are proposed:

(1) The parameters A, B, and C consist of reactivity coefficients such as $\alpha_D, \alpha_A, \alpha_R, \alpha_C$. Therefore, in addition to $\alpha_D, \alpha_A, \alpha_R, \alpha_C$ being negative, A, B, and C need to be less than 0.
(2) The cladding material (HT-9 steel) has a temperature limitation under accident conditions: T_{ct} = 650°C. Assuming that the temperature rise at the core coolant outlet is approximately equal to the rise in the coolant pipe surface temperature, the maximum temperature rise of the coolant at the core outlet is less than T_{ct}: $\delta T_{out} < T_{ct} - T_{out}$;
(3) The bubbles generated during coolant boiling result in reduced neutron absorption and increased neutron leakage from the moderator; the void coefficient α_V needs to be less than 0.

4 Maximum power calculation analysis

For a given reactor, the output power can be theoretically infinite when not considering its fuel consumption and lifecycle. When considering other factors, such as operating life, material life, and the maximum power consumed by the reactor, the reactor output power will be limited to the maximum. Therefore, achieving the maximum output power of a reactor is a multi-objective, complex, multidimensional, nonlinear, and constrained optimization problem. The proxy model is an analytical model with high computational efficiency and computational accuracy, which has been proposed to solve the problems of excessive computation and slow convergence during simulation and simulation experiments.

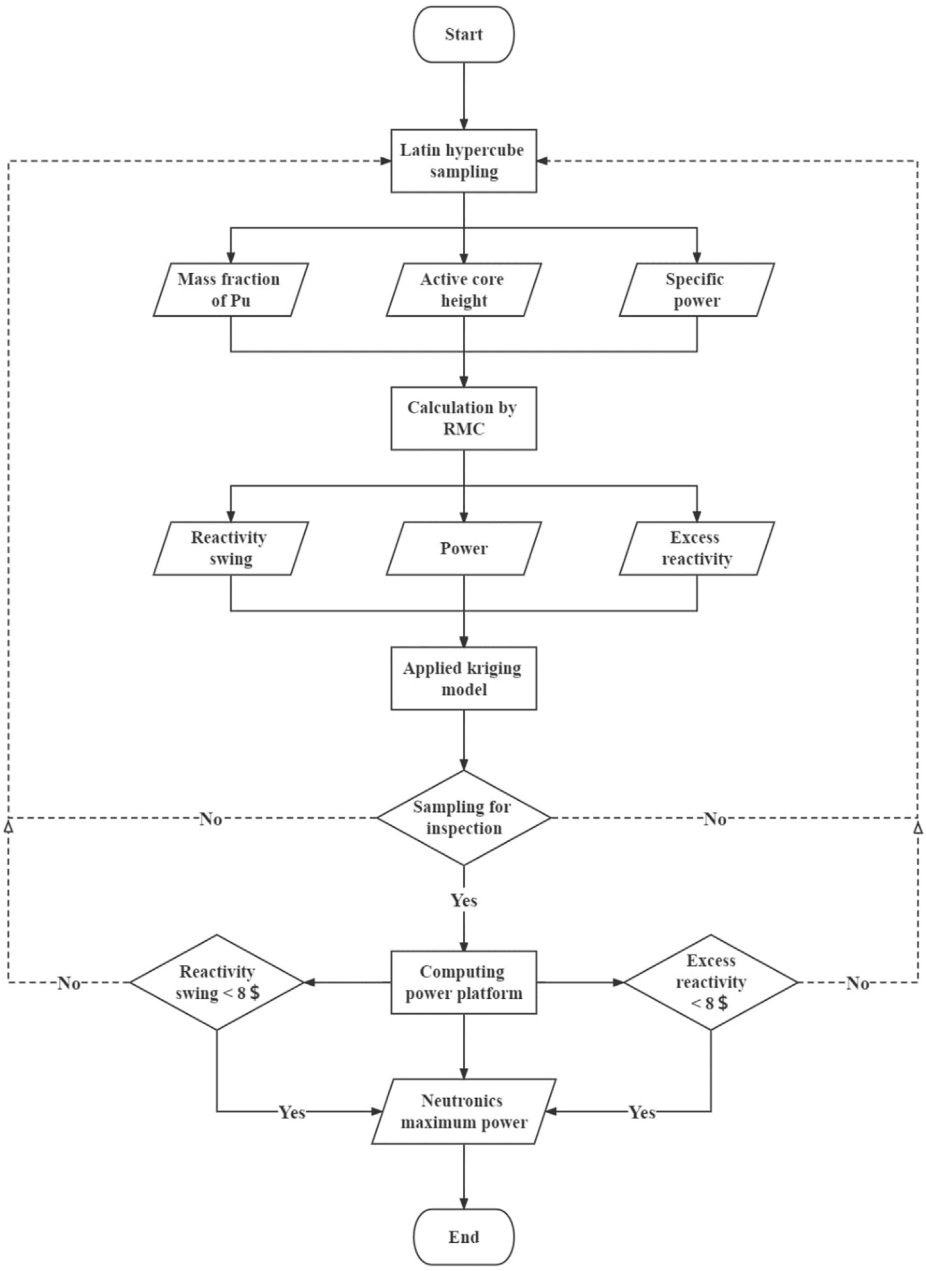

FIGURE 3
Flow chart of the platform used to calculate the maximum neutronic power.

4.1 Maximum neutronic power

4.1.1 Development of the neutronic power calculation platform

The platform developed in this study to calculate the maximum neutronic power of the reactor is based on Python; this platform utilizes the Monte Carlo code RMC (Liang et al., 2014) to calculate the initial sample points generated using the LHS method, thus generating data that will be used for training a Kriging model to produce a proxy model.

In this study, the SPALLER-100 reactor is taken as the research object. In fact, both the fuel mass fraction and the core height affect the fuel loading, which further influences the neutronic power of the core. Moreover, to ensure the safety of the reactor during operation, the reactivity swing should be as small as possible. Therefore, based on the steady-state limit, the fuel

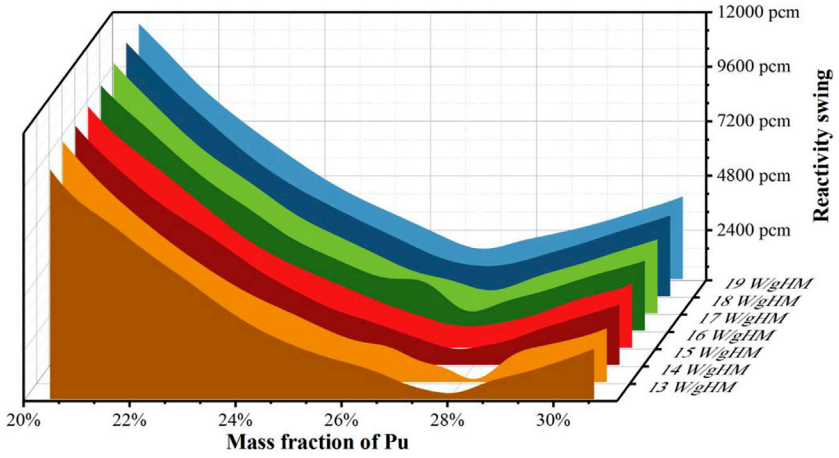

FIGURE 4
Plot of reactivity swing, specific power, and mass fraction.

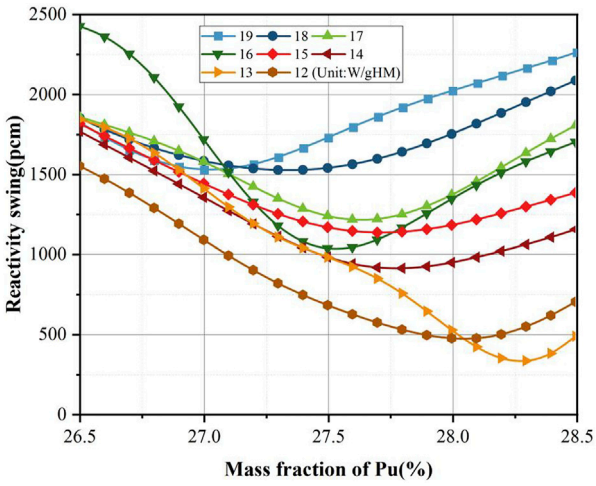

FIGURE 5
Plot of reactivity swing, specific power, and mass fraction (26.5%–28.5%).

mass fraction, core height, and specific power are selected as the sampling variables, while the reactivity swing, initial excess reactivity, and power are constrained. Figure 3 demonstrates the steps used to design the platform.

According to the steady-state limitations, the height of the core ranges from 1 to 2.5 m; the mass fractions in the inner zone and outer zone of the reactor are 20.5% and 30.8%, respectively. To ensure suitable material irradiation (200 dpa), 19.4 W/gHM is selected as the upper limit for specific power. By considering the sampling error caused by significant variations and ensuring a high neutronic power, the lower limit of specific power is assumed to be 12 W/gHM according to experience.

4.1.2 Platform prediction and verification

Figure 4 shows that with an increase in the fuel mass fraction of the Kriging model (also known as the neutronic power calculation platform, which is based on 1200 training sets at different specific powers), the predicted reactivity swing has minimum value (corresponding mass fraction is the optimal mass fraction).

Figure 5 shows that under different specific powers, the predicted reactivity swing of Pu mass fraction (26.5%–28.5%) is relatively small (less than 2500 pcm), which is conducive to the smooth operation of the reactor. Meanwhile, an increase in specific power tends to augment reactivity swing. When the specific power is approximately 19 W/gHM, the optimal mass fraction is 27%.

Twenty sample points were randomly generated *via* LHS, and the prediction results obtained using the platform were compared with the RMC calculation results to determine the accuracy of the values predicted by the platform. As shown in Figure 6, the absolute error between the reactivity swing and excess reactivity predicted by the platform and those calculated using the RMC procedure is 367 pcm at maximum. To ensure the safety of the reactor at maximum power, the reactivity swing should be as small as possible.

As seen from Figure 7, the maximum absolute error between the power predicted by the platform and the power calculated by the RMC is 5.4 MW for individual sampling points. This error may be due to an insufficient number of training sets for the Kriging model; however, the overall compliance is good, and a solution can be provided by increasing the number of training

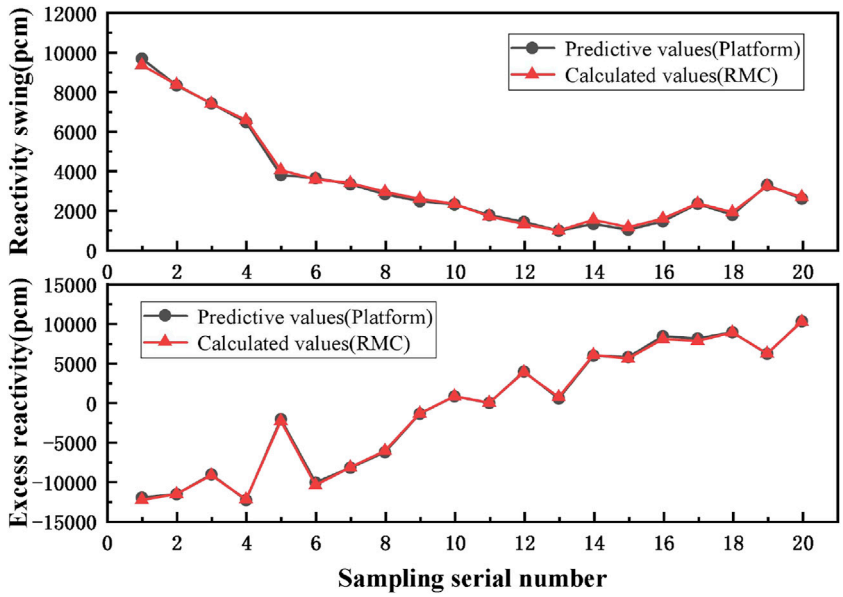

FIGURE 6
Comparison of the reactivity swing and excess reactivity. Predicted using the platform with the corresponding RMC results.

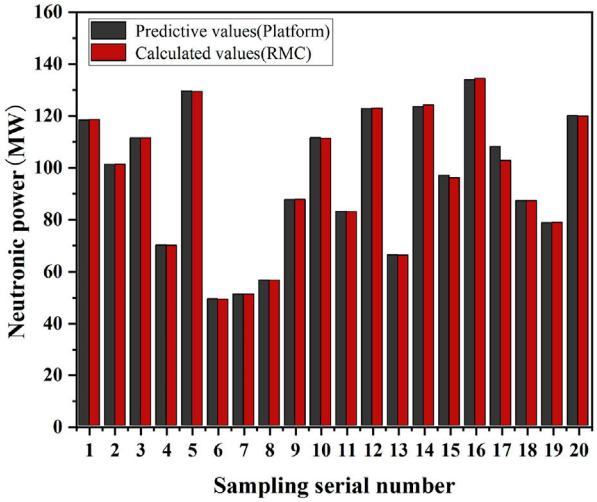

FIGURE 7
Comparison of the power predicted by the proposed platform with that predicted using RMC.

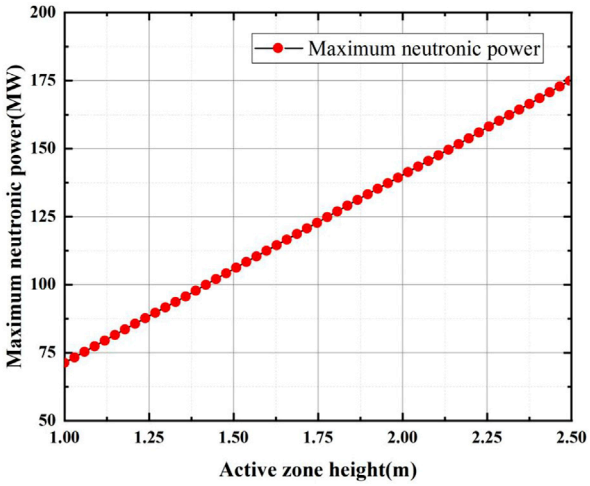

FIGURE 8
Maximum neutronic power of the SPALLER reactor at different heights.

sets. Therefore, the proposed platform exhibits decent accuracy as well as credibility.

4.1.3 Calculate the maximum neutronic power

Finally, based on the kriging proxy model, the maximum power that meets the permitted limits for burnup reactivity swing and excess reactivity at each height is determined. The fuel loading increases with rise in the active zone height of the reactor core, which in turn augments the neutronic power. Figure 8 shows that the maximum neutronic power of the reactor almost exhibits a linear relationship with the active zone height.

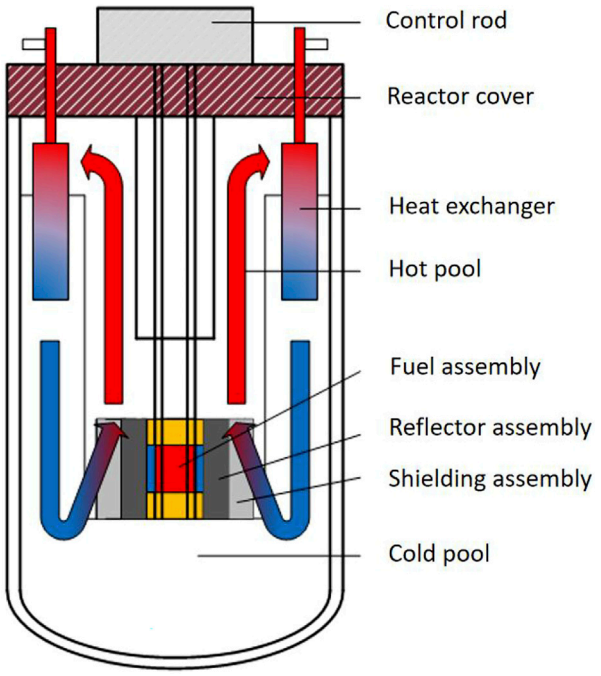

FIGURE 9
Natural circulation diagram.

4.2 Natural circulation power

In the reactor, natural circulation refers to the circulation that occurs without the driving force provided by the pump, which in turn depends on the driving force generated by the differences in density and height that brings out the core power. The pressure drop caused by various resistances has a significant influence on the calculation of cooling power produced *via* natural circulation because it is the most difficult to predict among many uncertain factors. Since the pressure drop in the primary circuit system is mainly sourced from the core and heat exchanger, this study only considers the friction pressure drop and local pressure drop of the core and heat exchanger for simplification (Figure 9).

4.2.1 Natural circulation capacity principle

In the reactor, the coolant flows into the lower chamber from the inlet connecting pipe, flows through the reactor core from bottom to top, carries the heat generated by nuclear fission in the reactor core, flows out from the outlet connecting pipe of the upper chamber, enters the steam generator through the rising section for heat exchange, and the cooled fluid flows out from the outlet of the steam generator. It then flows from the reactor inlet nozzle through the descending section to complete the natural circulation flow of the primary reactor circulation.

The pressure drop in the core mainly occurs due to the friction loss in the coolant channel and the core inlet and outlet. In addition, the pressure drop in the heat exchanger mainly includes the friction loss in the heat exchanger and the inlet and outlet losses.

The driving force of natural circulation is the buoyancy generated by the differences in density and height. The driving head P_d is given using Eq. 16:

$$P_d = gH\left(\rho_{in} - \rho_{out}\right) \tag{16}$$

where g is the gravitational acceleration (m/s^2), H is the natural circulation height (m), and ρ_{in} and ρ_{out} are the coolant densities at the inlet and outlet of the core (kg/m^3), respectively.

By employing Boussinesq approximation and ignoring the axial heat conduction, heat dissipation of the system, and work done by spatial pressure change, the above formula can be expressed as:

$$P_d = \rho_c g \beta_c H \Delta T \tag{17}$$

where ρ_c is the coolant density, β_c is the coefficient of thermal expansion (K^{-1}), and ΔT is the temperature difference in the coolant between the inlet and outlet (°C).

Therefore, to develop a method that maximizes the power generated by the reactor at a conceptual design level, it is necessary to satisfy the equation associated with a coolant natural circulation design. In steady-state operations, the driving force of natural circulation should be equal to the total pressure drop in the primary system; this ensures that the basic relationship between buoyancy (left) and resistance (right) is maintained:

$$\rho_c g \beta H \Delta T = \sum \frac{1}{2} \rho_c V_i^2 \left(k_i + f_i \frac{l_i}{d_i} \right) \tag{18}$$

where $V_i, k_i, f_i, l_i,$ and d_i represent the coolant flow rate, form resistance coefficient, friction coefficient, flow length, and hydraulic diameter of the $i-th$ area, respectively. The above formula shows that there are two values that have a great impact on the natural circulation power of the primary circulation system. The first is the pressure drop loss caused by the friction coefficient and local resistance coefficient in the primary circulation system; the second is the circulation height: the height difference from the center of the core to the center of the heat exchanger.

The natural circulation power is expressed using Eq. 19 as follows:

$$P_{core} = WC_P \Delta T = \rho_c A_i V_i C_P \Delta T \tag{19}$$

where P_{core} is the natural circulation power, W is the coolant mass flow, C_p is the specific heat capacity at constant pressure, and A_i represents the coolant flow area of the $i-th$ area.

According to Eqs 18, 19, the functional relationship of P_{core} can be derived *via* natural circulation:

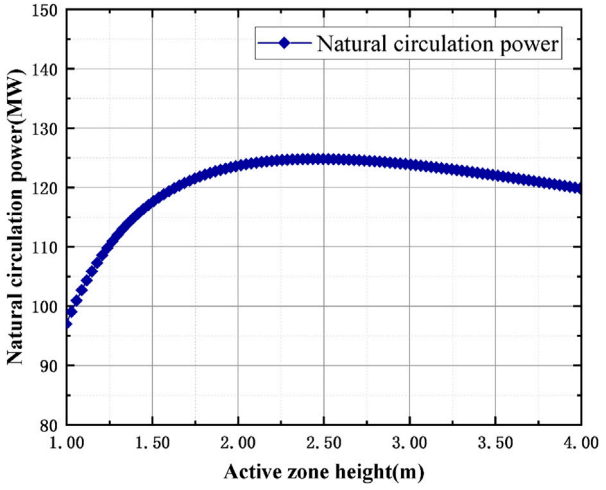

FIGURE 10
Natural circulation power of SPALLER at different heights.

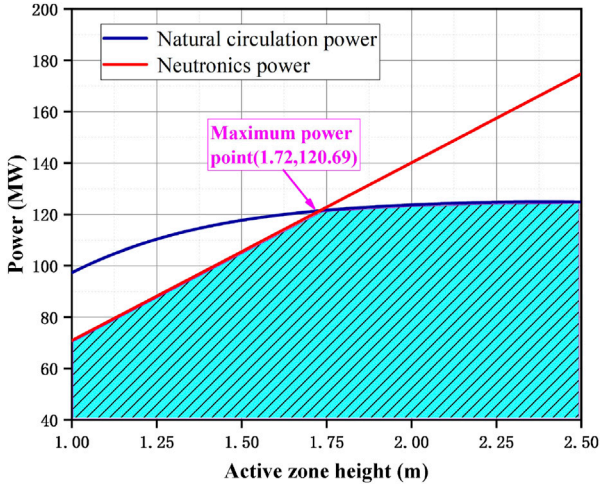

FIGURE 11
Maximum power of SPALLER.

$$2C_p^2\rho_c^2 g\beta\frac{\Delta T^3}{P_{core}^2} = \sum\frac{1}{H\cdot A_i^2}\left(f_i\frac{l_i}{d_i}+k_i\right) \tag{20}$$

4.2.2 Calculate the natural circulation power

By solving the above-mentioned theory and Eq. 20, Figure 10 shows the relationship between the natural circulation power and the active zone height in the core.

The corrosion and erosion limitations are considered to determine the natural circulation power. Since the pressure drop mainly occurs in the core, the active zone height of the core has a great influence on the total pressure drop. When calculating the natural circulation power, the circulation height must remain unchanged to ensure the advantage of miniaturization. As the active zone height increases, the core pressure drop and pitch-to-diameter ratio also increase. Because an increase in the pitch-to-diameter ratio reduces the total pressure drop in the system, the relationship between natural circulation power and core height is nonlinear. Therefore, based on the maximum neutronic power, these two factors (core height and pitch-to-diameter ratio) are critical for maximizing core power.

5 Power maximization and accident safety analysis

5.1 Maximum power research scheme

The actual maximum power of the reactor core is determined using the natural circulation power. As shown in Figure 11, the neutronic power and natural circulation power tend to be maximum at the same core height. If the reactor core height continues to increase, the rise in natural circulation power becomes negligible and the neutronic power improves significantly; however, this is not conducive to improving the cost-effectiveness of the reactor.

To determine neutronic power (red line), the influences of transport limitation, material irradiation limitation, and reactivity limitation are considered; meanwhile, to determine natural circulation (blue curve), the influences of corrosion limitation and temperature limitation are considered. The area below the intersection of the two lines meets the requirements for the natural circulation power and maximum neutronic power. When considering the maximum power constraints and miniaturization constraints of these reactors, increasing the core height implies further increasing the active zone height of the fuel, which leads to increased costs. Therefore, based on a comprehensive consideration of the safety and economical aspects associated with different limitations, the maximum power of SPALLER determined in this study is approximately 120.69 MW, optimal fuel mass fraction is 27%, and corresponding core height is approximately 1.72 m.

According to the above-mentioned research results, Table 2 shows the main design parameters used for maximizing the power of SPALLER. In Section 5.2, accident analysis applicable to the natural circulation QSRB approach has been carried out.

5.2 Accident safety analysis based on quasi-static reactivity balance

Compared with the original design, by implementing RMC modeling while ensuring maximum power, the relevant dynamic parameters at the beginning of life (BOL), middle of life (MOL),

TABLE 2 Necessary parameters for maximizing the reactor power.

Design parameters	Units	Original design values	Current design values
Power	MWt	100	120.69
Refueling cycle	a	20	20
Mass fraction of Pu	%	(20.5,30.8)	27
Circulation height	m	4	4
Active zone height	m	1.50	1.72
Pitch-to-diameter ratio	/	1.70	1.91
Specific power	W/gHM	18.26	19.2

TABLE 3 Dynamic parameters of SPALLER under different life cycles.

Parameters	BOL		MOL		EOL	
	Original	Current	Original	Current	Original	Current
β (pcm)	307	307	288	288	322	322
α_D (cents/°C)	−0.5208	−0.4290	−0.5927	−0.5550	−0.6047	−0.4973
α_C (cents/°C)	−0.3788	−0.6141	−0.3712	−0.7631	−0.3407	−0.6927
α_A (cents/°C)	−0.0635	−0.0631	−0.0580	−0.0709	−0.0472	−0.0601
α_R (cents/°C)	−0.0658	−0.0165	−0.0688	−0.0101	−0.0273	−0.0063
α_V (cents/1%)	—	−30.14	—	−34.37	—	−31.32
A (cents)	−153.11	−167.02	−170.49	−212.43	−170.80	−189.18
A' (cents)	−136.45	−145.60	−155.29	−188.37	−158.44	−168.78
B (cents)	−93.05	−91.14	−98.55	−112.74	−89.01	−101.02
C (cents/°C)	−1.03	−1.12	−1.09	−1.40	−1.02	−1.26

TABLE 4 Accident safety analysis of SPALLER under maximum power.

Accident	Parameters	BOL		MOL		EOL	
		Original	Current	Original	Current	Original	Current
ULOHS	Relative power	0.07	0.07	0.07	0.07	0.07	0.07
	δT_{out} (°C)	72.13	72.93	79.41	75.28	87.06	73.97
UTOP	Relative power	1.10	1.10	1.10	1.10	1.10	1.10
	δT_{out} (°C)	89.42	81.62	83.06	63.57	88.30	71.73
UCIT	Relative power	1.40	1.40	1.40	1.40	1.40	1.40
	δT_{out} (°C)	−21.85	7.59	−24.81	8.62	−27.96	8.54
$T_{ct} - T_{out}$	$T_{ct} = 650$, $T_{out} = 480$	<170	<170	<170	<170	<170	<170

and end of life (EOL) are calculated in Table 3, such as A, A', B, C, β, α_D, α_A, α_R, *and* α_C.

According to the dynamic parameters and QSRB equations, Table 4 lists the relative power and rise in coolant outlet temperature when the reactor core reaches the quasi-static state by relying on its own reactivity feedback after the ULOHS, UTOP, and UCIT accidents. Assuming that the rise in temperature at the outlet of the core coolant is approximately equal to the temperature rise on the surface of the coolant pipe, the maximum temperature of the cladding surface under accident conditions can be estimated.

The maximum temperature limit of the cladding under the SPALLER accident condition has been designed to be 650°C, as mentioned in the steady-state limitations. It can be seen from Table 4 that for the original design scheme and the another, the UTOP accident (introducing reactivity of 1 $) at BOL has the most serious consequences among the three accident conditions. The rise in coolant temperature at the outlet are 89.42°C and 81.62°C, respectively; thus, the maximum temperature on the coolant pipeline surface are predicted to be 569.42°C and 561.62°C. This value is slightly higher than the steady-state temperature limit of the cladding (550°C); however, it is far lower than the accidental temperature limit of the cladding (650°C).

Three accident limitations have been considered in the accident limitations analysis, and the calculation results meet the above conditions. First, in addition to the fuel Doppler coefficient α_D, axial expansion reactivity coefficient of fuel α_A, core radial expansion reactivity coefficient α_R, and coolant density reactivity coefficient α_C are less than 0; the coefficients A, B, and C calculated in Table 3 are also less than 0. Second, under ULOHS, UTOP, and UCIT accident conditions, δT_{out} does not exceed $T_{ct} - T_{out}$. Third, the void coefficient α_V is negative. All the above conditions are within the permitted limits, thereby further revealing the safety characteristics of the SPALLER.

6 Conclusion

To explore the maximum power that the reactor can output, the SPALLER-100 reactor is selected as the research object. The initial samples are generated using the LHS method and many training sets are trained. The Kriging proxy model is constructed and the neutronic power calculation platform is built to reduce the actual amount of calculations while ensuring accuracy. To improve the economy and safety, the maximum neutronic power and natural circulation power at different core heights are calculated by utilizing three steady-state limitations and three accident limitations as constraints. Considering the maximum power that can be achieved *via* natural circulation, the design scheme that maximizes the power output and meets both the rector thermal-hydraulic and rector physical requirements is finally obtained. The main conclusions of this study are as follows:

(1) The design scheme increases the power of SPALLER-100 from 100 MW thermal power to 120.69 MW maximum power (by more than 20%), which greatly improves the cost-effectiveness of the reactor and provides a reference method for designers.

(2) Three typical reactor accidents (ULOHS, UTOP, and UCIT) are analyzed by using the QSRB approach suitable for natural circulation. The results show that the proposed design scheme exhibits a good safety performance and can be used in future reactor engineering designs.

Data availability statement

The original contributions presented in the study are included in the article/Supplementary Material, further inquiries can be directed to the corresponding authors.

Author contributions

YX: data curation, writing- original draft preparation. JY: conceptualization, methodology, software. PZ: supervision. TY: visualization, investigation. ZL: reviewing and editing.

Funding

This work is supported by the "Coupled Response Mechanism of Lead-based Fast Reactor Hot Pool and Cold Pool Thermal stratification under Asymmetric Thermal Load Condition and its Influence on Natural Circulation Performance" project sponsored by the National Natural Science Foundation of China (Grant No. 11905101).

Conflict of interest

The authors declare that the research was conducted in the absence of any commercial or financial relationships that could be construed as a potential conflict of interest.

Publisher's note

References

Cao, Y, Wang, S, Xiong, W, et al. (2014). Features and application analysis of small modular reactor (in Chinese). *Nucl. Electron. Detect. Technol.* 34 (06), 801–806. doi:10.3969/j.issn.0258-0934.2014.06.029

Cheon, J. S., Lee, C. B., Lee, B. O., Raison, J., Mizuno, T., Delage, F., et al. (2009). Sodium fast reactor evaluation: Core materials. *J. Nucl. Mater.* 392 (2), 324–330. doi:10.1016/j.jnucmat.2009.03.021

Cho, J., Shin, Y. H., and Hwang, I. S. (2015). Power maximization method for land-transportable fully passive lead–bismuth cooled small modular reactor systems. *Nucl. Eng. Des.* 289, 240–251. doi:10.1016/j.nucengdes.2015.04.027

Duffey, R. B., and Sursock, J. P. (1987). Natural circulation phenomena relevant to small breaks and transients. *Nucl. Eng. Des.* 102 (2), 115–128. doi:10.1016/0029-5493(87)90244-5

Geng, L. (2004). An illustration for standard of P.R.C.《Limits of dimensions, axle load and masses for road vehicles》(in Chinese). *Traffic Stand.* 0 (8), 10–13. doi:10.3869/j.issn.1002-4786.2004.08.003

Hong, S. G., Kim, J. H., and You, W. S. (2015). A neutronic design study of lead-bismuth-cooled small and safe ultra-long-life cores. *Ann. Nucl. Energy* 85, 58–67. doi:10.1016/j.anucene.2015.04.032

Kempf, Stephanie, Forget, Benoit, and Hu, Lin-Wen (2012). Kriging-based algorithm for nuclear reactor neutronic design optimization. *Nucl. Eng. Des.* 247, 248–253. doi:10.1016/j.nucengdes.2012.03.001

Li, J., and Zhang, B. (2011). Probabilistic load flow based on improved Latin hypercube sampling with evolutionary algorithm (in Chinese). *Proc. CSEE* 31 (25), 90–96. doi:10.13334/j.0258-8013.pcsee.2011.25.012

Liang, J., Qiu, Y., Wang, K., and Chai, X. (2014). Research of full core burnup calculations based on tally data decomposition in RMC (in Chinese). *Nucl. Power Eng.* 35, 231–234. doi:10.13832/j.jnpe.2014.S2.0231

Liu, Z., Zhao, P., and Zhang, B. (2020). Research on core concept design of ultra-long life small natural circulation lead-based fast reactor. *Atomic Energy Sci. Technol.* 54 (7), 1254–1265. doi:10.7538/yzk.2019.youxian.0720

Müller, G., Heinzel, A., Konys, J., Schumacher, G., Weisenburger, A., Zimmermann, F., et al. (2002). Results of steel corrosion tests in flowing liquid Pb/Bi at 420–600 °C after 2000 h. *J. Nucl. Mater.* 301 (1), 40–46. doi:10.1016/s0022-3115(01)00725-5

Rivai, A. K., and Takahashi, M. (2008). Compatibility of surface-coated steels, refractory metals and ceramics to high temperature lead–bismuth eutectic. *Prog. Nucl. energy* 50 (2-6), 560–566. doi:10.1016/j.pnucene.2007.11.081

Todreas Neil, E., and Kazimi Mujid, S. Nuclear SystemsI: Thermal hydraulic fundamentals. 1990.

Wade, D. C., and Chang, Y. I. (1988). The integral fast reactor concept: Physics of operation and safety. *Nucl. Sci. Eng.* 100 (4), 507–524. doi:10.13182/nse88-2

Zhao, pengcheng (2017). *Thermal-hydraulic safety analysis of primary cooling system for small modular natural circulation LFR SNCLFR-100 (in Chinese)*. China: University of Science and Technology of China.

Zrodnikov, A. V., Toshinsky, G. I., Komlev, O. G., Dragunov, Y., Stepanov, V., Klimov, N., et al. (2006). Nuclear power development in market conditions with use of multi-purpose modular fast reactors SVBR-75/100. *Nucl. Eng. Des.* 236 (14-16), 1490–1502. doi:10.1016/j.nucengdes.2006.04.005

frontiers | Frontiers in Energy Research

TYPE Original Research
PUBLISHED 22 August 2022
DOI 10.3389/fenrg.2022.964171

OPEN ACCESS

EDITED BY
Songbai Cheng,
Sun Yat-sen University, China

REVIEWED BY
Xu Han,
The University of Tokyo, Japan
Antai Liu,
Harbin Engineering University, China

*CORRESPONDENCE
Di Wang,
wangdi2020@cgnpc.com.cn

SPECIALTY SECTION
This article was submitted to Nuclear Energy,
a section of the journal
Frontiers in Energy Research

RECEIVED 08 June 2022
ACCEPTED 27 June 2022
PUBLISHED 22 August 2022

CITATION
Wang D, Lu X, Qiu S, Liang R, Lin Z and Ouyang Y (2022), Development of drift-flux correlations for vertical forward bubble column-type gas-liquid lead-bismuth two-phase flow.
Front. Energy Res. 10:964171.
doi: 10.3389/fenrg.2022.964171

Development of drift-flux correlations for vertical forward bubble column-type gas-liquid lead-bismuth two-phase flow

Di Wang[1]*, Xianghui Lu[1], Suizheng Qiu[2], Ren Liang[1], Zhikang Lin[1] and Yong Ouyang[1]

[1]China Nuclear Power Technology Research Institute, Shenzhen, China, [2]School of Energy and Power Engineering, Xi'an Jiaotong University, Xi'an, China

Bubble columns represent an extreme case of gas-liquid two-phase flow, where net liquid velocity is zero and the gas simply bubbles up through the liquid. The bubble column-type gas-liquid metal two-phase flow always appears in an accident scenario for pool-type lead-bismuth eutectic cooled fast breeder reactors. To accurately predict the void fraction for the accident evaluation and design of a reactor system, nine existing drift-flux type constitutive correlations are evaluated with a nitrogen-liquid heavy metal two-phase flow test. Few correlations give a relatively good prediction and the basic assumption in the distribution parameter calculation is not applicable for a bubble column. To solve this problem, analysis based on Clark's theoretical model is carried out. The results show that the distribution parameter assumes very high values at a low Re number. As the Froude number increases, the distribution parameter tends to decrease. At lower void factions, the distribution parameter is also assumed to be at high values. This indicates that the pipe size, flow rate, and void fraction can all influence the distribution parameter. Considering the quantitative laws of these influence factors obtained by theoretical analysis and fitting the data of Ariyoshi's test, a new correlation for a bubble column-type gas-LBE two-phase flow is developed and evaluated. The results of the statistical analysis show that the new correlation gives the best prediction for gas-LBE two-phase flow in the void fraction range of 0.018–0.313.

KEYWORDS

gas-LBE two-phase flow, drift-flux model, fast reactor, void fraction, bubble column

1 Introduction

Gas-liquid two-phase flow is a kind of fluid mixture that is capable of efficiently transporting mass, momentum, and heat energy in various engineering fields (Han et al., 2020). A bubble column represents an extreme case of gas-liquid two-phase flow, where net liquid velocity is zero and the gas simply bubbles up through the liquid (Clark and Egmond, 1990). This phenomenon is frequently encountered, especially in chemical

TABLE 1 Summary of the nine correlations.

Description of correlation	Equation number	Allocated number
Ishii's correlation for bubbly flow	(7, 8)	1
Ishii's correlation for slug flow	(7, 8)	2
Ishii's correlation for churn flow	(7, 8)	3
Kataoka and Ishii's correlation	(7, 9)	4
Kocamustafaogullari and Ishii's correlation	(7, 11)	5
Mikityuk's pool correlation	(12)	6
Mikityuk's loop correlation	(12)	7
Shen's correlation for low wettability wall	(13)	8
Shen's correlation for high wettability wall	(13)	9

engineering and metallurgy. With the development of nuclear power technology, the bubble column-type gas-liquid metal two-phase flow has attracted more attention as a typical thermal-hydraulics phenomenon during a hypothetical accident in pool-type liquid metal cooled fast breeder reactors (FBRs). For instance, in the long-term stage (i.e., the main pump has been shut down) of a steam generator tube rupture (SGTR) in a lead-bismuth eutectic (LBE) alloy cooled fast reactor, steam released from the break of the tube into the reactor vessel may transport upward through the active section from the bottom inlet of the reactor core and introduce additional activity due to the moderation effect of water, which threatens the reactor's safety. During a severe accident scenario in FBRs, the gas generated from the melting and boiling of fuel, cladding, and liquid metal coolant may also form a multi-phase flow in a static liquid metal pool and relocate the fuel, which causes the risk of re-criticality in the molten core. Meanwhile, the gas-phase fission product may transport upward through the liquid metal into the cover gas and cause a risk of radioactivity release. The basic characteristic of these phenomena during an accident is a bubble column-type gas-liquid two-phase flow. Therefore, to determine the core activity introduced by gas bubbles and to evaluate the consequences of an accident, the void fraction in the vertical flow channel of the reactor core should first be obtained. Therefore, reliable prediction of the void fraction is necessary.

The one-dimensional correlation based on the drift-flux model has been often used for void-fraction prediction (Abbs and Hibiki, 2019), and is one of the most practical and accurate models to solve many engineering problems. In the past few decades, various correlations for calculating the drift-flux model parameters have been developed based on gas-water two-phase flow test with relatively high liquid velocity. Ishii (1977) first considered a fully developed bubbly flow, and assumed that the distribution parameter C_0 would depend on the density ratio and Reynolds number (Hibiki and Ishii, 2003), and also gave the correlations applied to fully developed flow in small diameter round pipe. The modified equations considering the Sauter mean diameter (Hibiki and Ishii, 2002) and for boiling bubbles (Ishii, 1977) were then developed. For large diameter pipes, Hills (1976), Shipley (1984), and Clark and Flemmer (1985) measured the void fraction of air-water and developed some correlations. Then, Kataoka and Ishii (1987) found the effect of tube diameter, pressure, gas flux, and fluid physical properties on drift velocity and develop a correlation of about v_{gj}^{+}. In Ishii's research, C_{∞}, the asymptotic value of C_0 is approximated to be constant ($C_{\infty} = 1.2$) for upward flow in a round pipe based on the water test data. Under this assumption, the C_0 only depends on the density ratio between gas and liquid. However, the applicability of the assumption of constant in a bubble column-type gas-liquid metal two-phase flow remains to be discussed. Shen and Hibiki (2020) evaluated the problem with several gas-liquid metal experimental data and showed that the distribution parameter correlation of Ishii with $C_{\infty} = 1.2$ or 1.35 (rectangular tube) predicted well the N_2-Na/K two-phase flow with high gas-to-liquid density ratio but cannot give reasonable predictions for the large C_0 values in the other two-phase flows with low gas-to liquid density ratios. Their study also pointed out the extremely high C_0 value may appear when the pipe's diameter is greater than 0.06 m in a N_2-Pb/Bi mixture. In another study of bubble column-type two-phase flow, Clark and Egmond (1990) found that the constants vary significantly due to the effect of buoyancy and low liquid velocity. Compared with water, the density of liquid lead-bismuth is about 10 times higher. Therefore, the buoyancy effect is more significant, which may lead to a higher distribution parameter. Consequently, the existing correlation can be further improved by considering the effect of liquid density, Reynolds number, and buoyancy to extend its applicability in bubble column-type gas-liquid metal flow. However, their work is limited by the lack of test data number of existing bubble column-type gas-LBE two-phase flow test because of the difficulty of void fraction and velocity measurement in a non-transparent liquid medium. This makes it difficult to analyze the gas bubble flow mechanism in liquid metal with high density. The existing method is to obtain a certain value of the parameter in a drift-flux model by directly fitting all of the available data points, such as in Mikityuk et al.'s

TABLE 2 Experiment study of liquid metal two-phase flow.

Institute/ Researchers	Flow channel geometry	D_h(m)	P (MPa)	T (°C)	j_f (m/s)	j_g (m/s)	α
JNC & KyotoU	Rectangular	0.033	0.1	200 (LBE)	0	0.0014–0.29	0.018–0.313
Saito-Ga/H_2O	Circular	0.1	0.1	80(Ga)/20(H_2O)	0	0.005–0.39/0.002–0.323	0.012–0.264/ 0.006–0.36
Ariyoshi	Circular	0.1023	0.1	200 (LBE)	0	0.013–0.09	0.017–0.11

TABLE 3 Physical property parameter of liquid in the experiment.

Fluid material	Density (kg/m^3)	Surface tension (N/m)	Viscosity (Pa·s)
LBE (200°C)	10,460	0.401	0.00170
Ga (80°C)	6060	0.735	0.00163
H_2O(20°C)	998	0.0732	0.001

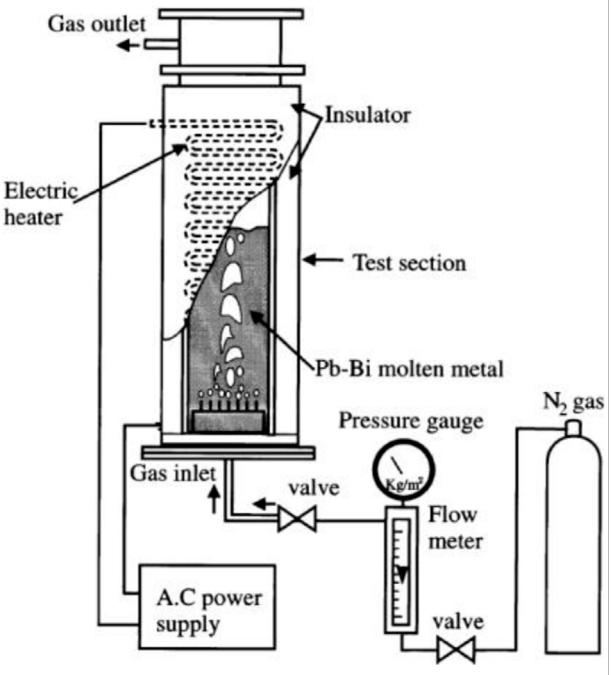

FIGURE 1
Diagram of the JNC & KyotoU test facility (Hibiki et al., 2000).

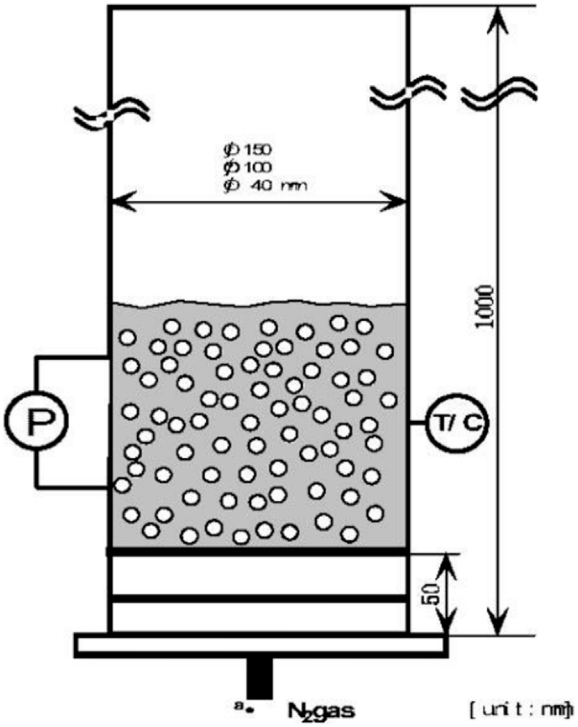

FIGURE 2
Diagram of Saito's test facility (Saito et al., 1998).

(2005) study, or by combining different correlations based on gas-water two-phase flow by interpolation to approximate the experimental data, such as the modified application in SIMMER-III code (Suzuki et al., 2003).

A method that combines theoretical analysis with experimental data is adopted in this study to clarify the effect of buoyancy, Reynolds number, and so on, on the distribution parameter. Therefore, a theoretical model for velocity radial distribution in bubble columns was proposed by Clark and Egmond. (1990), derived for gas-liquid metal two-phase flow to quantitatively achieve the effect of the above parameter. Based on the calculated result with the theoretical model and Ariyoshi et al.'s (2017) gas-LBE test data, a set of new correlations were applied for bubble column-type gas-liquid lead-bismuth two-

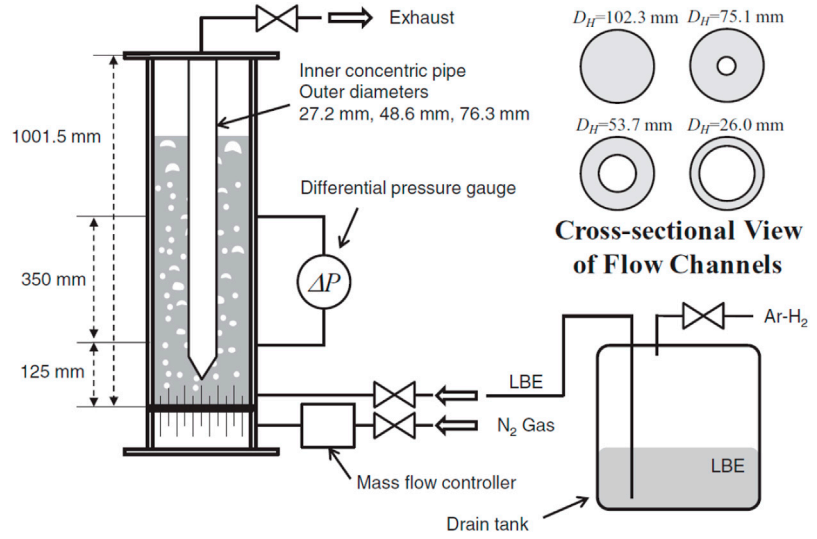

FIGURE 3
Diagram of Ariyoshi's test facility (Ariyoshi et al., 2017).

phase flow in the drift-flux model and developed and verified by comparing them with test data and other existing correlations.

2 Literature survey

2.1 Summary of the existing drift-flux model correlations

Zuber and Findlay (1965) were the first to take into account both the effect of nonuniform flow and concentration profiles, as well as the effect of the local relative velocity between the phases in analysis, and developed the following one-dimensional drift-flux model to predict the cross-sectional averaged void fraction in a flow channel:

$$\langle\langle v_g\rangle\rangle = \frac{\langle j_g\rangle}{\langle\alpha\rangle} = C_0\langle j\rangle + \langle\langle v_{gj}\rangle\rangle = C_0\left(\langle j_g\rangle + \langle j_f\rangle\right) + \langle\langle v_{gj}\rangle\rangle \tag{1}$$

Where v_g, α, j, j_g, j_f, C_0, and v_{gj} are gas velocity, void fraction, mixture volumetric flux, superficial gas velocity, superficial liquid velocity, distribution parameter, and drift velocity, respectively. < > and << >> are the area-averaged and void-fraction weighted mean quantities. The distribution parameter and drift velocity are defined as

$$C_0 = \frac{\langle\alpha j\rangle}{\langle\alpha\rangle\langle j\rangle}$$
$$\langle\langle v_{gj}\rangle\rangle = \frac{\langle\alpha v_{gj}\rangle}{\langle\alpha\rangle} \tag{2}$$

The non-dimensional expression is shown as follows, which is derived by dividing Equation 1 by the factor of $(\sigma g(\rho_f - \rho_g)/\rho_f^2)^{0.25}$.

$$\frac{\langle j_g^+\rangle}{\langle\alpha\rangle} = C_0\langle j^+\rangle + \langle\langle v_{gj}^+\rangle\rangle \tag{3}$$

where

$$X^+ = \frac{X}{\left(\sigma g\left(\rho_f - \rho_g\right)/\rho_f^2\right)^{0.25}} \tag{4}$$

X represents superficial gas and liquid velocity and drift velocity.

C_0 and v_{gj} represent the effect of void distribution and the relative velocity between phases. A number of constitutive correlations of C_0 and v_{gj} have been developed based on air/steam-water two-phase flow experimental data. In addition, several new correlations have been derived from the data of gas-liquid metal two-phase flows in recent years.

As mentioned in the introduction, Ishii has indicated that the distribution parameter is modeled by considering the density ratio of gas and liquid phases:

$$C_0 = C_\infty - (C_\infty - 1)\sqrt{\frac{\rho_g}{\rho_f}} \tag{5}$$

where C_∞ is the asymptotic value of the distribution parameter as the density ratio near zero. Meanwhile, as the density ratio approaches unity, the distribution parameter should also become unity. According to the experimental data of the fully developed flow in a round tube (Ishii, 1977), we have

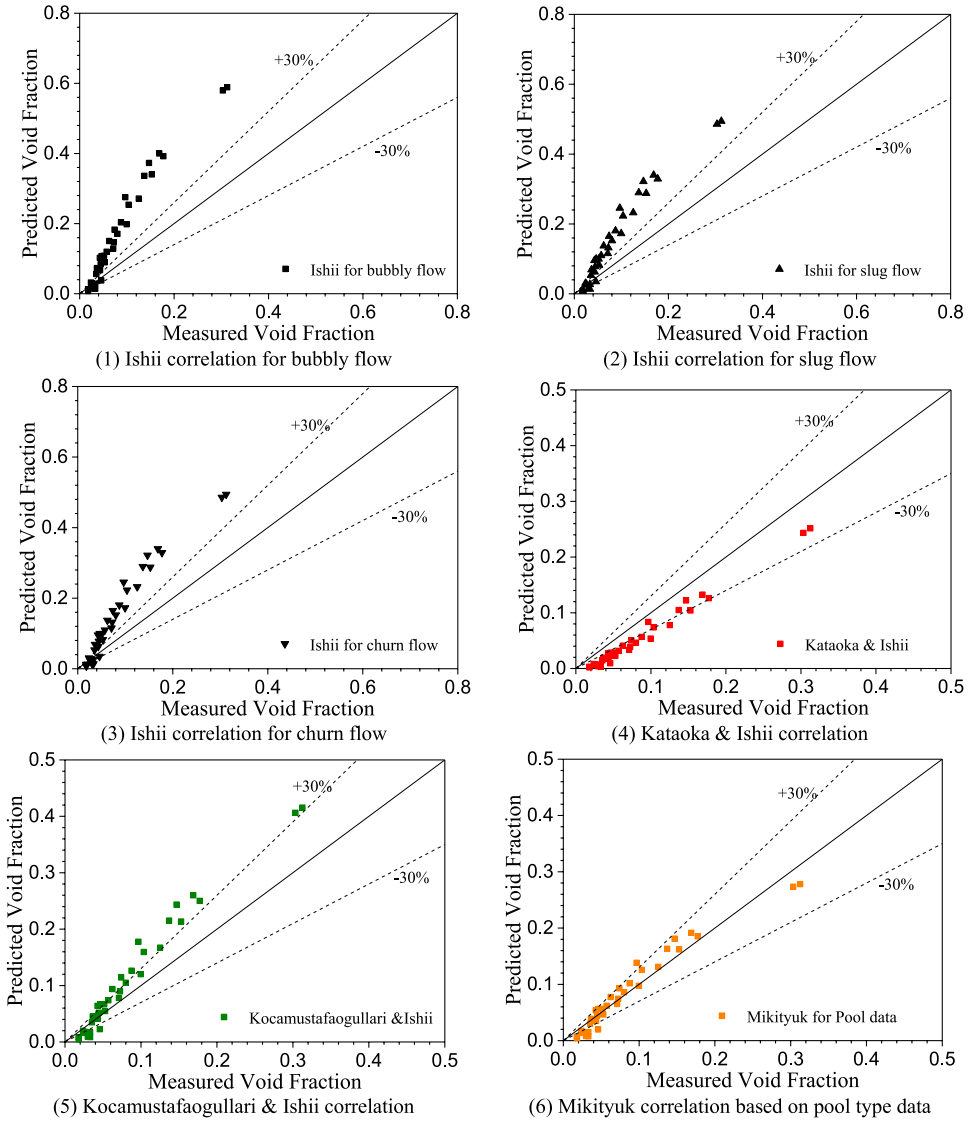

FIGURE 4
(Continued).

$$C_{\infty} = 1.393 - 0.0155\ln(\mathrm{Re}) \tag{6}$$

Over a wide range of Reynolds numbers, this equation can be approximated by $C_{\infty} = 1.2$ for a flow in a round tube. Thus, the following correlation for flow in small size tube:

$$\begin{aligned} C_0 &= 1.2 - 0.2\sqrt{\frac{\rho_g}{\rho_f}}, \text{ circular channel} \\ C_0 &= 1.35 - 0.35\sqrt{\frac{\rho_g}{\rho_f}}, \text{ rectangular channel} \end{aligned} \tag{7}$$

Drift velocity correlations for different flow regimes are developed by Ishii based on drag law (Ishii, 1977).

$$\begin{aligned} \langle\langle v_{gj}\rangle\rangle &= \sqrt{2}(1-\alpha)^{1.75}\left(\sigma g\left(\rho_f - \rho_g\right)/\rho_f^2\right)^{0.25}, \text{ bubbly flow} \\ \langle\langle v_{gj}\rangle\rangle &= 0.35\sqrt{gD_h\left(\rho_f - \rho_g\right)/\rho_f}, \text{ slug flow} \\ \langle\langle v_{gj}\rangle\rangle &= \sqrt{2}\left(\sigma g\left(\rho_f - \rho_g\right)/\rho_f^2\right)^{0.25}, \text{ churn flow} \end{aligned} \tag{8}$$

Compared with medium size channels, the different flow phenomena observed in large size channels are the formation of liquid recirculation (secondary flow) patterns in a bubbly flow and the disintegration of large bubbles due to surface instabilities (Abbs and Hibiki, 2019). Kataoka and Ishiii (1987) took the secondary flow in gas-water two-phase flow under the stagnant liquid conditions into account and developed the following correlations:

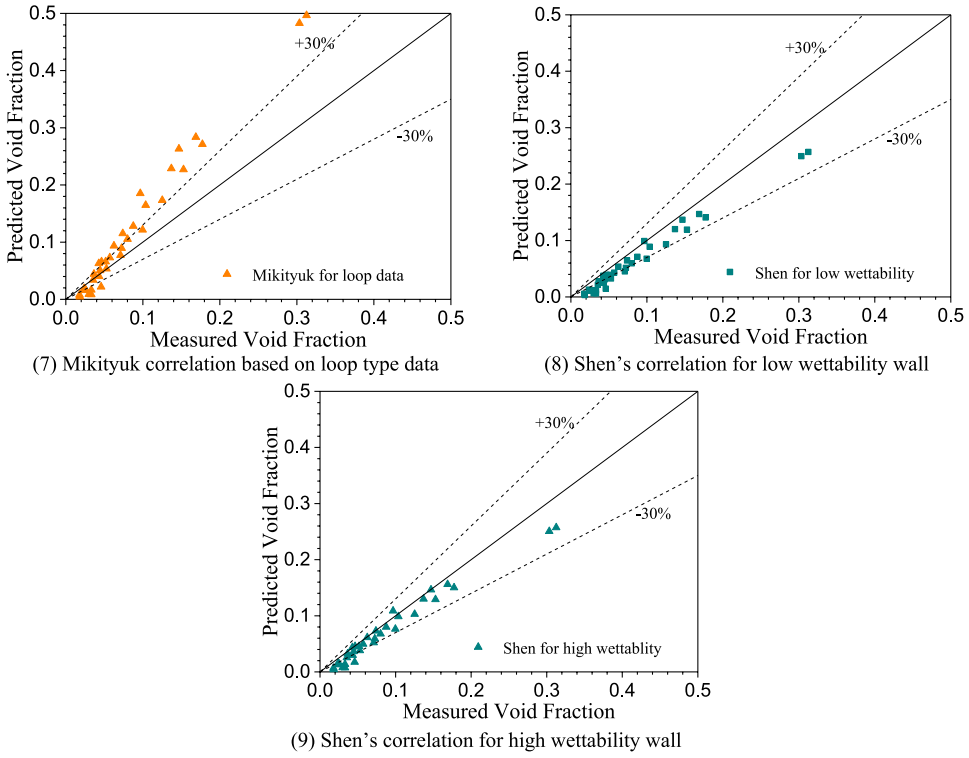

(7) Mikityuk correlation based on loop type data
(8) Shen's correlation for low wettability wall
(9) Shen's correlation for high wettability wall

FIGURE 4
(Continued). Comparisons between the measured (JNC experiment) and predicted void fraction. **(A)** Ishii correlation for bubbly flow. **(B)** Ishii correlation for slug flow. **(C)** Ishii correlation for churn flow. **(D)** Kataoka and Ishii correlation. **(E)** Kocamustafaogullari and Ishii correlation. **(F)** Mikityuk correlation based on pool type data. **(G)** Mikityuk correlation based on loop type data. **(H)** Shen's correlation for low wettability wall. **(I)** Shen's correlation for high wettability wall.

$$\begin{aligned}
\langle\langle v_{gj}\rangle\rangle &= 0.0019 D_h^{*0.809}\left(\rho_g/\rho_f\right)^{-0.157} N_{\mu_f}^{-0.562}\left(\sigma g\Delta\rho/\rho_f^2\right)^{0.25}, N_{\mu f} \le 0.0225, D_h^* \le 30\\
\langle\langle v_{gj}\rangle\rangle &= 0.03\left(\rho_g/\rho_f\right)^{-0.157} N_{\mu_f}^{-0.562}\left(\sigma g\Delta\rho/\rho_f^2\right)^{0.25}, N_{\mu f} \le 0.0225, D_h^* > 30\\
\langle\langle v_{gj}\rangle\rangle &= 0.92\left(\rho_g/\rho_f\right)^{-0.157}\left(\sigma g\Delta\rho/\rho_f^2\right)^{0.25}, N_{\mu f} > 0.0225, D_h^* > 30
\end{aligned} \tag{9}$$

where $N_{\mu f}$ is viscosity number

$$N_{\mu f} = \frac{\mu_f}{\sqrt{\sigma\rho_f\sqrt{\sigma/\left[g\left(\rho_f-\rho_g\right)\right]}}} \tag{10}$$

Kocamustafaogullari and Ishiii. (1985) considered the dominant effect of large cap bubbles on the drift velocity in two-phase flow and developed the following correlations for cap bubbly flow in vertical flow channels:

$$\langle\langle v_{gj}^+\rangle\rangle = \begin{cases} 0.54\sqrt{D_h^*}, & D_h^* \le 30 \\ 3.0, & D_h^* > 30 \end{cases} \tag{11}$$

As for gas-liquid metal two-phase flow, Mikityuk et al. (2005) analyzed five sets of experimental data with different geometries, working fluids, flow rates, and void fraction ranges and compared four types of correlations for pool-type (average superficial liquid velocity is zero) and loop-type channels. The recommended correlations are given by Equation 12. Because the high value of C_0 in the correlations for pool data shows that the liquid's velocity has a significant effect on the drift-flux parameter, their study indicated that the use of the correlation should be based not on the local characteristic length (bubble size) but on the pool diameter to reflect the fact that the multi-dimensional flow patterns, in this case, influence the two-phase flow parameters. In Mikityuk et al.'s study, the distribution parameter C_0 is a certain value, which is obtained by fitting test data directly:

$$\begin{aligned}
&C_0 = 2.4, \langle\langle v_{gj}\rangle\rangle = 0.61\sqrt{gD_h\Delta\rho/\rho_f}, \text{for pool data}\\
&C_0 = 0.9, v_{gj} = 2.33\sqrt[4]{g\sigma\Delta\rho/\rho_f^2}, \text{for loop data}
\end{aligned} \tag{12}$$

Shen and Hibiki. (2020) developed two correlations for the low and high wettability between the liquid metal and channel wall surface, respectively, as shown in Equation 13.

For the low wettability wall surface

$$C_0 = \left[1 + \frac{\langle j_g^+ \rangle^{0.00102}}{0.0667\langle j_g^+ \rangle^{0.690} + 1.36\langle j_f^+ \rangle^{3.29}}\right]\left(1 + 4.82e^{-0.186D_h^*}\right)$$

$$\left[1 - \left(\frac{\rho_g}{\rho_f}\right)^{0.0181}\right] + \left(\frac{\rho_g}{\rho_f}\right)^{0.0181}$$

$$\langle\langle v_{gj} \rangle\rangle = \begin{cases} 0.548\sqrt{D_h^*}\left(\sigma g \Delta\rho/\rho_f^2\right)^{0.25}, D_h^* \le 30 \\ 3.0\left(\sigma g \Delta\rho/\rho_f^2\right)^{0.25}, D_h^* > 30 \end{cases} \quad (13)$$

and for the high wettability wall surface

$$C_0 = \left[1 + \frac{\langle j_g^+ \rangle^{0.143}}{0.0853\langle j_g^+ \rangle^{0.719} + 0.115\langle j_f^+ \rangle^{1.08}}\right]\left(1 + 1.40e^{-0.0296D_h^*}\right)$$

$$\left[1 - \left(\frac{\rho_g}{\rho_f}\right)^{0.0137}\right] + \left(\frac{\rho_g}{\rho_f}\right)^{0.0137}$$

$$\langle\langle v_{gj} \rangle\rangle = \begin{cases} 0.508\sqrt{D_h^*}\left(\sigma g \Delta\rho/\rho_f^2\right)^{0.25}, D_h^* \le 30 \\ 2.78\left(\sigma g \Delta\rho/\rho_f^2\right)^{0.25}, D_h^* > 30 \end{cases}$$

Up to now, we have surveyed a total of nine correlations. Each correlation is allocated a number for comparison in Section 4, as shown in Table 1.

2.2 Summary of bubble column-type gas-liquid heavy metal two-phase flow experiments

Although many steam, nitrogen, and air-water two-phase flow tests have been carried out over the last few years, the number of gas-liquid LBE two-phase flow tests is much less due to the limitation of measurement difficulty and applied range, especially the bubble column. Three sets of bubble column-type tests are available and have been adopted for correlation evaluation and development, which is summarized in Table 2. In these tests, LBE and the similar heavy metal Gallium are used. The physical property parameters of liquid metal and water in tests are shown in Table 3.

2.2.1 JNC & KyotoU test

This test was performed under a joint research project by Japan Nuclear Cycle Development Institute (JNC) and Kyoto University (KyotoU) (Hibiki et al., 2000). Figure 1 shows a schematic diagram of the test facility. The test section is a rectangular tank whose inner height, width, and thickness are 530, 100, and 20 mm, respectively. Molten lead-bismuth eutectic is contained in the tank and nitrogen is injected uniformly from seven vertical nozzles that are mounted on the bottom of the tank. The experiment is conducted by varying gas superficial velocity j_g over range of 0.005–0.3 m/s while keeping the temperatures of nitrogen and molten lead–bismuth constant at 473 K.

In the experiment, high frame-rate neutron radiography technology is adopted to observe the flow regime and bubble shape. Void fraction can be also measured by the post process of the picture taken by a silicone intensifier target (SIT) tube camera (Hibiki et al., 2000). The test results show that a spherical or ellipsoidal bubble can be observed at a low gas velocity. As j_g increases, large slug bubbles or cap like bubbles appeared together with highly deformed small bubbles. The 35 sets of databases (time and space averaged void fraction vs. gas superficial velocity) from the three cases are used for correlation evaluation and validation in the current analysis.

2.2.2 Saito test

This experiment was performed by Saito et al. (1998) in the Tokyo Institute of Technology to study the hydraulic characteristics of a gas-liquid two-phase flow. As shown in Figure 2, the test section is a cylindrical vessel with an inner diameter of 10 cm. Through a plate with 2 mm diameter holes, nitrogen is injected into gallium and water in two cases. This allows the effect of liquid's physical property on two-phase flow to be compared directly. The void fraction is measured with a differential pressure gauge. The 68 and 43 sets of database (time and space averaged void fraction vs. gas superficial velocity) from gas-water and gas-gallium test cases are used for correlation evaluation and validation in the current analysis.

2.2.3 Ariyoshi test

This experiment was performed by Ariyoshi et al. (2017) at Kyoto University. Figure 3 shows the facility. A vertical circular pool is formed by a pipe with an inner diameter of 0.102 m. A three vertical annular pool is established by a combination of the pipe and inner concentric pipes with three different outer diameters. Nitrogen is injected from the bottom of the test section through the gas injector, which consists of 60 stainless steel needle tubes with 0.15 mm in inner diameter. The differential pressure was measured to estimate the time and space averaged void fraction at the measurement section. The database of the circular pool is used for new correlation development in the current analysis.

2.3 Evaluation of the applicability of the existing correlations of bubble-column flow

The void fraction under different gas superficial velocities can be predicted by Equation 1 with each of the above drift-flux correlations. A comparison between the predicted value of void fraction and the test data in the JNC & KyotoU test is shown in Figure 4. The void fraction calculated by Ishii correlation only agrees relatively well in the range of the void fraction lower than 0.05. When the void fraction is higher than 0.05, Equation 8 for bubbly flow overpredicts significantly. Although the Ishii correlations for

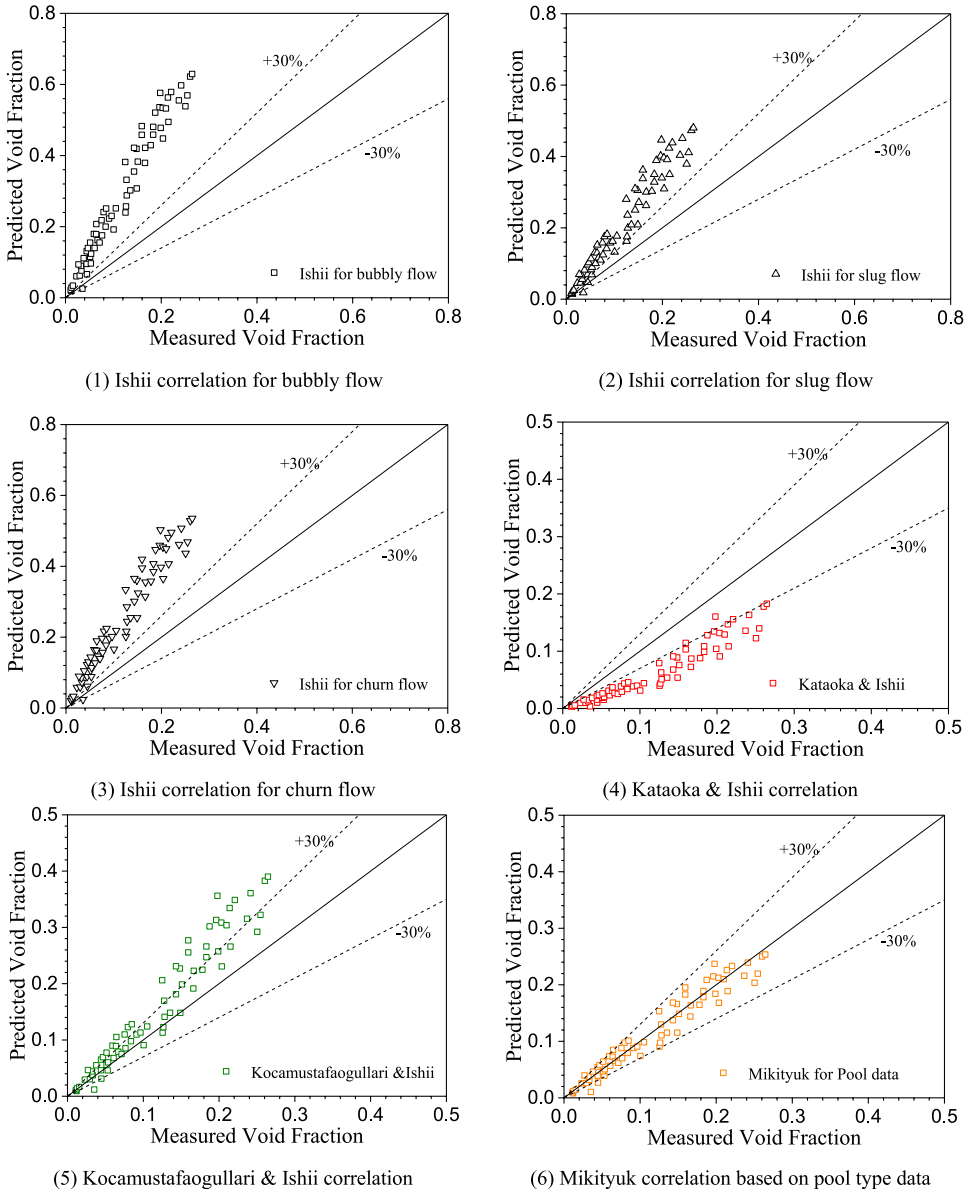

FIGURE 5
(Continued).

slug and churn flow are more applicable to the flow regime under a higher void fraction compared to the bubbly flow, the relative error is greater than 30% in gas-LBE two-phase flow.

In the range of 0.018–0.313, the void fraction is 30% underestimated by Kataoka and Ishii's correlation, as shown in Figure 4D. When the void fraction is lower than 0.05, this discrepancy increases to 80%. As a whole, as the void fraction increases, the prediction by Kataoka and Ishii's correlation is improved. This tendency is consistent with the research by Schlegel et al. (2010), who recommended the Kataoka and Ishii correlation for slug flow with cap bubble in gas-water two-phase flow. This happens because, in liquid heavy metal, a bubble is more likely to deform to a cap-shaped in higher gas fluxes (Suzuki et al., 2003), due to the high density ratio between phases.

A comparison between the prediction of Kocamustafaogullari and Ishii correlation and test data is shown in Figure 4E. The result indicates that in the range of 0–0.05, the correlation underpredicts the void fraction. As the void fraction increases, the overestimation is about 30%, which is less than that by Ishii correlations for different flow regimes.

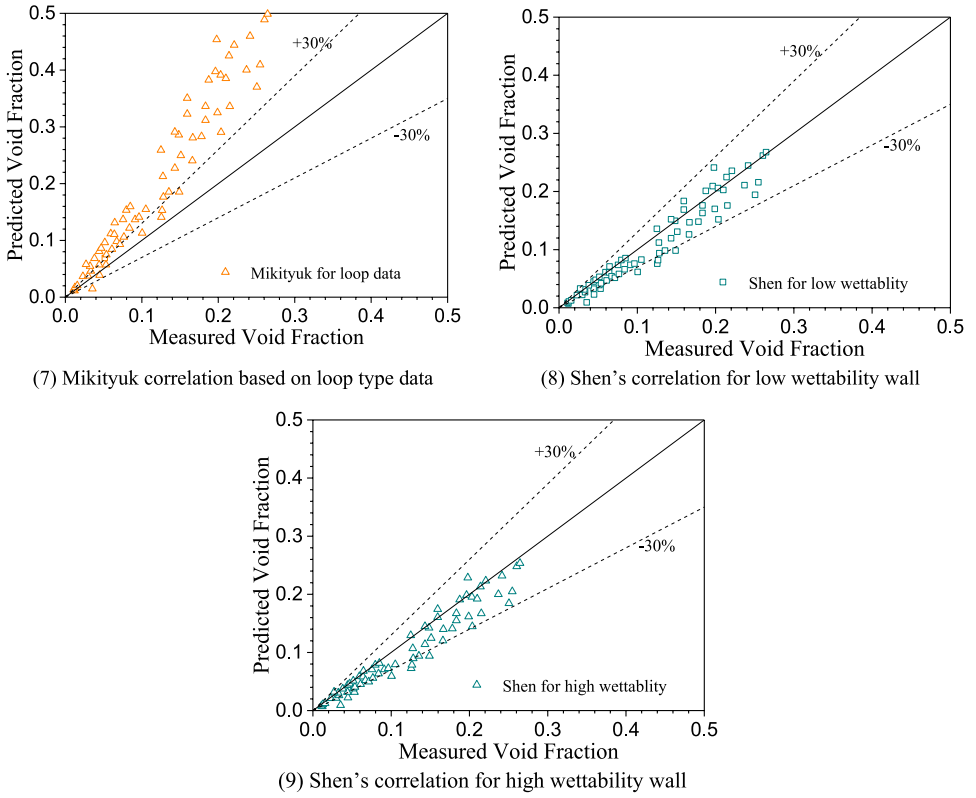

FIGURE 5
(Continued). Comparisons between the measured (Saito-Ga experiment) and predicted void fraction. **(A)** Ishii correlation for bubbly flow. **(B)** Ishii correlation for slug flow. **(C)** Ishii correlation for churn flow. **(D)** Kataoka and Ishii correlation. **(E)** Kocamustafaogullari and Ishii correlation. **(F)** Mikityuk correlation based on pool type data. **(G)** Mikityuk correlation based on loop type data. **(H)** Shen's correlation for low wettability wall. **(I)** Shen's correlation for high wettability wall.

For the drift-flux model based on gas-liquid metal two-phase flow, Mikityuk's pool-type correlation gives a good consistency with the test data. However, the loop-type correlation overestimates the void fraction, as shown in Figures 4F,G. This indicates that the distribution parameter tends to be greater than 1.0 when liquid velocity is relatively low so that the fitting value reaches 2.4 in Equation 12. It should be pointed out that the database of the JNC & KyotoU and Saito test has been also used for fitting in Mikityuk's correlations. Therefore, other independent tests are recommended for evaluation in the future.

Figures 4H,I show the comparisons between the void fraction calculated by Shen's correlation and measured in the JNC & KyotoU test. A little underestimation is observed in the void fraction range of 0.018–0.313. This demonstrates that the predictions of the drift-flux type correlation are in better agreement with the collected data than the correlations that only consider the density ratio in distribution parameter calculation.

Comparisons between predicted void fraction with drift-flux correlations and Saito's nitrogen-gallium two-phase flow test data are shown in Figure 5. The overall prediction trend is consistent with that observed in the JNC & KyotoU test with liquid lead-bismuth. All of the drift-flux models derived from the gas-water database give more than ±30% deviation of the predicted value. Among the correlations based on gas-liquid metal, Mikityuk's pool-type correlation and Shen's correlation for low wettability wall are in good agreement with the test data.

Correlations based on gas-water two-phase flow database are used to enhance the adequacy of the evaluation; that is, Equations 7–11 are further compared with the data obtained by the Saito-H_2O test. The predicted deviation by Ishii (for slug flow), Kataoka and Ishii, and Kocamustafaogullari and Ishii correlations is less than ±30%, which is improved compared with the prediction for nitrogen-gallium two-phase flow. It must be pointed out that this comparison is not intended to verify the applicability of these correlations in gas-water two-phase flow (because they have been fully demonstrated with large amounts of test data), but is intended to indicate that the density ratio between phases indeed affects flow characteristics and the drift-flux parameter can be improved when applying to void-fraction prediction in a gas-liquid metal two-phase flow.

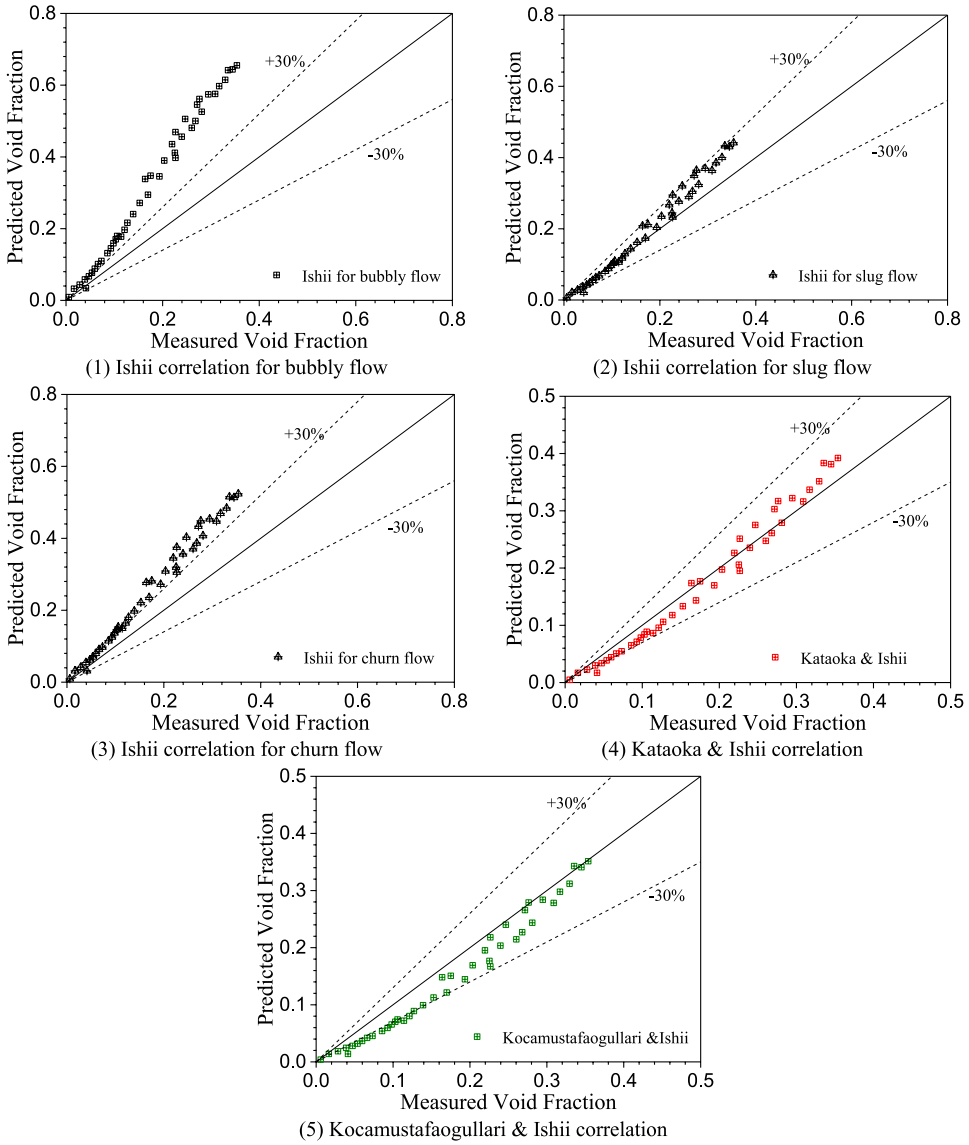

FIGURE 6
Comparisons between the measured (Saito-H_2O experiment) and predicted void fraction. **(A)** Ishii correlation for bubbly flow. **(B)** Ishii correlation for slug flow. **(C)** Ishii correlation for churn flow. **(D)** Kataoka and Ishii correlation. **(E)** Kocamustafaogullari and Ishii correlation.

In summary, it can be observed that the density difference between liquid metal and water shows an obvious effect on the drift-flux parameter by comparing the predicted void fraction by two types of correlations derived from gas-water and gas-liquid metal two-phase flow database, respectively. For the correlations for gas-liquid metal two-phase flow, Mikityuk's pool-type model agrees well with the test data. It should be noted that the test data has been also used for data fitting during the correlation development process, the application of which is beyond the range of the experimental parameter and should be further discussed. Other correlations can be further improved to apply better in bubble column-type gas-LBE two-phase flow, see Figure 6.

3 The influence factor of distribution parameter C_0

3.1 Clark's theoretical model

According to Clark and Van Egmond's (1990) model, the two-phase flow along axial direction in a round tube is assumed

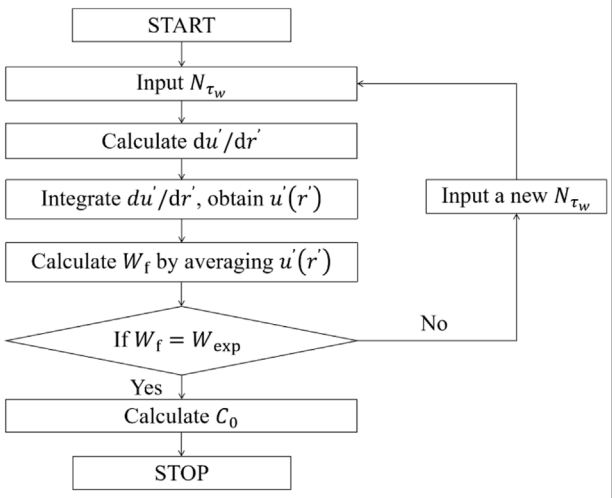

FIGURE 7
Calculation flow chart of Clark's theoretical model.

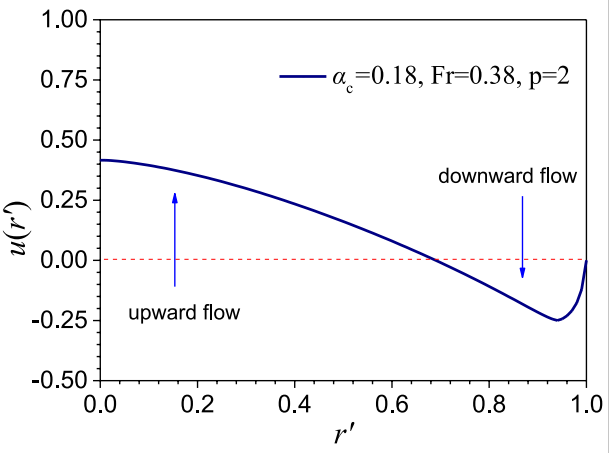

FIGURE 8
Calculated velocity along radial direction.

to be one-dimensional and the void-fraction profile along radial direction r is assumed as in the following equation:

$$\alpha(r) = \alpha_c\left[1 - \left(\frac{r}{R}\right)^p\right] \tag{14}$$

where α_c is the void fraction at the center of the tube and R is the radius of the flow channel.

The density of two-phase mixture $\rho(r)$ is given by

$$\rho(r) = \rho_f(1 - \alpha(r)) + \rho_g\alpha(r) \tag{15}$$

where ρ_f and ρ_g is liquid and gas density. Generally, ρ_g can be neglected due to order of magnitude difference. Substitute $\alpha(r)$ into Equations 2 and 3,

$$\rho(r) = \rho_f\left[1 - \alpha_c + \alpha_c\left(\sqrt{r/R}\right)^p\right] \tag{16}$$

the shear stress $\tau(r)$ can be calculated using force balance (Levy, 1963; Clark et al., 1987). It should be noted that in Clark and Flemmer's derivation, there is a clerical error in that the R is wrongly written in the denominator, which can be easily derived by dimensional analysis. The correct equation is shown as follows:

$$\tau(r) = \tau_w\frac{r}{R} + \frac{1}{2}rg[\bar{\rho} - \rho_i(r)] \tag{17}$$

where g is the gravitational acceleration and τ_w is wall shear stress, $\bar{\rho} - \rho_i(r)$ is the difference between the average density over the whole radius and the average density within radius r, which is given by integrating Equation 16. The result is shown in the following equation:

$$\bar{\rho} - \rho_i(r) = \rho_f\left(\frac{2\alpha_c}{p+2}\right)\left[1 - \left(\frac{r}{R}\right)^p\right] \tag{18}$$

As for $\tau(r)$, a rheological mixing length model which takes into account turbulent momentum transfer has been proposed by Clark and Egmond (1990). The shear stress was accordingly taken as

$$\tau(r) = -\mu\frac{dU}{dr} - l^2\left|\frac{dU}{dr}\right|\frac{dU}{dr} \tag{19}$$

where μ is dynamic viscosity, U is the liquid velocity, l is the mixing length used by Clark and Egmond (1990).

$$\frac{l}{R} = 0.14 - 0.08\left(\frac{r}{R}\right)^2 - 0.06\left(\frac{r}{R}\right)^4 \tag{20}$$

By combining Equations 17 and 19, a formula as follows about the U along radius is obtained by introducing Equation 21.

$$0 = \tau_w\frac{r}{R} + \frac{1}{2}rg[\bar{\rho} - \rho_i(r)] + \mu\frac{dU}{dr} + l^2\left|\frac{dU}{dr}\right|\frac{dU}{dr} \tag{21}$$

In Equation 21, the wall shear stress τ_w is unknown. Therefore, an assumed initial value should be input to obtain dU/dr by solving the quadratic equation. Then, $U = 0$ at $r = R$, the liquid velocity profile $U(r)$ can be found by integrating from the wall boundary condition.

The average liquid velocity can be solved by integrating $U(r)$ over the whole cross section of the channel, as shown in Equation 22:

$$W_f = \frac{2}{R^2}\int_0^R U(r)(1 - \alpha(r))rdr \tag{22}$$

For the convenience of solving, Equation 21 is converted into a dimensionless form:

$$0 = \left[N_{\tau_w} + \frac{\mathrm{Ga}}{2}\frac{\alpha}{p+2}\right]r' + 2\frac{du'}{dr'} + \left(\frac{l}{R}\right)^2(1-\alpha)\mathrm{Ga}\left|\frac{du'}{dr'}\right|\frac{du'}{dr'} \tag{23}$$

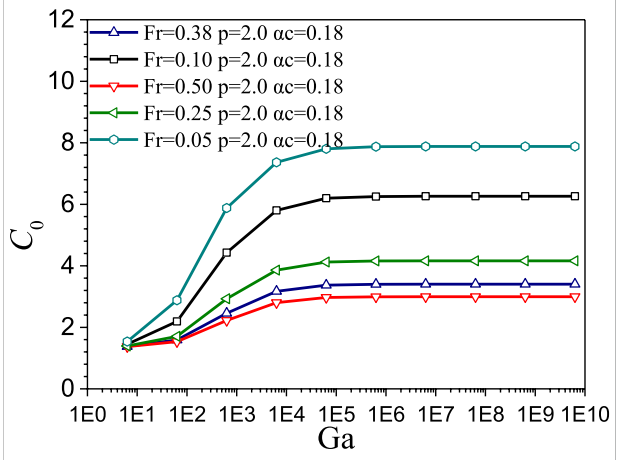

FIGURE 9
The effect of Ga on the distribution parameter.

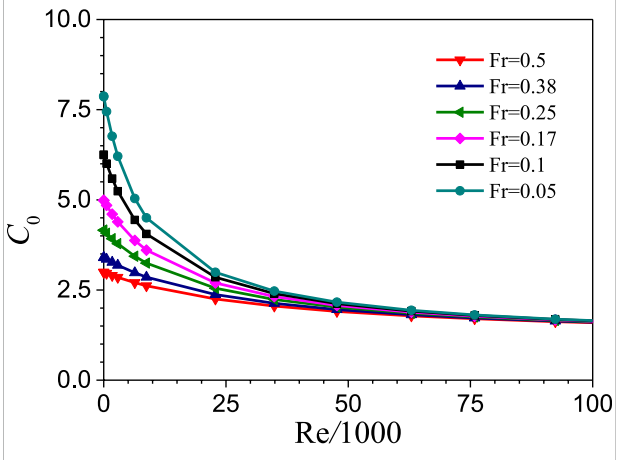

FIGURE 11
The effect of Re on the distribution parameter.

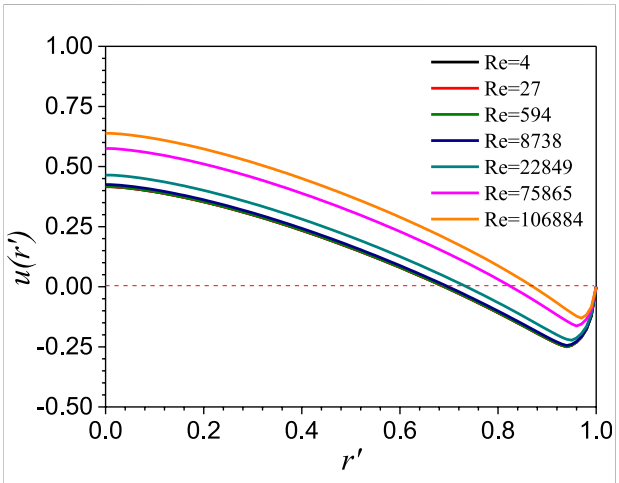

FIGURE 10
Velocity distribution along radial direction under different Reynolds numbers (Fr = 0.38, α_c = 0.18, p = 2.0).

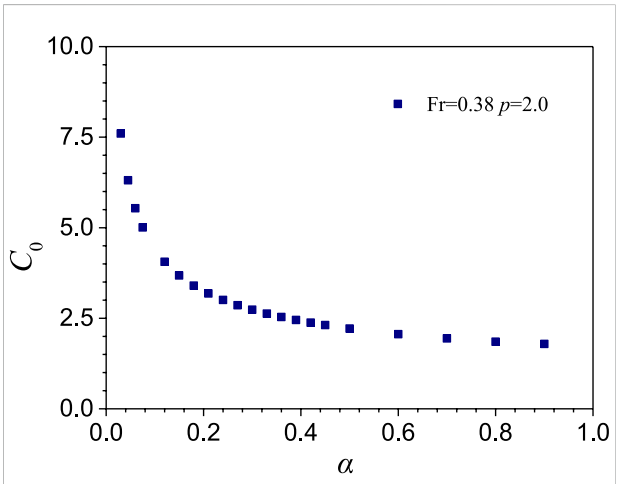

FIGURE 12
The effect of the void fraction on the distribution parameter.

where

$$N_{\tau_w} = \frac{\tau_w}{\mu}\sqrt{\frac{D}{g}}$$
$$u' = \frac{U}{\sqrt{gD}}$$
$$r' = \frac{r}{R} \quad (24)$$
$$\mathrm{Ga} = \frac{\sqrt{gD}D\rho_f}{\mu}$$

where Ga is Galileo number, D is the channel diameter, and Equation 22 can be rewritten as

$$\frac{W_f}{\sqrt{gD}} = 2\int_0^1 u'(1-\alpha)r'dr' \quad (25)$$

We iterate the wall shear stress until the calculated W_f is equal to the real value (W_{exp} = 0 in pool-type two-phase flow), and then the assumed τ_w and corresponding velocity profile is correct. Therefore, the distribution parameter C_0 can be determined by definition; that is, Equation 2:

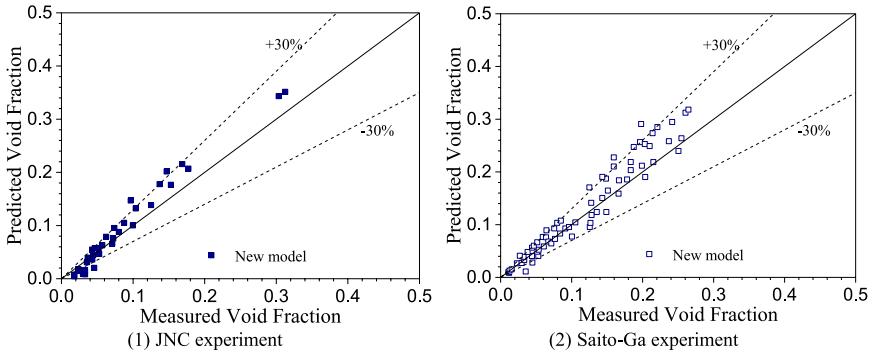

FIGURE 13
Comparisons between measured and predicted void fraction. **(A)** JNC experiment. **(B)** Saito-Ga experiment.

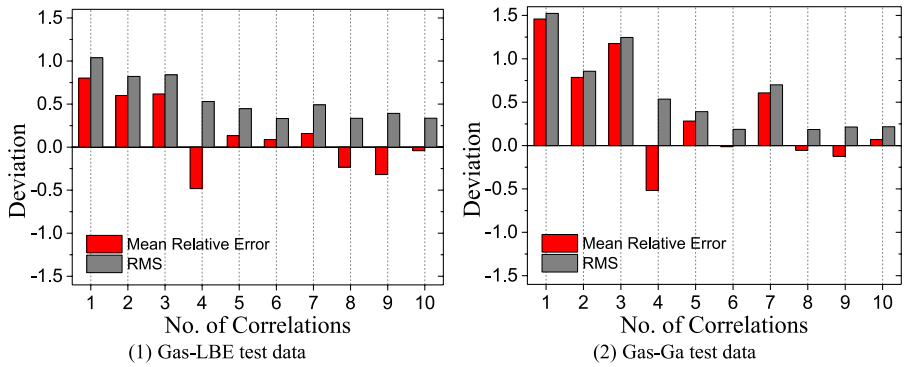

FIGURE 14
Statistical analysis of the predicted void fraction by correlations (1—Ishii for bubbly, 2—Ishii for slug, 3—Ishii for churn, 4—Kataoka and Ishii, 5—Koca and Ishii, 6—Mikityuk for pool, 7—Mikityuk for loop, 8—Shen for low wettability wall, 9—Shen for high wettability wall, 10—New developed model). **(A)** Gas-LBE test data. **(B)** Gas-Ga test data.

TABLE 4 Comparison of the predicted performance of all of the correlations, in terms of the benchmark coefficient ξ_j.

Correlations number, j	ξ_j for gas-LBE test	ξ_j for gas-Ga test
1	0.168	0.066
2	0.215	0.117
3	0.210	0.080
4	0.322	0.186
5	0.489	0.261
6	0.685	**0.995**
7	0.433	0.144
8	0.530	0.625
9	0.442	0.488
10	**0.939**	0.528

The bold value is the maximal value among corresponding column.

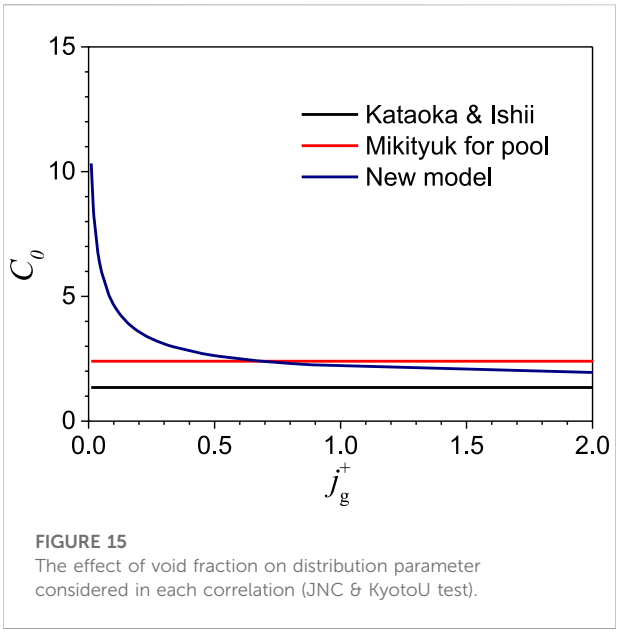

FIGURE 15
The effect of void fraction on distribution parameter considered in each correlation (JNC & KyotoU test).

$$C_0 = \frac{\int_0^1 \left[\alpha u' + \frac{\alpha^2}{1-\alpha}\mathrm{Fr}\right] r' dr'}{\alpha_c\left(1 - \frac{2}{p+2}\right)\int_0^1 \left[u' + \frac{\alpha}{1-\alpha}\mathrm{Fr}\right] r' dr'} \tag{26}$$

where Fr is the Froude number. To solve the problem of the unknown local drift velocity for Fr calculation due to lack of measured data, we refer the reader to the study by Ariyoshi et al. (2017), and the void-fraction-weighted mean drift velocity is applied to Equation 27 as the approximate value of the local drift velocity v_{gj}:

$$\mathrm{Fr} = \frac{\langle\langle v_{gj}\rangle\rangle}{\sqrt{gD_h}} \tag{27}$$

3.2 Calculation results

A program based on Fortran90 is coded to solve the distribution parameter by using this theoretical model. The calculation flow chart is shown in Figure 7, the centric void fraction (0.18), channel radius, and Froude number (0.38) are referred from the experiment case with a round tube that was conducted by Ariyoshi et al. (2017).

The calculated liquid velocity profile over radius is shown in Figure 8. In the center of the flow channel, the liquid metal is entrained by rising bubbles and flows upward. Correspondingly, liquid metal near the wall flows downward to fill the vacancy after the fluid in the center area leaves. A flow circulation over radius forms. Because the liquid metal is contained in a static pool during the experiment, the overall volume flux over channel cross section and the liquid Reynolds number based on average velocity are zero.

The distribution parameter calculated with Equation 26 *versus* Galileo number Ga is shown in Figure 9. Under the same Fr number, with Ga increasing, C_0 increases significantly when Ga is in the range of 0–1.0×10^5. When Ga > 1.0×10^5, C_0 remains almost unchanged. As shown in Equation 24, the definition of Ga includes liquid phase density and dynamic viscosity. It can be seen that the dynamic viscosity of the two kinds of liquid metal (LBE and Gallium) is close to that of water, and the density is about 5–10 times that of water. Therefore, under the same channel diameter, the Ga number of liquid heavy metal tends to be also larger than that of water, which leads to higher distribution parameters. This result is consistent with the phenomena observed in Saito et al.'s (1998) experiment.

Velocity profile along radial direction under different liquid Reynolds numbers (i.e., the velocity, viscosity, and density are based on liquid phase) is shown in Figure 10. The greater value of the Reynolds number represents a larger liquid velocity in the same channel. Figure 11 shows that as the Reynolds number increases, the distribution parameter reduces. When the Reynolds number is 100,000, the C_0 has reached 1.28. It can be inferred from this that in the pool-type test conducted by JNC and KyotoU, Saito, or Ariyoshi, the liquid superficial velocity and Reynolds number of which are zero, the liquid velocity profile is significantly affected by buoyancy and the distribution parameter could be much higher than 1. This indicates that existing correlations are not suitable for lower liquid velocity two-phase flow. Furthermore, another factor is the Fr number—under larger Fr, the distribution parameter tends to be near 1.

The effect of the void fraction on distribution is shown in Figure 12. Under the same power law (p = 2.0), for the calculated case (Fr = 0.38, Re = 0), when the center void fraction increases from 0.04 to 0.4, the distribution decreases from 6.3 to 2.45.

4 New correlation development and validation

Through the influence analysis of the distribution parameter based on Clark's theoretical model, it can be seen that the distribution parameter is not only affected by the density ratio of gas and liquid phase but is also affected by the liquid phase velocity, void fraction, and Fr number. In this regard, the following analysis is carried out to consider these factors and develop new correlations. First, the theoretical method in Section 3.1 is used to calculate velocity distribution, as shown in Figures 8 and 10. Based on the velocity distribution and assumed void fraction distribution, C_0 is calculated with Equation 26, so the relationship between C_0 and Re, Fr, the void fraction can be obtained in the form of calculated datasets, as shown in Figures 11 and 12. In this section, the functions that C_0 about Re, Fr, and void fraction is obtained by data fitting.

4.1 Development of the correlations

Ishii's (1977) study on gas-water two-phase flow, distribution parameter can be represented by replacing Equation 7, as follows:

$$C_0 = f(\mathrm{Re}) - [f(\mathrm{Re}) - 1]\sqrt{\frac{\rho_g}{\rho_f}} \tag{28}$$

According to the calculated result shown in Figure 11, the distribution parameter decreases with the increase of Re. At the same time, with the increase of Fr, the distribution parameter corresponding to different Re numbers decreases totally. Therefore, it can be assumed that the f (Re) under different Fr meets

$$f(\mathrm{Re}) = \begin{cases} X_1 g_1(\mathrm{Fr}), & lg(\mathrm{Re}) < 3.26 \\ X_2 g_2(\mathrm{Fr}) - X_3 g_3(\mathrm{Fr}) lg(\mathrm{Re}), & 3.26 \le lg(\mathrm{Re}) < 5 \end{cases} \tag{29}$$

By fitting the calculated C_0 versus Re dataset under the Fr is 0.38, the coefficients X_1, X_2, and X_3 are given

$$f(\mathrm{Re}) = \begin{cases} 3.4 g_1(\mathrm{Fr}), & lg(\mathrm{Re}) < 3.26 \\ 6.63 g_2(\mathrm{Fr}) - 0.99 g_3(\mathrm{Fr}) lg(\mathrm{Re}), & 3.26 \le lg(\mathrm{Re}) < 5 \end{cases} \tag{30}$$

Furthermore, the functions g_1, g_2, and g_3 about the Fr number are given by fitting the calculated result of C_0 versus Fr, as shown in following equation:

$$\begin{aligned} g_1(\mathrm{Fr}) &= 0.391 - 0.632\ln(\mathrm{Fr}) \\ g_2(\mathrm{Fr}) &= 0.449 - 0.58\ln(\mathrm{Fr}) \\ g_1(\mathrm{Fr}) &= -0.286 + 0.755\ln(\mathrm{Fr}) \end{aligned} \tag{31}$$

where the Fr number is obtained from Equation 27.

As can be seen from Figure 12, the distribution parameter decreases with the increase of the void fraction in the center of the flow channel. The function of C_0 about void fraction when Fr is 0.38 is given by fitting the dataset of void fraction and distribution parameter, as shown in Equation 32:

$$C_0 = 1.82 - 0.62\lg(\alpha_c) + 2.03[\lg(\alpha_c)]^2 \tag{32}$$

When p, the exponent of the power law of void fraction distribution along the radius, is 2.0, α_c is equal to $2.0\langle\alpha\rangle$, and $\langle\alpha\rangle$ is given by fitting the dataset from the nitrogen-LBE two-phase flow test case in circular channel conducted by Ariyoshi et al. (2017), as shown in Equation 33:

$$\langle\alpha\rangle = \frac{j_g^+}{3.92 j^+ + 3.5} \tag{33}$$

Consider the influence of void fraction in Equation 28, that is:

$$C_0 = \left\{ f(\mathrm{Re}) - [f(\mathrm{Re}) - 1]\sqrt{\frac{\rho_g}{\rho_f}} \right\} h(\alpha) \tag{34}$$

$$h(\alpha) = 0.535 - 0.182\lg(\alpha_c) + 0.597[\lg(\alpha_c)]^2 \tag{35}$$

As for the gas drift velocity, referring to Shen and Hibiki's (2020) evaluation result of v_{gj}^+ data variation with dimensionless hydraulic diameter, Kocamustafaogullari and Ishii correlations could give the best prediction v_{gj}^+ among chosen correlations. Consequently, this model is adopted:

$$\langle\langle v_{gj}^+ \rangle\rangle = \begin{cases} 0.54\sqrt{gD_h^*}, & D_h^* \le 30 \\ 3.0, & D_h^* > 30 \end{cases} \tag{36}$$

Finally, the new correlations consist of Equations 28, 30, and 31 and Equations 33–36.

4.2 Evaluation of the newly developed correlations

Figure 13A shows the comparison between the void fraction predicted by newly developed correlations and JNC & KyotoU test data. After considering the influence of liquid phase velocity, Froude number, and void fraction on the distribution parameter, the predicted results with new correlations show agreement with gas-LBE two-phase flow test data. In the void fraction range of 0.018–0.313, most data points fall into the error band of −30% to 30%. A similar predicted result is also observed in the comparison with the Saito-Ga test, as shown in Figure 13B.

For statistical analysis, the relative error of the jth correlation when predicting the ith data point, ε_{ij}, is defined as

$$\varepsilon_{ij} = \frac{\alpha_{predicted}}{\alpha_{measured}} - 1 \tag{37}$$

The statistical mean and root-mean-square (RMS) value of ε_{ij} are defined for a set of N data points in Equations 38 and 39:

$$\bar{\varepsilon}_{ij} = \frac{1}{N}\sum_{i=1}^{N}\varepsilon_{ij} \tag{38}$$

$$\varepsilon_{RMSj} = \sqrt{\frac{1}{N}\sum_{i=1}^{N}\varepsilon_{ij}^2} \tag{39}$$

These statistical relative errors are shown in Figure 14. It can be observed that the newly developed correlation (No. 10) tends to give the smallest mean relative error for predicting the void fraction in gas-LBE two-phase flow. The RMS of new correlations is also relatively small and comparable to Mikityuk's (for pool, No. 6) correlation and Shen's (for low wettability wall, No. 8) correlation. As for the evaluation with the Saito-Ga test, the new correlations also show good agreement with experimental data with a relatively small error.

To determine the best correlation for gas-liquid metal two-phase flow in a bubble column from the statistical result in Figure 14, a benchmark coefficient ξ_j is used which refers to the method adopted in the evaluation of convective heat transfer correlations (Pacio et al., 2015), as shown in Equation 40. In this coefficient, both the absolute mean relative error and RMS value

of correlation are considered. A larger value of the coefficient in the range of $0 \le \xi_j \le 1$ indicates a better prediction performance:

$$\xi_j = 0.5\left[\frac{\min_j|\varepsilon_j|}{|\varepsilon_j|} + \frac{\min_j \varepsilon_{RMSj}}{\varepsilon_{RMSj}}\right] \quad (40)$$

From Table 4, it can be seen that the new correlation (No. 8) gives a much better prediction for gas-LBE two-phase flow in the bubble column case than any other correlations. For gas-Ga two-phase flow, the prediction performance of the new model ranks third among all of the correlations. When compared with correlation No. 6, although the new model is developed as the best fit of relatively few data points, it has the smallest mean relative error, and the effect of liquid velocity and a void fraction (which generally increase with rising superficial gas velocity) on distribution parameter is considered. In addition, the gas-Ga test data are used for fitting to get the correlation. However, the applicability should be further evaluated beyond the range of $0 < j_g < 0.4$ m/s and $\alpha \le 0.3$. Therefore, the conclusion proposed by Clark's study that C_0 assumes very high values at a low net flow rate can be verified, as shown in Figure 15.

5 Conclusion and prospects

The drift-flux model is very important for gas-liquid two-phase flow analysis in the safety evaluation of an advanced nuclear system during an accident process. To study the bubble column-type gas-liquid lead-bismuth two-phase flow phenomenon, nine existing drift-flux type correlations are reviewed and evaluated. Based on one-dimensional theory analysis, the distribution parameter is estimated and the effect is quantitatively discussed. A new correlation is then developed. The obtained conclusions and prospects are as follows:

1) To predict the void fraction in a bubble column-type gas-liquid heavy metal two-phase flow, the evaluation result based on the data from JNC & KyotoU and Saito's test shows that only Mikityuk's correlation for pool-type flow and Shen's correlation for low wettability wall give relatively good prediction among the nine correlations. In Mikityuk's model, the distribution parameter is assumed to be a constant, the applicability of which can be further evaluated under a wider parameter range.
2) The analysis result based on Clark's theoretical model shows that the distribution parameter assumes very high values at a low Re number. As the Froude number increases, the distribution parameter tends to decrease. At lower void factions, the distribution parameter is also assumed to be a high value. This indicates that the pipe size, flow rate, and void fraction can all influence distribution parameter.
3) Considering the quantitative laws of the influence factors obtained by theoretical analysis and fitting the data of Ariyoshi's test, a new correlation for bubble column-type gas-LBE two-phase flow is developed and evaluated with JNC & KyotoU and Saito's test. The statistical analysis result shows that the new correlation gives the best prediction for gas-LBE two-phase flow in the void fraction range of 0.018–0.313.

In future work, a separated effect test of the gas-LBE bubble column in which the void fraction and liquid velocity along the radius are accurately measured is necessary to further verify or modify the initial assumption of the void-fraction profile in the existing theoretical analysis. In addition, an experiment with an extended range of void fractions and Froude numbers is required.

Data availability statement

The original contributions presented in the study are included in the article/supplementary material, and further inquiries can be directed to the corresponding author.

Author contributions

DW: methodology, coding, writing-original draft. XL: conceptualization, methodology, supervision. SQ: conceptualization, methodology, supervision. RL: analysis and writing-original draft. ZL: literature survey, proofread, and modification. YO: proofread and modification.

Conflict of interest

The authors declare that the research was conducted in the absence of any commercial or financial relationships that could be construed as a potential conflict of interest.

Publisher's note

References

Abbs, T., and Hibiki, T. (2019). One-dimensional drift-flux correlation for vertical upward two-phase flow in a large size rectangular channel. *Prog. Nucl. Energy* 110, 311–324. doi:10.1016/j.pnucene.2018.09.023

Ariyoshi, G., Inatomi, R., Ito, D., and Saito, Y. (2017). Effect of wall wettability condition on drift-flux parameters in lead-bismuth two-phase flow in circular and annular bubble columns. *J. Nucl. Sci. Technol.* 55, 239–253. doi:10.1080/00223131.2017.1394230

Clark, N. N., Flemmer, R., and Atkinson, C. (1987). Turbulent circulation in bubble columns. *AIChE J.* 33, 515–518. doi:10.1002/aic.690330321

Clark, N. N., and Flemmer, R. (1985). Predicting the holdup in two-phase bubble upflow and downflow using the Zuber and Findlay drift-flux model. *AIChE J.* 31, 500–503. doi:10.1002/aic.690310323

Clark, N. N., Van Egmond, J. W., and Nebiolo, E. (1990). The drift-flux model applied to bubble columns and low velocity flows. *Int. J. Multiph. Flow* 16 (2), 261–279. doi:10.1016/0301-9322(90)90058-q

Han, X., Shen, X., Yamamoto, T., Nakajima, K., and Hibiki, T. (2020). Drift-flux correlation for upward gas-liquid two-phase flow in vertical rod bundle flow channel. *Int. J. Heat Mass Transf.* 162, 120341. doi:10.1016/j.ijheatmasstransfer.2020.120341

Hibiki, T., and Ishii, M. (2002). Distribution parameter and drift velocity of drift-flux model in bubbly flow. *Int. J. Heat Mass Transf.* 45, 707–721. doi:10.1016/s0017-9310(01)00195-8

Hibiki, T., and Ishii, M. (2003). One-dimensional drift–flux model for two-phase flow in a large diameter pipe. *Int. J. Heat Mass Transf.* 46, 1773–1790. doi:10.1016/s0017-9310(02)00473-8

Hibiki, T., Saito, Y., Mishima, K., Tobita, Y., Konishi, K., and Matsubayashi, M. (2000). Study on flow characteristics in gas-molten metal mixture pool. *Nucl. Eng. Des.* 196, 233–245. doi:10.1016/s0029-5493(99)00293-9

Hills, J. H. (1976). The operation of a bubble column at high throughputs. *Chem. Eng. J.* 12, 89–99. doi:10.1016/0300-9467(76)87002-5

Ishii, M. (1977). One-dimensional drift-flux model and constitutive equations for relative motion between phases in various two-phase flow regimes. *ANL-* 77-47.

Kataoka, I., and Ishii, M. (1987). Drift flux model for large diameter pipe and new correlation for pool void fraction. *Int. J. Heat Mass Transf.* 30 (9), 1927–1939. doi:10.1016/0017-9310(87)90251-1

Kocamustafaogullari, G., and Ishii, M. (1985). "Maximum fluid particle size for bubbles and drops," in Proceedings of Fundamental Aspects of Gas-liquid Flows, FED-Vol. 29, ASME Winter Annual Meeting, Miami Beach, Florida, USA, 17-21 Nov 1985, 99–107.

Levy, S. (1963). Prediction of two phase pressure drop and density distribution from mixing length theory. *J. Heat Transf.* 85 (2), 137–150. doi:10.1115/1.3686033

Mikityuk, K., Coddington, P., and Chawla, R. (2005). Development of a drift-flux model for heavy liquid metal/gas flow. *J. Nucl. Sci. Technol.* 42 (7), 600–607. doi:10.1080/18811248.2004.9726427

Pacio, J., Marocco, L., and Wetzel, T. H. (2015). Review of data and correlations for turbulent forced convective heat transfer of liquid metals in pipes. *Heat. Mass Transf.* 51, 153–164. doi:10.1007/s00231-014-1392-3

Saito, M., Sawada, T., Teraoka, Y., and Nezu, A. (1998). "Dispersion characteristics of gas-liquid two-phase pools," in The 6th International Conference on Nuclear Engineering, May 10-14, 1998. ICONE-6118.

Schlegel, J., Hibiki, T., and Ishii, M. (2010). Development of a comprehensive set of drift-flux constitutive models for pipes of various hydraulic diameters. *Prog. Nucl. Energy* 52, 666–677. doi:10.1016/j.pnucene.2010.03.007

Shen, X., and Hibiki, T. (2020). Distribution parameter and drift velocity for upward gas-liquid metal two-phase flow. *Appl. Therm. Eng.* 184, 116242. doi:10.1016/j.applthermaleng.2020.116242

Shipley, D. G. (1984). Two phase flow in large diameter pipes. *Chem. Eng. Sci.* 39, 163–165. doi:10.1016/0009-2509(84)80143-8

Suzuki, T., Tobita, Y., Kondo, S., Saito, Y., and Mishima, K. (2003). Analysis of gas-liquid metal two-phase flows using a reactor safety analysis code SIMMER-III. *Nucl. Eng. Des.* 220, 207–223. doi:10.1016/s0029-5493(02)00349-7

Zuber, N., and Findlay, J. A. (1965). Average volumetric concentration in two-phase flow systems. *J. Heat Transf.* 87, 453–468. doi:10.1115/1.3689137

Nomenclature

C_0 distribution parameter
C_∞ the asymptotic value of C_0
D diameter of the flow channel (m)
D_h hydraulic diameter (m)
f function in new developed model
Fr Froude numberg
g ggravitational acceleration (9.8 m/s^2)
g_1 function in new developed model about Fr
g_2 function in new developed model about Fr
g_3 function in new developed model about Fr
Ga Galileo number
h function in new developed model about void fraction
j mixture volumetric flux (m/s)
j_g gas superficial velocity(m/s)
j_f liquid superficial velocity(m/s)
l mixing length (m)
N number of data points
N_{μ_f} viscosity number
$N\tau_w$ non-dimensional wall shear stress
p exponent (in Clark's model)
R radius of the flow channel
Re Reynolds number
r radial axis
r' non-dimensional radius
U liquid velocity (m/s)
v_g gas velocity (m/s)
v_{gj} drift velocity of gas phase (m/s)
W_{exp} real liquid average velocity in test case(m/s)
W_f liquid average velocity(m/s)
X velocity in general non-dimensional equation
X_1 fitting coefficient in new developed model
X_2 fitting coefficient in new developed model
X_3 fitting coefficient in new developed model

Subscripts

f liquid-phase
g gas-phase
c center of the tube

Superscripts

+ non-dimensional parameter
* non-dimensional parameter

Greek symbols

α void fraction
ε_{ij} the relative error of the jth correlation when predicting the ith data point
ε_{RMSj} the root-mean-square of the jth correlation
ξj benchmark coefficient
σ surface tension(N/m)
μ dynamic viscosity (Pa·s)
ρ density (kg/m^3)
τ shear stress (N/m^2)
τ_w wall shear stress (N/m^2)

Mathematical symbols

< > area-averaged quantity
<< >> void-fraction weighted mean quantity

frontiers | Frontiers in Energy Research

TYPE Review
PUBLISHED 24 August 2022
DOI 10.3389/fenrg.2022.893048

OPEN ACCESS

EDITED BY
Hitesh Bindra,
Kansas State University, United States

REVIEWED BY
Luteng Zhang,
Chongqing University, China
Laurent Trotignon,
Direction des Energies—IRESNE—CE Cadarache—CEA, France

*CORRESPONDENCE
Songbai Cheng,
chengsb3@mail.sysu.edu.cn

SPECIALTY SECTION
This article was submitted to Nuclear Energy,
a section of the journal
Frontiers in Energy Research

RECEIVED 09 March 2022
ACCEPTED 12 July 2022
PUBLISHED 24 August 2022

CITATION
Xu R and Cheng S (2022), Experimental and numerical investigations into molten-pool sloshing motion for severe accident analysis of sodium-cooled fast reactors: A review.
Front. Energy Res. 10:893048.
doi: 10.3389/fenrg.2022.893048

Experimental and numerical investigations into molten-pool sloshing motion for severe accident analysis of sodium-cooled fast reactors: A review

Ruicong Xu and Songbai Cheng*

Sino-French Institute of Nuclear Engineering and Technology, Sun Yat-Sen University, Zhuhai, Guangdong, China

Safety issues are particularly crucial for sodium-cooled fast reactors (SFRs). Data obtained from SFR safety analyses over recent years have shown that a specific type of sloshing motion probably occurs in the molten pool during core disruptive accidents (CDAs) of SFRs due to local neutronic power excursion or pressure developments, thereby significantly influencing recriticality. Recognizing the importance of improving the evaluation of CDAs of SFRs, extensive knowledge about this phenomenon has been garnered through experimental studies of their thermal-hydraulic mechanism and characteristics. Based on these studies, simulations using various numerical approaches, such as SIMMER code, the finite volume particle method, and the smoothed particle hydrodynamic method, have attempted to reproduce the sloshing motion under various experimental conditions to verify their reasonability and applicability, thereby promoting the development of SFR safety analysis. To provide useful references for future SFR safety analyses and assessments, we have systematically reviewed and summarized these experimental and numerical investigations into the thermal-hydraulic aspect of molten-pool sloshing motion. In addition, to enhance deeper and more comprehensive research into sloshing motion, we have also discussed future prospects. Knowledge gained from experimental and numerical investigations into molten-pool sloshing motion is valuable not only for improving and verifying SFR safety analysis codes but also for providing reference data for studies of sloshing motion in other fields of engineering.

KEYWORDS

experiments, numerical simulations, molten-pool sloshing motion, safety analysis, sodium-cooled fast reactor, review, thermal-hydraulics

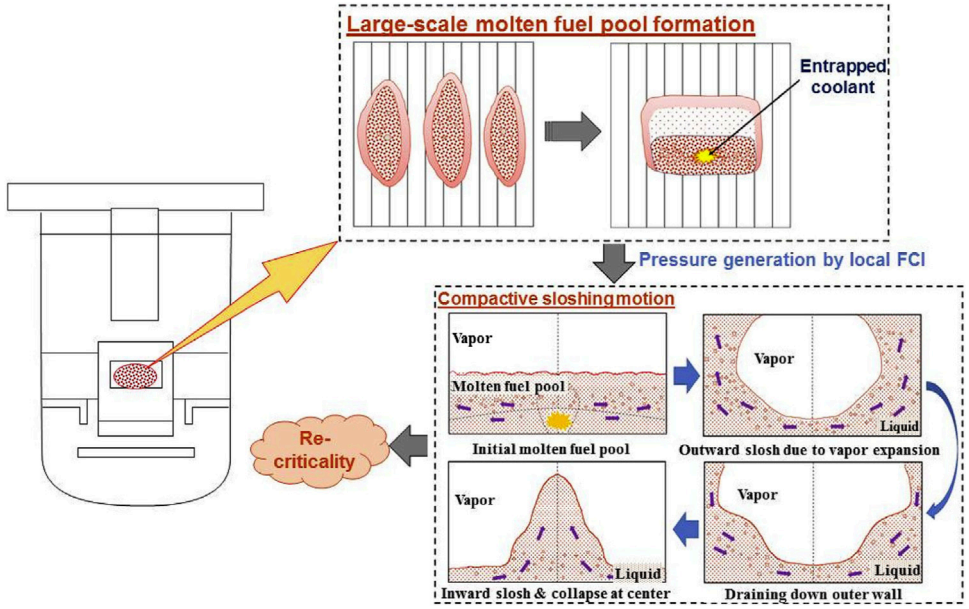

FIGURE 1
Molten pool formation and sloshing motion.

1 Introduction

Sodium-cooled fast reactor (SFRs) are considered to be predominant among Generation IV nuclear reactor systems due to their outstanding breeder characteristics and the considerable experience accrued in their construction and operation (Raj et al., 2015). Nevertheless, for the nuclear power industry, safety is always an important issue for its developments, and SFRs are no exception. Therefore, to accelerate SFR developments and applications, analysis of their safety is crucial, particularly for severe accidents such as core disruptive accidents (CDAs) (Tentner et al., 2010; Ohshima and Kubo, 2016). In the initiation phase of CDA, due to the specific core design of SFRs, the nonenergetic initial power transient could be generally brought by the negative reactivity effect as a result of fuel dispersion with pin disruption, which would be superior to the positive reactivity effects such as void reactivity (Maschek et al., 1992a; Suzuki et al., 2014). In such nonenergetic case, the accident scenario may proceed from the initiating phase to a transition phase (Maschek et al., 1992a; Suzuki et al., 2014; Suzuki et al., 2015). In this phase, due to the melting of the reactor core, a large molten pool at the whole-core scale can be formed, with an adequate molten fuel spatial configuration to exceed prompt criticality (see Figure 1). Within the molten pool, a complex system with multiphase flows is believed to form, including molten fuel, molten structure, refrozen fuel, liquid coolant, fission gas, fuel vapor, solid fuel pellets, and other materials (Liu et al., 2006, 2007; Tentner et al., 2010). Results calculated using SIMMER-II code (a Euler-based code for fast-reactor safety analysis) revealed that in the large molten pool, a specific flow pattern might exist that could trigger the central compacting fluid motions (Bohl, 1979; Maschek et al., 1982; Kondo et al., 1985; Theofanous and Bell, 1986). As shown in Figure 1, during the extension of the molten pool, portions of liquid coolant may be entrapped in the pool, thereby leading to a local fuel–coolant interaction (FCI), which could cause bubble expansion and pressure development, disturbing the stability of the pool by pushing the liquid fuel away from the central core region toward the peripheral regions, then impelling it back to the center through gravity (Maschek et al., 1992a; Yamano et al., 2009; Zhang et al., 2018; Cheng et al., 2019d). Therefore, taking into consideration the sensitivity of SFRs to dimensional variations or core-material relocations, such bubble expansion and subsequent centralized, inward sloshing motion could potentially promote recriticality and lead to an energetic power excursion due to fuel compactions in the molten pool (Theofanous and Bell, 1986; Maschek et al., 1992a; Yamano et al., 2009; Tatewaki et al., 2015). This could lead to the accident progressing to the core expansion phase, thereby threatening the structural stability of the reactor vessel. It should be noted that although the sloshing motion is also of great importance and has attracted great attention in fields other than nuclear energy (e.g., the steel industry, volcanology, Earth sciences, and fluidized beds) (Sakai et al., 1984; Bi, 2007; Hatayama, 2008; Namiki et al., 2016; Thaker

et al., 2020), this review will concentrate on investigations into molten-pool sloshing motion in relation to CDAs of SFRs due to its special pattern and mechanism compared with those seen in other science and engineering fields.

In recent decades, it has become clear that an understanding of molten-pool sloshing motion is very important for the improved evaluation of SFR severe accident scenarios, particularly regarding energetic recriticality. A series of experimental investigations was carried out at Karlsruhe Institute of Technology (KIT), Kyushu University, and Sun Yat-Sen University (SYSU) that considered various conditions, such as dam-break, fluid-step, and gas-injection conditions (Maschek et al., 1992a; Maschek et al., 1992b; Morita et al., 2014; Cheng et al., 2018c; Cheng et al., 2018d; Cheng et al., 2019a; Cheng et al., 2019b; Cheng et al., 2019c; Cheng et al., 2020; Xu et al., 2022). Basic mechanisms (e.g., peripheral pushing of molten fuel and gravitation-induced inward centralized sloshing) and important sloshing characteristics (e.g., the maximal inward and outward sloshing liquid heights) were phenomenologically observed via dam-break and fluid-step experiments (Maschek et al., 1992a; Maschek et al., 1992b), in which the outward and inward sloshing motions were both triggered by gravity. However, it should be pointed out that in an actual scenario of a CDA in an SFR, as the molten pool forms and enlarges (e.g., as a result of the failure of control rod guide tubes), and due to the possibility for a portion of the liquid sodium coolant to be entrapped in it, outward sloshing motion could be initiated by rapid vapor generation and pressure buildup around the central pool region through local FCI (Cheng et al., 2014; Cheng et al., 2015; Zhang et al., 2018). Therefore, it is reasonable to assume that the use of the gas-injection method for simulating vapor expansion can achieve more realistic conditions for the molten-pool sloshing motion triggered by local FCI. Furthermore, the vaporization of fuel or structural materials in cases of large power depositions may also contribute to the sloshing motion. In a preliminary study of molten-pool sloshing motion while taking into consideration thermal-hydraulic or neutronic disturbances, Morita et al. (2014) carried out gas-injection experiments to investigate the overlaying (i.e., mitigating or augmenting) effects of various modes of hydraulic disturbance. Furthermore, aimed at a deeper and more comprehensive understanding of the sloshing motion initiated by local FCI, a series of experimental investigations using the gas-injection method without hydraulic disturbances in pure liquid pools was conducted by Cheng et al. (2018c), to investigate the flow-regime patterns of sloshing motion in more detail. While observing that it is possible to find the co-existence of molten structural materials and fuel under actual accident conditions, Cheng et al. (2020) performed further experimental investigations into sloshing motion in pools with liquid stratification. In addition to experiments in liquid pools without solid phases and considering the fact that, in an actual reactor accident, solid phase materials may be present in the pool as a result of incomplete melting of structural materials and fuel pellets (Liu et al., 2006, 2007), experiments in liquid pools with solid phases (such as solid particles and solid obstacles with rod-shaped structures) have also been performed under dam-break and gas-injection conditions to accumulate valuable knowledge concerning the effects of solid phases on sloshing characteristics (Maschek et al., 1992a; Maschek et al., 1992b; Cheng et al., 2018d; Cheng et al., 2019a; Cheng et al., 2019b; Cheng et al., 2019c; Xu et al., 2022). These previous experimental investigations into sloshing motion are summarized in Figure 2.

In recent decades, however, to better reproduce sloshing motions and thereby improve the assessment of the evolution of severe SFR accidents, in addition to experimental investigations, numerical simulations and validations of molten-pool sloshing motion have been developed and greatly progressed by employing various computational fluid dynamics (CFD) codes and methods. Based on the dam-break and fluid-step experiments performed by Maschek et al. (1992a, 1992b), SIMMER-II, AFDM, and IVA3 codes were used by Munz and Maschek (1992) and Maschek et al. (1992a) to create a preliminary simulation of sloshing motion. Then, to improve the reliability and accuracy of SFR safety analysis, Pigny (2010) and Yamano et al. (2012) employed SIMMER-IV code to perform numerical simulations at the Commissariat à l'Energie Atomique et aux Energies Alternatives (CEA) and the Japan Atomic Energy Agency (JAEA), respectively. It was verified that experimental sloshing characteristics (such as compaction velocities) can be rationally reproduced by SIMMER-IV for both dam-break and fluid-step cases. The applicability of particle methods for simulating sloshing motion was also validated in accordance with dam-break experiments. For instance, the simulation rationality of the finite volume particle (FVP) method was demonstrated by Guo et al. (2010, 2012) at Kyushu University through simulations for dam-break sloshing with/without solid particles. Vorobyev et al. (2010, 2011) and Vorobyev (2012) at KIT, Buruchenko and Crespo (2014) at South Ural State University (SUSU) and University of Vigo (UVigo), and Jo et al. (2019, 2021) at Seoul National University (SNU) confirmed the reliability of simulation results obtained using the smoothed particle hydrodynamic (SPH) method. Furthermore, Morita et al. (2014) carried out SIMMER-III numerical simulations related to gas-injection experiments with hydraulic disturbances. These numerical investigations into sloshing motion are also summarized in Figure 2, where a brief introduction of each simulation code/method is provided.

Understanding and knowledge obtained from experiments and numerical simulations about the mechanisms and characteristics of molten-pool sloshing motion are of great importance for improving the safety evaluations of SFRs (e.g.,

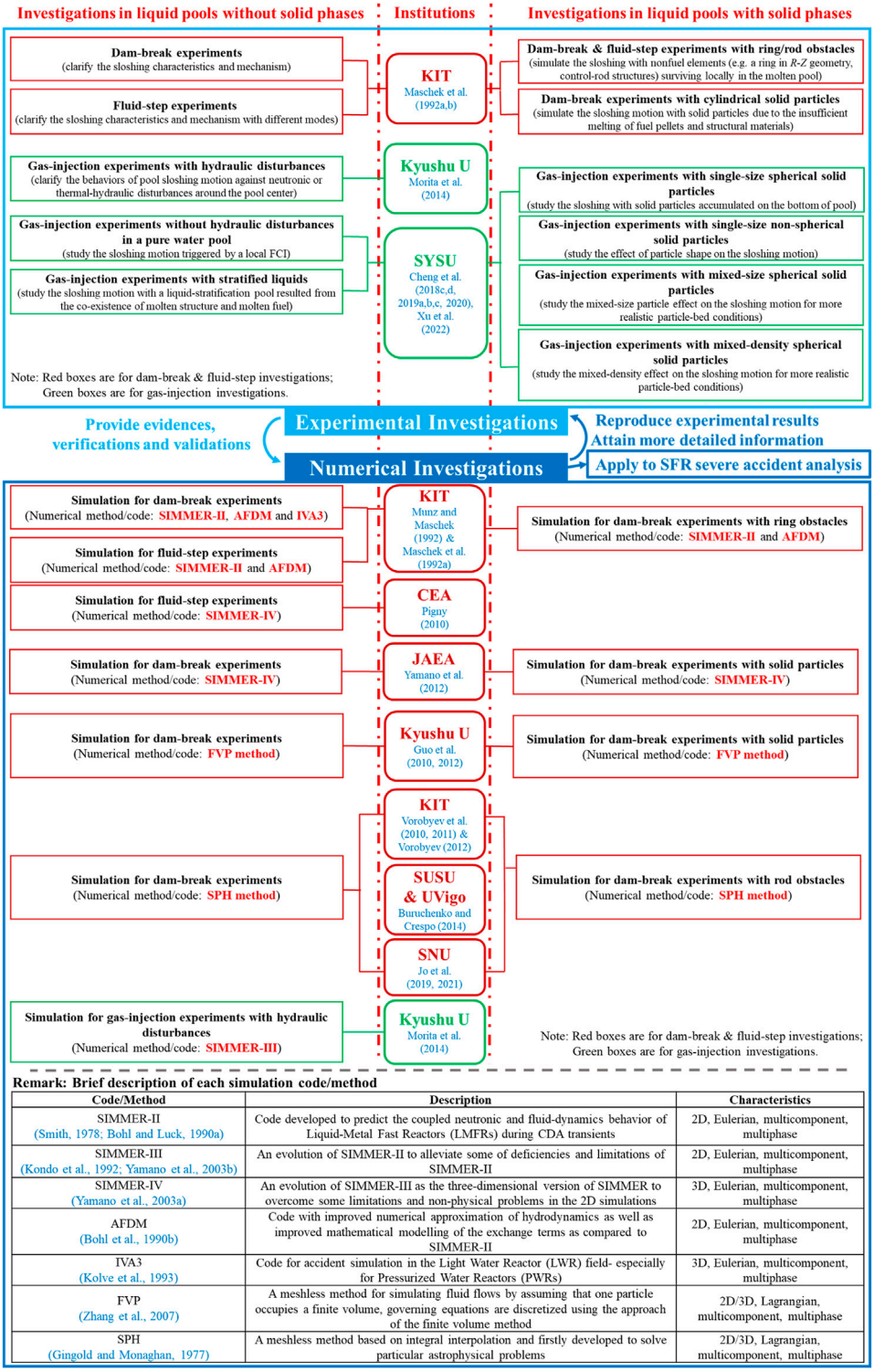

Remark: Brief description of each simulation code/method

Code/Method	Description	Characteristics
SIMMER-II (Smith, 1978; Bohl and Luck, 1990a)	Code developed to predict the coupled neutronic and fluid-dynamics behavior of Liquid-Metal Fast Reactors (LMFRs) during CDA transients	2D, Eulerian, multicomponent, multiphase
SIMMER-III (Kondo et al., 1992; Yamano et al., 2003b)	An evolution of SIMMER-II to alleviate some of deficiencies and limitations of SIMMER-II	2D, Eulerian, multicomponent, multiphase
SIMMER-IV (Yamano et al., 2003a)	An evolution of SIMMER-III as the three-dimensional version of SIMMER to overcome some limitations and non-physical problems in the 2D simulations	3D, Eulerian, multicomponent, multiphase
AFDM (Bohl et al., 1990b)	Code with improved numerical approximation of hydrodynamics as well as improved mathematical modelling of the exchange terms as compared to SIMMER-II	2D, Eulerian, multicomponent, multiphase
IVA3 (Kolve et al., 1993)	Code for accident simulation in the Light Water Reactor (LWR) field- especially for Pressurized Water Reactors (PWRs)	3D, Eulerian, multicomponent, multiphase
FVP (Zhang et al., 2007)	A meshless method for simulating fluid flows by assuming that one particle occupies a finite volume, governing equations are discretized using the approach of the finite volume method	2D/3D, Lagrangian, multicomponent, multiphase
SPH (Gingold and Monaghan, 1977)	A meshless method based on integral interpolation and firstly developed to solve particular astrophysical problems	2D/3D, Lagrangian, multicomponent, multiphase

FIGURE 2
Previous experiments and numerical investigations regarding sloshing motion.

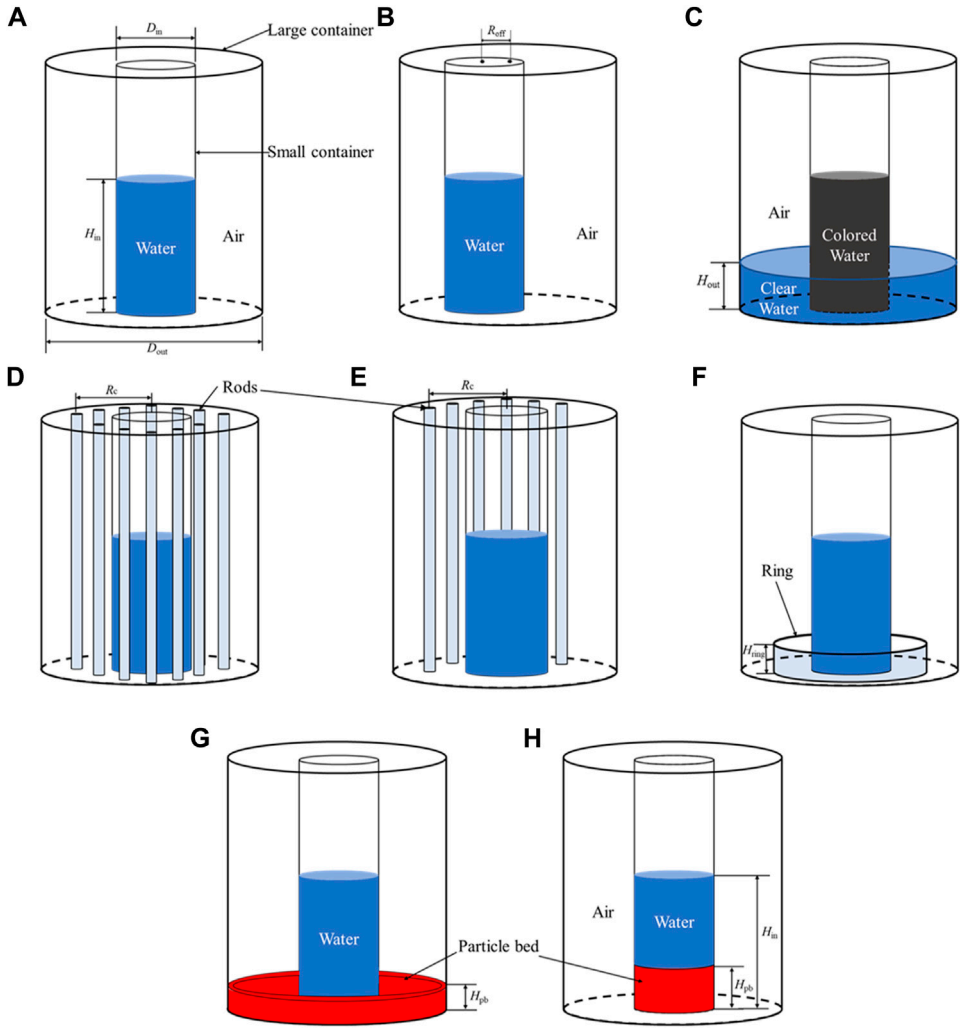

FIGURE 3
Main devices used for dam-break and fluid-step experiments under different conditions (containers that are open at the top). **(A)** Symmetrical dam-break condition. **(B)** Asymmetrical dam-break condition. **(C)** Fluid-step condition. **(D)** Dam-break condition with symmetrically distributed rod-shaped obstacles. **(E)** Dam-break condition with asymmetrically distributed rod-shaped obstacles. **(F)** Dam-break condition with ring-shaped obstacles. **(G)** Dam-break condition with a particle ring. **(H)** Dam-break condition with a central particle bed.

improvement and verification of SFR safety analysis codes with proper neutronic models) and providing reference data for investigations into sloshing motion in other fields of engineering. Considering these aspects, we aimed to carry out a comprehensive systematic review and discussion of previous experiments and numerical simulations of molten-pool sloshing motion in cases of CDAs in SFRs. In Section 2, the experimental and numerical investigations for dam-break and fluid-step sloshing are introduced, while investigations involving gas-injection conditions are discussed and summarized in Section 3. In Section 4, conclusions are described, and some future prospects are discussed to provide a valuable reference and guidance for encouraging deeper and more comprehensive investigations on this topic in the future.

2 Dam-break and fluid-step sloshing motions

2.1 Dam-break and fluid-step sloshing motions in pure liquid pools

2.1.1 Description of experiments

To provide experimental evidence for the numerical analysis of sloshing motion, Maschek et al. (1992a, 1992b) conducted several dam-break and fluid-step sloshing experiments. Figures 3A–C show the main experimental devices, which included two Plexiglas containers of cylindrical shape. For the dam-break and fluid-step experiments, the inner container was filled with water and rapidly pulled up to release this water so that the subsequent

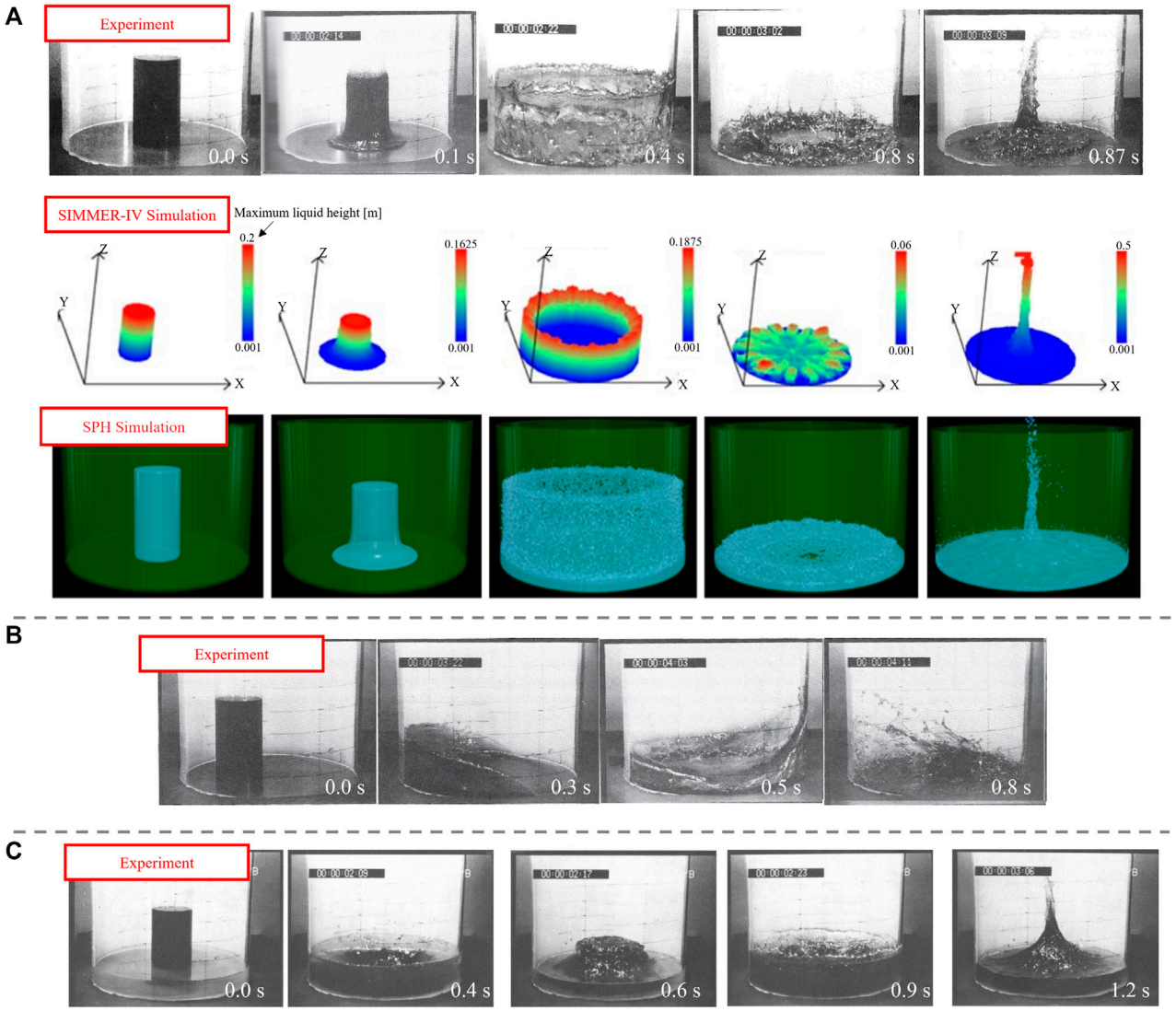

FIGURE 4
Typical dam-break and fluid-step sloshing motion (Maschek et al., 1992b; Yamano et al., 2012; Jo et al., 2021). **(A)** Symmetric dam-break sloshing motion (D_{in} = 11 cm, H_{in} = 20 cm). **(B)** Asymmetric dam-break sloshing motion (D_{in} = 11 cm, H_{in} = 20 cm, off-centeredness = 8.25 cm). **(C)** Fluid-step sloshing motion (D_{in} = 11 cm, H_{out} = 5 cm, H_{in} = 20 cm).

sloshing motion could be initiated through the gravitation. From symmetrical dam-break experiments, it was observed that the liquid would first slosh out toward the peripheral area of the outer container and then slosh inward to pile up in the central region, finally resulting in a central liquid peak (see Figure 4A). It was confirmed that, due to gravity, an inner container of larger diameter (D_{in}) or higher initial water height (H_{in}), which resulted in greater inertia of the liquid, increased the sloshing intensity, as characterized by the maximal water heights of peripheral outward and centralized inward sloshing motion (Maschek et al., 1992b). However, if the sloshing system was asymmetric, not only did the inward sloshing motion become chaotic with no centralized sloshing peak observed but the maximal peripheral sloshing heights were also observably different between the left and right sides due to the different lengths of the propagating liquid waves (see Figure 4B). This difference in peripheral sloshing heights increased when an asymmetric system with greater off-centeredness (R_{off}) was employed.

In addition to dam-break experiments, fluid-step experiments were performed to more comprehensively clarify the sloshing characteristics, by introducing additional liquid of various heights within the outer container (H_{out}) (see Figure 3C) and coloring the inner water to visually distinguish it from the

TABLE 1 Comparison of sloshing characteristics for experiments and numerical simulations under dam-break conditions with water at room temperature (D_{in} = 11 cm) (Maschek et al., 1992a; Maschek et al., 1992b; Munz and Maschek, 1992; Guo et al., 2012; Yamano et al., 2012; Buruchenko and Crespo, 2014; Jo et al., 2021).

Case[a]	H_{in} [cm]	R_{off} [cm]	Outward sloshing motion[b]			Inward sloshing motion[c]	
			Arrival time [s]	Time of max H [s]	Max H [cm]	Time of max H [s]	Max H [cm]
Case 1: Symmetric dam-break							
Experiment 1	20	0	0.20 ± 0.02	0.42 ± 0.02	16 ± 1	0.88 ± 0.04	40 ± 5
SIMMER-II	20	0	0.18	-	9.0	0.62	16.0
AFDM	20	0	0.18	-	13.0	0.61	50.0
SIMMER-IV	20	0	0.19	0.40	15.3	0.89	42.0
SPH	20	0	0.20	0.42	15.5	0.87	41.0
Experiment 2	10	0	0.21 ± 0.02	0.36 ± 0.02	9 ± 1	0.84 ± 0.04	25 ± 5
FVP	10	0	0.20	0.36	13.6	0.88	21.0
Case 2: Asymmetric dam-break							
Experiment	20	8.25	-	0.36 ± 0.02	14 ± 2	0.48 ± 0.02	24 ± 2
SIMMER-IV	20	8.00	-	0.36	17.25	0.48	21.0
FVP	20	8.25	-	0.34	16.0	0.47	23.0
SPH	20	8.25	-	0.36	14.5	0.48	21.5

[a]Although for one specific method (such as the SPH method) many simulations have been carried out for the numerical analysis, in this table the simulation cases were chosen by considering the most accurate simulation results in comparison with experimental data.
[b]For symmetric dam-break cases, outward sloshing motion means the sloshing at the wall of outer container, while for asymmetric ones it means the sloshing at the left wall (the wall closer to the inner container, as shown in Figure 3).
[c]For symmetric dam-break cases, inward sloshing motion represents the sloshing at the pool center, while for asymmetric ones it signifies the sloshing at the right wall (the wall closer to the inner container, as shown in Figure 3).

outer water. As shown in Figure 4C, experimental results showed that the inner colored water pushed the clear, outer water to the peripheries of the outer container after being discharged, before being compressed by the inward sloshing clear water to form a water hump. This would then collapse due to gravity, resulting in a second, outward sloshing motion in the deeper region, subsequently leading to a second inward sloshing motion that extruded a centralized sloshing peak. It was found that a higher H_{out} can lead to more repeats of sloshing as a result of less energy being dissipated in the deeper water region (Maschek et al., 1992b). Furthermore, a similar effect of a liquid's inertia on the enhancement of sloshing intensity was observed in experiments conducted under fluid-step conditions.

Briefly, based on the dam-break and fluid-step sloshing experiments using pure liquid pools, it was concluded that the symmetricity and the overall inertia of the liquid in a sloshing system noticeably affects the characteristics of the sloshing motion.

2.1.2 Numerical simulations

To reproduce the symmetric dam-break and fluid-step sloshing motions, three CFD codes, SIMMER-II (Smith, 1978; Bohl and Luck, 1990), AFDM (advanced fluid-dynamics model) (Bohl et al., 1990), and IVA3 (Kolev, 1993), were examined first (Munz and Maschek, 1992). However, although the basic sloshing process could be rationally reproduced, relatively inaccurate results were obtained, especially for the methods with a first-order differencing scheme (i.e., SIMMER-II and IVA3). With developments in computing science and technology, in recent years a SIMMER-IV code with a higher-order differencing scheme (Yamano et al., 2003a), the FVP method (Zhang et al., 2007), and the SPH method (Gingold and Monaghan, 1977) were used to simulate dam-break sloshing and obtain more accurate simulation results (Guo et al., 2010, 2012; Vorobyev et al., 2010; 2011; Vorobyev, 2012; Yamano et al., 2012; Buruchenko and Crespo, 2014; Jo et al., 2019, Jo et al., 2021). The SIMMER-IV code was also used in an attempt to simulate fluid-step sloshing motion (Pigny, 2010). Tables 1 and 2 summarize the results of simulated sloshing characteristics using different numerical methods for dam-break and fluid-step cases, respectively.

Simulation snapshots for the SIMMER-IV and SPH methods under dam-break conditions are shown in Figure 4A. It can be seen from these figures that the sloshing motion could be rationally reproduced by the simulations. The simulation results shown in Tables 1 and 2 further validate the

TABLE 2 Comparison of sloshing characteristics for experiments and numerical simulations under fluid-step conditions (D_{in} = 11 cm, H_{in} = 20 cm, H_{out} = 5 cm) (Maschek et al., 1992a; Maschek et al., 1992b; Pigny, 2010).

Case	Outward sloshing motion		Inward sloshing motion			
	Time of max H [s]	Max H [cm]	Time of first max H [s]	First max H [cm]	Time of second max H [s]	Second max H [cm]
Experiment	0.36 ± 0.02	11 ± 1	0.62 ± 0.04	15 ± 3	1.24 ± 0.04	22 ± 2
SIMMER-II	-	16.0	-	-	-	18.0
AFDM	-	12.0	-	-	-	28.0
SIMMER-IV	0.34	11.5	0.61	16.0	1.22	22.0

simulation accuracy of SIMMER-IV, SPH, and FVP. According to simulations performed by Yamano et al. (2012) using the SIMMER-IV code, it was found that the sloshing characteristics could be better simulated by using 3D R-θ-Z geometry (see the data in Table 1), while the centralized maximal height of sloshing and its time were both overestimated in 2D R-θ-Z simulations due to the larger momentum of inward sloshing liquid resulting from the lack of circumferential energy dissipation. On the other hand, compared with simulations with X-Y-Z geometry, the R-θ-Z simulations can effectively avoid the non-smooth curved boundary of liquid when sloshing outward (Yamano et al., 2012), thereby providing more reliable results for maximal sloshing heights. Nevertheless, irrespective of the simulation geometry, SIMMER-IV can generally provide reliable simulation results regarding the times of maximum heights, which represent that the compaction velocities determine significantly the ramp rates in CDA of SFR.

For simulations using particle methods (i.e., SPH and FVP methods), more information about the flow shape and fragmentation of the liquid was obtained (see Figure 4A). In addition, it was confirmed that simulations with a higher resolution showed greater agreement with experimental results; this is because lower resolution would generally lead to a lower particle number density for inward sloshing motion, causing a diminished bulk flow of liquid piling up motion, thereby underestimating the centralized sloshing height (Guo et al., 2010, 2012; Vorobyev, 2012; Buruchenko and Crespo, 2014; Jo et al., 2019; Jo et al., 2021). Furthermore, by referring to Richardson's extrapolation and the grid convergence index (GCI) (Roache, 1972, Roache, 1998), it was found that as the resolution increased (i.e., a larger particle number (N_p) was applied in calculations), the maximal centralized sloshing height tended to increase and converge to a maximal value close to the experimental data when the particle number became infinite, indicating the necessity of sufficient resolution for accurately reproducing sloshing motion (Jo et al., 2021). The FVP simulations conducted by Guo et al. (2010, 2012)showed that the choice of cut-off radius, which is a defined length characterizing the range of influence of each particle in a simulation, seemed to only have a slight impact on the simulation results. Additionally, it was determined that simulations that considered air particles (i.e., two-phase simulations) showed the best agreement with experiments due to the prevention of local numerical errors from particle deficiency in the free surface area, especially for the centralized sloshing peak (Jo et al., 2021). Through two-phase SPH simulations, it was found that gas might be entrapped in the water during the centralized sloshing motion, revealing the possibility of pressure buildup resulting from vapor trapped during the sloshing motion. Overall, more accurate simulation results were obtained using the SPH method.

2.2 Dam-break and fluid-step sloshing motions with solid obstacles

2.2.1 Description of experiments

To study the influence of the presence of solid obstacles (due to the possible incomplete melting of structural materials) on the sloshing motion, two types of obstacles, namely, rod- and ring-shaped obstacles, were employed. In the case of rod-shaped obstacles, as shown in Figures 3D,E, symmetrical (12 rods) and asymmetrical (half-symmetrical, 6 rods) distributions of rods around the inner column were considered, with varying distances from the centers of the rods to the center of the container, while the diameter of the rods was geometrically scaled down based on their blockage ratio (Maschek et al., 1992a; Maschek et al., 1992b). Figure 5B shows the sloshing motions seen in some typical cases with rod-shaped obstacles. It was found that the rod-shaped obstacles had no significant impact on the outward sloshing characteristics, but greatly dampened the inward sloshing (see Figures 4A, 5B, and compare the data with those of experiment 1 shown in Table 1 and experiments 1 and 2 shown in Table 3). This is because rod-shaped structures may impact on the inward centralized sloshing intensity to augment the inherent unsteadiness of the converging liquid waves moving inward. Such a dampening impact on inward sloshing intensity was

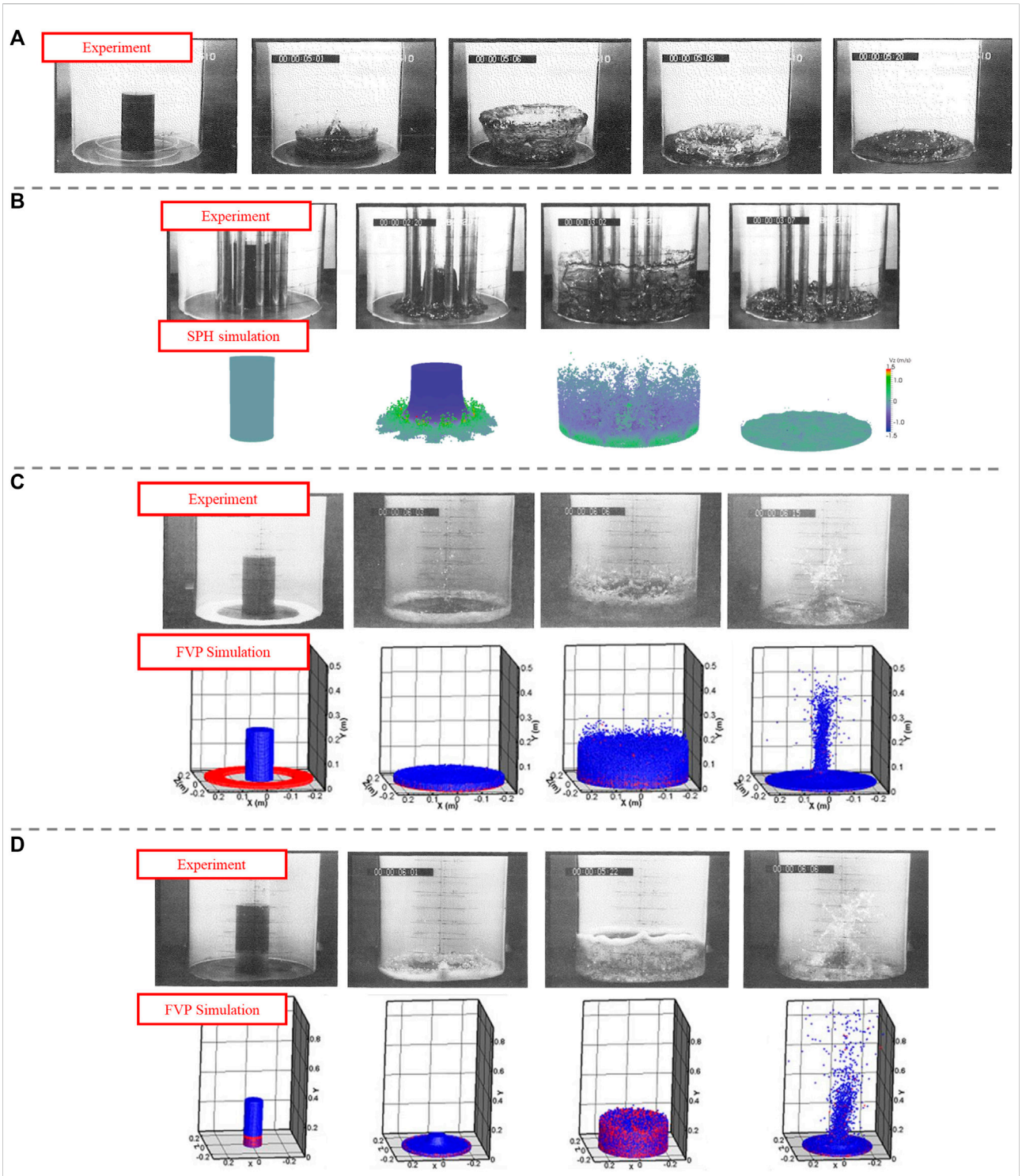

FIGURE 5
Typical dam-break and fluid-step sloshing motion with solid obstacles/particles (Maschek et al., 1992b; Guo et al., 2012; Vorobyev, 2012). **(A)** Dam-break experiment with ring-shaped obstacles (D_{in} = 11 cm, H_{in} = 20 cm, H_{ring} = 3 cm). **(B)** Dam-break experiment and simulation with symmetrically distributed rod-shaped obstacles (R_c = 9.9 cm, D_{in} = 11 cm, H_{in} = 20 cm) (for the simulation case, rods are hidden in the snapshots to allow better visualization). **(C)** Particle-ring dam-break experiment and simulation (H_{pb} = 1 cm, D_{in} = 11 cm, H_{in} = 20 cm). **(D)** Central-particle dam-break experiment and simulation (H_{pb} = 7 cm, D_{in} = 11 cm, H_{in} = 23 cm).

TABLE 3 Comparison of sloshing characteristics for dam-break experiments and numerical simulations with solid obstacles (D_{in} = 11 cm, H_{in} = 20 cm) (Maschek et al., 1992a; Maschek et al., 1992b; Munz and Maschek, 1992; Vorobyev et al., 2011; Vorobyev, 2012).

Case	R_c [cm]	H_{ring} [cm]	Outward sloshing motion[a]			Inward sloshing motion	
			Arrival time [s]	Time of max H [s]	Max H [cm]	Time of max H [s]	Max H [cm]
Case 1: Symmetrical distribution, rod-shaped obstacles							
Experiment 1	9.9	0	0.22 ± 0.02	0.44 ± 0.02	15 ± 1	0.90 ± 0.04	3 ± 2
SPH (without extra wall friction)	9.9	0	0.19	0.39	18.5	0.78	4.5
SPH (with extra wall friction)	9.9	0	0.19	0.38	15.5	0.78	5.0
Experiment 2	17.6	0	0.20 ± 0.02	0.42 ± 0.02	15 ± 1	0.88 ± 0.04	15 ± 3
SPH (without extra wall friction)	17.6	0	0.20	0.42	21.0	0.82	17.0
SPH (with extra wall friction)	17.6	0	0.20	0.41	18.5	0.84	15.5
Case 2: Ring-shaped obstacles							
Experiment	0	3	-	0.32 ± 0.02	14 ± 1 0.60 ± 0.06	5 ± 3	
SIMMER-II	0	3	-	-	- -	13.0	
AFDM	0	3	-	-	- -	10.0	

[a]For cases of ring-shaped obstacles, the data for outward sloshing motion was recorded for the upward deflection of the ring-shaped obstacles, as indicated in the third photo of Figure 5A.

restrained to some degree when a longer R_c (i.e., greater distance between the rods and the center) or asymmetrical distribution of rods was employed. For fluid-step cases, the effect of rod-shaped obstacles restricting inward sloshing motion seemed to be less evident. This is because in general, based on fluid-dynamics theory (Stoker, 1957), in such an oscillating sloshing system, most of the damping is relevant to the surface waves, and the kinetic energy is mostly stored in these wave packages. Therefore, compared with the dam-break cases, there was less energy dissipation in such oscillating sloshing systems with interactions between surface waves and deepwater waves (Maschek et al., 1992b).

For the experiments using ring-shaped obstacles, as shown in Figures 3A,G, Plexiglas rings of a specific height (H_{ring} = 2 or 3 cm) were placed at the bottom of the pool between the outer container and the inner liquid column. As can be seen from the dam-break sloshing motion with ring-shaped obstacles that is shown in Figure 5A, due to deflection by the ring-shaped obstacles, a bowl-type liquid structure formed first during the outward sloshing motion, and the intensity of the outward sloshing at the peripheral area of the outer container and the inward sloshing at the pool center was observably diminished. Similarly, the diminishing effect of ring-shaped obstacles on sloshing intensity could also be seen in fluid-step experiments. In summary, the dampening influence of solid obstacles on the intensity of pool sloshing motion was confirmed, suggesting it might be difficult to achieve an intensive, centralized sloshing motion in cases where solid obstacles were present in a molten pool under accident conditions.

2.2.2 Numerical simulations

To simulate sloshing motions in the presence of solid obstacles, the SIMMER-II, AFDM, and SPH methods were employed. As shown in Figure 5B, the dam-break sloshing motion with symmetrically distributed rod-shaped obstacles was rationally reproduced by the SPH method, and the dampening effect of these obstacles could be well described by SPH simulations (Vorobyev et al., 2010; Vorobyev et al., 2011; Vorobyev, 2012; Buruchenko and Crespo, 2014; Jo et al., 2019; Jo et al., 2021). In particular, Vorobyev et al. (2011) found that the effect of wall friction caused by rod-shaped obstacles, which is related to momentum dissipation, played an essential role in the sloshing motions. Generally, as shown in Table 3, underestimating the wall friction would lead to an overestimate of sloshing intensity. On the other hand, Munz and Maschek (1992) determined that SIMMER-II and AFDM can provide reasonable phenomenological simulations of dam-break sloshing motions with ring-shaped obstacles. Nevertheless, an obvious overestimate of sloshing intensity (e.g., maximal sloshing height) was observed (see Table 3), which may have been due to the 2D simulation conditions, although the dampening impact of ring-shaped obstacles on the centralized

TABLE 4 Comparison of sloshing characteristics for dam-break experiments and numerical simulations with solid particles (D_{in} = 11 cm) (Maschek et al., 1992b; Guo et al., 2012; Yamano et al., 2012).

Case	H_{pb} [cm]	H_{in} [cm]	Outward sloshing motion			Inward sloshing motion	
			Arrival time [s]	Time of max H [s]	Max H[a] [cm]	Time of max H [s]	Max H [cm]
Case 1: Particle-ring condition							
Experiment 1	1	20	0.28 ± 0.02	0.40 ± 0.02	10/8 ± 1	0.80 ± 0.04	25 ± 5
SIMMER-IV (without a momentum diffusion term)	1	20	0.21	0.36	11/11	0.82	32
SIMMER-IV (without a particle viscosity model)	1	20	0.21	0.35	10/10	0.83	36
SIMMER-IV (with a momentum diffusion term and particle viscosity model)	1	20	0.21	0.36	10.5/10.5	0.82	27
FVP	1	20	0.22	0.38	14/3	0.85	38
Case 2: Central particle condition							
Experiment	7	23	0.24 ± 0.02	0.40 ± 0.02	15.0 ± 1	0.84 ± 0.04	30 ± 8
FVP	7	23	0.20	0.41	19	0.92	65

[a]In this column, the maximal sloshing heights shown in the case of particle-ring conditions were identified for liquid and solid particles, respectively (e.g., 10/8 means the maximal sloshing height for liquid was 10 cm, while for solid particles it was 8 cm).

sloshing intensity could be effectively reproduced through comparison with the simulation results for dam-break sloshing motions in pure liquid pools.

2.3 Dam-break sloshing motions with one-sized cylindrical solid particles

2.3.1 Description of experiments

To investigate the influence of solid particles dispersed in the liquid pool, Maschek et al. (1992a, 1992b) carried out several dam-break experiments using cylindrical acrylic particles (ρ_p = 1130 kg/m^3) of height and diameter 3 and 2.5 mm, respectively, to form particle beds with a porosity of 40% (see Figure 3H). In the experiments, two types of initial particle location conditions (namely, particle-ring and central particle conditions) were applied. For the particle-ring experiments, a particle bed with a height (H_{pb}) of 1 or 2 cm was initially located in a ring, of which the inner diameter was 29 cm and the outer diameter was the same as D_{out}. As for the central particle experiments, a particle bed with a height of 7 or 22 cm was located on the bottom of the inner container. Figures 5C,D show the typical dam-break-sloshing motions under particle-ring and central particle conditions, respectively. According to Figure 5C, it can be observed that in case of particle-ring conditions, the released liquid would first push the particles outward and then slosh inward together with the particles to form an asymmetric multiphase centralized peak, which involved gas, liquid, and solid particles, thereby destroying the coherent sloshing motion and weakening the intensity of inward sloshing. Similarly, asymmetric multiphase centralized sloshing motion occurred in the central-particle experiments using a particle bed with a low height (7 cm), so that the inward sloshing intensity was diminished (see Figure 5D). However, it was found that if the particles dominated the pool (e.g., if the inner column was composed of water and a particle bed of the same height), the multiphase flow would slosh outward but no inward sloshing motion could be observed (Maschek et al., 1992b), indicating the complete dampening of centralized sloshing motion. Hence, based on these findings, it can be concluded that greater particulate domination plays a crucial role in diminishing the intensity of sloshing.

2.3.2 Numerical simulations

Regarding the simulations for dam-break sloshing motions involving solid particles, SIMMER-IV (for particle-ring cases) and FVP (for both particle-ring and central particle cases) were applied (Guo et al., 2012; Yamano et al., 2012). For the Eulerian-based SIMMER-IV code, the solid particles were represented by the volume fraction with a porosity of 40%, and their size was specified so that the same volume-equivalent diameter could be ensured in accordance with that of the particles used in the experiments. However, for this reason, the differences in the maximum sloshing height between solid particles and liquid were not identified. From the SIMMER-IV

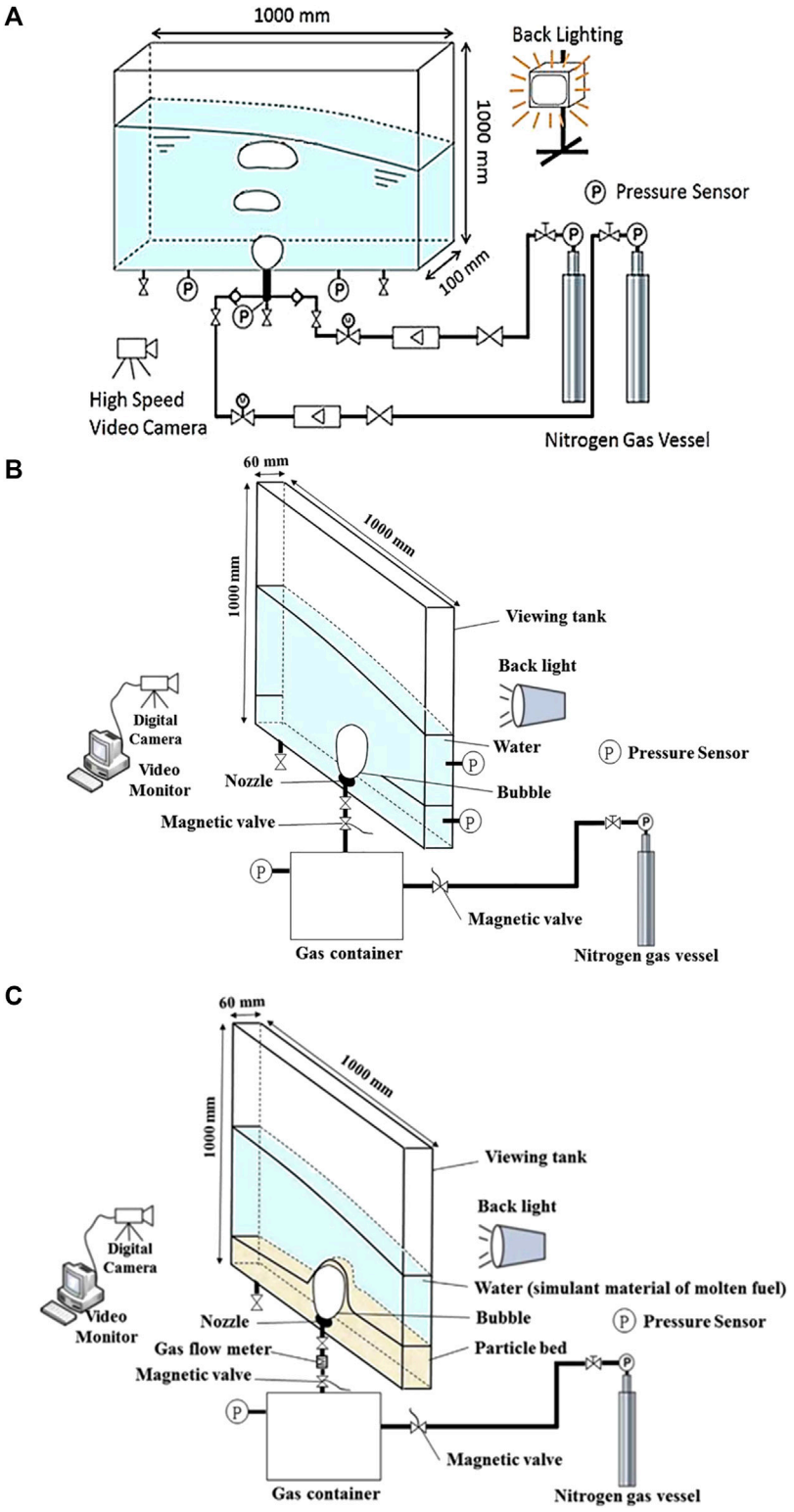

FIGURE 6
Experimental system for gas-injection experiments in liquid pools (Morita et al., 2014; Cheng et al., 2018c; Cheng et al., 2019b). **(A)** Pure liquid pool with hydraulic disturbances. **(B)** Pure liquid pool without hydraulic disturbances. **(C)** Liquid pool without hydraulic disturbances and with a solid particle bed.

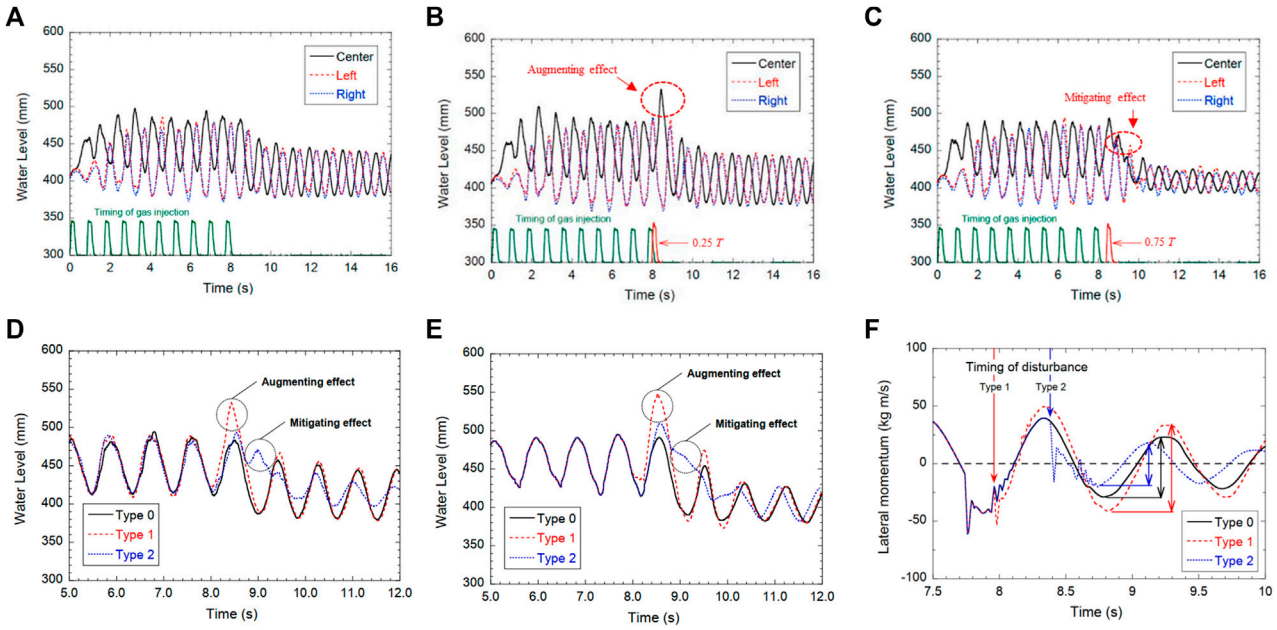

FIGURE 7
Water-level variations indifferent areas of the pool for gas-injection conditions with hydraulic disturbances (Morita et al., 2014). **(A)** Type 0 experiments: no disturbance. **(B)** Type 1 experiments: disturbance at 0.25 *T* (7.955 s). **(C)** Type 2 experiments: disturbance at 0.75 *T* (8.385 s). **(D)** Central water-level variations in experiments. **(E)** Central water-level variations in simulations. **(F)** Lateral momentum variations in simulations (a negative lateral momentum means an overall outward sloshing motion of liquid, while a positive one means an overall centralized inward sloshing motion of liquid).

simulations, the necessity for implementing the particle viscosity model and the momentum diffusion term in the momentum conservation equation (utilized to model the increase in fluid viscosity following the increment of particle volume fraction) was validated, so that the effect of solid particles on sloshing motions can be better reproduced (Yamano et al., 2012). As shown in Table 4, it was found that if the momentum diffusion term and the particle viscosity model were not involved in the calculations, the centralized sloshing intensity would be significantly overestimated due to the larger compaction of the multiphase sloshing mixture. On the other hand, although the sloshing motion could be qualitatively reproduced in the FVP simulations (see Figures 5C,D), it should be highlighted that, as shown in Table 4, the sloshing intensity was overestimated by FVP, which was probably due to the lack of models for the interaction of solid particles (Guo et al., 2012). In short, the lack of consideration of multiphase interactions, which may induce momentum and energy dissipation, seems to lead to the overestimation of sloshing intensity. Therefore, to better reproduce the experimental sloshing motion and achieve more accurate calculations under actual reactor conditions, multiphase interactions should be modeled more appropriately.

3 Sloshing motion under gas-injection conditions

3.1 Gas-injection sloshing motion with hydraulic disturbances in pure liquid pools

3.1.1 Description of experiments

Aimed at preliminarily studying the effect of thermal-hydraulic or neutronic disturbances on sloshing motions, Morita et al. (2014) conducted several experiments that involved introducing hydraulic disturbances by injecting nitrogen gas into a 2D water pool. Figure 6A shows the experimental devices. Before each experiment, the water level and the nitrogen gas pressure and flow rate were initially set at 400 mm, 56 kPa, and 230 L/min, respectively. In the experiments, gas was injected into the pool within 0.2 s through a square nozzle with a side length of 10 cm located at the bottom of the tank. This was performed 10 times with a fixed period (*T*) of 0.86 s. Then, additional gas at a similar flow rate and pressure (230 L/min and 56 kPa, respectively) was injected at different times (0.25 *T* or 0.75 *T*) after the 10 periodic injections, to induce hydraulic disturbances in the liquid pool.

Figures 7A–C compare the central and peripheral water-level variations in cases under different types of disturbance in the

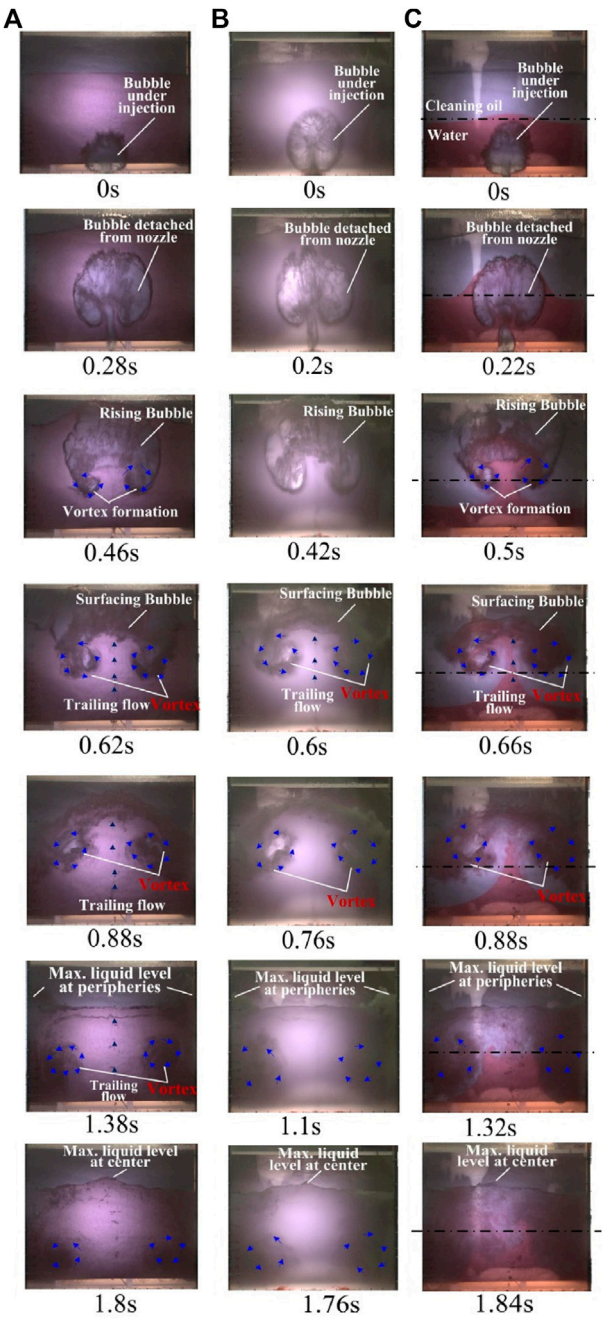

FIGURE 8
Typical sloshing motions in gas-injection experiments without disturbances (ΔT = 0.1 s, p = 4 bar) (Cheng et al., 2020). **(A)** Pure water pool (H_w = 60 cm, H_o = 0 cm). **(B)** Pure cleaning oil pool (H_w = 0 cm, H_o = 60 cm). **(C)** Stratified liquid pool (H_w = 30 cm, H_o = 30 cm).

experiments. It can be seen that the sloshing motion without disturbances (see Figure 7A) is relatively stationary, while observable variations in the water level can be seen after external disturbances were introduced (see Figures 7B,C). In more detail, it can be seen that the disturbance in Type 1 (see Figure 7B) would strengthen (augment) the sloshing motion but in Type 2 (Figure 7C) the sloshing intensity was weakened (mitigated). This was because in Type 1, the gas was injected at the moment when liquid sloshed out toward the wall, then the reflected inward sloshing liquid moved to the central area and joined with the upward gas, which subsequently detached from the liquid and enhanced (augmented) the outward sloshing motion to the peripheral areas (Morita et al., 2014). For Type 2, on the other hand, after being injected the gas reached the liquid surface at the moment when the outward sloshing motion occurred. As a result, the subsequent inward sloshing liquid wave interacted with the wave resulting from the gas detaching from the liquid, leading to a dampened (mitigated) sloshing motion. According to these typical cases of sloshing motion with hydraulic disturbances, the overlaying (namely augmenting or mitigating) effect resulting from interactions between local liquid flows was identified.

To sum up, although the thermal-hydraulic or neutronic disturbances resulting from local expansion in the molten pool could not be comprehensively represented through the introduced external disturbances triggered by injected gas in the experiments (e.g., the reactivity insertion resulted from the fuel compaction caused by the sloshing motion), it was confirmed that the timing of any external disturbances that were introduced would determine the (mitigating or augmenting) effects on the sloshing intensity.

3.1.2 Numerical simulations

Aiming to provide a deeper understanding of the effect of external disturbances, Morita et al. (2014) applied SIMMER-III codes to perform further analyses. The reliability of SIMMER-III for simulating sloshing motion initiated by injected gas with hydraulic disturbances was validated through comparisons with experimental water-level variations for different types of disturbance. The augmenting and mitigating effects were reasonably simulated as observed in the experiments (see Figures 7D,E). To more comprehensively investigate the characteristics of the entire sloshing system, the lateral liquid momentum was focused on, which was equal to the sum of the products of liquid velocity and liquid mass of all mesh cells (Morita et al., 2014). As shown in Figure 7F, there was generally good agreement between water-level and lateral momentum variations. In addition, Figure 7F shows that the introduction of external disturbances could augment the outward sloshing motion but mitigate the inward sloshing motion. This may indicate that the occurrence of augmented or mitigated sloshing motion following the introduction of an external disturbance could depend on the type of sloshing motion (i.e., outward or inward) at the timing of the disturbance, although further investigations are required to clarify this (e.g., Fourier analysis of signals collected from

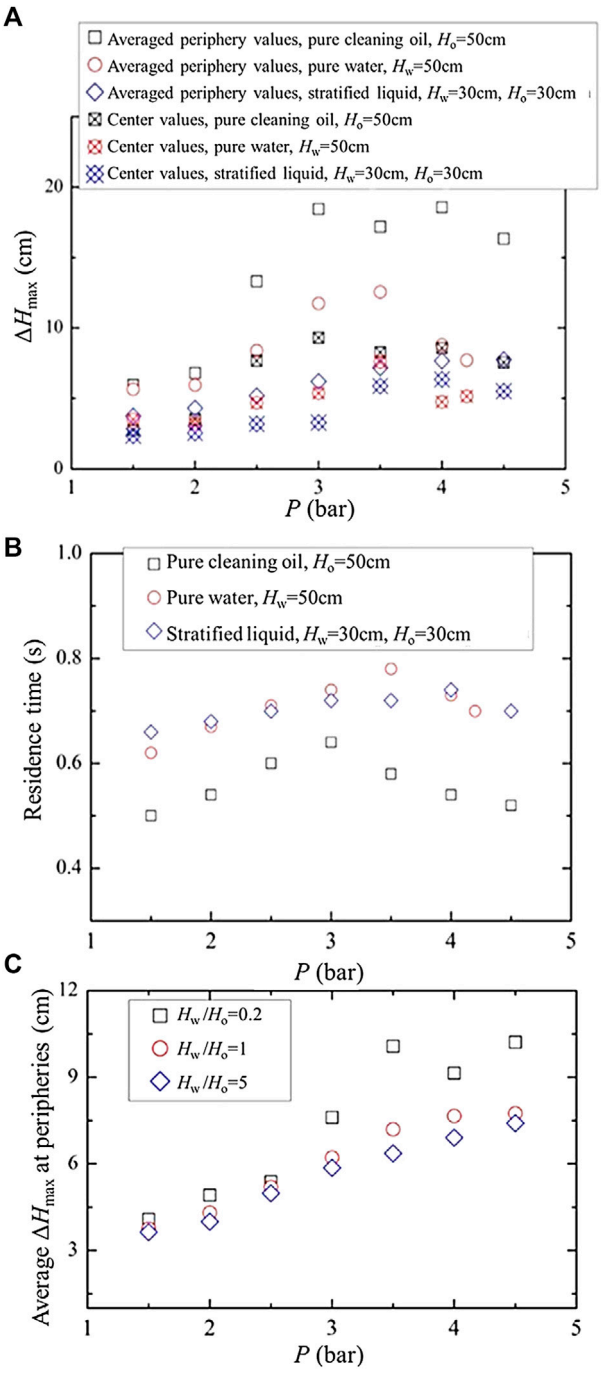

FIGURE 9
Influence of injected gas pressure on sloshing intensity (D_n = 50 mm, ΔT = 0.1 s) (Cheng et al., 2020). **(A)** Maximal liquid sloshing height. **(B)** Residence time. **(C)** Peripheral ΔH_{max} for stratified liquid (H_{pool} = 60 cm).

experiments along with an evaluation of the impulse of a single bubble to obtain fundamental quantities of the oscillator for such a quasi "forced oscillating system"). In addition, further studies that consider neutronic feedback are necessary to rationally evaluate the energetic potential of the molten pool and elucidate the sloshing motions in response to neutronic or thermal-hydraulic disturbances.

3.2 Gas-injection sloshing motion without hydraulic disturbances in liquid pools

Focusing on the sloshing motions induced by local FCI, extensive experiments without hydraulic disturbances were conducted by Cheng et al. (2018c, 2020), who injected nitrogen gas into narrow 2D liquid pools (including pure and stratified liquid pools) to obtain better visualization (see Figure 6B). To simulate the co-existence of molten fuel and molten stainless steel, the stratified liquid was composed of transparent oil and colored water, which possessed comparable density and viscosity ratios to those expected to be crucial parameters affecting sloshing characteristics (Fauske and Koyama, 2002; Cheng et al., 2020). Various parameters, such as the pressure of injected gas (P, 1.5–4.5 bar), the duration of gas injection (ΔT, 0.06–0.1 s), nozzle size (D_n, 10–50 mm), and initial liquid (water or cleaning oil) depth (H_w or H_o, 10–60 cm), were investigated in experiments to comprehensively study the parametric effect on the sloshing motion. Typically, the gas-injection durations were set with consideration of the durations of vapor expansion triggered by local FCIs, according to past investigations of FCIs (Cheng et al., 2014; Cheng et al., 2015; Zhang et al., 2018; Cheng et al., 2019d).

The transient sloshing motions under gas-injection conditions without disturbances are shown in Figure 8. From Figures 8A,B, it can be seen that the shape of the injected gas bubble initially had a concave lower surface following its detachment from the pool bottom, indicating a relatively higher (lower) pressure inside the bubble in comparison with the liquid static pressure at its upper (lower) surface. As the gas bubble rose up, probably due to this difference in pressure, two symmetric vortices with an upward trailing flow, as well as the continuous enlargement and geometrical elongation of the bubble, were observed. When the bubble arrived at the liquid surface, it tended to break up immediately, possibly as a result of the huge difference in pressure between the static water pressure at its base and the atmospheric pressure. Due to this rapid bubble bursting, the two symmetric vortices accelerated and moved to the peripheral areas, simultaneously impelling the central liquid out toward the peripheral areas. After that, the liquid was pushed back to the center of the pool under the gravitational effect and formed a centralized sloshing peak.

The sloshing flow-regime characteristics described above were found to be common for various experimental cases, but a comparatively larger bubble was observed in cases of lower liquid density (see Figures 8A,B). Nevertheless, compared with the cases with pure liquid pools, in the cases of pools with stratified liquid it was seen that during the process of the

FIGURE 10
Typical sloshing motion under gas-injection conditions with solid particles (spherical glass particles, ΔT = 0.1 s) (Cheng et al., 2019b). **(A)** Regime I (d_p = 0.125 mm, H_{pb} = 15 cm, p = 3 bar). **(B)** Regime II (d_p = 0.5 mm, H_{pb} = 15 cm, p = 3 bar). **(C)** Regime II (d_p = 0.5 mm, H_{pb} = 30 cm, p = 3 bar). **(D)** Regime II (d_p = 0.5 mm, H_{pb} = 30 cm, p = 2 bar). **(E)** Regime III (d_p = 6 mm, H_{pb} = 15 cm, p = 3 bar).

bubble rising upwards, much water was entrained upward by the two vortices along with the upward trailing flow and subsequently diluted the upper cleaning oil region (see Figure 8C). Although a centralized water peak emerged due to the entraining effect of the bubble (see the photo at 0.88 s in Figure 8C), recognizing the thinned colored region near the peak, it should be pointed out that the compaction of water in such situations was very limited. This is because compared with the initial depth of water, the vertical location of water peak was not obviously elevated, and was even lower than the initial water depth for some specific cases (Cheng et al., 2020). It was also verified that, in addition to the injected gas pressure, the ratio of the depth of the different liquids (H_w/H_o) played a prominent role in the abovementioned water entrainments (Cheng et al., 2020). For instance, in cases of a lower depth ratio (i.e., more oil and less water), the water region could remain more static under the influence of the weakened entrainment effect resulting from the greater distances from the water region to the upper surface of the liquid (Cheng et al., 2020). For cases with a greater water depth and a lower oil depth, although the entrainment effect caused by the generated vortices was strengthened, a large majority of the water was diluted and redistributed. Therefore, the above analysis reveals that if liquid stratification occurs under real accidental conditions in a reactor (i.e., a layer of molten structural materials covers the upper surface of molten fuel), regardless of the depth ratio, the fuel compaction may be generally diminished.

For the quantitative analyses of parametric effects, Figure 9A shows the influence of injected gas pressure on the peak height of the liquid level (ΔH_{max}) in the central and peripheral areas of the

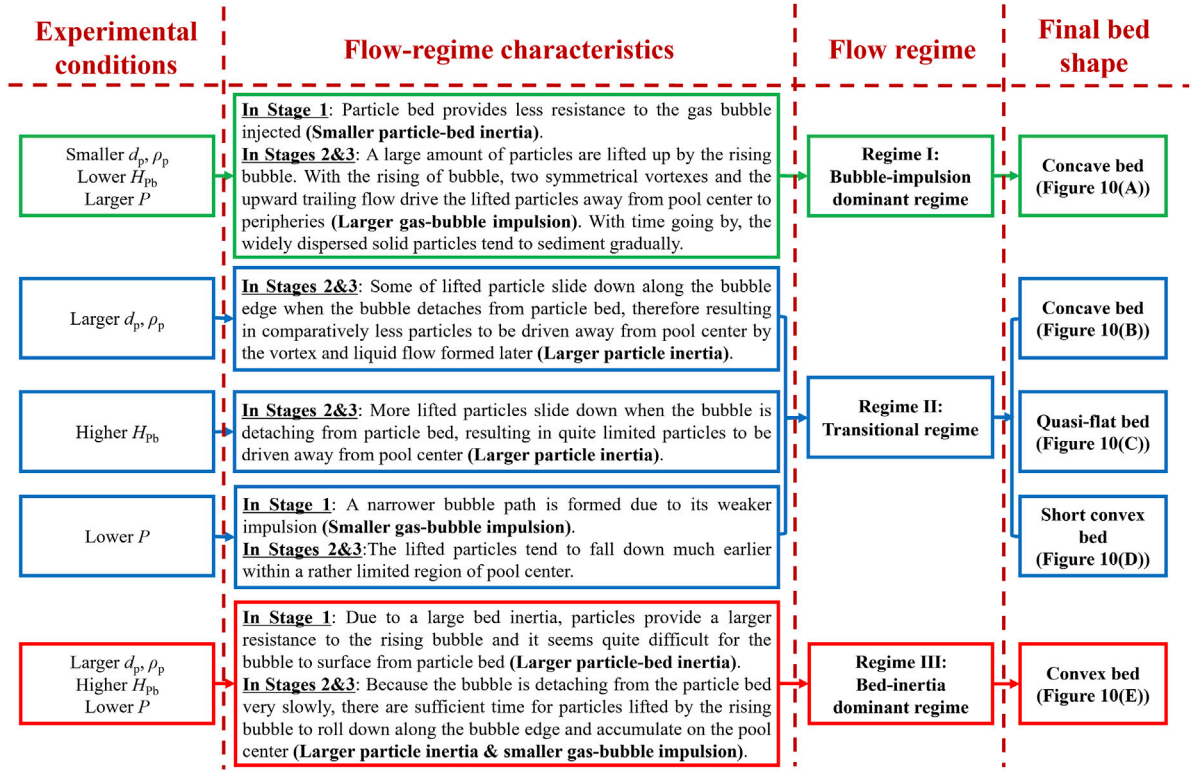

FIGURE 11
Illustrations for different flow-regime characteristics under different experimental conditions.

pool. From this figure, it can be observed that with increasing gas pressure, the sloshing intensity at the center and peripheral areas increased until a critical pressure was reached (i.e., approximately 3.5, 3, and 4 bar for pure water, pure cleaning oil, and stratified liquid, respectively) and subsequently tended to diminish, indicating a possibly saturated sloshing intensity. This may be understood through the fact that during the inceptive stage of increasing pressure, a more significant influence on the variations in liquid-level height could occur as a result of the much greater lifting force on the rising bubble caused by the higher pressure of injected gas. However, if the injected gas pressure became sufficiently high (such as larger than the critical value), as shown in Figure 9B, the time that the bubble resides in the liquid pool could be noticeably reduced by the much-increased velocity of the rising bubble, resulting in a dampening effect on the sloshing intensity. In Figures 9A,B, a similar tendency in the variation of the residence time of the bubble with gas-injection pressure can be seen. This may be the reason that although the speed of the rising bubble was expected to accelerate with increased injected gas pressure, some transient processes (e.g., bubble bursting as well as deformation and elongation) are likely to play a more prominent role during the bubble rising process (when the pressure was below the critical value). These transient processes therefore result in a longer residence time (Cheng et al., 2018c). Nevertheless, as the injected gas pressure augmented over the critical value, though such effect on extending the bubble residence time resulted from the transient processes still existed to some degree, the overall bubble rising velocity should become a more dominant factor on the residence time.

One more important point that can be seen from Figures 9A,B is that for experiments in pure liquid pools, a greater liquid density seemed to diminish the maximal elevation of the liquid level due to the larger resistance force on the rising bubble caused by greater inertia of the liquid. With cases of stratified liquid, as shown in Figure 9C, the sloshing intensity was clearly weakened by employing a greater water–oil depth ratio, which signified more fraction of larger-density water in the pool to restrain the upward movement of rising bubble due to its relatively larger liquid inertial force. Furthermore, due to this larger inertial force of liquid, the critical pressure was found to become relatively larger in cases of larger water–oil ratios (see Figure 9C), revealing that the a much intensive sloshing motion was difficult to attained in this case. It has been demonstrated that the sloshing intensity tended to be strengthened first then diminished afterward with the increasing initial depth of liquid in the pool (H_{pool}). This may be explained by the fact

that a greater depth of liquid could enhance the liquid's inertia (restricting effect) and prolong the bubble residence time (positive effect) within the liquid pool in such cases (Cheng et al., 2018a). Additionally, it was generally found that smaller nozzle size and longer gas-injection duration could effectively enhance the sloshing motion due to the much more violent hydraulic disturbances to the static liquid pool. However, more analyses are required to quantitatively considering the time-scale couplings and momentum injection rate during the sloshing motion for clarifying the correlations between sloshing intensity and varying parameters.

On balance, owing to the more comprehensive and detailed experiments conducted by Cheng et al. (2018c, 2020), various parametric effects on the sloshing intensity were validated e.g., depth ratio of stratified liquids, injected gas pressure, liquid depth, and gas-injection duration as well as nozzle size. Additionally, a possible way to mitigate fuel compaction in actual reactor accidents was identified, if a layer of molten structural materials exists at the upper area of the molten fuel pool.

3.3 Gas-injection sloshing motion with solid particles

Figure 6C shows the experimental system employed for investigations with solid particles by utilizing gas injection. Considering the probable situations that might occur in a CDA of an SFR, particle beds with different compositions (such as particles of different density, size (d_p, 0.125–8 mm), shape (spherical and non-spherical), components (single size and density, bicomponent mixed-size, bicomponent mixed density), and different initial height (H_{pb}, 5–30 cm) were used and placed on the bottom of pool, and gas-injection duration (0.06–0.1 s) as well as injected gas pressure (2–4 bar) were also treated as experimental parameters to obtain valuable experimental data for further numerical validation (Cheng et al., 2019a, 2019b, 2019c; Xu et al., 2022).

From the basic experiments with single-sized spherical particles, three stages of development for the sloshing process with solid particles were observed. The first and second experimental snapshots in Figures 10A–E illustrate Stage 1, in which the gas bubble entered at the bottom of a particle bed and rose to the top of the particle bed. In the third and fourth experimental snapshots in Figures 10A–E, Stage 2 is shown, in which the bubble detached from the particle bed with some possibility that particles could be pushed up and subsequently roll down along the edge of the bubble. After that, as displayed in the fifth and sixth experimental snapshots in Figures 10A–E, the bubble moved upward in the upper free liquid area to subsequently induce the outward peripheral and inward centralized sloshing motions. In addition, according to the multiphase interaction mechanism involving liquid, injected gas, and solid particles, three typical flow regimes (Regime I: bubble-impulsion dominant regime; Regime II: transitional regime; and Regime III: bed-inertia dominant regime), as shown in Figure 10, were specified and resulted in three corresponding final particle bed geometries. It should be noted that such characteristics might not emerge for fluidized beds (Didwania and Homsy, 1981; Bai et al., 1999), as under these experimental conditions the particles were far from being fluidized beds (i.e., no fluidization). Based on experimental analyses, as shown in Figure 11, the remarkable parametric effects on the flow-regime transitions and sloshing intensity were investigated and validated. In general, the flow-regime transitions were dictated by two important factors: particle-bed inertia and gas-bubble impulsion.

In the extended experiments with single-sized non-spherical particles, which were conducted considering the fact that various shapes of solid particles may be encountered in an actual CDA, particles of cylindrical, triangular prism, and irregular shapes were taken into account (Cheng et al., 2019c). Based on experimental observations, it was found that as the particle sphericity increased, due to the additional particle–particle friction and collisions resulting from some shape-relevant properties (Cheng et al., 2018b), not only was the overall particle-bed inertia diminished in Stage 1 but also the rolling-down process tended to be prevented in Stage 2, while interactions between the fluid flow and solid particles were enhanced, as a result facilitating regime transitions from a higher number to a lower one.

Recognizing that solid particles may also occur in various sizes in the molten pool of an actual CDA of an SFR, a large number of extended experiments using bicomponent mixed-sized spherical solid particles at the same densities but with different volumetric mixing ratios were conducted by Cheng et al. (2019a) to elucidate the effect of mixed sizes on sloshing motion. From the experiments, although the abovementioned key parametric effects on the flow-regime transitions were in general validated, typically the flow-regime characteristics tended to shift from a higher (e.g., Regime III) to a lower one (e.g., Regime II) if larger weights of smaller particles were employed in the particle mixtures. In addition, compared with the experimental results using single-sized solid particles, an incongruity could be found, especially for experiments employing more smaller particles within the particle mixtures. In the mixed-sized experiments, a quasi-flat bed was not only found in the transitional regime (namely Regime II) but also emerged in Regime II/III and Regime III/II, which signified the flow regimes involving the characteristics of Regime II and Regime III. Particularly, the symbols III/II and II/III were marked for such experimental cases which had more characteristics of Regimes III and II, respectively. The reason for this incongruity may be that although the overall impact of particle-bed inertia was comparatively somewhat larger than that of the gas-bubble

impulsion in cases of Regime III/II or II/III, the impulsion of the rising bubble might still exceed the inertia of smaller particles within the particle mixtures. This can cause the separation of particles of different sizes in the particle mixtures, which could lead to flow-regime deviation from a strict Regime II for instance (Cheng et al., 2019a). This may also explain why the in-between flow regimes were mostly emerged when more particles with small size presented in the particle mixtures. Noticing this point, further dimensional analysis may therefore be needed to classify the flow regimes and patterns more elaborately.

Considering the co-existence of other non-melted or refrozen materials (e.g., control rods and structures) in the molten pool during an actual scenario of a CDA in an SFR, further experiments were carried out by Xu et al. (2022) using bicomponent mixed-density particles of identical sizes. In general, they re-confirmed the fundamental effects of experimental parameters (such as particle size, injected gas pressure, and height of the particle bed) on the flow-regime transitions. For the effect of mixed-density particles, it was found that if the particle mixtures were composed of more high-density particles, the flow regimes would transit from a lower one to a higher one due to the relatively larger overall particle-bed inertia. However, compared with the mixed-size cases, the aforementioned in-between flow regimes were not found. This may be due to the smaller particles being more likely to pass through the larger gaps (or void spaces) among larger particles, while for mixed-density cases, due to the identical size of each component, the capability of lighter particles to pass through the gaps between heavier ones was thought to be largely restrained.

In short, based on experiments using gas injection with solid particles, it was demonstrated that through increasing the overall particle-bed inertia by particle-bed-related parameters (e.g., particle density, particle size, and height of the particle bed), not only would the gas-bubble impulsion effect in Stage 1 be to some extent limited within the particle bed but also the rolling-down effect of solid particles along with their sedimentation effect lifted by upward moving injected gas in Stage 2, resulting in the flow regimes shifting from lower to higher ones.

4 Conclusion and future prospects

4.1 Conclusion

Studies into molten-pool sloshing motion are important for the improved evaluation of the transition phase of CDAs in SFRs. Knowledge gained from experimental and numerical investigations into the mechanisms and characteristics of molten-pool sloshing motion are valuable not only for the improvement and verification of SFR safety analysis codes (which can invoke the simulation using actual materials in reactors and coupling with neutronic models) but also to provide reference data for studies of sloshing motion in other fields of engineering. We have systematically reviewed and discussed experimental and numerical studies into sloshing characteristics that have been performed in the past, focusing on thermal-hydraulics aspects under various conditions, including dam-break, fluid-step, and gas-injection conditions. Based on these studies, the important characteristics necessary for evaluating sloshing intensity (e.g., the maximal heights that emerge during peripheral outward and centralized inward sloshing motions) were identified, and the applicability of various simulation approaches (such as SIMMER code, SPH, and FVP methods) were validated through comparisons of both qualitative and quantitative experimental observations.

In the pioneering dam-break and fluid-step sloshing experiments in pure liquid pools, it was found that the sloshing characteristics were significantly affected by the overall liquid inertia and symmetricity of the sloshing system. With the further consideration of the non-melted or refrozen solid materials (e.g., control rods and structural materials) that may be present in a molten pool during an actual CDA in an SFR, dam-break and fluid-step experiments with solid phases (including rod- and ring-shaped obstacles, and solid particles) were conducted, and the dampening effect of the presence of solid phases on sloshing intensity was confirmed. This illustrated the difficulty of obtaining an intensive sloshing motion when sufficient amount of solid phases still existed in the molten pool during the CDA of SFR. As for the numerical simulations, the reasonability and applicability of SIMMER-IV code, SPH, and FVP methods for reproducing a dam-break along with the fluid-step sloshing motions in pure liquid pools (particularly for the compaction velocity) were validated. In general, for Eulerian-based methods (such as SIMMER code), the notable influences of the spatial differencing order and simulation geometries on the numerical accuracy were found. For the particle methods, more accurate results could be attained, with higher resolution, but this also caused an unavoidable reduction in numerical efficiency. In addition, it was revealed that vapor-trapping phenomena might occur during centralized sloshing motion, in accordance with the two-phase SPH simulations. However, from the simulations of dam-break experiments with solid phases, the necessity for modeling the multiphase interactions (particularly for those on solid phases) to obtain adequate simulation rationality and accuracy was demonstrated, whereas the dampening effect of solid phases on sloshing intensity could not observed or were underestimated.

As sloshing motion might be encountered as a result of rapid vapor generation and pressure buildup due to local FCIs within a large-scale molten pool during its formation and enlargement, the gas-injection method was used to study this type of sloshing motion. To study the effect of thermal-hydraulic disturbances on sloshing motions, several experiments using the gas-injection method were carried out with hydraulic disturbances in a pure-water pool. Based on

these experiments, the mitigating and augmenting effects on the sloshing intensity were found to depend on the timing of the external disturbances that were introduced, due to the interactions between local liquid flows; these could also be reproduced well through the SIMMER-III calculations. On the other hand, to more deeply and comprehensively elucidate the sloshing mechanism and the characteristics triggered by a local FCI, several experiments were conducted using the gas-injection method without hydraulic disturbances in liquid pools without solid phases, and various parametric effects were taken into account. Based on qualitative and quantitative experimental observations, it was confirmed that a maximal sloshing intensity was likely to emerge a critical pressure of injected gas, whose value is up to the liquid inertia (e.g., liquid density and liquid depth) as well as the depth ratio of stratified liquids, was reached. Moreover, it was revealed that fuel compaction might be diminished in real reactor accidents in cases where the stratification of molten fuel and molten structural materials was present, although the possibility of reactivity insertion due to molten-pool stratification should be noted for the real accidents. In the gas-injection experiments with solid particles, three typical flow regimes, referred to as the bubble-impulsion dominant regime, the transitional regime, and the bed-inertia dominant regime, were identifiable and were dominated by the overall gas-bubble impulsion and particle-bed inertia in different stages during the sloshing process. However, in the cases with mixed-size particles, some in-between flow regimes were found to appear due to the different prominence of larger-size particles and smaller-size particles in the particle bed against the gas-bubble impulsion, indicating a different time scale for momentum dissipation between larger and smaller particles.

4.2 Discussion and future prospects

Although much valuable knowledge and understanding concerning molten-pool sloshing motion have been gained through experiments and numerical simulations with their analyses of thermal-hydraulics mechanisms, in general, the analyses and discussions are lacking in their consideration of momentum dissipation processes (e.g., interfacial dynamics between fluid and particles). The contributors to the dissipation of momentum (e.g., particle size, particle density, particle components, intensity of gas-impulsion, and liquid properties) should be studied. In addition, the behaviors of the fluid and solid mixture may be different with the different time scale of impulsion built-up. Therefore, more elaborate studies into the initiators of sloshing motion (e.g., local FCIs and fuel or steel vapor generation) should be performed to better understand the mechanism and characteristics of molten-pool sloshing. On the other hand, it should be pointed out that compared with the parametric conditions that were considered in the experiments, the actual conditions in reactor accidents are more complicated. Furthermore, as experiments at real scale with real materials are difficult to perform, the verification of safety analysis codes/methods is of great significance if it is based on more elaborate experiments that clarify the mechanism of sloshing motion under the possible conditions that may occur during a CDA. The numerical accuracy for reproducing the sloshing motion (particularly for cases with solid phases) should also be further improved for the improved assessment of severe SFR accidents. In addition, investigations should focus on the sloshing intensity and fuel compaction velocity, which are anticipated to be of great importance to the power deposition and recriticality issues during a CDA of an SFR.

In the future, experimental and numerical studies into the sloshing mechanism and characteristics could include but are not limited to the following aspects.

1) Further gas-injection experiments with external disturbances that consider more complete parametric conditions. Although it has been confirmed that the timing of insertion of external disturbances is a key factor for augmenting or mitigating the sloshing intensity, it remains necessary to conduct additional experiments with a variety of other parameters (such as gas-injection duration period along with pressure, intensity of disturbances, and location of disturbance insertion) to gain a deeper clarification of the effect of external disturbances to study the determining regular for the overlaying (namely augmenting or mitigating) effects and the timing of introducing external disturbances.
2) Further experiments and validations for multicomponent (i.e., more than three components) mixed solid particles (including mixed-sized and mixed-density particles) using gas-injection methods. Although some important sloshing characteristics were captured in past investigations by using mixed-sized and mixed-density spherical particles under gas-injection conditions, it should be noted that only bicomponent particle mixtures were used. Therefore, to obtain more information regarding the sloshing motion under a more realistic particulate situation, further experimental investigations should be performed with multicomponent mixed particles. In addition, considering the incongruities found in the previous bicomponent mixed-sized experiments, elaboration of some dimensional analyses may be necessary to evaluate the flow-regime characteristics and identifications during the sloshing motion with particle bed consisted of multicomponent mixed particles.
3) Further gas-injection experiments in large-scale 3D pools. In earlier experiments that focused on sloshing motions initiated by local FCIs, 2D liquid pools were used to ensure sufficient experimental visualization so that the basic and essential

sloshing mechanisms and characteristics could be identified and understood. By referring the previous experimental studies regarding the debris bed self-leveling behavior by using gas-injection method for the CDA analysis of SFR (Cheng et al., 2011; Cheng et al., 2013a; Cheng et al., 2013b), it may be feasible that insights and fundamental understandings obtained through 2D experiments can be validated in large-scale 3D experiments, although some deviations or changes concerning the specific values of parameters (such as the critical gas-injection pressure) may occur due to the dimensional and scale changes (e.g., the length scale of the ratio of liquid pool height to diameter, and the time scale of bubble influence) and wall effects. Thus, to obtain a more comprehensive understanding of the molten-pool sloshing motion initiated by a local FCI, it will be necessary to perform large-scale 3D experiments with proper scale and dimensional analysis for space-, mass-, energy-, and time-scales to assess similarity rules. These large-scale 3D studies may validate the knowledge of the sloshing mechanism and characteristics accumulated from 2D experiments, while any changes in critical values following the dimensional and scale variations should also be investigated.

4) Numerical simulations for sloshing motion under gas-injection conditions without disturbances. In the earlier numerical studies, a variety of numerical approaches was attempted and validated in the dam-break and fluid-step sloshing experiments. However, the applicability of these approaches or other numerical methods, e.g., the moving particle semi-implicit (MPS) method that is applicable in the simulation of multiphase flows with various interfaces between phases (Park et al., 2016; Liu et al., 2021), should be continuously examined to obtain more reliable analysis for the evaluation of the sloshing motion in a CDA of an SFR based on the gas-injection experiments for simulating the sloshing motion triggered by local FCIs, during which the high-velocity gas flow along with large bubble deformation should be considered.
5) Further numerical simulations for sloshing motion with solid phases by appropriate treatment of the multiphase interactions involving the solid phases. In earlier numerical simulations for sloshing motion with solid phases, the need to appropriately estimate the multiphase interactions was demonstrated. Although reasonable simulation results could be obtained by employing some macroscopic models (such as the particle viscosity model) and technical approaches (e.g., adding a momentum diffusion term and wall friction), it should be recognized that the solid phase still played a less prominent role in the sloshing motion in such cases compared with other phases. Thus, the development and use is anticipated of more effective models or methods for reproducing the sloshing motion with a significant amount of solids (e.g., for gas-injection experiments with solid particles). For sloshing motion with solid particles, taking into account the past numerical investigations into particle-related phenomena for the assessment of severe accidents in SFRs (Shamsuzzaman et al., 2014; Tagami and Tobita, 2014; Guo et al., 2017; Tagami et al., 2018; Sheikh et al., 2020), in which solid particles played a major role in the multiphase behaviors, microscopic models for inter-particle collisions and contacts or the discrete element method (DEM) may additionally be considered in the simulations to provide appropriate estimates of particle–particle interactions.
6) Further investigations into the effect of coupling between nuclear power deposition as well as recriticality and pool sloshing motion based on the knowledge obtained from thermal-hydraulics studies. Some investigations have been performed to study the coupling between nuclear power deposition as well as recriticality and pool sloshing motion (e.g., a SIMMER-III simulation to study the power deposition and criticality during sloshing motion by assuming a mass of molten fuel fragment falls into the molten pool (Tatewaki et al., 2015)), and the effect of the power excursion and recriticality on the sloshing intensity were preliminarily studied. However, it should be noted that the knowledge from the studies into the thermal-hydraulic aspect of sloshing motion is of great importance to verify the reasonability and reliability of the simulation studies regarding power deposition and recriticality, which will also influence the sloshing characteristics in an actual CDA. Therefore, in the future, based on thermal-hydraulic experiments, investigations may be performed using the verified SFR safety analysis codes/methods coupled with reliable neutronic models for the further comprehensive evaluation of the transition phase of CDAs in SFRs.

Author contributions

RX performed the research and wrote the manuscript. SC guided the research and reviewed the manuscript.

Funding

The present work was performed with financial support from Guangdong Basic and Applied Basic Research Foundation (No. 2022A1515011582) and Science and Technology Program of Guangdong Province (No. 2021A0505030026) in China.

Conflict of interest

The authors declare that the research was conducted in the absence of any commercial or financial relationships that could be construed as a potential conflict of interest.

Publisher's note

References

Bai, D., Issangya, A. S., and Grace, J. R. (1999). Characteristics of gas-fluidized beds in different flow regimes. *Ind. Eng. Chem. Res.* 38 (3), 803–811. doi:10.1021/ie9803873

Bi, H. T. (2007). A critical review of the complex pressure fluctuation phenomenon in gas–solids fluidized beds. *Chem. Eng. Sci.* 62 (13), 3473–3493. doi:10.1016/j.ces.2006.12.092

Bohl, W., and Luck, L. B. (1990). SIMMER-II: A computer program for LMFBR disrupted core analysis. *Los Alamos Natl. Lab. Rep.* LA-11415-MS, 1–64. doi:10.2172/6851447

Bohl, W. (1979). "Some recriticality studies with SIMMER-II," in Proceedings of the International Meeting on Fast Reactor Technology, Washington, United States, August 19–23, 1979.

Bohl, W., Wilhelm, D., Parker, F. R., Berthier, J., Goutagny, L., and Ninokata, H. (1990). AFDM: An advanced fluid-dynamics model. *Los Alamos Natl. Lab. Rep.* LA-11692-MS. doi:10.2172/6664961

Buruchenko, S. K., and Crespo, A. J. C. (2014). "Validation DualSPHysics code for liquid sloshing phenomena," in Proceedings of the 2014 22nd International Conference on Nuclear Engineering, Cambridge, United Kingdom, July 28–30, 2014.

Cheng, S., Cui, J., Qian, Y., Gong, P., Zhang, T., Wang, S., et al. (2018a). An experimental investigation on flow-regime characteristics in debris bed formation behavior using gas-injection. *Ann. Nucl. Energy* 112, 856–868. doi:10.1016/j.anucene.2017.11.028

Cheng, S., Gong, P., Wang, S., Cui, J., Qian, Y., Zhang, T., et al. (2018b). Investigation of flow regime in debris bed formation behavior with nonspherical particles. *Nucl. Eng. Technol.* 50 (1), 43–53. doi:10.1016/j.net.2017.09.003

Cheng, S., Jin, W., Qin, Y., Zeng, X., and Wen, J. (2019a). Investigation of flow-regime characteristics in a sloshing pool with mixed-size solid particles. *Nucl. Eng. Technol.* 52 (5), 925–936. doi:10.1016/j.net.2019.11.006

Cheng, S., Li, S., Li, K., Zhang, N., and Zhang, T. (2018c). A two-dimensional experimental investigation on the sloshing behavior in a water pool. *Ann. Nucl. energy* 114, 66–73. doi:10.1016/j.anucene.2017.12.026

Cheng, S., Li, S., Li, K., and Zhang, T. (2019b). An experimental study on pool sloshing behavior with solid particles. *Nucl. Eng. Technol.* 51 (1), 73–83. doi:10.1016/j.net.2018.09.016

Cheng, S., Li, S., Li, K., Zhang, T., Zhang, N., Li, X. a., et al. (2018d). Prediction of flow-regime characteristics in pool sloshing behavior with solid particles. *Ann. Nucl. Energy* 121, 11–21. doi:10.1016/j.anucene.2018.07.017

Cheng, S., Li, X., Liang, F., Li, S., and Li, K. (2019c). Study on sloshing motion in a liquid pool with non-spherical particles. *Prog. Nucl. Energy* 117, 103086. doi:10.1016/j.pnucene.2019.103086

Cheng, S., Matsuba, K., Isozaki, M., Kamiyama, K., Suzuki, T., and Tobita, Y. (2015). A numerical study on local fuel–coolant interactions in a simulated molten fuel pool using the SIMMER-III code. *Ann. Nucl. Energy* 85, 740–752. doi:10.1016/j.anucene.2015.06.030

Cheng, S., Matsuba, K., Isozaki, M., Kamiyama, K., Suzuki, T., and Tobita, Y. (2014). An experimental study on local fuel–coolant interactions by delivering water into a simulated molten fuel pool. *Nucl. Eng. Des.* 275, 133–141. doi:10.1016/j.nucengdes.2014.05.003

Cheng, S., Tanaka, Y., Gondai, Y., Kai, T., Zhang, B., Matsumoto, T., et al. (2011). Experimental studies and empirical models for the transient self-leveling behavior in debris bed. *J. Nucl. Sci. Technol.* 48 (10), 1327–1336. doi:10.1080/18811248.2011.9711823

Cheng, S., Xu, R., Jin, W., Qin, Y., Zeng, X., Li, S., et al. (2020). Experimental study on sloshing characteristics in a pool with stratified liquids. *Ann. Nucl. Energy* 138, 107184. doi:10.1016/j.anucene.2019.107184

Cheng, S., Yamano, H., Suzuki, T., Tobita, Y., Gondai, Y., Nakamura, Y., et al. (2013a). An experimental investigation on self-leveling behavior of debris beds using gas-injection. *Exp. Therm. Fluid Sci.* 48, 110–121. doi:10.1016/j.expthermflusci.2013.02.014

Cheng, S., Yamano, H., Suzuki, T., Tobita, Y., Nakamura, Y., Zhang, B., et al. (2013b). Characteristics of self-leveling behavior of debris beds in a series of experiments. *Nucl. Eng. Technol.* 45 (3), 323–334. doi:10.5516/NET.02.2012.068

Cheng, S., Zhang, T., Meng, C., Zhu, T., Chen, Y., Dong, Y., et al. (2019d). A comparative study on local fuel-coolant interactions in a liquid pool with different interaction modes. *Ann. Nucl. Energy* 132, 258–270. doi:10.1016/j.anucene.2019.04.048

Didwania, A. K., and Homsy, G. M. (1981). Flow regimes and flow transitions in liquid fluidized beds. *Int. J. Multiph. Flow* 7 (6), 563–580. doi:10.1016/0301-9322(81)90031-8

Fauske, H. K., and Koyama, K. (2002). Assessment of fuel coolant interactions (FCIs) in the FBR core disruptive accident (CDA). *J. Nucl. Sci. Technol.* 39 (6), 608–614. doi:10.1080/18811248.2002.9715241

Gingold, R. A., and Monaghan, J. J. (1977). Smoothed particle hydrodynamics: Theory and application to non-spherical stars. *Mon. Notices R. Astronomical Soc.* 181 (3), 375–389. doi:10.1093/mnras/181.3.375

Guo, L., Morita, K., and Tobita, Y. (2017). Numerical simulations on self-leveling behaviors with cylindrical debris bed. *Nucl. Eng. Des.* 315, 61–68. doi:10.1016/j.nucengdes.2017.02.024

Guo, L., Zhang, S., Morita, K., and Fukuda, K. (2012). Fundamental validation of the finite volume particle method for 3D sloshing dynamics. *Int. J. Numer. Methods Fluids* 68 (1), 1–17. doi:10.1002/fld.2490

Guo, L., Zhang, S., Morita, K., and Fukuda, K. (2010). "Numerical simulation of 3D liquid sloshing motion with solid particles using finite volume particle method," in 18th International Conference on Nuclear Engineering, Xi'an, China, May 17–20, 2010, 585–592.

Hatayama, K. (2008). Lessons from the 2003 Tokachi-oki, Japan, earthquake for prediction of long-period strong ground motions and sloshing damage to oil storage tanks. *J. Seismol.* 12 (2), 255–263. doi:10.1007/s10950-007-9066-y

Jo, Y., Park, J., and Kim, E. (2019). "Numerical simulation on LMR molten-core sloshing behaviors using smoothed particle hydrodynamics method," in Proceeding of the Korean Nuclear Society Spring Meeting, Jeju, Korea, May 23–24, 2019.

Jo, Y., Park, S., Park, J., and Kim, E. S. (2021). Numerical simulation on LMR molten-core centralized sloshing benchmark experiment using multi-phase smoothed particle hydrodynamics. *Nucl. Eng. Technol.* 53 (3), 752–762. doi:10.1016/j.net.2020.07.039

Kolev, N. I. (1993). The code IVA 3 for modelling of transient three-phase flows in complicated 3D geometry/Das Programm IVA3 zur Modellierung transienter Dreiphasen- Strömungen in komplizierten dreidimensionalen Geometrien. *Kerntechnik* 58 (3), 147–156. doi:10.1515/kern-1993-580305

Kondo, S., Furutani, A., and Ishikawa, M. (1985). "SIMMER-II application and validation studies in Japan for energetics accommodation of severe LMFBR accidents," in Fast Reactor Safety: Proceedings of the International Topical Meeting, Knoxville, United States, April 21–25, 1985.

Kondo, S., Tobita, Y., Morita, K., and Shirakawa, N. (1992). "SIMMER-III: An advanced computer program for LMFBR severe accident analysis," in Proceedings of International Confefence on Design and Safety of Advanced Nuclear Power.Plants (ANP'92), Tokyo, Japan, October 25–29, 1992.

Liu, P., Yasunaka, S., Matsumoto, T., Morita, K., Fukuda, K., and Tobita, Y. (2006). Simulation of the dynamic behavior of the solid particle bed in a liquid pool: Sensitivity of the particle jamming and particle viscosity models. *J. Nucl. Sci. Technol.* 43 (2), 140–149. doi:10.1080/18811248.2006.9711076

Liu, P., Yasunaka, S., Matsumoto, T., Morita, K., Fukuda, K., Yamano, H., et al. (2007). Dynamic behavior of a solid particle bed in a liquid pool: SIMMER-III code verification. *Nucl. Eng. Des.* 237 (5), 524–535. doi:10.1016/j.nucengdes.2006.08.004

Liu, X., Morita, K., and Zhang, S. (2021). Direct numerical simulation of incompressible multiphase flow with vaporization using moving particle semi-implicit method. *J. Comput. Phys.* 425, 109911. doi:10.1016/j.jcp.2020.109911

Maschek, W., Fischer, E., and Asprey, M. (1982). "Transition phase and recriticality analyses for a SNR-type homogeneous core with the SIMMER-II code," in Proceedings of the LMFBR safety topical meeting, Lyon-Ecully, France, July 19–23, 1982.

Maschek, W., Munz, C.-D., and Meyer, L. (1992a). Investigations of sloshing fluid motions in pools related to recriticalities in liquid-metal fast breeder reactor core meltdown accidents. *Nucl. Technol.* 98 (1), 27–43. doi:10.13182/NT92-A34648

Maschek, W., Roth, A., Kirstahler, M., and Meyer, L. (1992b). Simulation experiments for centralized liquid sloshing motions. *Kernforsch. Karlsr. Rep*, 1–51. doi:10.5445/IR/270033132

Morita, K., Matsumoto, T., Emura, Y., Abe, T., Tatewaki, I., and Endo, H. (2014). "Investigation on sloshing response of liquid in a 2D pool against hydraulic disturbance," in The Ninth Korea-Japan Symposium on Nuclear Thermal Hydraulics and Safety (NTHAS-9), Buyeo, Korea, November 16–19, 2014.

Munz, C.-D., and Maschek, W. (1992). Comparison of results of two-phase fluid dynamics codes and sloshing experiments. *Kernforsch. Karlsr. Rep.*, 1–54. doi:10.5445/IR/270033133

Namiki, A., Rivalta, E., Woith, H., and Walter, T. R. (2016). Sloshing of a bubbly magma reservoir as a mechanism of triggered eruptions. *J. Volcanol. Geotherm. Res.* 320, 156–171. doi:10.1016/j.jvolgeores.2016.03.010

Ohshima, H., and Kubo, S. (2016). *Handbook of generation IV nuclear reactors*. Manchester: Woodhead Publishing.

Park, S., Park, H. S., Jang, B. I., and Kim, H. J. (2016). 3-D simulation of plunging jet penetration into a denser liquid pool by the RD-MPS method. *Nucl. Eng. Des.* 299, 154–162. doi:10.1016/j.nucengdes.2015.08.003

Pigny, S. L. (2010). Academic validation of multi-phase flow codes. *Nucl. Eng. Des.* 240 (11), 3819–3829. doi:10.1016/j.nucengdes.2010.08.007

Raj, B., Chellapandi, P., and Rao, P. V. (2015). *Sodium fast reactors with closed fuel cycle*. Boca Raton, United States: CRC Press.

Roache, P. J. (1972). *Computational fluid dynamics*. Albuquerque: Hermosa publishers.

Roache, P. J. (1998). *Verification and validation in computational science and engineering*. Albuquerque, United States: Hermosa publishers.

Sakai, F., Nishimura, M., and Ogawa, H. (1984). Sloshing behavior of floating-roof oil storage tanks. *Comput. Struct.* 19 (1), 183–192. doi:10.1016/0045-7949(84)90217-7

Shamsuzzaman, M., Zhang, B., Horie, T., Fuke, F., Matsumoto, T., Morita, K., et al. (2014). Numerical study on sedimentation behavior of solid particles used as simulant fuel debris. *J. Nucl. Sci. Technol.* 51 (5), 681–699. doi:10.1080/00223131.2014.887481

Sheikh, M., Liu, X., Matsumoto, T., Morita, K., Guo, L., Suzuki, T., et al. (2020). Numerical simulation of the solid particle sedimentation and bed formation behaviors using a hybrid method. *Energies* 13, 5018. doi:10.3390/en13195018

Smith, L. L. (1978). SIMMER-II: A computer program for LMFBR disrupted core analysis. *Los Alamos Natl. Lab. Rep*. LA-7515-M, 1–279.

Stoker, J. J. (1957). *Water waves, the mathematical theory with applications*. New York, United States: Interscience Publishers.

Suzuki, T., Kamiyama, K., Yamano, H., Kubo, S., Tobita, Y., Nakai, R., et al. (2014). A scenario of core disruptive accident for Japan sodium-cooled fast reactor to achieve in-vessel retention. *J. Nucl. Sci. Technol.* 51 (4), 493–513. doi:10.1080/00223131.2013.877405

Suzuki, T., Tobita, Y., Kawada, K., Tagami, H., Sogabe, J., Matsuba, K., et al. (2015). A preliminary evaluation of unprotected loss-of-flow accident for a prototype fast-breeder reactor. *Nucl. Eng. Technol.* 47 (3), 240–252. doi:10.1016/j.net.2015.03.001

Tagami, H., Cheng, S., Tobita, Y., and Morita, K. (2018). Model for particle behavior in debris bed. *Nucl. Eng. Des.* 328, 95–106. doi:10.1016/j.nucengdes.2017.12.029

Tagami, H., and Tobita, Y. (2014). "Numerical simulation for debris bed behavior in sodium cooled fast reactor," in The 10th International Topical Meeting on Nuclear Thermal-Hydraulics, Operation and Safety (NUTHOS-10), Okinawa, Japan, December 14–18, 2014.

Tatewaki, I., Morita, K., and Endo, H. (2015). "A study on characteristics of molten pool sloshing in core disruptive accidents of fast reactors," in 23rd International Conference on Nuclear Engineering: Nuclear Power-Reliable Global Energy (ICONE-23), Chibu, Japan, May 17–21, 2015.

Tentner, A., Parma, E., Wei, T., and Wigeland, R. (2010). *Severe accident approach-final report. Evaluation of design measures for severe accident prevention and consequence mitigation*. United States: Argonne National Laboratory.

Thaker, A. H., Bhujbal, S. V., and Buwa, V. V. (2020). Effects of sloshing gas–liquid interface on dynamics of meandering bubble plumes and mixing in a shallow vessel: PIV and PLIF measurements. *Chem. Eng. J.* 386, 122036. doi:10.1016/j.cej.2019.122036

Theofanous, T., and Bell, C. (1986). An assessment of Clinch River Breeder Reactor core disruptive accident energetics. *Nucl. Sci. Eng.* 93 (3), 215–228. doi:10.13182/NSE86-A17751

Vorobyev, A. (2012). *A Smoothed particle hydrodynamics method for the simulation of centralized sloshing experiments*. Baden-Württemberg: KIT Scientific Publishing.

Vorobyev, A., Kriventsev, V., and Maschek, W. (2010). "Analysis of central sloshing experiment using smoothed particle hydrodynamics (SPH) method," in 18th International Conference on Nuclear Engineering (ICONE18), Xi'an, China, May 17–20, 2010.

Vorobyev, A., Kriventsev, V., and Maschek, W. (2011). Simulation of central sloshing experiments with smoothed particle hydrodynamics (SPH) method. *Nucl. Eng. Des.* 241 (8), 3086–3096. doi:10.1016/j.nucengdes.2011.05.020

Xu, R., Cheng, S., Li, S., and Cheng, H. (2022). Knowledge from recent investigations on sloshing motion in a liquid pool with solid particles for severe accident analyses of sodium-cooled fast reactor. *Nucl. Eng. Technol.* 54 (2), 589–600. doi:10.1016/j.net.2021.08.024

Yamano, H., Fujita, S., Tobita, Y., Kamiyama, K., Kondo, S., Morita, K., et al. (2003b). *SIMMER-III: A computer program for LMFR core disruptive accident analysis version 3 A model summary and program description*. Ibaraki, Japan: Japan Nuclear Cycle Devlopment Institute. JNC-TN–9400-2003-071.

Yamano, H., Fujita, S., Tobita, Y., Kamiyama, K., Kondo, S., Morita, K., et al. (2003a). *SIMMER-IV: A three-dimensional computer program for LMFR core disruptive accident analysis version 2 A model summary and program description*. Japan Nuclear Cycle Devlopment Institute. JNC-TN–9400-2003-070.

Yamano, H., Onoda, Y., Tobita, Y., and Sato, I. (2009). Transient heat transfer characteristics between molten fuel and steel with steel boiling in the CABRI-TPA2 test. *Nucl. Technol.* 165 (2), 145–165. doi:10.13182/NT09-A4082

Yamano, H., Suzuki, T., Tobita, Y., Matsumoto, T., and Morita, K. (2012). "Validation of the SIMMER-IV severe accident computer code on three-dimensional sloshing behavior," in Proceedings of The 8th Japan-Korea Symposium on Nuclear Thermal Hydraulics and Safety (NTHAS-8), Beppu, Japan, December 9–12, 2012.

Zhang, S., Morita, K., Fukuda, K., and Shirakawa, N. (2007). A new algorithm for surface tension model in moving particle methods. *Int. J. Numer. Methods Fluids* 55 (3), 225–240. doi:10.1002/fld.1448

Zhang, T., Cheng, S., Zhu, T., Meng, C., and Li, X. a. (2018). A new experimental investigation on local fuel-coolant interaction in a molten pool. *Ann. Nucl. Energy* 120, 593–603. doi:10.1016/j.anucene.2018.06.031

Nomenclature

Symbols

D_{in} inner diameter of the inner cylinder
D_{out} inner diameter of the outer cylinder
d_p diameter of solid particles
H_{in} liquid height in the inner cylinder
H_{out} liquid height in the outer cylinder
H_{pb} particle-bed height
H_{ring} height of ring-shaped obstacle
H_w water depth
H_o depth of cleaning oil
H_{pool} total depth of liquid in the pool
ΔH_{max} maximum liquid-level elevation
N_p particle number
P gas-injection pressure
R_c distance of rods from the center of the container
R_{off} off-centeredness
T gas-injection period
ΔT gas-injection duration

Greek letters

ρ_p density of solid particles

frontiers | Frontiers in Energy Research

TYPE Original Research
PUBLISHED 15 September 2022
DOI 10.3389/fenrg.2022.1005171

OPEN ACCESS

EDITED BY
Wenzhong Zhou,
Sun Yat-sen University, China

REVIEWED BY
Yaou Shen,
Laboratory of Reactor System Design Technology (LRSDT), China
Bo Pang,
Shenzhen University, China

*CORRESPONDENCE
Tao Wan,
wantao@impcas.ac.cn

SPECIALTY SECTION
This article was submitted to Nuclear Energy,
a section of the journal
Frontiers in Energy Research

RECEIVED 28 July 2022
ACCEPTED 29 August 2022
PUBLISHED 15 September 2022

CITATION
Chen X and Wan T (2022), CFD analysis of Fe transfer on roughened wall caused by turbulent lead-bismuth eutectic flow. *Front. Energy Res.* 10:1005171. doi: 10.3389/fenrg.2022.1005171

CFD analysis of Fe transfer on roughened wall caused by turbulent lead-bismuth eutectic flow

Xiaolin Chen[1] and Tao Wan[1,2,3]*

[1]Advanced Energy Science and Technology Guangdong Laboratory, Huizhou, China, [2]Institute of Modern Physics, Chinese Academy of Sciences, Lanzhou, China, [3]School of Nuclear Science and Technology, University of Chinese Academy of Sciences, Beijing, China

Structural material compatibility with lead bismuth eutectic is one of the main challenges for design and operation of the LBE-cooled nuclear systems. To better understand the mechanisms of stainless steel corrosion behavior in LBE flow, the iron mass transfer phenomenon on roughened walls under various LBE pipe flow conditions are numerically investigated in this study. CFD simulations are performed, by applying a low Reynolds number k-ε model, in a range of Reynolds number from 5×10^3 to 10^5. Meanwhile, various pipe wall roughness conditions are considered, which are simulated by crests with different depths and periodic lengths. Effects of roughness dimensions and Reynolds numbers on the near-wall mass transfer rate are investigated. Results showed that higher flow velocities and shorter crest length led to higher mass transfer coefficient. On the basis of the results, the mass transfer coefficients are proposed both for smooth wall and roughened walls. The mass transfer enhanced by wall roughness is characterized by the ratio of rough-to-smooth mass transfer coefficient, and this ratio is demonstrated by a regression equation, in which dimensionless roughness number, Reynolds number and geometrical ratio of the roughness are included. Moreover, it is found that the ratio of rough-to-smooth mass transfer coefficient is relatively more dependent on Reynolds number.

KEYWORDS

LBE, corrosion, mass transfer, wall roughness, numerical simulation

Introduction

Lead-bismuth Eutectic (LBE) is a prominent candidate coolant for Lead-cooled Fast Reactors (LFRs) and Accelerator Driven Systems (ADS) due to its favorable thermal and physical properties (Zhang, 2014). However, the compatibility of structure material (e.g., stainless steel) with LBE is one of the key issues for design and operation of LBE-cooled nuclear systems. Stainless steels could be severely corroded when exposed to flowing LBE, which would challenge the structural integrity of and operation safety, especially at high working temperature.

To better understand the mechanism and characteristics of steel corrosion in LBE, many studies have been carried out in last two decades (Barbier et al., 2001; Benamati et al., 2006; Doubková et al., 2008; Zhang and Li, 2008; Del Giacco et al., 2014; Heinzel et al., 2014; Lambrinou et al., 2017; Chen et al., 2019). The state-of-art of steel corrosion in LBE pointed out four main mechanisms: oxidation, dissolution, erosion-corrosion and fretting wear (Ballinger and Lim, 2004; Zhang and Li, 2008; Zhang, 2009; Gong et al., 2022). Oxidation of steel occurs if oxygen concentration in LBE reaches appropriate value, Fe_3O_4-based oxide film or layer could be formed at the metal surface, which could be protective or rather non-protective to the metallic surface. Dissolution corrosion is facilitated when the oxygen concentration in LBE locates at a sufficient low level, steel elements dissolve directly into LBE since there is no protective oxide layer at surface. The dissolution is driven by the temperature-dependent chemical potential differences of elements in steels and those in LBE. Erosion-corrosion is also termed as flow-assisted corrosion, it is caused by the LBE penetration into grain boundaries of steel when dissolution of elements occurs, then the loose grains are stripped by high wall shear stress under high velocities, which leads to further penetration of LBE into steel. Fretting wear is considered as an interaction of flow-induced vibration and corrosion processes, which occurs most likely at fuel pins in core or heat exchanger tubes in steam generator.

The surface condition is one of the addressed factors that affects the LBE corrosion behavior (Gong et al., 2022). Discrepancies of liquid metal corrosion behavior of steels under different surface conditions were reported. Doubková et al. (2008) observed a different corrosion resistance for T91 steel specimens with ground and passivated surfaces in the same LBE environment. Tsisar et al. (2018) investigated effect of structure state and surface finishing of austenitic 1.4970 (15-15 Ti) steel on the corrosion under flowing oxygen-containing LBE condition, and they found out that specimens with polished surfaces were less resistant to dissolution corrosion. Ilinčev et al. (2004) carried out corrosion/oxidation behavior studies of 304 and 316 Austenitic steel in LBE with different oxygen concentrations, differences of corrosion rates were reported between specimens with ground, passivated, and as-produced surfaces. Thus, it is reasonable to consider that surface roughness, which could represent the surface condition, plays an important role in corrosion/oxidation behavior of steel in LBE.

The effect of surface roughness on mass transfer behavior has been investigated under different Reynolds numbers and Schmidt numbers. Mass transfer on various roughened surfaces including V-shaped grooves (Dawson and Trass, 1972; Tantirige and Trass, 1984; Grifoll et al., 1986; Zhao and Trass, 1997), erosion-corrosion roughness (Postlethwaite and Lotz, 1988), sandpaper-roughness (Lolja, 2005) and square ribs (Berger and Hau, 1979) have been studied by applying electrochemical method (Selman and Tobias, 1978). Equations of Sherwood number, Reynolds number and Schmidt number were proposed. Dimensionless wall roughness was considered as a factor enhancing the mass transfer. Recently, researchers investigated mass transfer enhancement on sinusoidal wavy wall, in which a plaster dissolution method was applied to measure the mass transfer coefficient (Fujisawa et al., 2017, 2020; Yamagata and Fujisawa, 2021). Meanwhile, CFD studies of roughness effect on mass transfer by using low Reynolds number (LRN) models are reported as well. Mass transfer behavior on a sinusoidal wavy wall was simulated and compared with the experimental results by Yamagata and Fujisawa (2021) and Fujisawa et al. (2017, 2020), respectively. Lari et al. (2013) investigated the mass transfer behavior on d-type rough wall under high Schmidt number by applying a LRN k-ε model, they concluded that mass transfer could be either enhanced or weakened by the roughness.

Mass transfer of elements in LBE is a crucial phenomenon in steel corrosion process. Due to the technical difficulties in experimental measurement, the CFD investigation is considered as a highly effective way. Zhang et al. (2021) used Ansys FLUENT code to simulate oxygen mass transfer for a packed bed of PbO spheres in flowing LBE in the CRAFT experiment. Ito and Sakai (2004) evaluated the oxygen concentration controllability in a LBE-cooled natural-circulation reactor using COCOA code. Feng et al. (2021) proposed a coupling method between the oxidation model and Ansys CFX code to simulate the oxidation reaction in fuel assemblies under flowing LBE. Marino et al. (2018) investigated the oxygen concentration profiles through the 19-pin scaled fuel assembly of MYRRHA reactor core with Ansys CFX tool and identified the regions which are prone to LBE corrosion. The investigation of oxygen transfer in LBE is necessary in environment of high oxygen concentration, while in environment of low oxygen concentration, the study of iron transfer is crucial when dissolution of iron occurs at the interface of structural steel and LBE. Investigation on iron mass transfer in dissolution corrosion under different surface states of steel, could provide considerable values for evaluation of dissolution damage of LBE to steel, like corrosion rate. However, to the best of the authors' knowledge, CFD investigation of iron transfer behavior under LBE flow condition is limited, especially transfer from roughened wall to bulk LBE. By using STAR-CD code to simulate the mass transfer behavior of dissolved iron, Wan and Saito (2018) evaluated the corrosion rate of 316L steel in LBE and compared with experimental data. More numerical investigations on iron transfer in LBE are required for the further analysis and model development of iron dissolution. Although experimental investigation has always been the main approach in the research of steel corrosion behavior in LBE, the CFD approach is thought to be an effective way to analyze the local mass transfer phenomenon on roughened walls and is able to provide considerable values for further development of corrosion/dissolution model of steel in LBE.

The aim of this study is to characterize the effect of rough walls on iron transfer behavior in LBE flow and to further enhance the understanding of steel dissolution in LBE. For this purpose, d-type roughened pipe wall geometries are chosen, numerical simulation of iron transfer in LBE flow at different Reynolds numbers is carried out. By applying LRN k-ε model, the mass transfer coefficient is obtained through the calculated near-wall iron concentration. Effect of different roughness is then analyzed by comparison with smooth wall, the rough-to-smooth ratio is characterized and correlated with several parameters.

Physical models

Corrosion and mass transfer model

In the steady state LBE pipe flow without protective oxide layer at wall under isothermal condition, the steel corrosion depends on the mass transfer rates and dissolution/reaction rates of steel constituents at wall. If the mass transfer rate is greater than dissolution rate, the corrosion is dominated by the mass transfer, which is called mass transfer controlled corrosion. In the other case, it is called activation controlled or dissolution controlled corrosion (Zhang et al., 2010). The dissolved iron at wall is firstly transferred through the diffusion boundary layer by molecular diffusion, then the transfer rate of iron becomes higher in the viscous sublayer. The diffusion boundary layer could be very thin as the Schmidt number is considerably high (order of 10^3).

The mass flux of iron J at wall obeys the Fick's law and could be expressed as follow:

$$J = D_m \frac{\partial C}{\partial n} = \frac{D_m}{y_0}(C_w - C_0) \tag{1}$$

where D_m is the molecular diffusion coefficient of iron, C and n are, respectively the concentration and normal distance to wall in Fick's law, respectively, C_w is the concentration of iron at wall, y_0 is the distance from wall and C_0 is the concentration of iron at distance y_0. In general, the distance y_0 represents the thickness of the first inflation mesh layer in CFD simulation. Meanwhile, the mass flux from dissolution location to bulk fluid can be expressed by the following equation, where C_w denotes concentration at wall, C_b denotes concentration in bulk fluid and K is mass transfer coefficient of iron:

$$J = K(C_w - C_b) \tag{2}$$

Since the mass transfer rate in diffusion boundary layer is very low, it dominates the mass transfer from wall to bulk fluid. Thus, the iron mass flux is the same in Eqs 1, 2, and the mass transfer coefficient can be deduced by

$$K = \frac{D_m}{y_0}\frac{(C_w - C_0)}{(C_w - C_b)} \tag{3}$$

For the mass transfer controlled corrosion, the corrosion rate (CR) is proportional to the mass flux and therefore can be directly calculated as follow (Davis and Frawley, 2009):

$$CR = \frac{JM}{\rho_{\mathrm{Fe}}} = K(C_w - C_b)\frac{M}{\rho_{\mathrm{Fe}}} \tag{4}$$

where ρ_{Fe} and M denote the density and molar mass of iron, respectively. In addition, many studies have found that local wall-to-liquid mass transfer behavior and corrosion rate in practical geometries have strong dependence on the near-wall turbulent level (Poulson, 1999; Nešić, 2006; Ikarashi et al., 2017), the near-wall concentration distributions of solutes are considered to be influenced by the near-wall turbulent kinetic energy (Wan and Saito, 2018).

For the mass transfer in a steady-state or fully developed flow, correlations between Sherwood number Sh, ($Sh = Kl/D_m$with l the characteristic length), Reynolds number Re and Schmidt number Sc [$Sc = \mu/(\rho D_m)$] were proposed as follow (Dawson and Trass, 1972; Grifoll et al., 1986; Postlethwaite and Lotz, 1988; Poulson, 1990):

$$Sh = a_1 Re^{a_2} Sc^{a_3} \tag{5}$$

where the coefficients a_1 depends on the geometry, a_2 generally ranges from 0.5 to 1, while a_3 is close to 1/3. As the near-wall mass transfer is affected by the wall roughness, the rough-to-smooth ratio of mass transfer coefficient K_r/K_s has been characterized by the similarity function (Dawson and Trass, 1972; Tantirige and Trass, 1984; Postlethwaite and Lotz, 1988; Mobarak et al., 1997; Zhao and Trass, 1997; Lolja, 2005). The mass transfer similarity function contains several parameters, such as the dimensionless roughness number, Schmidt number and Reynolds number:

$$\frac{K_r}{K_s} = f(e^+, Sc, Re, \ldots) \tag{6}$$

The dimensionless roughness number (or roughness Reynolds number) e^+ is defined by roughness height e and friction velocity u^*:

$$e^+ = \frac{\rho u^* e}{\mu},\ u^* = U\sqrt{\frac{f}{8}} \tag{7}$$

The dimensionless friction velocity $u*$ is determined by the stream flow velocity U and friction factor f, while the friction factor f could be determined by the measured pressure drop for pipe flow with roughened wall:

$$f = \frac{\Delta P}{\rho U^2}\frac{2D}{L} \tag{8}$$

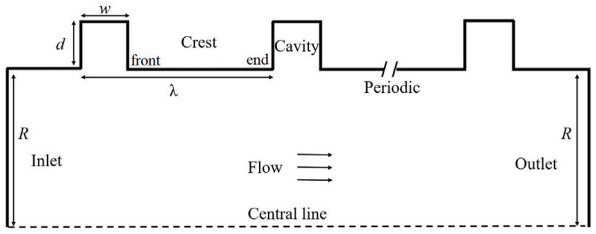

FIGURE 1
2D axisymmetric geometry of the rough wall pipe.

LRN turbulent model

The resolution of the near-wall iron concentration is critical since the near-wall concentration dominates the mass transfer behavior in LBE corrosion. To achieve a precise simulation of the near-wall flow behavior, LRN models with damping functions are used. LRN models have been proposed by Jones and Launder (1972), Launder and Sharma (1974), Lam and Bremhorst (1981), and Chien (1982). In this study, the Launder-Sharma LRN model is adopted for calculation, the transport equations of the turbulent kinetic energy and its dissipation rate are given as follows:

$$\frac{\partial \rho k}{\partial t} + \frac{\partial}{\partial x_j}\left[\rho k u_j - \left(\mu + \frac{\mu_t}{\sigma_k}\right)\frac{\partial k}{\partial x_j}\right] = P_k - \rho\varepsilon - 2\mu\left(\frac{\partial \sqrt{k}}{\partial y}\right)^2 \quad (9)$$

$$\frac{\partial \rho \varepsilon^*}{\partial t} + \frac{\partial}{\partial x_j}\left[\rho \varepsilon^* u_j - \left(\mu + \frac{\mu_t}{\sigma_\varepsilon}\right)\frac{\partial \varepsilon^*}{\partial x_j}\right] = \left(C_1 f_1 P_k - C_2 f_2 \rho \varepsilon^*\right)\frac{\varepsilon^*}{k} + \frac{2\mu\mu_t}{\rho}\left(\frac{\partial^2 u}{\partial y^2}\right)^2 \quad (10)$$

$$\mu_t = \rho C_\mu f_\mu \frac{k^2}{\varepsilon^*} \quad (11)$$

$$\varepsilon^* = D_\varepsilon + \varepsilon \quad (12)$$

In the above equations, μ_t and P_k denote turbulent viscosity and production rate of turbulence respectively. σ_k, σ_ε, C_1, C_2, and C_μ are constants which have the same values as those in the standard k-ε model (i.e. 1.0, 1.3, 1.44, 1.92, and 0.09, respectively). The modified turbulent dissipation rate ε^* is related to the origin turbulent dissipation rate ε with a damping term D_ε whose value is significant near wall but can be negligible away from the wall. With Eq. 12, equation of ε^* could be solved by applying a zero wall boundary condition, which greatly simplifies the computation. f_1, f_2, and f_μ are damping functions accounting for near-wall effects:

$$f_1 = 1.0,\ f_2 = 1 - 0.3\exp\left(-Re_t^2\right),\ f_\mu = \exp\left[\frac{-3.4}{(1 + 0.02Re_t)^2}\right] \quad (13)$$

wherein the turbulent Reynolds number Re_t is defined as:

$$Re_t = \frac{\rho k^2}{\mu \varepsilon^*} \quad (14)$$

The direct resolution of the viscous sublayer in LRN model requires very fine grids at walls, the first node (or cell centroid) should be located at $y^+ \leq 1$.

Numerical simulation

Rough wall geometry

The rough wall geometry consists of periodic square cavities, Figure 1 shows the 2D geometry of computational domain. An axis-symmetry model is adopted, with a radius of the cylinder pipe R = 4.9 mm. λ is the periodic distance between two adjacent cavities, while w and d denotes the width and depth of the cavity, respectively. The width-to-depth ratio w/d is one for square cavities, hence a d-type roughness is represented. The d-type roughness is considered as a good representative for a natural roughness and allows for comparison of the flow field with CFD and electrochemical experiments (Lari et al., 2013). Three different sizes of cavities w = 500, 250, 50 μm are adopted and the ratio λ/d = 2 and 4 are considered, respectively. The total length of computational domain is 80 mm, which is more than eight times of the inlet diameter, thus the pipe flow could be considered as fully developed. The mass transfer of smooth wall with the same radius R and length is also studied for comparison. Table 1 gives the models with different geometrical dimensions in this study.

Mesh generation

Unstructured triangle grid was applied to the LBE bulk, with coupled mesh inflation that consists of fine layers near the wall. The thickness of the first inflation layer was fixed approximately at y^+ = 0.1 or below for LRN model, which is considered as the thickness of the diffusion boundary layer (Nešić et al., 1992). Hence, in the above geometrical models, y^+ was set as approximately 0.1 in the whole computational domain. For the LBE flow in condition $Re = 5 \times 10^4$, the thickness of the first layer is 3.4×10^{-7} m. With extension ratio of 1.2 in normal direction to the wall, sixteen layers were defined, which could cover the viscous sublayer region. In the region away from the wall, coarse triangle meshes were applied. The maximal total number of cells does not exceed two million. A typical mesh structure is given in Figure 2.

Simulation set up

The steady-state simulation of LBE flow and iron transfer was carried out by the CFD code Ansys FLUENT. Table 2 summarizes the main boundary conditions applied in the

TABLE 1 Geometrical characteristics of considered models.

Wall type	Total length (mm)	w	λ/d	Number of cavities
Rough	80	500 μm	2	80
		500 μm	4	40
		250 μm	2	160
		250 μm	4	80
		50 μm	2	800
		50 μm	4	400
Smooth	80	—	—	0

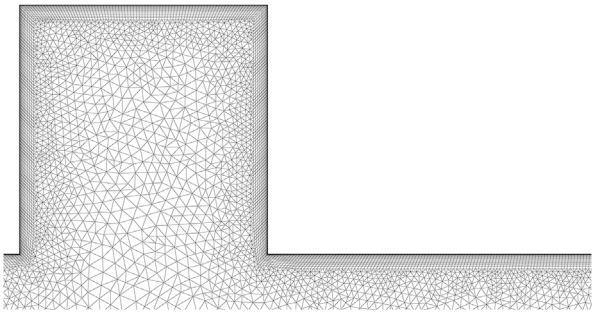

FIGURE 2
Mesh employed for computational domain (w = 500 μm, λ/d = 4).

Robertson's law (Abella et al., 2011; OECD, 2015). A mesh independent check was preliminarily performed in the smooth pipe geometry. The Figure 3 shows the radial distribution of iron concentration at pipe outlet under $Re = 5 \times 10^4$ for different meshes number. The convergence of the resolution is reached when the relative residuals are all below 10^{-7}.

Results and discussion

Iron mass transfer

The radial distributions of velocity at different positions near outlet are compared. In Figure 4, at distance of 70, 75, and 79 mm of

TABLE 2 Boundary conditions used in simulations.

Boundary	Boundary condition	Value
Inlet	Fluid velocity	0.07, 0.14, 0.25, 0.35, 0.53, 0.7, 1.05, 1.4 m/s
	Iron concentration	9.576×10^{-6} wt%
Central line of pipe	Axis-symmetry	—
Walls	Iron concentration	8.978×10^{-5} wt%
Outlet	Outflow	—

computation. In each model, the inlet bulk fluid velocity ranges from 0.07 to 1.4 m/s, correspondingly the Reynolds number ranges from 5×10^3 to 10^5. With an assumption that the oxygen concentration in LBE is sufficiently low, Fe_3O_4-based oxide film does not form at the metallic wall surface, so that LBE has direct contact with wall and the dissolution equilibrium of iron is established at wall. Thus, a constant iron concentration of 8.978×10^{-5} wt% is imposed at wall and the iron concentration in LBE bulk fluid is set as 9.576×10^{-6} wt% (Li, 2002). The viscosity of LBE adopted in calculation is 0.001402 kg/m.s, the density of LBE in simulation is 10130.2 kg/m^3 at 450°C, the molecular diffusion coefficient of iron in LBE at 450°C is 3.16×10^{-10} m^2/s, which is deduced through an extrapolation from the pipe, high consistency of the velocity profiles consist is observed respectively for smooth pipe and roughened pipe at $Re = 10^5$, which could verify the developed state of flow near outlet.

Since the mass transfer coefficient K is locally determined, a profile of K is obtained along the wall. The mass transfer coefficient of smooth wall K_s is the averaged value of K near the outlet. The mass transfer coefficient of rough wall K_r is the averaged value of K along the cavity walls and crest horizontal wall in a periodic length (see Figure 1). In addition, the mass transfer coefficient of the crest K_{cr} is the averaged value of K along the crest horizontal wall. The last periods of cavities in each roughness geometrical models are chosen in order to neglect the entrance effect of flow.

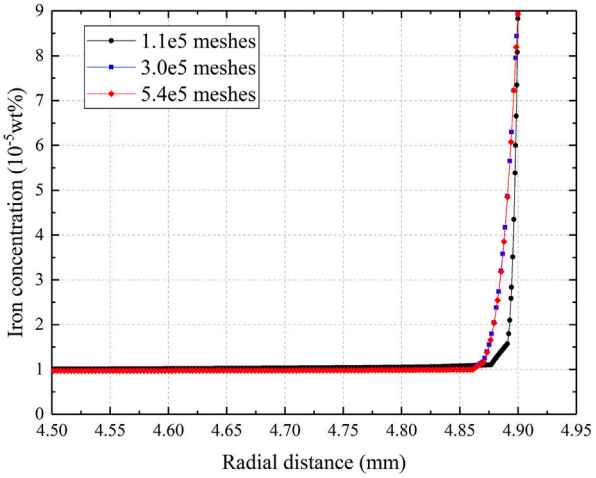

FIGURE 3
Radial distributions of iron concentration at $Re = 5 \times 10^4$ in mesh independent check.

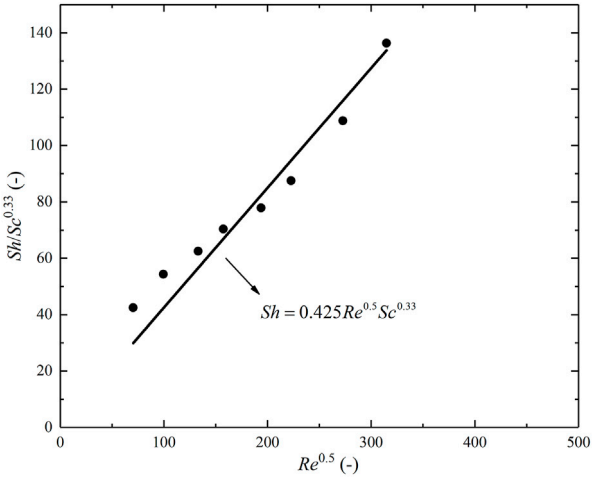

FIGURE 5
$Sh/Sc^{0.33}$ versus $Re^{0.5}$ for iron transfer on smooth wall (Re from 5×10^3 to 10^5).

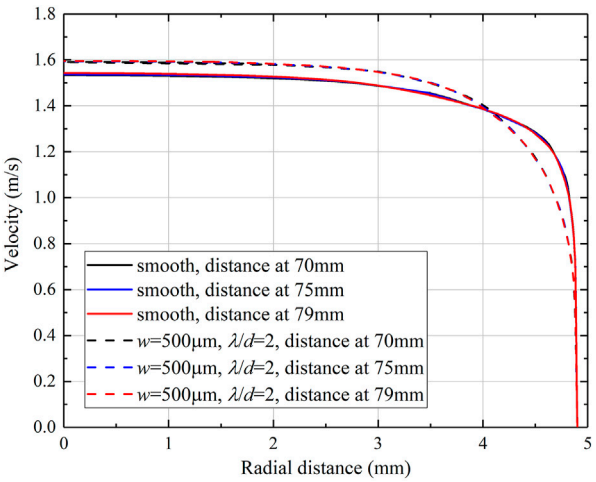

FIGURE 4
Radial distributions of velocity at distance of 70, 75, and 79 mm ($Re = 10^5$).

The results of mass transfer data Sherwood number Sh determined by predicted mass transfer coefficient are shown in Figure 5. Sh increased with a higher flow velocity, this is consistent with the fact that the diffusion boundary layer and viscous sublayer are thinner at high Re, therefore a higher near-wall concentration difference was formed and the mass transfer rate was enhanced. A higher corrosion rate could be observed for the flow at higher velocity. Berger and Hau (1977) have proposed a correlation for fully developed flow in smooth pipe where Re ranges from 8×10^3 to 2×10^5 and Sc varying from 1×10^3 and 6×10^3:

$$Sh = 0.165Re^{0.86}Sc^{0.33} \quad (15)$$

In previous mass transfer study, a relation between thickness of viscous sublayer δ_v and thickness of diffusion boundary layer δ_d was proposed (Levich, 1962; Nešić and Postlewaite, 1991):

$$\delta_d = \delta_v / \mathrm{Sc}^{0.33} \quad (16)$$

The diffusion boundary layer is much thinner than viscous sublayer. In this diffusion boundary layer, the mass transfer is dominated by molecular diffusivity, while out of this layer the mass transfer is dominated by turbulence in viscous region. In the correlation between Sh, Re and Sc, Re affects the viscous layer of flow, while the relation between δ_v and δ_d depends on Sc. For this reason, the variation of mass transfer is mainly impacted by Re. The factor $Sc^{0.33}$ in Eq. 16 is also verified by Wan and Saito (2018) in LBE pipe flow. Thus, we assume the same exponent value on Sc, which is the same approach as in Dawson and Trass (1972), Berger et al. (1979), and Postlethwaite and Lotz (1988), then the following correlation is obtained by regression:

$$Sh = 0.425Re^{0.5}Sc^{0.33} \quad (17)$$

The corrosion rate of smooth wall is also estimated and compared with experimental data which were reported by Wan and Saito (2018). The averaged corrosion depth of a 9.8 mm-diameter straight pipe under LBE flow at a velocity of 0.7 m/s ranges from 0.06–0.16 mm after 3,000 h operation. With the same flow condition, the predicted corrosion depth calculated by Eqs 3, 4 is about 0.22 mm, which is near 1.4 to 3.6 times of the measured value. This discrepancy may be caused by the varying surface condition of the pipe during operation and the assumption of saturated solute concentration at solid-fluid interface.

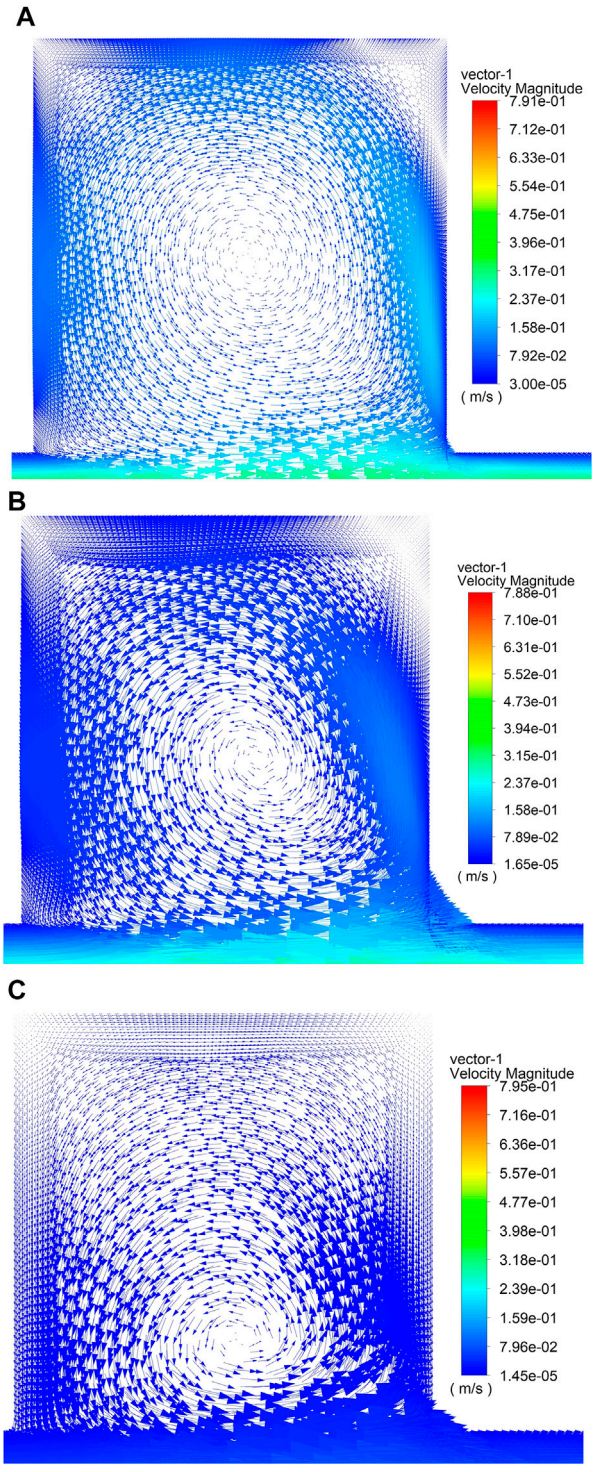

FIGURE 6
Velocity field in cavity for λ/d = 4 at Re = 5 × 10^4 **(A)** w = 500 μm; **(B)** w = 250 μm; **(C)** w = 50 μm.

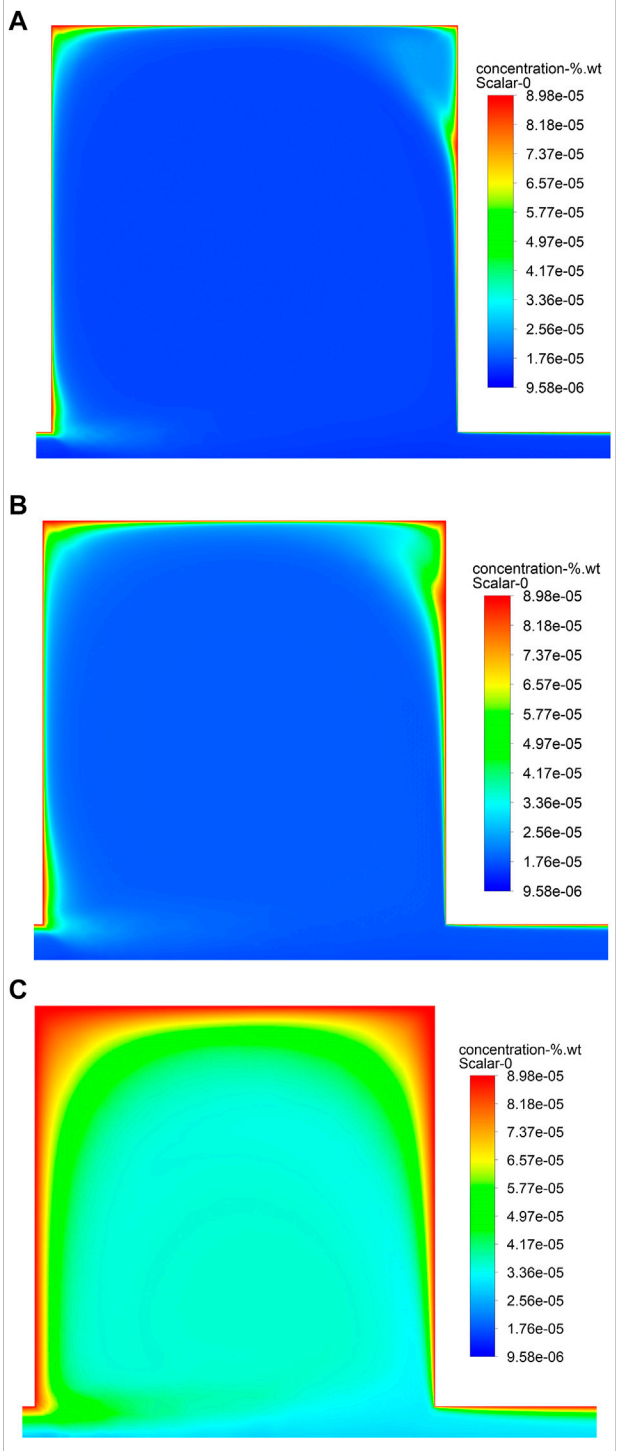

FIGURE 7
Iron concentration distribution in cavity for λ/d = 4 at Re = 5 × 10^4 **(A)** w = 500 μm; **(B)** w = 250 μm; **(C)** w = 50 μm.

Iron mass transfer from roughened walls is different compared to smooth wall, since the near-wall velocity field can be affected by the rough wall. The results show that stagnant flow is formed in cavities. Figure 6 gives the flow velocity fields in cavities under different roughness at Re = 5 × 10^4 and Figure 7 gives the corresponding iron concentration distributions. Given the same inlet condition, the

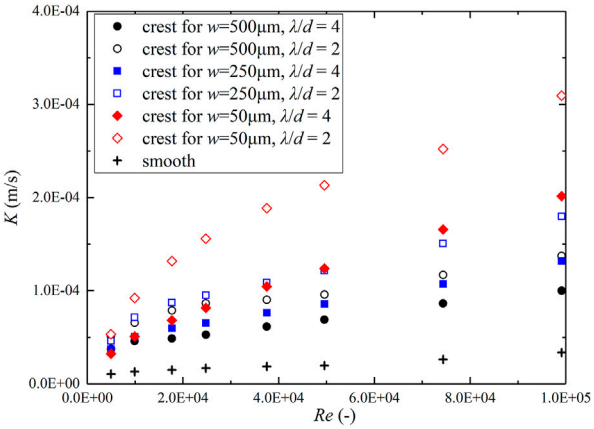

FIGURE 8
Mass transfer coefficient on crest wall and smooth wall, *Re* from 5×10^3 to 10^5.

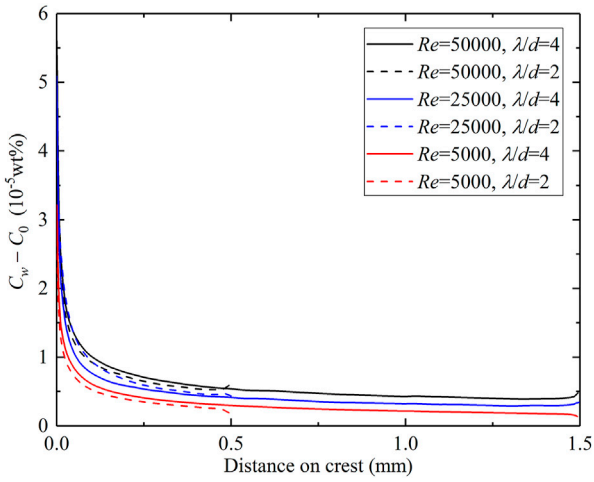

FIGURE 9
Distribution of (C_w–C_0) on the crest wall (d = 500 μm).

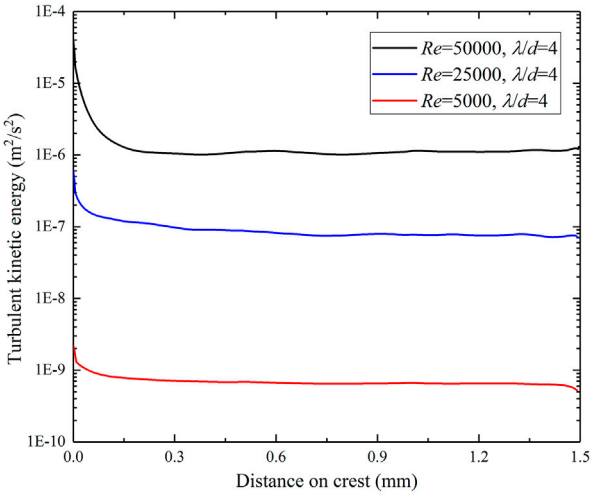

FIGURE 10
Distribution of turbulent kinetic energy on the crest wall (d = 500 μm).

velocity magnitude in cavity decreased as the size of cavity decreased, resulting in the increased near-wall concentration, which led to weaker transfer of iron from cavity wall to LBE bulk fluid. Similar results were observed at different Reynolds numbers as well.

The size of the crest can impose influence on the iron transfer at crest wall since it is depended by the distribution of K along the crest wall. The averaged coefficient K_{cr} of each rough geometry are given in case of *Re* from 5×10^3 to 10^5 in Figure 8, and are compared with K_s of smooth wall. It is shown that, as the flow velocity increased, K_{cr} increased obviously and the values are much greater than K_s. At the same ratio of λ/d, value of K_{cr} is larger as the cavity has a smaller size. For the same cavity size, value of K_{cr} is smaller with higher ratio of λ/d, which represents a longer crest.

The distribution of concentration at the first node, C_0, along the crest wall depends not only on the flow velocity, but also on the crest length. Figure 9 gives the distributions of (C_w–C_0) along the crest walls for d = 500 μm and for Re = 5×10^3, 2.5×10^4 and 5×10^4. At the same *Re*, compared with the relatively uniform distribution in the case of the smooth pipe, C_0 has much lower values at the front of the crest wall, while it increases along the crest, then it stays very close to C_w until the end of the crest wall. This distribution is similar to that of the entrance part of the smooth pipe wall. Hence, higher local mass transfer coefficients K are obtained at the front of crest wall. However, when λ/d = 4, which represents the horizontal length of crest is three times of that of λ/d = 2, K remains at a low level at the end of crest wall, so the average coefficient K_{cr} owns a lower value. The distributions of turbulent kinetic energy at the first node along the crest are given in Figure 10, for d = 500 μm and for *Re* = 5×10^3, 2.5×10^4, and 5×10^4. It is shown that, higher values of turbulent kinetic energy are obtained at higher flow velocities, the turbulent kinetic energy decreases from the front part of crest wall and then keeps at a stable level until the end of crest wall. It could be observed that the turbulent kinetic profiles are similar to those of (C_w–C_0), thus it is reasonable to relate the near-wall mass transfer rate to the near-wall turbulence level.

By calculating the mass transfer coefficients along the cavity walls and crest wall, the averaged coefficient K_r on a periodic length λ is determined for each rough geometry. The obtained Sherwood number for roughened walls Sh_r are correlated with *Sc* and *Re* by Eq. 5, which is shown in Figure 11. Assuming that the

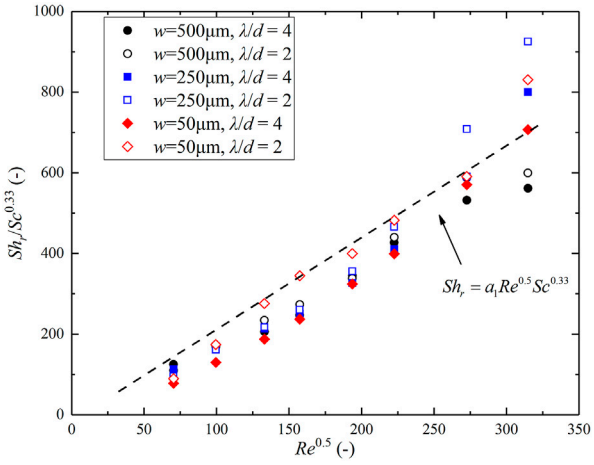

FIGURE 11
$Sh_r/Sc^{0.33}$ versus $Re^{0.5}$ for iron transfer, Re from 5×10^3 to 10^5.

correlation expression for Sh_r has the same exponent values on Re and Sc as in Eq. 16, Table 3 gives the correlative coefficient a for different cases. The value of a ranges from 1.810 to 2.357 for the correlations, which is thought to be a geometry-dependent coefficient for mass transfer in this study.

Effect of surface roughness

The mass transfer enhancement phenomenon caused by the roughen walls was described by the rough-to-smooth ratio K_r/K_s. The values of K_r/K_s for iron mass transfer in LBE are plotted against the dimensionless roughness number e^+ in Figure 12. At $Sc = 438$, for each rough geometry, K_r/K_s increased from near two to approximately six as e^+ increased. It should be noticed that for the same rough geometry, the increase of e^+ is due to the rise of flow velocity. Hence, K_r/K_s has low dependence on e^+ but has great dependence on the flow velocity. In previous reported researches, the mass transfer similarity functions have been developed and K_r/K_s was characterized under different roughness regimes depending on e^+ (Dawson and Trass, 1972; Postlethwaite and Lotz, 1988). However, the same approach cannot be adopted to analyze the results in this study, more parameters are required to characterize K_r/K_s. The difference between the results in previous studies and in this study can be explained from several aspects. First, the properties of fluid are involved in the definition of e^+, which could induce a great different range of e^+. Secondly, the Schmidt number characterizes the mass transfer properties of the species in fluid, the value is relatively much lower in this study comparing with Sc = 2,000–5,000 in previous reported researches. Moreover, in this study, K_r are determined by averaging the values along the cavity wall and crest wall in a roughness period, which is quite different from the electrochemical method.

In previous sections, the dimension and geometry of the crest and cavity are found to have considerable influence on C_0. The value of K_r is actually dominated by the value of K_{cr}. For this reason, a correlation of K_r/K_s is proposed with the following parameters: dimensionless roughness number e^+, Reynolds number Re and the geometrical ratio $(\lambda\text{-}d)/\lambda$:

$$\frac{K_r}{K_s} = b_1 + b_2 (e^+)^{b_3} Re^{b_4} \left(\frac{\lambda - d}{\lambda}\right)^{b_5} \tag{18}$$

In the correlation expression, the value of the first constant b_1 is one since it is the asymptotic value of K_r/K_s as e^+ and Re tend to zero, which means that the mass transfer behavior on rough walls is similar to that of smooth wall. The values of K_r/K_s are plotted by using Eq. 18 in Figure 13, fitting values of correlative constants in Eq. 18 are obtained with a deviation within 4%. Thus, the mass transfer enhancement is well correlated for Re ranging from 5×10^3 to 10^5:

$$\frac{K_r}{K_s} = 1 + 0.0117 (e^+)^{0.1} Re^{0.5} \left(\frac{\lambda - d}{\lambda}\right)^{0.1} \tag{19}$$

The exponent values on e^+ and Re are, respectively 0.1 and 0.5, which is consistent with the results that e^+ has less contribution while the flow velocity has higher contribution on K_r/K_s. To a certain degree, the mass transfer enhancement is also affected by the geometrical ratio of the crest. The effect of Sc is not included in the correlation since all predicted results are obtained at the same Sc = 438.

TABLE 3 Values of coefficient a in correlations for different roughness walls.

Cavity width w (μm)	Ratio λ/d	Number of cavities	Value of coefficient a_1	Value of R^2
500	2	80	1.924	0.993
500	4	40	1.810	0.995
250	2	160	2.357	0.950
250	4	80	2.075	0.965
50	2	800	2.271	0.983
50	4	400	1.920	0.970

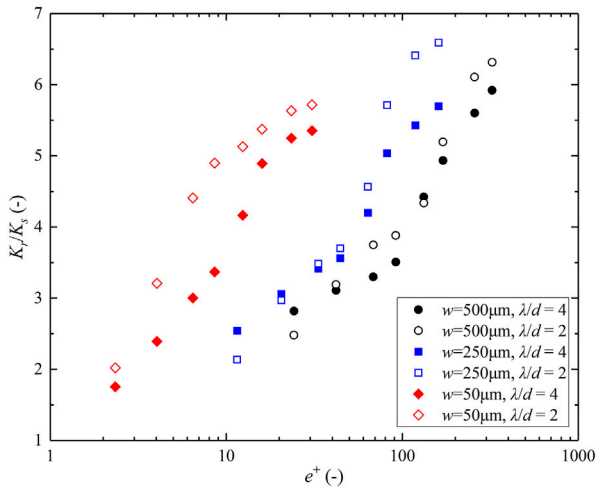

FIGURE 12
K_r/K_s versus e^+, Re from 5×10^3 to 10^5.

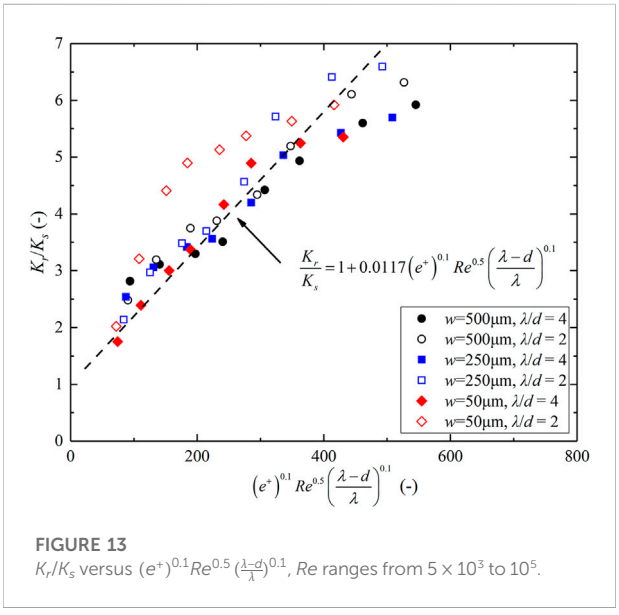

FIGURE 13
K_r/K_s versus $(e^+)^{0.1}Re^{0.5}\left(\frac{\lambda-d}{\lambda}\right)^{0.1}$, Re ranges from 5×10^3 to 10^5.

Conclusion

The Iron mass transfer on roughened walls in LBE turbulent pipe flow is studied by using CFD code. Steady-state simulations are performed with the LRN k-ε model. Based on the simulation results, the following main conclusion can be drawn:

(1) The mass transfer coefficient of iron from wall to LBE bulk fluid depends on the distribution of the near-wall iron concentration, which is highly affected by the near-wall flow velocity magnitude. Higher flow velocity induces higher mass transfer rate from the wall to fluid.

(2) Under the same Re condition, the local mass transfer is strongly affected by the roughness dimension. The mass transfer rate in the cavity of smaller size is lower due to the relatively lower velocity magnitude, while the mass transfer rate at crest wall has higher value when the crest length is shorter. The averaged mass coefficient K_r is dominated by the value K_{cr}, which has higher value than K_s.

(3) Based on the predicted results, mass transfer correlations relating Sh, Re and Sc are established both for smooth wall and roughened walls at $Sc = 438$ and Re ranging from 5×10^3 to 10^5. The mass transfer enhancement induced by roughened wall is confirmed through the computed data.

(4) The ratio K_r/K_s ranges from about 2 to 6, effects of different parameters on K_r/K_s are analyzed. A correlation is proposed and it indicates that the mass transfer enhancement has a higher dependence on Reynolds number than the dimensionless roughness number. The effect of the geometrical ratio of the crest is also included.

Further work is still needed to make progress in understanding the iron mass transfer in steel dissolution/corrosion phenomenon in LBE flow. Other factors, such as roughness types (k-type, V-grooved, and irregular roughness), Schmidt numbers (which varies with LBE working temperature) could be included in further investigation. The method and results obtained in this work could provide some values for the future numerical investigations on steel corrosion in LBE.

Data availability statement

The original contributions presented in the study are included in the article/supplementary material, further inquiries can be directed to the corresponding author.

Author contributions

XC: Writing–original draft; methodology; investigation. TW: Concept; software; methodology; writing–review and editing.

Conflict of interest

Author TW was employed by the company Institute of Modern Physics, Chinese Academy of Sciences.

The remaining author declares that the research was conducted in the absence of any commercial or financial relationships that could be construed as a potential conflict of interest.

Publisher's note

References

Abella, J., Verdaguer, A., Colominas, S., Ginestar, K., and Martinelli, L. (2011). Fundamental data: Solubility of nickel and oxygen and diffusivity of iron and oxygen in molten LBE. *J. Nucl. Mater.*415 (3), 329–337. doi:10.1016/j.jnucmat.2011.04.036

Ballinger, R. G., and Lim, J. (2004). An overview of corrosion issues for the design and operation of high-temperature lead- and lead-bismuth-cooled reactor systems. *Nucl. Technol.*147 (3), 418–435. doi:10.13182/NT04-A3540

Barbier, F., Benamati, G., Fazio, C., and Rusanov, A. (2001). Compatibility tests of steels in flowing liquid lead-bismuth. *J. Nucl. Mat.* 295 (2-3), 149–156. doi:10.1016/S0022-3115(01)00570-0

Benamati, G., Gessi, A., and Zhang, P. (2006).Corrosion experiments in flowing LBE at 450˚C. *J. Nucl. Mater.*356 (1-3), 198–202. doi:10.1016/j.jnucmat.2006.05.035

Berger, F. P., and Hau, F. L. (1977). Mass transfer in turbulent pipe flow measured by the electrochemical method. *Int. J. Heat Mass Transf.*20 (11), 1185–1194. doi:10.1016/0017-9310(77)90127-2

Berger, F. P., Hau, K. F., and Hau, F. L. (1979). Local mass/heat transfer distribution on surfaces roughened with small square ribs. *Int. J. Heat Mass Transf.*22 (12), 1645–1656. doi:10.1016/0017-9310(79)90081-4

Chen, G., Ju, N., Lei, Y., Wang, D., Zhu, Q., and Li, T. (2019).Corrosion behavior of 410 stainless steel in flowing lead-bismuth eutectic alloy at 550 ˚C. *J. Nucl. Mater.*522, 168–183. doi:10.1016/j.jnucmat.2019.05.029

Chien, K. Y. (1982). Predictions of channel and boundary-layer flows with a low-Reynolds-number turbulence model. *AIAA J.*20 (1), 33–38. doi:10.2514/3.51043

Davis, C., and Frawley, P. (2009). Modelling of erosion-corrosion in practical geometries. *Corros. Sci.*51 (4), 769–775. doi:10.1016/j.corsci.2008.12.025

Dawson, D. W., and Trass, O. (1972). Mass transfer at rough surfaces. *Int. J. Heat Mass Transf.*15 (7), 1317–1336. doi:10.1016/0017-9310(72)90015-4

Del Giacco, M., Weisenburger, A., and Mueller, G. (2014). Fretting corrosion of steels for lead alloys cooled ADS. *J. Nucl. Mater.*450 (1-3), 225–236. doi:10.1016/j.jnucmat.2013.07.005

Doubková, A., Di Gabriele, F., Brabec, P., and Keilová, E. (2008). Corrosion behavior of steels in flowing lead-bismuth under abnormal conditions. *J. Nucl. Mater.*376 (3), 260–264. doi:10.1016/j.jnucmat.2008.02.033

Feng, W., Zhang, X., Cao, L., Wang, S., and Chen, H. (2021). Development of oxygen/corrosion product mass transfer model and oxidation-corrosion model in the lead-alloy cooled reactor core. *Corros. Sci.*190, 109708. doi:10.1016/j.corsci.2021.109708

Fujisawa, N., Uchiyama, K., and Yamagata, T. (2017). Mass transfer measurements on periodic roughness in a circular pipe and downstream of orifice. *Int. J. Heat Mass Transf.*105, 316–325. doi:10.1016/j.ijheatmasstransfer.2016.10.002

Fujisawa, N., Yamagata, T., and Nagasaki, T. (2020). Mass transfer behavior on sinusoidal wavy walls at different Reynolds numbers. *Int. Commun. Heat Mass Transf.*110, 104383. doi:10.1016/j.icheatmasstransfer.2019.104383

Gong, X., Short, M. P., Auger, T., Charalampopoulou, E., and Lambrinou, K. (2022). Environmental degradation of structural materials in liquid lead- and lead-bismuth eutectic-cooled reactors. *Prog. Mater. Sci.*126, 100920. doi:10.1016/j.pmatsci.2022.100920

Grifoll, F., Farriol, X., and Giralt, F. (1986). Mass transfer at smooth and rough surfaces in a circular Couette flow. *Int. J. Heat Mass Transf.*29 (12), 1911–1918. doi:10.1016/0017-9310(86)90009-8

Heinzel, A., Weisenburger, A., and Müller, G. (2014). Corrosion behavior of austenitic steels in liquid lead bismuth containing 10^{-6} wt% and 10^{-8} wt% oxygen at 400-500 ˚C. *J. Nucl. Mat.* 448 (1-3), 163–171. doi:10.1016/j.jnucmat.2014.01.046

Ikarashi, Y., Taguchi, S., Yamagata, T., and Fujisawa, N. (2017).Mass and momentum transfer characteristics in and downstream of 90˚ elbow. *Int. J. Heat Mass Transf.*107, 1085–1093. doi:10.1016/j.ijheatmasstransfer.2016.11.014

Ilinčev, G., Kárník, D., Paulovič, M., and Doubková, A. (2004).The impact of the composition of structural steels on their corrosion stability in liquid Pb-Bi at 500 and 400 ˚C with different oxygen concentrations. *J. Nucl. Mater.*335 (2), 210–216. doi:10.1016/j.jnucmat.2004.07.015

Ito, K., and Sakai, T. (2004). Oxygen diffusion analysis of lead-bismuth-cooled natural-circulation reactor. *J. Nucl. Sci. Technol.*41 (3), 252–259. doi:10.1080/18811248.2004.9715482

Jones, W. P., and Launder, B. E. (1972). The prediction of laminarization with a two-equation model of turbulence. *Int. J. Heat Mass Transf.*15 (2), 301–314. doi:10.1016/0017-9310(72)90076-2

Lam, C. K. G., and Bremhorst, K. (1981).A modified form of the k-ε model for predicting wall turbulence. *J. Fluids Eng.* 103 (3), 456–460. doi:10.1115/1.3240815

Lambrinou, K., Charalampopoulou, E., Van der Donck, T., Delville, R., and Schryvers, D. (2017).Dissolution corrosion of 316L austenitic stainless steels in contact with static liquid lead-bismuth eutectic (LBE) at 500 ˚C. *J. Nucl. Mater.*490, 9–27. doi:10.1016/j.jnucmat.2017.04.004

Launder, B. E., and Sharma, B. I. (1974). Application of the energy-dissipation model of turbulence to the calculation of flow near a spinning disc. *Lett. Heat Mass Transf.*1 (2), 131–137. doi:10.1016/0094-4548(74)90150-7

Levich, V. G. (1962). *Physicochemical hydrodynamics*. Prentice-Hall.

Li, N. (2002). Active control of oxygen in molten lead-bismuth eutectic systems to prevent steel corrosion and coolant contamination. *J. Nucl. Mater.*300 (1), 73–81. doi:10.1016/S0022-3115(01)00713-9

Lolja, S. A. (2005). Momentum and mass transfer on sandpaper-roughened surfaces in pipe flow. *Int. J. Heat Mass Transf.*48 (11), 2209–2218. doi:10.1016/j.ijheatmasstransfer.2004.12.030

Marino, A., Lim, J., Keijers, S., Deconinck, J., and Aerts, A. (2018). Numerical modeling of oxygen mass transfer in a wire wrapped fuel assembly under flowing lead bismuth eutectic. *J. Nucl. Mater.*506, 53–62. doi:10.1016/j.jnucmat.2017.12.017

Mobarak, A. A., Farag, H. A., and H.Sedahmed, G. H. (1997). Mass transfer in smooth and rough annular ducts under developing flow conditions. *J. Appl. Electrochem.* 27, 201–207. doi:10.1023/A:1018408125105

Nešić, S., Postlethwaite, J., and Bergstrom, D. J. (1992). Calculation of wall-mass transfer rates in separated aqueous flow using a low Reynolds number *k-ε* model. *Int. J. Heat. Mass Transf.* 35 (8), 1977–1985. doi:10.1016/0017-9310(92)90200-C

Nešić, S. (2006). Using computational fluid dynamics in combating erosion-corrosion. *Chem. Eng. Sci.*61 (12), 4086–4097. doi:10.1016/j.ces.2006.01.052

Nesõić, S., and Postlethwaite, J. (1991). Hydrodynamics of disturbed flow and erosion-corrosion. Part I - single-phase flow study. *Can. J. Chem. Eng.* 69 (3), 698–703. doi:10.1002/cjce.5450690311

OECD (2015). *Handbook on lead-bismuth eutectic alloy and lead properties, materials compatibility, thermal-hydraulics and technologies*. Paris, France No: OECD/NEA, 7268.

Postlethwaite, J., and Lotz, U. (1988). Mass transfer at erosion-corrosion roughened surfaces. *Can. J. Chem. Eng.* 66 (1), 75–78. doi:10.1002/cjce.5450660111

Poulson, B. (1999). Complexities in predicting erosion corrosion. *Wear* 233-235, 497–504. doi:10.1016/S0043-1648(99)00235-5

Poulson, B. (1990). Mass transfer from rough surfaces. *Corros. Sci.* 30 (6-7), 743–746. doi:10.1016/0010-938X(90)90037-6

Selman, J. R., and Tobias, C. W. (1978). Mass-transfer measurements by the limiting-current technique. *Adv. Chem. Eng.* 10, 211–318. doi:10.1016/S0065-2377(08)60134-9

Sookhak Lari, K. S., van Reeuwijk, M., and Maksimović, Č. (2013). The role of geometry in rough wall turbulent mass transfer. *Heat. Mass Transf.* 49, 1191–1203. doi:10.1007/s00231-013-1165-4

Tantirige, S. C., and Trass, O. (1984). Mass transfer at geometrically dissimilar rough surfaces. *Can. J. Chem. Eng.* 62 (4), 490–496. doi:10.1002/cjce.5450620407

Tsisar, V., Schroer, C., Wedemeyer, O., Skrypnik, A., and Konys, J. (2018).Effect of structural state and surface finishing on corrosion behavior of 1.4970 austenitic steel at 400 and 500 ˚C in flowing Pb-Bi eutectic with dissolved oxygen. *J. Nucl. Eng. Radiat. Sci.* 4 (4), 041001. doi:10.1115/1.4040422

Wan, T., and Saito, S. (2018). Flow-accelerated corrosion of type 316L stainless steel caused by turbulent lead-bismuth eutectic flow. *Metals* 8 (8), 627. doi:10.3390/met8080627

Yamagata, T., and Fujisawa, N. (2021). Experimental and numerical studies of flow field and mass transfer phenomena on sinusoidal wavy walls. *Heat. Mass Transf.* 57, 715–722. doi:10.1007/s00231-020-02975-x

Zhang, J. (2009). A review of steel corrosion by liquid lead and lead-bismuth. *Corros. Sci.*51 (6), 1207–1227. doi:10.1016/j.corsci.2009.03.013

Zhang, J., Hosemann, P., and Maloy, S. (2010). Models of liquid metal corrosion. *J. Nucl. Mater.*404 (1), 82–96. doi:10.1016/j.jnucmat.2010.05.024

Zhang, J. (2014). Lead-bismuth eutectic (LBE): A coolant candidate for gen. IV advanced nuclear reactor concepts. *Adv. Eng. Mat.* 16, 349–356. doi:10.1002/adem.201300296

Zhang, J., and Li, N. (2008). Review of the studies on fundamental issues in LBE corrosion. *J. Nucl. Mater.*373 (1-3), 351–377. doi:10.1016/j.jnucmat.2007.06.019

Zhang, Y., Zhang, D., Wang, C., Lan, Z., Tian, E., Su, G., et al. (2021). Oxygen transport analysis in lead-bismuth eutectic coolant for solid-phase oxygen control. *Ann. Nucl. Energy*154, 108128. doi:10.1016/j.anucene.2021.108128

Zhao, W., and Trass, O. (1997). Electrochemical mass transfer measurements in rough surface pipe flow: Geometrically similar V-shaped grooves. *Int. J. Heat Mass Transf.*40 (12), 2785–2797. doi:10.1016/S0017-9310(96)00346-8

Nomenclature

Abbreviations

a_1, a_2, a_3 correlative constants in correlation linking *Sh* to *Sc* and *Re*

b_1, b_2, b_3, b_4, b_5 correlative constants in correlation of K_r/K_s

C concentration in Fick's law, kmol/m^3

C_1, C_2, C_μ constants in transport equations of k and ε

C_b, C_w, C_0 species concentration in bulk fluid, at wall, and at the first node, kmol/m^3

d depth of cavity, m

D diameter of pipe, m

D_m molecular diffusion coefficient, m^2/s

D_ε damping term of turbulent dissipation rate, m^2/s^3

$\mathbf{e}$ roughness height, m

$\mathbf{e}^+$ dimensionless roughness height

f friction factor

f_1, f_2, f_μ damping functions in Launder-Sharma LRN model

J mass flux of iron, kmol/(m^2 s)

k turbulent kinetic energy, m^2/s^2

K mass transfer coefficient, m

l characteristic length, m

L Length of pipe, m

M molar mass of iron, kg/mol

n normal distance to wall in Fick's law, m

P_k production rate of turbulence, kg/(m s^3)

ΔP Pressure drop through the pipe, Pa

R radius of pipe, m

Re, Re_t Reynolds number and turbulent Reynolds number

Sc Schmidt number

Sh Sherwood number

t time, s

u, u_j velocity and its components in transport equation of ε^*, m/s

u^* friction velocity

U velocity of stream flow, m/s

w width of cavity, m

x_j Cartesian coordinates, m

y distance from the wall, m

y_0 distance of the first node from the wall, m

y^+ dimensionless distance from the wall

Greek symbols

δ_v, δ_d Thickness of viscous layer and diffusion boundary layer, m

ε, ε^* origin and modified dissipation rate of turbulent kinetic energy, m^2/s^3

λ periodic length of adjacent cavities, m

μ molecular dynamic viscosity, kg/(m s)

μ_t turbulent viscosity, kg/(m s)

ρ, ρ_{Fe} density of fluid and density of iron, kg/m^3

σ_k, σ_ε constants in transport equations of k and ε

Subscripts

cr crest of roughness

r rough wall

s smooth wall

frontiers | Frontiers in Energy Research

TYPE Original Research
PUBLISHED 16 September 2022
DOI 10.3389/fenrg.2022.961901

OPEN ACCESS

EDITED BY
Shripad T. Revankar,
Purdue University, United States

REVIEWED BY
Xiang Chai,
Shanghai Jiao Tong University, China
Tengfei Zhang,
Shanghai Jiao Tong University, China

*CORRESPONDENCE
Pengcheng Zhao,
zpc1030@mail.ustc.edu.cn

SPECIALTY SECTION
This article was submitted to Nuclear Energy,
a section of the journal
Frontiers in Energy Research

RECEIVED 05 June 2022
ACCEPTED 30 August 2022
PUBLISHED 16 September 2022

CITATION
Yi J, Ji N, Zhao P and Wu H (2022), Research on the method of predicting CEFR core thermal hydraulic parameters based on adaptive radial basis function neural network.
Front. Energy Res. 10:961901.
doi: 10.3389/fenrg.2022.961901

Research on the method of predicting CEFR core thermal hydraulic parameters based on adaptive radial basis function neural network

Jinhao Yi, Nan Ji, Pengcheng Zhao* and Hong Wu

School of Nuclear Science and Technology, University of South China, Hengyang, Hunan, China

Alterations in thermal hydraulic parameters directly affect the safety of reactors. Accurately predicting the trends of key thermal hydraulic parameters under various working conditions can greatly improve reactor safety, thereby effectively preventing the occurrence of nuclear power plant accidents. The thermal hydraulic characteristic parameters in the reactor are affected by many factors, in order to preliminarily study whose forecasting methods and determine the feasibility of neural network forecasting, the China Experimental Fast Reactor (CEFR) is selected as the research target in this study, and the maximum surface temperature of fuel rod sheath and mass flow rate are used as predictive variables. After data samples are generated through the reactor sub channel analysis code (named SUBCHANFLOW), two widely used adaptive neural networks are used to perform the thermal hydraulic parameter forecast analysis of CEFR fuel assembly under steady-state conditions. The 1/2 core model of CEFR is used to perform a single-step predictive analysis of thermal hydraulic parameters under transient conditions. The results show that the adaptive radial basis function (RBF) neural network exhibits a better fitting ability and higher forecasting accuracy than that of the adaptive back propagation neural network, and the maximum error under steady-state conditions is 0.5%. Under transient conditions, poor forecasting accuracy is observed for some local points; however, the adaptive RBF neural network is generally excellent at predicting temperature and mass flow. The mean relative error of temperature does not exceed 1%, and the mean relative error of flow does not exceed 6.5%. The proposed RBF neural network model can provide real-time forecasting in a short time under unstable flow conditions, and its forecasting results have a certain reference value.

KEYWORDS

radial basis function neural network arithmetic, adaptive gradient descent, fast reactor, thermal hydraulic parameters, forecasting

1 Introduction

Reactor thermal hydraulic parameters, such as the maximum fuel sheath surface temperature, are closely related to the economics and safety of nuclear power plants. Accurately predicting the change trend of key thermal hydraulic parameters of reactors under various working conditions in a short time can enable operators and nuclear power plant systems to respond in advance, significantly improve the reactor safety, and effectively prevent nuclear power plant accidents. However, during reactor operation, the key thermal hydraulic parameters are affected by multiple physical quantities simultaneously and their change trends are complex; thus, it is difficult for adaptive forecasting methods to achieve accurate forecasts in a short time. Therefore, for improving reactor security, it is vital to develop a new forecasting method for the key thermal hydraulic parameters of reactors.

Neural network is a mathematical model that simulates the behavioral characteristics of animal neurons for information processing. Owing to its nonlinear, large-scale, strong parallel processing ability, robustness, fault tolerance, and strong self-studying ability, it has been triumphantly applied in many domains, such as nonlinear function approximation, information classification, type recognition, information processing, image-processing, control and hitch diagnosis, financial forecast, time series forecasting (Liang and Wang, 2021). Since the 1990s, many studies have made use of various neural network arithmetics to forecast core parameters. Huang et al. (2003) made use of the back propagation (BP) artificial neural network to forecast the critical heat flux density of reactors. Compared with the traditional method, this method exhibits a high forecasting accuracy and is more convenient to update and use, thereby making it easier to adopt. Taking the 10 MW high temperature gas-cooled reactor into consideration, Li et al. (2003) monitored and analyzed the changes in various parameters of reactors under various faults by using an artificial neural network. Mohamedi et al. (2015) used a neural network to predict the effective multiplication factor Keff and peak fuel power Pmax of a light water reactor; their results indicate a high forecasting accuracy, while demonstrating that the neural network analysis method can largely cut down the time acquired for this optimization process. Peng et al. (2014) proposed that the normalized adaptive radial basis function (RBF) neural network arithmetic can be used for accurately reconstructing the axial power array of the core; they also studied the power array of the ACP-100 modular reactor. Their study also found that this technique exhibits sufficient robustness to overcome the intrinsic ill-posedness during power array reconstruction. However, most of the existing studies are based on the widely used BP neural network, and rarely involve other neural networks. Furthermore, most of the current research focuses on forecasting and analyzing steady-state parameters of reactors. However, there are few studies on the transient-state condition, which significantly affects reactor security; therefore, forecasting its change trends is more important. Based on the adaptive RBF neural network, this study forecasts the maximum surface temperature of the fuel sheath of a reactor under steady-state and transient-state conditions, compares the adaptive RBF neural network with the widely used adaptive BP neural network, and elucidates the adaptability of the adaptive RBF neural network for forecasting key parameters.

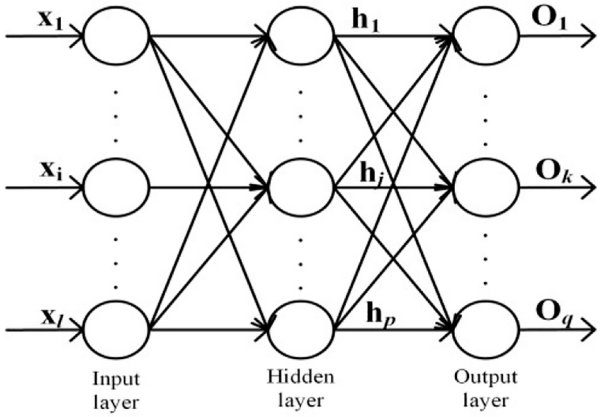

FIGURE 1
Structure of the 3-layer BP neural network.

2 Introduction of neural network model

2.1 Back propagation neural network

The traditional BP neural network is a feed forward neural network based on the error BP arithmetic (Huang et al., 2003). It simulates the reactive procedure of human brain neurons to external stimulus signals, constructs a multi-layer perceptron model, and adopts forward propagation and error backpropagation (Liang and Wang, 2021). Through multiple iterative studies, this neural network can describe numerous input-output pattern mappings without revealing their specific mathematical equations, and can successfully build an intelligent model for solving nonlinear data (Liang and Wang, 2021). As one of the mostly widely applied neural networks, its modeling process mainly includes forward transmission of information and error BP (Lyu et al., 2021). The traditional BP neural network has a simple construction and stable gradient descent. In theory, it can realize high-precision nonlinear fitting. Moreover, it can be utilized in the nonlinear function approach, time series forecasting, and other applications.

The traditional BP neural network is an arithmetic comprising an input layer, an output layer, and a hidden layer. The input and output layers are sufficiently connected, and there are no connections between neurons in the same layer (Li et al., 2003). Figure 1 shows the topology of a typical BP neural network. The input dimension is l, number of hidden layer nodes is p, and output dimension is q.

The traditional BP neural network is studied via a two-step procedure: forward propagation of signals and BP of signals (Huang et al., 2003). First, the input signal is transmitted through the input layer, hidden layer, and output layer (in that order) to complete the forward propagation of the signal. When the signal error of the output layer is larger than the anticipated error, the error BP process is performed. Second, the error values obtained via calculation are used to modify the weights of each layer one by one, and BP is carried out from the output layer to the hidden and input layers. Finally, through continuous forward propagation of signals and BP of errors, weights of each layer are continuously modified. This procedure is iterated until either the signal error of the output layer decreases to a tolerable level, or the predetermined number of iterations is reached.

According to the three-layer BP neural network method, the following presumptions are made: the input vector is $X = (x_1, x_2, ..., x_i, ..., x_l)^T$; output vector of the hidden layer is $H = (h_1, h_2, ..., h_j, ..., h_p)^T$; output vector is $O = (o_1, o_2, ..., o_k, ..., o_q)^T$; prospective output vector is $D = (d_1, d_2, ..., d_k, ..., d_q)^T$; weight matrix between the input layer and the hidden layer is $W = (W_1, W_2, ..., W_j, ..., W_p)$ (Li et al., 2003); weight matrix between the hidden layer and output layer is $V = (V_1, V_2, ..., V_k, ..., V_q)$; Wj is the weight vector consistent with the *j*th neuron in the hidden layer; and Vk is the weight vector consistent with the *k*th neuron in the output layer (Li et al., 2003).

2.1.1 Forward propagation of signals

The following equations are associated with the hidden layer:

$$net_j = \sum_{i=1}^{l} w_{ij} x_i, j = 1, 2, ..., p \tag{1}$$

$$h_j = f\left(net_j\right), j = 1, 2, ..., p \tag{2}$$

where netj is the input of the *j*th neuron in the hidden layer and f(x) is the transfer function.

The following equation is associated with the output layer:

$$o_k = \sum_{j=1}^{p} v_{jk} h_j, k = 1, 2, .., q \tag{3}$$

After using the transfer function f(x) as the bipolar sigmoid function, we obtain the following expression:

$$f(x) = \frac{2}{1 + e^{-2x}} - 1 \tag{4}$$

The derivative of this function is:

$$f'(x) = 1 - f^2(x) \tag{5}$$

2.1.2 Backward propagation of errors

The mean square error of the output is shown below:

$$E = \frac{1}{2}(D - O) = \frac{1}{2}\sum_{k=1}^{q}(d_k - o_k)^2 \tag{6}$$

By determining the gradient change of the loss function E with respect to each weight, the error is reversely transferred; this ensures that all the weights are adjusted in the direction in which the loss function E decreases the fastest. The loss function E can be continuously reduced, and the output constantly approaches the actual output value.

The network weight is updated as follows:

$$\Delta v_{jk} = -\eta \frac{\partial E}{\partial v_{jk}} = -\eta \frac{\partial E}{\partial o_k} \frac{\partial o_k}{\partial v_{jk}} = \eta (d_k - o_k) h_j \tag{7}$$

$$\Delta w_{ij} = -\eta \frac{\partial E}{\partial w_{ij}} = -\eta \frac{\partial E}{\partial h_j} \frac{\partial h_j}{\partial net_j} \frac{\partial net_j}{\partial w_{ij}} = \eta \left(\sum_{k=1}^{q} (d_k - o_k) v_{jk} \right) \left(1 - h_j^2\right) x_i \tag{8}$$

where η is the studying rate, which is a constant in the adaptive gradient descent method.

The structure of the traditional BP neural network is relatively simple, and the gradient descent is relatively stable (Wang et al., 2020). Theoretically, this network can achieve high precision nonlinear fitting, while exhibiting a certain application value for nonlinear function approximation, time series forecasting, and other approaches. However, the studying rate of the traditional BP neural network does not change once initialized, which makes it difficult to implement the correct studying process at minimum loss function values, thereby leading to a low convergence speed. Thus, the adaptive moment estimation (Adam) arithmetic (such as the adaptive BP neural network) has been used to improve the gradient descent method (Wang et al., 2020), which ensures that the studying rate can adapt to changes in the size of the loss function to improve the convergence speed.

The Adam arithmetic parameters are updated as follows:

$$\theta_{t+1} = \theta_t - \frac{lr_t}{\sqrt{v_t} + \epsilon} \overline{m_t} \tag{9}$$

where θ is any parameter; lr_t is the studying rate; ε is set as 10–8 to ensure that the division result is not 0; t is the number of iterations: $\bar{m}$ is the bias-corrected initial moment evaluation; and $\overline{v_t}$ is the bias-corrected second moment evaluation (Wang et al., 2020). Figure 2 indicates the calculation flow diagram of the neural network forecast method used in this study.

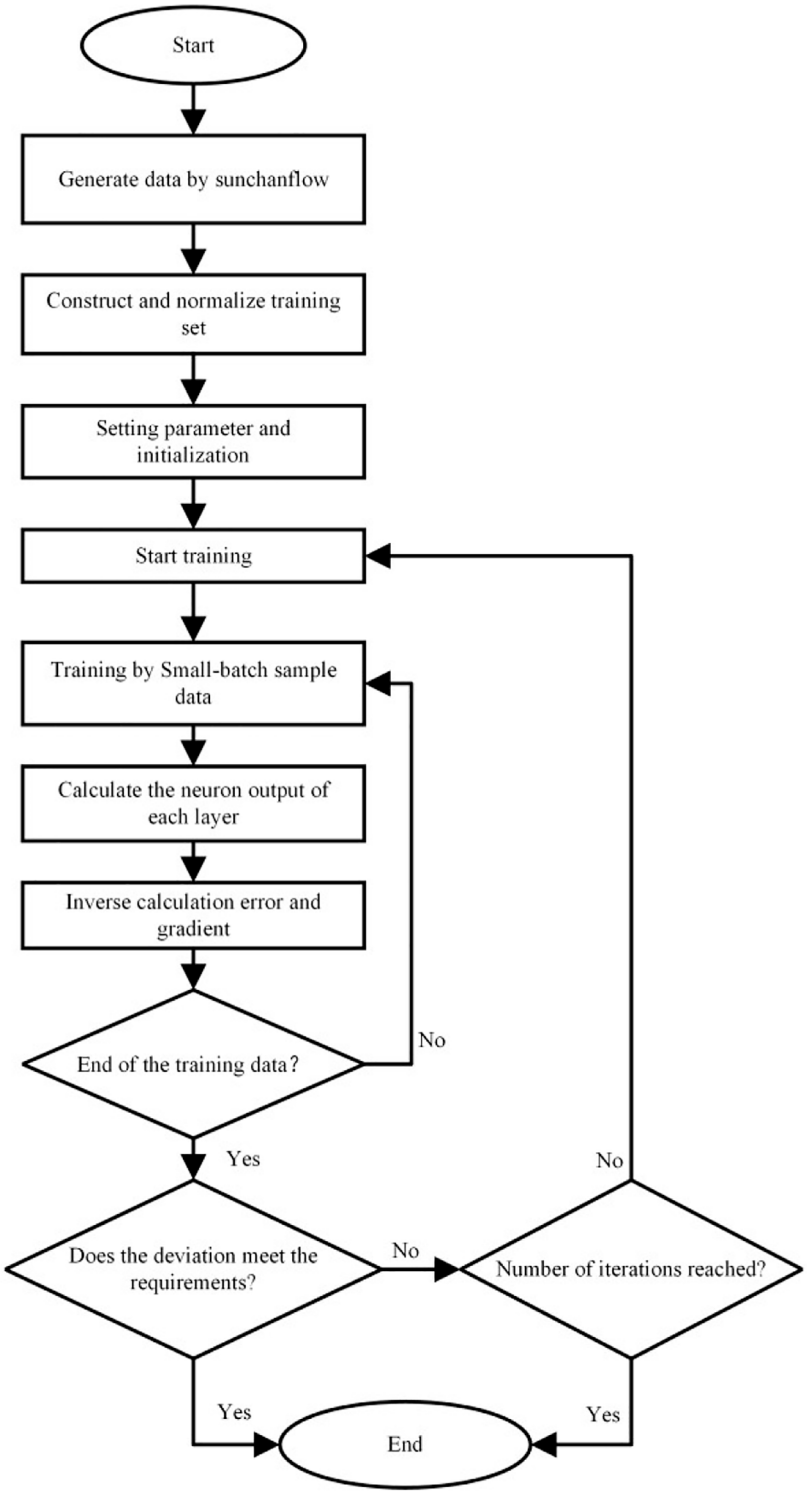

FIGURE 2
Flow-process diagram of neural network forecast model.

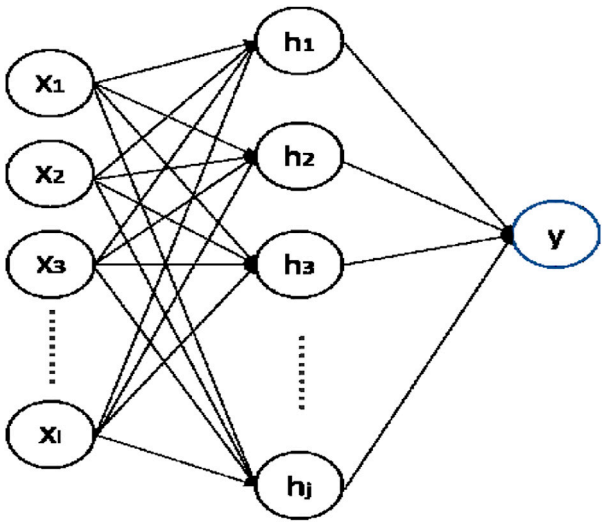

FIGURE 3
Structure of single output layer RBF neural network.

2.2 Adaptive radial basis function neural network

The generation of RBF neural network has a strong biological background. In human cerebral cortex, local regulation and overlapping receptive fields are the distinguishing features of human brain response. Based on the characteristics of receptive fields, Moody and Darken established a model, namely: RBF network.

The RBF neural network is a local approximate feed forward neural network, which can approach any nonlinear function. It exhibits an optimum generalization capability and a rapid convergence speed, even when dealing with mechanisms that are difficult to analyze in the system. One of the most commonly used in the RBF neural network is the Gaussian Kernel Function, which has the best forecasting performance compared to other kernel functions such as Linear Kernel Function and Polynomial Kernel Function (Lou et al., 2013). Compared with that of the BP neural network, the RBF neural network exhibits a faster convergence speed because it comprises only one middle hidden layer. The hidden layer considers the Euclidean distance as an independent variable between the input vector and central vector, while utilizing the Gaussian Kernel Function as the activation function, which can map the data to infinite dimensions. If the input is at a considerable distance from the middle of the activation function, the output value of the hidden layer tends to be significantly small. A real mapping effect is observed only when the Euclidean distance is negligible, thereby demonstrating local approximation. Poggio and Girosi have demonstrated that generalized RBF neural networks exhibit superior performance for continuous function approximation and has great noise immunity (Maruyama and Girosi, 1992). Currently, Gaussian radial basis neural networks is one of the most common RBF neural networks. The network construction and the RBF neural network arithmetic tend to differ in these neural networks, which overcomes the shortcomings that BP network is easy to fall into local optimal solution and its convergence speed is slow to a certain extent (Hong et al., 2021). Figure 3 shows the basic structure of single output layer RBF neural network.

In this work, the Gaussian kernel function is selected as the RBF, which is controlled by the central location and relevant width parameters. The width of the function unit controls the decline rate of the function. The output of the hidden layer is represented as:

$$h_j = \exp\left(-\frac{\|x - c_j\|^2}{2\sigma_j^2} \right), j = 1, 2, ..., p \tag{10}$$

$$y = \sum_{j=1}^{s} \omega_j * h_j \tag{11}$$

where $x - c_j$ is the Euclidean distance; $j$is the number of hidden layer nodes; c_j and σ_j are the central vector and distance of the jth node in the hidden layer, respectively; h_j is the output of the jth node in the hidden layer; $\omega_j$is the weight of the jth neuron; and y is the output of the network. In this article, these parameters are optimized using the Adam arithmetic.

The specific implementation steps of the generalized RBF neural network are similar to the BP neural network, that is, after a single training, the gradient descent method is used to iterate the weights of each neuron, when the termination condition is reached, the iteration is stopped and a group of optimal weights are obtained. The generalized RBF neural network also has the problem of constant learning rate in the iterative process. Therefore, this study has optimized the weight update method of the generalized RBF neural network through adaptive gradient descent method to obtain the adaptive RBF neural network arithmetic.

From the above analysis, it can be seen that the adaptive RBF neural network has better generalization capability and faster convergence speed than the adaptive BP neural network, which makes it have a better application prospect in nonlinear time series forecasting. In view of this, the performance of adaptive BP neural network and adaptive RBF neural network applied to steady-state and transient analysis of key thermal hydraulic parameters of reactor core is studied below.

3 Comparative analysis of different neural network models

For comparing the advantages and disadvantages of different adaptive neural network models, the maximum surface temperature of a fuel rod sheath of the China Experimental

TABLE 1 Main parameters of CEFR.

Parameters	Values	Parameters	Values
Rated thermal power	65 MW	Sheath thickness	0.3 mm
Outside distance across flats of the fuel assembly	59 mm	Outer/inner diameter of fuel pellets	5.2/1.6 mm
Wall thickness of wrapper tube	1.2 mm	Wire diameter	0.95 mm
Number of fuel rods	61	Wire pitch	100 mm
Height of active core	450 mm	Core inlet/outlet temperature	360/530°C
Fuel rod diameter	6.0 mm		

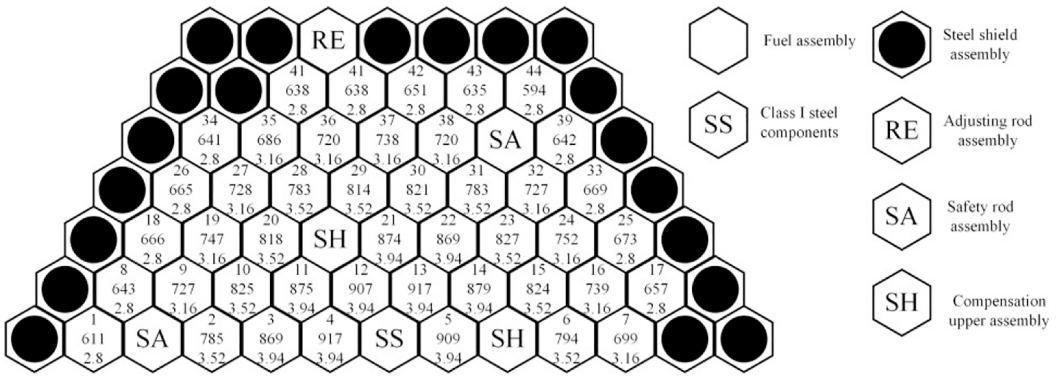

FIGURE 4
Distribution of channel number, power, and flow rate for analysis of the 1/2 core model.

Fast Reactor (CEFR) under different conditions is selected as the basis for comparison. The main dynamic thermal hydraulic parameters of CEFR are shown in Table 1. During the CEFR equilibrium cycle, the fuel power and reactor core flow rate of the fuel assembly are determined by referencing the CEFR safety analysis report. The specific values are shown in Figure 4, where the first line represents the sub channel number during the analysis of the 1/2 core model. The second line represents the power of the fuel assembly in kW, while the third line represents the coolant flow in kg/s.

3.1 Steady-state single assembly analysis

The normal operating state of reactors is steady-state condition. In that case, the boundary conditions such as inlet and outlet temperature and flow rate change little, in order to simplify the model, which can be approximately considered as unchanged. Studying the trends of key thermal hydraulic parameters under steady-state conditions can further improve the reactor safety and economy. For studying the forecasting performance of two neural networks under steady-state conditions, the core model of CEFR is used to perform steady-state analysis, which can be divided into three parts: acquisition of data samples, determination of network topology, and result and analysis.

3.1.1 Acquisition of data samples

The CEFR core is divided into four fuel zones, with 61 fuel rods in each assembly. Figure 5 shows the 126 sub channels obtained by using the SUBCHANFLOW code (Gomez et al., 2012) when building the CEFR single-assembly model.

According to the CEFR safety analysis report, the channel power and flow range of CEFR is 0–1,200 kW and 0–6 kg/s, respectively. Several datasets are arbitrarily selected, combined with the main parameters of CEFR in Table 1, and used as SUBCHANFLOW input. After calculations are performed by the code, 1,000 significant dataset samples are obtained.

The generalization capability of the adaptive BP neural network is relatively poor, and the most intuitive performance of the generalization capability is the overfitting and under fitting, both of which are two states in the neural network training process. At the beginning of the training, the error of the training set and the test set is relatively poor, and the entire

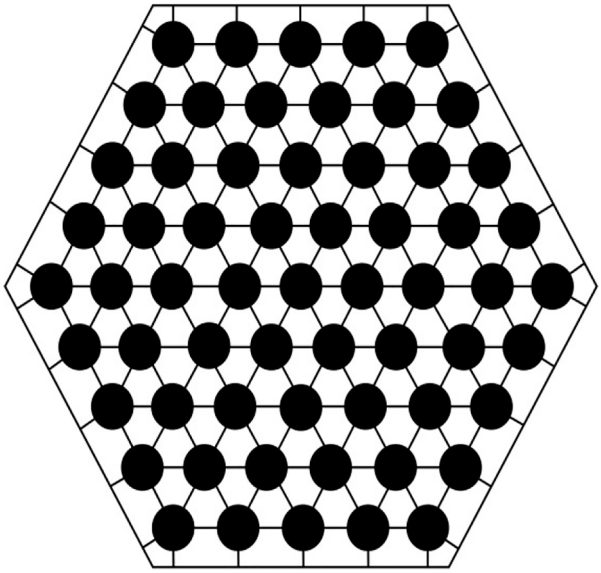

FIGURE 5
Number of coolant channels.

model is in the state of under fitting. With the increase of model complexity, the error of the training set and the test set will become smaller and smaller, the error of the test set will begin to rise after a certain demarcation point, and the entire model will enter the overfitting state. If the neural network training is stopped at the demarcation point, the generalization capability of the network will be best. Therefore, the generalization capability can be improved by introducing verification sets. Adding the validation set to the training network helps in determining the change in the forecast error at any time. When the error gradually decreases to the inflection point, the network training is stopped and the network weight can no longer be updated, which can avoid overfitting and under fitting of the model. Subsequently, the dataset is divided into two parts: training set (accounts for 80%) and the validation and test sets (account for 20%) (Yang et al., 2022); the number of samples in these two datasets is the same. Therefore, 800 datasets are randomly selected as the training samples, 100 are chosen as the verification samples, and the remaining 100 are used as the test samples. Since the adaptive RBF neural network exhibits optimum generalization capability and convergence speed, the training and test samples can be used directly in the ratio of 80 and 20%, respectively. Therefore, 800 datasets are stochastically chosen as the training samples, and the remaining 200 datasets are the test samples. The evaluation model is constructed by predicting the results of the test set. The training samples only participate in network training, and the test samples only participate in the forecasting process and result analysis. The training set is randomly disrupted before each training to avoid excessive recording of local features by the neural network.

3.1.2 Determination of network topology

The number of hidden layer nodes and hidden layers significantly affects the topology of neural networks. An excessive number of hidden layers tends to destabilize the network. An increasing trend in the number of hidden layers leads to an increased probability of local optimization in the training process. An excessive number of hidden layer nodes tends to affect the learning time of the network, while an extremely small number either leads to poor network learning or no learning at all. In addition, the number of hidden layer nodes and hidden layers is related to the generalization ability of the network (Li and He, 2006).

Nielson has theoretically proven that a neural network with one hidden layer can approach all functions that are continuous in a closed interval by changing the number of hidden layer nodes (Azghadi et al., 2007); consequently, a network with good performance can be obtained. Therefore, two different neural networks with a three-layer topology structure are chosen; that is, the number of hidden layers in these networks is one. The number of hidden layer nodes is continuously debugged by performing iterative calculations for each neural network, and the number of optimal hidden layer nodes in the final grid is determined using the grid error. The basic principle of selecting hidden layer nodes is that the overall degree of freedom of the network should equal the data samples; thus, every 10 nodes in the range of [20, 360] are selected as the current node number. This procedure is iterated 5,000 times, and the mean relative error associated with network forecasting is determined (Figure 6).

Figure 6 reveal that within the set number of nodes, the relative error of adaptive BP tends to increase as the number of nodes increases; the minimum number of nodes is 30. The change trend of the mean relative error of the adaptive RBF with the number of nodes is not obvious. Considering that the increase in the number of nodes will increase the amount of calculations, hidden layer nodes are selected to be 40.

3.1.3 Result and analysis

The adaptive BP neural network and the adaptive RBF neural network were used to repeat the experiment 10 times with the same datasets, and the mean values associated with the forecasting results of the test set were determined (Table 2).

MRE can reflect the degree of dispersion of data samples. The smaller the MRE, the higher the forecast accuracy. Maximum relative error can reflect the degree of maximum deviation from the actual value as well as the fitting ability of local data. By comparing the maximum relative error and MRE of the test sets of the two neural network arithmetics, it is determined that the MREs of both the test sets are less than 1%. A high forecasting accuracy implies that the maximum surface temperature of the

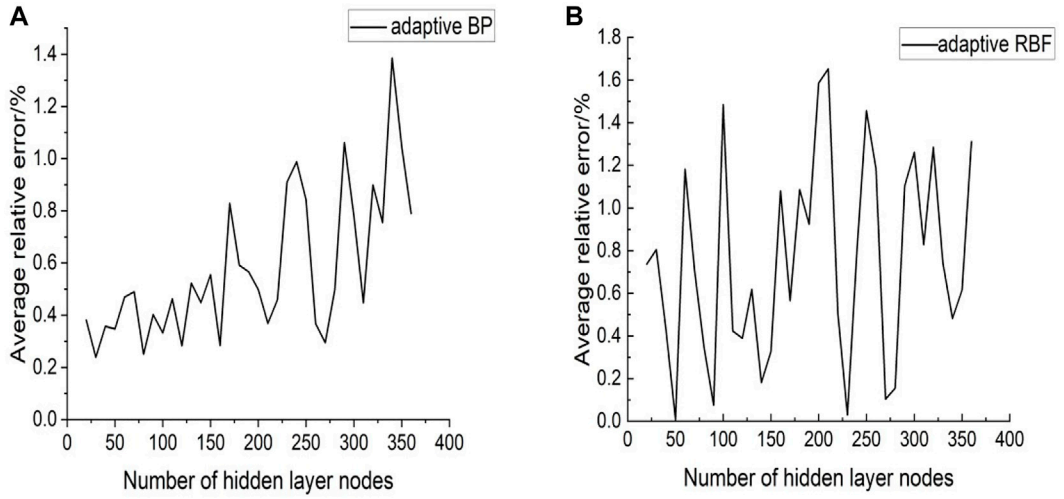

FIGURE 6
Number of hidden layer nodes-average relative error (A) adaptive BP, (B) adaptive RBF.

TABLE 2 Comparison of neural network forecast error.

Neural network arithmetic	MRE of test set/%	Maximum relative error of test set/%	Number of hidden layer nodes
Adaptive back propagation neural network	0.43	2.35	30
Adaptive radial basis function neural network	0.12	0.50	40

MRE: mean relative error.

fuel rod sheath can be better predicted. The MRE of the adaptive RBF neural network (less than 1%) is extremely similar to the MRE of the test set, indicating that the network has a good fitting effect for local points.

From the above results, it can be summarized that compared to the adaptive BP neural network arithmetic, the adaptive RBF neural network arithmetic exhibits a better forecasting ability for the maximum surface temperature of the fuel rod sheath in the fast reactor core. The reason is that in contrast to the adaptive BP neural network, the adaptive RBF neural network has better generalization capability, can approximate any complex nonlinear function with higher accuracy and obtain high-precision forecasting results for the input data, which shows that it has a good application prospect.

3.2 Transient full reactor analysis

The transient condition is that the coolant flow rate will change significantly with time due to accident working conditions or some reasons, and then other thermal hydraulic parameters of reactors will also change, among which flow instability has a significant impact on reactor safety under transient conditions, so studying the flow instability under the transient conditions is of great significance to the safe operation of reactors. The construction method of neural network under transient conditions is the same as that under steady-state conditions.

3.2.1 Acquisition of data samples

SUBCHANFLOW is used to construct the CEFR 1/2 core model. To reduce the number of calculations, the core sub channel is simplified. It is considered that the axial and radial power density distributions of all the fuel rods in the reactor core area are almost the same; thus, hypothetically combining all coolant channels leads to a bigger channel, whose center is located on the fuel rod with the relevant heating and wetting circumferences (Hu. 2019). For studying the forecasting performance of the neural network under flow instability, the flow change input into the CEFR 1/2 core model is set (Figure 7). This dataset comprises a sine signal and Gaussian white noise signal. Subsequently, the maximum temperature variation in the core fuel sheath is calculated (Figure 8).

Compared with the steady-state forecasting, the calculation and processing of sample data of transient forecasting will be more complex. To facilitate forecasting, the phase space

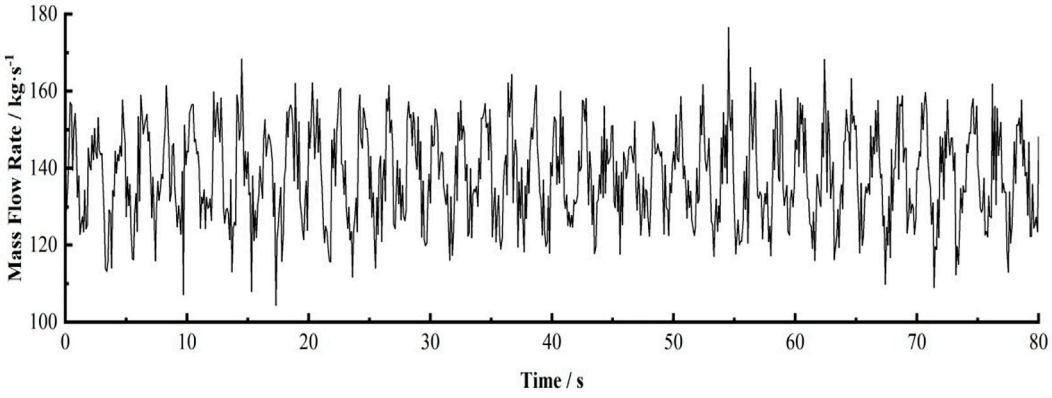

FIGURE 7
Variation in the core inlet flow.

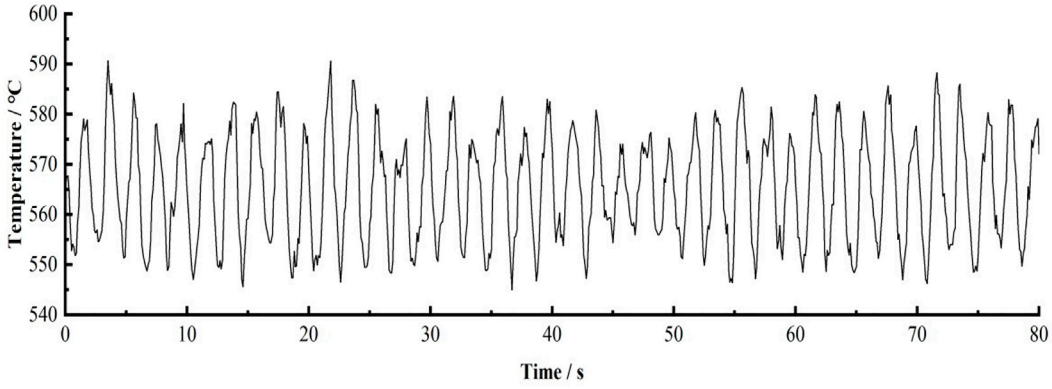

FIGURE 8
Variation in the maximum surface temperature of the fuel rod sheath.

reconstruction of the flow time series $f(i)$ and maximum temperature-time series of the sheath t(i) is carried out:

$$\begin{cases} F(i) = \left(f(i), f(i+\tau), f(i+2\tau), L, f(i+(\mathrm{m}-1)\tau)\right) \\ T(i) = \left(t(i), t(i+\tau), t(i+2\tau), L, t(i+(\mathrm{m}-1)\tau)\right) \end{cases} \tag{12}$$

$$\begin{bmatrix} F(1) \\ F(2) \\ . \\ . \\ . \\ F(\mathrm{n}) \end{bmatrix} = \begin{bmatrix} f(2+(m-1)\tau) \\ f(3+(m-1)\tau) \\ . \\ . \\ . \\ f(n+1+(m-1)\tau) \end{bmatrix} \tag{13}$$

The embedding dimension m is 30, and the time delay τ is 0.1. A total of 771 datasets were acquired by using the reconstructed core inlet flow vector $F(i)$ and highest shell temperature vector $T(i)$ as the input layer, and $F(i+\mathrm{m}\tau)$ and $T(i+\mathrm{m}\tau)$ as the output layer. The selection of each data set is consistent with the steady-state conditions. In the adaptive BP neural network, the number of training samples, verification samples, and test samples is 541, 115, and 115, respectively. In the adaptive RBF neural network, the number of training samples and test samples is 617 and 154, respectively. First of all, the neural network for forecasting mass flow rate is trained by Eq. (13), with the neural network input data on the left of the equal sign and the predictive data on the right, and then single-step and continuous forecasting are carried out on the test samples (the next input vectors are replaced by the existing forecasting results).

3.2 2 Analysis of results

The adaptive RBF neural network was used for single-step and continuous forecasting, and the forecasting results were compared with the test values. Figures 9, 10 show that when

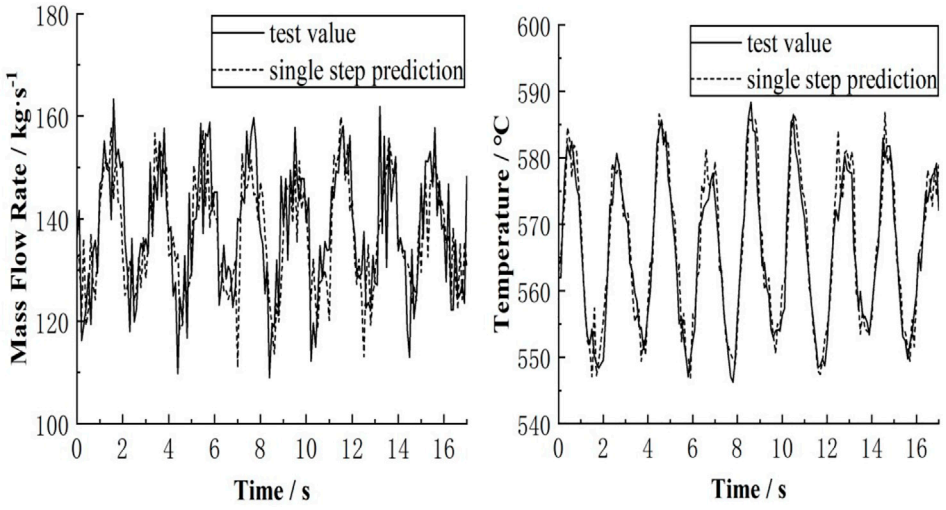

FIGURE 9
Contrast between the test samples and single-step forecasting results.

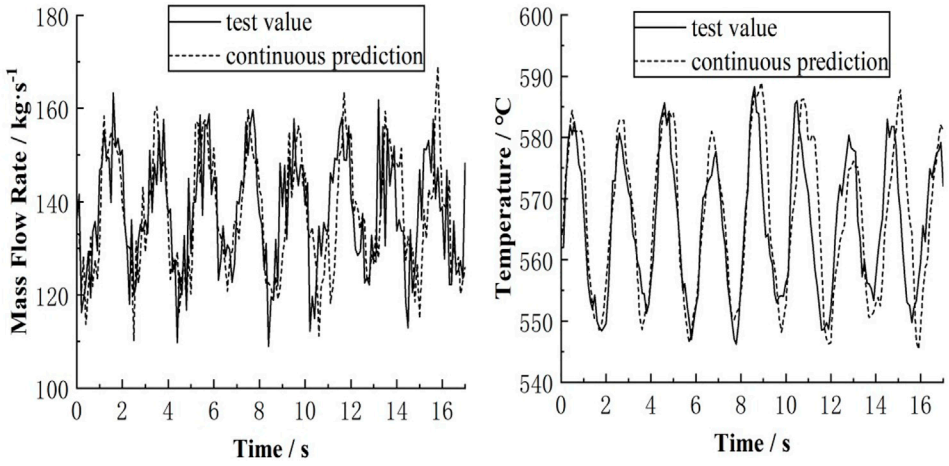

FIGURE 10
Contrast between the test samples and continuous forecasting results.

single-step forecasting is performed, the forecasting accuracy of the reactor core inlet flow is not as good as that of the maximum surface temperature of fuel sheath due to its large noise. The changes in the reactor core inlet flow can still be well controlled; however, in continuous forecasting, since the predictive value will be used as the input value for the next forecast, the error generated by each forecast will affect the next forecast. The predictive value of the core inlet flow is in perfect accordance with the measured value in the first 10 s (Figure 10). In the last 7 s, due to the accumulation of errors, there is a large offset between the predicted value and the measured value, as depicted by the peaks and troughs of the flow oscillation. The accuracy of long-term continuous forecasting is generally low; however, for a short term, the forecasting accuracy of the core inlet flow is higher.

In singe-step forecasting of the maximum surface temperature of fuel rod sheath, the predictive value is basically the same as the test value; thus, the forecasting accuracy is high. At 7 s, the forecast of the inlet flow of the core suffers a large deviation, leading to a poor forecasting accuracy is poor.

The above results show that for ensuring the accuracy of adaptive neural network prediction results, the time step

TABLE 3 Comparison of neural network forecasting results.

Predictive variables	Neural network arithmetic	MRE/%		Number of hidden layer nodes
		Single-step forecasts	Continuous forecasts	
Flow rate	Back propagation neural network	0.0578	0.0629	100
	Radial basis function neural network	0.0544	0.0592	300
Temperature	Back propagation neural network	0.0051	0.0113	100
	Radial basis function neural network	0.0047	0.0088	300

associated with continuous forecasting needs to be limited. Short-term continuous forecasting performed using the adaptive RBF neural network can accurately forecast the maximum surface temperature of the fuel rod sheath.

Single-step forecasting and continuous forecasting were performed using the adaptive BP neural network and the adaptive RBF neural network, and the forecasting results are listed in Table 3. Table 3 reveals that irrespective of using the adaptive BP neural network or adaptive RBF neural network, the error associated with single-step forecasts is smaller than that of continuous forecasts; however, for the core inlet flow, due to the noise produced by the adaptive RBF neural network, the MREs of single-step forecasting and continuous forecasting are high; there is little difference between the forecasts. The single-step forecasting error for the highest surface temperature of the fuel rod sheath is significantly smaller than the corresponding continuous forecasting error. Comparing the forecasting accuracy of the adaptive BP neural network and the adaptive RBF neural network, it is revealed that for forecasting the reactor core inlet flow and the maximum temperature of the fuel rod sheath, the adaptive RBF neural networks are superior to the adaptive BP neural networks; further, the MREs of single-step forecasting and continuous forecasting are less than those associated with the BP neural networks.

4 Conclusion

This study aimed to forecast the maximum surface temperature of the fuel rod sheath and the mass flow rate of CEFR under different working conditions. Consequently, different neural network arithmetics are analyzed and compared, and a forecasting method is established for steady-state and transient-state thermal hydraulic parameters of the adaptive RBF neural network model. The main conclusions are as follows:

1) By selecting the 1/2 core model of the CEFR fuel assembly as the research target, forecasting and analysis of the maximum surface temperature of fuel rod sheath under steady-state conditions were performed under the same core background values; the results were repeatedly verified. The results show that the forecasting accuracy of the adaptive RBF neural network is higher than that of the adaptive BP neural network, and its maximum error is 0.5%. Consequently, the adaptive RBF neural network arithmetic has a good application prospect for accurately forecasting the thermal hydraulic parameters of reactors under steady-state conditions.
2) Regardless of single-step or continuous forecasting, the adaptive RBF neural network exhibits a better forecasting accuracy than that of the adaptive BP neural network; however, due to the noise produced by the adaptive RBF neural network, forecasting for certain local points is poor. Nevertheless, the overall forecasting accuracy is good; the MRE associated with forecasting the maximum surface temperature of the fuel rod sheath is no more than 1%, and the MRE of the flow is no more than 6.5%. Therefore, the adaptive RBF neural network can provide reasonably accurate short-term forecasting results and maintain the accuracy under unstable flow conditions, which indicates that it has a good application prospect for real-time forecasting of reactor transients.
3) The adaptive RBF neural network can only complete continuous forecasting in a short time. In the forecasting of transient working conditions, the continuous forecasting error in a short time is acceptable, but with the increase of time, which will become larger because the continuous forecasting error is the superposition of multiple single-step forecasting errors. To solve this problem, further research is needed to improve the single-step forecasting accuracy of neural network; when studying the forecasting performance of the neural network under unstable flow conditions, we used the boundary condition of mass flow rate composed of a sine signal and Gaussian white noise signal. In that case, the transient forecasting accuracy of the adaptive RBF neural network is very good, but there are a large number of transient conditions in the reactor core. In order to further study the adaptability of the method for forecasting key thermal hydraulic parameters under transient conditions, it is necessary to carry out targeted research on different and more complicated boundary conditions.

Data availability statement

The original contributions presented in the study are included in the article/Supplementary Material, further inquiries can be directed to the corresponding author.

Author contributions

JY: analyze the results, writing-original draft preparation. NJ: design the program. PZ: supervision. HW: reviewing and editing.

Funding

This work is supported by the "Coupled Response Mechanism of Lead-based Fast Reactor Hot Pool and Cold Pool Thermal stratification under Asymmetric Thermal Load Condition and its Influence on Natural Circulation Performance" project of National Natural Science Foundation of China (Grant Nos. 11905101).

Acknowledgments

Thanks are due to all the reviewers who participated in the review and to MJEditor (www.mjeditor.com) for providing English editing services during the preparation of this manuscript.

Conflict of interest

The authors declare that the research was conducted in the absence of any commercial or financial relationships that could be construed as a potential conflict of interest.

Publisher's note

References

Azghadi, S., Bonyadi, M. R., and Shahhosseini, H. (2007). Gender classification based on FeedForward backpropagation neural network[J]. *Ifip Int. Fed. Inf. Process.* 96 (2), 299–304. doi:10.1007/978-0-387-74161-1_32

Gomez, A., Jger, W., and Sánchez, V. (2012). "On the influence of shape factors for CHF forecasts with SUBCHANFLOW during a rod ejection transient[C]," in International Topical Meeting on Nuclear Thermal-Hydraulics, Operation and Safety (NUTHOS-9), Taichung, Taiwan, September 4–9, 2022.

Hong, C., Huang, J., Guan, Y., and Ma, X. (2021). Combustion control of power station boiler by coupling BP/RBF neural network and fuzzy rules[J]. *J. Eng. Therm. Energy Power* 36 (4), 142–148. doi:10.16146/j.cnki.rndlgc.2021.04.021

Hu, P. (2019). *Study on multi-scale thermal-hydraulic coupling calculation method for reactor core[D]*. Harbin: Harbin Engineering University.

Huang, Y., Shan, J., Chen, B., Zhu, J., Lang, X., Jia, D., et al. (2003). Application of artificial neural networks in analysis of CHF experimental data in tubes[J]. *Chin. J. Nucl. Sci. Eng.* 23 (1), 45–51. doi:10.3321/j.issn:0258-0918.2003.01.008

Li, Hui, Wang, Ruipian, and Hu, Shouyin (2003). Application of artificial neural networks in fault diagnosis for 10MW high-temperature das-cooled reactor[J]. *Nucl. Power Eng.* 24 (6), 563–567. doi:10.3969/j.issn.0258-0926.2003.06.016

Li, Wulin, and He, Yujie (2006). The relationship between the number of hidden nodes and the computational complexity of BP network[J]. *J. Chengdu Inst. Inf. Eng.* (01), 70–73.

Liang, Xi, and Wang, Ruidong (2021). Optimization arithmetic of neural network structure based on adaptive genetic arithmetic[J]. *J. Harbin Univ. Sci. Technol.* 26 (1), 39–44. doi:10.15938/j.jhust.2021.01.006

Lou, jungang, Jiang, yunliang, Shen, qing, and Jiang, jianhui (2013). Evaluating the prediction performance of different kernal functions in kernel based software reliability models. *Chin. J. Comput.* 36 (06), 1303–1311. doi:10.3724/SP.J.1016.2013.01303

Lyu, Y., Zhou, Q. W., Li, Y. F., and Li, W. D. (2021). A predictive maintenance system for multi-granularity faults based on AdaBelief-BP neural network and fuzzy decision making. *Adv. Eng. Inf.* 49, 101318. doi:10.1016/j.aei.2021.101318

Maruyama, M., and Girosi, F., (1992). *A connection between GRBF and MLP[J]*. Boston, MA: laboratory massachusetts institute of technology.

Mohamedi, Brahim, Hanini, Salah, Ararem, Abdelrahmane, and Mellel, Nacim (2015). Simulation of nucleate boiling under ANSYS-FLUENT code by using RPI model coupling with artificial neural networks[J]. *Nucl. Sci. Tech.* 26 (04), 97–103. doi:10.13538/j.1001-8042/nst.26.040601

Peng, X., Ying, D., Qing, L. I., and Wang, K. (2014). Application of regularized radial basis function neural network in core axial power distribution reconstruction [J]. *Nucl. Power Eng.* 35 (S2), 12–15. doi:10.13832/j.jnpe.2014.S2.0012

Wang, D., Yang, H., Wang, D., Chao, L., and Wang, W. (2020). Research on adaptive BP neural network forecast method for thermal parameters of China experimental fast reactor[J]. *Atomic Energy Sci. Technol.* 54 (10), 1809–1816. doi:10.7538/yzk.2019.youxian.0751

Yang, Chenyi, he, Yuqing, Zhao, Junyuan, and Li, Guorong (2022). Lightweight neural network gesture recognition method for embedded platform[J]. *High Power Laser Paritricle Beams* 34 (03), 142–150.

frontiers | Frontiers in Energy Research

TYPE Original Research
PUBLISHED 26 September 2022
DOI 10.3389/fenrg.2022.973390

OPEN ACCESS

EDITED BY
Shripad T Revankar,
Purdue University, United States

REVIEWED BY
Jinbiao Xiong,
Shanghai Jiao Tong University, China
Pengcheng Zhao,
University of South China, China

*CORRESPONDENCE
Xianbao Yuan,
verona1206@163.com

SPECIALTY SECTION
This article was submitted to Nuclear Energy,
a section of the journal
Frontiers in Energy Research

RECEIVED 20 June 2022
ACCEPTED 01 September 2022
PUBLISHED 26 September 2022

CITATION
Guo Y, Zhang B, Yuan X, Du X, Zhang Y and Tan C (2022), Thermal-hydraulic characteristics in inner and outer wire-wrapped for a fast reactor annular fuel assembly.
Front. Energy Res. 10:973390.
doi: 10.3389/fenrg.2022.973390

Thermal-hydraulic characteristics in inner and outer wire-wrapped for a fast reactor annular fuel assembly

Yuefeng Guo[1,2], Binhang Zhang[1,2], Xianbao Yuan[1,2]*, Xiaochao Du[1,2], Yonghong Zhang[1,2] and Chao Tan[3]

[1]College of Mechanical and Power Engineering, China Three Gorges University, Yichang, China, [2]Hubei Key Laboratory of Hydroelectric Machinery Design and Maintenance, China Three Gorges University, Yichang, China, [3]China Nuclear Power Operation Technology Corporation Ltd, Wuhan, China

The annular fuel has dual-cooled surfaces internally and externally. Compared with traditional cylindrical fuel, the inner flow field is introduced on the annular fuel assembly, and wire-wrapped can influence the inner flow field. In order to research and compare the effect of wire-wrapped on the sub-channels and inner flow field of the fast reactor annular fuel assembly, thermal-hydraulic properties of the fast reactor annular fuel assembly with the inner and outer wire-wrapped are investigated in this research. The flow, heat transfer, and mechanical properties are analyzed, including temperature, transverse velocity, pressure drop, and thermal stress. The temperature of three sub-channels is the key that influences the temperature characteristics. The wire-wrapped reduces the coolant temperature gradient, flattens the coolant outlet temperature, and makes the coolant outlet temperature more uniform. The transverse velocity of coolant in the sub-channels is about three times that of in the inner flow field. From the perspective of the inner flow field, the increase in the number of wire-wrapped leads to an increase in transverse velocity. The number of wire-wrapped is not as good as possible from the perspective of sub-channels. The pressure drop of the sub-channels is larger than the pressure drop of the inner flow field. No matter the sub-channels or the inner flow field, the increase in the number of wire-wrapped will cause an increase in the pressure drop. The thermal-hydraulic properties of one inner and outer wire-wrapped are better than other models. The stress in the cladding is about 1.75 times the stress in the annular fuel rod, and the stress in the inner cladding is higher than that in the outer cladding. The research provides a reference for the optimization design of the fuel assembly.

KEYWORDS

annular fuel assembly, sodium-cooled fast reactor, inner and outer wire-wrapped, thermal stress, computational fluid dynamics

Introduction

Sodium-cooled fast reactors are one of the reactors selected by international forums for generation IV nuclear energy systems that can use nuclear energy efficiently. In sodium-cooled fast reactors fuel assemblies, helical wire-wrapped is widely used to promote coolant mixing and prevent mechanical vibration between the fuel assembly. Many experiments are mainly focused on the thermo-hydraulic properties of wire-wrapped. Some important correlations are also developed in the experiments. Novendstern (1972) developed a semi-empirical model that can predict the pressure loss for a turbulent region with wire-wrapped. Rehme (1973) introduced an effective velocity to take into account the helical flow velocity around the rods caused by the wire-wrapped. Engel et al. (2017) introduced the intermittency factor to correlate with a friction factor based on their experimental results. Cheng and Todreas (1986) developed their friction factor correlations with a complicated model and upgraded their correlations twice till now (Chen S. K. et al., 2018; Pacio et al., 2022). Choi et al. (2003)developed a series of water experiments using a helical wire-wrapped 19-pin fuel assembly and performed a comparative study of five existing correlations. Bertocchi et al. (2019) and Wang et al. (2020) conducted some experiments to study the cross-flow caused by the wire-wrapped using particle image velocimetry. Chun and Seo (2001), Pacio et al. (2016), Hou et al. (2019), and Liang et al. (2020)studied the flow and heat transfer characteristics with wire-wrapped along with different fuel bundles. The abovementioned experiments on wire-wrapped are based on cylindrical fuel bundles.

With the dramatic increase in computer performance, it is more efficient to use numerical simulation to study the characteristics of sodium-cooled fast reactors wire-wrapped. The CFD method has great potential in the study of detailed three-dimensional flow and heat transfer characteristics in wire-wrapped compared with the experimental method. Gajapathy et al. (2015) and Raj and Velusamy (2016) studied the characterization of velocity and temperature fields in a 217-pin wire-wrapped fuel bundle of a sodium-cooled fast reactor. Chen J. et al. (2018) and Bieder et al. (2021) invested the pressure loss and velocity distribution in a 217-pin wire-wrapped fuel bundle. Wang and Cheng (2018) and Song et al. (2019) analyzed the sweeping flow and vortex behavior in the 19-pin and 37-pin wire-wrapped fuel assembly for a sodium fast reactor. Thermal-hydraulic comparisons of 19-pin rod bundles with four circular- and trapezoid-shaped wire-wrapped were performed in Liu et al. (2017)'s research. All of the abovementioned researchers have conducted rich analyses of the wire-wrapped structure, which has great significance. The abovementioned research studies on wire-wrapped are all carried out on the basis of cylindrical fuel bundles, and the wire-wrapped is located in the sub-channels, which causes the change of the thermal-hydraulic properties in the sub-channels. Like pressurized water reactors, annular fuel assemblies are employed in the sodium-cooled fast reactors. It is possible to improve the overall performance of sodium-cooled fast reactors.

The annular fuel has been proposed as one of the options to achieve higher power density, larger safety margin, and reduced electricity generation cost (Feng et al., 2007; Lahoda et al., 2007). The annular fuel, mainly utilized in pressurized water reactors, is less adopted in generation IV reactors. The United States (Kazimi et al., 2006; El-Sahlamy et al., 2020), South Korea (Shin et al., 2012), Iran (Zaidabadi et al., 2017), and other countries have used annular fuel assembly for active pressurized water reactors, proving many advantages of the annular fuel assembly. Rowinski et al. (2015)described the innovative model of annular fuel design for lead-cooled fast reactors. Due to the introduction of the inner flow field, the research on the mechanical properties of annular fuel assembly is of great significance. Zhao et al. (2004), Kwon et al. (2013),and Xu et al. (2020) analyzed the mechanical properties, such as thermal stress and displacement of PWR with annular fuel assembly. The abovementioned studies on the annular fuel assembly are focused on the PWR without the effect of the wire-wrapped. There are few studies on the mechanical properties of Sodium-cooled fast reactor annular fuel assembly.

In this research study, the effects of the annular fuel assembly and wire-wrapped on the flow, heat transfer, and mechanical properties are considered together of the sodium-cooled fast reactor. Due to the introduction of the inner flow field, the thermal-hydraulic properties of the 7-pin annular fuel assembly with the inner and outer wire-wrapped are investigated in this research. It is a whole new way of wire-wrapped. The flow, heat transfer, and mechanical properties are analyzed, including temperature, transverse velocity, pressure drop, and thermal stress. This article is organized as follows. *Introduction* introduces the geometry, mesh, and boundary conditions. Model validation is introduced in *Introduction*. Analysis results and discussions include temperature field, flow field, pressure drop, and thermal stress performances, which are described in *Introduction*. Finally, the conclusion and future works are given in *Introduction*.

Computional models

The computational models of the annular fuel assembly with the inner and outer wire-wrapped for the Chinese Experimental Fast Reactor are developed in *Computational models*, which includes five parts, which are geometry models, mesh models, turbulence models, thermodynamic models, and boundary conditions.

Geometry models

The geometry models of the annular fuel assembly for the Chinese Experimental Fast Reactor (Cui et al., 2013) are established by 3D software based on the annular fuel assembly

TABLE 1 Geometric parameters.

Parameters	Symbol	Dimension
The number of the fuel bundle	N	7
Annular fuel inner diameter	D_1	4.4 mm
Annular fuel outer diameter	D_2	8 mm
Pitch of the annular fuel assembly	P	9 mm
Wire-wrapped diameter	D_w	0.95 mm
Helical pitch	H	100 mm
Annular fuel length	L	450 mm

design principles, and the geometric parameters are shown in Table 1. The models are created according to the difference between the number and position of the wire-wrapped. The solid domain and fluid domain of the geometry models are shown in Figures 1 and 2. In all models, the winding direction of the wire-wrapped is clockwise, and the winding angle at the outlet of the wire-wrapped is 30°. When the number of wire-wrapped is two, the winding angle at the outlet of the wire-wrapped is different by 180°.

Mesh models

The geometry models have been pre-processed by the design modeler. The geometry sharp angle is easily produced in the position where the connection between the wire-wrapped and the annular fuel rods, owing to the contraction in this location, is the line. In addition, it can cause an increase in the number of grids dramatically and a decrease in the quality easily. Both are moved toward each other by 0.05 mm in order to solve this problem. The effect of this treatment on the calculation can be ignored (Natesan et al., 2010). Fluent mesh is used to develop polyhedral mesh, and local meshes are refined around the wire-wrapped. The boundary layer is created at the contact surface between the fluid domain and the solid domain, and a high-quality mesh is obtained. Figure 3A shows the mesh for the thermal stress model at the outlet. Boundary layers are set where the solids and fluids are in contact. Table 2 depicts the number of grids of four cases in the five models. Figure 3B depicts the coolant average temperature in the interior sub-channel in different cases of the five models. The coolant average temperature in the interior sub-channel increases gradually with the increase of Z/Z_m. The maximum errors of the five models are 0.007%, 0.38%, 0.05%, 0.6%, and 0.41%, respectively. These errors are within acceptable limits. Finally, the cases with consistent grid sizes are selected. The number of grids for the five models is 2.31million, 1.04million, 1.28million, 3.73million, and 3.20million, respectively.

Governing equations and turbulent model

The equations that govern the steady-state sodium flow and heat transfer process in the annular fuel assembly are as follows.Continuity equation.

$$\frac{\partial(\rho u)}{\partial x}+\frac{\partial(\rho v)}{\partial y}+\frac{\partial(\rho w)}{\partial z}=0, \quad (1)$$

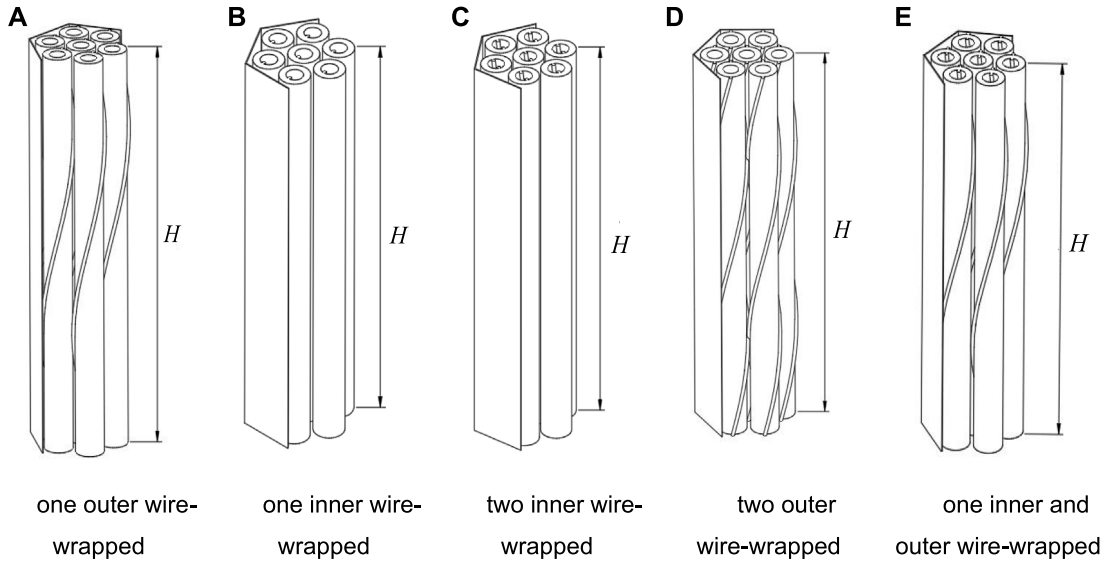

FIGURE 1
Geometry models (solid domain).

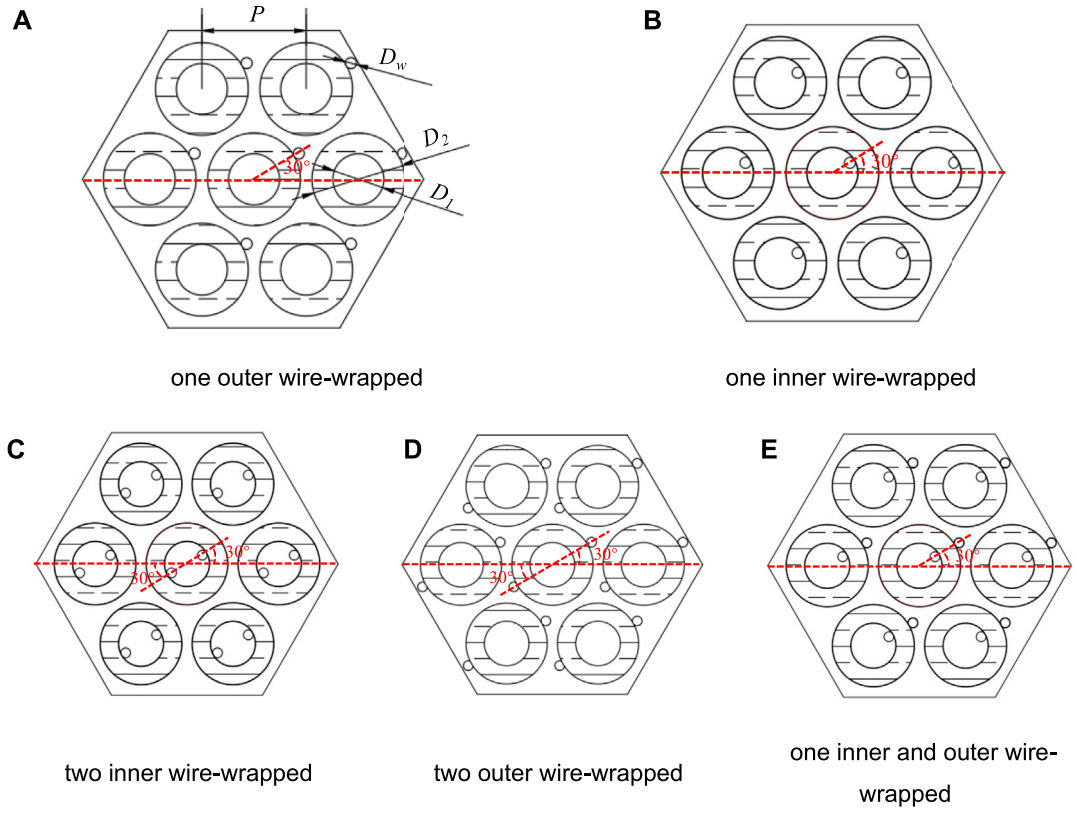

FIGURE 2
Geometry models (fluid domain).

where u, v, w is the velocity component of fluid in x, y, z directions, and ρ is the density of the coolant.Momentum equation.

$$\begin{cases} \frac{\partial(\rho uu)}{\partial x}+\frac{\partial(\rho vu)}{\partial y}+\frac{\partial(\rho wu)}{\partial z}=-\frac{\partial p}{\partial x}+\frac{\partial \tau_{xx}}{\partial x}+\frac{\partial \tau_{yx}}{\partial y}+\frac{\partial \tau_{zx}}{\partial z}+S_{Mx} \\ \frac{\partial(\rho uv)}{\partial x}+\frac{\partial(\rho vv)}{\partial y}+\frac{\partial(\rho wv)}{\partial z}=-\frac{\partial p}{\partial y}+\frac{\partial \tau_{xy}}{\partial x}+\frac{\partial \tau_{yy}}{\partial y}+\frac{\partial \tau_{zy}}{\partial z}+S_{My} \\ \frac{\partial(\rho uw)}{\partial x}+\frac{\partial(\rho vw)}{\partial y}+\frac{\partial(\rho ww)}{\partial z}=-\frac{\partial p}{\partial z}+\frac{\partial \tau_{xz}}{\partial x}+\frac{\partial \tau_{yz}}{\partial y}+\frac{\partial \tau_{zz}}{\partial z}+S_{Mz} \end{cases}, \tag{2}$$

where τ_{ij} is the component of the viscous stress, S_{Mx}, S_{My}, S_{Mz} is the momentum source term, and p is the pressure of the coolant.Energy equation.

$$\left(\frac{\partial(\rho uT)}{\partial x}+\frac{\partial(\rho vT)}{\partial y}+\frac{\partial(\rho wT)}{\partial z}\right)=\frac{\lambda}{C_p}\left(\frac{\partial^2 T}{\partial x^2}+\frac{\partial^2 T}{\partial y^2}+\frac{\partial^2 T}{\partial z^2}\right)+S_t, \tag{3}$$

where S_t is the viscous dissipation term, λ is the thermal conductivity of the coolant, T is the temperature of the coolant, and C_p is the heat capacity at constant pressure.

By solving the governing equations, the flow and heat transfer characteristics of the 7-pin annular fuel assembly with wire-wrapped are obtained in Table 3. The Standard k-ε model (Launder and Spalding, 1983), SST k-ω model (Menter, 1994), and Realizable k-ε model (Shih et al., 1995) are selected to compare the changes in the average temperature in the outlet of the interior sub-channel and pressure drop. The Y+ of the three turbulence models is 32.7 ≤ Y+≤76.4, Y+~1, 52.4 ≤ Y+≤72.8. The coolant temperature and pressure drop in different turbulence models are similar. The maximum error range is 5.1%, which is an acceptable range. The majority of wall Y+ cells are below 100, so the high Reynolds k, ε turbulence is well-adapted to represent the turbulence existing in the fluid domain. Moreover, the calculation time of the Standard k-ε model is shortest compared to the others. To sum up, the Standard k-ε model is selected as the turbulence model that can yield optimal results in terms of efficiency and accuracy.

As a double-equation model, the equation of turbulence dissipation rate is introduced based on the k equation. The double-equation is shown from Eqs. 4–7.

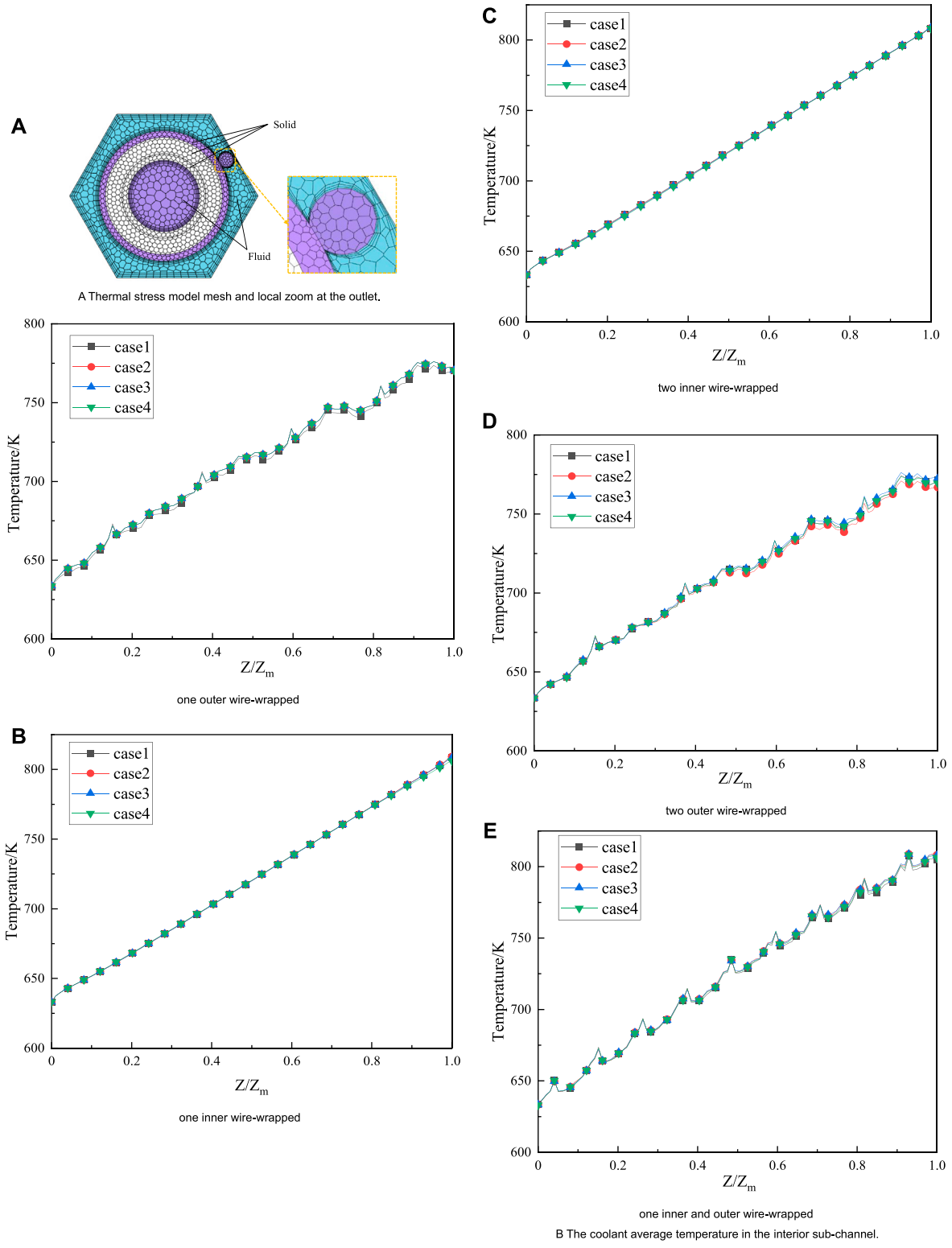

FIGURE 3
Mesh models and grid independence tests.

TABLE 2 Number of grids in different models (unit: million).

Model	Case1	Case2	Case3	Case4
One outer wire-wrapped	2.31	2.85	2.93	3.01
One inner wire-wrapped	0.95	0.98	1.00	1.04
Two inner wire-wrapped	1.28	1.30	1.33	1.36
Two outer wire-wrapped	2.84	3.05	3.58	3.73
One inner and outer wire-wrapped	2.10	2.30	3.20	3.24

$$\frac{\partial(\rho k u_i)}{\partial x_i} = \frac{\partial\left[\left(\mu + \frac{\mu_t}{\sigma_k}\right)\frac{\partial k}{\partial x_j}\right]}{\partial x_j} + 2\mu_t S_{ij} \cdot S_{ij} - \rho\varepsilon, \tag{4}$$

$$\frac{\partial(\rho\varepsilon u_i)}{\partial x_i} = \frac{\partial\left[\left(\mu + \frac{\mu_t}{\sigma_\varepsilon}\right)\frac{\partial k}{\partial x_j}\right]}{\partial x_j} + C_{2e}\frac{\varepsilon}{k}2\mu_t S_{ij} \cdot S_{ij} - C_{2e}\rho\frac{\varepsilon^2}{k}, \tag{5}$$

where

$$\mu_t = \rho C_\mu \frac{k^2}{\varepsilon}, \tag{6}$$

$$S_{ij} = \left(\frac{\partial u_i}{\partial x_j} + \frac{\partial u_j}{\partial x_i}\right), \tag{7}$$

where k is turbulent kinetic energy, ε is the rate of dissipation of turbulent kinetic energy, σ_k is the turbulent Prandtl number for k, σ_ε is the turbulent Prandtl number for ε, μ is molecular dynamic fluid viscosity, μ_t is turbulent viscosity, and S_{ij} is the rate of deformation. The coefficients of the Standard k-ε model are as follows: C_{1e} = 1.44, C_{2e} = 1.92, C_μ = 0.09, σ_k = 1.0, and σ_ε = 1.3.

Thermodynamic model

The annular fuel bundle is set in the condition of steady-state in this research. It is assumed that the physical parameters of the annular fuel bundle are constant and a uniform heat source is available. Then the equation of thermal conductivity can be simplified as Eq. (8).

$$\frac{\partial^2 T}{\partial x^2} + \frac{\partial^2 T}{\partial y^2} + \frac{\partial^2 T}{\partial z^2} + \frac{\Phi}{\lambda} = 0, \tag{8}$$

where T is the temperature of each part of the annular fuel, and Φ is the annular fuel heat source.

It is assumed that the material of the annular fuel bundle is uniform and homogeneous in calculating the thermal stress. The annular fuel bundle is approximated as an elastic object generating elastic strain because of the thermal stress with the following equations.

$$\begin{cases} \varepsilon_x = \frac{1}{E}\left[\sigma_x - \left(\eta\sigma_y + \sigma_z\right)\right] + \alpha T \\ \varepsilon_y = \frac{1}{E}\left[\sigma_y - \left(\eta\sigma_x + \sigma_z\right)\right] + \alpha T \\ \varepsilon_z = \frac{1}{E}\left[\sigma_z - \left(\eta\sigma_x + \sigma_y\right)\right] + \alpha T \\ \gamma_{yz} = \frac{2(1+\eta)}{E}\tau_{yz} \\ \gamma_{zx} = \frac{2(1+\eta)}{E}\tau_{zx} \\ \gamma_{xy} = \frac{2(1+\eta)}{E}\tau_{xy} \end{cases}, \tag{9}$$

where εx, εy, εz is the strain in x, y, z direction, E is Young's modulus, α is the thermal expansion coefficient, η is the Poisson's ratio, σ_x, σ_y, σ_z is the stress in x, y, z direction, γ is the shear strain, and τ is the shear stress.

Boundary conditions

Liquid sodium metal is the coolant for the sodium-cooled fast reactor. It is assumed that the physical parameters of the coolant are not constant, including density, thermal conductivity, heat capacity at constant pressure, and dynamic viscosity. the

TABLE 3 Flow and heat transfer characteristics with different turbulence models.

Models		Standard k-ε	SST k-ω	Realizable k-ε
Average temperature in the interior sub-channel/K	One outer wire-wrapped	770.45	764.04	766.19
	One inner wire-wrapped	808.17	809.03	809.31
	Two inner wire-wrapped	808.13	807.95	808.44
	Two outer wire-wrapped	804.84	803.17	804.14
	One inner and outer wire-wrapped	771.41	767.39	769.89
Pressure drop/Pa	One outer wire-wrapped	49574.96	48974.70	49406.41
	One inner wire-wrapped	35453.79	35963.91	36292.78
	Two inner wire-wrapped	34197.20	34396.63	32724.21
	Two outer wire-wrapped	61350.31	62068.14	63739.91
	One inner and outer wire-wrapped	49643.00	49046.96	49484.88

TABLE 4 The physical parameters of the fluid domain.

Physical parameters	Correlations
Density	$\rho = 16.0185 \times \left[\begin{array}{c} 59.566 - 7.9504 \times 10^{-3} (1.8t + 32) - 0.2872 \times 10^{-6} \\ (1.8t + 32)^2 + 0.603 \times 10^{-9} (1.8t + 32)^3 \end{array} \right]$
Thermal conductivity	$\lambda = 1.72958 \times \left[\begin{array}{c} 54.306 - 1.878 \times 10^{-2} (1.8t + 32) \\ +2.0914 \times 10^{-6} (1.8t + 32)^2 \end{array} \right]$
Heat capacity at constant pressure	$C_p = 4186.8 \times \left[\begin{array}{c} 0.389352 - 1.10599 \times 10^{-4} (1.8T) \\ +3.41178 \times 10^{-8} (1.8T)^2 \end{array} \right]$
Dynamic viscosity	$\mu = (0.1235 \pm 0.0018)\rho^{1/3} e^{\frac{(697 \pm 9)\rho}{T}}, T < 773K$
	$\mu = (0.0851 \pm 0.0013)\rho^{1/3} e^{\frac{(1040 \pm 19)\rho}{T}}, T \geq 773K$

TABLE 5 The physical parameters of the solid domain.

Solid domains	Physical parameters	Dimension
Cladding and wire-wrapped	Density	7,814 kg/m^3
	Thermal conductivity	19.47 W/(m·K)
	Heat capacity at constant pressure	550 J/(kg·K)
	Poisson's ratio	0.3
	Thermal expansion coefficient	1.8×10^{-5} 1/°C
	Young's modulus	1.8×10^{11} Pa
Annular fuel pellet	Density	10500 kg/m^3
	Thermal conductivity	4.5 W/(m·K)
	Teat capacity at constant pressure	300 J/(kg·K)
	Poisson's ratio	0.316
	Thermal expansion coefficient	1×10^{-5} 1/°C
	Young's modulus	1.42×10^{11} Pa

relationship with temperature is shown in Table 4 (Cui et al., 2013). These parameters are imported in the form of UDF. The solid part, which mainly includes an annular fuel pellet, inner and outer cladding, and wire-wrapped, and its thermal properties and mechanical parameters are shown in Table 5.

According to the parameters of the Chinese Experimental Fast Reactor, the coolant inlet temperature is 633.15 K, and the inlet velocity is 3.5–8 m/s. The outlet is the pressure outlet, and the outlet's static pressure is 0. The annular fuel rod is assumed to have the same heat flux on the inner and outer surfaces. The heat flux on the inner and outer surfaces are both 1.49×10^6W/m^3. The heat flux of the 7-pin bundle annular fuel assembly is set to the average surface heat flux density. The part of wire-wrapped is set to be without heat flux. The surface of the wrapper tube, the annular fuel rods surface, and the wire-wrapped surface are all no-slip surfaces. In this study, a pressure-based solver is used to calculate the discrete equations using the SIMPLE algorithm with the second-order upwind format. When the residuals of the momentum and turbulence equations reach 10^{-5} and the residuals of the energy equation reach 10^{-6}, the calculation is finished.

Model validation

In this research, the flow and heat transfer process in sub-channels of the 7-pin annular fuel assembly of sodium-cooled fast reactors is verified. Considering that the experiments of flow and heat exchange are based on the traditional fuel assembly with outer wire-wrapped, the model with one outer wire-wrapped is selected for verification in this research. The friction factor f is the most important dimensionless parameter to solve the pressure drop, and its value is related to the Reynolds number and the geometric structure of the fuel assembly, such as P/D and H/D. Its equation is as follows:

$$\Delta p = f \frac{L}{D_e} \frac{\rho v^2}{2}, \tag{10}$$

where Δp is the pressure drop, L is the length of the coolant channel, v is the velocity of the coolant, and D_e is the equivalent diameter. Friction factor correlations, such as the Rehme model and the Cheng and Todreas simplified model, are widely used for a wire-wrapped fuel bundle. Each friction factor is calculated using the following correlations. The Rehme model and the

TABLE 6 Applicable range of models.

Models	P/D	H/D	Re	Pe
Rehme	1.125 ≤ P/D ≤ 1.417	5 ≤ H/D ≤ 50	2000 ≤ Re ≤ 250000	-
Cheng and Todreas	1.067 ≤ P/D ≤ 1.35	4 ≤ H/D ≤ 52	400 ≤ Re ≤ 100000	-
Schad	1.1 ≤ P/D ≤ 1.5	-	-	150 ≤ Pe ≤ 1000
Westinghouse	1.1 ≤ P/D ≤ 1.4	-	-	10 ≤ Pe ≤ 5000
Mikityuk	1.1 ≤ P/D ≤ 1.95	-	-	30 ≤ Pe ≤ 5000
Borishanski	1.1 ≤ P/D ≤ 1.5	-	-	60 ≤ Pe ≤ 2200

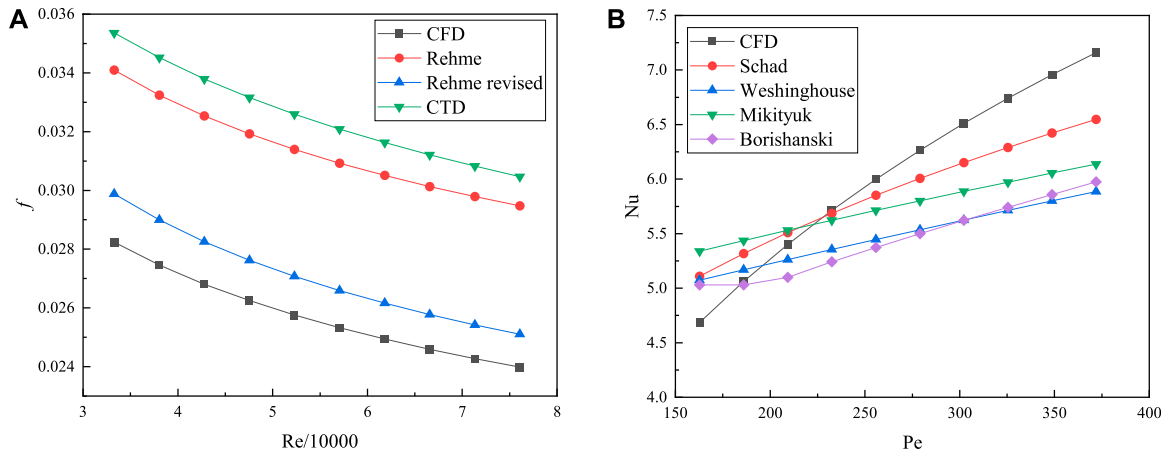

FIGURE 4
Comparison of the CFD analysis results **(A)** with the friction factor correlations and **(B)** with heat transfer correlations.

Cheng and Todreas simplified model can be defined by Eqs 11–15, and the applicable range of models is shown in Table 6.

Rehme model (Rehme, 1973):

$$f = \left(\frac{64}{Re}F^{0.5} + \frac{0.0816}{Re^{0.133}}F^{0.9335}\right)\frac{P_{wb}}{P_{wt}}. \tag{11}$$

Rehme revised model.

$$f = \left(\frac{64}{Re}F^{0.7} + \frac{0.0816}{Re^{0.133}}F^{0.9335}\right)\frac{P_{wb}}{P_{wt}} - 0.0045, \tag{12}$$

where Re is the Reynolds number, P_{wb} is the wetted perimeter of the rod bundle, P_{wt} is the total wetted perimeter, and F is the square of the ratio of this effective velocity to the bundle average axial velocity. It is related to the geometry parameters.

$$F = \left(\frac{P}{D}\right)^{0.5} + \left[7.6\frac{D + D_w}{H}\left(\frac{P}{D}\right)^2\right]^{2.16}. \tag{13}$$

Cheng and Todreas simplified model (Cheng and Todreas, 1986):

$$f = \frac{C_{fT}}{Re^{0.18}}, \tag{14}$$

$$C_{fT} = \left[0.8063 - 0.9022\log\left(\frac{H}{D}\right) + 0.3526\left(\log\left(\frac{H}{D}\right)\right)^2\right]\left(\frac{P}{D}\right)^{9.7}\left(\frac{H}{D}\right)^{1.78-2(P/D)}, \tag{15}$$

where C_{fT} is the friction factor in turbulence.

The average heat transfer coefficient at the outlet is calculated as

$$\begin{cases} h = \dfrac{q}{\Delta T} \\ Nu = \dfrac{hD_e}{\lambda} \end{cases}, \tag{16}$$

where $\Delta T = T_c\text{-}T_f$, T_c is the cladding temperature of all bundles at the outlet, T_f is the coolant temperature at the outlet, and q is the heat flux of the annular fuel rod. The Nusselt number is an important parameter to reflect the heat transfer

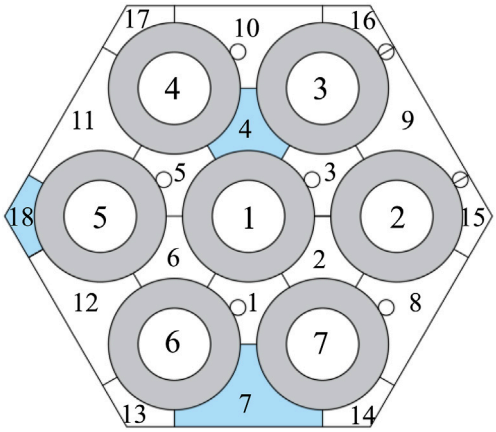

FIGURE 5
Serial number of sub-channels and inner flow field.

characteristics in the fuel assembly, and its value is not only related to the Peclet number but also to the structural parameter *P/D* of the fuel assembly. These models can be defined by Eqs 17–20, and the applicable range of models is shown in Table 5.

Schad model (Kazimi and Carelli, 1976):

$$Nu = \left(-16.15 + 24.96\frac{P}{D} - 8.55\left(\frac{P}{D}\right)^{2}\right)Pe^{0.3}. \quad (17)$$

Westinghouse model (Kazimi and Carelli, 1976):

$$Nu = 4.0 + 0.33\left(\frac{P}{D}\right)^{3.8}\left(\frac{Pe}{100}\right)^{0.86} + 0.16\left(\frac{P}{D}\right)^{5.0}. \quad (18)$$

Mikityuk model (Mikityuk, 2009):

$$Nu = 0.047\left(1 - e^{-3.8(P/D)-1}\right)\left(Pe^{0.77} + 250\right). \quad (19)$$

Borishanski model (Borishanskii et al., 1969):

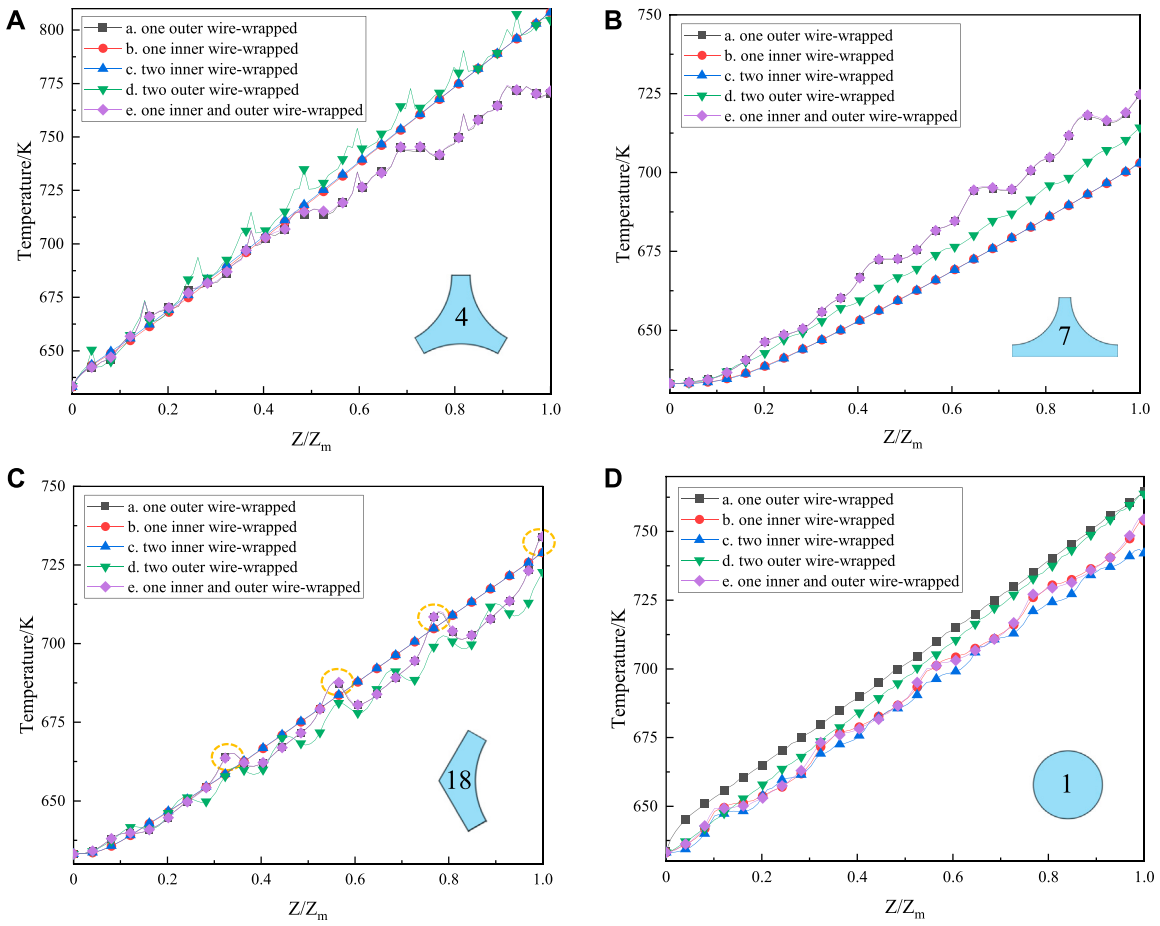

FIGURE 6
Distribution of temperature in the **(A)** interior sub-channel, **(B)** edge sub-channel, **(C)** corner sub-channel, and **(D)** inner flow field.

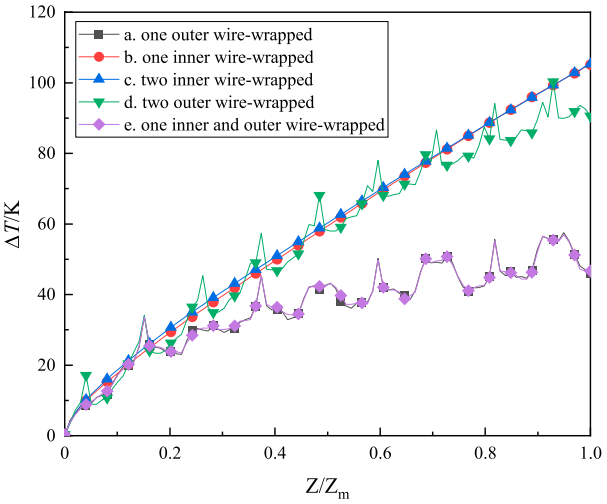

FIGURE 7
Temperature difference in different cross-sections.

$$Nu = 24.15\log\left(-8.12 + 12.76\frac{P}{D} - 3.65\left(\frac{P}{D}\right)^2\right) + 0.0174\left(1 - e^{-6(P/D)-1}\right)B, \tag{20}$$

where

$$B = \begin{cases} 0, & Pe < 200 \\ (Pe - 200)^{0.9}, & Pe \geq 200 \end{cases}$$

Figure 4A depicts the comparison results of the CFD analysis results and the friction factor correlations. With the increase of the Reynolds number, the friction factor decreases gradually. Each friction factor correlation tends to be consistent with the change of the Reynolds number. Compared with correlations, the friction factor of the CFD analysis results in this study is smaller because when the total pressure drop of the core is constant, the pressure drop of the inner flow field will affect the pressure drop of the sub-channels and affect the variety of the friction factor *f*. The turbulence model has the smallest error with the Rehme revised model, and the errors with other correlations are also within an acceptable range.

Figure 4B shows the comparison results of the CFD analysis results and the heat transfer correlations. With the increase of the Peclet number, the Nusselt number increases gradually. In terms of curve growth rate, the growth rate of the CFD analysis results is greater than that of the heat transfer correlations. The annular fuel assembly is developed in this research, so the heat exchange in the inner channels accounted for part of the share of the total heat flux in the annular fuel pellet, which will decrease the heat exchange in the sub-channels. Considering the various uncontrollable factors of the experiment itself and the difference between the Prandtl number of the liquid metal NaK or LBE used in the experiment and the Prandtl number of the liquid metal sodium used in the numerical simulation in this study, the errors are all within an acceptable range.

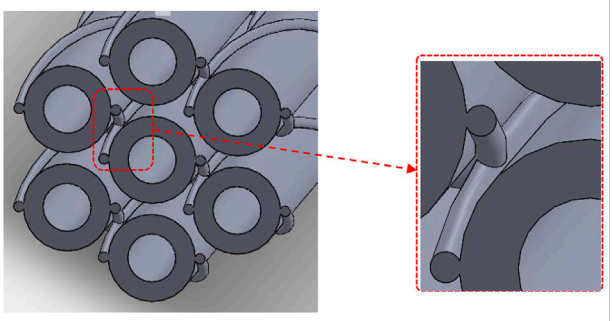

FIGURE 8
Overlap of wire-wrapped in the model of model (e).

Numerical results and analysis

Temperature distribution in the bundle

Figure 5 shows the serial number of the sub-channels and the inner flow field of the annular fuel assembly. Model (a) is taken as an example in Figure 5. The research selects the more representative sub-channels 4, 7, and 18 to analyze the change in the coolant temperature in different sub-channels. It is shown in Figure 6. Figure 6A shows the coolant temperature at the interior sub-channel 4. The coolant temperature increases gradually with the increase of Z/Z_m. When the sub-channel is winding with wire-wrapped, there are different numbers of peaks in the distribution of temperature. The coolant in the interior sub-channel is mainly affected by the surrounding wire-wrapped from three annular fuel rods, so the number of the peak is disordered. The temperature of model (d) is bigger than that of model (a) and model (e). Figure 6B depicts the coolant temperature at the edge sub-channel 7. The temperature of the edge sub-channel is mainly affected by the two surrounding annular fuel rods, and the number of peaks in the temperature is more obvious than that of the interior sub-channel. On the whole, the temperature of the sub-channel in model (a) and model (e) are the highest. Figure 6C is the coolant temperature at the corner sub-channel 18. The temperature distribution of the corner sub-channel is mainly affected by the wire-wrapped of the annular fuel rod adjacent to it. Therefore, there are four peaks for model (a) and model (e). The number of wire-wrapped increases by one time in model (d), so the number of peaks has also doubled. The temperature of the five models is the highest in the interior sub-channel, followed by the corner sub-channel, and the lowest temperature is in the edge sub-channel. The temperature

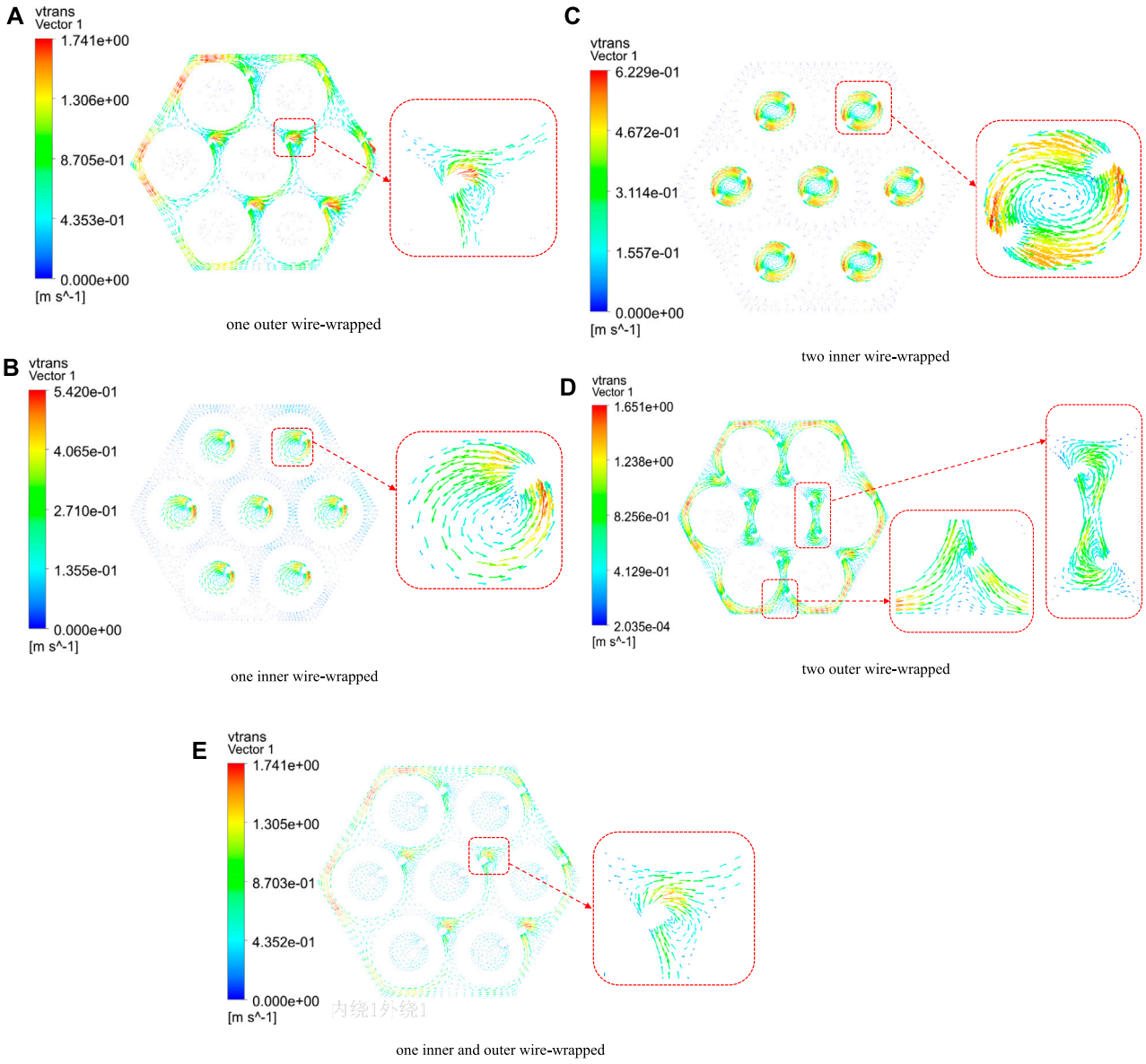

FIGURE 9
Velocity vector of the transverse velocity of cross-session with different models.

characteristics of model (a) and model (e) are better than others in the sub-channels. Figure 6D is the distribution of the coolant temperature in the inner flow field 1. The number of wire-wrapped is two in model (c), and the helical wire-wrapped mixes the coolant fully and strengthens the heat transfer between coolant and fuel bundles. The coolant outlet temperature is the lowest, which is about 742K. The number of wire-wrapped is only one of model (b) and model (e) in the inner flow field. The flow heat transfer effect of the wire-wrapped is inferior to the former slightly. The temperature of the two models is about 754K.

Figure 7 shows the temperature gradient of the five models. With the increase of Z/Z_m, the temperature difference of each model increases gradually. The temperature difference in model (b) and model (c) is the largest, which is 105K. The temperature difference in model (a) and model (e) is the smallest, only 46K. The temperature difference in model (d) is 90K. It is not difficult to find from the above data that the key to affecting the temperature difference is the temperature of the three sub-channels. The outer wire-wrapped reduces the coolant temperature difference and flattens the coolant outlet temperature difference, and makes the coolant outlet

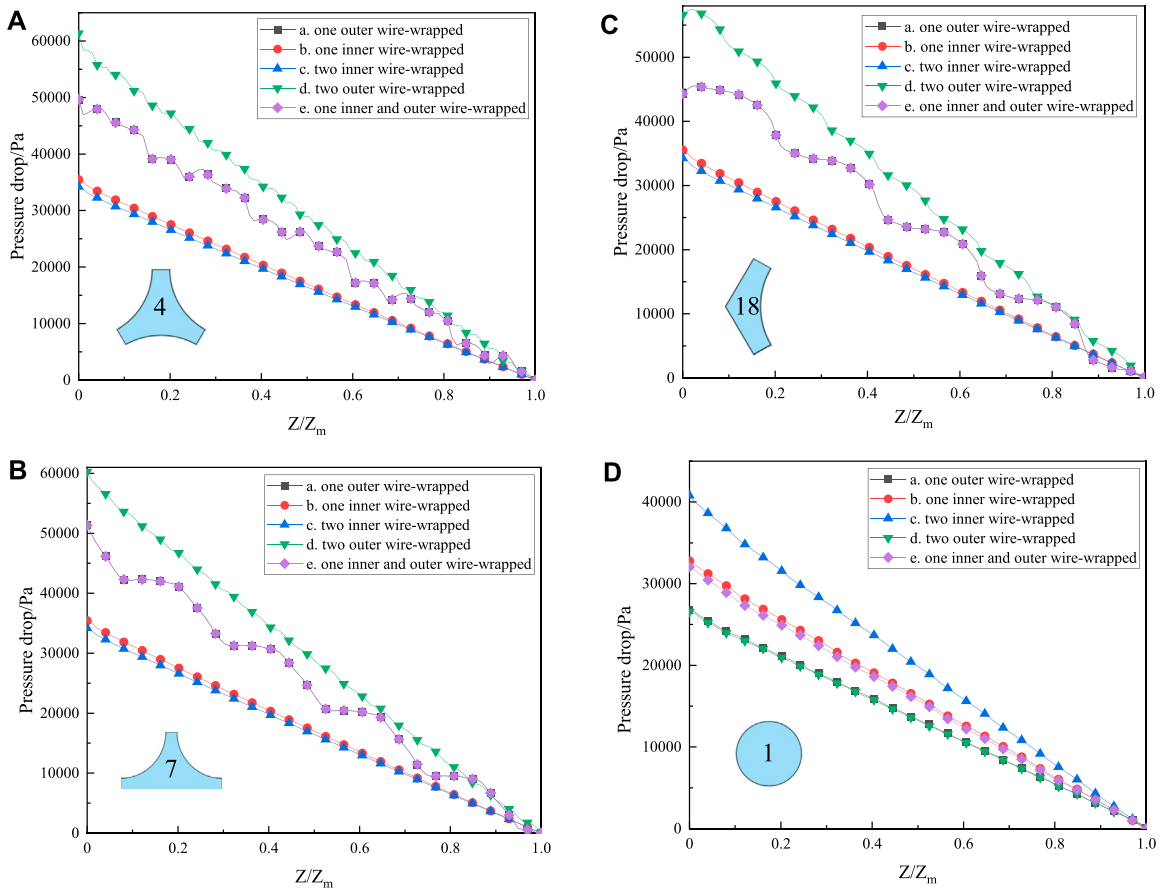

FIGURE 10
Distribution of pressure drop in the **(A)** interior sub-channel, **(B)** edge sub-channel, **(C)** corner sub-channel, and **(D)** inner flow field.

temperature more uniform. The effect of flattening the temperature difference in model (a) and model (e) is better than that in model (d). When the ratio of the rod pitch to rod diameter (P/D) is constant, the number of the outer wire-wrapped increases, which will cause overlap between the wire-wrapped and wire-wrapped from the adjacent fuel rod. It may cause the coolant flow channel and poor heat transfer. Figure 8 is the overlap of wire-wrapped in the model of one inner and outer wire-wrapped. Considering the sub-channels, inner flow field, and temperature difference, the temperature field characteristics of one inner and outer wire-wrapped (model e) are better than those of others.

Transverse velocity distribution in the bundle

Figure 9 is the velocity vector of the transverse velocity of cross-session for the five models. It can be seen from the figure that the transverse velocity of the five models is 1.74 m/s, 0.54 m/s, 0.62 m/s, 1.65 m/s, and 1.74 m/s, respectively. The transverse velocity of coolant in the sub-channels is about three times that of in the inner flow field. The sub-channels of the annular fuel assembly can be considered a whole, and the coolant can flow from one sub-channel to another sub-channel. Therefore, the flow of the coolant in the sub-channels is affected by all the wire-wrapped twined bundles. Every inner flow field is an independent individual. The inner flow fields do not affect each other. The transverse velocity of model (b) is smaller than that of model (c). It may be that because of the increase of the number of wire-wrapped, the direction of the coolant flow is hindered by the wire-wrapped. The velocity components in the *x* and *y* directions increase, which is behaved as an increase in the transverse velocity. From the perspective of the inner flow field, the increase in the number of wire-wrapped leads to an increase in transverse velocity. Due to the number of wire-wrapped being two in model (d), there will be an overlap between the wire-wrapped and the wire-wrapped adjacent rod bundles. The flow of the coolant is blocked, the velocity of the coolant decreases, and the transverse velocity also decreases. Thus, the effect of model

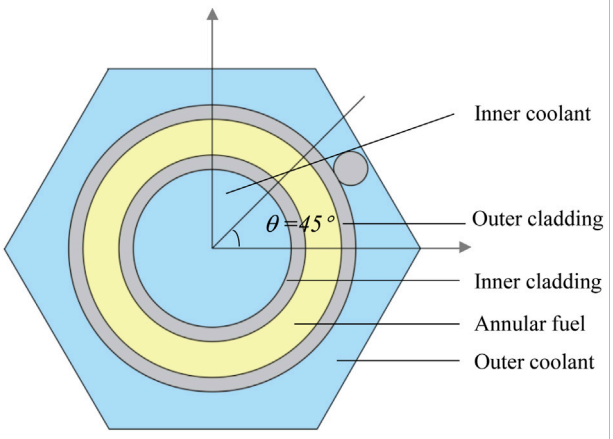

FIGURE 11
Cross-section of the thermal stress model.

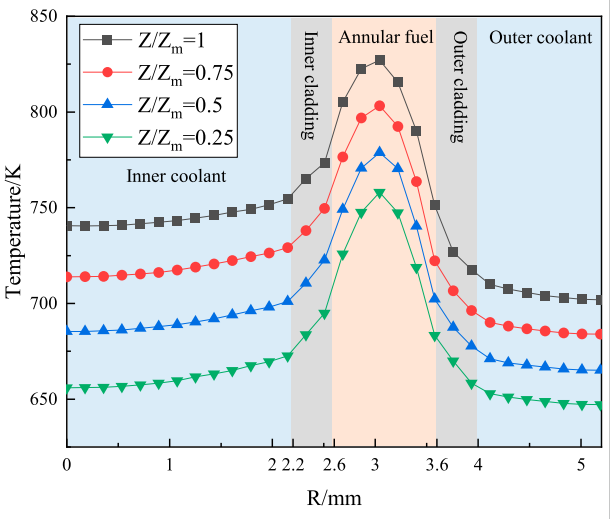

FIGURE 12
Distribution of temperature of the thermal stress model.

(a) and model (e) is better than that of model (d). The number of wire-wrapped is not as good as possible from the perspective of sub-channels. Overall, the transverse velocity of one inner and outer wire-wrapped (model e) is better than that of others.

It can be seen from the local enlarged vector of the transverse velocity in Figure 9 that the flow of coolant is blocked when the coolant encounters the wire-wrapped during the flow of the coolant. The flow area of the coolant decreases, and the advancing direction is hindered by the wire-wrapped. The coolant gathers in a narrow position between the annular fuel rod and the wire-wrapped. It appears that the transverse velocity is greatest at the narrow location between the wire-wrapped and the annular fuel rod. Figure 9A depicts the local enlarged vector of the transverse velocity that the flow of the coolant in the interior sub-channel is affected by the wire-wrapped from three directions of the adjacent three annular fuel rods, and a vortex appears at the gathering position.

Pressure drop in the bundle

Figure 10 shows the pressure drop of the coolant in different sub-channels and inner flow fields. With the increase of Z/Z_m, the pressure drop of the coolant decreases gradually, and it is 0 Pa at the outlet. The pressure drop of the sub-channels is all larger than the pressure drop of the inner flow field. Figure 10A–C are the coolant pressure drop at the sub-channels 4, 7, and 18. There is only one wire-wrapped in the sub-channels of models (a) and (e). The existence of the wire-wrapped in models (a), (d), and (e) causes the coolant pressure drop to increase in the sub-channel. The pressure drop is the largest in model (d), which reaches 6.1 × 10^4Pa. In addition, the pressure drop of the coolant exhibits a periodic decrease during the wire-wrapped outer. There are four peaks on the pressure drop curve. This is because the winding

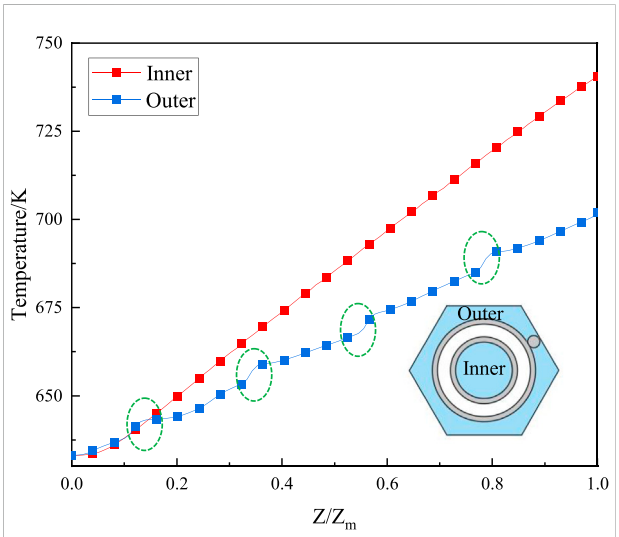

FIGURE 13
Distribution of temperature with inner and outer.

position of the wire-wrapped has an influence on the coolant flow. Therefore, the flow velocity of the coolant increases, and the pressure drop decreases. This phenomenon disappears when the coolant flows through the wire-wrapped.

Figure 10D depicts the pressure drop of the coolant in the inner flow field. The coolant pressure drop decreases linearly as Z/Z_m increases. The main factor that affects the pressure drop in the inner flow field is whether the wire-wrapped in the inner flow field. The number of wire-wrapped is two in model (c), so the pressure drop is the largest, which is reach to 4.1 × 10^4Pa. In

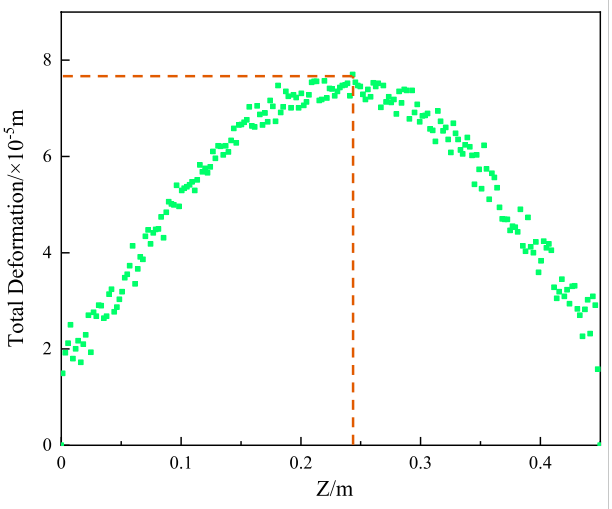

FIGURE 14
Total deformation of the solid domain.

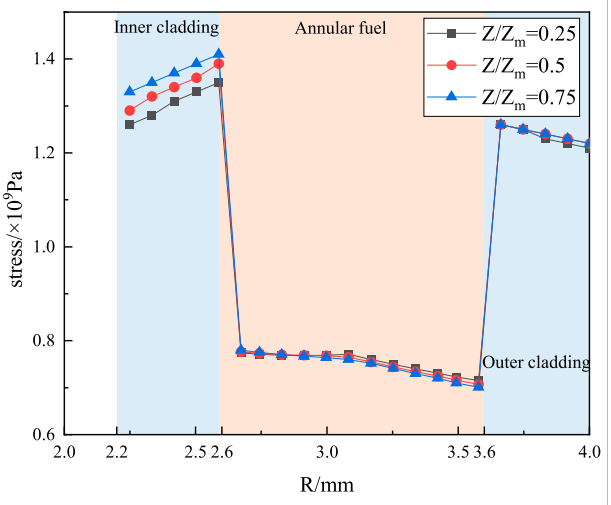

FIGURE 15
Stress of solid domain.

addition, the pressure drop of model (b) and model (e) is in the middle, and the pressure drop is 3.2×10^4Pa, which is about 22% smaller than the maximum pressure drop. No matter the sub-channels or the inner flow field, the increase in the number of wire-wrapped will cause an increase in the pressure drop. The increase in pressure drop may have an impact on the normal operating conditions of the core. Overall, the pressure drop of one inner and outer wire-wrapped (model e) is better than that of others. According to the design criteria of sodium-cooled fast reactors, the pressure drops of the above five models are all within their safety margins and meet the design criteria.

Thermal stress in the rod

The fuel pellets will have a visible temperature gradient from the center to the surface during the operation of the annular fuel rod in the reactor. The annular fuel rod will generate thermal stress by the influence of the temperature gradient, which leads to the deformation of the annular fuel rod. As the first shelter to tolerate the deformation of the annular fuel rod, it is very important to study the deformation and thermal stress of the annular fuel rod and the cladding. Figure 11 is the cross-section of the thermal stress model. At the same time, a line in $\theta = 45^\circ$ is selected to extract the data of temperature and thermal stress of coolant, cladding, and annular fuel rod in radial.

Figure 12 depicts the radial temperature of the annular fuel rod and cladding along the line of $\theta = 45^\circ$ with different Z/Z_m. Along the X-axial, from left to right, are the inner coolant, inner cladding, annular fuel rod, outer cladding, and outer coolant, respectively. The thickness of the inner and outer claddings is 4 mm. Here, Z is the Z-coordinate, and Z_m is the total length of the annular fuel rod. With the increase of Z/Z_m, the temperature of both the fluid domain and the solid domain increases, and the temperature at the outlet ($Z/Z_m = 1$) is the highest. Overall, the temperature of the annular fuel rod is high in the middle and low on both sides. At the radial midpoint of the fuel rod (R = 3.1 mm), the annular fuel rod temperature is the highest, reaching about 830K. The heat flux of the annular fuel rod is transferred to the inner and outer claddings on both sides through the method of heat conduction. Sufficient heat transfer can achieve the purpose of taking away the heat of the annular fuel rod by the inner and outer claddings and the coolant. The temperature on the left side of the symmetrical position (R = 3.1 mm) is higher than the temperature on the right side.

Figure 13 is the distribution of temperature with the inner and outer flow fields of the annular fuel rod. With the increase of Z/Z_m, the temperature of the inner and outer flow fields increases gradually. In addition, the temperature difference larger between the inner and outer flow fields increases with the increase of Z/Z_m. The maximum temperature difference is about 40K on the coolant outlet ($Z/Z_m = 1$). This may be caused by the fact that the surface area of the fuel pellet per unit of coolant flow which acts as the area for heat transfer from the fuel to the coolant at the inner flow field is larger than that of the outer flow field. In addition, the annular fuel rod is positioned by the wire-wrapped, and the spiral method of the wire-wrapped has an impact on the flow of the coolant in the outer flow field. Therefore, lower temperature in the outer flow field than in the inner. There are four peaks in the temperature curve. There is no wire-wrapped effect in the inner flow field, so the temperature rises linearly.

Figure 14 indicates the total deformation of the solid domain along the Z-axial. The total deformation of the middle part (Z =

0.24 m) of the solid domain is the largest and about 79 μm. Due to the fixing effect of the structure on both sides of the annular fuel rod, the displacement of both sides of the annular fuel rod and the inner and outer claddings is the smallest. Overall, the deformation of the whole solid domain is characterized by small at both slides and large in the middle. The total displacement distribution curve is similar to the shape of a parabola. Excessive displacement can affect the safety of the annular fuel rod and even the whole core. Swelling and cracking of the cladding will happen. Therefore, the total deformation of the annular fuel rod is considered an important parameter. Figure 15 shows the stress distribution of the annular fuel rod and claddings of the inner and outer. The stress variation in the solid domain is mainly along the radial direction. The axial variation tends to be consistent. The stress in the cladding is about 1.75 times the stress in the annular fuel rod, and the stress in the inner cladding is higher than that in the outer cladding.

Conclusion

Thermal-hydraulic characteristics of the 7-pin annular fuel assembly with the inner and outer wire-wrapped are investigated in this research. The flow, heat transfer, and mechanical properties are analyzed, and the conclusions are as follows.

The temperature of three sub-channels is the key that influences the temperature characteristics. The wire-wrapped reduces the coolant temperature gradient, flattens the coolant outlet temperature, and makes the coolant outlet temperature more uniform. The increase in the number of wire-wrapped is not better, and the geometry of the annular fuel assembly should be fully considered. Considering the sub-channels, inner flow field, and temperature difference, the temperature field characteristics of one inner and outer wire-wrapped (model e) are better than those of others.

The transverse velocity of coolant in the sub-channels is about three times that of in the inner flow field. From the perspective of the inner flow field, the increase in the number of wire-wrapped leads to an increase in transverse velocity. The number of wire-wrapped is not as good as possible from the perspective of sub-channels. The transverse velocity of one inner and outer wire-wrapped (model e) is better than that of others.

The pressure drop of the sub-channels is greater than the pressure drop of the inner flow field. No matter the sub-channels or the inner flow field, the increase in the number of wire-wrapped will cause an increase in the pressure drop. The pressure drop of one inner and outer wire-wrapped (model e) is better than that of others. In conclusion, the thermal-hydraulic properties of one inner and outer wire-wrapped (model e) are better than those of other models.

The temperature of the annular fuel rod is high in the middle and low on both sides. The total deformation of the middle part of the solid domain is the largest and about 79 μm. The stress variation in the solid domain is mainly along the radial direction. The axial variation tends to be consistent. The stress in the cladding is about 1.75 times the stress in the annular fuel rod, and the stress in the inner cladding is higher than that in the outer cladding because the inner cladding surface area is less than the outer cladding surface area. These findings provide a reference for the optimization design of the fuel assembly. In future work, special conditions or the effect of variable conditions on the fatigue life of wire-wrapped assemblies is yet to be investigated.

Data availability statement

The original contributions presented in the study are included in the article/Supplementary Material; further inquiries can be directed to the corresponding author.

Author contributions

YG has written and organized the structure of the manuscript and has performed some of the calculations presented in the manuscript. BZ and XY have performed some of the calculations in the manuscript. XD, YZ, and CT have given some advice about the manuscript.

Funding

This work is supported by the National Natural Science Foundation of China (Nos. 12175116 and 11805112). The authors would like to show their great appreciation to other members of the team for their support and contribution to this research.

Conflict of interest

The authors declare that the research was conducted in the absence of any commercial or financial relationships that could be construed as a potential conflict of interest.

Publisher's note

References

Bertocchi, F., Rohde, M., and Kloosterman, J. (2019). Understanding migratory flow caused by helicoid wire spacers in rod bundles: An experimental and theoretical study. *Int. J. Heat Fluid Flow* 80, 108491. doi:10.1016/j.ijheatfluidflow.2019.108491

Bieder, U., Uitslag-Doolaard, H., and Mikuž, B. (2021). Investigation of pressure loss and velocity distribution in fuel assemblies with wire-wrapped rods by using RANS and LES with wall functions. *Ann. Nucl. Energy* 152, 108025. doi:10.1016/j.anucene.2020.108025

Borishanskii, V., Gotovskii, M., and Firsova, E. (1969). Heat transfer to liquid metals in longitudinally wetted bundles of rods. *A. T. Energy* 27, 1347–1350. doi:10.1007/BF01118660

Chen, J., Zhang, D. L., Song, P., Wang, X. A., Wang, S. B., Liang, Y., et al. (2018a). CFD investigation on thermal-hydraulic behaviors of a wire-wrapped fuel subassembly for sodium-cooled fast reactor. *Ann. Nucl. Energy* 113, 256–269. doi:10.1016/j.anucene.2017.11.023

Chen, S. K., Chen, Y. M., and Todreas, N. E. (2018b). The upgraded Cheng and Todreas correlation for pressure drop in hexagonal wire-wrapped rod bundles. *Nucl. Eng. Des.* 335, 356–373. doi:10.1016/j.nucengdes.2018.05.010

Cheng, S.-K., and Todreas, N. E. (1986). Hydrodynamic models and correlations for bare and wire-wrapped hexagonal rod bundles - bundle friction factors, subchannel friction factors and mixing parameters. *Nucl. Eng. Des.* 92, 227–251. doi:10.1016/0029-5493(86)90249-9

Choi, S. K., Choi, I. K., Nam, H. Y., Choi, J. H., and Choi, H. K. (2003). Measurement of pressure drop in a full-scale fuel assembly of a liquid metal reactor. *J. Press. Vessel Technol.* 125, 233–238. doi:10.1115/1.1565076

Chun, M.-H., and Seo, K.-W. (2001). An experimental study and assessment of existing friction factor correlations for wire-wrapped fuel assemblies. *Ann. Nucl. Energy* 28, 1683–1695. doi:10.1016/S0306-4549(01)00023-8

Cui, M., Guo, Y., and Zhang, Z. (2013). Transient simulation code development of primary coolant system of Chinese Experimental Fast Reactor. *Ann. Nucl. Energy* 53, 158–169. doi:10.1016/j.anucene.2012.09.022

El-Sahlamy, N., Hassan, M., and Khedr, A. (2020). Comparison between standard solid fuel and a new annular fuel performance in the core of a PWR. *Kerntechnik* 85, 161–168. doi:10.3139/124.190020

Engel, F. C., Markley, R. A., and Bishop, A. A. (2017). Laminar, transition, and turbulent parallel flow pressure drop across wire-wrap-spaced rod bundles. *Nucl. Sci. Eng.* 69, 290–296. doi:10.13182/nse80-a2012710.13182/nse79-a20618

Feng, D., Morra, P., Sundaram, R., Lee, W.-J., Saha, P., Hejzlar, P., et al. (2007). Safety analysis of high-power-density annular fuel for PWRs. *Nucl. Technol.* 160, 45–62. doi:10.13182/NT07-A3883

Gajapathy, R., Velusamy, K., Selvaraj, P., and Chellapandi, P. (2015). CFD investigation of effect of helical wire-wrap parameters on the thermal hydraulic performance of 217 fuel pin bundle. *Ann. Nucl. Energy* 77, 498–513. doi:10.1016/j.anucene.2014.10.038

Hou, Y., Wang, L., Wang, M., Zhang, K., Zhang, X., Hu, W., et al. (2019). Experimental study of liquid sodium flow and heat transfer characteristics along a hexagonal 7-rod bundle. *Appl. Therm. Eng.* 149, 578–587. doi:10.1016/j.applthermaleng.2018.12.043

Kazimi, M., and Carelli, M. (1976). *Clinch river breeder reactor plant. Heat transfer correlation for analysis of CRBRP assemblies*. Madison, PA (United States): Westinghouse Electric Corp.Advanced Reactors Div.

Kazimi, M. S., Hejzlar, P., Carpenter, D., Feng, D., Kohse, G., Lee, W. J., et al. (2006). *High performance fuel design for next generation PWRs*.

Kwon, Y., Yang, Y., Kim, J., and Kwon, S. (2013). A study on the flow characteristics in an annular type fuel pellet of PWR. *J. Mech. Sci. Technol.* 27, 257–261. doi:10.1007/s12206-012-1205-x

Lahoda, E., Mazzoccoli, J., and Beccherle, J. (2007). High-power-density annular fuel for pressurized water reactors: Manufacturing costs and economic benefits. *Nucl. Technol.* 160, 112–134. doi:10.13182/NT07-A3887

Launder, B. E., and Spalding, D. B. (1983). "The numerical computation of turbulent flows," in *Numerical prediction of flow, heat transfer, turbulence and combustion* (Elsevier), 96–116. doi:10.1016/b978-0-08-030937-8.50016-7

Liang, Y., Zhang, D., Chen, Y., Zhang, K., Tian, W., Qiu, S., et al. (2020). An experiment study of pressure drop and flow distribution in subchannels of a 37-pin wire-wrapped rod bundle. *Appl. Therm. Eng.* 174, 115283. doi:10.1016/j.applthermaleng.2020.115283

Liu, L., Wang, S., and Bai, B. (2017). Thermal-hydraulic comparisons of 19-pin rod bundles with four circular and trapezoid shaped wire wraps. *Nucl. Eng. Des.* 318, 213–230. doi:10.1016/j.nucengdes.2017.04.017

Menter, F. R. (1994). Two-equation eddy-viscosity turbulence models for engineering applications. *AIAA J.* 32, 1598–1605. doi:10.2514/3.12149

Mikityuk, K. (2009). Heat transfer to liquid metal: Review of data and correlations for tube bundles. *Nucl. Eng. Des.* 239, 680–687. doi:10.1016/j.nucengdes.2008.12.014

Natesan, K., Sundararajan, T., Narasimhan, A., and Velusamy, K. (2010). Turbulent flow simulation in a wire-wrap rod bundle of an LMFBR. *Nucl. Eng. Des.* 240, 1063–1072. doi:10.1016/j.nucengdes.2009.12.025

Naveen Raj, M. N., and Velusamy, K. (2016). Characterization of velocity and temperature fields in a 217 pin wire wrapped fuel bundle of sodium cooled fast reactor. *Ann. Nucl. Energy* 87, 331–349. doi:10.1016/j.anucene.2015.09.008

Novendstern, E. (1972). Turbulent flow pressure drop model for fuel rod assemblies utilizing a helical wire-wrap spacer system. *Nucl. Eng. Des.* 22, 28–42. doi:10.1016/0029-5493(72)90059-3

Pacio, J., Chen, S.-K., Chen, Y.-M., and Todreas, N. (2022). Analysis of pressure losses and flow distribution in wire-wrapped hexagonal rod bundles for licensing. Part I: The Pacio-Chen-Todreas Detailed model (PCTD). *Nucl. Eng. Des.* 388, 111607. doi:10.1016/j.nucengdes.2021.111607

Pacio, J., Daubner, M., Fellmoser, F., Litfin, K., and Wetzel, T. (2016). Experimental study of heavy-liquid metal (LBE) flow and heat transfer along a hexagonal 19-rod bundle with wire spacers. *Nucl. Eng. Des.* 301, 111–127. doi:10.1016/j.nucengdes.2016.03.003

Rehme, K. (1973). Pressure drop correlations for fuel element spacers. *Nucl. Technol.* 17, 15–23. doi:10.13182/NT73-A31250

Rowinski, M. K., White, T. J., and Zhao, J. (2015). Innovative model of annular fuel design for lead-cooled fast reactors. *Prog. Nucl. Energy* 83, 270–282. doi:10.1016/j.pnucene.2015.04.002

Shih, T.-H., Liou, W. W., Shabbir, A., Yang, Z., and Zhu, J. (1995). A new k-ϵ eddy viscosity model for high Reynolds number turbulent flows. *Comput. fluids* 24, 227–238. doi:10.1016/0045-7930(94)00032-T

Shin, C.-H., Chun, T.-H., and Oh, D.-S. (2012). Thermal hydraulic performance assessment of dual-cooled annular nuclear fuel for OPR-1000. *Nucl. Eng. Des.* 243, 291–300. doi:10.1016/j.nucengdes.2011.12.010

Song, M. S., Jeong, J. H., and Kim, E. S. (2019). Numerical investigation on vortex behavior in wire-wrapped fuel assembly for a sodium fast reactor. *Nucl. Eng. Technol.* 51, 665–675. doi:10.1016/j.net.2018.12.012

Wang, H., Wang, S., and Lu, D. (2020). PIV measurements of the cross flow induced by a wrapped wire spacer. *Ann. Nucl. Energy* 146, 107634. doi:10.1016/j.anucene.2020.107634

Wang, X., and Cheng, X. (2018). Analysis of inter-channel sweeping flow in wire wrapped 19-rod bundle. *Nucl. Eng. Des.* 333, 115–121. doi:10.1016/j.nucengdes.2018.04.008

Xu, Z., Liu, Y., and Wang, B. (2020). Simulation and optimization design of fuel rod in pressurized water fuel assemblies. *Nucl. Eng. Des.* 370, 110856. doi:10.1016/j.nucengdes.2020.110856

Zaidabadi, M., Ansarifar, G., and Esteki, M. (2017). Thermal hydraulic analysis of VVER-1000 nuclear reactor with dual-cooled annular fuel using K–ω SST Turbulence model. *Ann. Nucl. Energy* 101, 118–127. doi:10.1016/j.anucene.2016.09.027

Zhao, J., No, H. C., and Kazimi, M. S. (2004). Mechanical analysis of high power internally cooled annular fuel. *Nucl. Technol.* 146, 164–180. doi:10.13182/NT04-A3496

frontiers | Frontiers in Energy Research

TYPE Original Research
PUBLISHED 27 September 2022
DOI 10.3389/fenrg.2022.993383

OPEN ACCESS

EDITED BY
Muhammad Saeed,
East China University of Technology, China

REVIEWED BY
Mohammad Alrwashdeh,
Khalifa University, United Arab Emirates
Yufeng Lv,
China Institute of Atomic Energy, China

*CORRESPONDENCE
Wenzhong Zhou,
zhouwzh3@mail.sysu.edu.cn
Long Gu,
gulong@impcas.ac.cn

SPECIALTY SECTION
This article was submitted to Nuclear Energy, a section of the journal Frontiers in Energy Research

RECEIVED 13 July 2022
ACCEPTED 05 September 2022
PUBLISHED 27 September 2022

CITATION
Cai Y, Chen K, Zhou W and Gu L (2022), Multiphysics thermo-mechanical behavior modeling for annular uranium-plutonium mixed oxide fuels in a lead-cooled fast reactor.
Front. Energy Res. 10:993383.
doi: 10.3389/fenrg.2022.993383

Multiphysics thermo-mechanical behavior modeling for annular uranium-plutonium mixed oxide fuels in a lead-cooled fast reactor

Yutai Cai[1], Ken Chen[1], Wenzhong Zhou[1,2]* and Long Gu[3]*

[1]Sino-French Institute of Nuclear Engineering and Technology Sun Yat-Sen University, Zhuhai, China, [2]Department of Mechanical Engineering City University of Hong Kong, Hong Kong, China, [3]Institute of Modern Physics Chinese Academy of Sciences, Lanzhou, China

Understanding and predicting nuclear fuel behavior is the cornerstone for fuel design and optimization, and the safe and economic operation of nuclear reactors. Due to the excellent neutronic economy and safe operational characteristics of lead/lead-bismuth-based liquid metal coolant, lead-cooled fast reactor (LFR) has received much attention and has been regarded as one of the top candidate reactors for Generation IV nuclear power plants. Mixed oxide (MOX) fuel is beneficial to improve fuel cycle utilization and consume weapons-grade plutonium, among which hollow MOX fuel has excellent heat transfer advantages, which can further improve fuel economy and safety, and has good development prospects. In this work, an annular uranium-plutonium mixed oxide (MOX) fuel operating in a liquid lead/lead-bismuth cooled fast reactor is modeled and simulated to predict its behavior under transient and steady-state operation. This model has several modules working in a fully coupled approach based on COMSOL Multiphysics, such as heat transfer, fuel burnup, oxygen redistribution, plutonium redistribution, porosity evolution, fission gas release, JOG growth, and grain size evolution. The modeling results were benchmarked with the existing codes and experimental data, and the results were in satisfactory agreement. The parameters analysis was carried out in this work. Consistent with the solid MOX fuel, the O/M ratio (or deviation from the stoichiometry of oxygen) significantly affects temperature evolution, fission gas migration and release behavior, and plutonium redistribution. Linear power also has a significant influence on fuel performance.

KEYWORDS

mixed oxide (MOX) fuels, lead-cooled fast reactor (LFR), multiphysics, annular fuel, nuclear fuel performance

Introduction

Understanding and predicting fuel behavior are essential for fuel design, operation, reprocessing, and reactor safety. The nuclear fuel operation involves coupling multiple thermal, mechanical, and chemical phenomena. Early fuel models, such as GAPCON (Singh, 1977), FALCON (Rashid et al., 2004), FEMAXI (Nakajima et al., 1994),

FRAPCON (Berna et al., 1997), and FRAPTRAN (Geelhood et al., 2011), typically used many correlations formulas to predict fuel behavior and had limited coupling between the physical fields. TOUTATIS (Bentejac and Hourdequin, 2005) and ALCYONE (Thouvenin et al., 2007) used 2D/3D models and expressions based on mathematical and physical principles to describe fuel behavior. However, fuel codes are usually written in programming languages, making code changes extraordinarily complex and challenging to apply the source code to other applications.

BISON is a code for simulating fuel performance developed by Idaho National Laboratory (INL) based on the Multiphysics Object-Oriented Simulation Environment (MOOSE). It is designed to solve the axisymmetric 1D, 2D, and 3D problems for fuel performance. The MOOSE framework has a limited graphical user interface and lacks pre- and post-processing tools.

The FAST code is based on the COMSOL Multiphysics platform and was developed to simulate the behavior of the CANDU reactor fuel under transient and steady-state operating conditions. The FAST code includes heat transfer, burnup, fuel densification, fission gas swelling and release. It also includes creep, pellet-cladding interaction, and other mechanics modules. The simulation results of the FAST code were benchmarked with ELESIM (Notley, 1979), ELESTRES (Chassie et al., 2005), and ELOCA (Williams, 2005) codes (the three codes were also developed for CANDU fuel) and experimental data, and good agreement was obtained.

CityU Advanced Multiphysics nuclear fuel Performance with User-defined Simulations (CAMPUS) (Liu et al., 2016) is an LWR fuel model based on MATPRO (Hagrman et al., 1995), BISON (Hales et al., 2016), and FAST (Prudil, 2013) code using the COMSOL Multiphysics platform. The predicted performance of a UO_2 fuel with zircaloy cladding in CAMPUS was compared with the results from BISON, ABAQUS, and FRAPCON, and good agreement was achieved. UO_2, composite (UO_2-10% volBeO), silicide (U_3Si_2), and mixed oxide [$(Th_{0.9},U_{0.1})O_2$] fuel performance are calculated and compared, which proves the flexibility and utility of the CAMPUS code. The CAMPUS code includes the modules of heat generation and production, oxygen diffusion, fuel deformation, fission gas release and swelling, gap/plenum pressure, and other models under transient and steady-state operating conditions.

In this paper, the development of a fuel code is described. This model is based on the COMSOL Multiphysics platform. COMSOL Multiphysics is a computational platform based on the finite element method with a variety of built-in physical fields such as mechanics, thermal, acoustics, and optics. Users can also implement physical fields by establishing PDEs and ODEs. COMSOL Multiphysics has comprehensive pre- and post-processing capabilities, including geometry construction, mesh generation and result plotting.

The model is based on the FAST and CAMPUS code framework described previously and simulated the behavior of annular MOX fuel in a liquid lead-bismuth eutectic cooled fast reactor. The model contains heat transfer, fuel burnup, oxygen redistribution, plutonium redistribution, fission gas release, porosity variation, and grain growth modules.

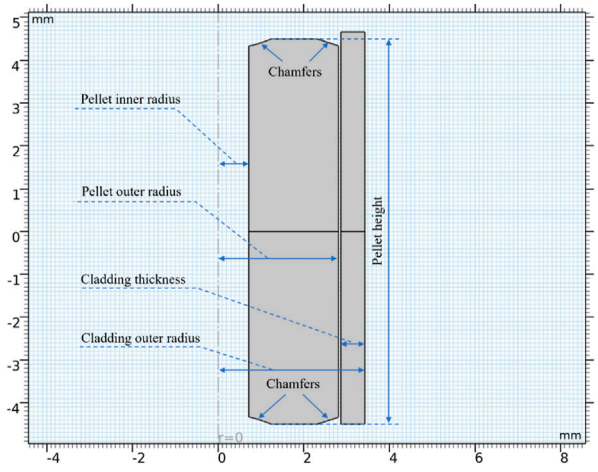

FIGURE 1
Schematic diagram of the annular MOX fuel used in this work.

TABLE 1 Specifications of pellet in ACO-3 fuel rod (Bridges et al., 1993; Karahan and Buongiorno, 2010).

Parameters	Value
Cladding material	HT9
Fuel density (%TD)	92.5
Pellet inner diameter(mm)	1.47
Pellet outer diameter(mm)	5.55
Cladding thickness(mm)	0.56
Outer diameter of cladding(mm)	6.86
Oxygen/Metal ratio (O/M)	1.95
Fuel composition [Pu/(Pu + U)] (wt%)	29
Maximum linear power (kW/m)	42.6
Maximum fuel burnup (at%)	16.3
Maximum integrated flux (10^{22}) (n/cm2)	19

Model development

Model geometry and mesh

The annular MOX fuel pellet used in this work is modeled based on the pellet and cladding dimensions in the experimental fuel rod numbered ACO-3 from the U.S. Department of Energy's CDE (Core Demonstration Experiment) experiment.

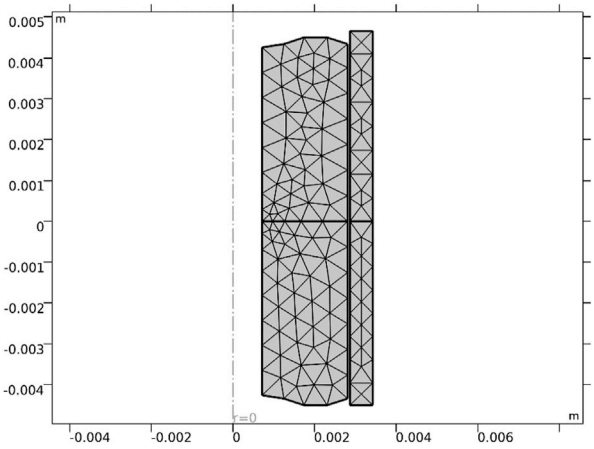

FIGURE 2
The mesh before refining.

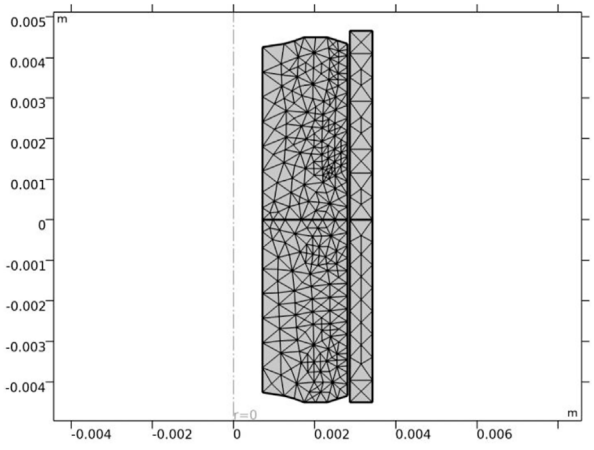

FIGURE 3
The mesh after refining.

Figure 1 shows a 2D axisymmetric geometry used in this work. Fuel specifications are listed in Table 1. During the pellet production, the edges of the pellet are chamfered to give space to the swelling of the fuel during operation and to reduce the interaction forces of the pellets in the axial direction. The chamfering dimensions in this work are based on the literature (Prudil, 2013).

The COMSOL built-in "Adaptive Mesh Refinement" is used to save computational resources and obtain sufficient computational accuracy. Adaptive mesh refinement automatically refines the mesh when the local gradient is too large and retains the original mesh in areas with smaller gradients during the solving process. Figure 2 and Figure 3 demonstrate the mesh before and after refining.

Heat transfer module

To solve the temperature distribution of the fuel pellet, the transient heat transfer equation needs to be solved

$$\rho C_p \frac{\partial T}{\partial t} = \nabla \cdot (k \nabla T) + Q \tag{1}$$

where ρ is the fuel density (kgm^{-3}), C_p is the heat capacity of the fuel ($Jmol^{-1}K^{-1}$), k is the thermal conductivity ($Wm^{-1}K^{-1}$), $T(K)$ is the temperature, and Q is the power density (Wm^{-3}). The material properties are listed in Table A1. The power density is calculated as the ratio of linear power and the cross-section area of the pellet as $Q = \frac{P_{lin}}{s_{pellet}}$.

Fuel burnup module

It is necessary to calculate the fuel burnup to accurately calculate properties such as thermal conductivity of fuels and predict fuel behavior. According to the literature (Morgan, 2007), the fuel burnup will be expressed through the ordinary differential equation and correlated with time and fuel power.

$$\frac{dBu}{dt} = \frac{P_{\text{lin}}\left((1-y)M_{\text{U}} + yM_{\text{Pu}} + (2-x)M_{\text{O}}\right)}{s_{pellet}\rho_0\left((1-y)M_U + yM_{Pu}\right)} \tag{2}$$

where Bu is the fuel burnup ($MW\,h/kg$). P_{lin} is the instantaneous linear power (W/m) and s_{pellet} is the cross-sectional area of the fuel pellet, ρ_o is the unirradiated fuel density, M_U, M_{Pu} and M_O are the molar masses of natural uranium, natural plutonium, and oxygen, respectively, y is the mass fraction of uranium in the fuel, and x is the deviation from the stoichiometry of oxygen.

Oxygen redistribution module

Liquid metal-cooled fast reactors operate at higher linear powers and higher coolant temperatures than light water reactors (LWRs). In addition, the effective fuel density (smear density) and the initial oxygen/metal ratio are lower than those of LWRs. As a result, the operating fuel temperature is much higher than LWRs. The high temperatures and high-temperature gradients lead to a complex chemical environment (Karahan, 2009) where the migration of fuel components such as cesium, oxygen, molybdenum, and plutonium significantly impacts the overall fuel performance.

To control the chemical reaction between the fuel and the cladding, the initial oxygen/metal ratio of the oxide fuel in the fast reactor is designed to be less than 2. Deviation from stoichiometry x is defined as:

$$x = \frac{O}{U + Pu} - 2 \tag{3}$$

For the hypostoichiometric case, defining $c = -\frac{x}{2}$ to denote oxygen vacancies.

Based on thermo-transport theory, the oxygen atom flux under temperature-driven $J\,(m^2/s)$ is

$$J = -D_O\left(\Delta c + c\frac{Q}{RT^2}\nabla T\right) \tag{4}$$

where Q is the molar effective heat of transport of oxygen, T is the temperature (K), and D_O is the diffusion coefficient of oxygen.

Bringing into the continuity equation $\frac{\partial c}{\partial t} = -\nabla.J$, the variable$c$ becomes a function of time t and position r.

Under axisymmetric conditions, the gradient in the axial direction can be neglected. Eq. 4 becomes

$$\frac{\partial c}{\partial t} = \frac{1}{r}\frac{\partial}{\partial r}\left\{rD\left(\frac{\partial c}{\partial r} + c\frac{Q}{RT^2}\frac{\partial T}{\partial r}\right)\right\} \tag{5}$$

Plutonium redistribution module

Plutonium migration mechanisms have been extensively investigated, and a large amount of basic information on plutonium migration mechanisms has been obtained. Bober (Bober et al., 1973) and Schumacher and Matzke (Glasser-Leme and Matzke, 1982) pointed out vapor transport and thermal diffusion as important mechanisms of plutonium migration, respectively. Vapor transport and thermal diffusion are mainly influenced by temperature, oxygen/metal ratio, and initial plutonium content (Olander, 1976).

Uranium and plutonium migrate under temperature gradients, especially in the radial direction where the temperature gradient is large (Ishii and Asaga, 2001). Such migration leads to local variations in plutonium concentration. The modeling of the radial distribution of plutonium is a critical issue for the design of MOX fuel pellets because the accumulation of plutonium in the central part of the fuel pellet during irradiation imposes significant limitations on the maximum fuel temperature, which affects the linear power of the fuel (Olander, 1976).

In this work, thermo-transport theory (Clement and Finnis, 1978; Ishii and Asaga, 2001) is used to simulate plutonium redistribution in the fuel pellet's radial direction.

Diffusion flow$J$ contains a concentration gradient term and a thermal diffusion term:

$$J = -D_{Pu}\left(\frac{\partial C}{\partial r} + C(1-C)\frac{Q_{Pu}}{RT^2}\frac{dT}{dr}\right) \tag{6}$$

The continuity equation is

$$\frac{\partial C}{\partial t} = -\nabla.J \tag{7}$$

Combining the above two equations gives the variation of plutonium concentration with time in the radial distribution. Q_{Pu} is the heat of transport, $Q_{Pu} = 35000cal/mol$, R is the universal gas constant, $R = 1.987cal/mol/K$, C is the mass fraction of plutonium. D_{Pu} is the coefficient of mutual diffusion of uranium and plutonium, $D_{Pu} = 0.34 \times 10^{-4}\exp\left(-\frac{55351}{T}\right)(\mathrm{m}^2/\mathrm{s})$.

Fission gas release module

Since the Booth diffusion model (Booth, 1957) agrees well with the experimental data, it is used for the fission gas diffusion calculations in this work. The fission gas concentration c_g is determined by

$$\frac{\partial c_g}{\partial t} = D_g\frac{1}{r}\frac{\partial^2\left(rc_g\right)}{\partial r^2} + B \tag{8}$$

where $D_g\,(\mathrm{m}^2/\mathrm{s})$ is the fission gas diffusion coefficient and the source term$B\,(\mathrm{atom}/\mathrm{m}^3/\mathrm{s})$ is the gas production rate due to fission, $B = \dot{F}z$, where $z = 0.25\,(atom/fission)$ is the fission gas yield. $\dot{F}\,(\mathrm{fissions}/\mathrm{m}^3/\mathrm{s})$ is the fission rate density, based on the approximation that the energy released per fission$is\ 200MeV$, therefore

$$\dot{F} = \left[200\frac{\mathrm{MeV}}{\mathrm{fission}} \times \frac{10^6 eV}{1\mathrm{MeV}} \times \frac{1.6\times10^{-19}\mathrm{J}}{\mathrm{eV}}\right]^{-1} Q$$

$$= \left(3.125\times10^{10}\right)Q \tag{9}$$

where $Q\,(\mathrm{W}/\mathrm{m}^3)$ is power density.

The fission gas atoms are released into the grain boundaries, and as the fuel burnup increases, the gas atoms saturate the grain boundaries, causing bubbles to interconnect, thus creating a diffusion path to the free volume of the fuel. The subsequent fission gas produced will be released into the free volume of the fuel. Grain boundary saturated gas density$G_{bsat}\,(\mathrm{atoms}/\mathrm{m}^3)$ from the literature (White and Tucker, 1983) is given by

$$G_{bsat} = \frac{4r_f f\left(\theta_{fg}\right)f_B}{3k_B T sin^2\left(\theta_{fg}\right)}\left(P_{ext} + \frac{2\gamma_{se}}{r_f}\right)\left(\frac{3}{g_r}\right) \tag{10}$$

$$f(\theta) = 1 - 1.5\cos(\theta) + 0.5\cos^3(\theta) \tag{11}$$

where $r_f = 5\times10^{-7}\mathrm{m}$ is the diameter of the grain boundary bubble, and $f(\theta_{fg})$ is a function of the bubble shape with respect to $\theta_{fg} = 50^\circ$, is the half dihedral angle between the bubbles, and $f_B = 0.5$ is the ratio of grain boundary saturation at saturation, and k_B is the Boltzmann constant, and $T(K)$ is the temperature, $\gamma_{se} = 0.626\ (Jm^{-2})$ is the surface tension of the gas, and g_r is the grain diameter. All coefficients are taken from the BISON manual (Hales et al., 2016).

Porosity variation module

Under the effect of the temperature gradient, the pores migrate toward the center of the fuel. The pores migrate

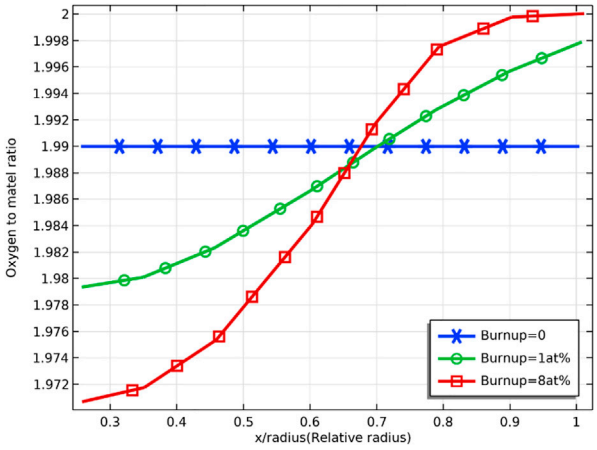

FIGURE 4
Radial distribution of oxygen/metal ratio at 0, 1 at% and 8 at% fuel burnup (with initial oxygen/metal ratio of 1.99)

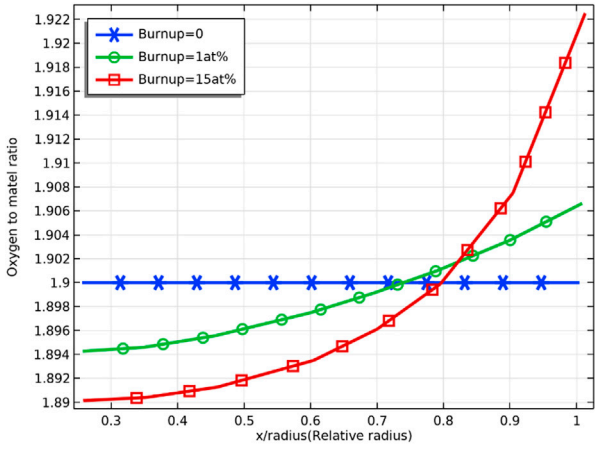

FIGURE 5
Radial distribution of oxygen/metal ratio at 0, 1 at% and 8 at% fuel burnup (with oxygen/metal ratio of 1.90)

toward the pellet center for solid MOX fuels, eventually forming a central void; for annular MOX fuels, they show an increase in porosity at the surface of the central hollow. The migration mechanism is vapor transport, where the fuel vaporizes on the hotter side of the pore and then condenses on the cooler side of the pore. The vapor transport results in the migration of the porosity to the center of the fuel, and the theoretical support for vapor transport comes from Nichols (Nichols, 1967) and Sens (Sens, 1972). The physical and mathematical models of the migration governing equations are well summarized in the literature (Vance, 2017).

During fuel production, pores are created, which are called initial porosity. Based on the initial porosity, the effect of fuel densification, fission gas, and solid fission product swelling on the porosity is considered.

$$P = P_0\left(1 - F_{\text{dens}} - \frac{\Delta V_{\text{sfp}}}{V}\right) + \frac{\Delta V_{\text{gfp}}}{V} \tag{12}$$

where $P_0 = 0.08$, is the initial porosity, and F_{dens} is the porosity eliminated under fuel densification as suggested in Ref. (Hastings and Evans, 1979)

$$F_{\text{dens}} = 0.6 - \exp\left(-0.506 - 8.67 \times 10^{-10} T^3 \times \left(1 - \exp\left(-2.867 \times 10^{-2}\beta\right)\right)\right) \tag{13}$$

$\frac{\Delta V_{\text{sfp}}}{V}$ is the swelling due to fissionable solids, typically 0.32% per at % burnup (Olander, 1976)

$$\frac{\Delta V_{\text{sfp}}}{V} = 0.0032\frac{\text{Bu}}{225} \tag{14}$$

The correlation of swelling caused by fission gas is taken from MATPRO nuclear fuel material properties database (Mihaila et al., 2012) as

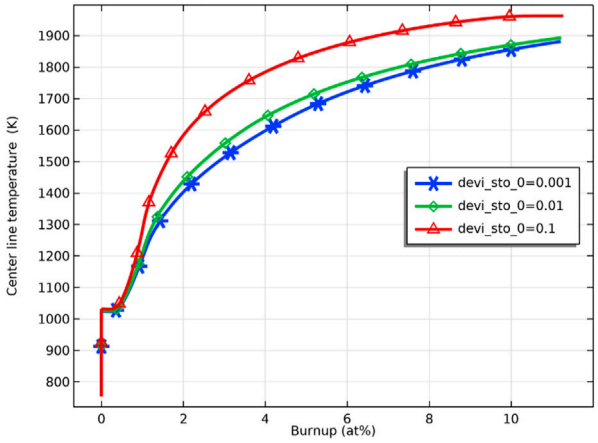

FIGURE 6
Pellet inner surface temperature against burnup for deviation from the stoichiometry of oxygen of 0.001, 0.01, and 0.1 (with Pu content = 29wt%).

$$\frac{d\left(\Delta V_{\text{gfp}}/V\right)}{dt} = \begin{cases} 9.42 \times 10^{-36}(2800 - T)^{11.73} \exp\left(-0.0162(2800 - T)\right) \exp\left(-8 \times 10^{-7}\text{Bu}\rho\right) \times \rho\frac{d\text{Bu}}{\text{dt}}, & \int_0^t F(t)B\,\text{dt} \le N_{\text{sat}}\frac{3}{a} \\ 0, & \int_0^t F(t)B\,\text{dt} \ge N_{\text{sat}}\frac{3}{a} \end{cases} \tag{15}$$

Grain growth module

During the irradiation process, high temperatures cause grain growth. In this work, the effective size of the grain is

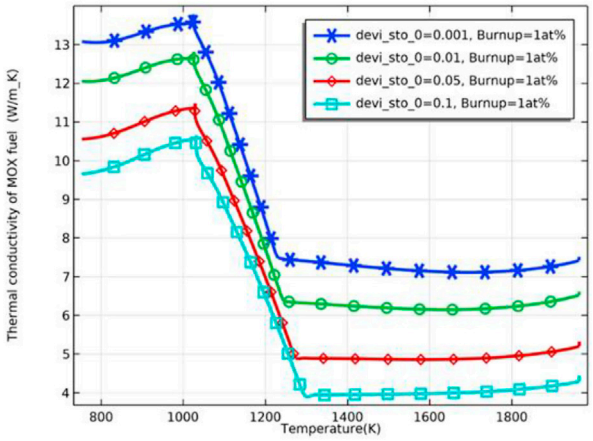

FIGURE 7
Fuel thermal conductivity against temperature for deviation from the stoichiometry of oxygen of 0.001, 0.01, 0.05 and 0.1 (burnup = 1 at%).

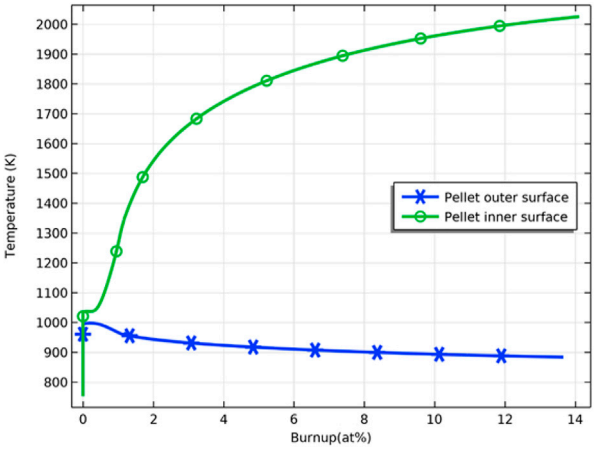

FIGURE 9
Pellet inner/outer surface temperature variation against burnup.

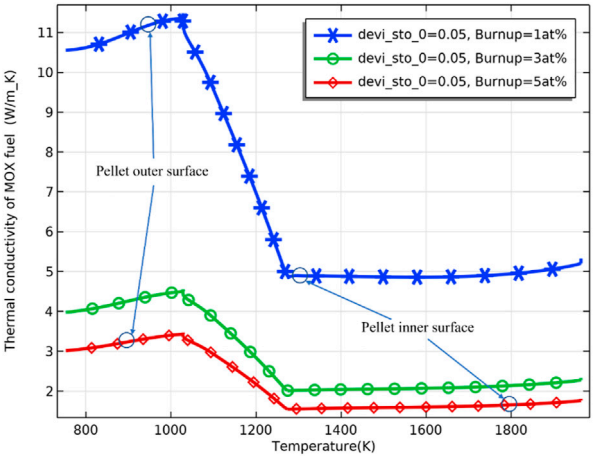

FIGURE 8
Fuel thermal conductivity against temperature for burnup of 1 at%, 3 at%, and 5 at% (deviation from the stoichiometry of oxygen = 0.05).

assumed to be the average grain diameter, which is obtained by solving the equation given in the literature (Khoruzhii et al., 1999)

$$\frac{dg_d}{dt} = k_g\left(\frac{1}{g_d} - \frac{1}{g_{max}} - \frac{1}{g_{ir}}\right) \tag{16}$$

where $k_g\,(m^2 s^{-1})$ is the grain growth rate, defined as

$$k_g = 1.46 \times 10^{-8} \exp\left(\frac{-32100}{T}\right) \tag{17}$$

$T\,(K)$ is the temperature, and $g_{max}\,(\mu m)$ is the maximum stable size of the grain, defined as

$$g_{max} = 2.23 \times 10^{-3} \exp\left(\frac{-7620}{T}\right) \tag{18}$$

The effect of irradiation on grain growth $g_{ir}\,(\mu m)$ is considered and defined as

$$g_{\mathrm{ir}} = \frac{6.71 \times 10^{18}\, exp\,\left(\frac{-5620}{T}\right)}{\dot{F}T} \tag{19}$$

Results and discussions

The Heat Transfer Module in COMSOL was used to solve the heat transfer in fuel. The thermal deformation was calculated using the Solid Mechanics module in COMSOL. The modules of oxygen redistribution, plutonium, grain growth, and fission gas release are implemented with user-defined PDEs. The MUMPS (Multi-frontal Massively Parallel sparse) direct solver in COMSOL is used to solve the coupled multiphysics. In all calculations, except those with marked power, the rest are calculated with a linear power of $40kW/m$.

The migration of oxygen has a significant impact on the overall performance of the fuel. To control the chemical reaction of the pellet with the cladding, the initial oxygen/metal ratio of MOX fuel is designed to be less than 2. The oxygen is redistributed in the radial direction under the temperature gradient during operation.

Figure 4 and Figure 5 demonstrate the radial distribution of oxygen to the burnup for an initial oxygen/metal ratio of

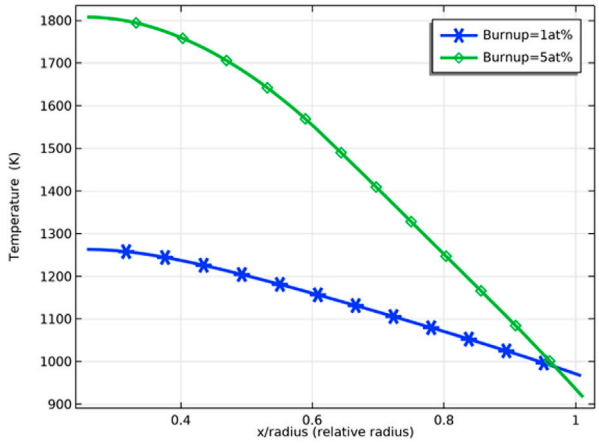

FIGURE 10
Pellet radial temperature for burnup = 1 at% and 5 at%.

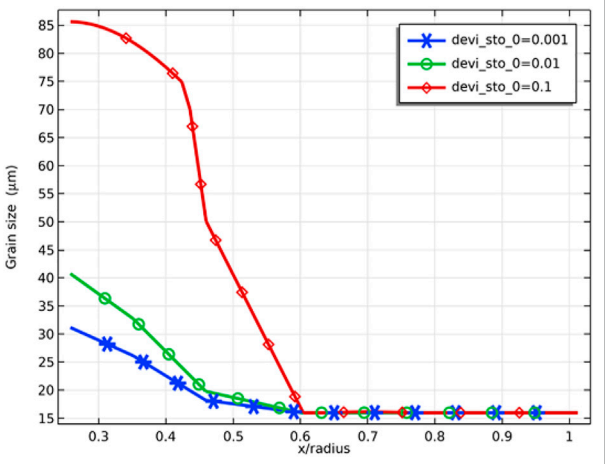

FIGURE 12
Radial variation of grain size at deviation from the stoichiometry of oxygens of 0.001, 0.01, and 0.1 (fuel burnup of 8 at%).

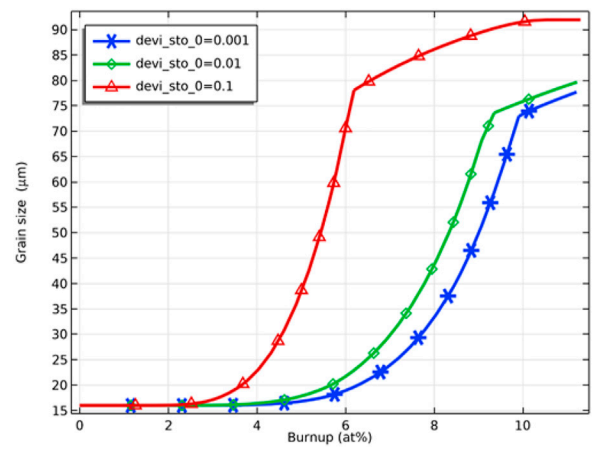

FIGURE 11
Variation of pellet inner surface grain size with fuel burnup for deviation from the stoichiometry of oxygen of 0.001, 0.01 and 0.1.

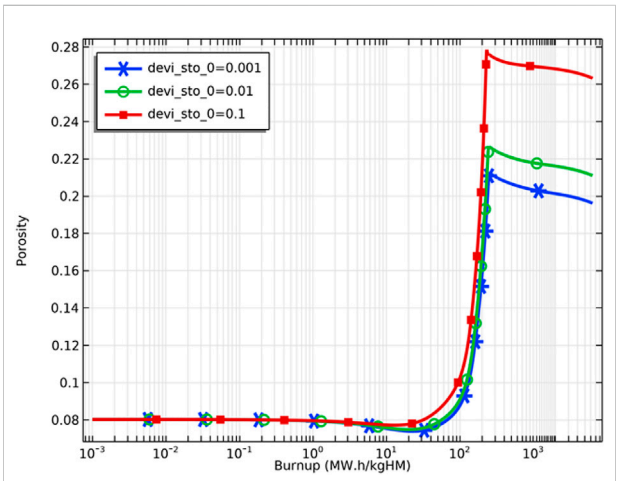

FIGURE 13
Variation of pellet inner surface porosity for deviation from the stoichiometry of oxygens of 0.001, 0.01 and 0.1.

1.99 and 1.90, respectively. The deviation from the stoichiometry of oxygen (devi_sto) is defined in the chemical expression of the fuel $(PuU)O_{2-devi\_sto}$. The oxygen migrates toward the outer surface of the fuel under a temperature gradient. As shown in Figure 4, with a small initial deviation from the stoichiometry of oxygen, the O/M ratio in the outer region of the pellet reaches 2 (saturation value) when the fuel burnup reaches 8 at%, while the oxygen atoms inside the pellet still tend to migrate to the outer part of the pellet. On the contrary, when the initial deviation from the stoichiometry of oxygen is large, the O/M ratio on the outer surface of the fuel does not reach 2 even when the fuel burnup reaches 15 at%. It can be explained by the fact that the O/M ratio inside the fuel is already low, and the migration rate of oxygen to the outer surface is reduced or even stopped.

As shown in Figure 6, the inner surface temperature of the pellet is sensitive to the deviation from the stoichiometry of oxygen. The fuel temperature rises faster when the deviation from the stoichiometry of oxygen increases, and the temperature difference between the inner surface of the pellet reaches the maximum value at the fuel burnup of about 4 at%, which are 1600 K and 1780 K for the deviation from the stoichiometry of oxygen of 0.001 and 0.1, respectively, the difference reaches 180 K.

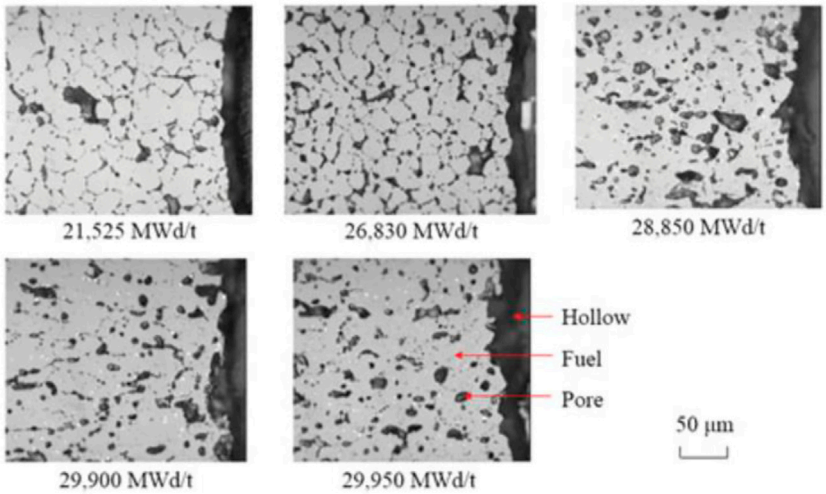

FIGURE 14
Microstructures of fuel region around the hollow fuel pellets at different burnups (Ishimi et al., 2016).

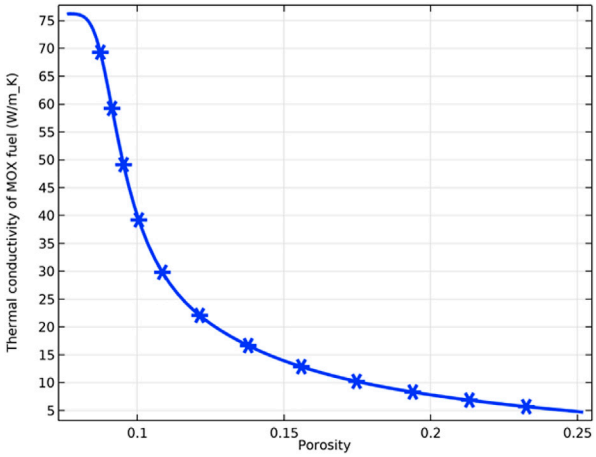

FIGURE 15
Variation of fuel thermal conductivity with porosity.

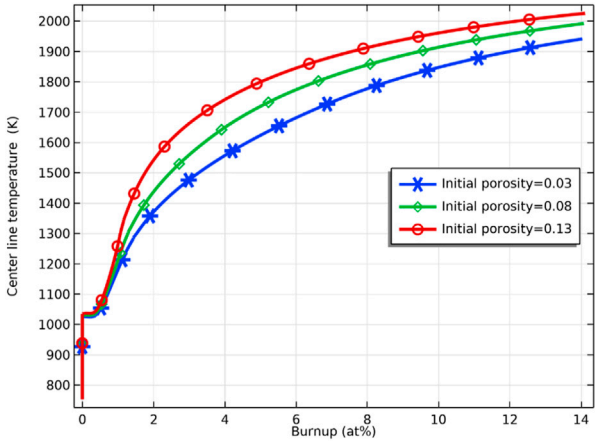

FIGURE 16
Variation of fuel inner surface temperature with fuel burnup for initial porosity of 0.03, 0.08 and 0.13.

As the burnup further increases, the difference in the fuel inner surface temperature due to different deviations from the stoichiometry of oxygen decreases, and the fuel temperature stabilizes. The difference in fuel temperature can be explained by the effect of the deviation from the stoichiometry of oxygen on the fuel thermal conductivity. The thermal conductivity of the pellet was plotted against different deviations from stoichiometry, as shown in Figure 7, where the thermal conductivity of the pellet decreases with an increase of deviation from the stoichiometry of oxygen. The decrease in thermal conductivity leads to higher fuel temperature. Plotting the thermal conductivity against temperature for different fuel burnups at the same deviation from the stoichiometry of oxygen, as shown in Figure 8, the thermal conductivity of the fuel decreases with an increase in burnup at the same temperature. On the other hand, the difference in thermal conductivity due to temperature difference decreases as burnup increases, resulting in a decrease in the difference in thermal conductivity of the inner and outer surfaces of the pellet. However, the difference in temperature increases with deepening burnup. As shown in Figure 9, the difference in thermal conductivity between the inner and outer surfaces of

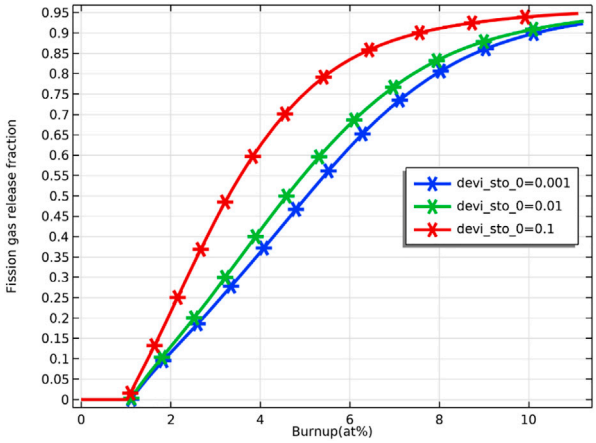

FIGURE 17
Variation of pellet inner surface fission gas release rate with fuel burnup for deviation from the stoichiometry of oxygen of 0.001, 0.01 and 0.1.

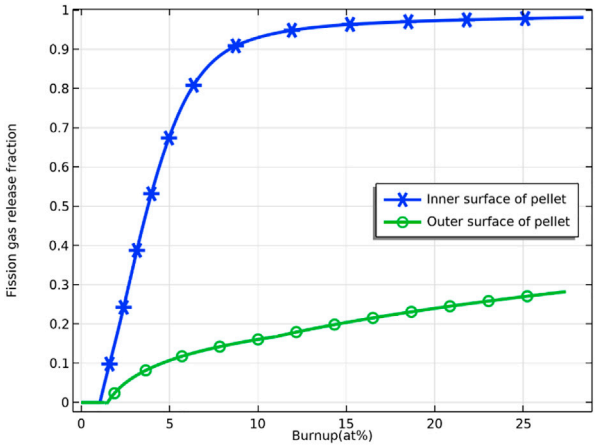

FIGURE 18
Variation of fission gas release ratio on the inner and outer surfaces of fuel pellets with fuel burnup.

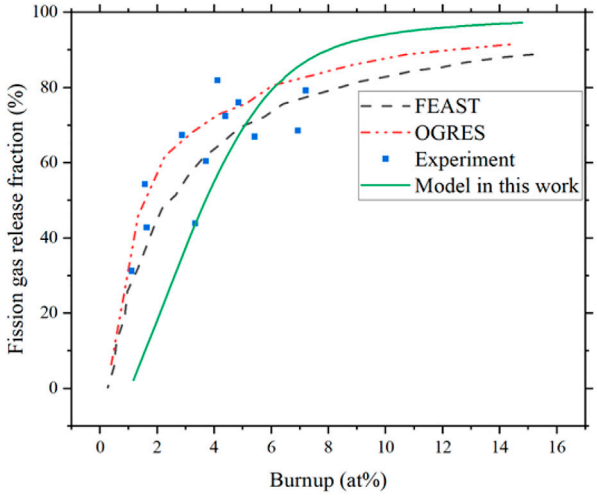

FIGURE 19
Fission gas release ratio from FEAST, OGRES model, experiment data (Karahan and Buongiorno, 2010), and compared with model in this work.

the pellet is about 6 W/m_K (5 W/m_K on the inner surface and 11.3 W/m_K on the outer surface) at 1 at% burnup. This value decreases to less than 2 W/m_K (1.7 W/m_K on the inner surface and 3.2 W/m_K on the outer surface) at 5 at% burnup. The temperature of the inner and outer surfaces of the pellet against burnup is shown in Figure 9, and the radial temperature at 1 at% and 5 at% is shown in Figure 10.

As Figure 11 shows, the grain size increases rapidly with an increase in burnup in the initial stage. Then the grain size increase rate slows down due to reaching the maximum grain size allowed at the corresponding temperature (Eq. 16). The effect of deviation from the stoichiometry of oxygen on grain size is significant, with grain size increasing within 50% for deviation from the stoichiometry of oxygen of 0.001 and 0.01 at 6 at% fuel burnup. In contrast, grain size has increased to more than 4 times the original size for deviation from stoichiometry of oxygen of 0.1. With the further increase of fuel burnup, the grain size difference under different deviations from the stoichiometry of oxygen conditions decreases and tends to the maximum grain size.

As Figure 12 shows, the grains grow in the range of relative radius less than 0.6, which is due to the fact that grain growth requires a temperature higher than 1300 K (Sari, 1986). At a fuel burnup of 8 at%, the grain size of the pellet inner surface is 30 and 40 μm at deviation from the stoichiometry of oxygen of 0.001 and 0.01, respectively, while at deviation from the stoichiometry of oxygen of 0.1, the grain size of the pellet inner surface reaches 85 μm. This can be explained by the fact that when the deviation from the stoichiometry of oxygen increases, the fuel thermal conductivity decreases, and the fuel temperature increases, resulting in an increase in the grain size.

Figure 13 demonstrates the variation of the porosity of the fuel inner surface with increasing fuel burnup for different deviations from the stoichiometry of oxygen. At the initial stage, there is a slight decrease in porosity caused by fuel densification. The fuel porosity then increases rapidly and reaches saturation. After the fuel porosity saturation, the porosity decreases due to continued fission gas release, and the swelling of the solid fission products takes voids in the fuel matrix. The porosity increasing on the pellet's inner surface was confirmed by the experiments. The microstructure around the hollow at different burnups is shown in Figure 14.

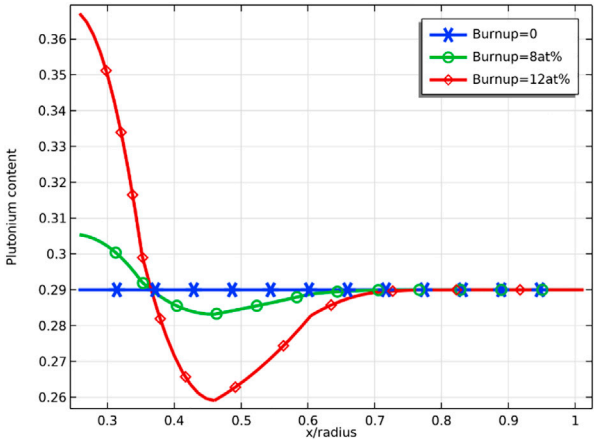

FIGURE 20
Radial distribution of plutonium at 0,8 at% and 12 at% fuel burnup.

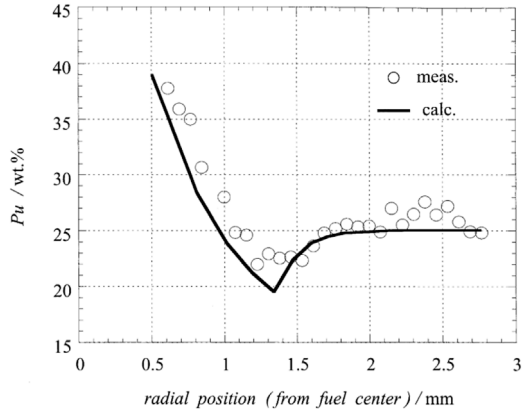

FIGURE 22
Radial distribution of plutonium predicted by CEDAR model and comparison of experimental data (experimental data from XD0992 fuel rod with 11 at% burnup, initial oxygen/metal ratio of 1.99, and initial plutonium content of 27 wt%) (Ishii and Asaga, 2001).

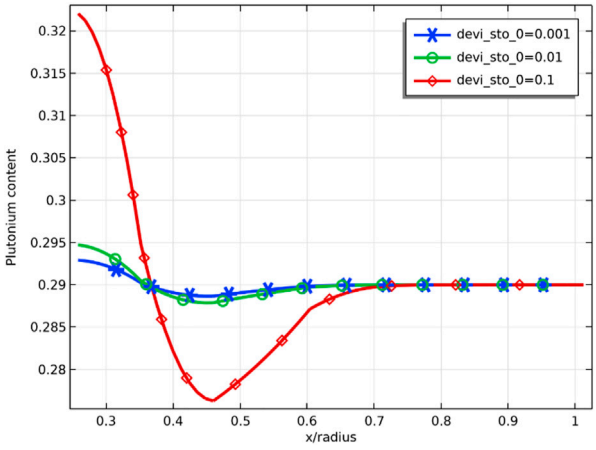

FIGURE 21
Radial distribution of plutonium content (mass fraction) for deviation from the stoichiometry of oxygens of 0.001, 0.01, and 0.1 (fuel burnup of 8 at%).

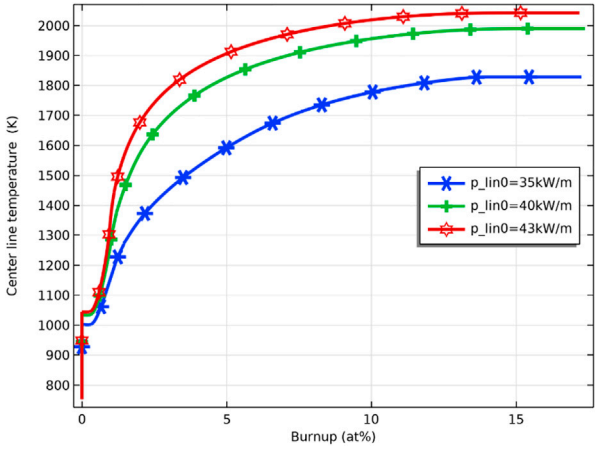

FIGURE 23
Variation of pellet inner surface temperature at initial linear power of 35 kW/m, 40 kW/m and 43 kW/m.

The pores formed by the void migration and growth of fission gas bubbles moved to the hollow edge part and became coarsened (Ishimi et al., 2016). Compared with the porosities for different deviations from the stoichiometry of oxygen, the porosity of the pellet inner surface increases when the deviation from the stoichiometry of oxygen increases, which is caused by the rise in temperature and the swelling of fission gas. As Figure 15 shows, the increase in porosity leads to a decrease in fuel thermal conductivity and a further rise in pellet inner surface temperature. Because the thermal conductivity of the fuel decreases as the porosity increases, the fuel temperature is higher for the same fuel burnup when the initial porosity of the fuel increases, as Figure 16 shows.

As Figure 17 shows, no fission gas is released from the pellet at the initial stage of fuel irradiation because the fission gas in the grain boundaries does not saturate yet (Eq. 10), and no fission gas has escaped. When the fuel burnup reaches about 1 at%, the fission gas starts to be released from the pellet and increases logarithmically with the fuel burnup, which is consistent with the literature (Karahan and Buongiorno, 2010) (see Figure 17). Figure 17 demonstrates the effect of deviation from the stoichiometry of oxygen on fission gas release. There is an

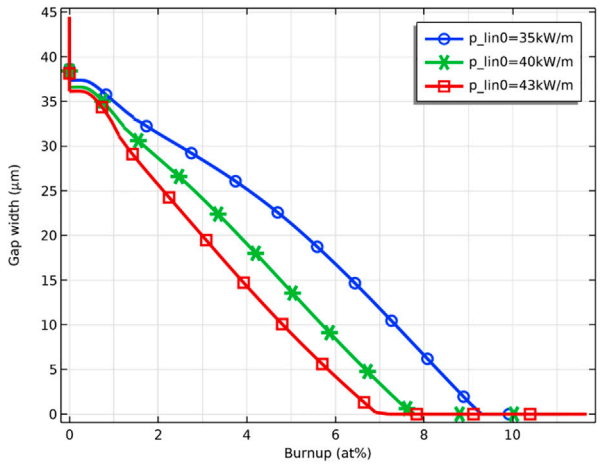

FIGURE 24
Gap closure process for initial linear power of 35 kW/m, 40 kW/m and 43 kW/m.

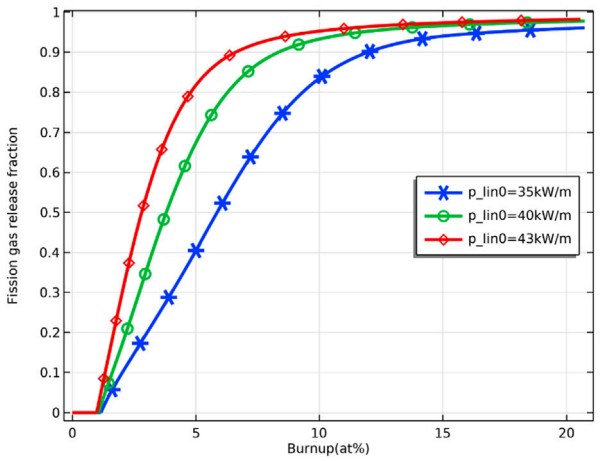

FIGURE 25
Fission gas release fraction at initial linear power of 35 kW/m, 40 kW/m and 43 kW/m.

increasing trend of fission gas release with increasing deviation from the stoichiometry of oxygen. The effect of deviation from the stoichiometry of oxygen on fission gas release is significant from 2 at% to 8 at% fuel burnup, with the percentage of fission gas release at 4 at% fuel burnup being about 63% for deviation from the stoichiometry of oxygen of 0.1 and about 36% for a deviation from the stoichiometry of oxygen of 0.001. The release of fission gas leads to an increase in gap pressure, which increases the pressure on the cladding and thus increases the risk of breakage.

Figure 18 demonstrates the comparison of the fission gas release from the fuel pellet's inner and outer surfaces of the fuel pellet. Since the temperature of the outer surface of the pellet is lower than that of the inner surface, the fission gas at the grain boundaries on the outer surface of the pellet saturates later in the initial stage of irradiation and therefore released later. Since the inner surface temperature of the pellet is higher than the outer surface temperature, the release of fission gas on the inner surface of the pellet is much larger than that on the outer surface.

Figure 19 compares the results of the FEAST model (Karahan (Karahan, 2009; Karahan and Buongiorno, 2010)), the OGRES model (Matthews and Wood (Matthews and Wood, 1980)), and experimental data for fission gas release predictions. As shown in Figure 19, the fission gas release from the FEAST model, OGRES model, and experimental data all show a logarithmic trend, which is consistent with the trend predicted for fission gas release in this work. The differences in slope and maximum value may arise from temperature and fuel composition differences.

Plutonium migrates under a temperature gradient, especially in a zone with a significant temperature gradient. The distribution of plutonium is a slow process, as shown in Figure 20, with plutonium migrating toward the center of the fuel pellet during irradiation, which is consistent with the literature (Valentino et al., 2012). Since the diffusion of plutonium in uranium accelerates with the temperature increase, the plutonium content remains unchanged at 29 wt% in the outer part of the pellet, where the temperature is low. In the region where the relative radius is smaller than 0.7, plutonium migrates toward the center of the pellet.

Figure 21 demonstrates the radial distribution of plutonium content for different deviations from the stoichiometry of oxygen at a burnup of 8 at%. The radial distribution of plutonium is sensitive to the deviation from the stoichiometry of oxygen, and the difference in plutonium content in the radial direction is less than 0.5 wt% at deviation from the stoichiometry of oxygen of 0.001, while plutonium content difference is greater than 4 wt% at deviation from the stoichiometry of oxygen of 0.1. This can be explained by the fact that the increase in deviation from the stoichiometry of oxygen reduces the thermal conductivity of the fuel, which leads to an increase in fuel temperature and accelerates the migration of plutonium. The accumulation of plutonium leads to an increase in local power, so the swelling of solid fission products and the swelling of gas fission products will be more significant at these locations. In the case of uniform power distribution, the temperature at the center of the fuel is already higher due to the poor thermal conductivity of MOX fuel, and the power rise due to plutonium enrichment at the center of the pellet will further increase the temperature at the center of the pellet. Compared with a solid pellet, an annular pellet can avoid high pellet center temperature and leave some space for fuel swelling, delaying fuel failure.

Figure 22 is taken from the CEDAR code developed by Japan Nuclear Cycle Development Institute (JNC) (Uwaba et al., 2014) and experimental measurements. The measurements were taken

from XD0992 fuel rods with an initial linear power of 44 kW/m, and the plutonium distribution was obtained by electron probe microanalysis (EPMA) after running for 560 effective full power days (EFPD). Comparing the line of "Burnup = 12 at%" in Figure 20 and Figure 22, the distribution trend of plutonium is the same, showing a trend of enrichment against the temperature gradient and toward the center. Meanwhile, the plutonium content redistribution prediction in this model calculation agrees well with the CEDAR model and the experimental data. The plutonium content is close to 40% at the center of the fuel, while the plutonium content on the outer surface of the fuel is almost unchanged.

Three initial linear power (35 kW/m, 40 kW/m, and 43 kW/m) are simulated to investigate the effect of power increase on fuel performance. As shown in Figure 23, the temperature of the fuel inner surface increases with the increase of the initial linear power. The maximum fuel inner surface temperature at initial linear power of 35 kW/m, 40 kW/m, and 43 kW/m are 1820, 2000, and 2050 K, respectively, and the highest simulated linear power is 43 kW/m, at which the maximum fuel temperature does not reach the melting point.

The effect of pellet thermal expansion and JOG growth in the gap closure process is considered. Figure 24 shows the gap closure process for initial linear power of 35 kW/m, 40 kW/m and 43 kW/m. As the linear power increases, the pellet-cladding closure is advanced. On the one hand, the rise in linear power causes an increase in fuel temperature, which in turn increases the thermal expansion of the pellet; on the other hand, as shown in Figure 25, the release of fission gas increases due to the rise in fuel linear power, which leads to faster growth of JOG. The increase in fuel linear power causes the pellet-cladding gap to close earlier due to the increased thermal expansion and the accelerated JOG growth.

Conclusion

A fuel performance simulation model based on the COMSOL Multiphysics platform was developed, which contains modules such as heat transfer, oxygen redistribution, plutonium redistribution, and fission gas release, which could be used for transient and steady-state simulation. In this work, a 2D axisymmetric model is developed for operating a single MOX fuel pellet and cladding in a liquid lead-bismuth eutectic cooled fast reactor. The material and geometry of the ACO-3 fuel were used. The simulation results are compared with existing codes and experimental data, and a good agreement is achieved. This model has a visual interface for easy modification and adjustment of parameters and is suitable for simulation and analysis of different fuel types and sizes.

The O/M ratio (or deviation from the stoichiometry of oxygen) significantly affects temperature evolution, fission gas migration and release behavior, and plutonium redistribution. In the initial stage of fuel operation, oxygen is redistributed in the radial direction and migrates from the center to the outer surface of the fuel. This effect is affected by the fuel's initial oxygen/metal ratio. The oxygen/metal ratio of the fuel has a significant influence on the thermal conductivity, grain growth, fuel porosity, and fission gas release of the fuel. As the deviation from the stoichiometry of oxygen increases, the thermal conductivity of the fuel decreases, resulting in a higher fuel temperature. The fuel grain size tends to increase with increasing the deviation from the stoichiometry of oxygen, with the most pronounced grain size change on the inner surface of the fuel, where the temperature is highest. With the increase of the deviation from the stoichiometry of oxygen, the saturation value of the fuel porosity shows an upward trend, and the increase of the porosity results in a decrease in the thermal conductivity of the fuel, which in turn results in a higher fuel temperature. The fission gas release amount and release rate showed an upward trend with the increase of the deviation from the stoichiometry of oxygen. The release of fission gas occurs mainly on the inner surface of the fuel, whose temperature is highest. Plutonium shows a tendency to migrate toward the center during fuel operation, and this trend is exacerbated with the increase of the deviation from the stoichiometry of oxygen. Higher fuel temperature resulted in faster fission gas release, faster JOG growth, and earlier closure of the pellet-cladding as fuel line power rose.

The operation of nuclear fuel involves coupling many physical and chemical phenomena, and the model established in this work has many areas worthy of further improvement. In order to make the simulation results more in line with the actual operation of the reactor, improvements can be made, such as 1) considering the power history during reactor operation; 2) modeling multiple pellets, taking into account power differences at different positions of the fuel rods; 3) using a 3D model; and 4) enhancing the mechanics module, taking cracking and creep into consideration.

Data availability statement

The raw data supporting the conclusions of this article will be made available by the authors, without undue reservation.

Author contributions

The work is mainly done by YC. WZ is the advisor of YC. KC and LG contributed to the accomplishment of this work. All authors contributed to the article and approved the submitted version.

Funding

The financial support from the Nuclear Power Technology Innovation Center of China (No. 45000-41020012) and the

Fundamental Research Funds for the Central Universities of China (No. 45000-18841210) is highly appreciated.

Conflict of interest

The authors declare that the research was conducted in the absence of any commercial or financial relationships that could be construed as a potential conflict of interest.

Publisher's note

References

Bentejac, F., and Hourdequin, N. (2005). Toutatis: An application of the CAST3M finite element code for PCI three-dimensional modeling. *Proc. Pellet-clad Interact. Water React. Fuels* 37, 9–11.

Berna, G. A., Beyer, G. A., Davis, K. L., and Lanning, D. D. (1997). *FRAPCON-3: A computer code for the calculation of steady-state, thermal-mechanical behavior of oxide fuel rods for high burnup*. Maryland, United States: US Nuclear Regulatory Commission. doi:10.2172/576110

Bober, M., Schumacher, G., and Geithoff, D. (1973). Plutonium redistribution in fast reactor mixed oxide fuel pins. *J. Nucl. Mater.* 47 (2), 187–197. doi:10.1016/0022-3115(73)90101-3

Booth, A. H. (1957). *A method of calculating fission gas diffusion from UO_2 fuel and its application to the X-2-f loop test*. Chalk River, Canada: AECL.

Bridges, A. E., Waltar, A. E., Leggett, R. D., Baker, B., and Ethridge, J. L. (1993). A liquid-metal reactor core demonstration experiment using HT-9. *Nucl. Technol.* 102 (3), 353–366. doi:10.13182/nt93-a17034

Carbajo, J. J., Yoder, G. L., Popov, S. G., and Ivanov, V. K. (2001). A review of the thermophysical properties of MOX and UO_2 fuels. *J. Nucl. Mater.* 299 (3), 181–198. doi:10.1016/s0022-3115(01)00692-4

Chassie, G. G., Sim, K.-S., Wong, B., and Papayiannis, G. (2005). *ELESTRES code Upgrades*. Vienna, Austria: International Nuclear Information System.

Clement, C., and Finnis, M. (1978). Plutonium redistribution in mixed oxide (U, Pu)O_2 nuclear fuel elements. *J. Nucl. Mater.* 75 (1), 193–200. doi:10.1016/0022-3115(78)90044-2

Geelhood, K. J., Luscher, W. G., Beyer, C. E., and Cuta, J. M. (2011). *Fraptran 1.4: A computer code for the transient analysis of oxide fuel rods*. Maryland, United States: US Nuclear Regulatory Commission.

Glasser-Leme, D., and Matzke, H. (1982). Interdiffusion and chemical diffusion in the UO_2 - (U, Pu)O_2 system. *J. Nucl. Mater.* 106, 211–220. doi:10.1016/0022-3115(82)90350-6

Hagrman, D. T., Allison, C. M., and Berna, G. A. (1995). *SCDAP/RELAP5/MOD 3.1 code manual: MATPRO, A library of materials properties for light-water-reactor accident analysis*. United States: N: Web. doi:10.2172/100327

Hales, J. D., Novascone, S. R., Pastore, G., Perez, D. M., Spencer, B. W., and Williamson, R. L. (2016). *BISON theory manual the Equations behind nuclear fuel analysis. INL/EXT-13-29930 rev. 3*. Idaho Falls, Idaho: Idaho National Laboratory.

Hastings, I. J., and Evans, L. E. (1979). Densification algorithm for irradiated UO_2 fuel. *J. Am. Ceram. Soc.* 62, 217–218. doi:10.1111/j.1151-2916.1979.tb19061.x

Ishii, T., and Asaga, T. (2001). An investigation of the Pu migration phenomena during irradiation in fast reactor. *J. Nucl. Mater.* 294, 13–17. doi:10.1016/s0022-3115(01)00445-7

Ishimi, A., Katsuyama, K., Kihara, Y., and Furuya, H. (2016). Fuel performance of hollow pellets for fast breeder reactors. *J. Nucl. Sci. Technol.* 53 (7), 951–956. doi:10.1080/00223131.2015.1085337

Karahan, A., and Buongiorno, J. (2010). Modeling of thermo-mechanical and irradiation behavior of mixed oxide fuel for sodium fast reactors. *J. Nucl. Mater.* 396 (2), 272–282. doi:10.1016/j.jnucmat.2009.11.021

Karahan, A. (2009). Modelling of thermo-mechanical and irradiation behavior of metallic and oxide fuels for sodium fast reactors. United States: Massachusetts Institute of Technology. Ph.D. thesis.

Khoruzhii, O. V., Kourtchatov, S. Y., and Likhanskii, V. V. (1999). New model of equiaxed grain growth in irradiated UO_2. *J. Nucl. Mater.* 265 (1), 112–116. doi:10.1016/s0022-3115(98)00632-1

Liu, R., Prudil, A., Zhou, W., and Chan, P. K. (2016). Multiphysics coupled modeling of light water reactor fuel performance. *Prog. Nucl. Energy* 91, 38–48. doi:10.1016/j.pnucene.2016.03.030

Matthews, J. R., and Wood, M. H. (1980). A simple operational gas release and swelling model: II. Grain boundary gas. *J. Nucl. Mater.* 91 (2), 241–256. doi:10.1016/0022-3115(80)90224-x

Mihaila, B., Stan, M., and Crapps, J. (2012). Impact of thermal conductivity models on the coupling of heat transport and oxygen diffusion in UO_2 nuclear fuel elements. *J. Nucl. Mater.* 430 (1), 221–228. doi:10.1016/j.jnucmat.2012.07.007

Morgan, D. (2007). *A thermomechanical model of CANDU fuel*. Canada: Web.

Nakajima, T., Saito, H., and Osaka, T. (1994). FEMAXI-IV: A computer code for the analysis of thermal and mechanical behavior of light water reactor fuel rods. *Nucl. Eng. Des.* 148 (1), 41–52. doi:10.1016/0029-5493(94)90240-2

Nichols, F. A. (1967). Theory of columnar grain growth and central void formation in oxide fuel rods. *J. Nucl. Mater.* 22 (2), 214–222. doi:10.1016/0022-3115(67)90031-1

Notley, M. (1979). Elesim: A computer code for predicting the performance of nuclear fuel elements. *Nucl. Technol.* 44 (3), 445–450. doi:10.13182/nt79-a32279

Olander, D. R. (1976). *Fundamental aspects of nuclear reactor fuel elements*. United States: Web.

Prudil, A. A. (2013). Fast: A fuel and sheath modeling tool for CANDU reactor fuel. Kingston, Ontario, Canada: Royal Military College of Canada. Ph.D. thesis.

Rashid, Y., Dunham, R., and Montgomery, R. (2004). Fuel analysis and licensing code: Falcon MOD01. EPRI Report.

Sari, C. (1986). Grain growth kinetics in uranium-plutonium mixed oxides. *J. Nucl. Mater.* 137 (2), 100–106. doi:10.1016/0022-3115(86)90038-3

Sens, P. F. (1972). The kinetics of pore movement in UO_2 fuel rods. *J. Nucl. Mater.* 43 (3), 293–307. doi:10.1016/0022-3115(72)90061-x

Singh, R. N. (1977). Isothermal grain-growth kinetics in sintered UO2 pellets. *J. Nucl. Mater.* 64 (1), 174–178. doi:10.1016/0022-3115(77)90021-6

Teague, M., Tonks, M., Novascone, S., and Hayes, S. (2014). Microstructural modeling of thermal conductivity of high burnup mixed oxide fuel. *J. Nucl. Mater.* 444 (1-3), 161–169. doi:10.1016/j.jnucmat.2013.09.035

Thouvenin, G., Michel, B., Sercombe, J., Plancq, D., and Thevenin, P. (2007). *Multidimensional modeling of a ramp test with the PWR fuel performance code ALCYONE*. United States: Web.

Uwaba, T., Mizuno, T., Nemoto, J., Ishitani, I., and Ito, M. (2014). Development of a mixed oxide fuel pin performance analysis code "CEDAR": Models and analyses of fuel pin irradiation behavior. *Nucl. Eng. Des.* 280, 27–36. doi:10.1016/j.nucengdes.2014.08.032

Valentino, D. M., Arndt, S., Jacques, V. D., and Paul, V. U. (2012).Revision of the transuranus PUREDI model. Technical report for the JRC-ITU Action No. 52201 – Safety of Nuclear Fuels and Fuel Cycles.

Vance, I. (2017). Computer simulation of pore migration due to temperature gradients in nuclear oxide fuel. Arkansas, Fayetteville: scholarworks.uark.edu. Thesis.

White, R., and Tucker, M. (1983). A new fission-gas release model. *J. Nucl. Mater.* 118 (1), 1–38. doi:10.1016/0022-3115(83)90176-9

Williams, A. (2005). *The ELOCA fuel modelling code: Past, present and future*. Toronto, Ontario (Canada): International Nuclear Information System.

Appendix

TABLE A1 Summary of MOX $U_{1-y}Pu_yO_{2-x}$ fuel property

Property	Functional form of property	Unit	Source
Fuel density $\rho(U_{1-y}Pu_yO_{2-x})$	$273K \le T \le 923K$ $\rho_s(T) = (10970 + 490y)(9.9734 \times 10^{-1} + 9.802 \times 10^{-6} - 2.705 \times 10^{-10}T^2 + 4.391 \times 10^{-13}T^3)(kg/m^3)$ $923K < T <$ Melting point of MOX $\rho_s(T) = (10970 + 490y)\begin{pmatrix} 9.9672 \times 10^{-1} + 1.179 \times 10^{-5}T \\ -2.429 \times 10^{-9}T^2 + 1.219 \times 10^{-12}T^{3)} \end{pmatrix}$	Kg/m^3	Carbajo et al., 2001
Heat capacity $C_p(U_{1-y}Pu_yO_{2-x})$	$C_P(T, \mathrm{MOX}) = (1-y)C_P(T, UO_2) + yC_P(T, PuO_2)$ $C_P = c_2 + 2c_3t + 3c_4t^2 + 4c_5t^3 + 5c_6t^4 - c_7t^{-2}$ For UO_2 $c_1 = -21.1762$ J/mol, $c_2 = 52.1743$ J/mol/K $c_3 = 43.9735$ J/mol/K^2, $c_4 = -28.0804$ J/mol/K^3, $c_5 = 7.88552$ J/mol/K^4, $c_6 = -0.52668$ J/mol/K^5, $c_7 = 0.71391$ J/mol For PuO_2 $c_1 = -32.0342$ J/mol, $c_2 = 84.495$ J/mol/K, $c_3 = 5.3195$ J/mol/K^2, $c_4 = -0.20379$ J/mol/K^3, $c_5 = 0$ J/mol/K^4, $c_6 = 0$ J/mol/K^5, $c_7 = 1.90056$ J K/mol	J/kgK	Carbajo et al., 2001
Thermal conductivity k$(U_{1-y}Pu_yO_{2-x})$	$k = F_1F_2F_3F_4k_o$ $k_o = \frac{1}{0.06059+0.2754\sqrt{\lvert 2-O/M\rvert}+2.011\times10^{-4}T}\frac{4.715\times10^9}{T^2}\exp\left(-\frac{16361}{T}\right)$ $F_1 = \left(\frac{1.09}{\beta^{3.265}} + \frac{0.0643}{\sqrt{\beta}}\sqrt{T}\right)\arctan\left(\frac{1}{\frac{1.09}{\beta^{3.265}}+\frac{0.0643}{\sqrt{\beta}}\sqrt{T}}\right)$ $F_2 = 1 + \frac{0.019\beta}{(3-0.019\beta)}\frac{1}{1+\exp\left(-\frac{T-1200}{100}\right)}$ $F_3 = 1 - \frac{0.2}{1+\exp\left(\frac{T-900}{80}\right)}$ $F_4 = 1 - \alpha P$	W/(mK)	Karahan., 2009, Teague et al., 2014

frontiers | Frontiers in Energy Research

TYPE Original Research
PUBLISHED 30 September 2022
DOI 10.3389/fenrg.2022.965319

OPEN ACCESS

EDITED BY
Hidemasa Yamano,
Japan Atomic Energy Agency, Japan

REVIEWED BY
Takayuki Ozawa,
Japan Atomic Energy Agency, Japan
Yasushi Okano,
Japan Atomic Energy Agency, Japan

*CORRESPONDENCE
Ho Jin Ryu,
hojinryu@kaist.ac.kr

SPECIALTY SECTION
This article was submitted to Nuclear Energy,
a section of the journal
Frontiers in Energy Research

RECEIVED 09 June 2022
ACCEPTED 08 September 2022
PUBLISHED 30 September 2022

CITATION
Mun J, Kim H-J and Ryu HJ (2022), Analysis of fuel performance under normal operation conditions of MicroURANUS: Micro long-life lead-bismuth-cooled fast reactor.
Front. Energy Res. 10:965319.
doi: 10.3389/fenrg.2022.965319

Analysis of fuel performance under normal operation conditions of MicroURANUS: Micro long-life lead-bismuth-cooled fast reactor

Jiwon Mun, Hyeong-Jin Kim and Ho Jin Ryu*

Department of Nuclear and Quantum Engineering, KAIST, Daejeon, South Korea

An innovative ultra-long-life lead-bismuth eutectic (LBE)-cooled fast reactor called MicroURANUS has been designed to prevent severe accidents. It utilizes the remarkable natural circulation capability of the LBE coolant. Furthermore, it can be operated at 60 MW_{th} without refueling for 30 effective full-power years (EFPY). In this study, the thermal and mechanical performance of the highest linear power rod of MicroURANUS was evaluated by modifying the fuel performance code FRAPCON-4.0, which is the normal operation fuel performance code for light water reactors (LWRs). A plutonium generation model was added to consider changes in the physical properties of the UO_2 fuel. Furthermore, mechanical and oxidation models of 15–15Ti were added, and the coolant models were modified for liquid metal. According to the unique design of MicroURANUS, a maximum low linear power density of 12.5 kW/m ensures that the highest linear power rod can operate below the safety limit. A low fuel temperature provides a large safety margin for fuel melting, as well as low-pressure build-up fission gas release. In addition, low inlet and outlet coolant temperatures of 250 and 350°C cause the cladding to display a low degree of swelling (a maximum diametral strain of 1.5%) while maintaining high mechanical integrity with negligible cumulative damage fraction (CDF). The modified fuel performance code for lead-cooled fast reactors exhibited the capability to be utilized for fuel performance evaluation and design feedback of MicroURANUS.

KEYWORDS

MicroURANUS, fast reactor, long-life, UO_2, fuel performance, lead-bismuth

1 Introduction

The importance of the northern sea route (NSR) for international trade and energy supply stability is increasing. For ships to navigate through the NSR, it is necessary to construct an icebreaker capable of crushing ice thicker than 5 m. Diesel icebreakers have difficulty breaking the ice with a thickness of over 2 m. In addition, these generate fine dust, which causes air pollution. The ships registered with International Maritime Organization (IMO) are required to reduce the sulfur content of diesel fuel to less than 0.5% by 2020 and to reduce CO_2 by 40 and 50% by 2030 and 2050, respectively, compared with 2008 (IMO, 2018). Although LNG-propelled ships have lower sulfide emissions than diesel ships, the problem of high methane emissions exists (Stern, 2020). Therefore, nuclear-propelled ships are a good alternative to fossil-fueled marine ships because they have high energy density and no greenhouse gas emissions. Furthermore, the industry has considerable experience in operating nuclear-powered submarines and aircraft carriers worldwide. Icebreakers that utilize propellant systems such as KLT-40s light water reactors (LWRs) are being developed and operated in Russia. In the case of a pressurized water reactor (PWR) that uses low enriched uranium (LEU), fuel replacement is essential after a maximum of 2.3 years (Afrikantov OKB Mechanical Engineering, 2013). This short refueling period requires a nuclear-only port facility and significantly increases the total life cycle cost of nuclear reactors. These, in turn, result in disadvantages in terms of ship economy and disposal of spent nuclear fuel.

To compensate for these shortcomings of LWR, research is being conducted to use fast reactors with remarkable fuel utilization as propulsion reactors. Among these, the lead-cooled fast reactor (LFR) is considered the most potential Generation-IV (GenIV) innovative reactor concept. A non-refueling ultra-long-life LFR called MicroURANUS is presently being developed in Korea as a nuclear propellant system for marine ships or icebreakers (Nguyen et al., 2021). MicroURANUS is a micro-reactor of 20 MWe. It can be operated for 30 effective full power years (EFPY), which is the full life of the nuclear reactor. This substantially reduces the risk of radioactive leakage in the event of an accident scenario and the problem of spent nuclear fuel. The fuel power density of MicroURANUS is four times lower than that of KLT-40s. In addition, the amount of heavy metal loaded initially is approximately 10 times higher. However, the fuel utilization is superior owing to the characteristic of the fast spectrum reactor. The average conversion ratio is 0.8. In addition, MicroURANUS is designed to operate for 30 EFPY, whereas KLT-40s can be operated for 2.3 years.

Three reference systems were adopted by LFR-provisional System Steering Committee (pSSC): ELFR, ALFRED (EU), BREST-OD-300 (Russia), and SSTAR (United States) (Alemberti et al., 2014). SCK-CEN (Belgium) developed FEMALE for evaluating the fuel performance of mixed oil fuel (MOX), particularly for LFR and ITU (Germany). In addition, they developed and validated the TRANSURANUS code for an application to the ALFRED reactor (Rozzia et al., 2012; Luzzi et al., 2014).

As a preliminary result of accident frequency evaluation through Probabilistic Safety Assessment (PSA), design base events such as Loss of Flow (LOF), Transient Over Power (TOP), Loss of Offsite Power (LOOP), and Loss of Heat Sink (LOHS) are considered Design Bases Accident (DBA), not Anticipated Operational Occurrences (AOOs). Therefore, in this reactor, the failure of minor equipment inside the reactor is defined as AOO, and it is expected that the transient thermal hydraulic phenomenon expected from AOO will have little negligible compared to the transient phenomenon caused by the described DBA and Beyond Design Bases Accident (BDBA). Therefore, the purpose of this study was to analyze the thermal and mechanical behavior of nuclear fuel during its full-life normal operation and evaluate its stability. For this purpose, the steady-state fuel performance code FRAPCON-4.0 was modified for a lead-bismuth-cooled reactor. The LFR fuel performance code was developed by altering the properties of the fuel, cladding, and coolant in the MicroURANUS reactor design. The thermal and mechanical performance of the nuclear fuel during steady-state operation for 30 years (the full life of the reactor) was evaluated using the developed LFR fuel performance code.

2 Modification of material properties

The normal operation fuel performance code for an LWR was modified through correlation alterations using FRAPCON-4.0. The objective was to develop an LFR fuel performance code applicable to the present fast reactor conditions. Fuel performance models such as the gap conductance model (GAPCON-2) and mechanical analysis model subroutine (FRACAS-1) are applied the same as FRAPCON-4.0 with some module changes to adapt to the conditions of MicroURANUS lead-cooled fast reactor (Beyer et al., 1975; Bohn, 1977). The modified material and material properties of LFR fuel performance code are summarized in Table 1. In addition, the correlations of the fuel and the cladding used in this study is summarized in Tables 2, 3, respectively. In this sector, a detailed explanation of updated modules was described.

2.1 Fission gas release

The fission gas release (FGR) was calculated using the modified Forsberg–Massih model in FRAPCON-4.0 (Forsberg

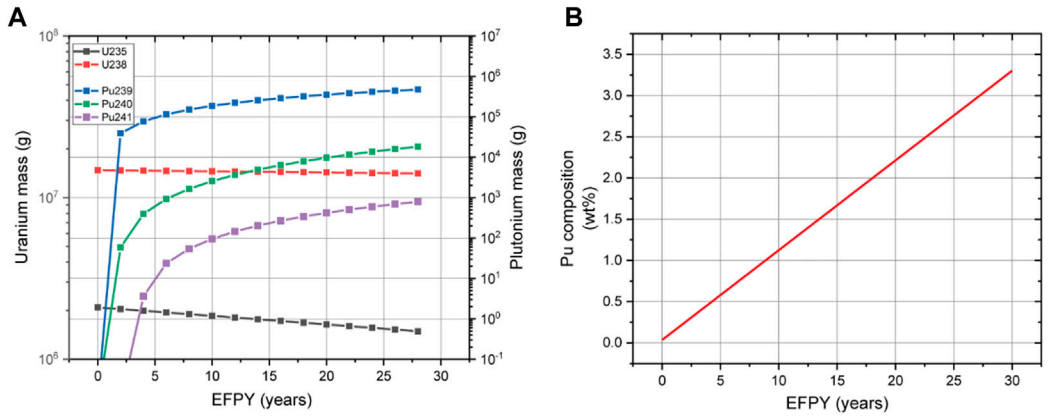

FIGURE 1
(A) Mass variation profiles of U and Pu isotopes and **(B)** composition profile of plutonium (Nguyen et al., 2021).

and Massih, 1985). Fission gas is released with a fraction F if the calculated surface gas area density N (atoms/m^2) is larger than the saturation concentration N_s.

Equation 1 Forsberg–Massih fission gas release model

$$N_S = \left[\frac{4rF(\theta)V_c}{3K_BTsin^2(\theta)}\right]\left(\frac{2\gamma}{r} + P_{ext}\right), F = \frac{N - N_s}{N}$$

N_s = saturation concentration (atoms/m^2)
θ = dihedral half-angle = 50°
K_B = Boltzmann constant.
γ = surface tension = 0.6 (J/m^2)
V_c = critical area coverage fraction = 0.25
r = bubble radius = 0.5 (μm)
$F(\theta)$ = 1–1.5 cos (θ) + 0.5 cos^3 (θ)
P_{ext} = external pressure on bubbles = gas pressure (Pa)

In the case of the Forsberg–Massih model, when the temperature of the nuclear fuel is sufficiently high to allow interconnection among intergranular bubbles, it simulates the release when the opening pathway to release is created. Thus, this is a general thermal release process that assumes that fission gas is released from a high-temperature fuel. However, at a low temperature, athermal fission gas release which is owing to the recoil and knock-out of fission gas atoms is the dominant mechanism, and the Forsberg–Massih model predicts a release of less than 1–2%, whereas 4–5% FGR values have been measured at burn-ups of 60 GWd/MTU (Killeen, Turnbull and Sartori, 2007). Therefore, an empirical athermal release model was suggested that can predict fission gas release at relatively low temperatures (as stated in Equation 2) (Turnbull, 1996). If the temperature of the nuclear fuel is sufficiently low, the higher F_{LT} value from the low-temperature model will be calculated than F from Forsberg–Massih model. In this case, the code was set to use the F_{LT} value instead of the F.

Equation 2 Low-temperature fission gas release model

$$F_{LT} = 7 \times 10^{-5}\, BU + C$$

F_{LT} = fission gas release fraction by low temperature model.
BU = local burnup (GWd/tU)
C = 0; for BU ≤ 40 GWd/tU.
= 0.01(BU - 40)/10; (BU > 40 GWd/tU and F ≤ 0.05)

2.2 Pu generation and radial power profile

The amount of plutonium produced by breeding is larger than that produced by the LWR owing to the characteristic of the fast reactor fuel. The major fissile isotope is Pu-239. Furthermore, in the case of MicroURANUS, the production of approximately 465 kg during 30 EFPY was calculated in the core design process (as shown in Figure 1A) (Nguyen et al., 2021). Variations in the thermal conductivity, heat capacity, and thermal expansion of the fuel caused by plutonium generation were considered as variations during operation through the weight fraction and composition of Pu-239, Pu-240, and Pu-241. The properties that vary during operation owing to Pu generation include density, heat capacity, thermal expansion, enthalpy, modulus, and thermal conductivity.

In addition to the fuel material properties, the influence of the variations in fuel irradiation behavior caused by plutonium generation was investigated. It is reported that a fission gas release enhancement effect occurs in the case of a MOX with 20 wt% plutonium (which is operated in a fast reactor) it is reported that there is a fission gas release enhancement effect owing to inhomogeneity caused by the segregation of PuO_2

(Walker, Goll, and Matsumura, 1996). However, in the case of nuclear fuel operating at low power and temperature, the fission gas release enhancement effects owing to plutonium segregation are negligible, and the plutonium composition at the end of life of the current nuclear fuel is approximately 3 wt% (as shown in Figure 1B) (White et al., 2001). This is significantly low to be considered in the MicroURANUS case.

Plutonium generation also affects the radial flux inside the pellet because of the generation of the local fissile element Pu-239. In the LWR, owing to the self-shielding effect by resonance capture of the thermal neutron, it has a higher burnup and neutron flux at the edge part of the pellet. However, radial flux depression can be disregarded in fast reactors because of the low-resonance capture of neutrons (Guerin, 2012; Medvedev et al., 2018). A few studies were conducted to develop a new burn-up module for fast-reactor MOX fuel that considers the generation of minor actinide elements (MA) and helium from the decay of MA (Cechet et al., 2021). The plutonium generation is considerably marginal in the present design (a maximum of 3 wt%). Furthermore, the initial fuel form is UO_2 rather than MOX. Therefore, a flat power profile was applied to the present code.

2.3 Model of cladding material properties

The most important life-limiting factor of cladding in the case of the fast reactor is irradiation-induced void swelling. Meanwhile, ferritic/martensitic stainless steel has been used widely in SFR because of the superior resistance to irradiation void swelling. However, when it is irradiated at a relatively low temperature (below approximately 400°C), it considerably affects the decrease in fracture resistance owing to irradiation embrittlement (Chen, 2013; Cabet et al., 2019). In addition, the ductile-to-brittle transition temperature (DBTT) of ferritic/martensitic stainless steel increases with irradiation at a low irradiation temperature. This could induce brittle fracture of cladding. Therefore, austenitic stainless steel cladding is used in the case of the present MicroURANUS core design because the inlet/outlet temperature is 250°C/350°C. This temperature is lower than the irradiation temperature of the existing fast reactor (approximately 500°C).

Conventional 304 and 316 grades were mainly used for austenitic stainless steel cladding, which is mainly used in SFR in the early stage of development. In addition, 304LN and 316 L(N) grades were applied gradually (these are low-carbon and nitrogen-controlled austenitic stainless steels) (Dai, Zheng, and Ding, 2021). This could suppress the decrease in corrosion resistance owing to grain boundary carbon precipitation and improve the mechanical strength owing to the high nitrogen content (Mathew, 2010; Ravi et al., 2012). In addition, swelling of cladding is the most crucial life-limiting factor in high burn-up and high neutron energy environments. Ti-stabilized austenitic stainless steels such as 316Ti and 15-15Ti have been developed to solve this problem (Maillard et al., 1994). These are swelling-resistant alloys. 15-15Ti shows a remarkable void swelling resistance of up to 130 dpa (Courcelle et al., 2016). Therefore, 15-15Ti steel was adopted as the cladding material because the peak cladding radiation damage attained approximately 120 dpa under the present reactor operating conditions. Luzzi *et al.* developed a "generalized 15-15Ti" model to fit the swelling data of several 15-15Ti steel groups in a conservative manner, and this model was used in this work (Luzzi et al., 2014). The irradiation swelling data of 15–25% cold worked 15–15Ti steels were used to establish the model (Hübner, 2000; Bergmann et al., 2003; Cheon et al., 2009; Dubuisson, 2013). The cladding correlations show the swelling correlation of 15-15Ti applied to this code (see Table 1). It has a peak value at 450°C. Furthermore, it increases exponentially with the increase in temperature and increases by a factor of 2.75 for fast fluence on cladding.

The corrosion of cladding in an LBE flow environment is also one of the highly important degradation mechanisms. The approximate coolant limit temperature is acknowledged to be 550°C (Li et al., 2017). In general, austenitic steels in lead-bismuth eutectic systems between 450 and 500°C oxidize with the formation of dual-layer porous magnetite (Fe_3O_4)/compact inner spinel layer for short-term operation (Müller, Schumacher and Zimmermann, 2000). However, it was verified that a uniform and protective Fe-Cr spinel single layer is formed in austenitic steel SS316L and 15–15Ti during long-term operation at a temperature below 450°C (Tsisar et al., 2016; Lee et al., 2021) Therefore, the single layer oxidation parabolic law of 15-15Ti was applied, and the parabolic rate constant and activation energy were calculated by fitting the literature data on long-term oxidation at 400°C, 450°C, and 550°C in flowing LBE (2 m/s) with 10^{-7} mass% of dissolved oxygen. (Tsisar et al., 2016). In addition, the existing ZrO_2 thermal conductivity model was modified to the thermal conductivity of Fe–Cr spinel obtained from first-principle calculations (Liu et al., 2016).

Equation 3 Parabolic law and constants for 15-15Ti

$$x = \sqrt{2k_p t}\,,\ k_p = Z \cdot \exp\left(-\frac{Q}{RT}\right)$$

x: corrosion thciness,
k_p: corrosion constant, and
t: corrosion time

Q: *activation energy*, R: *gas contant*, *and* T: *Temperature* (K)

$Q = 176.07 \pm 22.98$ kJ/mol, $RlnZ = 1.7417 \pm 31.84$

3 Results and analysis

3.1 Simulation conditions

The operating conditions of MicroURANUS are summarized in Table 4. The linear power of the rod of the MicroURANUS core was calculated based on a reactor

TABLE 1 Material property correlation of 15-15Ti.

Model parameter	Correlation used in the present work	References
Melting point [K]	1,673	Schumann, (1970)
Thermal conductivity [W/mK]	$k = 13.95 + 0.01163\,T$ [°C]	Tobbe, (1975)
Thermal expansion [%]	$B = -3.101 \times 10^{-4} + 1.545 \times 10^{-5}\,T$ [°C] $+ 2.75 \times 10^{-9}\,T^2$ [°C]^2	Tobbe, (1975)
Elastic modulus [GPa]	$E = 202.7 - 81.67 \times 10^{-3} \times T$ [°C]	Tobbe, (1975)
Specific heat [J/kgK]	$c_p = 450.74 + 1.333 \times 10^{-1} \times T$ [K]	Banerjee et al. (2007)
Irradiation swelling [%]	$\frac{\triangle V}{V}$ [%] $= 1.5 \times 10^{-3} \exp[-2.5\,(\frac{T[°C]-450}{100})^2]\varnothing^{2.75}$ $\varnothing[\frac{10^{22}}{cm^2}]$: neutron fast fluence, T [°C] : cladding temperature	Luzzi et al. (2014)
Irradiation creep	$\dot{\varepsilon}_i$ [$\%h^{-1}$] $= 3.2 \times 10^{-24}\overline{E}\varnothing\sigma, \overline{E}$ [MeV] = average neutron energy, $\varphi[\frac{n}{m^2 s}]$: fast flux, $\overline{E}$ $\varphi = 5 \times 10^{14}$ MeV/cm^{2}s , σ [MPa] cladding equivalent stress	Tobbe, (1975)

TABLE 2 Correlations adopted in fuel modeling.

Model parameter	Correlation used in the present work	References
Melting point [K]	MATPRO	Siefken et al. (2001)
Thermal conductivity	Duriez/modified NFI model	Duriez et al. (2000)
Thermal expansion [%]	Luscher/Geelhood model	Luscher, Geelhood and Porter, (2015)
Emissivity	MATPRO	Siefken et al. (2001)
Specific heat [J/kgK]	MATPRO	Siefken et al. (2001)

TABLE 3 Operation conditions of MicroURANUS.

Design parameter	Value
Fuel	
Fuel material	UO_2
Fuel diameter [mm]	17.1
Fuel column length [m]	1.55
Rod axial peaking factor	1.2
Effective full power operation year [year]	30
Cladding and plenum	
Cladding material	15–15Ti
Cladding outer diameter [mm]	20
Cladding thickness [mm]	0.95
Radial gap thickness [mm]	0.15
Rod fill gas	He
Initial fill gas pressure [MPa]	1
Fission gas plenum size [mm]	100

(Continued on following page)

TABLE 3 (*Continued*) Operation conditions of MicroURANUS.

Design parameter	Value
Coolant	
Primary coolant material	Lead-Bismuth Eutectic (LBE)
Coolant composition Pb/Bi [%]	44.5/55.5
Coolant pressure [MPa]	0.1
Average coolant heat transfer coefficient of the rod [W/m^{2}K]	30869
Coolant velocity [m/s]	0.77

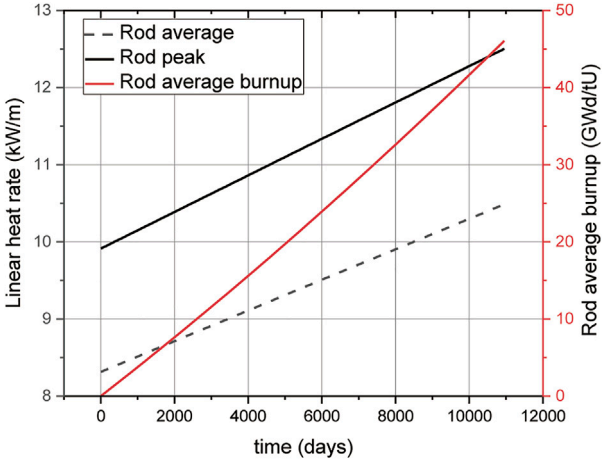

FIGURE 2
Average burn-up and linear heating rate profile of the rod.

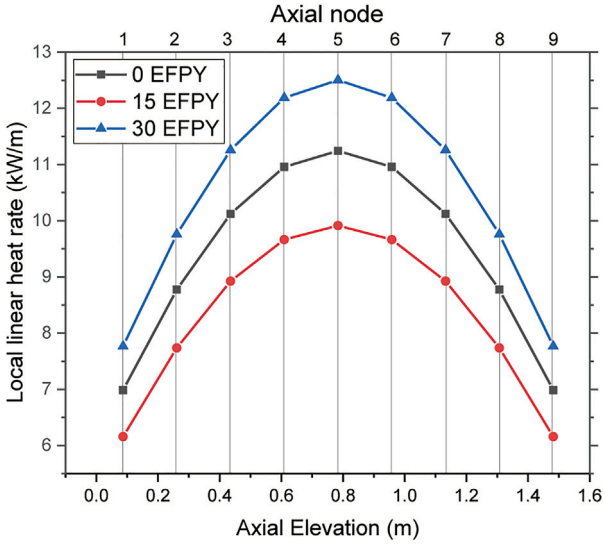

FIGURE 3
Axial peaking for fuel rod.

physics study (Nguyen et al., 2021). The performance of the peak power rod was evaluated to consider the safety margin of this core from the operation limit, through thermal and mechanical calculations of the nuclear fuel rod. Figure 2 shows the average and peak linear heat rates of the peak power rod and the average burn-up of the rod. These were calculated using the LFR fuel performance code. The MCS calculation in the reactor physics study revealed that the local peak linear heat rates of the hottest assembly were 9.91, 11.24, and 12.50 at 0, 15, and 30 EFPY, respectively. In the actual core design, the top and bottom 25 cm of the fuel rod have different enrichment designs, called onion zoning. However, simple cosine-shaped axial zoning is considered for the present calculations to evaluate nuclear fuel performance. An average-to-peak power ratio of 1.2 was applied. The rod average linear heat rate was calculated to be approximately 8.26, 9.37, and 10.42 at 0, 15, and 30 EFPY, respectively. The rod average discharged burn-up was approximately 46 GWd/tU when operated for 30 EFPY. Figure 3 shows the linear heat rate as a function of the axial elevation location of the fuel rod during operation.

The flow velocity variation between assembly channels should be treated carefully for the hot channel analysis. However, in the case of the current reactor system called MicroURANUS, it is a conceptual design stage, and the reactor physics study was based on constant fluid velocity obtained from a one-dimensional thermal hydraulics code (Nguyen et al., 2021). Therefore, the preliminary fuel performance analysis was performed on the unit cell without considering detailed assembly and grid structure to consider the coolant assembly velocity variation. For this reason, the core averaged mass flow rate is used in the current stage which is the

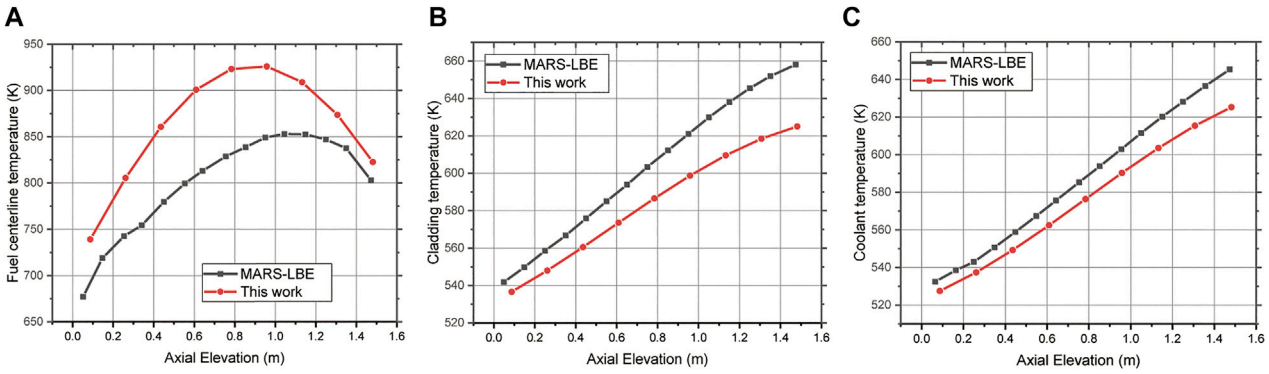

FIGURE 4
MARS-LBE code comparison results of **(A)** Fuel centerline temperature **(B)** Cladding average temperature **(C)** Coolant temperature.

TABLE 4 Modified material and material properties in LFR fuel performance code.

Module	Modified material	Modified properties
Fuel	UO_2	Pu generation
Cladding	Zircaloy → 15–15Ti	Swelling, Thermal conductivity, Heat capacity, Thermal expansion, Transition temperature Modulus, Creep (Thermal, Irradiation)
Coolant	Water → LBE	Constant heat transfer coefficient, Heat capacity, Mass flux

same value as the current study (see Table 4). In addition, the axial temperature distribution data was calculated based on an average bundle mass flow rate.

3.2 Validation of code

Figure 4 compares the temperature calculation results with the preliminary thermal-hydraulics analysis results obtained by MARS-LBE (Shin et al., 2017). Thermo-mechanical feedback of the material was not considered in the case of the RELAP5/MOD3 code and COBRA-TF used in the MARS code. The initial gap at cold zero power (CZP) was set to 150 μm in the MARS-LBE and LFR fuel performance codes in this study. However, in the case of the LFR fuel performance code, the thermo-mechanical response in both fuel and cladding owing to thermal expansion from CZP to hot zero power (HZP) was considered. The fuel surface and cladding inner radius displacements at the HZP were calculated to be approximately 60 and 110 μm, respectively. Consequently, the increase in the initial gap was approximately 200 μm at the beginning of life condition in the LFR fuel performance code. This is 50 μm larger than the initial inputted cold gap of 150 μm. Thereby, the LFR fuel performance code fuel rod temperature calculation result differed from the fuel centerline temperature (see Figure 4A). The fuel temperature was determined to be about 150 K higher in the case of the LFR fuel performance code. In the case of cladding and coolant temperatures, the MARS-LBE temperature was higher than the LFR fuel performance code results in Figures 4B,C. The differences among these codes exist mainly because of the 1) heat transfer coefficient models and the 2) calculation methods. 1) In MARS-LBE, convective heat transfer is obtained by calculating the convective heat transfer coefficient from Nu which is given by the function of Re and Pr. Seban-Shimazaki correlation is applied to obtain Nu in the MARS-LBE system (Seban and Shimazaki, 1949). Therefore, the heat transfer coefficient value is calculated and updated simultaneously according to the fuel rod axial position and temperature of the coolant using the Seban-Shimazaki correlation. Also, the MARS-LBE code considers mass, momentum, and flow condition change due to pressure loss by friction on the fluid flow model. However, in this work, the LFR fuel performance code was developed to verify that the reactor can be operated safely during steady-state operation from a nuclear fuel perspective through multiphysics modeling of fuel and cladding. Therefore, the characteristics of the fluid, which were considered in detail in the thermal-hydraulics code (MARS-LBE), were simplified in this work. In this work, the core-averaged constant heat transfer coefficient obtained by MARS-LBE was applied as stated in Table 4. In addition, the coolant temperature is calculated as an energy balance through a one-dimensional convection heat transfer coefficient without considering momentum change or friction. 2)

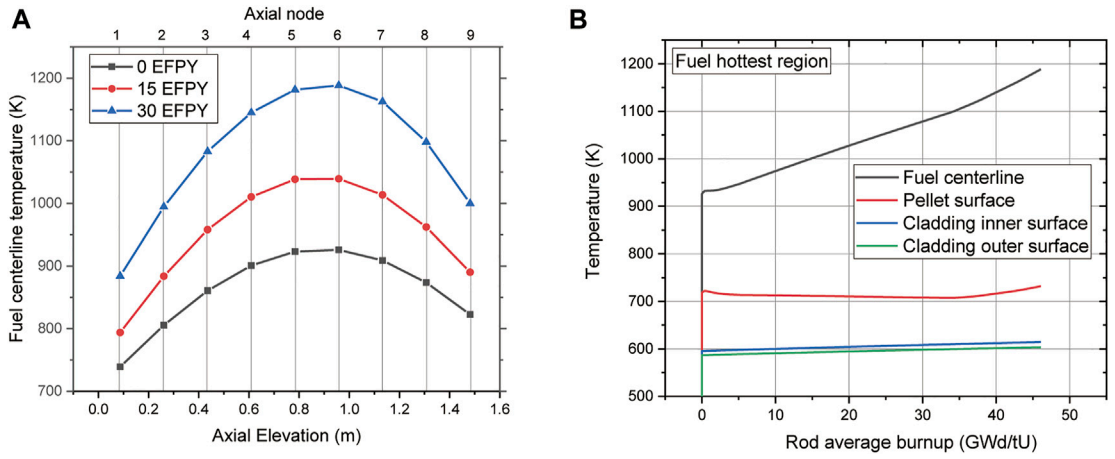

FIGURE 5
(A) Axial distribution of fuel centerline and **(B)** temperature evolution profile of the hottest axial region.

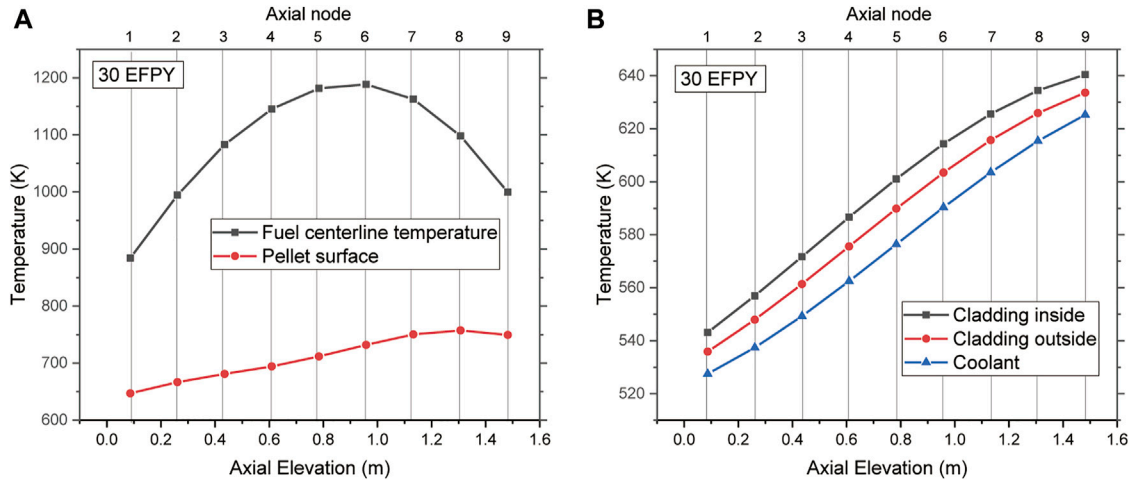

FIGURE 6
End-of-life Temperature of **(A)** fuel pellet and **(B)** cladding and coolant.

In the MARS-LBE code, the temperature calculation proceeds from the initial geometry without considering the thermomechanical deformation of the fuel rod. On the other hand, in this work, heat flux emitted out of the rod due to the He gap size increase caused by the thermal expansion of the cladding. As mentioned, there is a slight difference in the temperature calculation results due to the heat exchange capability of coolant and the effect of the geometry difference caused by the difference in detailed calculation methods among these two codes. Therefore, although the inlet temperature was set to have the same value of 523 K, the coolant temperature was calculated to be relatively low to be a maximum of about 20 K in the LFR fuel performance code. Furthermore, a low coolant temperature causes the cladding temperature to be calculated low and the maximum difference was calculated to be about 40 K in the outlet region. If we consider the different characteristics between the two codes, the temperature results were slightly different. However, thermomechanical iterations and a series of interactions can provide a more realistic simulation to analyze fuel rod multiphysics behavior with acceptable coolant temperature difference with thermal-hydraulics code. In the case of fuel temperature, the maximum temperature of the fuel at a point slightly higher than the mid-region was identical in both code

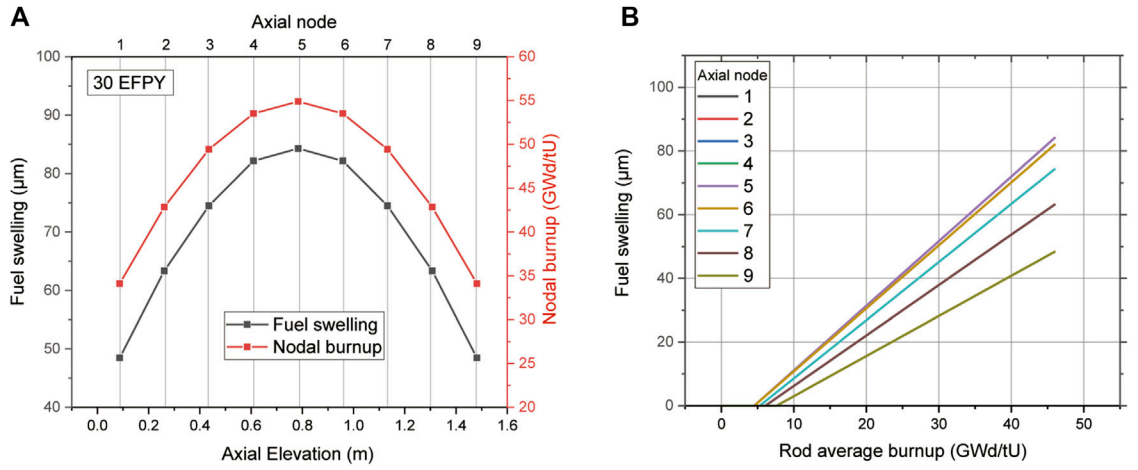

FIGURE 7
Fuel swelling **(A)** nodal burn-up relationship and **(B)** rod average burn-up profile.

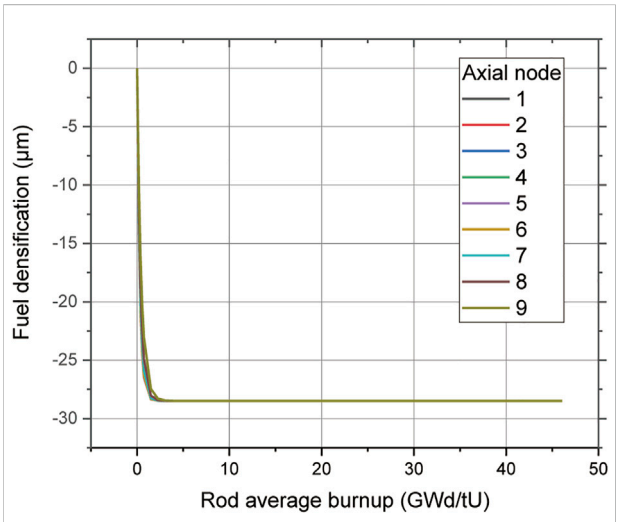

FIGURE 8
Fuel densification.

cases. In addition, it was confirmed that the cladding and coolant temperatures were well increased according to the axial elevation.

3.3 Thermo-mechanical behavior of peak power fuel rod

3.3.1 Thermal behavior of fuel rod

Figure 5A illustrates in detail the calculation results for the axial profile of the variation in fuel centerline temperature during operation. Because cosine-shaped power peaking was applied axially, the highest temperatures were observed in axial regions 5 and 6. These were 0.8 and 1.0 m above the center of the nuclear fuel. The fuel temperature continued to increase from 0 EFPY to 15 EFPY and 30 EFPY at each axial region. Figure 5B shows the long-term behavior of nuclear fuel. It illustrates the evolution of the fuel centerline, surface temperature, and temperature of the inner and outer surfaces of the cladding in the fuel rod hottest region (i.e., axial region 6). The centerline temperature of nuclear fuel shows an increase of approximately 250 K during operation. This is because the linear heat rate continues to increase during operation (as shown in Figure 3) and because of the effect of the degradation of fuel thermal conductivity owing to irradiation. It was determined that these factors that increase the fuel temperature are more significant than the effect of the increase in gap conductance owing to the decrease in pellet cladding gap. The variations in gap width and the effect of gap conductance are analyzed in detail in a subsequent section.

The calculated axial temperature distribution of the fuel rods at the end of life after the reactor was operated for 30 EFPY is shown in Figure 6. The temperature of the fuel was the highest at axial region 6 and was approximately 1200 K at 30 EFPY. Considering that the operating temperature of nuclear fuel in a conventional fast reactor is approximately 2000 K owing to the low linear power of the reactor in this study, the present calculation result is significantly low and ensures a thermal margin for fuel melting. In the case of the LBE coolant, the outlet temperature was approximately 623 K (an increase of 100 K) when the inlet temperature was set to 523 K. The maximum temperature of the cladding did not exceed 650 K. Therefore, it was operated at a lower temperature than that of the steel cladding of a conventional fast reactor, which is in the range of

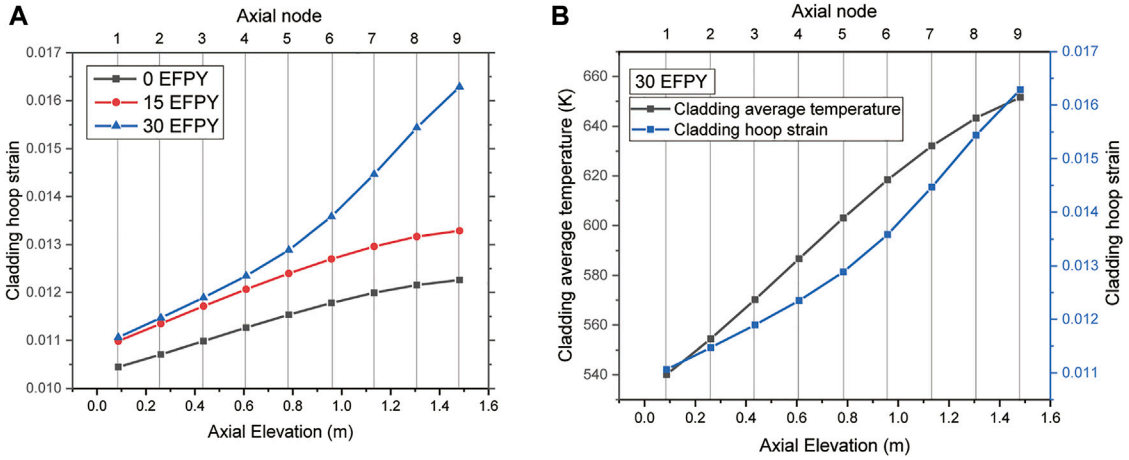

FIGURE 9
Cladding hoop strain **(A)** evolution profile and **(B)** temperature relationship at 30 EFPY.

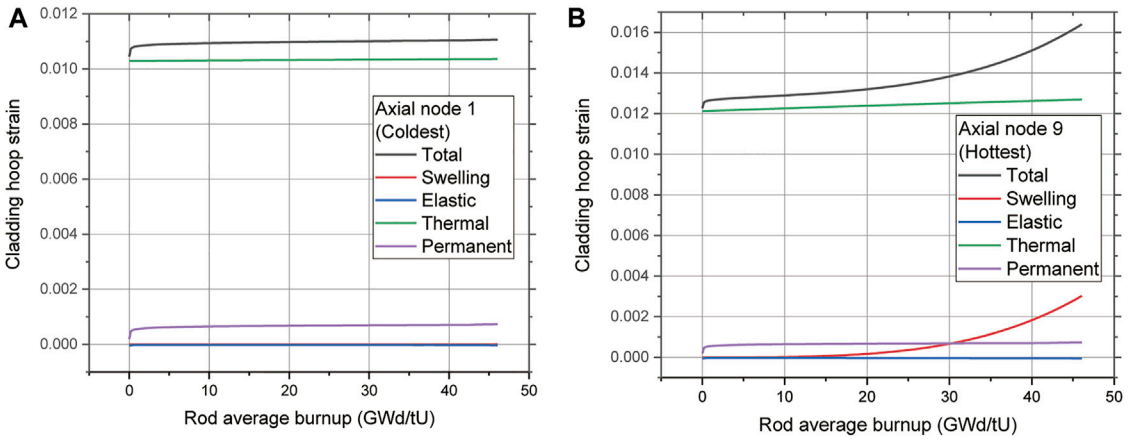

FIGURE 10
Cladding deformation mechanism of **(A)** coldest axial region and **(B)** hottest axial region.

700–800 K. Thus, stability can be secured by mechanisms that degrade material property, such as oxidation, creep, and swelling of cladding.

3.3.2 Mechanical behavior of fuel rod

The fuel, cladding deformation, and gap size evolution are discussed in detail in this section. Figure 7A shows the fuel swelling at 30 EFPY. Because the axial peaking of the fuel rods was considered, the average rod burn-up at 30 EFPY operations was 46 GWd/tU, whereas the maximum nodal burnup was calculated to be approximately 55 GWd/tU at the center of the fuel rod. Therefore, because a linearly increasing fuel swelling model was used for burn-up (as stated in Equation 4), the deformation caused by swelling was observed with an identical tendency as the burn-up profile. The highest swelling at the center of the fuel rod was approximately 85 μm, and the volume fraction was determined to be a maximum of approximately 3.3 vol%. Figure 7B shows the fuel swelling at each axial node according to the average burn-up of the rod. At the early stage of operation, the fuel surface deformed inward owing to the densification effect (see Figure 8).

Equation 4 Fuel swelling model used in the present study (Luscher, Geelhood, and Porter, 2015)

$$\text{For burnup} < 6\,\text{GWd/tU}: \quad solidswell = 0$$

$$\text{For burnup} > 6\,\text{GWd/tU and} < 80\,\text{GWd/tU}: \quad solidswell = bus \times \left(2.315 \times 10^{-23}\right)$$

$$bus = fdens \times 2.974 \times 10^{10} \times (bu - bul)$$

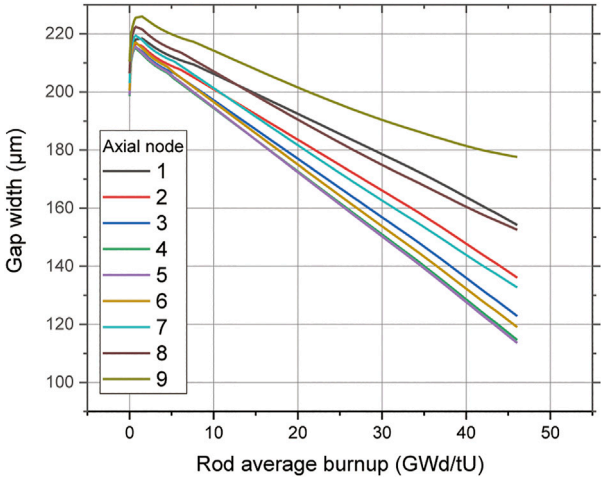

FIGURE 11
Profile of gap width evolution.

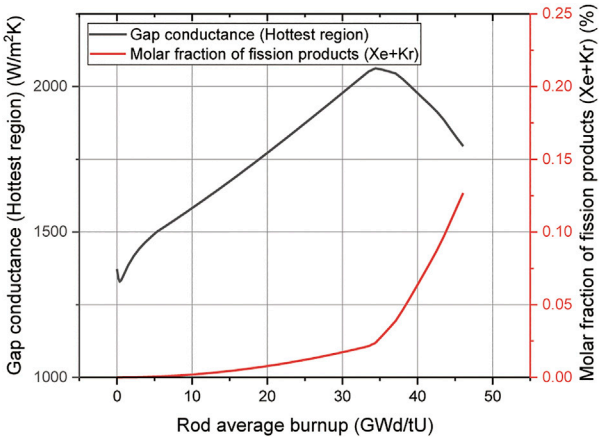

FIGURE 13
Gap conductance of peak power rod.

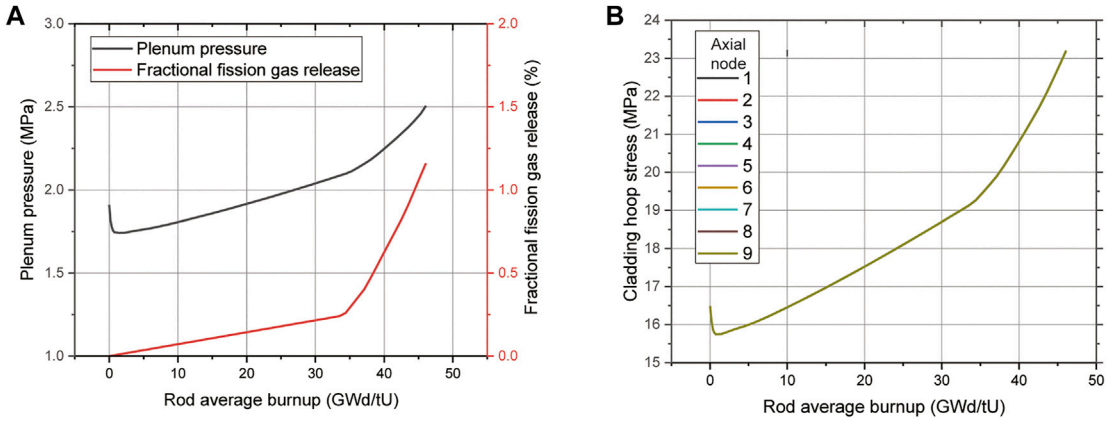

FIGURE 12
(A) Plenum pressure build-up and fission gas release and **(B)** Cladding hoop stress result.

solidswell = fractional volume fraction owing to solid fission product

bus = fuel burn-up during time-step

fdens = initial fuel density (kg/m3)

bu, bul = burn-up at the end of the time-step, previous time-step (GWd/tU)

The hoop strain of the cladding increased during operation as explained in Figure 9A. Although the neutron damage was highest at the center of the fuel rod owing to the high fission rate, the cladding of the hottest region (which is axial region 9) was observed to have the largest hoop strain according to Figure 9B. Figure 10 describes the hoop strain components of the 15–15Ti cladding of the coldest and hottest axial regions. At zero power, the thermal strain component caused by thermal expansion from room temperature cold zero power to hot zero power in both the coldest and hottest cladding regions was calculated. Thereafter, a marginal increase in thermal strain was observed as the cladding temperature increased. The elastic mechanical strain components generated by the difference between rod inner pressure and coolant pressure were determined to be significantly low. In addition, because the temperature of the cladding was inadequate to induce creep deformation, the permanent deformation owing to creep was also determined to be insignificant. However, there was a significant difference in swelling strain between the coldest and hottest regions. As shown in Figure 10A, the temperature of the cladding in the coldest region was sufficiently low for the increase in swelling strain

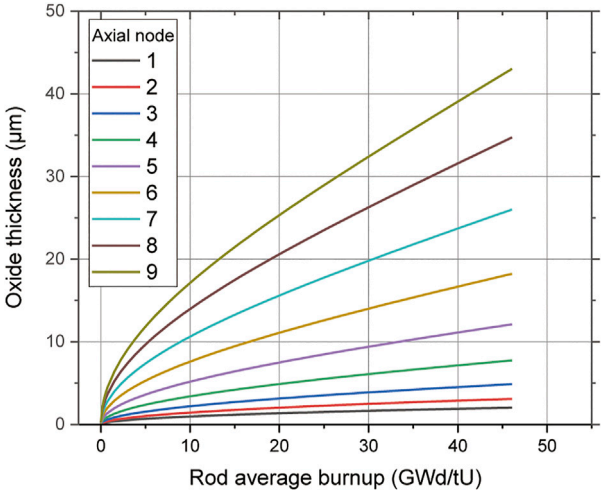

FIGURE 14
Calculated oxide thickness.

to be marginal. However, as can be observed in Figure 10B, the behavior of the hottest region was different from that of the coldest region. The swelling of 15–15Ti increases in proportion to the square of the temperature as it approaches 450°C. Therefore, the hottest cladding was determined to have a temperature sufficient for swelling to occur. Hence, the fast neutron fluence increment and temperature increment affect the swelling of the cladding during operation. The swelling deformation was the major component of the hottest cladding region. Furthermore, the hoop strain profile was consistent with the increasing tendency of swelling strain.

Based on the calculated fuel and cladding deformations, the evolution of the gap size between fuel cladding during operation is shown in Figure 11. The initial gap size was calculated to be approximately 200–210 μm depending on the axial region owing to the zero-power initial thermal expansion. At the early stage of operation, the fuel-cladding gap increased temporarily owing to fuel densification. Thereafter, the fuel-cladding gap decreased gradually owing to fuel swelling (which increased linearly), although the cladding deformed outward. This calculation of gap size verified that MicroURANUS can mitigate the fuel cladding mechanical interaction (FCMI) caused by fuel-cladding contact with a cold gap of 150 μm (which is a key factor that causes fuel failure during its entire life). Thereby, it can ensure the safety of fuel rods.

Figure 12A shows the fractional fission gas release of the peak power fuel rod of MicroURANUS and the corresponding plenum pressure calculated using the gap gas concentration and total void volume. The low-temperature fission gas release model was applied as described in Section 2.1. This was because the temperature of the fuel was low, wherefore the release fraction was evaluated as significantly low when the Forsberg–Massih model was used. Consequently, the release fraction increased linearly. In addition, the slope was determined to be steep when the local burnup exceeded 40 GWd/tU. It was determined that enhanced release was achieved when the rod average burn-up attained approximately 35 GWd/tU. This was because the nodal burn-up exceeded 40 GWd/tU in the mid-region of the highest rod. The fractional fission gas release at 30 EFPY was approximately 1.2%. This was maintained significantly low during the entire operation. Owing to the fission gas release, the plenum pressure attained approximately 2.5 MPa, and the cladding hoop stress showed a tendency identical to that of the plenum pressure build-up (see Figure 12B). This was because contact stress was absent owing to gap closure. Therefore, the gap conductance increased because the decrease in the fuel-cladding gap was dominant at the beginning of the operation. However, the gap conductance decreased abruptly owing to the release of fission gases such as Xe and Kr. These have low thermal conductivity after the average rod burn-up of approximately 35 GWd/tU (see Figure 13). The fuel temperature continued to increase owing to the thermal feedback phenomenon, wherein the decrease in gap conductance and degradation of fuel thermal conductivity occur simultaneously.

The oxide scale thickness was calculated using the parabolic law for 15-15Ti steel (Figure 14). It was calculated to be larger in the axial region where the cladding temperature was high. However, it was calculated to be approximately 40 μm at the end of the operation in axial region 9.

3.4 Calculation of mechanical integrity and comparison of design limit

Table 5 summarizes the comparison results of the thermomechanical behavior of the peak power fuel rod of the MicroURANUS system and the design limit factors. First,

TABLE 5 Design limit analysis results of MicroURANUS.

	MicroURANUS	Design limits	Reference
Max. pellet center temperature [K]	1,200	2,200	Grasso et al., 2013
Initial He pressurization/Max plenum pressure [MPa]	1/2	Max. 5	Grasso et al., 2013
Max. cladding temperature [K]	640	823	Grasso et al., 2013
Cladding diametral strain [%]	1.5	3	International Atomic Energy Agency, (2012)
Cumulative damage fraction	9.08×10^{-13}	0.2	International Atomic Energy Agency, (2012)

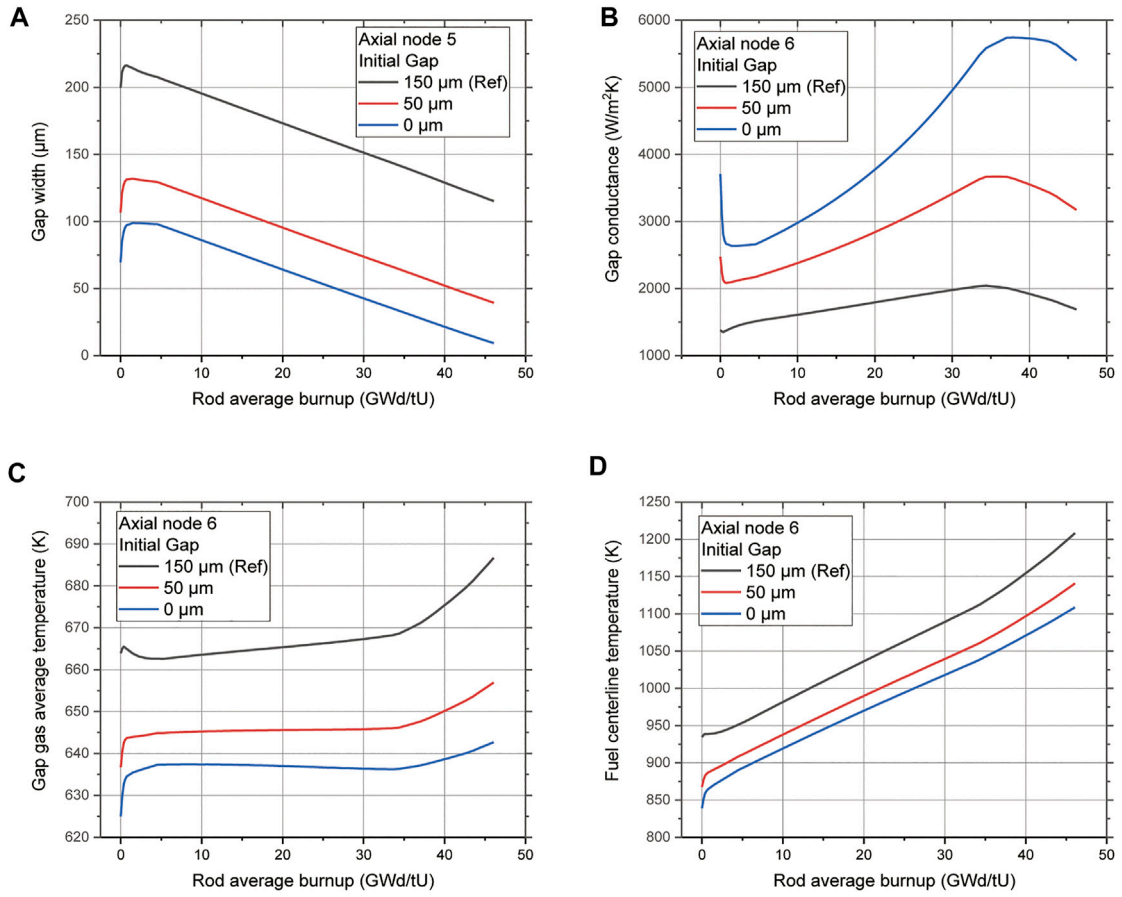

FIGURE 15
Initial gap size effects on **(A)** gap width, **(B)** gap conductance, **(C)** gap average temperature, and **(D)** fuel centerline temperature.

the maximum fuel temperature was evaluated as 1200 K. A sufficiently low fuel temperature provided a large safety margin for fuel melting and low pressure build-up fission gas release. The cumulative damage fraction (CDF) was calculated to predict the probability of creep rupture failure using the Larson–Miller parameter (LMP) for 15-15Ti steel (Filacchioni et al., 1990). Because the cladding hoop stress showed an equal value at all the axial nodes, the CDF of the hottest part of the cladding (which is aixial region 9) was calculated as 9.08×10^{-13} using Equation 5. This result reveals a negligibly low failure probability when a limit of approximately 0.2 is considered to account for the safety margin for the mechanical integrity of cladding (International Atomic Energy Agency, 2012).

Equation 5 Larson–Miller Parameter for 15-15Ti

$$LMP = T\left[16.0 + log_{10}\left(t_R\right)\right] = \left(2060 - \sigma_H\right)/0.095$$

t_R = rupture time (h), σ_H = hoop stress (MPa), and T = cladding temperature

$$CDF = \int_0^t \frac{dt}{t_R}$$

4 Design optimization of MicroURANUS

This section describes the optimization of the fuel rod design of MicroURANUS by using the developed LFR fuel performance code. As explained in Figure 11, the cold gap of MicroURANUS is set to 150 μm. However, considering the cladding thermal expansion in the room-temperature reference, it has a gap of approximately 210 μm for hot zero power. This indicates that gap closure does not occur. In this case, FCMI can be prevented. However, if the gap is excessively large, the temperature of the fuel may increase owing to the low thermal conductivity of the gap. Therefore, the fuel rod design was optimized by adjusting the size of the initial gap to 150 μm, which is the reference case.

The effects of initial gaps of 50 and 0 μm on the gap size, gap average temperature, and fuel centerline temperature were compared and analyzed.

In Figure 15A, the gap size evolution profile is compared by varying the size of the initial gap in axial region 5. This is the rod's mid-region with the smallest gap size owing to the largest fuel swelling. The decreasing tendency obtained when the initial gap was set to 50 and 0 μm was similar to that at 150 μm. This was because the fuel swelling model described in Equation 4 is related only to the burn-up, and there was no significant difference in cladding deformation. It was determined that gap closure did not occur even when there was no initial gap. Thus, Figure 15B verifies that the gap conductance increased as the size of the gap decreased. It is also shown in Figures 15C,D that the gap gas temperature and fuel centerline temperature decreased as the gap size decreased and gap conductance increased. Thus, it was demonstrated that a reduction in the size of the initial gap reduces the temperature of the nuclear fuel and excludes the possibility of FCMI for MicroURANUS design using the developed LFR fuel performance code. Considering the manufacturability of the actual fuel rod, the initial gap could not be set to 0 μm. However, the fuel design could be optimized by reducing it to approximately 50 μm.

5 Conclusion

In this study, the LFR fuel performance code (which is a normal operation fuel performance code for the LBE coolant fast reactor) was developed based on the LWR normal operation fuel performance code FRAPCON-4.0. The material properties and mechanisms were modified to adopt the fast spectrum characteristics of the current reactor. The full core life fuel performance of MicroURANUS was analyzed using the modified code to evaluate safety in terms of thermal stability and mechanical integrity.

Owing to the low linear power of this reactor (MicroURANUS), the maximum fuel temperature was determined to be 1200 K. Consequently, a low fuel temperature provides a large safety margin for fuel melting, as well as low pressure build-up fission gas release. The maximum fractional fission gas release does not exceed 1.2%, which can reduce the internal pressure build-up of the rod and enable high initial He pressurization to effectively reduce the fuel temperature. In addition, the results show that the fuel temperature is sufficiently low to enable safe operation without gap closure during the entire core life. This can prevent mechanical interaction between fuel and cladding, which is a key mechanism of fuel pin failure in conventional reactors. The cladding shows low degrees of swelling while maintaining high mechanical integrity because of the low temperatures of the cladding and coolant.

Data availability statement

The raw data supporting the conclusions of this article will be made available by the authors, without undue reservation.

Author contributions

JM: code development, performance calculation, H-JK: fuel and reactor design, HJR: conceptualization, manuscript review, project supervision.

Funding

This work was supported by the National Research Foundation of Korea (NRF, No. 2019M2D1A1067210 and 2022M2E9A304619011) grant funded by the Korea government (MSIT).

Conflict of interest

The authors declare that the research was conducted in the absence of any commercial or financial relationships that could be construed as a potential conflict of interest.

Publisher's note

All claims expressed in this article are solely those of the authors and do not necessarily represent those of their affiliated organizations, or those of the publisher, the editors and the reviewers. Any product that may be evaluated in this article, or claim that may be made by its manufacturer, is not guaranteed or endorsed by the publisher.

References

Afrikantov OKB Mechanical Engineering (2013). KLT-40S design description, 1–35.

Alemberti, A., Frogheri, M. L., Hermsmeyer, S., Ammirabile, L., Smirnov, V., Wu, Y., et al. (2014). Lead-cooled fast reactor (LFR) risk and safety assessment white paper. GENIV International Forum. Available at: https://www.gen-4.org/gif/upload/docs/application/pdf/2014-11/rswg_lfr_white_paper_final_8.0.pdf.

Banerjee, A., Raju, S., Divakar, R., and Mohandas, E. (2007). High temperature heat capacity of alloy D9 using drop calorimetry based enthalpy increment measurements. *Int. J. Thermophys.* 28, 97–108. doi:10.1007/s10765-006-0136-0

Bergmann, H., Dietz, W., Ehrlich, K., Muhling, G., and Schirra, M. (2003). Entwicklung des Werkstoffs X10CrNiMoTiB 15 15 als Strukturmaterial für Brennelemente. Available at: http://bibliothek.fzk.de/zb/berichte/FZKA6864.pdf.

Beyer, C. E., Geelhood, K. J., and Luscher, W. G. (1975). *GAPCONTHERMAL-2: A computer program for calculating the thermal behavior of an oxide fuel rod*. Richland, Wash. (USA): Battelle Northwest Laboratory.

Bohn, M. P. (1977). *'FRACAS : A subcode for the analysis of fuel pellet-cladding mechanical interaction*. Idaho Falls (USA): Idaho National Engineering Laboratory.

Cabet, C., Dalle, F., Gaganidze, E., Henry, J., and Tanigawa, H. (2019). Ferritic-martensitic steels for fission and fusion applications. *J. Nucl. Mater.* 523, 510–537. doi:10.1016/j.jnucmat.2019.05.058

Cechet, A., Barani, T., Cognini, L., Magni, A., Pizzocri, D., Altieri, S., et al. (2021). A new burn-up module for application in fuel performance calculations targeting the helium production rate in (U,Pu)O2 for fast reactors. *Nucl. Eng. Technol.* 53, 1893–1908. doi:10.1016/j.net.2020.12.001

Chen, Y. (2013). Irradiation effects of HT-9 martensitic steel. *Nucl. Eng. Technol.* 45, 311–322. doi:10.5516/NET.07.2013.706

Cheon, J. S., Lee, C. B., Lee, B. O., Raison, J. P., Mizuno, T., Delage, F., et al. (2009). Sodium fast reactor evaluation: Core materials. *J. Nucl. Mater.* 392 (2), 324–330. doi:10.1016/j.jnucmat.2009.03.021

Courcelle, A., Bisor, C., Piozin, E., Kountchou, M., Gavoille, P., Le Flem, M., et al. (2016). Evolution under irradiation of optimized austenitic steel for gen-IV reactors. Impact on fuel cladding properties and performances. *EPJ Web Conf.* 115, 47. doi:10.1051/epjconf/201611504003

Dai, Y., Zheng, X., and Ding, P. (2021). Review on sodium corrosion evolution of nuclear-grade 316 stainless steel for sodium-cooled fast reactor applications. *Nucl. Eng. Technol.* 113, 2327–2337. doi:10.1016/j.net.2021.05.021

Dubuisson, P. (2013). Core structural materials - feedback experience from phénix, design, manufacturing and irradiation behaviour of fast reactor. Fuel IAEA TECDOC 1689. Available at: https://www.iaea.org/publications/8881/design-manufacturing-and-irradiation-behaviour-of-fast-reactor-fuel.

Duriez, C., Alessandri, J. P., Gervais, T., and Philipponneau, Y. (2000). Thermal conductivity of hypostoichiometric low pu content (u, pu)o2-x mixed oxide. *J. Nucl. Mater.* 277, 143–158. doi:10.1016/S0022-3115(99)00205-6

Filacchioni, G., De Angelis, U., Ferrara, D., and Pilloni, L. (1990). Mechanical and structural behaviour of the second double stabilized stainless steels generation. Available at: https://www.icevirtuallibrary.com/doi/abs/10.1680/frcafsb.15661.0038.326

Forsberg, K., and Massih, A. R. (1985). Diffusion theory of fission gas migration in irradiated nuclear fuel UO2. *J. Nucl. Mater.* 135, 140–148. doi:10.1016/0022-3115(85)90071-6

Guerin, Y. (2012). Fuel performance of fast spectrum oxide fuel. *Compr. Nucl. Mater.* 5, 1–10. doi:10.1016/B978-0-08-056033-5.00043-4

Hübner, H. (2000). *Das Bestrahlungsverhalten des austenitischen Stahls DIN 1.4970*. Karlsruhe: Forschungszentrum Karlsruhe.

IMO (2018). *MEPC.304(72) IMO Strategy on reduction of GHG emissions from shipsStrategy on reduction of GHG emissions from ships*'. London: International Maritime Organization.

International Atomic Energy Agency (2012). *Structural materials for liquid metal cooled fast reactor fuel assemblies — operational behaviour STI/PUB/1548*. UK: IAEA Nuclear Energy Series, 103.

Killeen, J. C., Turnbull, J. A., and Sartori, E. (2007). *Fuel modelling at extended burnup: IAEA coordinated research project FUMEX-II*. Vienna: American Nuclear Society - 2007 LWR Fuel Performance/Top Fuel, 261–273.

Lee, S. G., Shin, Y. H., Park, J., and Hwang, I. S. (2021). High-temperature corrosion behaviors of structural materials for lead-alloy-cooled fast reactor application. *Appl. Sci. Switz.* 11 (5), 2349–2420. doi:10.3390/app11052349

Li, H., Bai, P., Lin, Z., Zhang, J., Tang, Q., and Pan, Y. (2017). Corrosion resistance in Pb-Bi alloy of 15-15Ti steel coated with Al2O3/SiC bilayer thin films by magnetron sputtering. *Fusion Eng. Des.* 125, 384–390. doi:10.1016/j.fusengdes.2017.04.089

Liu, Y., Xing, J., Li, Y., Tan, J., Sun, L., and Yan, J. (2016). Mechanical properties and anisotropy of thermal conductivity of $Fe_{3-x}Cr_xO_4$(x= 0–3). *J. Mat. Res.* 31 (23), 3805–3813. doi:10.1557/jmr.2016.425

Luscher, W. G., Geelhood, K. J., and Porter, I. E. (2015). *Material property correlations : Comparisons between FRAPCON-4.0, FRAPTRAN-2.0 and MATPRO* Richland, Washington: Pacific Northwest National Laboratory.

Luzzi, L., Cammi, A., De Marcello, V., Lorenzi, S., Pizzocri, D., Van Uffelen, P., et al. (2014). Application of the TRANSURANUS code for the fuel pin design process of the ALFRED reactor. *Nucl. Eng. Des.* 277, 173–187. doi:10.1016/j.nucengdes.2014.06.032

Maillard, A., Touron, H., Seran, J-L., and Chalony, A. (1994). Swelling and irradiation creep of neutron-irradiated 316Ti and 15-15Ti steels. *ASTM Spec. Tech. Publ.* 3, 824–837. doi:10.1520/stp23974s

Mathew, M. D. (2010). Evolution of creep resistant 316 stainless steel for sodium cooled fast reactor applications. *Trans. Indian Inst. Metals* 63, 153–158. doi:10.1007/s12666-010-0021-1

Medvedev, P., Hayes, S., Bays, S., Novascone, S., and Capriotti, L. (2018). Testing fast reactor fuels in a thermal reactor. *Nucl. Eng. Des.* 328, 154–160. doi:10.1016/j.nucengdes.2017.12.034

Müller, G., Schumacher, G., and Zimmermann, F. (2000). Investigation on oxygen controlled liquid lead corrosion of surface treated steels. *J. Nucl. Mater.* 278 (1), 85–95. doi:10.1016/S0022-3115(99)00211-1

Nguyen, T. D. C., Khandaq, M. F., Jeong, E., Choe, J., Lee, D., and Fynan, D. A. (2021). MicroURANUS: Core design for long-cycle lead-bismuth-cooled fast reactor for marine applications. *Int. J. Energy Res.* 45, 12426–12448. doi:10.1002/er.6661

Ravi, S., Laha, K., Mathew, M., Vijayaraghavan, S., Shanmugavel, M., Rajan, K., et al. (2012). Influence of flowing sodium on creep deformation and rupture behaviour of 316L(N) austenitic stainless steel. *J. Nucl. Mater.* 427, 174–180. doi:10.1016/j.jnucmat.2012.04.030

Rozzia, D., Del Nevo, A., Tarantino, M., and Forgione, N. (2012). Preliminary discussion on LFR fuel pin design: Current status, fuel modeling and open issues. *Int. Conf. Nucl. Eng. Proc. ICONE* 1, 467–473. doi:10.1115/ICONE20-POWER2012-54728

Schumann, U. (1970). *MAPLIB, A program system for provision of material property data to computer programs*.

Seban, R. A., and Shimazaki, T. (1949). *Heat trasnfer to a fluid flowing turbulently in a smooth pipe with walls at constant temperature*. Berkely (USA): California Univ.

Shin, Y. H., Cho, J., Lee, J., Ju, H., Sohn, S., Kim, Y., et al. (2017). Experimental studies and computational benchmark on heavy liquid metal natural circulation in a full height-scale test loop for small modular reactors. *Nucl. Eng. Des.* 316, 26–37. doi:10.1016/j.nucengdes.2017.03.001

Siefken, L. J., Coryell, E. W., Harvego, E. A., and Hohorst, J. K. (2001). *SCDAP/RELAP5/MOD 3.3 code manual* Rockville: U.S. Nuclear Regulatory Commission (NRC).

Stern, J. (2020). *Methane emissions from natural gas and LNG imports : An increasingly urgent issue for the future of gas in europe*. Oxford: Oxford Institute for Energy .

Többe, H. (1975). Das Brennstabrechenprogramm IAMBUS zur Auslegung von Schellbrüter–Brennstäben The Fuel Rod Calculation program IAMBUS for the Design of Fast Breeder Fuel Rods Bergisch Gladbach, Germany: Interatom GmbH.

Tsisar, V., Schroer, C., Wedemeyer, O., Skrypnik, A., and Konys, J. (2016). Long-term corrosion of austenitic steels in flowing LBE at 400 °c and 10-7 mass% dissolved oxygen in comparison with 450 and 550 °c. *J. Nucl. Mater.* 468, 305–312. doi:10.1016/j.jnucmat.2015.09.027

Turnbull, J. A. (1996). *Presentation at the IAEA reserach coordination meeting on fuel modelling at extended burnup*. Bombay, India: FUMEX.

Walker, C. T., Goll, W., and Matsumura, T. (1996). Effect of inhomogeneity on the level of fission gas and caesium release from OCOM MOX fuel during irradiation. *J. Nucl. Mater.* 228, 8–17. doi:10.1016/0022-3115(95)00191-3

White, R. J., Fisher, S., Cook, P., Stratton, R., Walker, C., and Palmer, I. (2001). Measurement and analysis of fission gas release from BNFL's SBR MOX fuel. *J. Nucl. Mater.* 288, 43–56. doi:10.1016/S0022-3115(00)00591-2

frontiers | Frontiers in Energy Research

TYPE Original Research
PUBLISHED 09 November 2022
DOI 10.3389/fenrg.2022.1041900

OPEN ACCESS

EDITED BY
Songbai Cheng,
Sun Yat-sen University, China

REVIEWED BY
Xingkang Su,
Lanzhou University, China
Kai Wang,
Sun Yat-sen University, China

*CORRESPONDENCE
Zhigang Zhang,
zg_zhang@hrbeu.edu.cn

SPECIALTY SECTION
This article was submitted to Nuclear Energy, a section of the journal Frontiers in Energy Research

RECEIVED 11 September 2022
ACCEPTED 24 October 2022
PUBLISHED 09 November 2022

CITATION
Liu H, Zhang Z, Du H and Cong T (2022), Numerical study on the heat transfer characteristics of a liquid lead–bismuth eutectic in a D-type channel. *Front. Energy Res.* 10:1041900. doi: 10.3389/fenrg.2022.1041900

Numerical study on the heat transfer characteristics of a liquid lead–bismuth eutectic in a D-type channel

Hong Liu[1], Zhigang Zhang[1]*, Haisu Du[1] and Tenglong Cong[2]

[1]Fundamental Science on Nuclear Safety and Simulation Technology Laboratory, Harbin Engineering University, Harbin, China, [2]School of Mechanical Engineering, Shanghai Jiao Tong University, Shanghai, China

A printed circuit heat exchanger (PCHE) can offer superior performance in area concentration and heat transfer efficiency. A PCHE with a liquid lead–bismuth eutectic (LBE) and supercritical carbon dioxide as working media can use these materials as intermediate heat exchangers in lead–bismuth eutectic-cooled reactors to reduce facility size and improve economy. To ensure the reliability of a numerical simulation for a liquid LBE in PCHE channels, the flow and heat transfer characteristics of a liquid LBE were investigated in a single D-type channel. The existing turbulent Prandtl number (Pr_t) models and the shear–stress transport (SST) $k-\omega$ model were evaluated first by using experimental liquid metal data. Then, a suitable Pr_t model was proposed for the numerical simulation of the liquid LBE. Finally, the flow and heat transfer characteristics of the liquid LBE were studied in D-type straight channels and D-type zigzag channels. The study presented the effects of flow velocity, wall heat flux, equivalent diameter and zigzag channel angle on the flow resistance and heat transfer characteristics. Meanwhile, a heat transfer correlation suitable for a D-type straight channel was also proposed. The research results in this paper lay a good foundation for the development of PCHEs with an LBE as the working fluid.

KEYWORDS

printed circuit heat exchange, turbulent Prandtl number, lead-bismuth eutectic, D-type channel, heat transfer correlation

1 Introduction

Liquid–metal cooled nuclear reactors are recognized as promising generation-IV reactors due to their low melting point, high boiling point, excellent heat absorption capacity, high molecular heat conduction, good neutron performance and radiation resistance. Moreover, the liquid lead alloy (typically a liquid lead–bismuth eutectic) offers good passive safety characteristics and superior economy as a coolant for nuclear reactors (Roelofs et al., 2019). The main characteristics of typical lead-based fast reactors (LFRs) worldwide have been summarized by Zhang et al. (2020). They noted the current

challenges in their development and discussed the research progress of four main thermohydraulic aspects.

The flow and heat transfer characteristics of liquid lead–bismuth eutectics (LBEs) have been studied extensively by experiments and numerical simulations. An experiment considering a 19-pin hexagonal rod bundle cooled by a forced-convective LBE was completed at the Karlsruhe Liquid Metal Laboratory (KALLA) (Pacio et al., 2016). Their experimental results had good repeatability in the uncertainty range, and correlations for predicting the drag coefficient and Nusselt number (Nu) were recommended. Moreover, research on the flow and heat transfer characteristics of a liquid LBE in annular channels has been conducted. An experimental investigation in the annular channel showed that the flow and heat transfer characteristics of a liquid LBE are obviously influenced by gas injection (Zhu et al., 2019). To overcome these experimental limitations, numerical simulations have been widely applied in analysing heat transfer characteristics. The RANS method and turbulent viscosity model were used to predict the forced convective heat transfer of a liquid LBE (Thiele and Anglart, 2013). Turbulent heat fluxes were modelled with a simple gradient diffusion hypothesis (Marocco et al., 2017), and the results showed that the turbulent Prandtl number (Pr_t) can be locally evaluated either with a correlation or by solving some additional transport equations. Furthermore, mixed large eddy simulation (LES) and direct numerical simulation (DNS) methods were also used to calculate the mixed convection of a liquid metal (Marocco and Garita, 2018), and the difference between the forced and assisted convection for the liquid metal was assessed at the same Reynolds number in detail. In addition, the flow and heat transfer characteristics of a liquid LBE in circular pipes were extensively studied. The heat transfer characteristics of a liquid LBE were also studied by experiments and numerical simulations methods in circular pipes (Chen et al., 2013). First, the numerical simulation results of different Pr_t models were evaluated. Then, they recommended a Pr_t model suitable for a liquid LBE in their investigation. The standard $k-\varepsilon$ model was adopted to analyse the heat transfer and flow characteristics of a liquid LBE in circular tubes under different heat flux conditions (Guo and Huai, 2013). The research results showed that the heat transfer entropy generation rate decreased with increasing Peclet number (Pe), and the fluid friction entropy generation rate increased. The direct numerical simulation method was used to calculate the liquid LBE in a vertical heating tube (Zhao et al., 2018). The study showed that when the turbulence attenuation increases with increasing buoyancy, the surface friction coefficient decreases significantly, and Nu decreases slightly. The physical properties of 12 liquid metals were collected and analysed by Jaeger (2016), and the heat transfer correlations in circular tubes, rectangular channels and circular channels were evaluated and compared with the experimental data. Moreover, the influence of inlet on heat transfer characteristics was analysed (Jaeger 2017). Jaeger predicted that the heat transfer at the inlet is 100% higher than that at the fully developed fluid and emphasized that optimizing the heat exchanger structure is helpful when strengthening the heat transfer.

In a nuclear reactor, heat is transferred from the primary circuit to a secondary circuit through an intermediate heat exchanger, and a regenerator is arranged in the second loop. The intermediate heat exchanger and the regenerator take the form of a shell and tube heat exchanger. This configuration requires that both heat exchangers have high heat transfer efficiency, and the safety of the heat exchangers must be guaranteed. Usually, shell and tube heat exchangers are used in conventional nuclear power plants. In recent years, the application of gas Brayton cycle power generation systems in liquid metal reactors has attracted extensive attention. Therefore, the characteristics between liquid metals and gas have been investigated. A numerical simulation method was used to analyse the characteristics of heat transfer and flow resistance between a liquid LBE and helium (Chen et al., 2013). Wang et al. (2017) experimentally investigated the heat transfer characteristics of a liquid LBE and helium in a heat exchanger, and the influences of inlet temperature and inlet fluid mass flow rate on the total heat transfer coefficient were analysed. Liu et al. (2018) designed a noncontact double-wall straight tube heat exchanger for a Kylin-II circuit, and the SST $k-\omega$ model was adopted to calculate the flow rate and temperature distribution of a liquid LBE in the heat exchanger. However, shell and tube heat exchangers are traditional heat exchanger equipment and cannot offer superior performance in area concentration and heat transfer efficiency.

It is well known that the heat needed to be recovered in the gas Brayton cycle is considerable, so the heat exchange efficiency and size of the regenerator are more prominent (Xu et al., 2020). Compared with shell and tube heat exchangers, printed circuit heat exchangers (PCHEs) have been applied in thermal power and solar power generation systems because of their high heat exchange efficiency, small size and high safety. The development of supercritical carbon dioxide flow and heat transfer characteristics have been classified and summarized in PCHEs according to experimental and numerical simulation results (Huang et al., 2019). An experimental study was conducted on a PCHE regenerator with discontinuous biased rectangular and airfoil fins (Pidaparti et al., 2019), and the local and average heat transfer coefficients and pressure drops under different operating conditions related to the supercritical carbon dioxide (SCO_2)-Brayton cycle were measured. Li et al. (2019) studied the influence of inlet temperature and pressure of SCO_2 on the overall heat transfer performance of a sawtooth finned PCHE, and an evaluation method was proposed for the overall heat transfer performance considering the influence of operating temperature and pressure. Aneesh et al. (2018) performed a numerical analysis on a simplified numerical model of a single-

row PCHE in a helium–helium countercurrent loop and studied the properties of local flow and heat transfer in a periodic channel. Saeed and Kim, 2017 performed a regional optimization of a SCO_2 PCHE, which significantly reduced the computation time without affecting the accuracy of the solution.

Most of the literature above has shown PCHEs used as regenerators in the Breton cycle, and the heat transfer characteristics were mainly studied between gases. However, there are few studies on PCHEs as intermediate heat exchangers for primary and secondary circuits of nuclear reactors. The thermal-hydraulic performance of a PCHE was studied with FLiNaK and helium as working fluids (Kim and Sun. 2014), and a reasonable PCHE design method was proposed. FLiNaK and carbon dioxide as working fluids were considered in a PCHE by Kim et al. (2016). They evaluated the influences of the different channel types on economy and proposed the best kinds of channel configuration for PCHEs. To obtain the heat transfer characteristics of SCO_2 and liquid metal in PCHEs, Cong et al. (2021) performed a numerical simulation on liquid metal sodium and SCO_2 by using SST $k-\omega$ and Abid low Reynolds $k-\varepsilon$ turbulence models for SCO_2 and sodium domains, respectively. They compared the heat transfer coefficient and friction coefficient calculated by numerical simulation with the empirical correlation. It was concluded that the mass flow and inlet working medium temperature have a significant influence on the heat transfer of the two kinds of working fluids.

At present, model tests and numerical simulations of liquid LBEs are widely performed in circular pipes, annular channels or outside tube bundles. Meanwhile, the heat transfer characteristics of fluids in the D-type channels of PCHEs are mainly focused on fluids such as supercritical carbon dioxide, helium and sodium. Nevertheless, no experimental data or simulation results for the flow and heat transfer characteristics of a liquid LBE in D-type channels have been published thus far. In the current work, to predict the convective heat transfer characteristics of a liquid LBE, a numerical simulation method with the SST $k-\omega$ model was performed in a single D-type channel of a PCHE. A new Pr_t model was proposed that is suitable for the numerical simulation of a liquid LBE. Meanwhile, a new correlation for calculating the heat transfer of D-type channels was also proposed. These research results can be used for developing a liquid metal PCHE that can be applied to a generation-reactor.

2 Numerical calculation models and methods

2.1 Geometry of the D-type channel

A PCHE is fabricated by flat metal plates with photochemically etched D-type channels. The diameter of the D-type channel is generally 1–2 mm. Compared with shell and tube heat exchangers, the PCHE has a smaller size and superior heat transfer efficiency; the diffusion welding process is used to ensure safety. In this paper, the heat transfer and resistance characteristics of D-type channels with different equivalent diameters are studied by a numerical simulation method. Based on the operational experience of a Russian liquid lead–bismuth reactor, it is believed that the liquid flow rate should be less than 2 m/s because mechanical corrosion can become a serious problem when the fluid velocity is high, especially for liquid heavy metals (Zhang et al., 2013). Therefore, the flow and heat transfer characteristics of the liquid LBE were studied at velocities of 0.2–2.2 m/s in this paper. The structural details of the D-type channel are shown in Figure 1. A shows a straight channel model, B and C show zigzag channels with different angles, and D shows a cross section of the D-type channel. Numerical simulation working conditions and the structural details for the D-type channels are described in Table 1.

2.2 Governing equations for flow and heat transfer

In recent years, computational fluid dynamics (CFD) has been widely used in the prediction of flow and heat transfer characteristics of liquid metals. Under the condition of constant wall heat flux, the $k-\varepsilon$ model was used to evaluate Pr_t in a two-dimensional model by Cheng and Tak. (2006); they proposed Cheng's Pr_t model. The $k-\varepsilon$ model was also adopted to calculate the heat transfer of a liquid LBE in a three-dimensional circular pipe (Chen et al., 2013); they evaluated Pr_t models and suggested correlations of Nu and Pr_t. However, the near-the-wall function was used to estimate the heat transfer in the $k-\varepsilon$ model, which cannot accurately calculate the heat transfer of the fluid in the viscous sublayer. The real heat transfer of the fluid in the viscous sublayer is bound to affect the accuracy of the numerical simulation results. Therefore, it is necessary to reassess the Pr_t model of a liquid LBE in the near wall. Although direct numerical simulation (DNS) and large eddy simulation (LES) can well calculate the real flow and heat transfer of a fluid near a wall, they are not suitable for engineering projects due to the large grid quantity. The $k-\omega$ model can be used to calculate the flow and heat transfer characteristics of a fluid near a wall; however, the $k-\varepsilon$ model is used to calculate the flow and heat transfer characteristics of the fluid outside the boundary layer. Moreover, the computational resources required by the $k-\omega$ model are far less than those of the DNS and LES. The $k-\omega$ model is considered an advantageous computational model for future engineering applications.

To comprehensively assess the applicability of the Pr_t models and study the flow and heat transfer characteristics of a liquid LBE, the SST $k-\omega$ model was adopted. The SST $k-\omega$ model can not only accurately calculate the flow and heat transfer in the viscous sublayer but also avoid the sensitivity of the standard $k-\omega$ model to incoming flow (Menter. 1993). The solved governing equations are as follows:

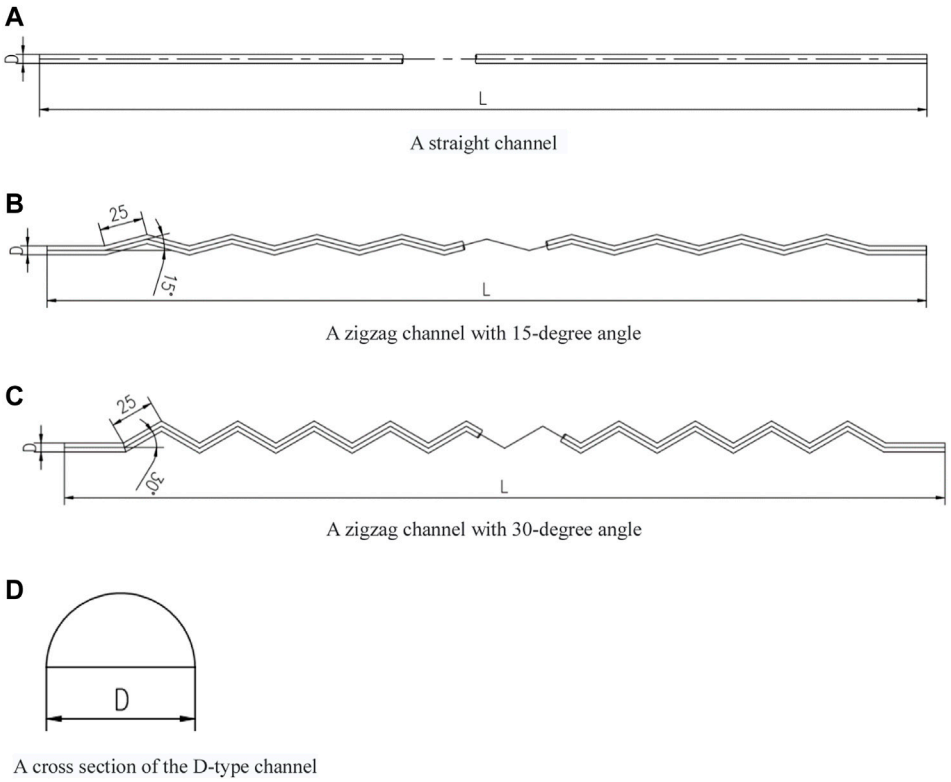

FIGURE 1
Geometry of the D-type channel.

TABLE 1 Numerical simulation working conditions for the D-type channels.

Case no.	D-type channel diameter(mm)	Equivalent diameter (mm)	Channel length (mm)	Velocity (m/s)	Wall heat flux (kW/m^2)	Inlet temperature (K)	Channel form
#1	10	6.11	900	0.2–2.2	−200	773.15	Straight channel
#2	7.5	4.58	900	0.2–2.2	−200	773.15	Straight channel
#3	5	3.05	900	0.2–2.2	−200	773.15	Straight channel
#4	2.5	1.53	900	0.2–2.2	−200	773.15	Straight channel
#5	10	6.11	900	0.2–2.2	−200	773.15	Straight channel
#6	5	6.11	900	1.0	−500 −100	773.15	Straight channel
#7	5	6.11	900	1.0	−200	573.15–773.15	Straight channel
#8	5	3.05	900	0.2–2.2	−200	773.15	zigzag channel(15°)
#9	5	3.05	900	0.2–2.2	−200	773.15	zigzag channel(30°)

TABLE 2 Constants used in the turbulence models.

$\sigma_{k,1}$	$\sigma_{\omega,1}$	$\sigma_{k,2}$	$\sigma_{\omega,2}$	α_1	$\beta_{i,1}$	$\beta_{i,2}$
1.176	2.0	1.0	1.168	0.31	0.075	0.0828

Mass equation:

$$\frac{\partial \rho}{\partial t} + \frac{\partial}{\partial x_i}(\rho u_i) = 0 \tag{1}$$

Momentum equation:

$$\frac{\partial}{\partial t}(\rho \overline{u_i}) + \frac{\partial}{\partial x_j}(\rho u_i u_j) = -\frac{\partial p}{\partial x_i} + \frac{\partial}{\partial x_j}(\sigma_{ij}) + \frac{\partial}{\partial x_j}\left(\mu_t\left(\frac{\partial u_i}{\partial x_j} + \frac{\partial u_j}{\partial x_i}\right) - \frac{2}{3}\left(\rho k + \mu_t \frac{\partial u_k}{\partial x_k}\right)\delta_{ij}\right) \tag{2}$$

Energy equation:

$$\frac{\partial}{\partial t}(\rho E) + \frac{\partial}{\partial x_i}(u_i(\rho E + p)) = \frac{\partial}{\partial x_j}\left(\left(k + \frac{c_p \mu_t}{Pr_t}\right)\frac{\partial T}{\partial x_j} + u_i(\tau_{ij})_{eff}\right) + S_h \tag{3}$$

where $\rho, u, p, \mu, \mu_t, k, T, c_p, (\tau_{ij})_{eff}, E, S_h, \sigma_{ij}$, and Pr_t are the density, velocity, pressure, laminar viscosity, turbulent viscosity, thermal conductivity, temperature, specific heat, deviatoric stress tensor, total energy, source items, stress tensor, and turbulent Prandtl number, respectively.

Shear–stress transport (SST) k–ω equations:

$$\frac{\partial}{\partial t}(\rho k) + \frac{\partial}{\partial x_i}(\rho k u_i) = \frac{\partial}{\partial x_j}\left[(\mu + \frac{\mu_t}{\sigma_k})\frac{\partial k}{\partial x_j}\right] + G_k - Y_k + S_k \tag{4}$$

$$\frac{\partial}{\partial t}(\rho \omega) + \frac{\partial}{\partial x_i}(\rho \omega u_i) = \frac{\partial}{\partial x_j}\left[(\mu + \frac{\mu_t}{\sigma_\omega})\frac{\partial \omega}{\partial x_j}\right] + G_\omega - Y_\omega + S_\omega \tag{5}$$

where G_k represents the production rate of turbulence due to the mean velocity gradients, G_ω represents the production ω, Y_k represents the dissipation of k due to turbulence, Y_ω represents the dissipation of ω due to turbulence, and S_k and S_ω represent source items for the user. σ_k represents the turbulent Prandtl number for turbulent kinetic energy k, and σ_ω represents the turbulent Prandtl number of specific dissipation rate ω.

$$\mu_t = \alpha^* \frac{\rho k}{\omega} \tag{6}$$

where α^* can reduce the viscosity of turbulence to correct for low Reynolds number

$$\alpha^* = \alpha^*_\infty\left(\frac{\alpha^*_0 + Re_t/R_k}{1 + Re_t/R_k}\right) \tag{7}$$

where $e_t = \frac{\rho k}{\mu \omega}$, $R_k = 6$, $\alpha^*_0 = \frac{\beta_i}{3}$, and $\beta_i = 0.072$.

At a high Reynolds number, $\alpha^* = \alpha^*_\infty = 1$. To accurately calculate the influence of the turbulent Prandtl number (Pr_t) on heat transfer characteristics at low Reynolds numbers, turbulent shear stress should be considered in the definition of turbulent viscosity in the SST $k-\omega$ model. The calculation method of μ_t is given in Eq. 8. This model is more accurate and reliable than the standard $k-\omega$ model and has a wider application range.

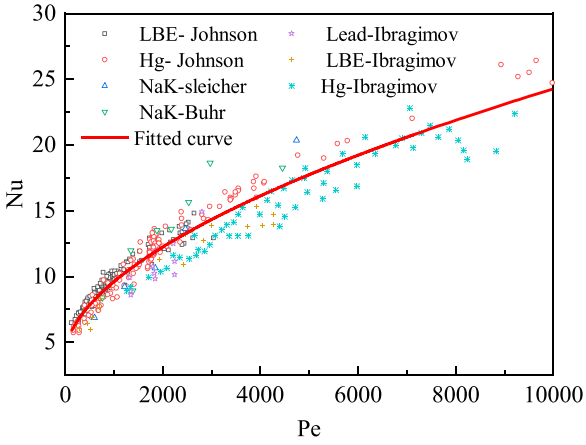

FIGURE 2
Experimental data and the fitted curve.

Turbulent viscosity:

$$\mu_t = \frac{\rho k}{\omega}\frac{1}{\max\left[\frac{1}{\alpha^*}, \frac{SF_2}{\alpha_1 \omega}\right]} \tag{8}$$

$$F_2 = \tanh(\phi_2^2) \tag{9}$$

$$\phi_2 = \max\left[2\frac{\sqrt{k}}{0.09\omega y}, \frac{500\mu}{\rho y^2 \omega}\right] \tag{10}$$

where y is the distance to the next surface.

The constants in the SST $k-\omega$ turbulence model are presented in Table 2. More details on the SST $k-\omega$ model can be found in Menter (1994).

3 Assessment of heat transfer correlations and Pr_t models

3.1 Assessment of heat transfer correlations

For liquid metals, numerous correlations have been proposed for convective heat transfer calculations by theoretical analysis and experimental research. Universally, the Nusselt number (Nu) is expressed as a function of the Prandtl number (Pr) and Peclet number (Pe). The correlation of heat transfer is given in the following.

$$Nu = a + bPr^m Pe^n \tag{11}$$

TABLE 3 Convective heat transfer correlation for liquid metals.

Investigator	Correlation	Remark
Lyon (1951)	$Nu = 7.0 + 0.025(Pe/Pr_t)^{0.8}$	$0 < Pr < 0.1$
		$4 \times 10^4 < Re < 3.24 \times 10^6$
Skupinski et al. (1965)	$Nu = 4.82 + 0.0185Pe^{0.827}$	$10^4 < Re < 5 \times 10^6$
Kirillov et al. (2001)	$Nu = 4.5 + 0.018Pe^{0.8}$	$10^4 < Re < 5 \times 10^6$
Azer and Chao. (1961)	$Nu = 7.0 + 0.05Pr^{0.25}Pe^{0.77}$	$0 < Pr < 0.1$
		$0 < Pe < 1.5 \times 10^4$
Sleicher et al. (1973)	$Nu = 6.3 + 0.0167Pr^{0.08}Pe^{0.85}$	$0.004 < Pr < 0.1$
		$10^4 < Re < 10^6$
Chen and Chiou. (1981)	$Nu = 5.6 + 0.0165Pr^{0.01}Pe^{0.85}$	$0 < Pr < 0.1$
		$10^4 < Re < 5 \times 10^6$
Stromquist (1953)	$Nu = 3.6 + 0.018Pe^{0.8}$	$88 < Pe < 4000$
Subbotin et al. (1963)	$Nu = 5 + 0.025Pe^{0.8}$	
Ibragimov et al. (1962)	$Nu = 4.5 + 0.014Pe^{0.8}$	
Cheng and Tak. (2006)	$Nu = A + 0.018Pe^{0.8}$	$A = \begin{cases} 4.5 & Pe \le 1000 \\ 5.4 - 9 \times 10^{-4}\,Pe & 1000 \le Pe \le 2000 \\ 3.6 & Pe \ge 2000 \end{cases}$

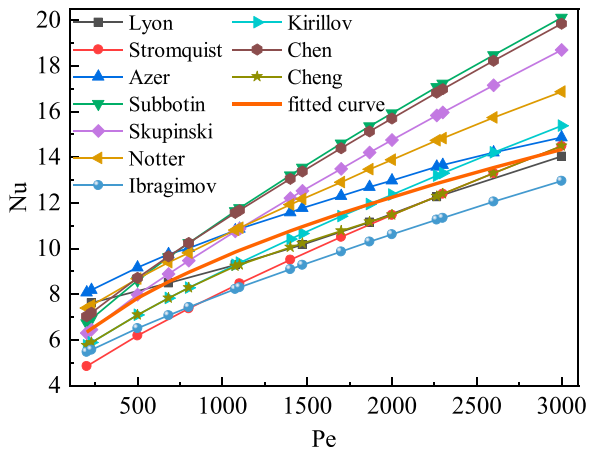

FIGURE 3
Comparison of heat transfer correlations and the fitted curve in Figure 2.

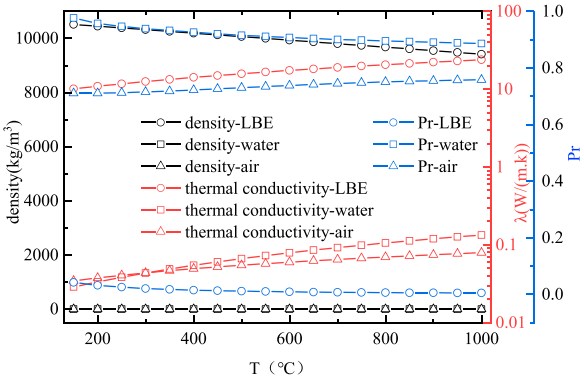

FIGURE 4
Variation in the physical properties of liquid LBE, air and water with different temperatures.

where α, b, m, and n are all constants.

Johnson et al. (1953), Buhr et al. (1968) and Ibragimov et al. (1962) used experimental methods to investigate the heat transfer characteristics of a liquid LBE in a vertical circular pipe, and they obtained experimental data in the range of 200–10,000. The experimental data and their fitted curves are presented in Figure 2. The correlations proposed by scholars are summarized in Table 3; a comparison between the fitted curves of the experimental data and the correlations proposed by scholars is shown in Figure 3.

As seen in Figure 2, the calculation results of the correlations proposed by Lyon. (1951), Stromquist (1953), Azer and Chao. (1961), Skupinski et al. (1965), Chen and Chiou. (1981), Sleicher et al. (1973) and Subbotin et al. (1963) are larger than the fitted curve, and the deviations are large. The calculated result of the correlation proposed by Ibragimov et al. (1962) is less than the fitted curve. Therefore, these models are not effective in describing the turbulent heat transfer of liquid metals. The heat transfer correlation proposed by Cheng and Tak. (2006) is in piecewise form. When Pe is less than 1,000, the correlation proposed by Kirillov et al. (2001) is adopted. When Pe is more than 2000, Stromquist's correlation is recommended. When $1000 < Pe < 3000$, a new correlation was reproposed. The

TABLE 4 Turbulent Prandtl number models of liquid metals.

Investigator	Correlation	Remark
Aoki. (1963)	$Pr_t^{-1} = 0.014Re^{0.45}Pr^{0.2}[1 - \exp(-1/0.014Re^{0.45}Pr^{0.2})]$	
Reynolds (1975)	$Pr_t = (1 + 100Pe^{-0.5})(1/1 + 120Re^{-0.5} - 0.15)$	
Jischa and Rieke. (1979)	$Pr_t = 0.9 + \frac{182.4}{PrRe^{0.888}}$	
Kays. (1994)	$Pr_t = 0.85 + 0.7/Pe_t$	
Chen et al. (2013)	$Pr_t = \begin{cases} 4.12 & Pe \le 1000 \\ 0.01Pe/[0.018Pe^{0.8} - (7.0 - A)]^{1.25} & 1000 \le Pe \le 6000 \end{cases}$	$A = \begin{cases} 5.4 - 9 \times 10^{-4}Pe & 1000 \le Pe \le 2000 \\ 3.6 & 2000 \le Pe \le 6000 \end{cases}$
ANSYS Default value	$Pr_t = 0.85$	

maximum deviation between Cheng's model and the fitted curve is less than 13.5%. Figure 3 shows that the correlations proposed by Kirillov agree well with the calculated results of the fitted curve, and the maximum deviation is less than 10%. Through comparative analysis, it is recommended to use the correlation proposed by Kirillov to assess the Pr_t model for a liquid LBE under the condition of constant wall heat flux.

3.2 Assessment of Pr_t models

The melting point of the liquid LBE is 125°C, and the physical properties of the liquid LBE are only a function of temperature (Organisation For Economic Co-Operation And Development Nuclear Energy Agency, 2015). At atmospheric pressure, the physical parameters of the liquid LBE are completely different from those of conventional fluids such as air and water. The density of the liquid LBE is 12,500–35,000 times that of air and 20,000–55,000 times that of water in the range of 150–1,000°C. The Prandtl number (Pr) of the liquid LBE is 6.5‰–6.5% for air and 5‰–4.3% for water. The thermal conductivity of the liquid LBE is 285–300 times that of air and 170–350 times that of water. The variation trends of the liquid LBE, air and water vapour with temperature are shown in Figure 4. The Pr of the liquid LBE is much smaller than that of a conventional fluid, but its thermal conductivity is three orders of magnitude higher than that of a conventional fluid. As a result, the fluid molecular thermal conductivity still dominates, even in a turbulent flow state. Therefore, the Pr_t model applied to a conventional fluid is no longer suitable for a liquid LBE.

3.2.1 Turbulent Prandtl number model

For conventional fluids, Pr is defined as the ratio of kinematic viscosity to thermal diffusivity, which reflects the comparison between momentum diffusion and thermal diffusivity. Similar to the molecular Prandtl number, Pr_t is defined as the ratio of momentum vortex diffusivity to heat transfer vortex diffusivity. The correlation of Pr_t is calculated according to Eq. 12 (Kays et al., 2004). To accurately calculate

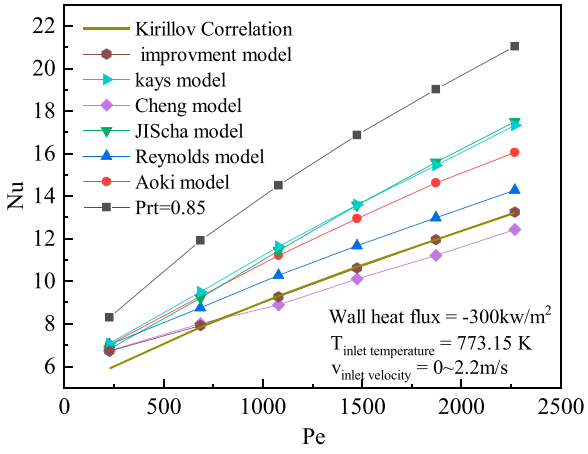

FIGURE 5
Comparison between the calculation results of 7 Pr_t models and Kirillov's correlation.

Pr_t, data such as the gradient of the mean temperature and velocity, turbulent shear stress and turbulent heat flux should be measured. In general, turbulent heat transport is strictly analogous to turbulent momentum transport (Groetzbach. 2003).

$$Pr_t = \frac{\varepsilon_M}{\varepsilon_H} = \frac{\overline{u_x' u_y'} \frac{\partial T}{\partial y}}{\overline{T' u_y'} \frac{\partial u_x}{\partial y}} \tag{12}$$

where ε_M represents momentum vortex diffusivity, ε_H represents heat transfer vortex diffusivity, and $\overline{u_x'}$, $\overline{u_y'}$, and $\overline{T'}$ are the average velocity and temperature.

To obtain more accurate prediction results, the SST $k-\omega$ model is used to assess the Pr_t models, which are summarized in Table 4, including the constant model with $Pr_t = 0.85$.

The Pr_t models proposed by Cheng, Aoki, Reynolds and Jischa are a series of global parameters related to flowing/transport conditions, such as Pr, Re (or Pe), which are equivalent to a fixed value on a certain cross section and do not involve the local spatial distribution of parameters. The

TABLE 5 Geometry and numerical calculation boundary conditions.

Name	Units	Value
Diameter	mm	5, 10, 15, 20, 25
Length	mm	1,500–2,500
Inlet temperature	°C	500
Wall heat flux	kw/m^2	−500 −100
Inlet velocity	m/s	0.2–2.2

TABLE 6 Grid independence verification.

Case no.	Grid number	Nu	Pressure drops (Pa)
1	346,500	12.67	13,499
2	478,500	12.83	13,868
3	630,500	12.88	14,087
4	770,000	13.0	14,342
5	927,500	13.03	14,403

Pr_t model proposed by Kays is a function of the turbulent Pe number, as shown in Table 4. The turbulent Pe number is a function of the turbulent viscosity ratio and Pr, which is shown in Eq. 13. The turbulent viscosity ratio is a local spatial parameter that needs to be extracted and updated in each simulation iteration during the numerical calculation. Duponcheel et al. (2014) verified that the Kays model was the best choice, which was in good agreement with LES results, but there is still a large discrepancy between the experimental data and the calculated results using the $k-\omega$ model. To improve the prediction accuracy of the heat transfer of the liquid metal, the Kays model was modified, and the constant 0.7 was replaced by 3.5 in the Kays model, the improved model was then proposed as shown in Eq. 14. The numerical simulation result of Nu calculated by Eq. 14 agrees with the correlation best, and the numerical results comparison of each Pr_t model can be found in Figure 5. The Eq. 14 can be applied to liquid metal sodium, lead-bismuth eutectic, sodium-potassium alloy and mercury.

$$Pe_t = \frac{\mu_t}{\mu} p_r \tag{13}$$

$$Pr_t = 0.85 + \frac{3.5}{Pe_t} \tag{14}$$

3.2.2 Assessment of the Pr_t model

3.2.2.1 Mesh independency verification

The physical properties of the liquid LBE, such as viscosity, specific heat, thermal conductivity and density, are based on the thermophysical relationships recommended in the guidance manual prepared by the Organization for Economic Cooperation and Development and Nuclear Energy Agency (OECD/NEA) (Organisation For Economic Co-Operation And Development Nuclear Energy Agency, 2015). In this paper, the Pr_t models of the liquid LBE were evaluated in a vertical circular pipe. The geometry of the circular pipe and the calculation boundary conditions are described in Table 5.

The structured mesh with O-type division is adopted for the calculation model, and the grid quantity of meshes ranges between 346,500 and 957,500. The number of boundary layers is set to 10, y+<1, and the Pr_t number is assumed to be 0.85. Without considering the influence of gravity, the pressure drops and Nu of liquid LBE with different grid quantities are obtained by numerical simulation. The calculation results are shown in Table 6.

The calculation results show that with the increase in the grid quantity, the difference in liquid LBE pressure drops and Nu decreases. The Nu deviations between the grid quantity of 630,500 and 770,000, 770,000 and 927,500 are less than 1%, and the pressure drop deviations are less than 1.7%, which indicates that the three grids are independent. Considering both the accuracy and the speed of the numerical simulation, the model with a grid quantity of 770,000 was selected to calculate the flow and heat transfer characteristics of the liquid LBE in a circular pipe.

3.2.2.2 Assessment of Pr_t models

In the present study, 7 Pr_t models were assessed by a numerical simulation method. The comparison between the calculation results and the correlation proposed by Kirillov is shown in Figure 5. The Pe number varies from 200 to 2,500. Under the same conditions of constant wall heat flux and inlet temperature conditions, numerical results show that Nu increases with increasing fluid velocity and Pe number. When Pe is larger than 500, the Nu calculated by the improvement model is in good agreement with the correlation proposed by Kirillov. When the Pe number is less than 500, the deviation with Kirillov's correlation is less than 10%, and as the PE number decreases, the calculation results of each Pr_t model have little difference.

To further verify the applicability of the Pr_t models at constant heat flux conditions, the numerical simulation was performed considering the changes in fluid temperature, wall heat flux, pipe tilt angle, and pipe diameter. As seen in Figure 6A, the results show that Nu increases with increasing wall heat flux when the fluid velocity and inlet temperature are constant, and the deviation between Nu calculated by numerical simulation and Kirillov's correlation is less than 1.4%. Figure 6B shows that Nu decreases with increasing inlet temperature when the wall heat flux and fluid velocity are constant, and the maximum deviation between Nu calculated by numerical simulation and

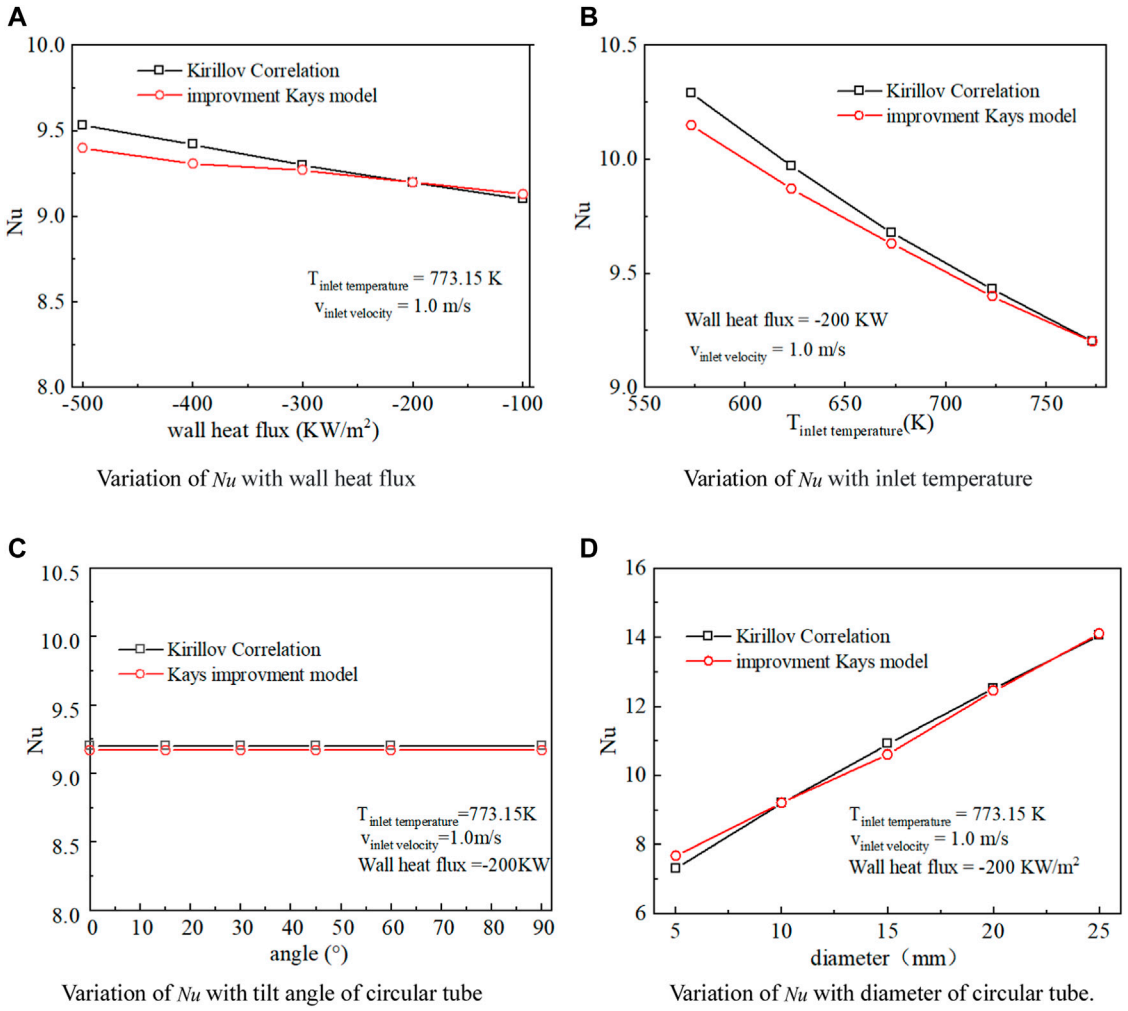

FIGURE 6
Variation of *Nu* with wall heat flux, inlet temperature, tilt angle and diameter.

Kirillov's correlation is less than 1.3%. Figure 6C illustrates that *Nu* basically did not change with increasing tube tilt angle when the wall temperature, fluid velocity and inlet temperature were constant, and the deviation between *Nu* calculated by numerical simulation and Kirillov's correlation was less than 0.3%. Figure 6D shows that *Nu* increases with increasing pipe diameter when the inlet fluid temperature, wall heat flux and fluid velocity are constant, and the deviation between *Nu* calculated by numerical simulation and Kirillov's correlation is less than 4.7%. The research results show that when the inlet temperature, wall heat flux, fluid velocity, tilt angle and pipe diameter change under the condition of constant wall heat flux, *Nu* calculated by the improvement model agrees well with the correlation proposed by Kirillov. The applicability of numerical methods and model have been verified with experimental data in circular channel. The Configuration of D-type channel is different from Circular

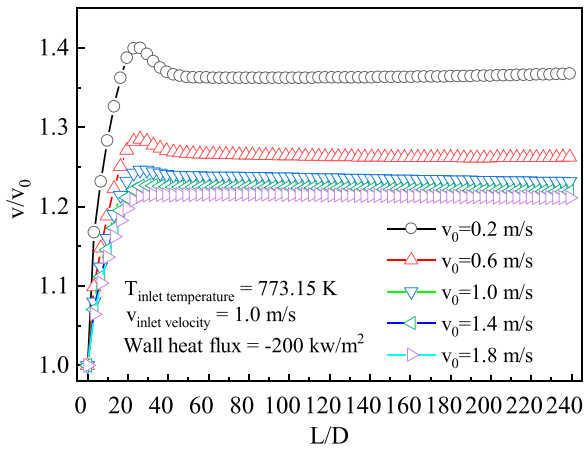

FIGURE 7
Variation in the velocity ratio along the circular tube.

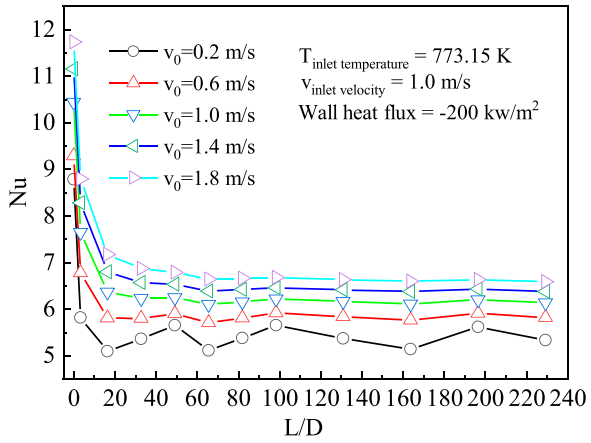

FIGURE 8
Variation of *Nu* along the circular tube.

channel. In this paper, the improvement Pr_t model was used to calculate the flow and heat transfer characteristics of the liquid LBE in the D-type channel.

4 Results and discussion

4.1 Variation in the velocity and heat transfer characteristics of a D-type straight channel

Taking a D-type straight channel with an equivalent diameter of 3.05 mm as an example, when the fluid velocity varies from 0.2 to 2.2 m/s and the inlet temperature of the liquid LBE and the wall heat flux are constants, the calculated results of the flow and heat transfer characteristics are analysed. Figure 7 shows that the centre flow velocity of the D-type channel reaches the maximum when L/D is

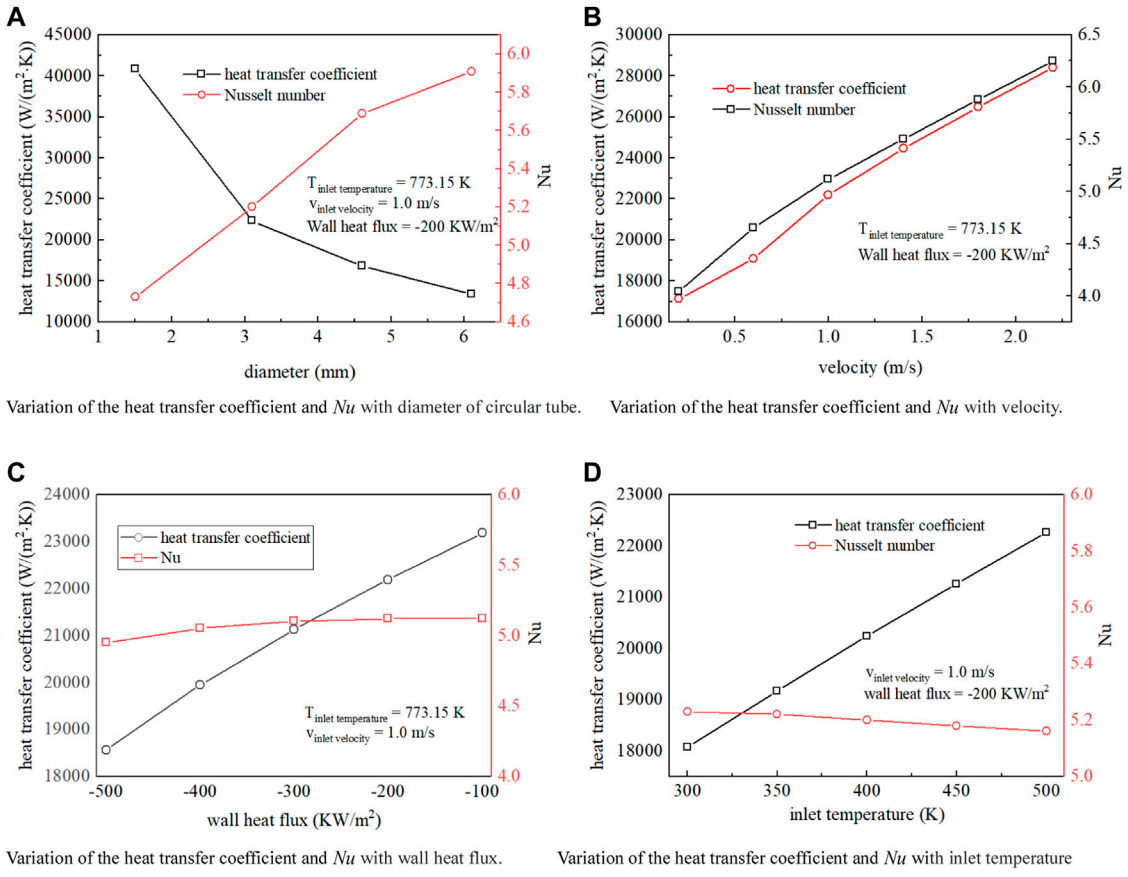

Variation of the heat transfer coefficient and *Nu* with diameter of circular tube.

Variation of the heat transfer coefficient and *Nu* with velocity.

Variation of the heat transfer coefficient and *Nu* with wall heat flux.

Variation of the heat transfer coefficient and *Nu* with inlet temperature

FIGURE 9
Variation of the heat transfer coefficient and *Nu* with diameter, velocity, wall heat flux and inlet temperature.

equal to 30. If the inlet fluid velocity is less than 1.0 m/s, the flow velocity decreases rapidly. When L/D is equal to 40, the flow velocity reaches a stable value, indicating that the liquid LBE has fully developed. When the fluid velocity is greater than 1.0 m/s, the fluid velocity reaches the maximum value and then maintains the stable value directly. Figure 8 illustrates that if the fluid velocity is low, the thickness of the boundary layer in the channel is large, and the heat transfer coefficient of the fluid fluctuates along the pipe length. When the flow velocity is greater than 1.0 m/s, the heat transfer coefficient of the fluid along the pipe length decreases to a certain value and then tends to be stable.

4.2 Analysis of the heat transfer characteristics of liquid LBE in straight channels

The liquid LBE in D-type channels with equivalent diameters of 1.53 mm, 3.05 mm, 4.58 mm and 6.1 mm were studied by a numerical simulation method, and the effects of diameters, fluid velocity, inlet temperature and wall heat flux on the heat transfer characteristics were analysed. As seen in Figure 9A, the calculation results show that *Nu* decreases gradually with decreasing diameter of the D-type channel at the given boundary conditions; however, the convective heat transfer coefficient increases gradually. This indicates that the microchannel heat exchanger has the advantage of a strong heat transfer capacity. The model with an equivalent diameter of 3.05 mm was adopted to analyse the effects of thermophysical properties on liquid LBE. Figure 9B illustrates the effect of the velocity on the heat transfer characteristics. The heat transfer coefficient and *Nu* of liquid LBE increase with increasing flow velocity. With the increase in flow velocity, the turbulent characteristics of the liquid LBE will be enhanced, which can effectively further strengthen the convective heat transfer characteristics of liquid LBE. Figure 9C shows that with the absolute value increase of the wall heat flux, the heat transfer coefficient of liquid LBE decreases greatly; however, *Nu* decreases slightly. When the absolute value of the wall heat flux increases, the temperature difference between the fluid and the wall gradually increases, so *Nu* only changes slightly. As shown in Figure 9D, the convective heat transfer coefficient of liquid LBE gradually increases with increasing fluid inlet temperature, but *Nu* slightly decreases. This indicates that if the fluid inlet temperature increases, the temperature difference between the fluid and wall gradually decreases, and the convective heat transfer characteristics of liquid lead–bismuth are strengthened.

Compared with the circular tube, for the special structural form of the D-type channel, under the condition of constant wall heat flux, the liquid LBE convective heat transfer correlation was proposed. The equation shown in Eq. 17. The application scope of *Pe* is from 100 to 1,500, the application scope of *Re* is from 8,000 to 130,000, the application scope of temperature is from 200°C to 550°C, and the fitting variance is 0.956.

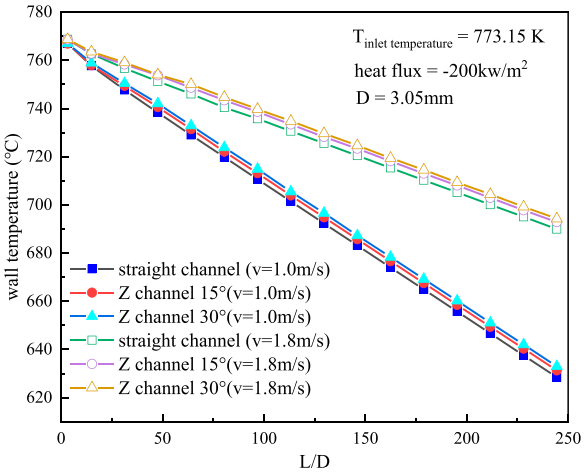

FIGURE 10
Variation in wall temperature along the circular tube for different D-type channels at different velocities.

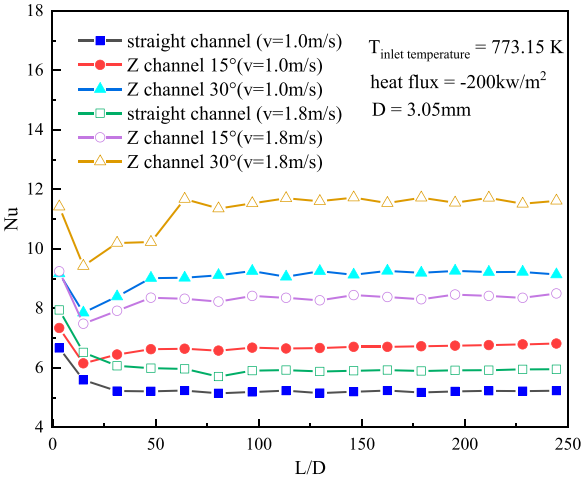

FIGURE 11
Variation in *Nu* along the circular tube for different D-type channels at different velocities.

$$Nu = 3.85 + 0.01Pe^{0.834} \quad (17)$$

4.3 Analysis of the heat transfer characteristics of liquid LBE in the zigzag channel

Generally, the design of a special structure can strengthen the heat transfer characteristics of the fluid. Numerical simulation calculation for the heat transfer characteristics

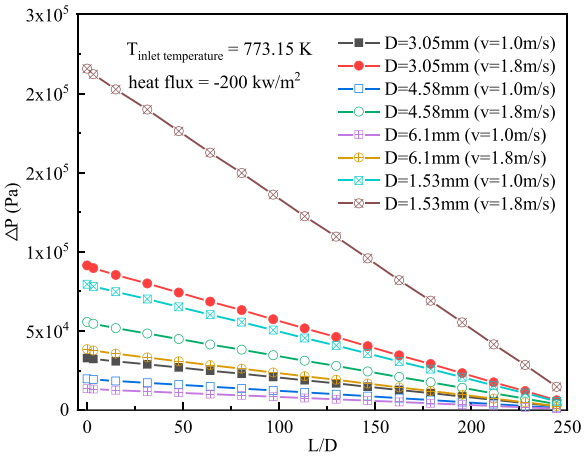

FIGURE 12
Variation in the pressure drop along the circular tube for different diameter channels at different velocities.

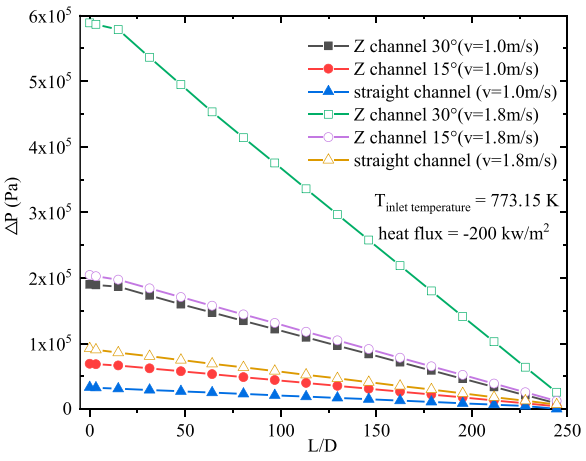

FIGURE 13
Variation in the pressure drop along the circular tube for different D-type channels at different velocities.

of liquid LBE was performed on the straight channel and the zigzag channel at the same boundary conditions. As seen in Figure 10, the wall temperature of the zigzag channel is higher than that of the straight channel at the same flow velocity. The calculation results also show that the wall temperature decreases with increasing flow velocity, and the wall temperature increases with increasing zigzag channel angle. As shown in Figure 11, with increasing fluid flow velocity, *Nu* increases. The *Nu* of liquid LBE in the Z-channel channel is higher than that in the straight channel at the same flow velocity, and the larger the angle of the Z-channel is, the larger the *Nu* of liquid LBE is. According to the analysis of the calculation results, the zigzag channel structure can strengthen the convective heat transfer characteristics of liquid LBE. Therefore, when the flow velocity of liquid LBE meets the requirement, the zigzag channel will be considered to enhance the convective heat transfer, which can effectively reduce the volume of the heat transfer equipment.

4.4 Analysis of the resistance characteristics of D-type channels

Although the design of the special structure can strengthen the convective heat transfer of the liquid LBE, it also increases the resistance of the fluid. In the current research, numerical simulation calculations were performed on the resistance characteristics of a straight channel with four equivalent diameters. As seen in Figure 12, at specified boundary conditions, the fluid resistance of liquid LBE increases with the velocity. At the same flow velocity, the smaller the equivalent diameter is, the greater the fluid resistance is. Figure 13 shows the resistance characteristics of the straight channel and zigzag channel. When the equivalent diameter of D-type channels and flow velocity are the same, the resistance of the fluid in the zigzag channel is greater than that in the straight channel, and the larger the angle of the zigzag channel is, the greater the resistance of the liquid LBE is, which is more obvious at high flow velocity. At the same zigzag channel angle, the fluid resistance increases with the flow velocity, which is in accord with the variation tendency of fluid resistance in the straight D-type channel, and the increase in fluid resistance is much larger than that caused by the increase in flow velocity in the straight channel. Therefore, if the design of the D-type channel heat exchanger is performed, the flow velocity of the fluid could not be too high, such as the choice of zigzag channel. It is suggested that the angle of the zigzag channel should not exceed 15°; otherwise, the resistance of the heat exchanger will be very large, resulting in the economic decline of the whole heat exchange system.

5 Conclusion

In this paper, the SST $k-\omega$ model was used to investigate the flow and heat transfer characteristics of liquid LBE in D-type channels. The main conclusions obtained from the present work are as follows:

1) The *Nu* calculated by the correlation proposed by Kirillov agrees well with the fitted curve of the experimental data

in a circular pipe at constant wall heat flux conditions, and the correlation proposed by Kirillov was used to assess the different Pr_t models in this paper.

2) To obtain the numerical simulation results of liquid LBE in a circular pipe, the improvement model was proposed in this paper. In addition, the improvement Pr_t model was used to calculate the heat transfer of liquid LBE at different boundary conditions, such as different fluid velocities, inlet temperatures, wall temperatures, fluid velocities, tube diameters and tube tilt angles. The numerical simulation results agree well with the heat transfer correlation proposed by Kirillov.
3) The heat transfer characteristics of liquid LBE were analysed in the current study, including variation of the heat transfer coefficient and Nu with equivalent diameter, wall heat flux, inlet fluid temperature and fluid velocity. A new correlation for calculating Nu of liquid LBE in the D-type straight channel was proposed.
4) The numerical simulation results of liquid LBE in D-type channels show that the heat transfer can be enhanced by reducing the equivalent of the D-channel or adopting a zigzag channel. The zigzag channel could obviously strengthen the heat transfer effect, but the increase in resistance was also particularly prominent. Therefore, it is necessary to comprehensively evaluate the resistance and heat transfer characteristics of zigzag channels when designing PCHEs with special D-type channels.

Data availability statement

The original contributions presented in the study are included in the article/Supplementary Material, further inquiries can be directed to the corresponding author.

Author contributions

HL: experimental data analysis, writing. ZZ: supervision, review and editing. HD: resources, conceptualization. TC: project review.

Funding

This research was supported by National Key R&D Program of China (grant number 2020YFB1901804), CNNC's Pilot-innovation Research Project, National Natural Science Foundation of China (grant number 52176151) and Fundamental Research Funds for the Central Universities of China (grant number 3072022TS1503).

Acknowledgments

The authors thank them for their financial support.

Conflict of interest

The authors declare that the research was conducted in the absence of any commercial or financial relationships that could be construed as a potential conflict of interest.

Publisher's note

References

Aneesh, A. M., Sharma, A., Srivastava, A., and Chaudhury, P. (2018). Effects of wavy channel configurations on thermal-hydraulic characteristics of printed circuit heat exchanger (pche). *Int. J. Heat Mass Transf.* 118, 304–315. doi:10.1016/j.ijheatmasstransfer.2017.10.111

Aoki, S. (1963). A consideration on the heat transfer in liquid metal. *Grafit-Gabrijel D.o.o.* doi:10.1016/S0016-5085(13)60330-3

Azer, N. Z., and Chao, B. T. (1961). Turbulent heat transfer in liquid metals-fully developed pipe flow with constant wall temperature. *Int. J. Heat Mass Transf.* 3 (2), 77–83. doi:10.1016/0017-9310(61)90069-2

Buhr, H. O., Carr, A. D., and Balzhiser, R. E. (1968). Temperature profiles in liquid metals and the effect of superimposed free convection in turbulent flow. *Int. J. Heat Mass Transf.* 11 (4), 641–654. doi:10.1016/0017-9310(68)90067-7

Chen, C. J., and Chiou, J. S. (1981). Laminar and turbulent heat transfer in the pipe entrance region for liquid metals. *Int. J. Heat. Mass Transf.* 24 (7), 1179–1189. doi:10.1016/0017-9310(81)90167-8

Chen, F., Huai, X., Cai, J., Li, X., and Meng, R. (2013). Investigation on the applicability of turbulent-Prandtl-number models for liquid lead-bismuth eutectic. *Nucl. Eng. Des.* 257, 128–133. doi:10.1016/j.nucengdes.2013.01.005

Cheng, X., and Tak, N. I. (2006). Investigation on turbulent heat transfer to lead–bismuth eutectic flows in circular tubes for nuclear applications. *Nucl. Eng. Des.* 236 (4), 385–393. doi:10.1016/j.nucengdes.2005.09.006

Cong, T., Wang, Z., Zhang, R., Wang, B., and Zhu, Y. (2021). Thermal-hydraulic performance of a pche with sodium and sco2 as working fluids. *Ann. Nucl. Energy* 157, 108210. doi:10.1016/j.anucene.2021.108210

Duponcheel, M., Bricteux, L., Manconi, M., Winckelmans, G., and Bartosiewicz, Y. (2014). Assessment of RANS and improved near-wall modeling for forced convection at low Prandtl numbers based on LES up to Reτ=2000. *Int. J. Heat. Mass Transf.* 75, 470–482. doi:10.1016/j.ijheatmasstransfer.2014.03.080

Groetzbach, G. (2003). "Turbulence modeling issues in ADS thermal and hydraulic analyses," in IAEA Technical Meeting on Theoretical and Experimental Studies of Heavy Liquid Metal Thermal Hydraulics, Karlsruhe, Germany, November 2003 (IAEA-TEC-DOC).

Guo, J., and Huai, X. (2013). Thermodynamic analysis of lead–bismuth eutectic turbulent flow in a straight tube. *Energy* 57 (1), 600–606. doi:10.1016/j.energy.2013.05.008

Huang, C., Cai, W., Wang, Y., Liu, Y., and Li, B. (2019). Review on the characteristics of flow and heat transfer in printed circuit heat exchangers. *Appl. Therm. Eng.* 153, 190–205. doi:10.1016/j.applthermaleng.2019.02.131

Ibragimov, M. K., Subbotin, V. I., and Ushakov, P. A. (1962). Investigation of heat transfer for turbulent flow of heavy liquid metals in tubes. *J. Nucl. Energy. Parts A/B. React. Sci. Technol.* 16 (3), 174–175. doi:10.1016/0368-3230(62)90094-0

Jaeger, W. (2016). Empirical models for liquid metal heat transfer in the entrance region of tubes and rod bundles. *Heat. Mass Transf.* 53 (5), 1667–1684. doi:10.1007/s00231-016-1929-8

Jaeger, W. (2017). Heat transfer to liquid metals with empirical models for turbulent forced convection in various geometries. *Nucl. Eng. Des.* 319, 12–27. doi:10.1016/j.nucengdes.2017.04.028

Jischa, M., and Rieke, H. B. (1979). About the prediction of turbulent Prandtl and schmidt numbers from modeled transport equations. *Int. J. Heat. Mass Transf.* 22 (11), 1547–1555. doi:10.1016/0017-9310(79)90134-0

Johnson, H. A., Hartnett, J. P., and Clabaugh, W. J. (1953). Heat transfer to molten lead-bismuth eutectic in turbulent pipe flow. *J. Fluids Eng.* 75 (6), 1191–1198. doi:10.1115/1.4015579

Kays, W. M. (1994). Turbulent Prandtl number—Where are we? *J. Heat. Transf.* 116 (2), 284–295. doi:10.1115/1.2911398

Kays, W. M., Crawford, M. E., and Weigand, B. (2004). *Convective heat and mass transfer*. New York: The McGraw-Hill Companies, Inc.

Kim, I., and Sun, X. (2014). CFD study and PCHE design for secondary heat exchangers withFLiNaK-Helium for SmAHTR. *Nucl. Eng. Des.* 270, 325–333. doi:10.1016/j.nucengdes.2014.02.003

Kim, I., Zhang, X., Richard, C., and Sun, X. (2016). Design study and cost assessment of straight, zigzag, S-shape, and OSF PCHEs for a FLiNaK–SCO2 Secondary Heat Exchanger in FHRs. *Ann. Nucl. Energy* 94, 129–137. doi:10.1016/j.anucene.2016.02.031

Kirillov, P. L., and Ushakov, P. A. (2001). Heat transfer to liquid metals: Specific features, methods of investigation, and main relationships. *Int. J. Heat. Mass Transf.* 48 (1), 50–59.

Li, H., Deng, T., Ma, T., Ke, H., and Wang, Q. (2019). A new evaluation method for overall heat transfer performance of supercritical carbon dioxide in a printed circuit heat exchanger. *Energy Convers. Manag.* 193, 99–105. doi:10.1016/j.enconman.2019.04.061

Liu, S., Jin, M., Lyu, K., Zhou, T., and Zhao, Z. (2018). Flow and heat transfer behaviors for double-walled-straight-tube heat exchanger of HLM loop. *Ann. Nucl. Energy* 120, 604–610. doi:10.1016/j.anucene.2018.06.016

Lyon, R. N. (1951). Liquid metal heat transfer coefficients. *Chem. Eng. Prog.* 47, 75–79. doi:10.1007/BF00412000

Marocco, Luca, and Garita, Francesco (2018). Large eddy simulation of liquid metal turbulent mixed convection in a vertical concentric annulus. *J. Heat. Transf.* 140 (7), 072504. doi:10.1115/1.4038858

Marocco, L., Valmontana, A., and Wetzel, T. (2017). Numerical investigation of turbulent aided mixed convection of liquid metal flow through a concentric annulus. *Int. J. Heat Mass Transf.* 105, 479–494. doi:10.1016/j.ijheatmasstransfer.2016.09.107

Menter, F. R. (1994). Two-equation eddy-viscosity turbulence models for engineering applications. *AIAA J.* 32 (5), 1598–1605. doi:10.2514/3.12149

Menter, F. R. "Zonal two equation k-w turbulence models for aerodynamic flows," in 24th Fluid Dynamics Conference, Orlando,FL,U.S.A, July 1993 (Reston: AIAA). doi:10.2514/6.1993-2906

Organisation For Economic Co-Operation And Development Nuclear Energy Agency (2015). *Handbook on lead-bismuth Butectic alloy and lead properties, materials Compatibility, thermal-hydraulics and Technologies*. OECD.

Pacio, J., Daubner, M., Fellmoser, F., Litfin, K., and Wetzel, T. (2016). Experimental study of heavy-liquid metal (LBE) flow and heat transfer along a hexagonal 19-rod bundle with wire spacers. *Nucl. Eng. Des.* 301, 111–127. doi:10.1016/j.nucengdes.2016.03.003

Pidaparti, Sandeep R., Anderson, Mark H., and Ranjan, Devesh (2019). Experimental investigation of thermal-hydraulic performance of discontinuous fin printed circuit heat exchangers for supercritical CO2 power cycles. *Exp. Therm. Fluid Sci.* 106, 119–129. doi:10.1016/j.expthermflusci.2019.04.025

Reynolds, A. J. (1975). The prediction of turbulent Prandtl and schmidt numbers. *Int. J. Heat. Mass Transf.* 18 (9), 1055–1069. doi:10.1016/0017-9310(75)90223-9

Roelofs, F., Gerschenfeld, A., Tarantino, M., Tichelen, K., and Pointer, W. D. (2019). "Thermal-hydraulic challenges in liquid-metal-cooled reactors-sciencedirect," in *Thermal Hydraulics aspects of liquid metal cooled nuclear reactors*, 17–43. doi:10.1016/B978-0-08-101980-1.00002-8

Saeed, M., and Kim, M. H. (2017). Thermal and hydraulic performance of SCO2 PCHE with different fin configurations. *Appl. Therm. Eng.* 127, 975–985. doi:10.1016/j.applthermaleng.2017.08.113

Skupinski, E., Tortel, J., and Vautrey, L. (1965). Determination des coefficients de convection d'un alliage sodium-potassium dans un tube circulaire. *Int. J. Heat Mass Transf.* 8 (6), 937–951. doi:10.1016/0017-9310(65)90077-3

Sleicher, C. A., Awad, A. S., and Notter, R. H. (1973). Temperature and eddy diffusivity profiles in NaK. *Int. J. Heat. Mass Transf.* 16 (8), 1565–1575. doi:10.1016/0017-9310(73)90184-1

Stromquist (1953). *Effect of WETTING on heat transfer characteristics of liquid metals*. [Tennessee Univ]. The University of Tennessee. [Technical Report].

Subbotin, V. I., Papovyants, A. K., Kirillov, P. L., and Ivanovskii, N. N. (1963). A study of heat transfer to molten sodium in tubes. *Soviet J. Atomic Energy* 13 (4), 991–994. doi:10.1007/BF01480861

Thiele, R., and Anglart, H. (2013). Numerical modeling of forced-convection heat transfer to lead–bismuth eutectic flowing in vertical annuli. *Nucl. Eng. Des.* 254, 111–119. doi:10.1016/j.nucengdes.2012.09.006

Wang, C., Wang, C., Zhang, Y., Zhang, D., Tian, W., Qiu, H., et al. (2021). Investigation on flow heat transfer characteristic of lead-bismuth eutectic alloy. *Atomic Energy Sci. Technol.* 55 (5), 822–828. doi:10.7538/yzk.2020.youxian.0356

Wang, Y., Li, X., Huai, X., Cai, J., and Xi, W. (2017). Experimental investigation of a lbe-helium heat exchanger based the ads. *Prog. Nucl. Energy* 99, 11–18. doi:10.1016/j.pnucene.2017.04.013

Xu, J., Liu, C., Sun, E., et al. (2020). Review and perspective of supercritical carbon dioxide power cycles. *Therm. Power Gener.* 49 (10), 1–10. doi:10.19666/j.rlfd.202004089

Zhang, J., Kapernick, R. J., Mcclure, P. R., and Trapp, T. J. (2013). Lead-bismuth eutectic technology for hyperion reactor. *J. Nucl. Mater.* 441 (1-3), 644–649. doi:10.1016/j.jnucmat.2013.04.079

Zhang, Y., Wang, C., Lan, Z., Wei, S., Chen, R., Tian, W., et al. (2020). Review of thermal-hydraulic issues and studies of lead-based fast reactors. *Renew. Sustain. Energy Rev.* 120, 109625. doi:10.1016/j.rser.2019.109625

Zhao, P., Zhu, J., Ge, Z., Liu, J., and Li, Y. (2018). Direct numerical simulation of turbulent mixed convection of LBE in heated upward pipe flows. *Int. J. Heat. Mass Transf.* 126, 1275–1288. doi:10.1016/j.ijheatmasstransfer.2018.05.104

Zhu, F., Junmei, W. U., Shi, L., and Guanghui, S. U. (2019). Experimental study on flow and heat transfer characteristic of liquid lead-bismuth eutectic in annular channel. *Atomic Energy Sci. Technol.* 53 (5), 819–825. doi:10.7538/yzk.2018.youxian.0495

Nomenclature

c_p specific heat
G mass flux
h enthalpy
k thermal conductivity; turbulent kinetic energy
Pr Prandtl number
p pressure
Pe Peclet number
Re Reynolds number
T temperature
u velocity
y distance from wall

Greek symbols

μ viscosity
ν kinematic viscosity
ω specific dissipation rate
ρ density
ε turbulence dissipation rate

Superscripts and subscripts

k turbulent kinetic energy
t turbulent
ω specific dissipation rate

frontiers | Frontiers in Energy Research

TYPE Original Research
PUBLISHED 10 January 2023
DOI 10.3389/fenrg.2022.991763

OPEN ACCESS

EDITED BY
Songbai Cheng,
Sun Yat-Sen University, China

REVIEWED BY
Shuo Li,
The University of Tokyo, Japan
Ting Zhang,
Kyushu University, Japan
Shangzhen Xie,
Wuhan Institute of Technology, China

*CORRESPONDENCE
Xiaoxue Huang,
xiaoxue.hi@gmail.com,
xiaoxue.huang@sheffield.ac.uk

SPECIALTY SECTION
This article was submitted to Nuclear Energy,
a section of the journal
Frontiers in Energy Research

RECEIVED 11 July 2022
ACCEPTED 28 September 2022
PUBLISHED 10 January 2023

CITATION
Duan J and Huang X (2023), An unsteady RANS study of thermal striping in a T-junction with sodium streams mixing at different temperatures.
Front. Energy Res. 10:991763.
doi: 10.3389/fenrg.2022.991763

An unsteady RANS study of thermal striping in a T-junction with sodium streams mixing at different temperatures

Jinping Duan[1] and Xiaoxue Huang[2]*

[1]State Key Laboratory of Nuclear Power Safety Monitoring Technology and Equipment, China Nuclear Power Engineering Co, Ltd, Shenzhen, Guangdong, China, [2]Department of Mechanical Engineering, The University of Sheffield, Sheffield, United Kingdom

Thermal striping in a T-junction with sodium streams mixing at different temperatures is studied using unsteady Reynolds-averaged simulation (RANS). Different parameters including the momentum ratio of the streams (0.2–4.3), the temperature difference between the streams (15–35 K), and the bulk Reynolds number (5,000–9,000) are investigated. Simulation results demonstrate that the flow pattern is mainly determined by the momentum ratio, while the temperature difference and the bulk Reynolds number have little influence within the range considered. The location of the separation point of the recirculation zone increases with the momentum ratio while the location of the thermal front decreases with it. In addition, the sensitivity of the temperature fluctuations to a range of low-Reynolds-number turbulence models are studied, which demonstrate that the time-varying temperature fluctuations predicted by these turbulence models are significantly smaller than the experimental measurements. High-fidelity simulations which fully resolve the temperature fluctuations will be carried out as the future work to complement the statistics of the temperature fluctuation.

KEYWORDS

liquid metal-cooled fast reactor, T-junction, URANS, thermal stripping, thermal mixing

1 Introduction

Thermal striping is often observed in the piping of liquid metal-cooled fast reactors (LMFRs) where two or more fluid streams at different temperatures meet. This is characterized by temperature fluctuations which can potentially cause cyclical thermal stresses and therefore fatigue cracking of the structures. Prediction of the thermal fatigue in the mixing region is important as it is important in terms of life cycle management of the piping systems.

Studies of thermal mixing in T-junctions have been reported by many authors (Lee et al., 2009; Walker et al., 2009; Ndombo and Howard, 2011; Gauder et al., 2016; Zhou et al., 2018). The complex features such as secondary flow, separation, recirculation, and reattachment have been investigated. Walker et al. (2009) studied the scalar mixing of water and identified four characteristic regions in the vicinity of the junction interface.

It comprises a mixing region with high fluctuations, a recirculation region containing two contra-rotating vortices, and two regions with small fluctuations. Ndombo and Howard (2011) examined the effect of the inlet turbulence on the unsteadiness of the flow. The turbulence at the inlet does not seem to have significant effect on the bulk flow, whereas it influences the near-wall flow, i.e., the wall temperature fluctuation and the temperature-velocity correlation are moved downstream with reduced magnitude with the inclusion of turbulence at the inlet. Similar results were presented by Gauder et al. (2016) through comparing the simulation results with and without turbulence at the inlets. Zhou et al. (2018) carried out experiments to investigate the thermal mixing with varied temperature differences. The temperature difference ranges from 140 K to 220 K and it has been found the temperature difference has a significant influence on the thermal stratification in the mixing flow as well as the reverse flow, and thus a significant influence on the thermal fatigue in the T-junction. Numerical analysis carried out by Lee et al. (2009) also identified the temperature difference (up to 150 K) between the two streams as the dominant factor among various parameters that affects the thermal fatigue. It is established that high-fidelity simulations such as large eddy simulation (LES) can capture the unsteadiness, which is responsible for the mechanical stresses that cause the thermal fatigue, whereas RANS (Reynolds Averaged Navier Stokes) models or URANS (Unsteady RANS) models to calculate the mean temperature and the temperature variance has been found unable to directly identify the local fluctuations associated with the thermal mixing.

In liquid metal-cooled fast reactors, there are several areas susceptible to thermal striping where hot and cold fluids merge, including the core outlet region, the upper plenum, and the flow guide tube, etc. Due to the high-temperature, opaque, and corrosive features of liquid metal experiments, the record of experimental data of liquid metal is scarce and most experimental studies use water as the working fluid. The large diffusivity for heat and the small diffusivity for momentum makes the liquid metal convection different from ordinary fluid convection, such as water. It has been shown that the results of water are not transferable to liquid metal especially under mixed convection as the velocity field depends strongly on the temperature field and the heat transfer behavior is significantly different from that of fluids at higher Prandtl number due to the dominance of molecular diffusion in heat transport (Huang and He, 2022a; Huang and He, 2022b). Dimensional analysis and experimental study have shown that the spectral distribution of temperature fluctuations of low Prandtl number fluids displays different characteristics compared with that of water (Bremhorst and Krebs, 1992). On the other hand, turbulence modelling of liquid metal convection is a topic requiring thorough investigation as the low Prandtl number induces different scales of the velocity field

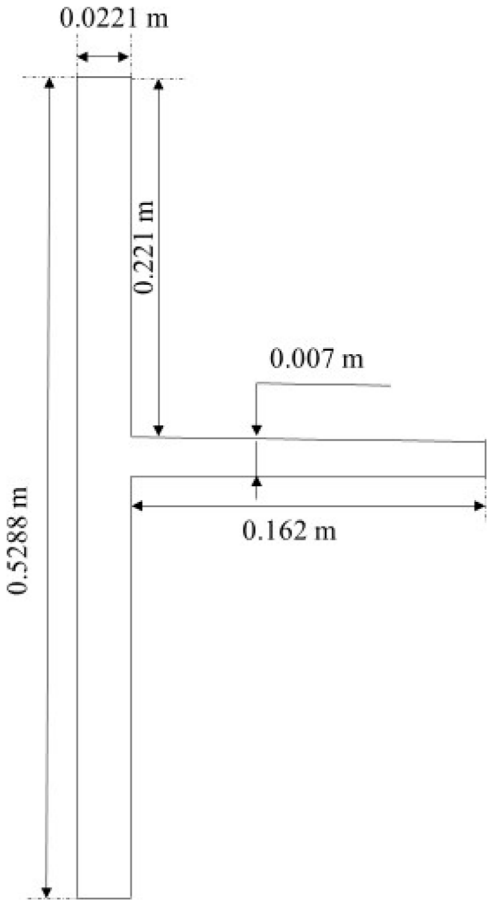

FIGURE 1
Schematic of the simulation domain of T-junction.

and the temperature field (Kawamura et al., 2000; Otic and Grötzbach, 2007). The properties of liquid metal pose difficulties on the turbulence modelling as the widely employed assumptions such as Reynolds analogy may not be applicable to liquid metal convection (Arien, 2002; Grötzbach, 2007; Shams, 2018). Otic and Grötzbach (2007) demonstrated incomplete modelling of turbulence heat flux with eddy diffusivity model. Roelofs et al. (2019) summarized dissimilarity in velocity and thermal fields for liquid metal as the wall layer thickness and the fluctuation fields do not behave similarly. Kawamura et al. (2000) performed direction numerical simulation of forced convection and demonstrated that the timescale ratio shows similar behavior in the near-wall region while it depends significantly on the boundary conditions in the bulk region. Otic and Grotzbach showed that using a thermal timescale or combining thermal and mechanical timescales improves the modelling of the turbulent heat transport in Rayleigh-Benard convection (Otić et al., 2005). Different approaches to model the turbulent heat transfer have been

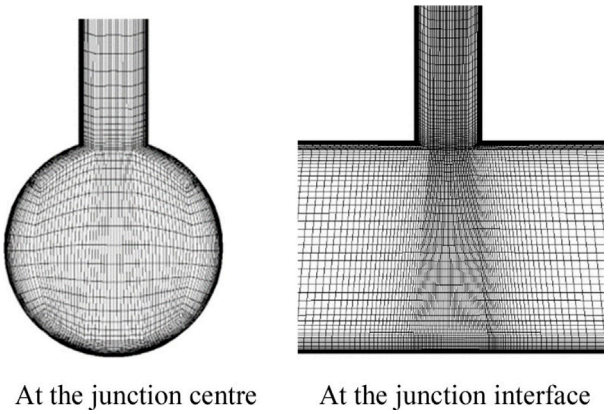

FIGURE 2
Mesh for the T-junction (full inlets and outlets have been cropped).

developed for liquid metal flows (Carteciano and Groetzbach, 2003; Manservisi and Menghini, 2014), however, further development and validation is still needed for complex configurations and for all flow regimes.

This paper investigates the thermal mixing in the T-junction. The computational model replicates the geometry and the experimental conditions of a rig detailed in Weathered (2017). A range of low-Reynolds-number turbulence models are employed, and the experimental data are used to compare with the simulation results. This is a preliminary numerical investigation of the thermal stripping phenomenon of sodium with a focus on the parametrical study and the performance estimation of various turbulence models.

2 Methodology

2.1 Experimental setup

A schematic of the T-junction is given in Figure 1. The test section has two streams of sodium impinging onto each other at different temperatures and flow rates. The temperature difference and the flow rates were varied to parametrically study the thermal striping phenomenon. Optical fibre sensors were employed for the temperature measurements in the experiments. The vertical main pipe with diameter of 22.1 mm delivered hot sodium, and the horizontal branch pipe with diameter of 7 mm delivered cold sodium. The entry length of the main pipe is 308 mm. The vertical length from the branch pipe to the exit of the main pipe is 221 mm, which is 10 times of the diameter. The entry and the exit lengths ensure sufficiently developed upstream and downstream flows.

2.2 Turbulence models

The unsteady RANS equations for the flow are expressed as follows:

$$\frac{\partial \rho}{\partial t} + \frac{\partial (\rho < U_i >)}{\partial x_i} = 0, \tag{1}$$

$$\frac{\partial \rho < U_i >}{\partial t} + \left(\rho < U_j >\right)\frac{\partial < U_i >}{\partial x_j} = -\frac{\partial < P >}{\partial x_i} + \frac{\partial}{\partial x_j}\left(\mu \frac{\partial < U_i >}{\partial x_j}\right) - \frac{\partial \left(\tau_{ij}\right)}{\partial x_j} + \rho g, \tag{2}$$

$< \ldots >$ denotes the Reynolds-averaged quantities. $\tau_{ij} = \rho < u_i' u_j' >$ are the Reynolds stress components to account for turbulent fluctuations in fluid momentum. In this study, we consider a range of low-Reynolds-number eddy-viscosity models and Reynolds-stress transport models as the closure for τ_{ij}.The eddy-viscosity models (EVMs) calculate τ_{ij} as follows

$$\tau_{ij} = \frac{1}{3}\delta_{ij}\tau_{kk} - 2\mu_t < S_{ij} > \tag{3}$$

Where $< S_{ij} > = \frac{1}{2}\left(\frac{\partial \overline{u_i}}{\partial x_j} + \frac{\partial \overline{u_j}}{\partial x_i}\right)$ is the mean rate of the strain tensor, μ_t is the turbulent viscosity. The low-Reynolds-number EVMs resolve the entire boundary layer, i.e., $y^+ < 1$. Two-equation models including Launder-Sharma k-ε and k-ω Shear Stress Transport (SST models), and v2-f model that solves additional transport equations to account for the anisotropy of wall-normal stresses are considered.

The Launder-Sharma k-ε model differs from the standard k-ε model as damping functions to account for the viscous and wall effects are included. The k-ω SST model uses a standard k-ω closure in the near-wall region and a k-ε model in the free-shear region. The v2-f model can be considered as a k-ε model with

TABLE 1 Properties of liquid sodium.

Property	Value	Unit
Thermal conductivity	104–0.047 × T	W/m/K
Density	1,014–0.235 × T	kg/m^3
Specific heat capacity	-3.001 × 10^6/T^2 + 1,658–0.8479 × T + 4.454 × 10^{-4} × T^2	J/kg/K
Dynamic viscosity	exp (556.835/T—0.3958 lnT—6.4406)	Pa·s

TABLE 2 Parameters of the simulation cases.

Case no.	1	2	3	4	5	6	7	8
M_R	0.2	1.3	3.27	4.31	0.87	0.87	0.83	0.84
$\triangle T$ (°C)	30	30	30	30	15	35	35	35
Re_{mix}	7,135	7,974	7,556	7,495	7,142	7,369	9,005	4,893
T_{branch} (°C)	250	250	250	250	265	245	245	245
T_{main} (°C)	280	280	280	280	280	280	280	280
Q_{branch} (L/min)	0.978	0.531	0.336	0.295	0.551	0.581	0.723	0.392
Q_{main} (L/min)	2.006	2.808	2.828	2.841	2.386	2.52	3.07	1.669

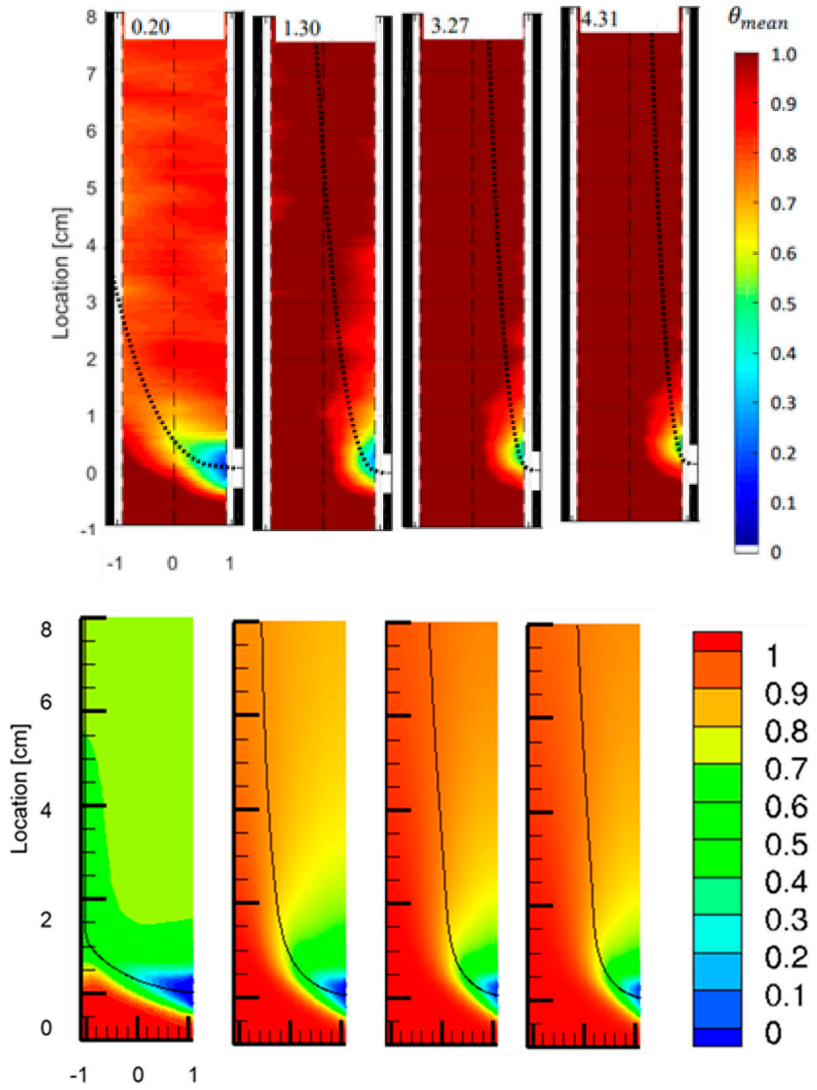

FIGURE 3
Normalized mean temperature for various momentum ratios. Top row: results from experiments, predicted jet trajectories displayed with dotted black lines. Bottom row: results from simulations (cases 1–4 from left to right), jet trajectories displayed with solid black line.

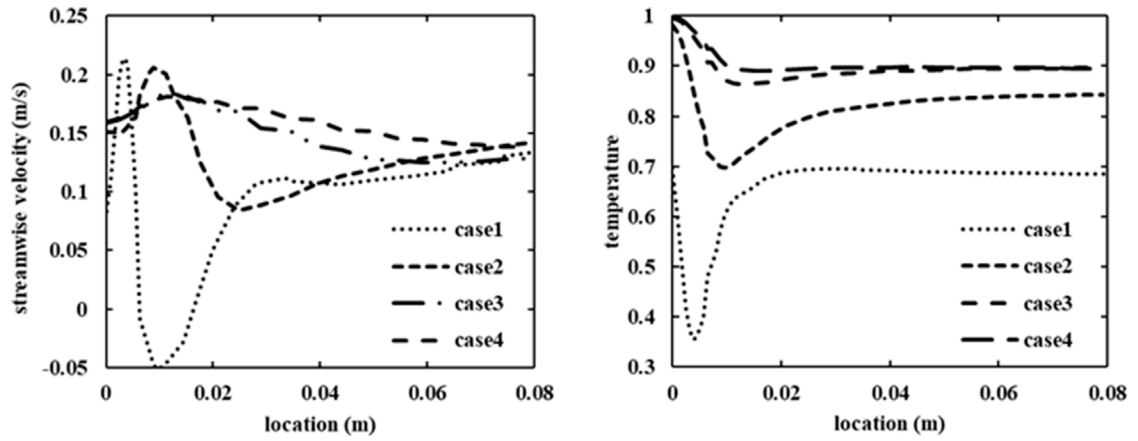

FIGURE 4
Streamwise velocity (left) and normalized temperature (right) along the centerline of the main pipe for cases 1–4.

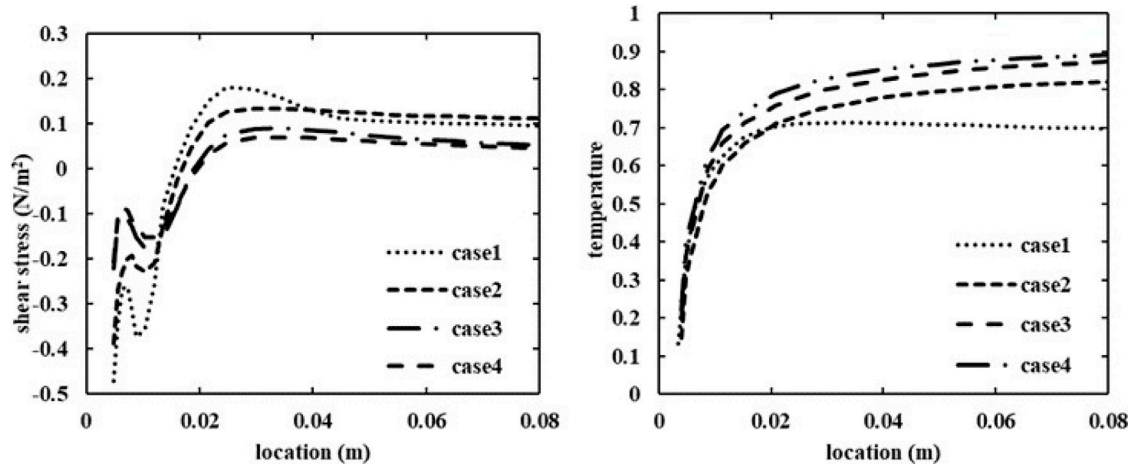

FIGURE 5
Wall shear stress (left) and normalized temperature (right) along the near side wall of the main pipe for cases 1–4.

wall-normal stress anisotropy by solving an additional transport equation for the wall-normal stress.

Reynolds-stress models (RSMs) solve a transport equation for each stress component. The elliptic blending Reynolds-stress model (EBRSM) which solves an elliptic equation for the pressure-strain term in the near-wall and the outer region is employed. The low-*Re* variant of RSM accounts for the difference in the turbulence near the wall and that at some distances away from the wall.

The simulations are carried out using Code_Saturne, version 6.0.8, an open-source finite volume solver developed by Electrictite de France (EDF) (EDF R&D, 2019). Second order centered scheme is employed for spatial and temporal discretization. The solver of the linear system is Jacobi for velocity and temperature, algebraic multigrid for pressure.

2.3 Mesh setup

The mesh is generated with the first cell wall spacing $y^+ \leq 1$ to resolve the viscous sublayer and 5–10 cells placed below $y^+ = 20$. The total number of elements of the mesh is 601,008 (shown in Figure 2). In the streamwise and the transverse directions, the sizes Δx and Δz are kept under 40 and 20, respectively. A mesh independence study has been carried out prior to the simulation. Temperature at selected downstream locations were monitored and it demonstrated that the solution is invariant when the mesh is further refined.

TABLE 3 Locations of the separation point and the thermal front for Cases 1– 4.

Case no.	Separation point (mm)	Thermal front simulation (mm)	Thermal front experiment (mm)
1	15.6	N/A	N/A
2	16.9	53.4	40.0
3	19.0	29.6	21.3
4	19.6	23.0	17.2

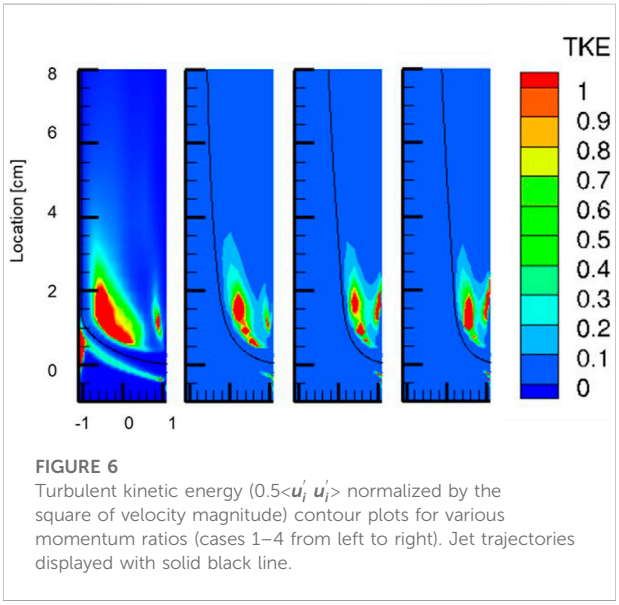

FIGURE 6
Turbulent kinetic energy ($0.5\langle u_i' u_i' \rangle$ normalized by the square of velocity magnitude) contour plots for various momentum ratios (cases 1–4 from left to right). Jet trajectories displayed with solid black line.

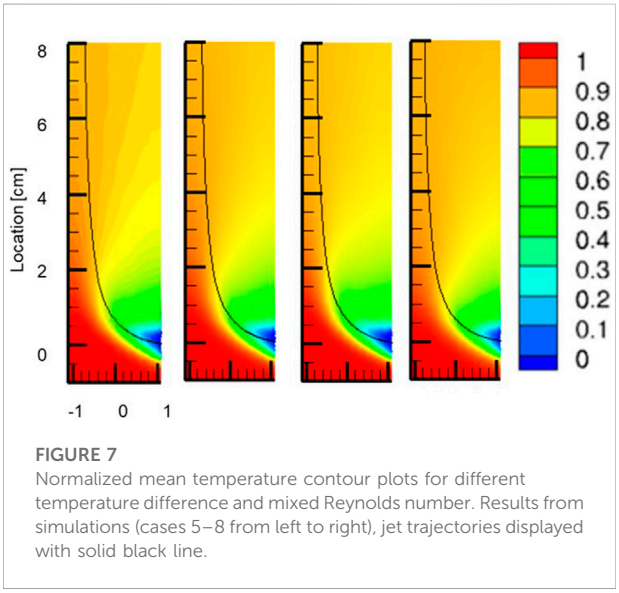

FIGURE 7
Normalized mean temperature contour plots for different temperature difference and mixed Reynolds number. Results from simulations (cases 5–8 from left to right), jet trajectories displayed with solid black line.

2.4 Thermophysical properties

The thermophysical properties of sodium are taken from Sobolev (2011). Table 1 gives the details of the properties.

2.5 Boundary conditions

Volumetric flow rate and constant temperature are prescribed at both inlets, a free outlet, i.e., zero-flux condition for the velocity and the temperature is prescribed at the outlet. Table 2 gives details of eight cases for the simulation.

To fully characterize thermal striping at the T-junction, the relevant parameters including the Momentum Ratio (M_R), the temperature difference (ΔT) between the main pipe and the branch pipe, and the bulk Reynolds number (Re_{mix}) are varied.

The momentum is defined as the volumetric flow rate multiplied by the momentum per unit volume. M_R is thus given as follows

$$M_m = (D_m D_b V_m)(\rho_m V_m)$$
$$M_b = \left(\frac{\pi}{4} D_b^2 V_b\right)(\rho_b V_b)$$
$$M_R = \frac{M_m}{M_b} \quad (4)$$

where D_m and D_b are the diameters, V_m and V_b are the bulk velocities and ρ_m and ρ_b are the densities. The subscripts m and b denotes the main pipe and the branch pipe, respectively.

The inlet flow rates range from 1.67 L/min to 3.07 L/min at the main pipe and 0.3 L/min to 0.98 L/min at the branch pipe, thus the range of Re_{mix} is 4,900 to 7,000. The range of the temperature difference between the main pipe flow and the branch pipe flow is 15°C to 35°C.

Among the eight cases, cases 1–4 vary the M_R, cases 5–6 vary ΔT, cases 7–8 vary Re_{mix}.

3 Results

This section details the simulation results of the T-junction. The results in Section 3.1, 3.2 employ k-ω SST model, and a comparison of different turbulence models (EBRSM, k-ω SST, Launder-Sharma k-ε and v2-f) is presented for Case 1 in Section 3.3. The time step size is 0.01s and the Courant number is kept lower than 1. Time-averaged data are collected for 50 flow through times after the

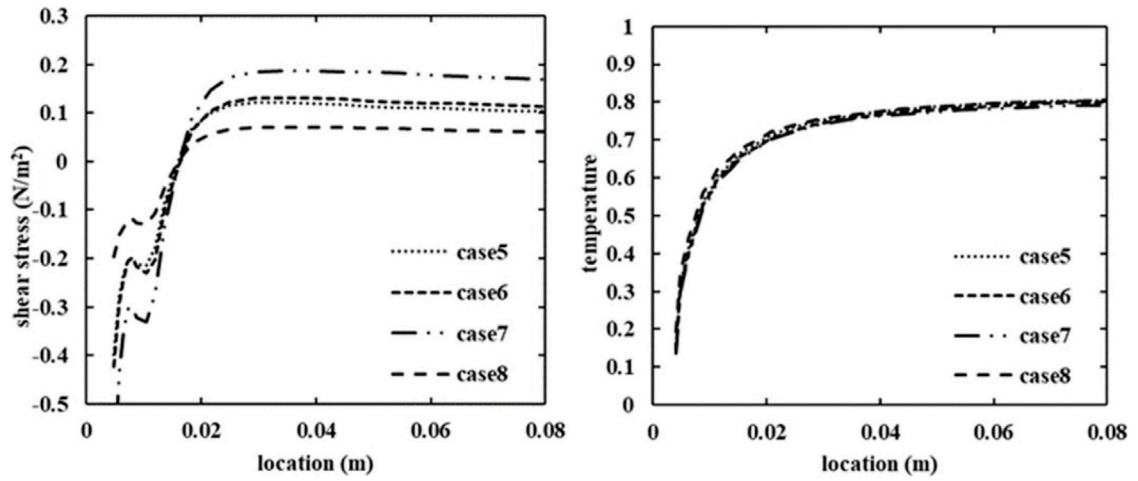

FIGURE 8
Wall shear stress and normalized temperature along the near side wall of the main pipe for cases 5–8.

domain reaches a statistically converged state, i.e., when the mean temperature value at the outlet keeps unchanged.

Time-averaged temperature and jet trajectory of cases 1–4 are compared against experimental results for investigation of the general flow patterns of the jet with various momentum ratios. Line plots of temperature, velocity and shear stress along the centerline and the near side wall of the main pipe are presented to investigate the locations of the thermal front of the jet and the size of the recirculation zone. The turbulent kinetic energy (indications of the level of turbulent temperature fluctuations, i.e., small-scale fluctuations), and the time variations of temperature (represent large-scale fluctuations in temperature) are given together with the experimentally measured peak-to-peak temperature variations for understanding of the thermal striping locations and levels.

Section 3.1 gives the results of cases 1–4, Section 3.2 gives the results of cases 5–8. In addition, a comparison between various low-*Re* turbulence models for case 1 is given in Section 3.3.

3.1 Results with various momentum ratios

The normalized mean temperature is defined as follows

$$\theta_{mean} = \frac{\bar{T} - T_b}{T_m - T_b} \tag{5}$$

Where $\bar{T}$ is the time-averaged temperature, $T_b$is the inlet temperature at the branch pipe and T_m is the inlet temperature at the main pipe. Figure 3 shows a comparison of the normalized mean temperature of the simulations and the experiments.

The jet trajectory is defined as the location of the maximum velocity of the downstream flow, thus it defines the flow path of it. In the simulation results, the trajectory is denoted by the stream trace from the centerline of the branch pipe. In the experimental results, the predicted trajectory shown was calculated using a correlation for the trajectory of a jet from a junction positioned flush with a flat plate (Kamotani and Greber, 1974). The correlation is given as

$$\frac{Z}{D_b} = 0.81 M_R^{-0.47} \left(\frac{X}{D_b}\right)^{0.36} \tag{6}$$

where Z is the spanwise direction parallel to the branch pipe, X is the streamwise direction parallel to the main pipe, D_b is the branch pipe diameter and M_R is the momentum ratio of the main to branch flow.

The top row in Figure 3 shows the experimental results (Weathered, 2017). M_R of different cases are labelled on the top of each contour plot. The bottom row shows the simulation results of cases 1–4. As shown both from the experiments and the simulations, the flow pattern changes from impinging jet to wall jet with M_R increasing from 0.2 to 4.31, which is consistent with the flow categories in literature (Hosseini et al., 2008). A reasonable agreement is observed between the simulations and the experiments in terms of the mean temperature.

TABLE 4 Locations of the separation point and the thermal front for Cases 5–8.

Case no.	Separation point (mm)
5	15.9
6	16.3
7	16.0
8	15.9

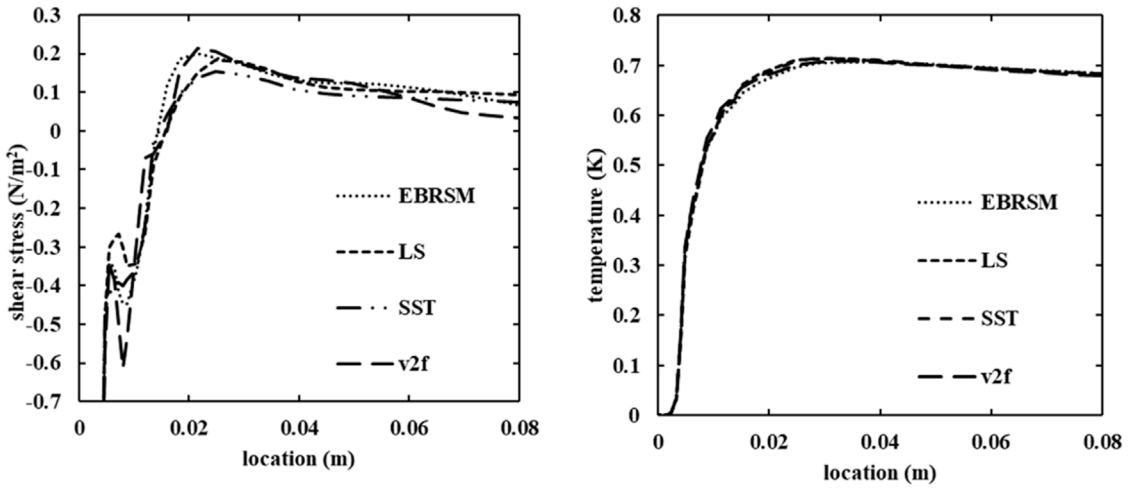

FIGURE 9
Wall shear stress and temperature along the near side wall of the main pipe in the simulations using different turbulence models.

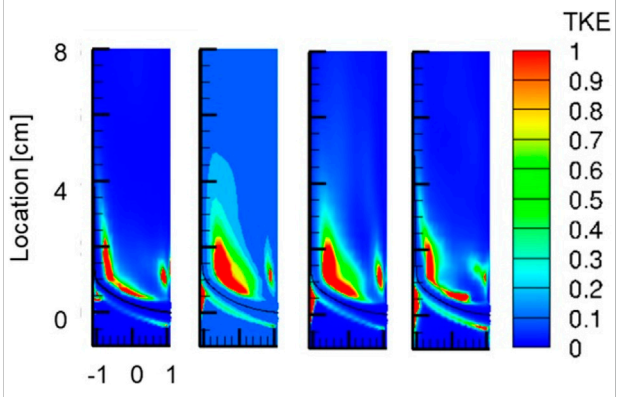

FIGURE 10
TKE in the simulations using different turbulence models (from left to right: EBRSM, LS k-ε and k-ω SST, v2-f).

The jet trajectories in the simulations differ from the trajectories predicted by Eq. 5 as they generally shift towards the far side wall in the simulations. This can be attributed to the different configurations between the simulation and the experiment in Kamotani and Greber (1974). In the simulation, the branch jet flow mixes with the pipe flow in the main pipe, whereas in the experiment in Kamotani and Greber (1974), the branch flow mixed with the cross flow over a flat plate. Besides, buoyancy effects may also contribute to this difference as Eq. 5 does not include the influence of buoyancy while the simulation has non-negligible buoyancy effect due to thermal mixing. An estimation of the trajectory location at 8 cm downstream from the branch pipe, i.e., the exit location of the trajectory in the figure, is made. It is found to be −0.122, 0.255, and 0.345 cm from the centerline of the pipe (the negative sign indicates further away from the jet side) in the experiments, compared to −0.539, −0.225, and −0.166 cm in the simulations (cases 2–4).

Figure 4 shows the temperature and streamwise velocity along the centerline of the main pipe. Following an increase in the velocity close to the junction interface due to the mixing of the streams, the velocity decreases as a result of the fast decay of the jet and increases again in cases 1 and 2 as the impinged jet mixes with the main pipe flow again. Correspondingly, the temperature decreases at the beginning due to the cold branch flow then increases due to the thermal mixing of the two streams.

Figure 5 shows the wall shear stress and the normalized temperature along the near side wall for cases 1–4. A recirculation zone is formed where the wall shear stresses are negative at the side wall. The location of the separation point between the recirculation zone and the upward main flow where the wall shear stress is zero is given in Table 3 for cases 1–4. The temperature increases monotonically along the near side wall as the two streams mix. The thermal front of the jet is defined as the location where the normalized mean temperature is 0.8. In case 1, the temperature has not reached 0.8 before the impingement. In cases 2–4, the thermal front predicted by the simulations and that estimated from the contour plots of experiments are given in Table 3. It is worth pointing out that the contour plots for the experiments in Figure 3 were interpolated from the measurements and uncertainties in the thermal front location in experiments may arise from the interpolation.

The time-dependent temperature data was collected by the optical fiber. The peak-to-peak normalized temperature range was calculated as

$$\theta_{p-p} = \frac{T_{max} - T_{min}}{\Delta T} \quad (7)$$

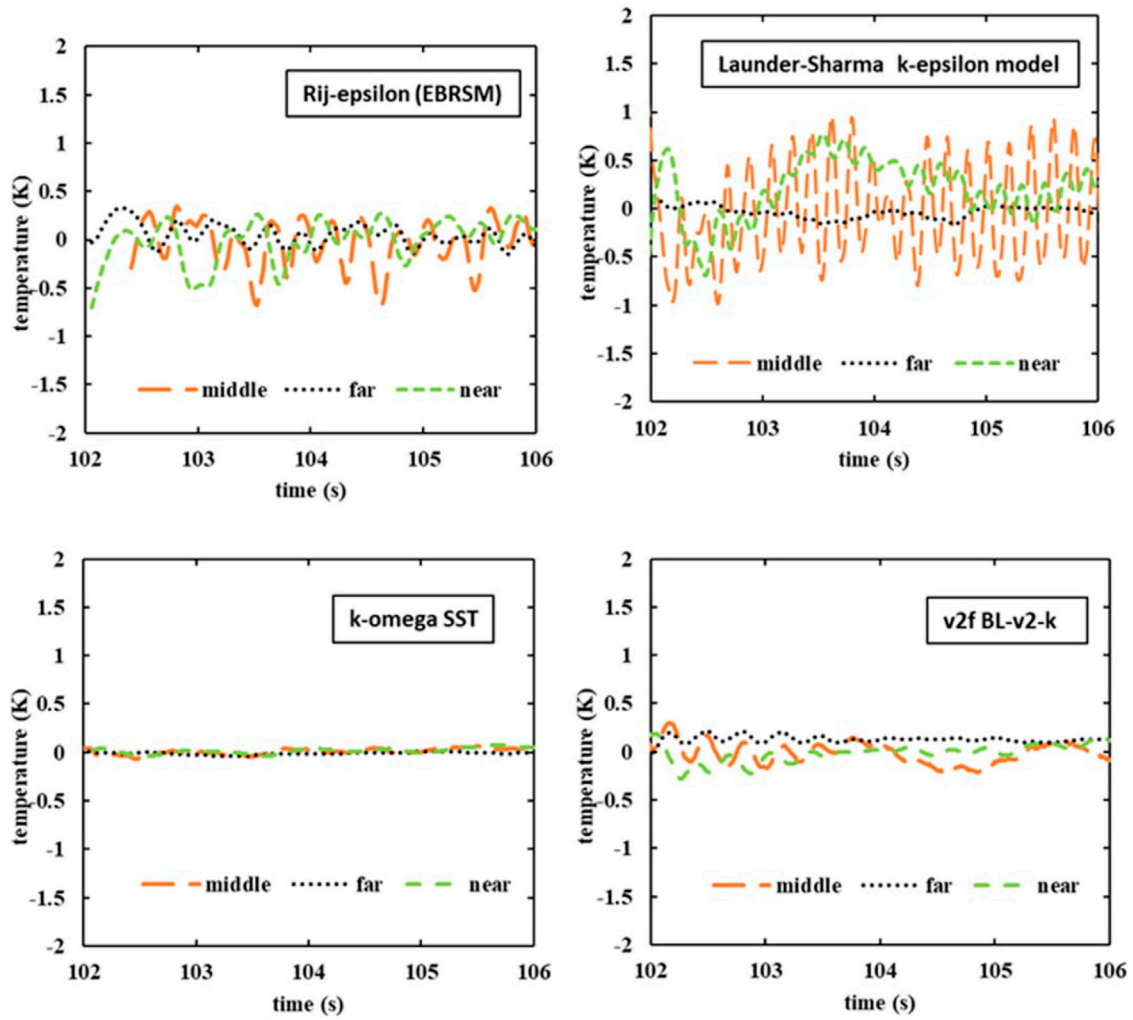

FIGURE 11
Temperature variations with time with different turbulence models.

where T_{max} and T_{min} are the maximum and minimum temperatures over the acquisition period and ΔT is the sodium temperature difference between the main pipe and the branch pipe.

The temperature fluctuations captured by experiments cannot be resolved directly in the turbulence modelling as the temperature fluctuation variance ($<\theta'^2>$) is not available in the present URANS simulations. Instead, the small scale (turbulent) fluctuations can be indirectly inferred using turbulent kinetic energy (TKE), whereas the large-scale fluctuations can be directly inspected by the time-varying temperature fluctuations in the simulation.

For an indicative comparison with the experiments, TKE (normalized by velocity squared) is shown in Figure 6 to demonstrate the level of turbulence over the domain. The distribution of TKE largely follows the streamline as a result of shearing between the jet and the main pipe flow. The TKE level in case 1 is the highest as the shear flow is strong due to the low M_R of the main flow over the branch flow. In each case, the highest TKE is seen slightly downstream from the trajectories as the recirculation zone is formed in those regions.

The temperature variations with time predicted by the URANS models are not significant (lower than 1K) in the current simulations, showing that the k-ω SST model is not able to predict the large-scale temperature fluctuations. A comparison of different URANS models in terms of this time-varying temperature fluctuation will be given in this Section 3.3.

3.2 Results with various temperature differences and bulk Reynolds numbers

Figure 7 gives the normalized mean temperature distribution of cases 5–8. A turning jet is observed in these cases as the M_R is fixed at 0.85. Figure 8 shows the

wall shear stress and the temperature along the near side wall. The wall shear stress increases with the Remix comparing cases~8), however, it does not vary significantly with the ΔT (cases 5–6). The locations of the separation points are given in Table 4. The normalized temperature profiles collapse together for cases 5–8 as shown in Figure 8, therefore, the locations of the thermal fronts for those cases are almost the same and not included in Table 4 for comparison.

3.3 Comparison of different turbulence Models

A comparison of different turbulence models has been conducted using the boundary conditions of case 1. This case has been selected for comparison as temperature fluctuations observed are strong at both the far side wall and the near side wall in the experiments.

The results of case 1 with various turbulence models are shown in Figures 9–11. The mean temperature distributions are largely the same for the tested turbulence models. Therefore, the contour plots of temperature are omitted and the plots of total shear stress and temperature along the near side wall are shown in Figure 9 instead. Besides, the locations of the separation point, and the thermal front produced by different turbulence models are almost the same. The wall shear stress in the recirculation center is the highest with v2-f model and lowest with the LS k-ε turbulence model.

Figure 10 shows the TKE distribution for the tested turbulence models. The LS k-ε turbulence model predicted the strongest turbulence level, while EBRSM and v2-f produce a low level of turbulence.

Figure 11 shows the time variation of the temperature at different locations. Three locations are monitored: 1D downstream at the near side wall, 0D downstream at the centerline and 0D downstream at the far side wall (D is the diameter of the main pipe). Among the tested turbulence models, k-ω SST is not able to reproduce the large-scale temperature fluctuations, while LS k- ε produces the strongest temperature fluctuations. The middle location, i.e., the location at the centerline, has shown low frequency with high magnitude of temperature variations, whereas the far location, i.e., the location at the far side wall, is comparatively silent. Correspondingly, the TKE level at the far location is high while it is relatively low at the middle location as shown in Figure 10. In the results from EBRSM and v2-f, the difference between the three locations is not as significant as that in the LS k-ε result.

According to the experimental results of the peak-to-peak temperature range in Weathered (2017), the fluctuation level is around 50% of the temperature difference (i.e., about 15 K), however, the simulation predicted temperature variation is just around 1 K in the case with strongest temperature fluctuations, i.e., the case using LS k-ε model. LES or unsteady RANS with transport equations for the temperature invariance and turbulent heat flux are needed for such predictions and this is the next step of the current study.

4 Conclusion

Unsteady RANS studies have been carried out for the thermal striping phenomena of a non-isothermal T-junction at various momentum ratios, temperature differences and bulk Reynolds numbers. The sensitivity to different turbulence models is also investigated. The main conclusions are as follows:

Within the range of the parameters considered, the flow pattern, including the distribution of the mean temperature, distribution of the recirculation zone and the location of the thermal front, is mainly determined by the momentum ratio while the temperature difference and the bulk Reynolds number have little influence. The location of the separation point of the recirculation zone increases with the momentum ratio while the location of the thermal front decreases with it.

According to the experiments, the temperature fluctuation level is around 50% of the temperature difference and it increases with the momentum ratio. Such fluctuations cannot be resolved directly in URANS simulations. Instead, the small-scale (turbulent) fluctuations can be indirectly inferred from TKE, whereas the large-scale fluctuations can be directly resolved and represented by the unsteady temperature variations. The simulation results show that the TKE level decreases with the momentum ratio. The TKE level is high in the cases with Launder-Sharma k-ε and k-ω SST compared to the rest of the turbulence models. On the other side, the time-varying temperature fluctuations predicted in the case with Launder-Sharma k-ε is the highest (but still around 1K) and it is nearly 0 in the case with k-ω SST.

LES simulations and URANS simulations with transport equations for the temperature invariance and turbulent heat flux are undertaken to directly resolve the temperature fluctuations associated with thermal striping as the next step of this study.

Data availability statement

The original contributions presented in the study are included in the article/Supplementary Material, further inquiries can be directed to the corresponding author.

Author contributions

JD: Conceptualization, Methodology, and Investigation. XH: Data curation and Writing.

Funding

This work has been performed using resources provided by the Cambridge Tier-2 system operated by the University of Cambridge Research Computing Service (www.hpc.cam.ac.uk) funded by EPSRC Tier-2 capital grant EP/P020259/1.

Conflict of interest

Author JD was employed by China Nuclear Power Engineering Co, Ltd.

The remaining authors declare that the research was conducted in the absence of any commercial or financial relationships that could be construed as a potential conflict of interest.

Publisher's note

References

Arien, B. (2002), Assessment of computational fluid dynamics codes for heavy liquid metals, Mol, Belgian: ASCHLIM EC-Con. FIKW-CT-2001-80121-Final Report.

Bremhorst, K., and Krebs, L. (1992). Experimentally determined turbulent Prandtl numbers in liquid sodium at low Reynolds numbers. *Int. J. Heat. Mass Transf.* 35 (2), 351–359. doi:10.1016/0017-9310(92)90273-u

Carteciano, L. N., and Groetzbach, G. (2003). *Validation of turbulence models in the computer Code FLUTAN for a free hot sodium jet in different buoyancy flow regimes*. Germany: ETDEWEB.

EDF R&D (2019). *Code_Saturne version 6.0.5 practical user's guide*. France, Europe: EDF R&D.

Gauder, P., Selvam, P. K., Kulenovic, R., and Laurien, E. (2016). Large eddy simulation studies on the influence of turbulent inlet conditions on the flow behavior in a mixing tee. *Nucl. Eng. Des.* 298, 51–63. doi:10.1016/j.nucengdes.2015.12.001

Grötzbach, G. (2007). *Anisotropy and buoyancy in nuclear turbulent heat transfer – critical assessment and needs for modelling*. FZKA: Forschungszentrum Karlsruhe.

Hosseini, S. M., Yuki, K., and Hashizume, H. (2008). Classification of turbulent jets in a T-junction area with a 90-deg bend upstream. *Int. J. Heat Mass Transf.* 51 (9-10), 2444–2454. doi:10.1016/j.ijheatmasstransfer.2007.08.024

Huang, X., and He, S. (2022). Study of a lead-bismuth eutectic jet issued into a heated cavity using large eddy simulation. *Int. J. Heat Mass Transf.* 198, 123407. doi:10.1016/j.ijheatmasstransfer.2022.123407

Huang, X., and He, S. (2022). Study of a negatively buoyant jet of liquid metal in a density-stratified ambient. *Int. Commun. Heat Mass Transf.* 138, 106351. doi:10.1016/j.icheatmasstransfer.2022.106351

Kamotani, Y., and Greber, I. Experiments on confined turbulent jets in cross flow (1974). Technical report, Cleveland: Case Western Reserve University,

Kawamura, H., Abe, H., and Shingai, K. (2000). *DNS of turbulence and heat transport in a channel flow with different Reynolds and Prandtl numbers and boundary conditions, 3rd International Symposium on Turbulence*. Nagoya, Japan: Heat Mass Transf.

Lee, J. I., Hu, L., Saha, P., and Kazimi, M. S. (2009). Numerical analysis of thermal striping induced high cycle thermal fatigue in a mixing tee. *Nucl. Eng. Des.* 239 (5), 833–839. doi:10.1016/j.nucengdes.2008.06.014

Manservisi, S., and Menghini, F. (2014). Triangular rod bundle simulations of a CFD κ-ϵ-κθ-ϵθ heat transfer turbulence model for heavy liquid metals. *Nucl. Eng. Des.* 273, 251–270. doi:10.1016/j.nucengdes.2014.03.022

Ndombo, J., and Howard, Richard J. A. (2011). Large Eddy Simulation and the effect of the turbulent inlet conditions in the mixing Tee. *Nucl. Eng. Des.* 241 (6), 2172–2183. doi:10.1016/j.nucengdes.2011.03.020

Otic, I., and Grötzbach, G. (2007). Turbulent heat flux and temperature variance dissipation rate in natural convection in lead-bismuth. *Nucl. Sci. Eng.* 155, 489–496. doi:10.13182/nse07-a2679

Otić, I., Grötzbach, G., and Wörner, M. (2005). Analysis and modelling of the temperature variance equation in turbulent natural convection for low-Prandtl-number fluids. *J. Fluid Mech.* 525, 237–261. doi:10.1017/s0022112004002733

Roelofs, F., Gerschenfeld, A., Tarantino, M., Van Tichelen, K., and Pointer, W. D. (2019). *Thermal-hydraulic challenges in liquid-metal-cooled reactors*. Sawston, United Kingdom: Woodhead Publishing.

Shams, A. (2018). Towards the accurate numerical prediction of thermal hydraulic phenomena in corium pools. *Ann. Nucl. Energy* 117, 234–246. doi:10.1016/j.anucene.2018.03.031

Sobolev, V. (2011). *Database of thermophysical properties of liquid metal coolants for GEN-IV*. 2nd ed. Belgium: SCK·CEN.

Walker, C., Simiano, M., Zboray, R., and Prasser, H. M. (2009). Investigations on mixing phenomena in single-phase flow in a T-junction geometry. *Nucl. Eng. Des.* 239 (1), 116–126. doi:10.1016/j.nucengdes.2008.09.003

Weathered, M. (2017). "Characterization of sodium thermal hydraulics with optical fiber temperature sensors,". Thesis (Ph.D.) (Madison: University of Wisconsin).

Zhou, M., Kulenovic, R., and Laurien, E. (2018). Experimental investigation on the thermal mixing characteristics at a 90° T-Junction with varied temperature differences. *Appl. Therm. Eng.* 128, 1359–1371. doi:10.1016/j.applthermaleng.2017.09.118

frontiers | Frontiers in Energy Research

TYPE Original Research
PUBLISHED 25 January 2023
DOI 10.3389/fenrg.2022.988745

OPEN ACCESS

EDITED BY
Muhammad Zubair,
University of Sharjah, United Arab Emirates

REVIEWED BY
Zhangjian Zhou,
University of Science and Technology Beijing, China
Aniruddh Das,
Technical University Dresden, Germany

*CORRESPONDENCE
Di Yun,
diyun1979@xjtu.edu.cn

SPECIALTY SECTION
This article was submitted to Nuclear Energy, a section of the journal Frontiers in Energy Research

RECEIVED 07 July 2022
ACCEPTED 13 December 2022
PUBLISHED 25 January 2023

CITATION
Xu Y, Yun D, Yan X, Zhang P, Yan W, Li Y, Li C, Li J, Zhang T, Li J, Zhou J, Kang L and Lu C (2023), Effects of Fe self-ion irradiation on a low carbon MX-ODS steel at 550°C.
Front. Energy Res. 10:988745.
doi: 10.3389/fenrg.2022.988745

Effects of Fe self-ion irradiation on a low carbon MX-ODS steel at 550°C

Yuwen Xu[1], Di Yun[1,2]*, Xu Yan[1], Ping Zhang[1], Wei Yan[3,4], Yanfen Li[3,4], Chao Li[5], Jiao Li[5], Tongmin Zhang[6], Jun Li[6], Junjun Zhou[6], Long Kang[6] and Chenyang Lu[1]

[1]School of Nuclear Science and Technology, Xi'an Jiaotong University, Xi'an, China, [2]State Key Laboratory of Multiphase Flow, Xi'an Jiaotong University, Xi'an, China, [3]CAS Key Laboratory of Nuclear Materials and Safety Assessment, Institute of Metal Research, Chinese Academy of Sciences, Shenyang, China, [4]Shi-Changxu Innovation Center for Advanced Materials, Institute of Metal Research, Chinese Academy of Sciences, Shenyang, China, [5]Instrumental Analysis Center, Xi'an Jiaotong University, Xi'an, China, [6]Institute of Modern Physics (IMP), Chinese Academy of Sciences, Lanzhou, China

Oxide Dispersion Strengthened (ODS) steels with nano-scale oxides have become one of the candidate materials used in advanced nuclear reactor systems. A novel MX-ODS steel with extremely low carbon content was irradiated with 3 MeV Fe ions at 550°C up to peak damage of 70 dpa. The steel contains uniformly distributed Y_2O_3 nano-precipitates with an average size of 3.5 nm and a number density of 5 × 10^{22}/m^3. A V-rich shell was found surrounding the core of Y, O, and Si at some particles. Two types of large precipitates, Y-Ta-Si oxides, and VN, were observed in the steel instead of carbides. Voids of very small size are present due to irradiation and the calculated void swelling was only 0.004%, suggesting good irradiation tolerance of the MX-ODS steel in this study. Fine and dense oxide nano-precipitates and their shell-core structure remained stable while the shape of large precipitates changed after irradiation.

KEYWORDS

ODS steel, ion irradiation, void swelling, oxide nano-precipitate, MX phase

1 Introduction

Advanced nuclear reactor systems with higher safety, reliability, and thermal efficiency are being developed as sustainable and clean energy sources. In the fourth generation fission reactors and fusion reactors, structure materials have to sustain harsh environments such as high temperatures and neutron irradiation of especially high doses, and this sets a limit for the development of advanced nuclear reactors. Nanostructured oxide dispersion strengthened (ODS) steels have become one of the promising candidate materials because of their outstanding high-temperature properties and remarkable tolerance to irradiation-induced swelling (Ukai et al., 2017; Odette, 2018). The oxide nano-precipitates should be of small size, high number density, uniform distribution, and should retain good stability in high temperature and irradiation environment. They could

pin dislocations and grain boundaries, and could serve as defect sinks to achieve good swelling resistance (Lin et al., 2021).

A series of ODS steels has been developed and tested to be used as the fusion blanket structural material (Zinkle et al., 2017) or in liquid lead-bismuth eutectic (LBE) or lead cooled reactors (Kimura et al., 2011; Song et al., 2019). $M_{23}C_6$ carbides, which commonly appear in ferritic/martensitic ODS steels and pin the grain boundaries, would be unstable in the high-temperature environment (Zheng et al., 2020), setting a limitation on the working temperature for such ODS steels. A novel MX-ODS steel with extremely low carbon content was developed (RUI, 2022) to eliminate $M_{23}C_6$ carbides and take the advantage of MX (M = Ta/V, X = C/N) precipitates as second-phase strengthening (Tan et al., 2016).

Both MX and $M_{23}C_6$ phases suffered from instability issues during irradiation, which may affect void swelling and mechanical properties. Several studies have been carried out to examine their stability under irradiation. Kano et al. (2018a) suggested that the size of both MX and $M_{23}C_6$ phase decreased slightly after ion irradiation of 50 dpa (damage per atom). The reduction of the MX phase was less severe than $M_{23}C_6$ in neutron irradiation according to Tan et al. (2020), while Tanigawa et al. (2007) reported that TaC disappeared when $M_{23}C_6$ reduced in size and became amorphous after ion irradiation. Furthermore, the MX phase of different elements responded differently to irradiation. TaN dissolved under ion irradiation while TaC and VN tended to further precipitate as reported by Tan et al. (2014), depending both on their chemical compositions and shapes. The excess vacancies created by irradiation can affect the stability of the MX phase, and the properties of the second phase may determine the behavior of point defects in return. Thus, based on these previous results, it is determined that in order to predict the response and the effect of the MX phase in the MX-ODS steel during irradiation, more investigations still need to be carried out in a systematic way.

In this work, a heavy ion irradiation experiment was conducted on an MX-ODS steel with 3 MeV Fe ions at 550°C to peak damage of 70 dpa. Ion irradiation with a high damage rate, no sample activation, and economical efficiency, has been widely used as a screening tool for alloy development (WAS, 2017). Fe ions were chosen to exclude the effects of injected atoms of other types. The steel is envisaged to be used in the lead-cooled fast reactor as fuel cladding with an outlet temperature of 550°C, which is slightly higher than the peak swelling temperature in ferritic/martensitic steel at about 420°C–470°C according to Toloczko et al. (2014). However, the peak swelling temperature may shift due to the differences of melting temperature of different steels. Considering a relatively good resistance to swelling commonly expected for ODS steels, a peak damage of 70 dpa was reached in the experiment. Such choice of ion irradiation dose serves two purposes: 1) To clarify the swelling resistance of the MX-ODS steel, and 2) To investigate the stability of MX phases under ion irradiation to an intermediate dose level.

In this work, the fine oxides of Y_2O_3 and large precipitates of metallic oxides and VN were characterized in the as-received materials first. Attention was paid to oxide nano-precipitates, which contribute to the resistance of irradiation effects. Then after irradiation, voids distribution and void swelling were particularly concerned. The response of oxide nano-precipitates to irradiation was examined as well.

2 Materials and methods

2.1 Materials preparation and characterization

The MX-ODS steel used in this study was produced by powder metallurgy. The pre-alloy powder smaller than 150 μm produced by gas atomization was mixed with 0.30 wt % Y_2O_3 power with the particle size of 100–200 nm. Mechanical alloying (MA) of the powder was conducted with grinding rotate peed of 150 r/min for 90 h under the protection of high purity Ar gas (99.99%). Then the powder was vacuum degassing and consolidated by hot forging. Finally, heat treatment was conducted at 980°C for 1 h and 750°C for 1 h. A detailed fabrication process can be found elsewhere (Rui et al., 2022). The chemical compositions are shown in Table 1. Carbon content was controlled to an extremely low level to eliminate carbides in the steel. The addition of N was expected to form the MX phase (M = Ta, V, X = N) to strengthen the steel. A tempered martensitic structure can be seen and the average grain size is 0.93 μm, as shown in Figure 1.

Non-irradiated specimens for TEM characterization were prepared by jet electropolishing. Samples were mechanically ground with SiC paper to less than 100 μm of thickness and punched into 3 mm discs. A solution of 10% perchloric acid in ethanol was used as an electrolyte and electropolishing was conducted at −20°C with a potential of 19 V. A focused ion beam (FIB) lift-out specimen with a thickness of 80 nm was fabricated to examine the cross-section after irradiation. Another FIB lift-out specimen was prepared in the same irradiation sample, but in the area which was covered by part of the holder during irradiation. Thus the specimen did not receive irradiation but went through the same condition (a high temperature of 550°C) during irradiation.

Microstructures of samples before and after irradiation were characterized by field emission transmission electron microscopy (TEM) using JEOL-F200 and Talos-F200X. Under-focus and over-focus of both 1000 nm in bright-field TEM were used to manifest voids. High angle annular dark field (HADDF) STEM and energy-dispersive X-ray spectroscopy (EDS) were performed for distinguishing and conducting the chemical analysis of nanoparticles and precipitates in the samples.

TABLE 1 Chemical composition of the MX-ODS steel (wt%).

C	Cr	N	W	Mn	Ta	V	Y	O	H	Si	Al
0.0115	7.69	0.110	1.14	0.94	0.11	0.39	0.23	0.163	0.00021	0.0124	0.0052

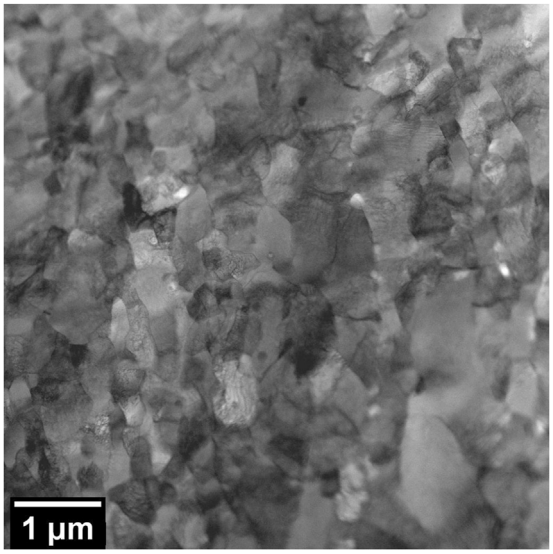

FIGURE 1
A tempered martensitic structure of the as-received sample with fine grains in TEM.

2.2 Irradiation experiment

The steel received was a rod with a radius of 7.5 mm. The samples for the irradiation experiment were prepared by wire-cut electric spark to a thickness of about 3 mm. The surfaces were mechanically ground with SiC paper and then polished by alumina paste. A vibratory polishing was conducted to remove surface stress.

Ion irradiation experiment was carried out at the 320 keV multi-discipline research platform for highly charged ions equipped with the ECR (electron cyclotron resonance) ion source in the Institute of Modern Physics, Chinese Academy of Sciences (IMP, CAS). Samples were irradiated with 3 MeV Fe ions at 550°C to a total fluence of 6.78×10^{16} ions/cm^2. The damage and injected Fe ion profiles along depth were calculated using Stopping and Range of Ions in Matter (SRIM) 2013 (Biersack, 2013) with the Kinchin-Pease mode and the displacement threshold energy of Fe was set to 40 eV (Greenwood, 1985; Stoller et al., 2013). As illustrated in Figure 2, the area from the surface down to the depth of 1.4 μm was influenced by irradiation and a peak damage of 70 dpa was obtained at a depth of around 0.8 μm.

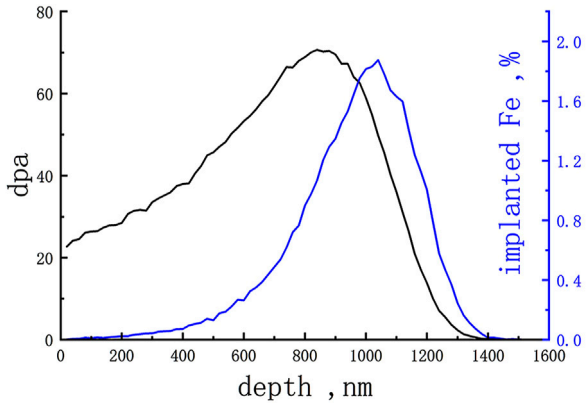

FIGURE 2
Damage (dpa) and implanted Fe ions distribution (%) along depth calculating by SRIM.

3 Results and discussion

3.1 Microstructure of as-received samples

3.1.1 Oxide nano-precipitates

The dispersive nano-precipitates of small size and high number density account for the advanced mechanical property and resistance to irradiation void swelling of ODS steel. The distribution, structure, and chemical composition of oxide nano-precipitates are characterized and analysed as follows.

Nano-precipitates of high number density and near-uniform distribution were observed in TEM bright field in Figure 3A. Precipitate size distribution was calculated using TEM bright field images and more than 1000 precipitates were measured, as shown in Figure 3B. The size of oxide precipitates varies from about 1 nm in diameter to 20 nm. Most of the precipitates are under 10 nm and the average size is 3.5 nm. The thickness of the TEM specimen prepared by electropolishing was estimated to be 100 nm and the number density of oxide precipitates is 5×10^{22}/m^3. The size and number density of the oxide precipitates in this ODS steel are the same levels as several kinds of ODS steels, with a number density of 10^{22}–10^{24}/m^3 and an average size from 2 to 10 nm (Klimiankou et al., 2005; Aleev et al., 2011; Hirata et al., 2012; Wu et al., 2012; Rahmanifard et al., 2015; Liu et al., 2017).

Y_2O_3 powder was added to produce oxide precipitates and the expected structure of nano-precipitates is Y_2O_3. TEM images in Figure 4 show an oxide nano-precipitate with a diameter of

3.5 nm in the steel matrix together with its fast Fourier transform (FFT) image. A structure of Y_2O_3 (PDF#01-075-3096) in the direction of (0 2 2) can be seen. The d-spacings of 0.26 and 0.31 nm accord with the d-spacings of (4 0 0), (2 2 2) in Y_2O_3, respectively, and the corresponding angles are 73 and 53°.

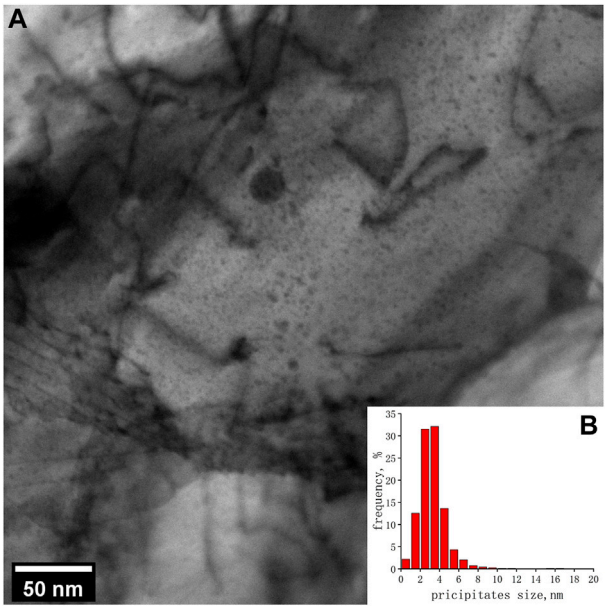

FIGURE 3
(A) High-density oxide nano-precipitates inside a grain in TEM bright field. **(B)** Size distribution of nano-precipitates in the as-received sample.

Structures of 10 nano-precipitates and their FFT were examined and all of them were the same Y_2O_3 structure. No specific orientation relationship between precipitates and the steel matrix was observed.

The chemical compositions of Y-O nano-precipitates acquired by EDS are shown in Figure 5. Precipitates vary from 1 to 10 nm in diameter in the HADDF image. These larger precipitates were chosen to illustrate element distribution clearly. Precipitates of Y and O, lacking Fe can be seen, and some of the precipitates contain Si and a small amount of Ta as well. A shell structure of V surrounding oxide is clearly demonstrated with the element map of Y and V. Element map of Cr shows its slight aggregation around the oxides.

It has been reported that other trace elements, such as Mn, Si, V, and Ta, could take part in the formation of oxide nano-precipitates, and some of the precipitates with these minor elements have different structures instead of Y_2O_3. Uchidi et al. (2011) reported that in 9YWT ODS steel with an extra 1 wt% Si added, besides fine precipitates of Y_2O_3, complex oxide of Y_2SiO_5 appeared during the annealing process after MA. An atom probe tomography (APT) study of ODS-EURORFER 97 steel showed the presence of Mn and Si at both 5%–10% in oxide precipitates (Williams et al., 2010). Klimenkov et al. (2009) reported the presence of Mn inside nano-precipitates, with a chemical composition of $(Y_{1.8}Mn_{0.2})O_3$ of the oxides in ODS-EUROFER alloy by electron energy loss spectroscopy (EELS). Mn seemed to dissolve in the Y_2O_3 phase and the structure of oxides was not changed.

The presence of minor elements in oxide can be explained by the formation enthalpy of their oxides. Among all the minor elements in the MX-ODS steel in this study, the formation

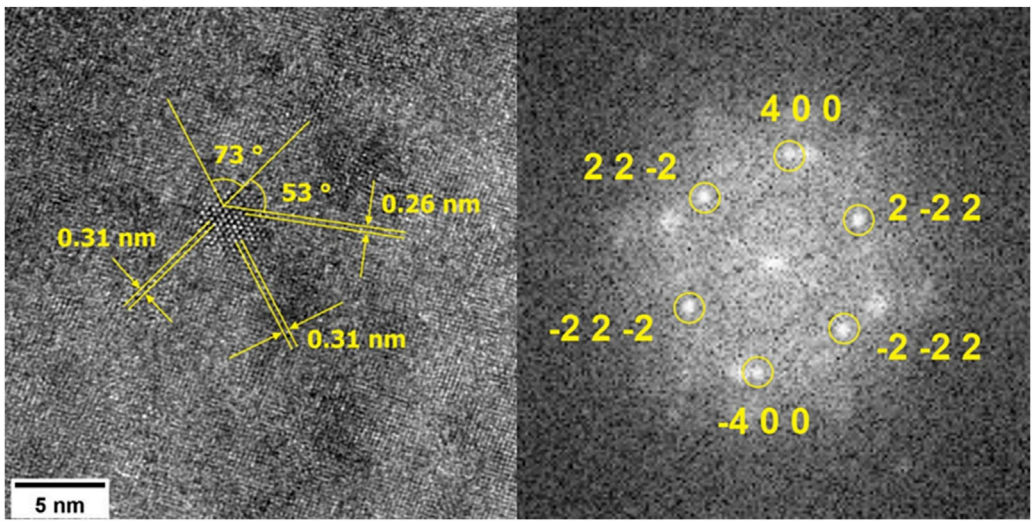

FIGURE 4
TEM image of an oxide nano-precipitate with a diameter of 3.5 nm together with its fast Fourier transform (FFT) image, showing a structure of Y_2O_3 (PDF#01-075-3096).

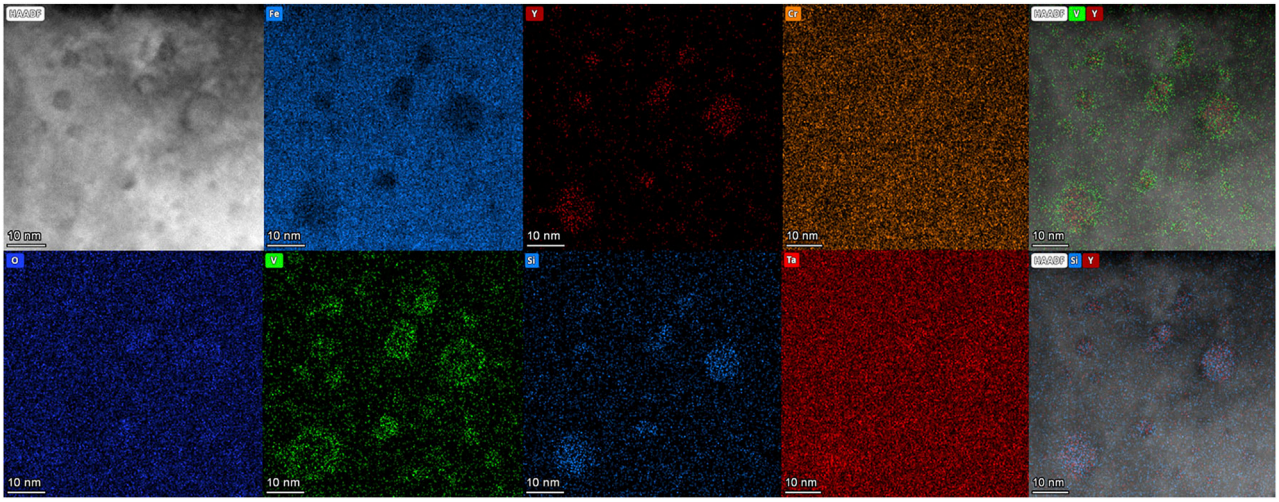

FIGURE 5
HADDF image and EDS elemental mappings showing the chemical compositions of oxide nano-precipitates and shell-core structures.

enthalpy of Y_2O_3 consuming per mole O at 298 K is 635 kJ, the largest, followed by SiO_2 of 455 kJ, the second, and Ta_2O_5 of 409 kJ (Rumble, 2021). Oxygen prefers to form oxides with Y first during the fabrication process since it is the most stable oxide from thermodynamic perspectives. It is reasonable for Si to enter the oxide precipitates of Y and O as its formation enthalpy is the second highest. Considering the small amount of Si totally contained in the steel (only 0.0124 wt%), even though it has a different structure of binary oxide, Si in precipitates did not influence the structure of Y_2O_3 of nano-precipitates.

The presence of shell structure around the oxide nano-precipitates has been reported in several works of ODS EUROFER steels. ODS EUROFER steel has similar chemical compositions of minor elements with that of the MX-ODS steel used in this study and Y_2O_3 oxide nano-precipitates are observed in ODS EUROFER steel although the presence of large carbide is also present due to higher carbon content. A Cr and V-rich shell surrounding the oxide nano-precipitates of Y-O core or Ti-O particles was reported (Williams et al., 2010; Oksiuta et al., 2013; Fu et al., 2021). Klimenkov et al. (2009) suggested that a V-Cr-O shell of 0.5–1.5 nm thickness formed around oxide nano-precipitates. Besides, in the study of a model ODS alloy containing Fe-12Cr-0.4 Y_2O_3 wt%, a Cr-rich shell of 3 nm was found in some of the oxides, which were still present after annealing for 96 h (de Castro et al., 2011b).

The formation of the shell structure of V and Cr around nano-oxides can be explained by the following two reasons.

1) The originally formed oxides contained Cr and V and other minor elements besides Y, and in the following process at high temperature, V and Cr atoms were expelled from oxides due to their weaker bond with O atoms compared with the bonds with Y, Si, and Ta (Williams et al., 2010). With smaller formation enthalpy of V and Cr, they were adjacent to O in the oxide core as a shell structure. The distribution of elements inside oxide nano-precipitates and the shell structure around is the result of reaching lower energy locally. In the study by Aleev et al. (2011), instead of a V-shell around, V was found inside the oxide in ODS EUROFER characterized by ATP, and the concentration of V equaled or exceeded that of Y in some particles. This suggests that V atoms were concentrated in the oxides at one time, and might participate in the formation of oxides. Therefore the later expelling of V out of oxides could be possible.
2) The oxides originally formed with Y, and a small amount of Si, Ta, with V and Cr diffusing and segregating around oxides in the following process. Cr and V atoms have a relatively high diffusivity in bcc-Fe. The trace diffusion coefficients of V and Cr at 1150 K are in the order of 10^{-11} and 10^{-15} cm^2/s, respectively, both higher than that of Fe, which is in the order of 10^{-15} cm^2/s, but smaller than Cr (Choudhury et al., 2011; Obrtlik and Kuöeka, 2022). Segregation of Cr along grain boundaries was observed in some prior works (Zhou et al., 2016). The interface of oxides nano-precipitates and the steel matrix provides sites for segregation. The diffusion of these elements at high temperatures during fabrication resulted in their segregation around oxides.

3.1.2 Large precipitates

Common carbides formed in steel such as MC, $M_{23}C_6$ (M = Fe, Cr, Mn) can be unstable during long-term high-temperature conditions and irradiation environments. The coarsening or dissolution of carbides results in the degradation of

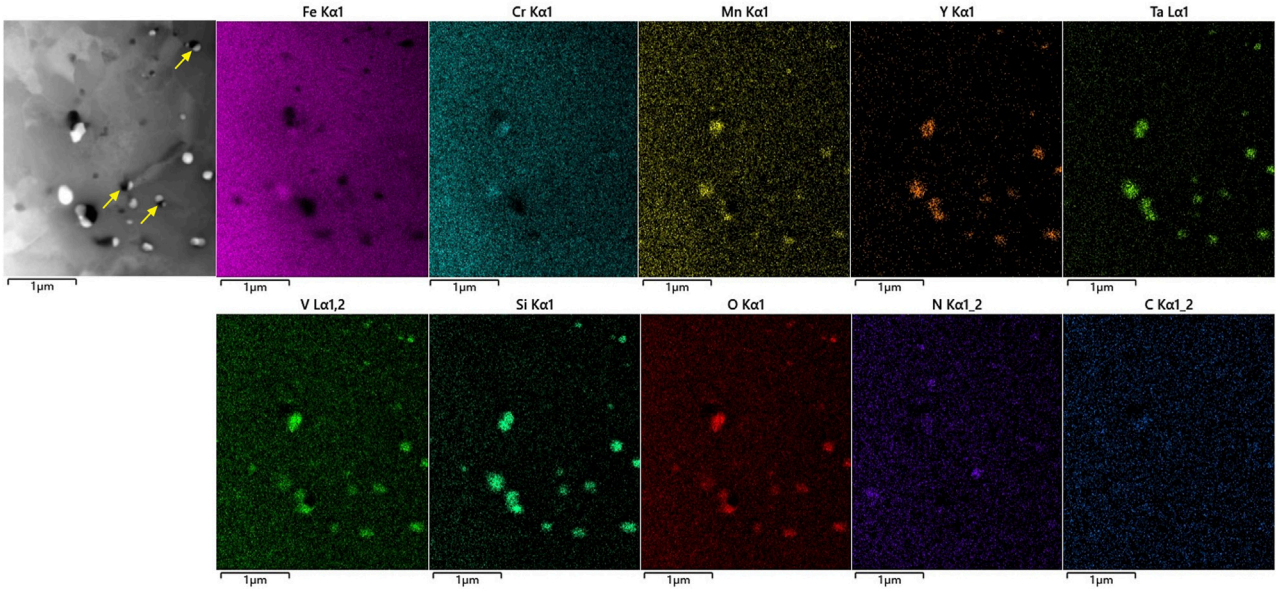

FIGURE 6
STEM image and elemental mappings of two types of large precipitates.

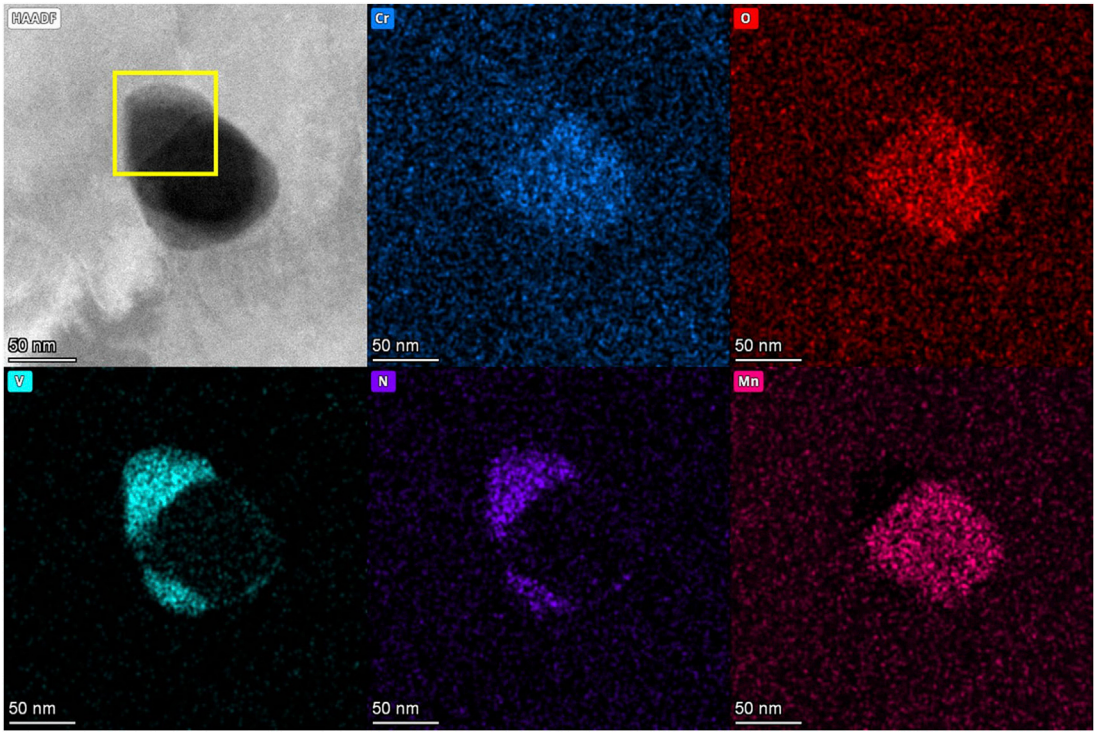

FIGURE 7
HADDF image and EDS elemental mappings of VN near an Y-Ta-Si type oxide. The area of TEM image in Figure 8 is illustrated with a yellow box.

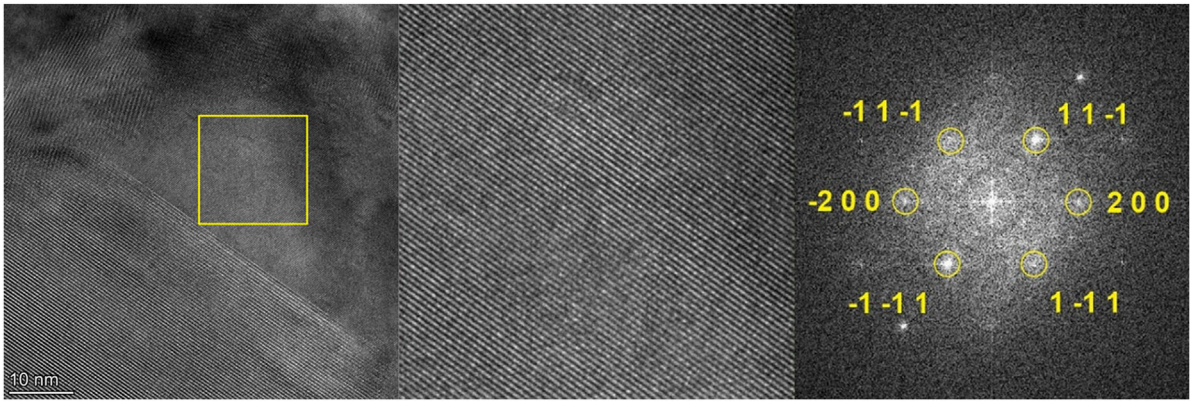

FIGURE 8
TEM bright field image of VN in high magnification, together with its FFT image showing a structure of VN (PDF#00-035-0768).

mechanical properties, threatening the safety of nuclear reactors (Grybėnas et al., 2017; Kano et al., 2018b). MX-ODS steel in this study was designed with extremely low carbon content to avoid the formation of carbides. Carbides were not found in the TEM examination of large areas in the electropolished specimens.

Two kinds of second phase precipitates of a rather large size (more than 40 nm in diameter) were found both on grain boundaries and inside the grains. The two types of large precipitates can be distinguished by their chemical composition and size.

The first type of large precipitates is the oxides of various metallic elements characterized as bright structures in the STEM images shown in Figure 6. The size of these oxides varies from 100nm to 250 nm and most of them contain Y, Ta, Si, thus named Y-Ta-Si oxide in this article. These oxides possess complex structures and some of them contain other elements such as Mn, Cr and V.

The second type of large precipitates is the VN particles characterized as dark structures in Figure 6. The size of VN particles is from 40 to 200 nm and the average size is smaller than 100 nm. It is noticed that some of the two kinds of large precipitates are present adjacent to each other, as indicated with arrows in Figures 6, 7 also shows a Y-Ta-Si-type oxide adjacent with VN, where the area of TEM image in Figure 8 is illustrated with a yellow box. The structure of VN is shown in Figure 8, with FFT of the TEM image in high magnification, in accord with VN (PDF#00-035-0768) in the direction of (0 2 2).

3.1.3 Voids in as-received samples

Voids of very small size (less than 1 nm) and high number density (about $10^{22}/m^3$) were observed in the as-received specimen prepared by electropolishing, in the FIB specimen of unirradiated area, as well as in the area far from irradiation depth in the irradiated FIB specimen, using over focus and under focus in bright field TEM. Thus the presence of voids was not due to FIB preparation or high temperature during irradiation. Figures 9A, B show the voids in the as-received sample. The distribution of small voids was rather uniform and a preferred attachment of small voids to nano-precipitates was not observed.

These pre-existing voids before irradiation were most probably produced during the hot forging and hot rolling process in the fabrication stage. Several works reported the presence of voids in ODS steel fabricated by the HIP process. It was reported that small voids of 2 nm in ODS-Fe12Cr or 5 nm in ODS-Fe14Cr alloys and voids were frequently found near oxide nano-precipitates, carbides, or Cr-rich precipitates (de Castro et al., 2009; de Castro et al., 2011a). Positron annihilation results of EUROFER steels with and without oxide dispersive strengthened particles suggested that Ar atoms were absorbed during the mechanical alloying process and vacancy clusters were captured by the interface between nano-precipitates and steel matrix, and hence, cavities nucleated grow next to precipitates (Ortega et al., 2008). The fabrication process of MX-ODS steel in this study included mechanical alloying in Ar atmosphere and hot forging as well as hot rolling instead of HIP. During the hot forging and hot rolling processes, materials were densified through rapid plastic deformation under high stress and the voids were not fully eliminated, thus small voids exist.

3.2 Microstructure of samples after irradiation

3.2.1 Precipitates

Oxide nano-precipitates were observed to be stable after high-temperature irradiation. Uniform distribution of fine and dense oxides was observed using HADDF as shown in Figure 10. The image was captured at the depth of 400 nm below surface, corresponding to a damage of about 35 dpa as calculated by

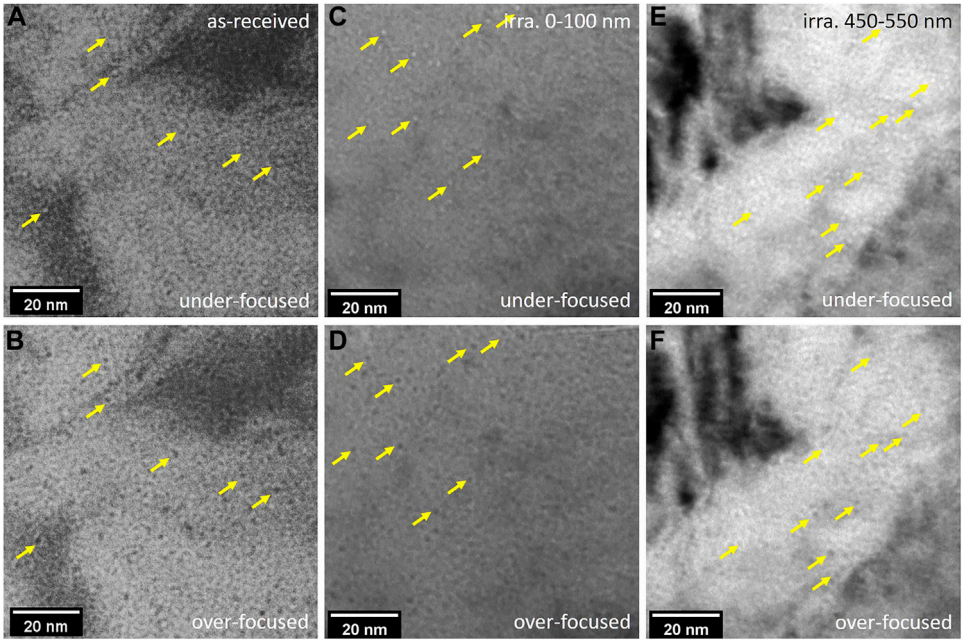

FIGURE 9
Voids in under-focused and over-focused TEM bright field. Some of the voids are illustrated with arrows. **(A,B)** Voids in the as-received sample. **(C,D)** Voids at the near surface area (0–100 nm in depth) of irradiated sample. **(E,F)** Voids in the irradiated sample in depth of 450–550 nm.

SRIM. The oxides in the images presented an average size of about 3 nm in diameter and their chemical compositions are shown in EDS images. The nano-precipitates contained mainly Y and O, with Si not clearly seen inside these oxides. A shell rich in V is present clearly in the overlapped element maps of V and Y. Distribution of Cr shows a slight gathering around the oxide particles. It can be concluded that a shell-core structure remained and the composition of oxides did not change after irradiation, although a careful and detailed comparison of the shell-core structures before and after irradiation can be hard using EDS. The changes of oxide nano-precipitates after irradiation, such as coarsening or dissolution of oxides, have been widely studied, and in most cases, Y-O oxides remained stable after irradiation (Wharry et al., 2017). In this study, the oxide nano-precipitates in MX-ODS steel remained stable after self-ion irradiation, showing a good tolerance to irradiation.

Large precipitates became unstable after irradiation, showing an irregular shape instead of a perfect sphere. Due to the limited irradiated area in the FIB specimen and a relatively low number density of large precipitates, only three precipitates after irradiation were observed and characterized, as shown in Figure 11A. The three precipitates are at about 200, 300, and 900 nm in depth, respectively, corresponding to damage levels of 28, 33, and 70 dpa. The bright field images in Figures 11B, C and HADDF image in Figure 11D show the irregular shape of the precipitates, with several bulges attaching together and comprising the precipitates. The three large precipitates have crystal structures and contain various mantellic elements and O, N atoms. Figure 11E shows the elementary mapping of the precipitate in Figure 11D and it contains Cr, Mn, V, N, and O. Pure VN was not found in the irradiation affected area. These three large precipitates could be developed from Y-Ta-Si-type oxides and VN since they appeared adjacently as mentioned before. During irradiation, both excess point defects and displacement cascade account for the instability of precipitates. Binding between point defect and solute atom could lead to the dissolution of atoms in precipitates where point defect gradient occurs (Abe et al., 2014; Kano et al., 2018b), while a number of atoms may be ejected when a displacement cascade locates at least partly within a precipitate (Russell, 1993). Shape change of precipitates was most probably caused by dissolution and subsequent precipitation. Atoms were knocked off the precipitates and dissolved into the matrix in displacement cascades, then formed smaller precipitates clinging to the original one.

3.2.2 Nano-voids and swelling

A much higher number density of voids appeared after irradiation in the irradiation influenced regions. As shown in Figure 9, voids are presented in bright and dark spots in under-focused and over-focused TEM bright field images. Images in Figures 9C, D were captured in the near-surface area, in the depth

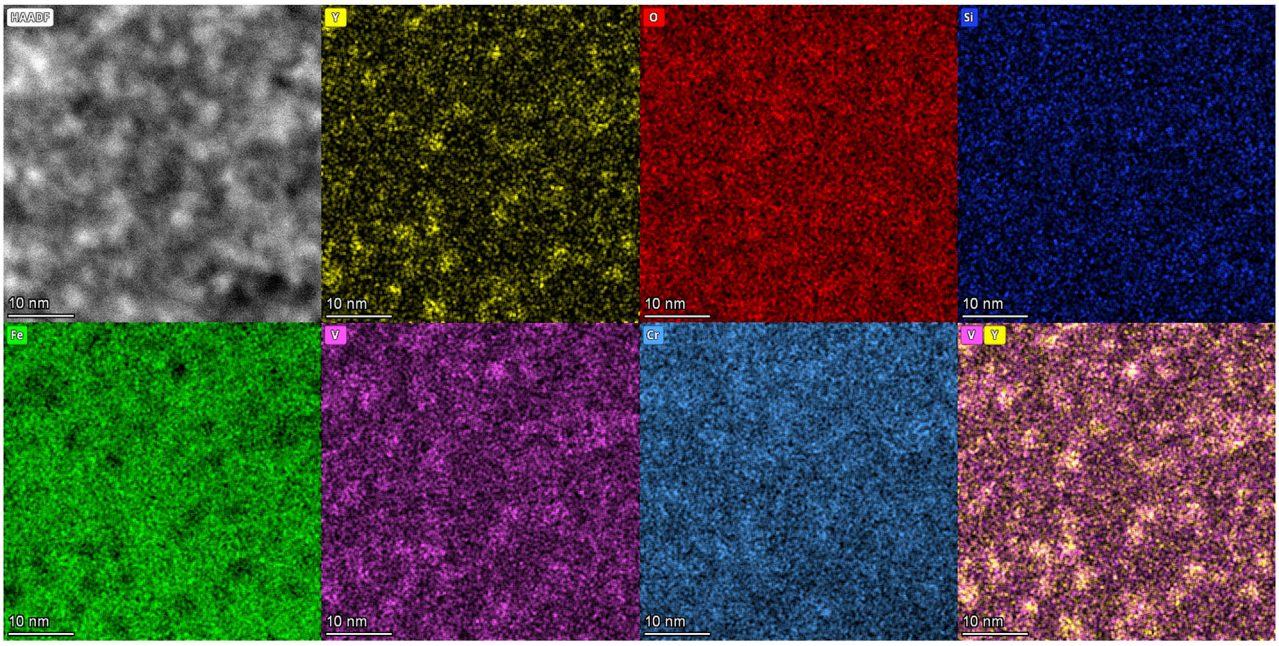

FIGURE 10
HADDF image and EDS elemental mappings of oxide nano-precipitates after irradiation, captured in the depth of 400 nm, corresponding to a damage of about 35 dpa.

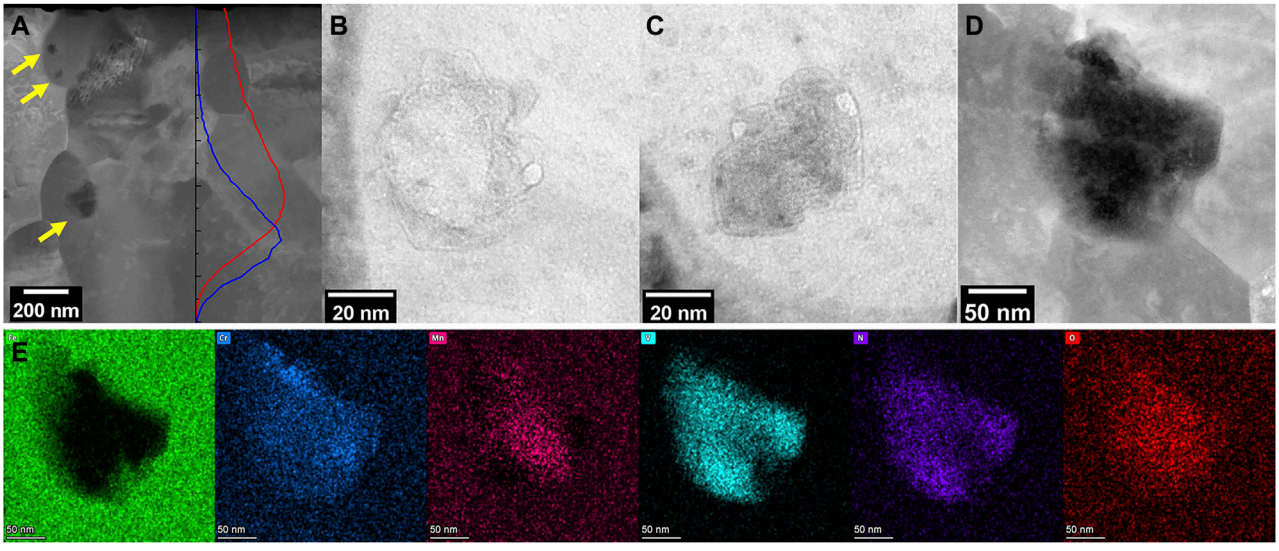

FIGURE 11
(A) HADDF image showing three precipitates in the irradiated area. Large precipitates are indicated with arrows and the dpa and implanted Fe ions distribution along depth are shown as lines in red and blue. **(B,C)** Bright field images of the upper precipitates. **(D)** HADDF image of the precipitates at the depth of damage peak. **(E)** EDS elemental mapping of the large precipitate in **(D)**.

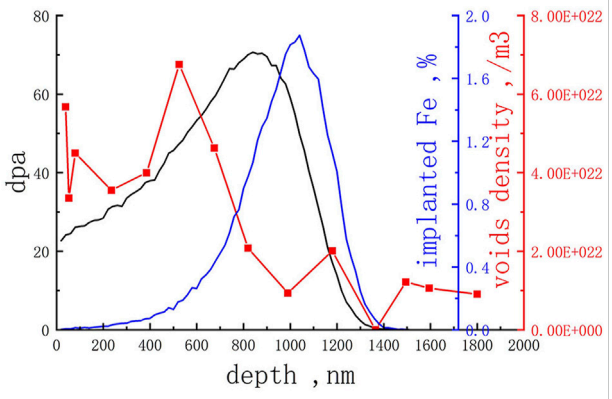

FIGURE 12
Distribution of voids density along depth with the irradiation damage and implanted ions distribution calculated by SRIM.

of 0–100 nm. Some of the voids are indicated with arrows in order to be clearly identifiable.

The size of voids remained small and statistics of their sizes can be fairly inaccurate, thus only numbers of voids in different depths were counted. A series of under-focused and over-focused TEM bright field images were captured along depth to calculate voids number density in different depths. A number density of $10^{22}/m^3$ was calculated in the FIB specimen prepared in the unirradiated area. This statistics was set as a background to be subtracted when estimating voids distribution produced by irradiation.

The distribution of voids number density along depth, along with the irradiation damage and implanted ions distribution calculated by SRIM is shown in Figure 12. Voids of the largest number density, a number density of four times that of the unirradiated area, were observed at the depth of approximately 500 nm, shallower than the damage peak at 800 nm depth. Another area with a high number density of voids appeared at the surface of the sample, at a depth of about 50 nm.

Void swelling due to irradiation was estimated using the number density of voids at 400–700 nm depth and an average size of 1 nm in diameter. Voids in the depth of 450–550 nm were shown in Figures 9E,F. Voids in this area was chosen to calculate void swelling in order to reduce implanted ion effects near peak damage area as well as to avoid the surface effect of the sample surface. The following formula (Velikodnyi et al., 2022) was used to calculate void swelling:

$$S = \frac{\pi/(6Ah)\sum_{i=1}^{N} d_i^3}{1 - \pi/(6Ah)\sum_{i=1}^{N} d_i^3} \cdot 100\%$$

Where A and h stand for the area and the thickness of the images examined, d_i and N_i stand for the diameter of i-void and number of voids counted. The void swelling due to irradiation was only 0.004%, indicating a reasonably good resistance to void swelling during irradiation. Besides, the pre-existing voids seem not to grow to a larger size during irradiation.

Ferritic martensitic ODS steels present very small void swelling compared to steels without ODS structure (Shao et al., 2015). No voids were found or only 0.5% swelling occurred at peak damage under 50 dpa (Tanaka et al., 2004; Song et al., 2018). 0.05% and 1.5% swelling were found after self-ion irradiation up to 800 dpa at 475°C in tempered martensite and ferrite phases respectively (Chen et al., 2015). The void swelling calculated in this study is reasonable compared to previous observations by other researchers. The oxide nano-precipitates with high number density, small size, and uniform distribution contribute to the good void swelling resistance of ODS steels. A large number of vacancies and interstitials are produced during irradiation, resulting in a much higher concentration of point defects in the steel matrix. Some of the defects are captured by sinks such as dislocations, grain boundaries, and free surfaces, becoming immobilized or annihilated there (WAS, 2017). The diffusivity of interstitials is higher than that of vacancies, leading to the supersaturation of vacancies and hence the formation of voids. High-density nano-oxides act as trapping sites for defects and delay the supersaturation of vacancies, thus suppressing void swelling. The sink strength contributed by line dislocations, grain boundaries and oxide nano-precipitates were calculated and oxides contributed the most in ODS steels (Song et al., 2018). The ability of nano-precipitates to reduce freely migrating defects is even better than that of dislocations and grain boundaries according to a rate theory calculation (Liu et al., 2018).

The peak void number density appearing ahead of peak damage calculated by SRIM is due to the following two reasons. First, implanted Fe ions as extra interstitial atoms entered the matrix, reducing vacancy concentration by enhancing recombination between vacancies and interstitials and suppressing void density. Second, the irradiation was conducted at a relatively high temperature of 550°C, and the thermal diffusion was enhanced and depth-dependent radiation enhanced diffusion should be taken into consideration as well. The affected area of implanted Fe ions may expand to a wider range as suggested by Doyle et al. (2018). Thus, the peak void swelling area was observed prior to the peak swelling depth.

A high number density of voids appeared in the near-surface area because of a biased loss of interstitials to the surface. Planar sinks such as grain boundaries or free surfaces can cause local defect-depleted zones in irradiation since they capture free point defects (Zinkle and Snead, 2018). Both interstitial-type and vacancy-type defect clusters were found to deplete near surfaces (Gigax et al., 2016; Short et al., 2016). Interstitials diffuse faster than vacancies, resulting in a severe depletion of interstitials. Therefore, the void swelling was enhanced in the near-surface area.

4 Conclusion

A self-ion irradiation experiment was conducted on the MX-ODS steel and samples before and after irradiation were characterized using TEM. The following conclusions were obtained.

The MX-ODS steel in this study contains uniformly distributed oxide nano-precipitates of small size and high number density. The average diameter and number density of the nano-precipitates are 3.5 nm and 5×10^{22} /m^3 respectively. The structure of fine oxides is Y_2O_3. Some nano-precipitates contain Si and present a V-rich shell surrounding Y and O. With an extremely low carbon continent, no carbides such as M23C6 or MC were found in the steel. Two types of large precipitates, Y-Ta-Si oxides, and VN, are present in grains and on grain boundaries, with a size of 100–250 nm and 40–200 nm respectively.

Heavy ion irradiation of 3 MeV Fe was conducted at 550°C to a peak damage of 70 dpa. After irradiation, fine and dense oxide nano-precipitates and their shell-core structure remained stable while large precipitates became instable, changing from globe to irregular shape with humps. Voids smaller than 1 nm appeared due to irradiation and the corresponding void swelling was only 0.004%, indicating a reasonably good swelling resistance of the MX-ODS steel in this study. The largest number density of voids occurred at the near-surface area and the depth ahead of peak damage calculated by SRIM, and this can be explained by the effects of implanted ions and the effects of surface.

Data availability statement

The raw data supporting the conclusions of this article will be made available by the authors, without undue reservation.

Author contributions

YX and DY contributed to conception and design of the study. YX, DY, and XY analysed and discussed the results. YX wroted the first draft of the manuscript. DY reviewed and edited the manuscript. WY, YL, PZ, and CL provided and prepared the sample. CL and JL contributed to TEM characterization. TZ, JL, JZ, and LK conducted the irradiation experiment.

Funding

This work was supported by the State Key Research and Development Program of China, Grant No. 2020YFB1902100.

Conflict of interest

The authors declare that the research was conducted in the absence of any commercial or financial relationships that could be construed as a potential conflict of interest.

Publisher's note

All claims expressed in this article are solely those of the authors and do not necessarily represent those of their affiliated organizations, or those of the publisher, the editors and the reviewers. Any product that may be evaluated in this article, or claim that may be made by its manufacturer, is not guaranteed or endorsed by the publisher.

References

Abe, H., Ishizaki, T., Kano, S., Li, F., Satoh, Y., Tanigawa, H., et al. (2014). Mechanism of instability of carbides in Fe–TaC alloy under high energy electron irradiation at 673K. *J. Nucl. Mater.* 455 (1), 695–699. doi:10.1016/j.jnucmat.2014.08.032

Aleev, A. A., Iskandarov, N. A., Klimenkov, M., Lindau, R., Möslang, A., Nikitin, A. A., et al. (2011). Investigation of oxide particles in unirradiated ODS Eurofer by tomographic atom probe. *J. Nucl. Mater.* 409 (2), 65–71. doi:10.1016/j.jnucmat.2010.09.008

Biersack, J. F. Z. J. P., SRIM Program, 2013 [Online]. Available: http://www.srim.org/[Accessed]

Chen, T., Aydogan, E., Gigax, J. G., Chen, D., Wang, J., Wang, X., et al. (2015). Microstructural changes and void swelling of a 12Cr ODS ferritic-martensitic alloy after high-dpa self-ion irradiation. *J. Nucl. Mater.* 467, 42–49. doi:10.1016/j.jnucmat.2015.09.016

Choudhury, S., Barnard, L., Tucker, J. D., Allen, T. R., Wirth, B. D., Asta, M., et al. (2011). *Ab-initio* based modeling of diffusion in dilute bcc Fe–Ni and Fe–Cr alloys and implications for radiation induced segregation. *J. Nucl. Mater.* 411 (1), 1–14. doi:10.1016/j.jnucmat.2010.12.231

de Castro, V., Leguey, T., Auger, M. A., Lozano-Perez, S., and Jenkins, M. L. (2011a). Analytical characterization of secondary phases and void distributions in an ultrafine-grained ODS Fe–14Cr model alloy. *J. Nucl. Mater.* 417 (1), 217–220. doi:10.1016/j.jnucmat.2010.12.067

de Castro, V., Leguey, T., Muñoz, A., Monge, M. A., Pareja, R., Marquis, E. A., et al. (2009). Microstructural characterization of Y2O3 ODS–Fe–Cr model alloys. *J. Nucl. Mater.* 386-388, 449–452. doi:10.1016/j.jnucmat.2008.12.136

de Castro, V., Marquis, E. A., Lozano-Perez, S., Pareja, R., and Jenkins, M. L. (2011b). Stability of nanoscale secondary phases in an oxide dispersion strengthened Fe–12Cr alloy. *Acta Mater.* 59 (10), 3927–3936. doi:10.1016/j.actamat.2011.03.017

Doyle, P. J., Benensky, K. M., and Zinkle, S. J. (2018). Modeling the impact of radiation-enhanced diffusion on implanted ion profiles. *J. Nucl. Mater.* 509, 168–180. doi:10.1016/j.jnucmat.2018.06.042

Fu, J., Davis, T. P., Kumar, A., Richardson, I. M., and Hermans, M. J. M. (2021). Characterisation of the influence of vanadium and tantalum on yttrium-based nano-oxides in ODS Eurofer steel. *Mater. Charact.* 175, 111072. doi:10.1016/j.matchar.2021.111072

Gigax, J. G., Chen, T., Kim, H., Wang, J., Price, L. M., Aydogan, E., et al. (2016). Radiation response of alloy T91 at damage levels up to 1000 peak dpa. *J. Nucl. Mater.* 482, 257–265. doi:10.1016/j.jnucmat.2016.10.003

Greenwood, L. R. S., and Smither, R. K. (1985). Specter: Neutron damage calculations for materials irradiations. RN:16073192. doi:10.2172/6022143

Grybėnas, A., Makarevičius, V., Baltušnikas, A., Lukošiūtė, I., and Kriūkienė, R. (2017). Correlation between structural changes of M23C6 carbide and mechanical behaviour of P91 steel after thermal aging. *Mater. Sci. Eng. A* 696, 453–460. doi:10.1016/j.msea.2017.04.103

Hirata, A., Fujita, T., Liu, C. T., and Chen, M. W. (2012). Characterization of oxide nanoprecipitates in an oxide dispersion strengthened 14YWT steel using

aberration-corrected STEM. *Acta Mater.* 60 (16), 5686–5696. doi:10.1016/j.actamat.2012.06.042

Kano, S., Yang, H., Shen, J., Zhao, Z., McGrady, J., Hamaguchi, D., et al. (2018a). Instability of MX and M23C6 type precipitates in F82H steels under 2.8 MeV Fe2+ irradiation at 673 K. *Nucl. Mater. Energy* 17, 56–61. doi:10.1016/j.nme.2018.08.001

Kano, S., Yang, H., Shen, J., Zhao, Z., McGrady, J., Hamaguchi, D., et al. (2018b). Investigation of instability of M23C6 particles in F82H steel under electron and ion irradiation conditions. *J. Nucl. Mater.* 502, 263–269. doi:10.1016/j.jnucmat.2018.02.004

Kimura, A., Kasada, R., Iwata, N., Kishimoto, H., Zhang, C. H., Isselin, J., et al. (2011). Development of Al added high-Cr ODS steels for fuel cladding of next generation nuclear systems. *J. Nucl. Mater.* 417 (1), 176–179. doi:10.1016/j.jnucmat.2010.12.300

Klimenkov, M., Lindau, R., and Möslang, A. (2009). New insights into the structure of ODS particles in the ODS-Eurofer alloy. *J. Nucl. Mater.* 386-388, 553–556. doi:10.1016/j.jnucmat.2008.12.174

Klimiankou, M., Lindau, R., Möslang, A., and Schröder, J. (2005). TEM study of PM 2000 steel. *Powder Metall.* 48 (3), 277–287. doi:10.1179/174329005X64171

Lin, Y.-R., Chen, W.-Y., Tan, L., Hoelzer, D. T., Yan, Z., Hsieh, C.-Y., et al. (2021). Bubble formation in helium-implanted nanostructured ferritic alloys at elevated temperatures. *Acta Mater.* 217, 117165. doi:10.1016/j.actamat.2021.117165

Liu, X., Miao, Y., Li, M., Kirk, M. A., Zhang, G., Ukai, S., et al. (2018). Radiation resistance of oxide dispersion strengthened alloys: Perspectives from *in situ* observations and rate theory calculations. *Scr. Mater.* 148, 33–36. doi:10.1016/j.scriptamat.2018.01.018

Liu, X., Miao, Y., Wu, Y., Maloy, S. A., and Stubbins, J. F. (2017). Stability of nanoclusters in an oxide dispersion strengthened alloy under neutron irradiation. *Scr. Mater.* 138, 57–61. doi:10.1016/j.scriptamat.2017.05.023

Obrtlik, K., and Kuöeka, J. (2022). "Diffusion of vanadium in the Fe-V system, *Phys. status solidi(a)*Volume 53, Number 2 June 16, " ed. Görlich. De Gruyter), 589–597. doi:10.1002/pssa.2210530223

Odette, G. R. (2018). On the status and prospects for nanostructured ferritic alloys for nuclear fission and fusion application with emphasis on the underlying science. *Scr. Mater.* 143, 142–148. doi:10.1016/j.scriptamat.2017.06.021

Oksiuta, Z., Lewandowska, M., Kurzydlowski, K. J., and Baluc, N. (2013). Effect of vanadium addition on the microstructure and mechanical properties of the ODS ferritic steels. *J. Nucl. Mater.* 442 (1Suppl. 1), S84–S88. doi:10.1016/j.jnucmat.2012.10.022

Ortega, Y., de Castro, V., Monge, M. A., Muñoz, A., Leguey, T., and Pareja, R. (2008). Positron annihilation characteristics of ODS and non-ODS EUROFER isochronally annealed. *J. Nucl. Mater.* 376 (2), 222–228. doi:10.1016/j.jnucmat.2008.03.005

Rahmanifard, R., Farhangi, H., and Novinrooz, A. J. (2015). Effect of zirconium and tantalum on the microstructural characteristics of 12YWT ODS steel nanocomposite. *J. Alloys Compd.* 622, 948–952. doi:10.1016/j.jallcom.2014.11.018

Rui, X., Li, Y., Zhang, J., Wang, Q., Yan, W., and Shan, Y. (2022). Microstructure and mechanical properties of a novel designed 9Cr-ODS steel synergically strengthened by nano precipitates. *Acta Metall. Sin.* 0-0. doi:10.11900/0412.1961.2021.00534

Rumble, J. R. (2021). *CRC handbook of chemistry and Physics*. Boca Raton, FL: CRC Press/Taylor & Francis.

Russell, K. C. (1993). Phase instability under cascade damage irradiation. *J. Nucl. Mater.* 206 (2), 129–138. doi:10.1016/0022-3115(93)90120-N

Shao, L., Toloczko, M., Maloy, S., and Voyevodin, V. N. (2015). "Use of self-ion bombardment to study void swelling in advanced radiation-resistant alloys", in: Proceedings of the International Conference on Environmental Degradation of Materials in Nuclear Power Systems - Water Reactors. (Ottawa, Canada), August 2015

Short, M. P., Gaston, D. R., Jin, M., Shao, L., and Garner, F. A. (2016). Modeling injected interstitial effects on void swelling in self-ion irradiation experiments. *J. Nucl. Mater.* 471, 200–207. doi:10.1016/j.jnucmat.2015.10.002

Song, L., Yang, X., Zhao, Y., Wang, W., and Mao, X. (2019). Si-containing 9Cr ODS steel designed for high temperature application in lead-cooled fast reactor. *J. Nucl. Mater.* 519, 22–29. doi:10.1016/j.jnucmat.2019.03.029

Song, P., Morrall, D., Zhang, Z., Yabuuchi, K., and Kimura, A. (2018). Radiation response of ODS ferritic steels with different oxide particles under ion-irradiation at 550 °C. *J. Nucl. Mater.* 502, 76–85. doi:10.1016/j.jnucmat.2018.02.007

Stoller, R. E., Toloczko, M. B., Was, G. S., Certain, A. G., Dwaraknath, S., and Garner, F. A. (2013). On the use of SRIM for computing radiation damage exposure. *Nucl. Instrum. Methods Phys. Res. Sect. B Beam Interact. Mater. Atoms* 310, 75–80. doi:10.1016/j.nimb.2013.05.008

Tan, L., Byun, T. S., Katoh, Y., and Snead, L. L. (2014). Stability of MX-type strengthening nanoprecipitates in ferritic steels under thermal aging, stress and ion irradiation. *Acta Mater.* 71, 11–19. doi:10.1016/j.actamat.2014.03.015

Tan, L., Snead, L. L., and Katoh, Y. (2016). Development of new generation reduced activation ferritic-martensitic steels for advanced fusion reactors. *J. Nucl. Mater.* 478, 42–49. doi:10.1016/j.jnucmat.2016.05.037

Tan, L., Zhong, W., and Chen, T. (2020). Microstructural stability of tantalum-alloyed ferritic-martensitic steel with neutron irradiation to 7.4 dpa at ~490 °C. *Materialia* 9, 100608. doi:10.1016/j.mtla.2020.100608

Tanaka, T., Oka, K., Ohnuki, S., Yamashita, S., Suda, T., Watanabe, S., et al. (2004). Synergistic effect of helium and hydrogen for defect evolution under multi-ion irradiation of Fe–Cr ferritic alloys. *J. Nucl. Mater.* 329-333, 294–298. doi:10.1016/j.jnucmat.2004.04.051

Tanigawa, H., Sakasegawa, H., Ogiwara, H., Kishimoto, H., and Kohyama, A. (2007). Radiation induced phase instability of precipitates in reduced-activation ferritic/martensitic steels. *J. Nucl. Mater.* 367-370, 132–136. doi:10.1016/j.jnucmat.2007.03.155

Toloczko, M. B., Garner, F. A., Voyevodin, V. N., Bryk, V. V., Borodin, O. V., Mel'nychenko, V. V., et al. (2014). Ion-induced swelling of ODS ferritic alloy MA957 tubing to 500dpa. *J. Nucl. Mater.* 453 (1), 323–333. doi:10.1016/j.jnucmat.2014.06.011

Uchidi, Y., Ohnuki, S., Hashimoto, N., Suda, T., Nagai, T., Shibayama, T., et al. (2011). Effect of minor alloying element on dispersing nano-particles in ODS steel. *MRS Online Proc. Libr.* 981 (1), 709. doi:10.1557/PROC-981-0981-JJ07-09

Ukai, S., Ohtsuka, S., Kaito, T., de Carlan, Y., Ribis, J., and Malaplate, J. (2017). "Oxide dispersion-strengthened/ferrite-martensite steels as core materials for Generation IV nuclear reactors," in *Structural materials for generation IV nuclear reactors*. Editor P. Yvon (Sawston, Cambridge: Woodhead Publishing), 357–414.

Velikodnyi, A. N., Voyevodin, V. N., Kalchenko, A. S., Karpov, S. A., Kolodiy, I. V., Tikhonovsky, M. A., et al. (2022). Impact of nano-oxides and injected gas on swelling and hardening of 18Cr10NiTi stainless steel during ion irradiation. *J. Nucl. Mater.* 565, 153666. doi:10.1016/j.jnucmat.2022.153666

Was, G. S. (2017). *Fundamentals of radiation materials science*. New York, NY: Springer.

Wharry, J. P., Swenson, M. J., and Yano, K. H. (2017). A review of the irradiation evolution of dispersed oxide nanoparticles in the b.c.c. Fe-Cr system: Current understanding and future directions. *J. Nucl. Mater.* 486, 11–20. doi:10.1016/j.jnucmat.2017.01.009

Williams, C. A., Marquis, E. A., Cerezo, A., and Smith, G. D. W. (2010). Nanoscale characterisation of ODS–Eurofer 97 steel: An atom-probe tomography study. *J. Nucl. Mater.* 400 (1), 37–45. doi:10.1016/j.jnucmat.2010.02.007

Wu, Y., Haney, E. M., Cunningham, N. J., and Odette, G. R. (2012). Transmission electron microscopy characterization of the nanofeatures in nanostructured ferritic alloy MA957. *Acta Mater.* 60 (8), 3456–3468. doi:10.1016/j.actamat.2012.03.012

Zheng, P., Li, Y., Zhang, J., Shen, J., Nagasaka, T., Muroga, T., et al. (2020). On the thermal stability of a 9Cr-ODS steel aged at 700 °C up to 10000 h - Mechanical properties and microstructure. *Mater. Sci. Eng. A* 783, 139292. doi:10.1016/j.msea.2020.139292

Zhou, X., Yu, X.-x., Kaub, T., Martens, R. L., and Thompson, G. B. (2016). Grain boundary specific segregation in nanocrystalline Fe(Cr). *Sci. Rep.* 6 (1), 34642. doi:10.1038/srep34642

Zinkle, S. J., Boutard, J. L., Hoelzer, D. T., Kimura, A., Lindau, R., Odette, G. R., et al. (2017). Development of next generation tempered and ODS reduced activation ferritic/martensitic steels for fusion energy applications. *Nucl. Fusion* 57 (9), 092005. doi:10.1088/1741-4326/57/9/092005

Zinkle, S. J., and Snead, L. L. (2018). Opportunities and limitations for ion beams in radiation effects studies: Bridging critical gaps between charged particle and neutron irradiations. *Scr. Mater.* 143, 154–160. doi:10.1016/j.scriptamat.2017.06.041

frontiers | Frontiers in Energy Research

TYPE Original Research
PUBLISHED 08 February 2023
DOI 10.3389/fenrg.2023.1041986

OPEN ACCESS

EDITED BY
Songbai Cheng,
Sun Yat-sen University, China

REVIEWED BY
Zidi Wang,
Japan Atomic Energy Agency, Japan
Xiaoxing Liu,
Sun Yat-sen University, China

*CORRESPONDENCE
Zhi-Gang Zhang,
zg_zhang@hrbeu.edu.cn

SPECIALTY SECTION
This article was submitted to Nuclear Energy,
a section of the journal
Frontiers in Energy Research

RECEIVED 12 September 2022
ACCEPTED 02 January 2023
PUBLISHED 08 February 2023

CITATION
Wang F, Zhang Z-G and Wu Q (2023), An improved multiphase SPH algorithm with kernel gradient correction for modelling fuel–coolant interaction.
Front. Energy Res. 11:1041986.
doi: 10.3389/fenrg.2023.1041986

An improved multiphase SPH algorithm with kernel gradient correction for modelling fuel–coolant interaction

Fang Wang, Zhi-Gang Zhang* and Qi Wu

Fundamental Science on Nuclear Safety and Simulation Technology Laboratory, Harbin Engineering University, Harbin, China

Fuel–coolant interaction (FCI) has a pivotal role in the development of core disruptive accident in a sodium-cooled fast reactor. The drastic deformation of multiphase interface in the FCI is hard to deal with in the traditional grid method. In this paper, an improved multiphase smoothed particle hydrodynamics (SPH) algorithm corrected with the kernel gradient correction (KGC) technique is presented for multiphase flow with a large density ratio and complex interfacial behaviors. The density discontinuity across the multiphase interface is described with the use of special volume, which only depends on the position information of adjacent particles. This multiphase SPH algorithm, which is troubled by an unstable and mixed-interface problem under a large density ratio, is significantly improved with the KGC technique. The accuracy and robustness of the improved method are demonstrated in the numerical simulations of the deformation of a square droplet, Rayleigh–Taylor instability, and bubble rising in water. The verified corrected multiphase SPH is applied to simulate the hydrodynamic behaviors of the general FCI and the interaction between fuels coated with stainless steel film and coolant. Boundary layer stripping, Rayleigh–Taylor instability, and Kelvin–Helmholtz instability are observed as important mechanisms of hydraulic fracturing. The fragments' distribution and the influence of stainless steel film are analyzed. The existence of a stainless steel film has been shown to inhibit breakage.

KEYWORDS

smoothed particle hydrodynamics, kernel gradient correction, fuel-coolant interaction, multiphase flow, large density ratio, fragmentation

1 Introduction

As the most mature reactor of Generation-IV advanced reactor systems, a sodium-cooled fast reactor (SFR) has advantages such as good inherent safety, high breeding ratio, high thermal conductivity, and long-life radioactive waste transmutation. Rich experience with operating systems laid the foundation of its commercialization. However, once the anticipated transients without scram, including unprotected transient overpower and unprotected loss of flow, happened, the boiling coolant could cause an increase in reactivity, exacerbating the consequences and leading to core disruption and fuel melting (Tobita et al., 2016). Although the probability of core disruptive accident (CDA) is very low, it is crucial for reactor safety assessment. Molten fuel ejected from the cladding rupture is mixed with the coolant and forms fragments. The behavior and size of fuel fragments formed in the fuel–coolant interaction (FCI) significantly affect the heat transfer deterioration in core as well as cooling and re-criticality in the lower head and core catcher (Cheng et al., 2019).

From this point of view, a number of experimental research studies have been conducted on the FCI related to an SFR to figure out the fragmentation characteristics over the past decades (Iwasawa and Abe, 2018). Some researchers used molten fuel materials (U/UO_2) in pursuit of a realistic core condition. Armstrong reported a series of experiments about the interactions between UO_2/stainless steel and liquid sodium in a dropping mode (Armstrong 1971) (Armstrong et al., 1976). Gabor et al. (1988) performed experiments by pouring molten metallic fuel and its alloy in quantities of kilogram into a sodium pool and focused on breakup behaviors. In most of the later experiments, as core materials are not readily available, materials with physical properties similar to fuel, such as copper, were often used as substitutes (Schins and Gunnerson, 1986; Nishimura et al., 2007; Nishimura et al., 2010; Zhang and Sugiyama, 2012). The fragmentation mechanisms are usually inferred based on the size and morphology of the solid fragments. Nishimura et al. (2010) carried out the FCI experiment in the form of a single molten copper jet penetrating into a sodium pool and analyzed the fragmentation characteristics from hydraulic and thermal perspectives. The processes of a single molten copper droplet (Nishimura et al., 2007; Zhang et al., 2009; Zhang and Sugiyama, 2010; Zhang and Sugiyama, 2012) and continuous copper droplets (Yang et al., 2018; Yang et al., 2019) interacting with liquid sodium have also been studied, and a thermal fragmentation mechanism of sodium entrainment was proposed and fragmentation due to a sodium microjet was presented.

In order to get rid of the limitation of core materials and obtain a visible development process, some scholars chose numerical methods to study the FCI. Cheng et al. (2015b) used SIMMER-III, which is a safety analysis code characterized by multivelocity field, multiphase, and multicomponent modeling to simulate the experimental tests of fuel–water interaction conducted at the Japan Atomic Energy Agency (Cheng et al., 2015a), to figure out the characteristics including pressure buildup and mechanical energy release. Because the FCI is a complex phenomenon involving multiphase flow, intense interfacial motion, drastic heat transfer, and phase transitions, it is challenging for traditional grid methods to capture these details, and some technical limitations emerge, such as grid distortion in the Lagrange grid method or difficult interface tracking in the Euler grid method when dealing with such large deformation multiphase flow problems. Therefore, some scholars have turned to meshfree methods, which have received extensive attention in recent years. The computational domain of the particle method is represented by a series of randomly distributed particles carrying material properties. Due to these moving Lagrange particles, the meshfree particle methods obtain attractive features and inherent advantages in solving complex hydrodynamics problems. The moving particle semi-implicit (MPS) method and smoothed particle hydrodynamics (SPH) are two typical meshfree particle methods. MPS was first proposed by Koshizuka and Oka (1996) and focused on thermal–hydraulic simulations in nuclear field. Abundant models related to incompressible flow have been developed in the MPS framework for calculating surface tension, heat conduction and convection, open inlet and outlet boundaries, fluid–structure interaction, and other problems. The development and application of MPS in nuclear engineering are well-reviewed by Li et al. (2020). SPH is the first meshfree particle method proposed by Lucy (1977) and Gingold and Monaghan (1977). With sufficient development, it has been widely used in marine, aerospace, and other fields covering compressible, weakly compressible, and incompressible flows (Lind et al., 2020). The fundamental difference between MPS and SPH lies in the solution of pressure. The pressure of incompressible flow in MPS is calculated by implicitly solving the pressure Poisson equation, which requires solving a super large-scale matrix. It is a severe test of computational cost and parallel feasibility, especially with a huge number of particles (Li et al., 2020). Considering the large-scale particle computation and parallel algorithms are the general trend, although SPH is rarely used in nuclear field compared with MPS, SPH is chosen in this paper for its development potential with explicit solution, which makes it easy to improve the computational efficiency through parallelism. In order to handle the density discontinuity across the multiphase interface, a few solutions have been proposed. In this paper, one of the popular ideas based on particle number density is adopted (Hu and Adams, 2006; Hu and Adams, 2007; Szewc et al., 2015). However, there are still errors under this approximation idea, and the accumulated errors lead to the situation where the stability and accuracy of the calculation cannot be maintained for a long time. Therefore, this study introduced kernel gradient correction (KGC) and combined it with the use of particle number density. The significantly better performance of the improved method in dealing with multiphase flow has been demonstrated and emphasized. The multiphase SPH corrected with KGC is abbreviated as KGC-MSPH in this paper. The program in this paper is developed based on FORTRAN language and uses OpenMP to realize parallel computation.

This paper is organized as follows: in the second section, the basic physical models, namely, conservation equations and equations of state, are introduced. Then, the third section describes the numerical scheme, including the basic principle of SPH and models and corrections used in multiphase SPH. In the fourth section, the numerical investigation of KGC-MSPH is explained with the test cases. Finally, we apply the validated method to the simplified FCI condition and discuss the simulation results.

2 Physical models

The Navier–Stokes equations used to describe the flow system in a Lagrangian frame are applied. The continuity equation and the momentum equation are as follows:

$$\frac{d\rho}{dt} = -\rho\nabla\cdot\boldsymbol{v}, \tag{1}$$

$$\frac{d\boldsymbol{v}}{dt} = \frac{1}{\rho}\left(-\nabla p + \boldsymbol{f}_v + \boldsymbol{f}_s\right) + \boldsymbol{g}, \tag{2}$$

where ρ is the density, $\boldsymbol{v}$ is the velocity vector, p is the pressure, and t is the time. The pressure gradient $-\nabla p$, viscous stress $\boldsymbol{f}_v$, surface tension force $\boldsymbol{f}_s$, and the gravity $\boldsymbol{g}$ are contained in the momentum equation. In the SPH framework, the incompressible fluids are usually assumed to be weakly compressible. Thus, the pressure is directly related to the density and can be calculated explicitly *via* the equation of state. Here, the commonly used Tait equation (Monaghan, 1994) is applied,

$$p = \frac{\rho_0 c_0^{\,2}}{\gamma}\left[\left(\frac{\rho}{\rho_0}\right)^{\gamma} - 1\right] + p_b, \tag{3}$$

where, c_0 is the artificial sound speed. The value of c_0 determines the compressibility of the fluid and it must be ten times greater than the maximum value of the fluid velocity to satisfy the weakly compressibility hypothesis (Monaghan and Kos, 1999). For single-phase flow and the denser phase in multiphase flow, γ is usually set to be 7, and it takes a smaller value for the lighter phase, which is usually 1.4 under the large density ratio of water to air (Colagrossi and Landrini, 2003; Grenier et al., 2009). The relation of the artificial sound speeds for different phases,

phase X and phase Y, satisfies the condition $\rho_{0,X}{c_{0,X}}^2/\gamma_X = \rho_{0,Y}{c_{0,Y}}^2/\gamma_Y$. p_b is the background pressure. It has a positive value for the multiphase flow to avoid negative pressures. The application of background pressure is beneficial to the uniformity of particle distribution and the stability of calculation (Marrone et al., 2013; Zhang et al., 2015).

3 Numerical scheme

3.1 Basic principle of SPH

In SPH, the computational domain is represented by a finite number of particles, which carry physical properties like real fluid elements. A kernel function is applied to establish the relationship between particles. The kernel approximation works by integrating over the surrounding particles to express the central one. The arbitrary function $A(\boldsymbol{x})$ at a general position $\boldsymbol{x}$ in the domain Ω and its derivative in SPH form are obtained,

$$A(\boldsymbol{x}) = \int_{\Omega} A(\boldsymbol{x}')W(\boldsymbol{x}-\boldsymbol{x}', h)d\boldsymbol{x}' \approx \sum_{j=1}^{N}\frac{m_j}{\rho_j}A(\boldsymbol{x}_j)W(\boldsymbol{x}-\boldsymbol{x}_j, h), \quad (4)$$

$$\nabla A(\boldsymbol{x}) = \int_{\Omega} A(\boldsymbol{x}')\nabla W(\boldsymbol{x}-\boldsymbol{x}', h)d\boldsymbol{x}' \approx \sum_{j=1}^{N}\frac{m_j}{\rho_j}A(\boldsymbol{x}_j)\nabla W(\boldsymbol{x}-\boldsymbol{x}_j, h), \quad (5)$$

where, $W(\boldsymbol{x}-\boldsymbol{x}', h)$ is the smoothing kernel function. The support domain of the kernel function is measured by the smoothing length h and it is discretized into N particles. When h becomes 0, $W(\boldsymbol{x}-\boldsymbol{x}', h)$ has the characteristic of the Dirac function and the kernel integral over the support domain is equal to 1. The subscript j is used to label the variables of these adjacent particles, like the mass m_j and the density ρ_j. All the particles in the computational domain can be expressed by contributing to each other in the summations.

The kernel function plays an important role in the SPH simulation and significantly affects the numerical results. Here, we consider two kernel functions. One is the renormalized Gaussian kernel (Grenier et al., 2009; Molteni and Colagrossi, 2009) used in the deformation of square droplet, given as follows:

$$W(r,h) = \begin{cases} \frac{1}{\pi h^2}\left(\frac{e^{-q^2}-C_0}{1-C_1}\right) & if\ q \le 2 \\ 0 & otherwise, \end{cases} \quad (6)$$

where, $r = |\boldsymbol{x}_i - \boldsymbol{x}_j|$ is the distance between two particles, $q = r/h$ and $C_0 = e^{-9}$ and $C_1 = 10C_0$. The cut-off radius is set to be $3h$.

The other one is the Wendland kernel (Dehnen and Aly, 2012; Ferrand et al., 2013) used in the other cases, given as

$$W(r,h) = \begin{cases} \frac{7}{64\pi h^2}(1+2q)(2-q)^4 & if\ q \le 2 \\ 0 & otherwise, \end{cases} \quad (7)$$

where, the cut-off radius is set to be $2h$.

3.2 MSPH formulations

The density estimation is the basis in the SPH frame and is achieved either by the continuity equation or by the density summation approach. In order to handle the density discontinuity across the multiphase interface, a few variants of density estimation have been developed. The special volume proposed by Hu and Adams (2006) is used in the present work. It is based on the density summation theory with the use of an interpolating function, given as

$$\chi_j(\boldsymbol{x}_i) = \frac{W_j(\boldsymbol{x}_i)}{\sum_{k=1}^{N}W_k(\boldsymbol{x}_i)} = \frac{W_j(\boldsymbol{x}_i)}{\sigma(\boldsymbol{x}_i)}, \quad (8)$$

where, $W_j(\boldsymbol{x}_i)$ is the abbreviation of $W_j(\boldsymbol{x}_i - \boldsymbol{x}_j, h)$. $\sigma(\boldsymbol{x}_i)$ is the particle density number. The special volume calculated with the interpolating function is as follows:

$$V_i^{\sigma} = \sum_{j=1}^{N}\chi_j(\boldsymbol{x}_i)V_j = \frac{\sum_{j=1}^{N}W_j(\boldsymbol{x}_i)V_j}{\sigma(\boldsymbol{x}_i)} \approx \frac{1}{\sigma(\boldsymbol{x}_i)}. \quad (9)$$

After the aforementioned derivation, the special volume V_i^{σ} is the inverse of σ_i, which only requires the position information of the adjacent particles. With the mass of particle i known as a constant, the density can be approximated as,

$$\rho_i = m_i/V_i^{\sigma} = m_i\sigma_i. \quad (10)$$

The density of particle i is not influenced by the mass or density of the neighbors, and this multiphase model is able to reproduce the discontinuous density field.

Based on the multiphase SPH idea, the momentum conservation equation Eq. 2 can be discretized as,

$$\frac{d\boldsymbol{v}_i}{dt} = \frac{1}{\rho_i}\left[-\frac{1}{V_i^{\sigma}}\sum_{j=1}^{N}\left(p_iV_i^{\sigma 2} + p_jV_j^{\sigma 2}\right)\nabla W_j(\boldsymbol{x}_i) + \boldsymbol{f}_{v,i} + \boldsymbol{f}_{s,i}\right] + \boldsymbol{g}. \quad (11)$$

The acceleration term driven by the pressure gradient in Eq. 11 has the anti-symmetric form, which is variationally consistent with the form of density estimation.

In addition to density, some other physical properties are discontinuous across the multiphase interface, such as viscosity. To deal with the viscosity jump, the viscous coefficient is calculated in a harmonic mean form proposed by Hu and Adams (2006). The formula of the viscous force $\boldsymbol{f}_{v,i}$ is given as,

$$\boldsymbol{f}_{v,i} = \sum_{j=1}^{N}\frac{2\eta_i\eta_j}{\eta_i+\eta_j}\left(V_i^{\sigma 2} + V_j^{\sigma 2}\right)\frac{(\boldsymbol{x}_i-\boldsymbol{x}_j)\cdot\nabla W_j(\boldsymbol{x}_i)}{|\boldsymbol{x}_i-\boldsymbol{x}_j|^2 + (\xi h)^2}\frac{(\boldsymbol{v}_i-\boldsymbol{v}_j)}{V_i^{\sigma}}, \quad (12)$$

where, η is the dynamic viscous coefficient and ξ is a small constant, usually taken to be 0.01, to prevent the denominator from being 0 when two particles coincide.

Here, the surface tension force is calculated using the CSF model (Brackbill et al., 1992) in the form $\boldsymbol{f}_s = -\alpha\kappa\boldsymbol{n}\lambda$. α is the surface tension coefficient, κ is the curvature of the interface, and $\boldsymbol{n}$ is the unit normal vector. λ is a weight function used to define a transition zone near the interface and determine the magnitude of the surface tension across the zone. The calculation of $\boldsymbol{n}$ and λ requires a density-weighted color function c such that $\boldsymbol{n} = \nabla c/|\nabla c|$ and $\lambda = |\nabla c|$. The formulas are given as (Adami et al., 2010)

$$c_i^j = \begin{cases} 1 & if\ i \in S, \quad j \notin S \\ 0 & if\ i \in S, \quad j \in S, \end{cases} \quad (13)$$

$$c_{i,W}^j = \frac{\rho_j}{\rho_i+\rho_j}c_i^j + \frac{\rho_i}{\rho_i+\rho_j}c_i^j, \quad (14)$$

where, c_i^j represents the relationship between particle i and the neighbor particle j, S is the phase to which particle i belongs to, and $c_{i,W}^j$ is the density-weighted color function. The SPH approximation of the unit normal vector is obtained as,

$$\nabla c_i = \sum_{j=1}^{N} \left(V_i^{\sigma 2} + V_j^{\sigma 2}\right) c_{i,W}^j \frac{\nabla W_j(x_i)}{V_i^{\sigma}}. \tag{15}$$

$$\boldsymbol{n}_i = \nabla c_i / |\nabla c_i| . \tag{16}$$

The curvature κ presented in Adami et al. (2010) using a reproducing divergence is applied here. The benefit of this reproducing divergence is that the support domain truncated condition can be handled more accurately. The curvature in the CSF model can be calculated as follows:

$$\phi_i^j = \begin{cases} -1 & if\ i \in S, \quad j \notin S \\ 1 & if\ i \in S, \quad j \in S, \end{cases} \tag{17}$$

$$\kappa_i = -\nabla \cdot \boldsymbol{n}_i = -d \frac{\sum_{j=1}^{N} \left(\boldsymbol{n}_i - \phi_i^j \boldsymbol{n}_j\right) \cdot \nabla W_j(\boldsymbol{x}_i) V_j^{\sigma}}{\sum_{j=1}^{N} |\boldsymbol{x}_i - \boldsymbol{x}_j| \left|\nabla W_j(\boldsymbol{x}_i)\right| V_j^{\sigma}}, \tag{18}$$

where, ϕ_i^j is used to describe the direction of the unit vector by determining whether the particles i and j belong to the same phase and d is the spatial dimension. Then, the surface tension force is obtained.

$$\boldsymbol{f}_{s,i} = \alpha_i d \frac{\sum_{j=1}^{N} \left(\boldsymbol{n}_i - \phi_i^j \boldsymbol{n}_j\right) \cdot \nabla W_j(\boldsymbol{x}_i) V_j^{\sigma}}{\sum_{j=1}^{N} |\boldsymbol{x}_i - \boldsymbol{x}_j| \left|\nabla W_j(\boldsymbol{x}_i)\right| V_j^{\sigma}} \nabla c_i . \tag{19}$$

The good performance of this surface tension model in multiphase flow is demonstrated in this study by simulating the oscillatory deformation of a square droplet.

3.3 Time-stepping scheme

The time-stepping scheme is fully explicit. Similar to Zhang et al. (2015), a modified predictor-corrector time-stepping scheme is used in this paper to integrate Eqs 1, 2. The integration process is divided into two steps. The following equation gives the prediction step of the algorithm.

$$\begin{cases} V_i^{\sigma,n+1/2} = \dfrac{1}{\sigma_i^n}, \quad \rho_i^{n+1/2} = m_i \sigma_i^n \\ \boldsymbol{v}_i^{n+1/2} = \boldsymbol{v}_i^n + \dfrac{\Delta t}{2} \left(\dfrac{d\boldsymbol{v}}{dt}\right)^n \\ \boldsymbol{x}_i^{n+1/2} = \boldsymbol{x}_i^n + \dfrac{\Delta t}{2} \boldsymbol{v}^{n+1/2} \end{cases}, \tag{20}$$

where, the subscripts n and $n+1/2$ represent, respectively, the previous step and the prediction step. Δt is the timestep which is determined by the CFL condition. The correction step, namely, the present $n+1$ step is updated as,

$$\begin{cases} V_i^{\sigma,n+1} = \dfrac{1}{\sigma_i^{n+1/2}}, \quad \rho_i^{n+1} = m_i \sigma_i^{n+1/2} \\ \boldsymbol{v}_i^{n+1} = \boldsymbol{v}_i^n + \Delta t \left(\dfrac{d\boldsymbol{v}}{dt}\right)^{n+1/2} \\ \boldsymbol{x}_i^{n+1} = \boldsymbol{x}_i^n + \Delta t \boldsymbol{v}_i^{n+1}. \end{cases} \tag{21}$$

3.4 Solid boundary treatment

In this paper, the solid boundary condition is carefully set with ghost particles, which have a mirroring relationship with the fluid particles within $3h$ of the boundary. Here, we use the lower subscripts g, f, and w to mark the information of the ghost particles, fluid particles, and the wall, respectively. The subscripts n and t, respectively, mean the normal and tangential direction. The position of the ghost particle is easy to obtain with the mirroring relation as $\boldsymbol{x}_g = 2\boldsymbol{x}_w - \boldsymbol{x}_f$. The common conditions of regular boundaries are mainly divided into no-slip and slip. The boundary conditions are expressed by the tangential velocity with $\boldsymbol{v}_{g,t} = -\boldsymbol{v}_{f,t}$ for no-slip and $\boldsymbol{v}_{g,t} = \boldsymbol{v}_{f,t}$ for slip condition. The normal velocity of ghost particles is opposite to that of liquid particles to prevent particles from penetrating the wall. In the case of intense flow, the opposite normal velocity is not enough to stop the particle penetration. Therefore, an additional repulsive force (Monaghan, 1994) is needed, and its formula is as follows:

$$\boldsymbol{f}_w\left(r_{gf}\right) = \begin{cases} D\left[\left(\dfrac{r_w}{r_{gf}}\right)^{n_1} - \left(\dfrac{r_w}{r_{gf}}\right)^{n_2}\right] \dfrac{r_w}{r_{gf}^2} & if\ \dfrac{r_w}{r_{gf}} \geq 1 \\ 0 & otherwise, \end{cases} \tag{22}$$

where, the distance between the ghost particle and the fluid particle is calculated as $r_{gf} = |\boldsymbol{x}_{i,g} - \boldsymbol{x}_{j,f}|$. r_w is the cut-off radius, and it is taken as the initial spacing. The two powers are set as $n_1 = 4$ and $n_2 = 2$. The value of D is on the order of the square of the maximum velocity.

3.5 Kernel gradient correction

Kernel gradient correction was developed to improve the simulation accuracy, and Bonet and Lok (1999) proved that by theoretical derivation. Shao et al. (2012) and Zhang and Liu (2017) have applied KGC in SPH simulation of liquid sloshing dynamics, high velocity impact, and violent impinging flow problems (Shao et al., 2016), which all focus on single-phase flow problems. Zhu et al. (2018) presented a SPH model for simulating multiphase flows with the use of KGC. In their work, the density is evaluated by the continuity equation, and the interface sharpness was maintained by developing an interface treatment algorithm, which consists of a virtual particle technique and an interface force. Here, the density discontinuity is handled by calculating the special volume based on density summation idea. The introduction of KGC can significantly improve the multiphase SPH model in this work, and the solution procedure of KGC-MSPH is relatively simple. The remarkable performance of KGC will be discussed in the numerical cases. The KGC formulation can be derived as follows:

$$\sum_{j=1}^{N} \frac{m_j}{\rho_j} \left(\boldsymbol{x}_j - \boldsymbol{x}_i\right) \otimes \nabla W_j^{KGC}(\boldsymbol{x}_i) = \boldsymbol{I} . \tag{23}$$

The corrected kernel gradient can be obtained by modifying the original gradient with a reversible matrix,

$$\nabla W_j^{KGC}(\boldsymbol{x}_i) = \boldsymbol{L}_i \nabla W_j(\boldsymbol{x}_i). \tag{24}$$

$$\boldsymbol{L}_i = \left[\sum_{j=1}^{N} \frac{m_j}{\rho_j} \nabla W_j(\boldsymbol{x}_i) \otimes \left(\boldsymbol{x}_j - \boldsymbol{x}_i\right)\right]^{-1} . \tag{25}$$

Since the $d \times d$ matrix is defined by the local particle information, a high computation cost is required, which is a drawback.

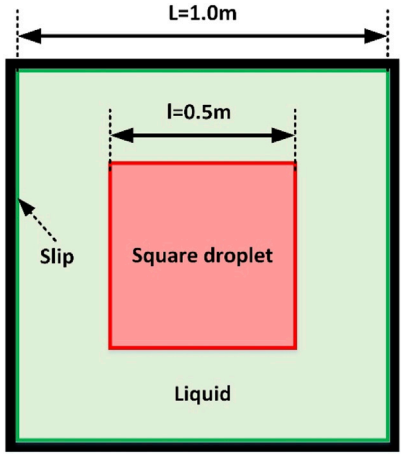

FIGURE 1
Initial setup of square droplet deformation.

3.6 The interfacial repulsive force

The interfacial repulsive force is commonly used in multiphase SPH-related studies (Monaghan, 2000; Grenier et al., 2009). If surface tension force is not considered, a spurious fragmentation can happen on the interface. The application of interfacial repulsive force can maintain the interface sharpness. This repulsive force is added to the pressure term depending on different situations and requirements. The discretized momentum equation considering the interfacial repulsive force can be written as follows:

$$\frac{d\boldsymbol{v}_i}{dt} = \frac{1}{\rho_i}\left[-\frac{1}{V_i^{\sigma}}\sum_{j=1}^{N}\left(p_i V_i^{\sigma 2} + p_j V_j^{\sigma 2}\right)\nabla W_j(\boldsymbol{x}_i)\right.$$
$$\left.-\varepsilon\frac{1}{V_i^{\sigma}}\sum_{j=1}^{N}\frac{\left|\rho_{0i}-\rho_{0j}\right|}{\left|\rho_{0i}+\rho_{0j}\right|}\left(\left|p_i\right|V_i^{\sigma 2} + \left|p_j\right|V_j^{\sigma 2}\right)\nabla W_j(\boldsymbol{x}_i) + \boldsymbol{f}_{v,i} + \boldsymbol{f}_{s,i}\right] + \boldsymbol{g}. \tag{26}$$

The interfacial repulsive force only appears near the interface and vanishes if the neighbor particles belong to the same phase. The effect of the interfacial repulsive force is negligible on the surface tension force, and the magnitude of the force is determined by the coefficient ε, where ε is generally less than 0.1 (Grenier et al., 2009; Monaghan and Rafiee, 2013). We introduced the interfacial repulsive force in this study and discussed the coefficient value applicable to our method.

4 Numerical investigations

4.1 Deformation of square droplet

In this section, the KGC-MSPH method is analyzed and verified by a 2D simulation of the deformation of a square droplet. This case has been studied by Ming et al. (2017), and Patiño-Nariño et al. (2019) simulated a simple case of a circle drop resettling under a zero gravity condition. The multiphase SPH models adopted in their work are also based on calculations of particle number density and specific volumes. Distorted and mixed-interface problem plagued them. In order to maintain the sharpness under the high density ratio and suppress the instabilities, some treatments, like background pressure and interface sharpness control and inter-particle approximation of average pressure value, are applied in their simulations. Here, we use the same case to demonstrate the effectiveness of KGC on this problem and make comparative analysis with their treatments.

The initial condition is shown in Figure 1. A square droplet with side length $l = 0.5\ m$ is located in the center of a square cavity with side length $L = 1.0\ m$. The computational domain is discretized into 80 × 80 particles with uniform spacing $\Delta x = 0.0125\ m$. The timestep is set as $\Delta t = 10^{-4} s$. The wall boundary is simulated with the free-slip condition using mirror ghost particles without additional repulsive force. The liquid inside the droplet is marked with subscript *in*, and the subscript *out* is used for marking the liquid outside the droplet in the cavity. The density ratio is defined as $\Psi = \rho_{in}/\rho_{out}$, and the viscosity ratio is $\Phi = \eta_{in}/\eta_{out}$. The density of the liquid inside and the dynamic viscous coefficient of the liquid outside are fixed as $\rho_{in} = 1000\ kg/m^3$ and $\eta_{out} = 0.2\ Pa \cdot s$, respectively. The prominent driven force, surface tension, is simulated with the density-weighted CSF model and $\alpha = 10.0\ N/m$. The background pressure is introduced here to prevent the tensile instability, and it is set as $P_b = 500\ Pa$.

For comparison, the MSPH basic method without correction is used in this case where $\Psi = 1000$ and $\Phi = 1$. The same condition is simulated with KGC-MSPH. Under the action of surface tension, the square droplet oscillated periodically and gradually converged to a circular droplet. Several typical moments in the first oscillation period of droplet deformation simulated by MSPH and KGC-MSPH are shown in Figure 2. The first two figures on the top row indicate that, without correction, the results of MSPH calculation are reasonable at the initial stage of calculation. However, such a smooth interface cannot be maintained for a long time. As the calculation is performed, the problems of mixing and distortion breakage appear on the interface and gradually become worse. The problem is completely solved with the use of KGC. The interface is smooth, and the calculation is stable. The whole process of the droplet periodic oscillation and convergence into a circle has been simulated. The axial and diagonal size changes of the droplet during the deformation process are shown in Figure 3. The droplet had completed more than ten significant oscillation periods within 20 s, and the final axial and diagonal sizes converged to the analytical equivalent diameter. The theoretical value of the oscillation period is calculated $t_{period} = 2\pi\sqrt{\rho_{in} R_a/60\alpha} = 1.215 s$, where R_a is the analytic radius of the circle. The simulated oscillation period is in good agreement with t_{period}. We further increased the density ratio to 10000 and increased the range of viscosity ratio to 10–100. The total kinetic energy fluctuated with the oscillation in these conditions as shown in Figure 4. When $\Psi = 10000$, KGC-MSPH is still competent for the simulation of deformation. Since the momentum of the external fluid is negligible for its small density, the variation of total kinetic energy is basically consistent with the curve of $\Psi = 1000$. In the oscillation process of the square droplet with a high viscosity ratio, the kinetic energy is rapidly transformed into potential energy, the oscillation period is obviously reduced, and the droplet converged into a circle more rapidly. The results indicate that KGC-MSPH is capable of simulating the multiphase flow with a high density ratio and a high viscosity ratio. With KGC, a simple correction operation, stable and accurate results can be obtained in this case.

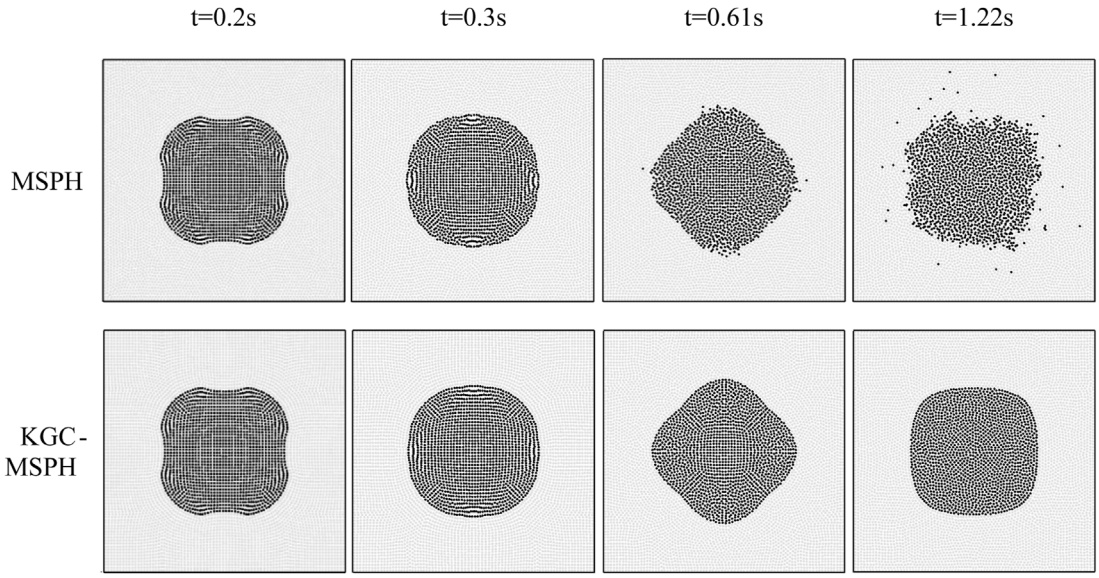

FIGURE 2
Comparison of square droplet oscillation simulated with MSPH and KGC-MSPH.

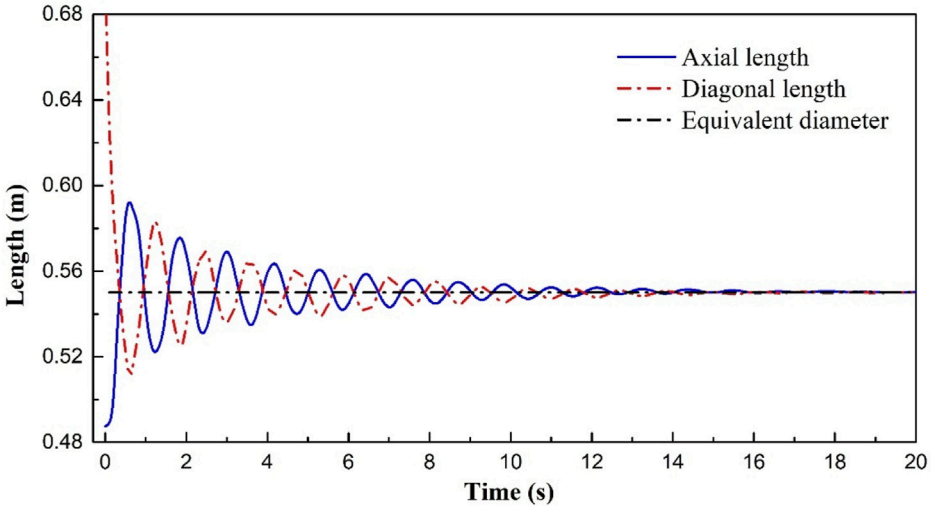

FIGURE 3
The variation of axial and diagonal sizes of the droplet.

4.2 Rayleigh–Taylor instability

In order to further demonstrate the good performance of KGC-MSPH in gravity flow, we select a classic case, Rayleigh-Taylor (R–T) instability, which has been studied by Cummins and Rudman (1999), Grenier et al. (2009), and Hu and Adams (2009) in many ways. The computational domain is rectangular with size of 1.0 m ×2.0 m and is discretized into 150 × 300 particles. The timestep is set at $\Delta t = 10^{-4}s$. The heavier fluid in the upper layer with density $\rho_h = 1800kg/m^3$ and the lighter fluid in the lower layer with density $\rho_l = 1000kg/m^3$ are separated by the interface at $y = 1.0 - 0.15\sin(2\pi x)$. The Reynolds number is set as $Re = \sqrt{H^3 g}/\upsilon$ =420, where $H = 1.0\ m$ and the gravity acceleration is $g = 1.0\ m/s^2$. The fluids have no initial velocity and begin to flow gradually driven by gravity. The boundary condition is set as no-slip, and no surface tension is considered here. The initial setup of this case is shown in Figure 5.

With KGC modification, MSPH is qualified for simulating R–T instability, and the contour of the interphase interface is well-described. The variation of the highest front position of the lighter fluid is in good agreement with the Layzer theory as shown in Figure 6. Because no external force is applied to the interface, slight unsmoothness occurred as shown in Figure 7A. The repulsive force model commonly used by scholars (Monaghan, 2000; Grenier et al., 2009; Monaghan and Rafiee, 2013) to stabilize multiphase interfaces was introduced. Snapshots of simulation results under repulsive forces

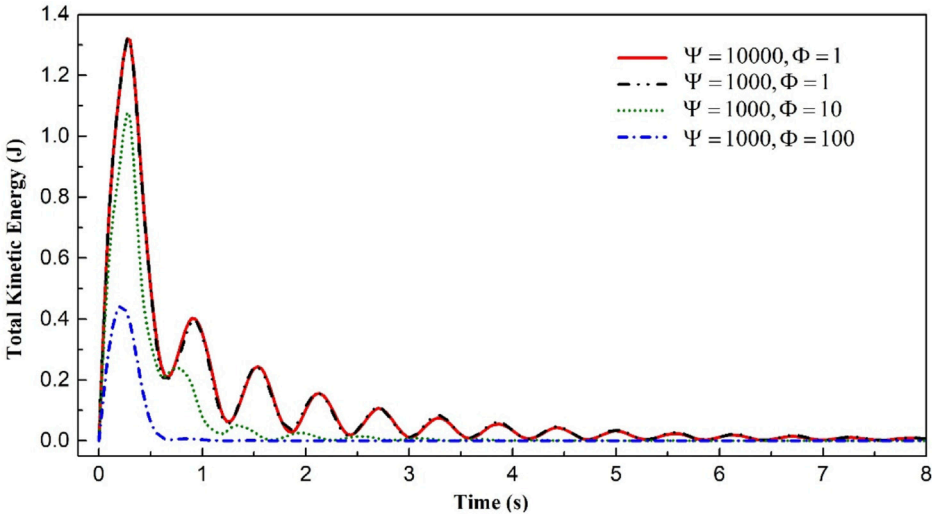

FIGURE 4
The variation of total kinetic energy of the droplet deformation with different density ratio and viscosity ratio.

of varying magnitude with $\varepsilon = 0.01$ and $\varepsilon = 0.08$, at $t = 0.5\ s$, are shown in Figures 7B, C, respectively. The smoothing effect of the repulsive force is clearly observed in the enlarged images. The interface is moderately smoothed with $\varepsilon = 0.01$. However, with $\varepsilon = 0.08$, the interface is overly smoothed and many details are erased, which is unreasonable. We suggest that in KGC-MSPH, the value should not be too large and preferably around 0.01 to avoid excessive influence on the interface.

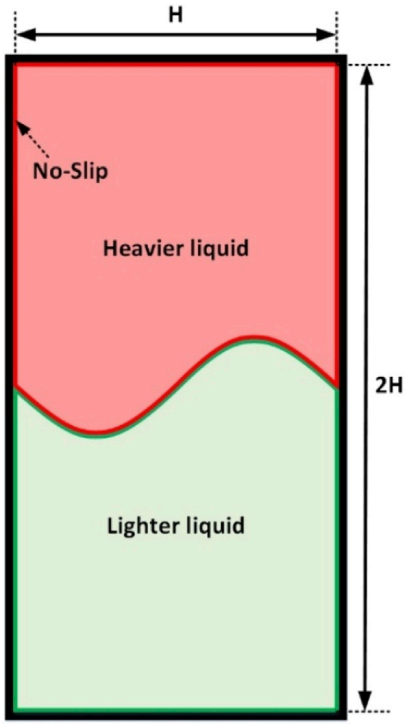

FIGURE 5
Initial setup of Rayleigh-Taylor instability.

We can conclude in this section that KGC-MSPH is capable of simulating R–T instability problem. The KGC correction fundamentally stabilizes the calculation and improves the calculation accuracy. If a smooth interface is desired, surface tension can be applied or an appropriate repulsive force can be introduced.

4.3 Bubble rising

Bubble dynamics plays an important role in multiphase flow. The bubble rising problem has been studied with experiments, such as Collins (1967); Liu et al. (2016), and it has been extensively simulated, such as Sussman et al. (1994) with a level set method and Krishna et al. (2000) with a VOF method. As an important multiphase benchmark case, the bubble rising process is accompanied with interface deformation subjected to gravity force, viscosity, and surface tension, and it is a test to the algorithms. We applied KGC-MSPH

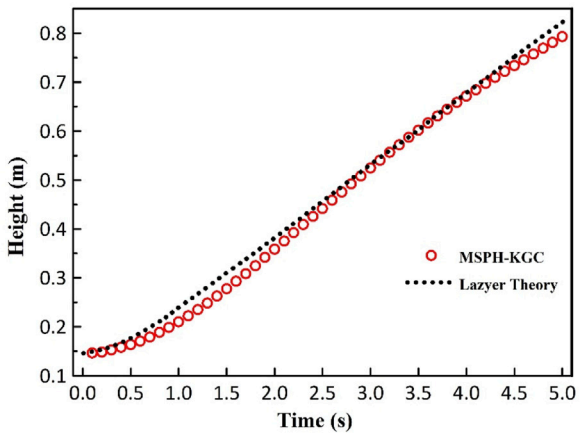

FIGURE 6
The highest front position of a light fluid over time with ε = 0.01.

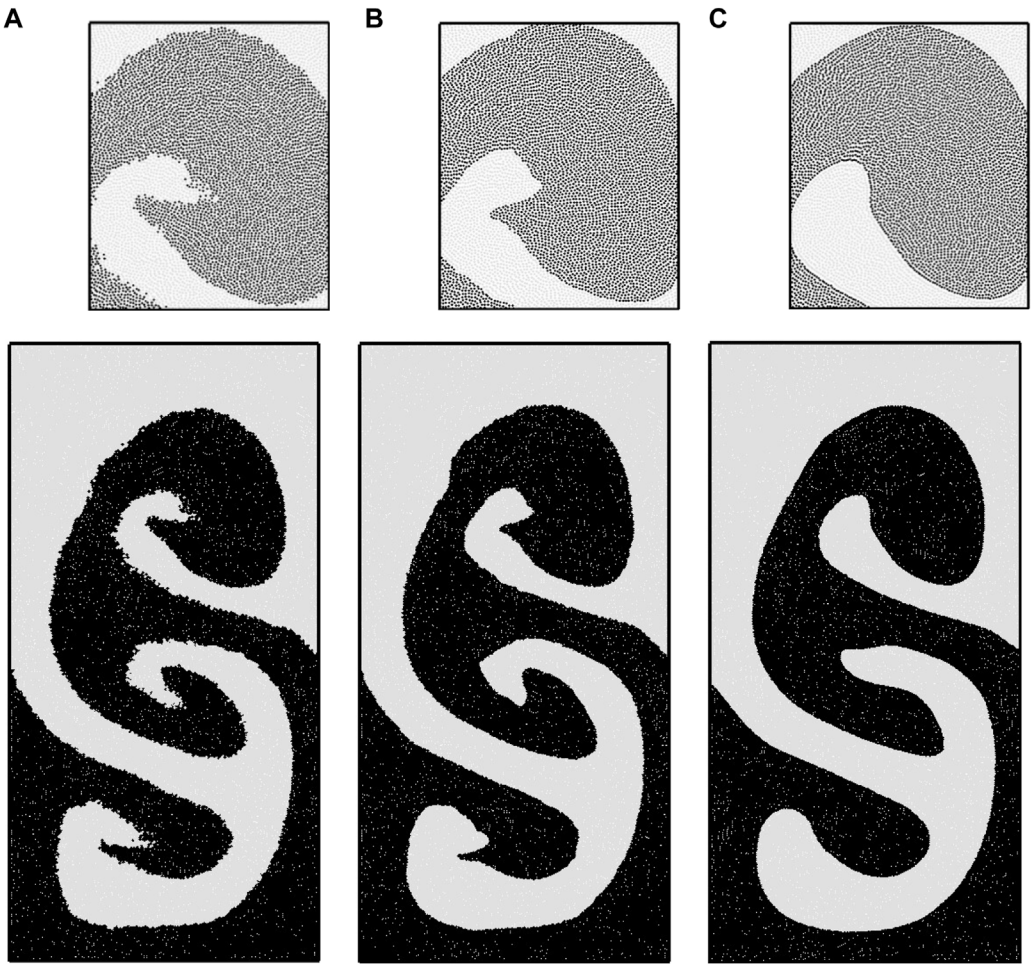

FIGURE 7
Snapshots of R-T instability at t = 5.0 s obtained by A MSPH-KGC, B MSPH-KGC with repulsive force ε = 0.01, C MSPH-KGC with repulsive force ε = 0.08.

to simulate the bubble rising process, and the results are compared to those in previous literature (Sussman et al., 1994) obtained with the level set method to prove the effectiveness of KGC-MSPH. The initial condition of this case is shown in Figure 8, and the bubble with radius $R = 1.0\ m$ rests in a rectangular container. The width of the container is $6R$ and the height $H = 10R$. The center of the bubble is located on the axis of the container and $2R$ away from the bottom of the container. We use the subscript m for referring to the bubble and n for the heavier liquid outside. The densities are set as $\rho_m/\rho_n = 1/1000$. The viscosity is defined by the Reynolds number $Re = \sqrt{(2R^3)g}/\upsilon_n = 1000$, where υ is the kinematic viscous coefficient and $\upsilon_m/\upsilon_n = 128$. The surface tension is defined by the Bond number $Bond = 4\rho_n g R^2/\alpha = 200$. A small repulsive force is considered here with $\varepsilon = 0.01$. The background pressure is set to be $P_b = 1000Pa$, and the artificial sound speeds of the two phases are, respectively, as $c_n = 5\sqrt{gH}$ and $c_m = 42.5\sqrt{gH}$.

The timestep is set as $\Delta t = 10^{-5}s$. The computational domain is discretized into two resolutions, 192×320 and 384×640, and it is placed in a Cartesian coordinate system with the origin of the coordinates in the lower left corner. Those snapshots demonstrating typical shapes, including horseshoe-shaped, mushroom-shaped, daughter bubble formation, and detachment, are shown in Figure 9. In this condition, the bubble body is elongated and pinched off, forming the daughter bubbles. This process, which is tricky for the multiphase methods, is well-handled here. The evolutions under the two resolutions are almost consistent with each other, and the details in higher resolution are slightly better. It is further compared with the level set results, and good agreement can be observed.

5 FCI simulation and mechanism analysis

Considering economy, safety, and reliability as well as engineering technology foundation, various countries have gradually agreed on the design scheme of the SFR. The core is made of metal fuel or MOX fuel, and stainless steel is used as the cladding material. Metal-fueled fast reactors are promising because metal fuels have better proliferative properties than MOX fuels, which is an important advantage for fast reactors (Carmack et al., 2009). However, metal uranium fuel has poor irradiation stability, low melting point, and is easy to crystallize with cladding at low temperature (Ogata, 2014). These shortcomings threaten the safety of the reactor core in serious accidents and may lead to CDAs. As an important phenomenon

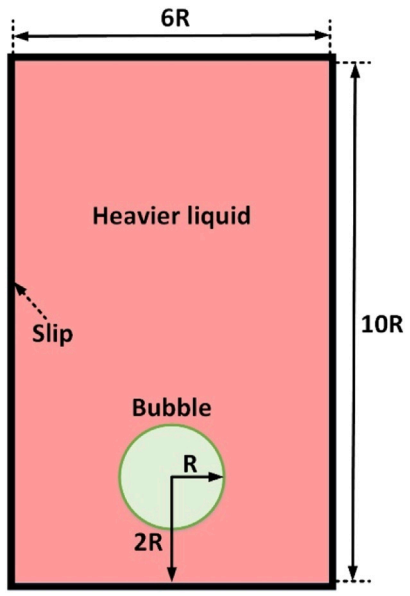

FIGURE 8
Initial setup of bubble rising.

contained in CDAs (Tobita et al., 2016), molten fuel is fragmented and solidified into debris surrounding by the coolant in the FCI. The debris is relocated on the lower head or the core catcher. The fragmentation characteristics of the FCI significantly affect the heat transfer deterioration in core as well as cooling and re-criticality in the lower head and core catcher. The FCI is numerically studied with the developed KGC-MSPH method in this work. The fuel material is uranium, and the coolant is sodium. The interactions between the fuel, which is coated with melted cladding material, and the coolant were simulated as well. In practice, such mixed situations may be more common and equally valuable; however, they are rarely studied in the published literatures.

Regardless of heat transfer and phase transition, we assume that uranium, stainless steel, and sodium remain liquid and interact with each other. The hydrodynamic fragmentation in the FCI is our focus. The sodium pool is placed in a 2D Cartesian coordinate system with a width of 0.6 m and height of 1.2 m. The uranium droplet, which has no initial velocity, with a radius of r = 0.08 m and with a center of (0.3, 1.0) is placed in the sodium pool. The computational domain is discretized into 450 × 900 particles. The timestep is set as $\Delta t = 10^{-5}s$. All the boundaries are considered free-slip. The gravity acceleration is g = 9.81 m/s^2. The density ratio between U, stainless steel (SS), and Na is 20:7.8:1 with ρ_U = 17797 kg/m^3, ρ_{SS} = 6920 kg/m^3, and ρ_{Na} = 892 kg/m^3. The other physical properties of the three materials used in this simulation are $\eta_U = 5.5 \times 10^{-3}\ Pa \cdot s$, α_U =1.55 N/m, $\eta_{SS} = 5.36 \times 10^{-3}\ Pa \cdot s$, α_{SS} =1.83 N/m, $\eta_{Na} = 4.067 \times 10^{-4}\ Pa \cdot s$, and α_{Na} = 0.182 N/m. The artificial sound speeds are $c_U = 40\sqrt{gH}$, $c_{SS} = 32\sqrt{gH}$, and $c_{Na} = 20\sqrt{gH}$. We first simulated the direct interaction between a single uranium droplet and sodium coolant. Then, the uranium droplet wrapped in stainless steel was further considered, and the thickness of the stainless steel film is set as

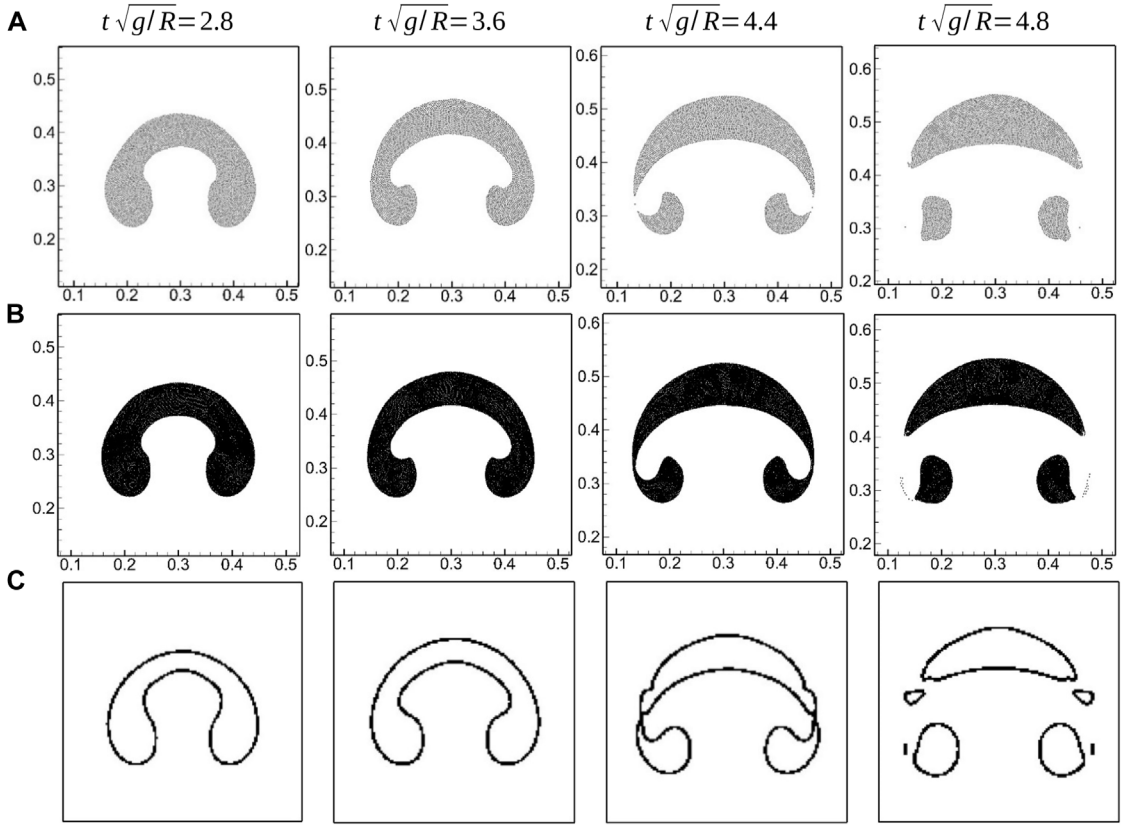

FIGURE 9
Snapshots of bubble rising. A MSPH-KGC solution with resolution of 192 × 320, B MSPH-KGC solution with resolution of 384 × 640, C Level set solution in (Sussman et al., 1994).

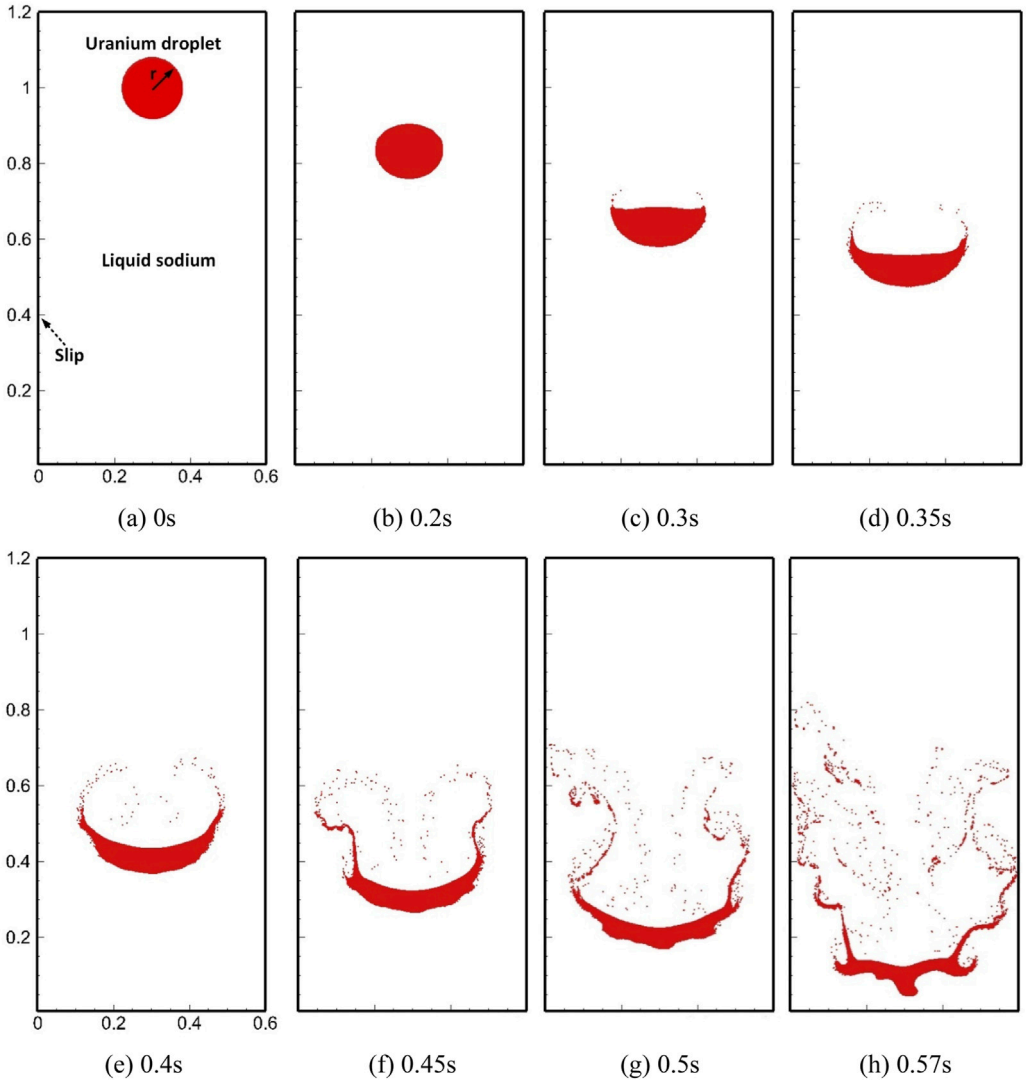

FIGURE 10
Initial setup and images in U-Na interaction.

0.01 *m* and 0.02 *m*. The thinner film thickness refers to the ratio of fuel cladding size to fuel pellet size in SFRs, which is 10% or slightly larger. The thicker film represents the condition that other stainless steel structures in the core also melt and participate in the FCI.

5.1 Breakup behavior

Figures 10, 11, 12 show the images of typical moments in the aforementioned three FCI processes, respectively. In order to clearly present the details of fragment distribution, we show uranium particles in red, stainless steel particles in green, and hide sodium particles. The simulated processes ended before liquid uranium hit the bottom of the sodium pool, which took about 0.57 s in all three cases. The initial layout for each case is shown in subfigure (a) of the series. In the process of direct interaction between uranium and sodium, as shown in Figure 10, the initially stationary uranium droplet began to slowly accelerate downward under gravity, and the circular droplet gradually developed into a crescent-shape droplet. Before 0.3 s, the droplet basically maintained good integrity. After that, the liquid sodium beneath the uranium droplet quickly flowed over the lower surface and carried a few small fragments away from the main body, rolling toward the low-pressure region behind the droplet and forming two vortexes, as shown in Figures 10D,E. As the falling speed of molten uranium increased, a large amount of uranium was elongated and stripped at the edge and is continuously taken away by the mainstream. The trailing vortices formed on both sides make the fragments more fully broken and dispersed in space. This is the typical phenomenon of boundary layer stripping. In addition, the main uranium body was obviously affected by Kelvin–Helmholtz (K–H) instability due to the relative velocity parallel to the interface and R–T instability due to gravity, both of which appeared later than the boundary layer stripping. Figure 13 shows the local magnified image at 0.57 s. The three hydraulic phenomena which are mentioned lead to the fragmentation which occurred simultaneously at that moment. They are in agreement with the discussion given by Nishimura et al. (2010) in form of a jet penetrating a surrounding fluid. Gray sodium particles are also shown in the magnified image included in Figure 13. We can observe that

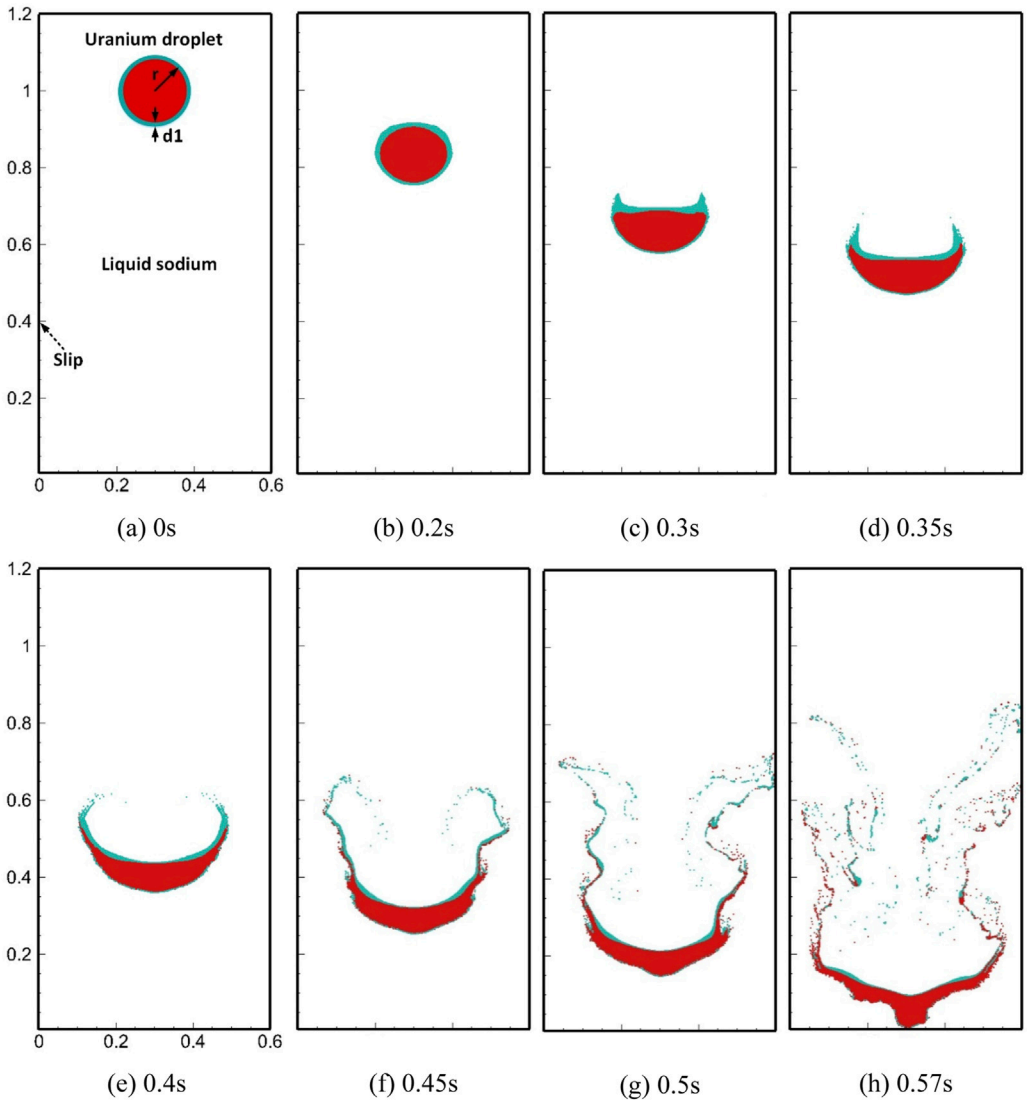

FIGURE 11
Initial setup and images in the interaction between U coated with Stainless steel film with thickness of 0.01 m and Na.

the complex interface can be clearly captured and particles near the interface with high density ratio are evenly distributed and accurately described. It proves the effectiveness of the KGC-MSPH method in solving FCI problems.

In the interactions between the uranium droplet coated with the stainless steel film and sodium coolant, the process can also be divided into two stages according to the integrity of the droplet. As shown in Figures 11, 12, the shape change of the uranium droplet in the first stage (0–0.35 s) is similar to that in the direct interaction and no fragments are generated. As mentioned previously, the dynamic viscosities of uranium and stainless steel are very close, and the density difference is not large, so the stainless steel film prevented the shear force from liquid sodium directly acting on the uranium surface. The isolation from the stainless steel film allowed the uranium droplets to remain unbroken for much longer than that in direct interaction, and the obtained droplet remained crescent-shaped. With falling speed, the lower stainless steel film gradually thinned under the shear forces and accumulated on the upper surface of the droplet. The stainless steel film was gradually elongated with the boundary layer movement and will be separated from the main body. In the later stage (0.35–0.57 s), the uranium at the crescent tips began to detach from the main body with the liquid stainless steel and formed uranium fragments which are adhered to stainless steel. The stainless steel film on the underlying surface of the main uranium body continued to be stretched and remained attached to the surface. The upper surface was always covered with a thicker film of stainless steel.

5.2 Result analysis

It can be observed from the FCI cases that the fragments formed mainly include a main uranium body with the largest mass and a large number of small fragments caused by boundary layer stripping. In order to illustrate the fragment distributions and analyze the influence of the stainless steel film, we made statistics on the total number of fragments and the mass change

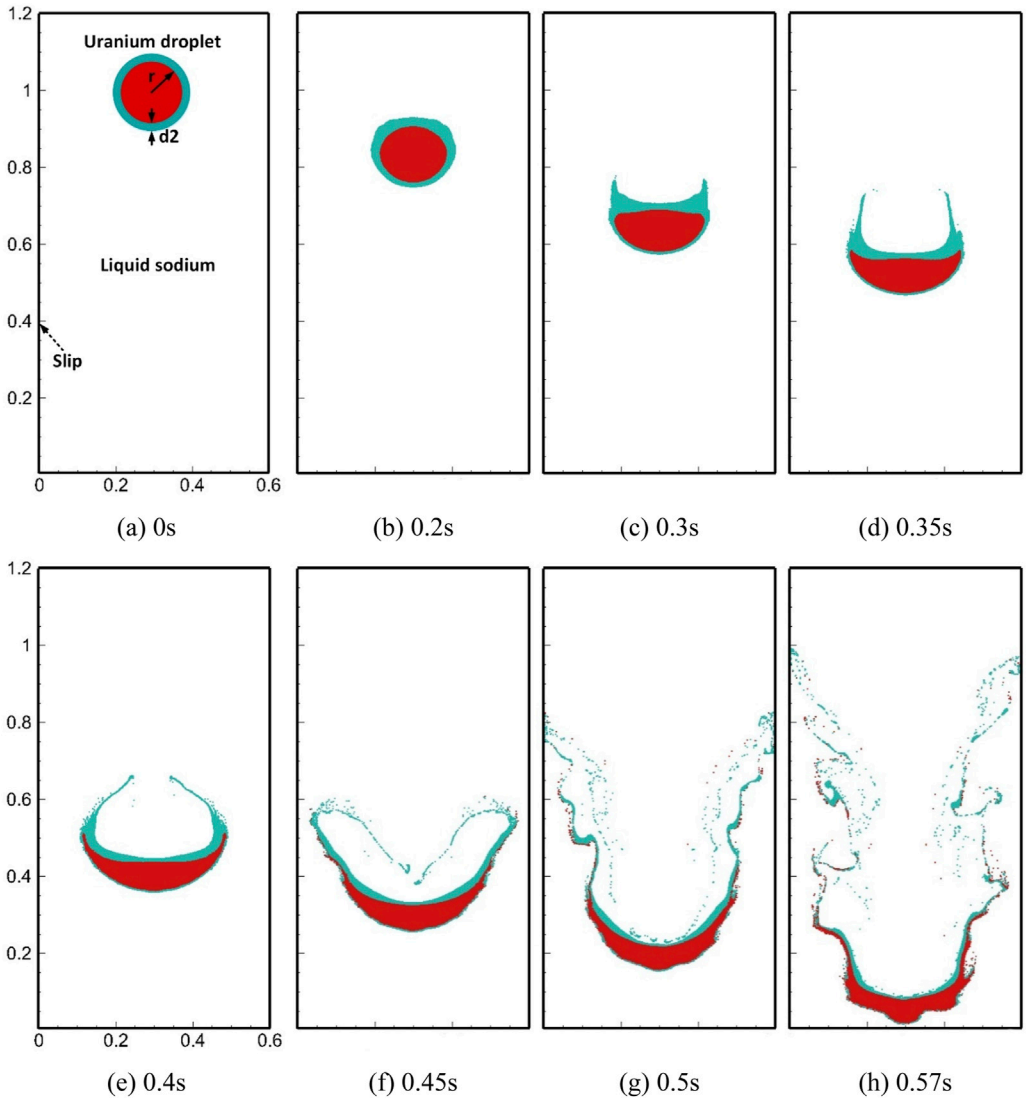

FIGURE 12
Initial setup and images in the interaction between U coated with Stainless steel film with thickness of 0.02 m and Na.

of the main uranium body. As shown in Figure 14, from the development trend of the total number of fragments, represented by N_{total}, it can be seen that the fragments in the direct U–Na interaction appeared earlier and were increasingly formed. We further analyzed the mass of the main body over time, as shown in Figure 15, expressed as the percentage of the mass of the main uranium body (M_{max}) to the total uranium mass (M_{total}). During the direct interaction, the mass detached from the main body is larger, resulting in the smallest mass of the final main body, about 73% of the total mass. In the other two cases, the mass of the main body is larger due to the isolation effect of the stainless steel film; the final mass fraction is 79% and 89%, respectively; and the interface deformation of the main body is less obvious and less easily broken.

Therefore, according to the aforementioned simulation results, it can be concluded that the KGC-MSPH method can realize the simulation of multiphase flow with intense interface deformation under a large density ratio. The obtained interface is smooth, and the calculation is stable. In the 2D FCI simulation results, we can clearly observe the effect of boundary layer stripping, R–T instability and K–H instability. Boundary layer stripping is the main reason for the generation of small fragments, while R–T instability and K–H instability mainly cause the deformation of the main body. In addition to the direct interaction between uranium and sodium, we also considered the influence of the stainless steel film. The presence of the stainless steel film has a significant inhibition effect on uranium droplet fragmentation. The thicker the liquid film is, the more obvious the inhibition is, the smaller the number of fragments is, and the larger the size of the main body is. In addition, the obtained fragments of all sizes were adhered to stainless steel or wrapped by a thin stainless steel film. Our further analysis suggests that the hydraulic fragmentation of the molten fuel is impeded with the stainless steel film, and the larger debris produced is more likely to block coolant channels, leading to deterioration in core. On the other hand from the thermal perspective, the thermal conductivity of stainless steel is lower

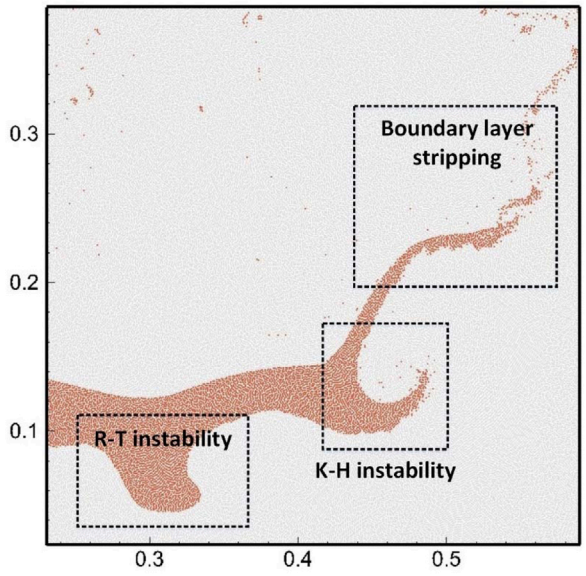

FIGURE 13
Local magnification in U-Na interaction at t = 0.57 s.

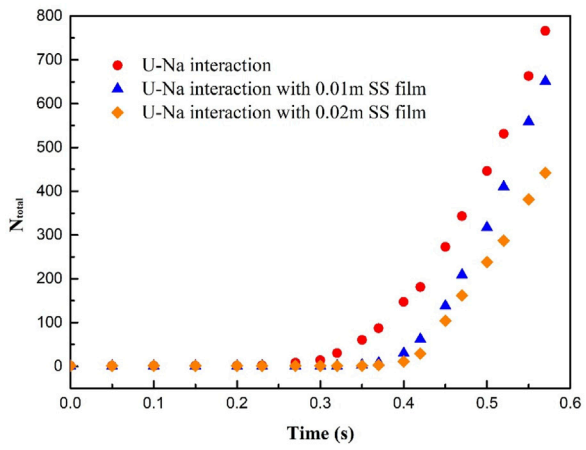

FIGURE 14
The variation of total number of uranium fragments.

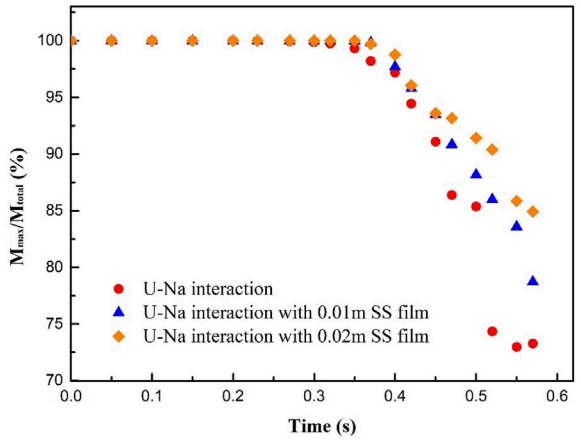

FIGURE 15
The variation of the mass fraction of the main uranium body relative to the total mass.

than that of uranium, and the stainless steel coat has a negative effect on the cooling of the molten fuel. The risk of re-criticality may arise, resulting in a pessimistic result. It is adverse to the safety of the reactor.

6 Conclusion

An improved MSPH with KGC is developed in this work to solve the simulation problem of multiphase flow with a large density ratio and drastic interface deformation. The KGC-MSPH is further applied to simulate FCI problems including the U–Na direct interaction and the interactions between uranium coated with stainless steel films of different thickness and sodium. The breakup behaviors, the number of fragments, and the mass of the main uranium body in each case are comparatively studied. The conclusions are drawn as follows:

1) Remarkable performance of KGC-MSPH is obtained; the unstable and mixed-interface problems are significantly solved. The capability of KGC-MSPH was validated by simulating the deformation of square droplet, R-T instability, and bubble rising in water.
2) Smoother interfaces can be obtained by considering the repulsive force model. The coefficient of this model applicable to this improved method is suggested to be around 0.01.
3) The breakup behaviors in all three FCI cases are similar, which are mainly affected by three hydraulic factors. Boundary layer stripping is the cause of the formation of a large number of small fragments. R–T instability and K–H instability act on the main body to deform the interface.
4) The stainless steel film can inhibit the breakup of the uranium droplet so that the integrity of the droplet can be maintained for a longer time, the number of fragments formed is less, and the main body size is larger. The thicker the liquid film is, the more obvious the inhibition effect is. The formed fragments and the main body are adhered to liquid stainless steel. The presence of the stainless steel film is suggested to be adverse to the safety of the reactor.

There are still some deficiencies in the simulation of FCI problems, which need to be improved in the future. The spatial scale of the sodium pool is limited, resulting in a short simulation process and the model is 2D. It can be further expanded in the computational domain scale and spatial dimension by solving the problem of computational cost. The thermal hydraulics behaviors closer to the actual situation can be simulated by further considering the thermodynamic model. With continuous development, the improved MSPH is expected to be a powerful tool for nuclear safety analysis and thermohydraulic calculation.

Data availability statement

The raw data supporting the conclusions of this article will be made available by the authors, without undue reservation.

Author contributions

FW carried out the method research and developed the code, performed the simulations, analyzed results, and wrote the manuscript. Z-GZ supervised the research and revised the manuscript. QW assisted in analyzing the results and writing the manuscript.

Funding

This research was supported by Projects of the National Natural Science Foundation of China [grant numbers 52176151 and 51476040], CNNC's Pilot-innovation Research Project, and Fundamental Research Funds for the Central Universities of China [grant number 3072022TS1503].

Acknowledgments

The authors thank the projects for the financial support.

Conflict of interest

The authors declare that the research was conducted in the absence of any commercial or financial relationships that could be construed as a potential conflict of interest.

Publisher's note

References

Adami, S., Hu, X. Y., and Adams, N. A. (2010). A new surface-tension formulation for multi-phase SPH using a reproducing divergence approximation. *Journal of Computational Physics*. 229 (13), 5011–5021. doi:10.1016/j.jcp.2010.03.022

Armstrong, D. R., Goldfuss, G. T., and Gebner, R. H. (1976). *Explosive interaction of molten UO2 and liquid sodium*. Lemont, United States: Argonne National Lab. Ill.(USA).

Armstrong, D. R. (1971). "Interaction of sodium with molten U02 and stainless steel using a drop mode of contact,". Report No.: ANL-7890. doi:10.2172/4696446

Bonet, J., and Lok, T. (1999). Variational and momentum preservation aspects of smooth particle hydrodynamic formulations. *Computer Methods in Applied Mechanics and Engineering*. 180 (1-2), 97–115. doi:10.1016/s0045-7825(99)00051-1

Brackbill, J. U., Kothe, D. B., and Zemach, C. (1992). A continuum method for modeling surface tension. *Journal of Computational Physics*. 100 (2), 335–354. doi:10.1016/0021-9991(92)90240-y

Carmack, W. J., Porter, D. L., Chang, Y. I., Hayes, S. L., Meyer, M. K., Burkes, D. E., et al. (2009). Metallic fuels for advanced reactors. *Journal of Nuclear Materials*. 392 (2), 139–150. doi:10.1016/j.jnucmat.2009.03.007

Cheng, S., Matsuba, K.-I., Isozaki, M., Kamiyama, K., Suzuki, T., and Tobita, Y. (2015b). SIMMER-III analyses of local fuel-coolant interactions in a simulated molten fuel pool: Effect of coolant quantity. *Science and Technology of Nuclear Installations*. 2015, 1–14. doi:10.1155/2015/964327

Cheng, S., Matsuba, K.-I., Isozaki, M., Kamiyama, K., Suzuki, T., and Tobita, Y. (2015a). The effect of coolant quantity on local fuel-coolant interactions in a molten pool. *Annals of Nuclear Energy*. 75, 20–25. doi:10.1016/j.anucene.2014.07.042

Cheng, S., Zhang, T., Meng, C., Zhu, T., Chen, Y., Dong, Y., et al. (2019). A comparative study on local fuel-coolant interactions in a liquid pool with different interaction modes. *Annals of Nuclear Energy*. 132, 258–270. doi:10.1016/j.anucene.2019.04.048

Colagrossi, A., and Landrini, M. (2003). Numerical simulation of interfacial flows by smoothed particle hydrodynamics. *Journal of Computational Physics*. 191 (2), 448–475. doi:10.1016/s0021-9991(03)00324-3

Collins, R. (1967). The effect of a containing cylindrical boundary on the velocity of a large gas bubble in a liquid. *Journal of Fluid Mechanics*. 28 (1), 97–112. doi:10.1017/s0022112067001922

Cummins, S. J., and Rudman, M. (1999). An SPH projection method. *Journal of Computational Physics*. 152 (2), 584–607. doi:10.1006/jcph.1999.6246

Dehnen, W., and Aly, H. (2012). Improving convergence in smoothed particle hydrodynamics simulations without pairing instability. *Monthly Notices of the Royal Astronomical Society*. 425 (2), 1068–1082. doi:10.1111/j.1365-2966.2012.21439.x

Ferrand, M., Laurence, D. R., Rogers, B. D., Violeau, D., and Kassiotis, C. (2013). Unified semi-analytical wall boundary conditions for inviscid, laminar or turbulent flows in the meshless SPH method. *International Journal for Numerical Methods in Fluids*. 71 (4), 446–472. doi:10.1002/fld.3666

Gabor, J. D., Purviance, R. T., Aeschlimann, R., and Spencer, B. W. (1988). Breakup and quench of molten metal fuel in sodium. *Proc. Int. Top. Mtg. on Safety of Next Generation Power Reactors, Seattle* 1988, 838–843.

Gingold, R. A., and Monaghan, J. J. (1977). Smoothed particle hydrodynamics: Theory and application to non-spherical stars. *Monthly Notices of the Royal Astronomical Society*. 181 (3), 375–389. doi:10.1093/mnras/181.3.375

Grenier, N., Antuono, M., Colagrossi, A., Le Touzé, D., and Alessandrini, B. (2009). An Hamiltonian interface SPH formulation for multi-fluid and free surface flows. *Journal of Computational Physics*. 228 (22), 8380–8393. doi:10.1016/j.jcp.2009.08.009

Hu, X. Y., and Adams, N. A. (2009). A constant-density approach for incompressible multi-phase SPH. *Journal of Computational Physics*. 228 (6), 2082–2091. doi:10.1016/j.jcp.2008.11.027

Hu, X. Y., and Adams, N. A. (2006). A multi-phase SPH method for macroscopic and mesoscopic flows. *Journal of Computational Physics*. 213 (2), 844–861. doi:10.1016/j.jcp.2005.09.001

Hu, X. Y., and Adams, N. A. (2007). An incompressible multi-phase SPH method. *Journal of Computational Physics*. 227 (1), 264–278. doi:10.1016/j.jcp.2007.07.013

Iwasawa, Y., and Abe, Y. (2018). Melt jet-breakup and fragmentation phenomena in nuclear reactors: A review of experimental works and solidification effects. *Progress in Nuclear Energy* 108, 188–203. doi:10.1016/j.pnucene.2018.05.009

Koshizuka, S., and Oka, Y. (1996). Moving-particle semi-implicit method for fragmentation of incompressible fluid. *Nuclear Science and Engineering*. 123 (3), 421–434. doi:10.13182/nse96-a24205

Krishna, R., Van Baten, J., Urseanu, M., and Ellenberger, J. (2000). Rise velocity of single circular-cap bubbles in two-dimensional beds of powders and liquids. *Chemical Engineering and Processing-Process Intensification*. 39 (5), 433–440. doi:10.1016/s0255-2701(99)00108-7

Li, G., Gao, J., Wen, P., Zhao, Q., Wang, J., Yan, J., et al. (2020). A review on MPS method developments and applications in nuclear engineering. *Computer Methods in Applied Mechanics and Engineering*. 367, 113166. doi:10.1016/j.cma.2020.113166

Lind, S. J., Rogers, B. D., and Stansby, P. K. (2020). Review of smoothed particle hydrodynamics: Towards converged Lagrangian flow modelling. *Proceedings Mathematical, physical, and engineering sciences*. 476 (2241), 20190801. doi:10.1098/rspa.2019.0801

Liu, L., Yan, H., Zhao, G., and Zhuang, J. (2016). Experimental studies on the terminal velocity of air bubbles in water and glycerol aqueous solution. *Experimental Thermal and Fluid Science*. 78, 254–265. doi:10.1016/j.expthermflusci.2016.06.011

Lucy, L. (1977). A numerical approach to the testing of the fission hypothesis. *The Astrophysical Journal*. 82, 1013–1024. doi:10.1086/112164

Marrone, S., Colagrossi, A., Antuono, M., Colicchio, G., and Graziani, G. (2013). An accurate SPH modeling of viscous flows around bodies at low and moderate Reynolds numbers. *Journal of Computational Physics*. 245, 456–475. doi:10.1016/j.jcp.2013.03.011

Ming, F. R., Sun, P. N., and Zhang, A. M. (2017). Numerical investigation of rising bubbles bursting at a free surface through a multiphase SPH model. *Meccanica* 52 (11-12), 2665–2684. doi:10.1007/s11012-017-0634-0

Molteni, D., and Colagrossi, A. (2009). A simple procedure to improve the pressure evaluation in hydrodynamic context using the SPH. *Computer Physics Communications*. 180 (6), 861–872. doi:10.1016/j.cpc.2008.12.004

Monaghan, J. J., and Kos, A. (1999). Solitary waves on a cretan beach. *Journal of Waterway, Port, Coastal, and Ocean Engineering*. 125 (3), 145–155. doi:10.1061/(asce)0733-950x(1999)125:3(145)

Monaghan, J. J., and Rafiee, A. (2013). A simple SPH algorithm for multi-fluid flow with high density ratios. *International Journal for Numerical Methods in Fluids*. 71 (5), 537–561. doi:10.1002/fld.3671

Monaghan, J. J. (1994). Simulating free surface flows with SPH. *Journal of Computational Physics*. 110 (2), 399–406. doi:10.1006/jcph.1994.1034

Monaghan, J. J. (2000). SPH without a tensile instability. *Journal of Computational Physics*. 159 (2), 290–311. doi:10.1006/jcph.2000.6439

Nishimura, S., Sugiyama, K.-I., Kinoshita, I., Itagaki, W., and Ueda, N. (2010). Fragmentation mechanisms of a single molten copper jet penetrating a sodium pool-transition from thermal to hydrodynamic fragmentation in instantaneous contact interface temperatures below its freezing point. *Journal of Nuclear Science and Technology*. 47 (3), 219–228. doi:10.1080/18811248.2010.9711948

Nishimura, S., Zhang, Z.-G., Sugiyama, K.-I., and Kinoshita, I. (2007). Transformation and fragmentation behavior of molten metal drop in sodium pool. *Nuclear Engineering and Design*. 237 (23), 2201–2209. doi:10.1016/j.nucengdes.2007.03.021

Ogata, T. (2014). Irradiation behavior and thermodynamic properties of metallic fuel. *Journal of Nuclear Science and Technology*. 39 (Suppl. 3), 675–681. doi:10.1080/00223131.2002.10875558

Patiño-Nariño, E. A., Galvis, A. F., Sollero, P., Pavanello, R., and Moshkalev, S. A. (2019). A consistent multiphase SPH approximation for bubble rising with moderate Reynolds numbers. *Engineering Analysis with Boundary Elements*. 105, 1–19. doi:10.1016/j.enganabound.2019.04.002

Schins, H. E. J., and Gunnerson, F. S. (1986). Boiling and fragmentation behaviour during fuel-sodium interactions. *Nuclear Engineering and Design*. 91, 221–235. doi:10.1016/0029-5493(86)90077-4

Shao, J. R., Li, H. Q., Liu, G. R., and Liu, M. B. (2012). An improved SPH method for modeling liquid sloshing dynamics. *Computational and Structural Biotechnology Journal*. 100-101, 18–26. doi:10.1016/j.compstruc.2012.02.005

Shao, J. R., Li, S. M., and Liu, M. B. (2016). Numerical simulation of violent impinging jet flows with improved SPH method. *International Journal of Computational Methods*. 13 (04), 1641001. doi:10.1142/s0219876216410012

Sussman, M., Smereka, P., and Osher, S. (1994). A level set approach for computing solutions to incompressible two-phase flow. *Journal of Computational Physics*. 114 (1), 146–159. doi:10.1006/jcph.1994.1155

Szewc, K., Pozorski, J., and Minier, J. P. (2015). Spurious interface fragmentation in multiphase SPH. *International Journal for Numerical Methods in Engineering*. 103 (9), 625–649. doi:10.1002/nme.4904

Tobita, Y., Kamiyama, K., Tagami, H., Matsuba, K.-I., Suzuki, T., Isozaki, M., et al. (2016). Development of the evaluation methodology for the material relocation behavior in the core disruptive accident of sodium-cooled fast reactors. *Journal of Nuclear Science and Technology*. 53 (5), 698–706. doi:10.1080/00223131.2016.1143409

Yang, Z., Zhang, Z.-G., Liu, C., Ji, B., and Ahmed, R. (2019). Thermal and hydrodynamic fragmentation of continuous molten copper droplets penetrating into sodium pool. *International Communications in Heat and Mass Transfer*. 108, 104317. doi:10.1016/j.icheatmasstransfer.2019.104317

Yang, Z., Zhang, Z.-G., Liu, X.-C., and Ahmed, R. (2018). Fragmentation of continuous molten copper droplets penetrating into sodium pool. *Journal of Nuclear Science and Technology*. 56 (2), 150–159. doi:10.1080/00223131.2018.1539350

Zhang, A., Sun, P., and Ming, F. (2015). An SPH modeling of bubble rising and coalescing in three dimensions. *Computer Methods in Applied Mechanics and Engineering*. 294, 189–209. doi:10.1016/j.cma.2015.05.014

Zhang, Z.-G., and Sugiyama, K.-I. (2012). Fragmentation of a single molten metal droplet penetrating into sodium pool. IV. Thermal and hydrodynamic effects on fragmentation in copper. *Journal of Nuclear Science and Technology*. 49 (6), 602–609. doi:10.1080/00223131.2012.686811

Zhang, Z.-G., and Sugiyama, K.-I. (2010). Fragmentation of a single molten metal droplet penetrating sodium pool II stainless steel and the relationship with copper droplet. *Journal of Nuclear Science and Technology*. 47 (2), 169–175. doi:10.1080/18811248.2010.9711942

Zhang, Z.-G., Sugiyama, K.-I., Itagaki, W., Nishimura, S., Kinosita, I., and Narabayashi, T. (2009). Fragmentation of a single molten metal droplet penetrating sodium pool I copper droplet and the relationship with copper jet. *Journal of Nuclear Science and Technology*. 46 (5), 453–459. doi:10.1080/18811248.2007.9711552

Zhang, Z. L., and Liu, M. B. (2017). Smoothed particle hydrodynamics with kernel gradient correction for modeling high velocity impact in two- and three-dimensional spaces. *Engineering Analysis with Boundary Elements*. 83, 141–157. doi:10.1016/j.enganabound.2017.07.015

Zhu, G. X., Zou, L., Chen, Z., Wang, A. M., and Liu, M. B. (2018). An improved SPH model for multiphase flows with large density ratios. *International Journal for Numerical Methods in Fluids*. 86 (2), 167–184. doi:10.1002/fld.4412

Nomenclature

Abbreviations

Symbols

A Arbitrary function

c Color function

c_0 Artificial sound speed (m/s)

d Spatial dimension

$\boldsymbol{f}_w$ Repulsive force acceleration of wall (m/s^2)

$\boldsymbol{f}_s$ Surface tension force (Kg/m^2/s^2)

$\boldsymbol{f}_v$ Viscous stress (Kg/m^2/s^2)

$\boldsymbol{g}$ Gravity acceleration (m/s^2)

h Smoothing length (m)

H Height (m)

$\boldsymbol{I}$ Unit matrix

i Center particle

j Adjacent particle

m Mass (kg)

$\boldsymbol{n}$ Unit normal vector

N Total number of particles

p Pressure (Pa)

p_b Background pressure (Pa)

r Distance between two particles (m)

R Radius (m)

t Time (s)

Δt Timestep (s)

$\boldsymbol{v}$ Velocity vector (m/s)

V Volume (m^3)

V^σ Special volume (m^d)

W Kernel function (m^{-d})

$\boldsymbol{x}$ Position vector (m)

Δx Uniform spacing (m)

Creek

α Surface tension coefficient (N/m)

γ Stiffness parameter

κ Curvature (m^{-1})

λ A density-weighted color function (m^{-1})

η Dynamic viscous coefficient (Pa·s)

ε Coefficient of repulsive force

ρ Density (kg/m^3)

ρ_0 Reference density (kg/m^3)

σ Particle density number (m^{-d})

υ Kinematic viscosity (m^2/s)

Ω Volume of arbitrary domain (m^3)

χ Interpolating function

Ψ Density ratio

Φ Viscosity ratio

Frontiers in
Energy Research

Advances and innovation in sustainable, reliable and affordable energy

Explores sustainable and environmental developments in energy. It focuses on technological advances supporting Sustainable Development Goal 7: access to affordable, reliable, sustainable and modern energy for all.

Discover the latest Research Topics

See more →

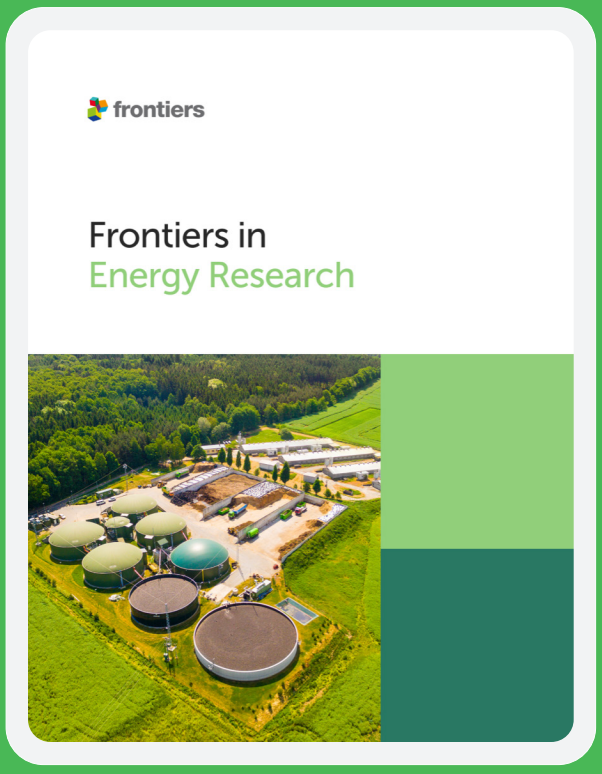

Frontiers

Avenue du Tribunal-Fédéral 34
1005 Lausanne, Switzerland
frontiersin.org

Contact us

+41 (0)21 510 17 00
frontiersin.org/about/contact